DOE/ER-0313/11

Fusion Reactor Materials

Semiannual Progress Report
for Period Ending
September 30, 1991

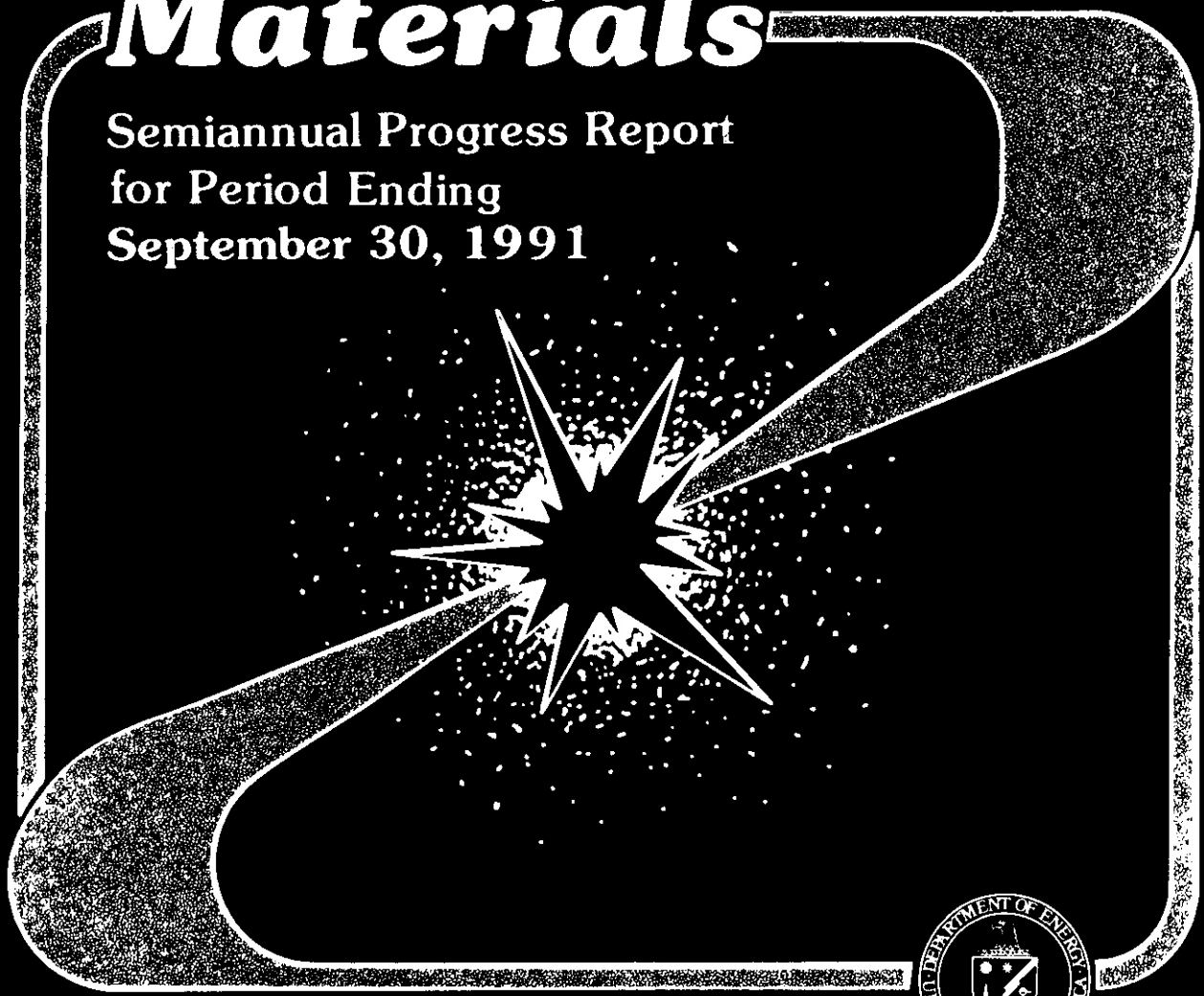

U. S. Department of Energy
Office of Fusion Energy

DOE/ER-0313/11
Distribution
Categories
UC-423, -424

FUSION REACTOR MATERIALS SEMIANNUAL PROGRESS REPORT FOR THE PERIOD ENDING SEPTEMBER 30, 1991

DATE PUBLISHED: APRIL 1992

Prepared for
DOE Office of Fusion Energy
(AT 15 02 03 A)

Prepared by
OAK RIDGE NATIONAL LABORATORY
Oak Ridge, Tennessee 37831
Managed by
MARTIN MARIETTA ENERGY SYSTEMS, INC.
for the
U.S. DEPARTMENT OF ENERGY
under Contract DE-AC05-84OR21400

FOREWORD

This is the eleventh in a series of semiannual technical progress reports on fusion reactor materials. This report combines research and development activities which were previously reported separately in the following progress reports:

- Alloy Development for Irradiation Performance
- Damage Analysis and Fundamental Studies
- Special Purpose Materials

These activities are concerned principally with the effects of the neutronic and chemical environment on the properties and performance of reactor materials; together they form one element of the overall materials program being conducted in support of the Magnetic Fusion Energy Program of the U.S. Department of Energy. The other major element of the program is concerned with the interactions between reactor materials and the plasma and is reported separately.

The Fusion Reactor Materials Program is a national effort involving several national laboratories, universities, and industries. The purpose of this series of reports is to provide a working technical record for the use of the program participants, and to provide a means of communicating the efforts of materials scientists to the rest of the fusion community, both nationally and worldwide.

This report has been compiled and edited under the guidance of A. F. Rowcliffe and Frances Scarboro, Oak Ridge National Laboratory. Their efforts, and the efforts of the many persons who made technical contributions, are gratefully acknowledged. F. W. Wiffen, Reactor Technologies Branch, has responsibility within DOE for the programs reported on in this document.

R. Price, Chief
Reactor Technologies Branch
Office of Fusion Energy

Reports previously listed in this series are as **fallows:**

DOEIER-031311	Period ending September 30, 1986
DOE/ER-0313/2	Period ending March 31, 1987
DOE/ER-0313/3	Period ending September 30, 1987
DOE/ER-03 1314	Period ending March 31, 1988
DOE/ER-03 1315	Period ending September **30,** 1988
DOE/ER-0313/6	Period ending March 31, 1989
DOE/ER-0313/7	Period ending September **30,** 1989
DOE/ER-03 1318	Period ending March 31, 1990
DOE/ER-03 1319	Period ending September 30, 1990
DOE/ER-0313/10	Period ending March 31, 1991

Two silicon-modified alloy series, one based on Fe-15Cr-20Ni and another based on Fe-15Cr-25Ni were irradiated at target temperatures between 399 and 649°C in EBR-II. The influence of silicon on swelling is more complex than previously envisioned and indicates that silicon plays two or more competing roles while in solution. Radiation-induced formation of γ' (Ni_3Si) precipitates is dependent on silicon and nickel content, as well as temperature. Precipitation of γ' appears to play only a minor role in void formation.

Microstructural evolution in response to 1MeV irradiation has been investigated for three simple ferritic alloys, pure beryllium, pure vanadium, and two simple vanadium alloys over a range of temperatures and doses. Microstructural evolution in Fe-3, -9, and -18Cr ferritic alloys is found to consist of crenelated, faulted a<100> loops and circular, unfaulted a/2 <111> loops at low temperatures, but with only unfaulted loops at high temperatures, The complex dislocation evolution is attributed to sigma phase precipifaults arising from chromium segregation to point defect sinks. Beryllium is found to be resistant to electron damage; the only effect observed was enhanced dislocation mobility. Pure vanadium, V-5Fe, and V-1Ni microstructural response was complicated by precipitation on heating to 400°C and above, but dislocation evolution was investigated in the range of room temperature to 300°C and at 600°C. The three materials behaved similarly, except that pure vanadium showed more rapid dislocation evolution. This difference does not explain the enhanced swelling observed in vanadium alloys.

Research efforts at UCLA on the effects of fusion neutron irradiation on structural materials covered a wide range of theoretical and materials engineering problems during the six year period supported by the DOE grant No. DE-FG03-84ER52110. In this brief report, highlights of research accomplishments are presented in the following areas:

(1) Atomic Displacements
(2) Microstructure Evolution
(3) Materials Engineering, Mechanics and Design
(4) Invention of Low-Activation Steels
(5) Research Motivated by Grant Support

Tensile specimens of tempered martensitic 9Cr-1MoVNb and 12Cr-1MoVW steels with and without additions of 2% Ni were irradiated in the High Flux Isotope Reactor (HFIR) at 400 and 600°C to displacement damage levels of up to 72 dpa. Nickel was added to the steels to produce transmutation helium, and up to 700 appm He was produced in the steels with 2% Ni. Irradiation at 400°C caused an increase in strength and decrease in ductility, while irradiation at 600°C caused a decrease in strength and an increase in ductility. Results at 400°C were similar to data from previous tests on steel irradiated to ≈11 dpa (up to 110 appm He), where it was concluded that helium caused a strength increase in addition to the hardening caused by displacement damage alone. The present results indicate that the helium-enhanced strengthening at 400°C saturates with increasing helium concentration, similar to the saturation (at a lower strength level) with displacement-damage dose found in the absence of helium.

Specimens of solution-annealed (SA) and 25% cold-worked (CW) PCA austenitic stainless steel were irradiated in ORR in spectrally-tailored experiments specially designed to produce fusion-relevant He/dpa ratios (12-18 appm He/dpa). SA and CW PCA were irradiated at 330 and 400°C to 13 dpa while only CW PCA was irradiated at 60, 200, 330 and 400°C to 7.4 dpa. While cavities and fine MC precipitates were only detectable at 330 and 400°C, dislocations were a major component of the radiation-induced microstructure at 60-400°C. The mixtures of 'black-dot" loops, larger Frank loops, and network that comprised the total dislocation structure were very dependent on irradiation temperature. Both SA and CW PCA contained Frank loops and network dislocations at 330 and 400°C. Frank loop concentrations were maximum at 330°C and dislocation evolution with dose was most evident at 400°C. At 60 and 200°C, the microstructure was dominated by very dense dispersions of (1-3 nm diam.) "black-dot" loops. Some Frank loops were observed at 200°C, hut almost none were found at 60°C. Surprisingly, there was significant radiation-induced recovery of the as-cold-worked dislocation network in CW PCA at all irradiation temperatures. There appears to be a distinguishable transition in the nature of the radiation-induced microstructure between 200 and 330°C.

The low-temperature tensile properties of type 316 stainless steel (5316) and Japanese Primary Candidate Alloy (JPCA) irradiated in spectrally tailored Oak Ridge Research Reactor (ORR) and in High Flux Isotope Reactor (HFIR) capsules are summarized. The yield and tensile strengths in the ORR-irradiated specimens were found to increase with increasing irradiation temperatures up to 330°C followed by a decrease with increasing temperature. This strength maximum was accompanied by an elongation minimum. Similar trend curves were observed in the HFIR-irradiated specimens, although the temperature of peak strength was shifted higher. The behavior can be understood roughly in terms of microstructural development of dislocation loops and recovery of network dislocations during irradiation. The temperature of peak strength seems to depend on irradiation conditions such as He:dpa ratio and irradiation dose rate.

Fe-15Cr-XNi alloys irradiated at both low (0.66 to 1.2) and very high (27 to 58) helium/dpa levels exhibit significantly different levels of strengthening due to an unprecedented refinement of cavity microstructure at the very high helium levels. When compounded with the nickel dependence of helium generation, the cavity distribution for some irradiation conditions and alloy compositions can be driven below the critical radius for bubble-to-void conversion, leading to a delay in swelling. The critical radius also appears to be dependent on the nickel level. The refinement may not have resulted from the high helium levels alone, however, but also may have been influenced by differences in displacement rate and temperature history in the two experiments.

At very low levels (<0.02 wt%), phosphorus additions to austenitic stainless steels often cause a substantial increase in void swelling. This phenomenon occurs in both simple model alloys and more complex solute-modified alloys typical of materials being considered for breeder reactor or fusion reactor service. This effect is observed in both annealed and cold-worked steels. At levels above 0.02% phosphorus, there is a reversal in behavior and swelling declines. This non-monotonic behavior tends to occur at lower irradiation temperatures in relatively simple alloys, but often persists to much higher temperatures in more complex titanium-modified alloys employed in the fusion and breeder reactor programs.

Although cold working is known to strongly influence neutron-induced swelling of austenitic stainless steels, it also appears that the annealing temperature employed before cold working has an equally large effect. Two irradiation studies conducted on AISI **316** stainless steel indicate that increasing the temperature of the intermediate temper anneal leads in general to a shortening of the transient regime of swelling. The evidence is consistent with the influence of both annealing temperature and irradiation temperature on carbide formation and its subsequent influence on the microchemical evolution and swelling of the steel.

A titanium-modified austenitic type stainless steel was tested at three cold work levels to determine its creep and creep rupture properties under both thermal aging and neutron irradiation conditions. Both the thermal and irradiation creep behavior exhibit a complex non-monotonic relationship with cold work level that reflects the competition between a number of stress-sensitive and temperature-dependent microstructural processes. Increasing the degree of cold work to **30%** from the conventional **20%** level was detrimental to its performance, especially for applications about 550°C. The **20%** cold work level is preferable to the **10%** level, in terms of both in-reactor creep rupture response and initial strength.

Irradiation creep data from FFTF-MOTA at ~400°C were analyzed for nine 20% cold-worked titanium-modified type **316** stainless steels, each of which exhibits a different duration for the transient regime of swelling. One of these steels was the fusion prime candidate alloy designated PCA. The others were various developmental breeder reactor heats. The analysis was based on the assumption that the $B_o + DS$ creep model applies to these steels at this temperature. This assumption was found to be valid. A creep-swelling coupling coefficient of $D \approx 0.6 \times 10^{-2}$ MPa^{-1} was found for all steels that had developed a significant level of swelling. This result is in excellent agreement with the results of earlier studies conducted in EBR-II using annealed AISI **304L** and also 10% and **20%** cold-worked AISI **316** stainless steels. There appears to be some enhancement of swelling by stress, contradicting an important assumption in the analysis and leading to an apparent but misleading nonlinearity of creep with respect to stress.

The microstructures of V-Ti, V-Cr-Ti, and V-Ti-Si alloys were characterized by transmission electron microscopy (TEM) after neutron irradiation in the FFTF at **420** and 600°C to fluences up to **114** dpa. Two types of irradiation-induced precipitates were identified, i.e., Ti_2O and $Ti_5(Si,P)_3$. Blocky Ti(O,N,C) precipitates, which form by thermal processes during ingot fabrication, **also** were observed in all unirradiated and irradiated specimens. Irradiation-induced precipitation of spherical (< **15** nm in diameter) $Ti_5(Si,P)_3$ phase was associated with superior resistance to void swelling. In specimens with negligible swelling, $Ti_5(Si,P)_3$ precipitation was significant. Irradiation-induced precipitation of the Ti_2O phase, a phase with needlelike morphology and approximately <**20** nm thick and < 200 nm long, was more pronounced in high-oxygen specimens irradiated at 600°C. It seems that ductility is significantly reduced when the precipitation of Ti_2O and $Ti_5(Si,P)_3$ is pronounced. These observations indicate that initial composition; fabrication processes; actual solute compositions of Ti, O, N, C, P, and Si after fabrication; O, N, and C uptake during service; and irradiation-induced precipitation are interrelated and are important factors to consider in developing an optimized alloy.

Ductile-brittle transition temperatures (DBTTs) were determined for dehydrogenated and hydrogenated unalloyed V and V-1Ti, V-10Ti, and V-7Cr-5Ti alloys from Charpy-impact tests. These DBTT data complement the data previously reported by Loomis et al.[1,2] on Charpy impact testing of V-3Ti-1Si, V-5Ti, V-5Cr-5Ti, V-10Cr-5Ti, V-20Ti, V-10Cr-10Ti, V-15Cr-5Ti, V-15Ti-7.5Cr, and Vanstar-7 alloys. The present experimental results show that V alloys with Ti additions (0-20 wt.%) have a minimum DBTT (≈-250°C) in an alloy containing ≈5 wt.% Ti, that addition of up to 15 wt.% Cr to V-5Ti alloy results in a substantial increase (90-160°C) of the DBTT, and that Si additions (0.25-1.0 wt.%) to V-3Ti alloy result in a significant increase (≈60°C) in DBTT. In addition, the current results show that the presence of 400-1200 appm H in unalloyed V and V alloys causes a significant increase (60-250°C) in DBTT. The DBTT of V-5Ti, V-5Cr-5Ti, V-7Cr-5Ti, and V-10Ti alloys is least affected by H. The DBTT dependence of these materials on H, Cr, Ti, and Si concentration is presented in the form of tables, graphs, and parametric equations.

Additions of 5 to 14 wt % chromium to vanadium lead to very large swelling rates during neutron irradiation of the binary alloys, with swelling increasing strongly at higher irradiation temperatures. Addition of 2 wt % silicon to vanadium also leads to very large swelling rates, but swelling decreases with increasing irradiation temperature. Addition of 1 wt % zirconium does not yield high swelling rates, however.

Results have been obtained on the post-irradiation properties of various oxide dispersion strengthened copper alloys irradiated from 34 to 150 dpa at 415°C in the Fast Flux Test Facility. The GlidCop™ alloys strengthened by Al_2O_3 continue to outperform other alloys with respect to swelling resistance, and retention of both electrical conductivity and yield strength. Several castable ODS alloys and a Cr_2O_3-strengthened alloy show increasingly poor resistance to radiation, especially in their swelling behavior. A HfO_2-strengthened alloy retains most of its strength and its electrical conductivity reaches a constant level after 50 dpa, but it exhibits a higher residual radioactivity.

Induction brazed butt joints were produced from which subsize fatigue samples were fabricated. Some fatigue samples have survived over 2×10^6 cycles in a tension-compression cantilever fatigue mode.

Specimens of a type 316 stainless steel (SS) that had been irradiated in the fusion spectrally-tailored MFE-6J/7J experiments in the Oak Ridge Research (ORR) to 7.4 dpa at temperatures of 400, 330, 200, and 60°C were SSRT tested in a recirculating autoclave system in oxygenated, high-purity water. Complete intergranular (IG) failure was observed only for the specimen irradiated at 400°C. Only 10% IG failure was observed for the 330°C irradiated specimen and no IG failure was observed for the specimens irradiated at 200 and 60°C.

Silicon Carbide (SiC) fiber reinforced composites (FRC's) are strong potential candidate structural and high heat flux materials for fusion reactors. During this past decade, they have been vigorously developed for use in aerospace and transportation applications. Recent fusion reactor system studies, such as ARIES, have concluded that further development of SiC composites will result in significant safety, operational, and waste disposal advantages for fusion systems. A concise discussion of the main material and design issues related to the use of SiC FRC's as structural materials in future fusion systems is given in this paper. The status of material processing of SiC/SiC composites is first reviewed. The advantages and shortcomings of the leading processing technology, known as Chemical Vapor Infiltration are particularly highlighted. A brief outline of the design-relevant physical, mechanical, and radiation data base is then presented. SiC/SiC FRC's possess the advantage of increased apparent toughness under mechanical loading conditions. This increased toughness, however, is associated with the nucleation and propagation of small crack patterns in the structure. Design approaches and failure criteria under these conditions are discussed.

This report presents a renew and analysis of the hermetic, thermal conductivity, corrosion, crack growth and radiation damage properties of CMCs. It was concluded that the leak rates of a gaseous coolant into the plasma chamber or tritium nut of the blanket could exceed design criteria if matrix microcracking causes existing porosity to become interconnected. Thermal conductivities of unirradiated SiC/SiC and C/SiC materials are about 1/2 to 2/3 that of Type 316SS whereas the thermal conductivity for C/C composites is seven times larger. The thermal stress figure-of-merit value for CMCs exceeds that of Type 316 SS for a single thermal cycle. SiC/SiC composites are very resistant to corrosion and are expected to be compatible with He or Li coolants if the O_2 concentrations are maintained at the appropriate levels. CMCs exhibit subcritical crack growth at elevated temperatures and the crack velocity is a function of the corrosions conditions. The radiation stability of CMCs will depend on the stability of the fiber, microcracking of the matrix, and the effects of gaseous transmutation products on properties.

Permeation rates for He through a SiC/SiC composite have been estimated using gas flow equations for viscous and molecular flow through small orifices. The total helium leak rate was determined for a composite material, SiC/SiC, utilized as a pressure boundary between a He coolant and the plasma. The calculated flow rates were determined for the residual porosity resulting from SiC/SiC manufacture and the total first wall surface area. This leak rate was compared to previous estimates of the tolerable leak rate limits established by plasma removal rates and recycling of He in a power reactor. The calculated estimates suggest that the He leak rates are within tolerable limits if the porosity is not interconnected or is interconnected by cracks with openings no larger than 0.3 nm. Increased crack opening, induced by creep or more extensive microcracking induced by radiation or stress, could cause He leak rates to exceed the tolerable limit. These estimates suggest that the use of SiC/SiC composites for structural applications in fusion reactors will require the use of seal coatings if these materials must also perform as a pressure boundary. Similar conclusions should also apply for tritium containment.

SiC/C/Nicalon Composite materials have been irradiated at 300°C in HFIR to a dose of 1 dpa. Three point bend tests demonstrate a marked decrease in ultimate tensile strength while showing added composite toughness. Both strength and toughness changes are shown to be caused by a large decrease in both interfacial shear strength and interfacial friction as measured using a thin section push-out test. The degradation in interfacial properties is attributed to a debonding at the fiber/interface interface due to fiber shrinkage during irradiation.

Room temperature carbon ion irradiations cause amorphization of both CVD SiC and Nicalon fiber. The elastic modulus and hardness have been measured using a microindentation method and the results compared with those of neutron irradiations in HFIR and FFTF at 300 and 435 °C, respectively. It is observed that the randomization/amorphization of CVD SiC significantly reduces both hardness and modulus for both carbon beam and neutron irradiations. The Nicalon fiber shows the opposite behavior yielding higher modulus and hardness for both neutron and carbon irradiations. This change in Nicalon mechanical properties occurs whether the microstructure has been amorphized, as is the case for the room temperature carbon irradiations, or if the microstructure appears unchanged leading to the assertion that the cause of the mechanical property change is the densification of the fiber.

Changes in the dielectric constant and loss tangent of alumina have been measured *in-situ* during proton irradiation. In these experiments, single crystal sapphire specimens were irradiated with 3 MeV protons which passed through the sample and were stopped in a copper-block heat sink. Dielectric properties were measured between 100 Hz and 10 MHz using a guard ring capacitor configuration. The proton irradiation caused an immediate increase in loss tangent from about 10^{-4} to more than 1.0. We have evaluated these changes at 300 K and 373 K, vs irradiation time, flux and frequency. While the *in-situ* radiation-induced conductivity (RIC) depends on these variables as well as on the history of previous irradiation, we believe that it is caused by a balance between the generation rate of electrons and holes, and their trapping and annihilation at displacement-type defects.

1.0 IRRADIATION FACILITIES, TEST MATRICES, AND EXPERIMENTAL METHODS

FABRICATION OF CREEP AND SWELLING SPECIMENS FOR MOTA-28 IRRADIATION - C. R. Eiholzer (Westinghouse Hanford Company) and D. S. Gelles (Pacific Northwest Laboratory*)

OBJECTIVE

The objective of this effort is to determine irradiation creep response in ferritic alloys. The ferritic alloys include three of the most promising low activation alloys and a simple alloy in the same composition range to provide fundamental response.

SUMMARY

Forty-five pressurized tubes and five open tubes have been made from four ferritic alloys. The alloys include a simple binary alloy, Fe-9Cr, two low activation ferric alloys in the Fe-9Cr range and one low activation alloy in the llCr range. Specimens were made for irradiation in the Materials Open Test Assembly (MOTA), starting in cycle 12 of the Fast Flux Test Facility (FFTF), and for corresponding thermal controls. This report documents how the specimens were made and defines the pre-test geometries.

PROGRESS AND STATUS

Introduction

As part of a study to define low activation ferritic alloy response to very high displacement dose, we had previously begun irradiation of three promising alloys in the FFTF/MOTA in order to obtain as complete a mechanical properties data base as possible.' Testing presently includes uniaxial tension, fracture toughness, Charpy impact response, disk bend, swelling and microstructural evolution at temperatures from 365 to 600°C with doses planned to 200 dpa or higher. Companion specimens of HT-9 are also being tested. The present effort expands the test matrix to creep and irradiation creep response. At issue is whether the creep and irradiation creep of low activation ferritic alloys are similar to HT-9. A few specimens of a simple Fe-9Cr binary alloy are also included in the matrix in order to study swelling-enhanced creep and stress-enhanced swelling response in a ferritic material already known to develop void swelling at low dose.[2]

A limited amount of tubing was manufactured using cold drawing and annedling processes to a final sire of 5.84 mm (0.230 in) by 0.381 mm (0.015 in) wall. (Efforts to oroduce a final size of 4.57 mm (0.180 in) bv 0.254 mm (0.010 in) were unsuccessful.) 'This report describes the procedure whereby pressurized tube specimens were manufactured from the tubing.

Exuerimental Procedure

Specimen Fabrication

Fabrication of pressurized tubes is an eight step process which involves making components, cleaning, engraving, electron beam welding, heat treating, determining fill pressures, pressurizing, and diameter measuring. Each step is addressed in the sections below. Open tube fabrication will be addressed in the components, cleaning, engraving, and measuring sections.

1. Components and Materials

Four different tubing lots were used to make the open tubes and the gage sections for the pressurized tubes. The alloys were E61, F82H, GA3X, and GA4X. The alloy chemistries are given in Table 1. All the tubing materials had 5.84 mm (0.23 in) outside diameter and 0.381 mm (0.015 in) wall thickness. The tubing was cut into 25.65 mm (1.01 in) lengths for pressurized tube gage sections and 9.525 mm (0.375 in) lengths for the open tubes.

Table 1. Nominal Chemical Composition of Tubing and End Cap Material for Fusion Creep and Swelling Specimens

		Composition (wt%)															
Material	Use	Fe	Cr	Ni	Mo	V	W	Mn	C	Si	Nb	P	S	Al	N	Ta	B
GA3X	Tube	Bal	9 0	0.02	0.01	0.3	2.0	0.04	0.15	0.06	-	0.001	0.001	0.02	0.002		
GALX	lube	8al	11.0	0.01	-	0.3	2.0	004	0.14	0.05	-	0.001	0.001	0.01	0.002		
E61	Tube	Bal	9.6	-				-	0.002	-					0.0014		
F82H	Tube	Bal	7.84	0 01	-	0 19	2.0	0.49	0.10	0.10	-	Ø 002	0.001	Ø.01	0 001	0 026	Ø 004
HT-9	End Caps	Bal	11.75	0.59	1.04	0.29	050	057	0.18	0.30	0.01	0.014	0.002	Ø.003			

*Operated for the U.S. Department of Energy by Battelle Memorial Institute under Contract DE-AC06-76RLO 1830.

Tie end caps for the pressurized tubes were made from HT-9. The composition of this material is also given in table 1.

2. Cleaning

fill the components were cleaned before assembly. The components were ultrasonically cleaned in acetone for five minutes and then in alcohol for five minutes. The components were air dried. The cleaned components were handled with clean cotton gloves.

3. Identification codes and Engraving

A laser engraver was used to place identification (ID) codes on sets of top and bottom pressurized tube end caps and on the sides of the open tubes. The ID codes consist of two characteristic letters followed by a two number sequence starting with either 00 or 01. Each set of characteristic letters is associated with an alloy. The open tubes and the pressurized tubes from the same alloy have the same two characteristic letters. Table 2 gives the identification codes and related alloys used for this group of specimens.

4. Electron Beam Welding

The end caps were electron beam weldea to the gage sections of the pressurized tube:. Before the test specimens were welded, qualification welds were made to determine if the welding parameters were correct for the material. A weld qualification is needed for each alloy/end cap combination. A qualification procedure usually consists of making six welds that have the same geometry and materials that. would be welded on the test specimens. However, the number of tubes available for qualifications and testing was limited. The welding engineer wrote a justification for reducing qualification samples which allows a minimum of two welds be made to qualify a procedure. The justification is based on the welding parameters for pressurized tubes not changing from alloy to alloy. Two welds for each alloy/end cap combination were used for qualifying the welding procedures for these specimens.

The qualification welds were leak checked and then metallographically examined for penetration. The required penetration is 85% of the wall thickness. The qualification welds passed both tests. All production welds were made to the qualified procedures.

The electron beam production welds were inspected before the specimens were accepted for further fabrication steps. A visual inspection was made on all the production welds. All the welds passed the inspection.

One specimen from the pressurized tube production of each alloy was sacrificed to determined if the penetration for that lot of specimens was correct. These specimens had the beginning and end of production welds made on them. The penetration was examined metallographically, and for each alloy, the correct weld penetration was found. Therefore, all four lots of specimens were accepted for further fabrication steps.

5. Post-Weld Heat treatment

After the electron beam welding, the pressurized tubes were subject to a post-weld heat treatment. The specimens were encapsulated in a glass capsule backfilled with argon. All specimens were heat treated in furnace 469569. The PNL recorder number was W446964. Table 3 gives the post-weld heal treatment for each alloy.

Table 2. Identification Codes for Fusion Pressurized Tubes and Open Tubes

Identification Code*	Alloy
DAnn	GA3X
DCnn	E61
DEnn	F82H
DGnn	GA4X

* nn refers to a two digit numerical code identifying each specimen.

Table 3. Post-Weld Heat Treatment For Fusion Pressurized Tubes

Alloy	Post-Weld Heat Treatment
GA3X	1100°C/3 min/AC t 700°C/2 hr/AC
GA4X	975°C/5 min/AC t 700°C/2 hr/AC
E61	1040°C/60 min/AC t 700°C/2 hr/AC
F82H	1100°C/3 min/AC t 700°C/2 hr/AC

6. Determination of stress and fill pressures

The fill pressures, based on the desired hoop stresses, were determined before the pressurized tubes were filled with gas. A computer program was used to determine the fill pressures. The program, FILPRES, uses elastic stress-strain relationships for cylindrical tubes to calculate fill pressures for the specimens to achieve the desired stress at temperature.[3] The code also incorporates the effects of wall thickness, material type, fill gas, and test temperature. For these specimens, the fill pressures were based on the thick wall equation for hoop stress, ferritic materials, helium fill gas, and the desired temperature-pressure matrix. Table 4 gives the temperature-pressure matrix and the fill pressures for the specimens.

Table 4. Pre-test Data and Specimen Disposition for Ferritic Creep Specimens

Spec. ID	Hoop Stress (MPa)	Test Temp. (C)	Fill Pressure (psig)	Prefill Dia. (in)	Postfill Dia. (in)	Specimen Usage	Material
DA01	0	600	NA+	NA	0.22929	REACTOR	GA3X
DA02	0	520	NA	NA	0,2293	REACTOR	GA3X
DA03	30	420	283.3	0.22941	0.2292	REACTOR	GA3X
DA04	60	420	572.9	0.22928	0.22931	REACTOR	GA3X
DA05	100	420	961.6	0.22914	0.22916	REACTOR	GA3X
DA06	15	600	108.87	0.22921	0.22921	REACTOR	GA3X
DA07	0	420	-4.57	0.22904	0.22905	REACTOR	GA3X
DA08	30	520	247.6	0.22927	0.22928	REACTOR	GA3X
DA09	60	520	502.6	0.22919	0.2292	REACTOR	GA3X
DAIO	100	520	844.7	0.22918	0.22923	REACTOR	GA3X
DA11	30	600	224.9	0.22912	0.22913	REACTOR	GA3X
DA12	60	600	457.8	0.22907	0.22909	REACTOR	GA3X
DC01	0	420	NA	NA	0.22922	REACTOR	E61
DC03	0	420	-4.6	0.22914	0.22915	REACTOR	E61
DC04	7	420	61.4	0.22874	0.22877	REACTOR	E61
DC05	30	420	283.3	0.22929	0.22934	REACTOR	E61
DC06	60	420	572.88	0.22926	0.22930	REACTOR	E61
DC07	7	420	61	0.22921	0.22921	TC	E61
DC08	30	420	283	0.22932	0.22931	TC	E61
DC09	60	420	573	0.22901	0.22903	TC	E61
DE00	0	520	NA	NA	0.22924	REACTOR	F82H
DE01	0	600	NA	NA	0.22921	REACTOR	F82H
DE02	0	420	NA	NA	0.22924	REACTOR	F82H
DE03	30	420	283.3	0.22910	0.22911	REACTOR	F82H
DE04	60	420	572.9	0.22917	0.22918	REACTOR	F82H
DE05	100	420	961.6	0.22919	0.22923	REACTOR	F82H
DE06	140	420	1353.4	0.22923	0.2293	REACTOR	F82H
DE07	30	520	247.6	0.22917	0.22918	REACTOR	F82H
DE08	60	520	502.6	0.22922	0.22924	REACTOR	F82H
DE09	100	520	844.7	0.22923	0.22927	REACTOR	F82H
DE10	15	600	108.9	0.22920	0.22921	REACTOR	F82H
DE11	30	600	224.9	0.22924	0.22927	REACTOR	F82H
DE12	60	600	457.85	0.22919	0.22922	REACTOR	F82H
DE13	140	420	1354	0.22913	0.22919	TC	F82H
DG01	0	420	NA	NA	0.22939	REACTOR	GA4X
DG03	30	420	283.3	0.22921	0.22924	REACTOR	GA4X
DG04	60	420	572.9	0.22930	0.22932	REACTOR	GA4X
DG05	100	420	961.6	0.22926	0.22931	REACTOR	GA4X
DG06	140	420	1353.4	0.22924	0.2293	REACTOR	GA4X
DG07	0	600	-6.6	0.22931	0.22932	REACTOR	GA4X
DG08	15	600	108.9	0.22917	0.22919	REACTOR	GA4X
DG09	30	600	224.9	0.22927	0.22928	REACTOR	GA4X
DG10	60	600	457.8	0.22921	0.22923	REACTOR	GA4X
DG11	60	420	573	0.22933	0.22936	TC	GA4X
DG12	100	420	962	0.22932	0.22937	TC	GA4X
DG13	140	420	1354	0.22930	0.22938	TC	GA4X
DG14	60	520	503	0.22930	0.22933	TC	GA4X
DG15	100	520	845	0.22931	0.22936	TC	GA4X
DG16	30	600	225	0.22925	0.22926	TC	GA4X
DG17	60	600	458	0.22930	0.22933	TC	GA4X

+ NA not applicable to open tubes
* TC thermal control

7. Gas Filling of Pressurized tubes

The pressurized tubes were filled in a laser weld chamber. The specimens were put in a pressure vessel that has a quartz port on top. The fill gas, which was ultra-pure helium, was put in the specimens until the desired fill pressure was obtained. After filling, a closure weld was performed with a laser pulse through the quartz port of the pressure vessel.

The laser welding parameters were qualified before the production welds on the test specimens were performed. The qualification procedure consisted of making six laser closure welds on the HT-9, heat 92231, top end caps. Six end caps were available lor qualification welds. The laser qualification welds were leak checked and then metallographically examined for fill hole closure. The qualification welds passed both examinations, and the qualifying welding parameters were used for the production welds.

The production laser closure welds were visually inspected and helium leak tested before the pressurized tubes were accepted for testing. The leak check has a sensitivity of 1×10^{-6} atm/cc/s, and all specimens passed the visual inspection and leak test.

8. Diametral measurements

The diameters of the pressurized tubes and open tubes were measured using a non-contacting laser system. The laser system takes five equidistant diameter measurements along the open tubes and the gage section of the pressurized tubes. The third measurement is taken at the center of the specimen. The distance between measurements on the pressurized tubes was 4.37 mm (0.172 in). The distance between measurements on the open tubes was 1.27 mm (0.05 in). The accuracy of the measurements is ± 0.00102 mm (0.00004 in). The average of the three middle measurements determines the average diameter. If the middle three measurements are not within 0.00127 mm (50 pin), then the specimen is remeasured two more times. For the pressurized tubes, diametral measurements were take before and after pressurizing. The open tubes were only measured once. Table 4 gives the pre-testing diametral measurements for the specimens.

Results

Specimen disposition

All the specimens made were used for either in-reactor tests, thermal controls, or metallographic weld checking. Table 4 gives the specimen disposition for the in-reactor and thermal control specimens. The in-reactor test specimens were put in MOTA-2B, and Table 5 gives the canisters and basket numbers for these specimens.

For each alloy, the pressurized tubes with numbers 01 and 02 were used for electron bean weld qualifications and lot weld penetration examination, respectively.

Discussion

Irradiation of open and pressurized tube specimens began in FFTF/MOTA 2B in May 1991 and is expecied to attain a maximum of about 30 dpa per MOTA cycle. This corresponds to about six years of irradiaticn required to achieve 200 dpa. At the end of each cycle, specimens will be removed from the reactor, measured for diameter change, and returned to the reactor. If diameter change is found to have exceeded about 2%, irradiations are expected to be discontinued. Swelling will be determined based on assuming isotropic swelling of open tubes according to the relationship $\Delta V = 3\Delta D$; however, effects of stress on swelling will be determined only by density change after specimens are permanently removed from the reactor.

Specimens prepared for thermal control testing are awaiting testing. The thermal creep test facility is being relocated. Relocation should be completed in the next six months and thermal control testing is then expected to begin.

CONCLUSIONS

Forty-five pressurized tubes and five open tubes have been made from tubing of four ferritic alloys. The alloys include a simple binary alloy, Fe-9Cr, two low activation ferritic alloys in the Fe-9Cr range and one low activation alloy in the 11Cr range. Specimens made for irradiation in the Materials Open Test Assembly, were placed in FFTF/MOTA 2B starting in cycle 12, and corresponding thermal control tests are expected to be started in the next reporting period.

Table 5. MOTA-28 Matrix Ferritic Creep Specimens

Specimen ID	Test Temp. (C)	Canister/basket
DA03	420	3A-2
DA04	420	3A-2
DA05	420	3A-2
DA07	420	3A-2
DC01	420	3A-1
DC03	420	3A-1
DC04	420	3A-1
DC05	420	3A-1
DC06	420	3A-1
DE02	420	3A-1
DE03	420	3A-1
DE04	420	3A-1
DE05	420	3A-1
DE06	420	3A-1
DG01	425	5E-1
DG03	425	5E-1
DG04	425	5E-1
DG05	425	5E-1
DG06	425	5E-1
DA02	520	2F-2
DA08	520	2F-2
DA09	520	2F-2
DAIO	520	2F-2
DE00	520	2F-2
DE07	520	2F-2
DE08	520	2F-2
DE09	520	2F-2
DA01	600	4c-1
DA06	600	4C-1
DAII	600	4C-1
DA12	600	4C-1
DE01	600	4C-1
DE10	600	4c-1
DE11	600	4c-1
DE12	600	4C-1
DG07	600	5B-1
DG08	600	5B-1
DG09	600	5B-1
DG10	600	5B-1

FUTURE WORK

The results of diameter measurements of neutron irradiated specimens and thermal controls will be reported as they become available.

REFERENCES

1. M. L. Hamilton and R. M. Ermi, Fusion Reactor Materials Semiannual Progress Report for the Period Ending March 31, 1990, DOE/ER-0313/8, 3.

2. D. S. Gelles, in Effects of Radiation on Materials: 14th International Symposium, Volume 1, ASTM STP 1046, N. H. Packan, R. E. Stoller and A. S. Kumar, Eds., (ASTM, Philadelphia, 1989) 73.

3. E. R. Gilbert and L. D. Blackburn, J. Engr. Matl. & Tech., Vol. 99 (1977) 168.

EFFECT OF MOTA SHUTDOWN PROCEDURE ON RADIATION-INDUCED MICROSTRUCTURAL EVOLUTION - F. A. Garner, Pacific Northwest Laboratory, A. M. Ermi, Westinghouse Hanford Company, N. Sekimura, University of Tokyo, and J. W. Newkirk, University of Missouri-Rolla

OBJECTIVE

The objective of this study is to determine the influence of reactor environment and history on the evolution of radiation-induced microstructure in metals.

SUMMARY

From the standpoint of MOTA operation, reactor scrams are the optimum method of ending an irradiation sequence. However, this procedure induces thermal stresses in core components that shorten their life. Thus, scrams are usually reserved for safety-related considerations only. Of the other shutdown procedures available, one involving helium purging of the MOTA can lead to substantial temperature reduction: cf the hotter canisters while the reactor is still producing power. At the end of FFTF Cycle 10C, helium purging caused a significant alreration of microstructure at the end of the MOTA 1F experiment. This procedure probably did not alter the total amount of void swelling, but most likely altered the mechanical properties due to additional hardening associated with the formation of a high density of small dislocation loops. In MOTA 1G and MOTA 2A, this purging procedure was not employed and no alteration of microstructure is anticioated.

irradiation.

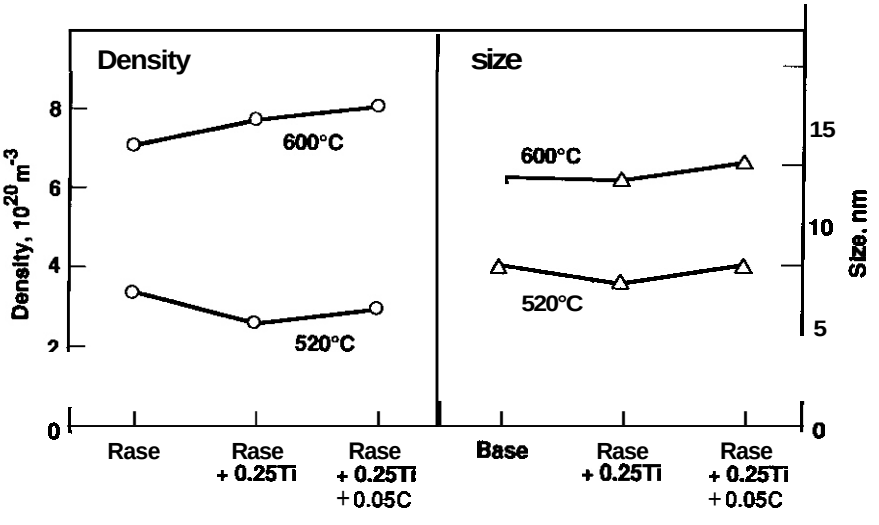

Fig. 1. Description of small dislocation loops observed in three Fe-15Cr-16Ni alloys irradiated in FFTF Cycle 10 by Sekimura and Ishino."'

Similar behavior has recently been observed in Fe-15Cr-25Ni-xP alloys that were also irradiated in FFTF Cycle 10 at compardble dpa levels and temperatures,[3,4] as shown in Figure 2. In order to explain the formation of these small loops, a review of the temperature history of MOTA 1F uas conducted. The temperature histories of MOTA 1G and MOTA 2A were also reviewed to assess whether a similar probiem might have occurred in FFTF Cycle 11.

*Operated for the U.S. Department of Energy by Battelle Memorial Institute under Contract DE-AC06-76RLO 1830.

Fig. *2.* Small **loops** observed in Fe-15Cr-25Ni-XP alloys after irradiation at 600°C to 31.8 dpa in FFTF Cycle 10. Alloys are *20%* cold worked, 50.005 **P** (top); annealed, 0.013 P (middle); and annealed, 0.10 **P** (bottom).

MOTA Temperature Histories Ouring Shutdowns

There are a number of ways in which the MOTA temperatures and FFTF power can vary during an FFTF cycle shutdown. Four combinations which have occurred are as follows:

(1) Controlled reactor shutdown over a period of several hours; MOTA not helium purged

(2) Controlled reactor shutdown over a period of several hours; MOTA helium purged before shutdown

(3) Reactor scrammed over a period of minutes.

(4) Reactor power and flow reduced to 75% during a reactivity feedback measurement test, followed by a controlled reactor shutdown over a period of several hours; MOTA not helium purged.

Controlled shutdowns involve reducing the power several percent at a time and then holding each new power level for 20-25 minutes. This produces an approximate ramp-down in power with "stairstep" reductions in temperature occurring in the MOTA canisters.

The controlled shutdowns without helium purging of the MOTA, (1) and (4) above, are the preferred methods of shutdown. The procedures employed for MOTA operation now require this kind of shutdown. The controlled shutdown of the reactor is used to minimize thermally-induced stresses in piping, instrument trees, drive lines, etc. Reactor scrams are permitted, but excessive numbers of reactor scrams reduce the plant life and are thus reserved for safety considerations involving the termination or avoidance of off-normal behavior.

Purging the MOTA before a controlled shutdown, (2) above, was the policy on earlier MOTAs, and was used primarily to obtain end-of-cycle helium purge data. Although this is no lonyer considered to be desirable, this procedure was used as recently as Cycle 10C. Reactor scrams occasionally occur during cycles, but an FFTF cycle and MOTA irradiation sequence sometimes also end on a reactor scram, as was the case for MOTA 1G and MOTA 2A, both conducted in FFTF Cycle 11C.

Figures 3-7 illustrate the end-of-cycle temperatures and reactor power levels associated with the three major FFTF Cycles for each of MOTA 1F, MOTA 1G and MOTA 2A. Intermediate shutdowns are not shown except in Figure 3. Note also that the curves for MOTA 1G and MOTA 2A are very similar since they were both irradiated in Cycle 11.

Figure 3 summarizes the full temperature histories for FFTF Cycles for MOTA 1F, MOTA 1G, and MOTA 2A respectively, and serves as a guide for subsequent figures. Figure 4 shows the histories for the ends of Cycles 10A, 10B, and 10C.l for three MOTA 1F canisters operating at 405, 520, and 600°C. Figure 5 shows similar histories for the ends of Cycles 118.1, 11B.2, and 11C for MOTA 1G. Figure 6 expands the scale to show in greater detail the reactor scram history for Cycle 11C as observed in both MOTAs. Figure 7 shows histories for the ends of Cycles 11B.1, 11B.2, and 11C for MOTA 2A. The "stairstep" type of shutdown observed in some figures is a result of using a five-minute data logging freauency that is smaller than the power reduction frequency. The "stairstep" is still present but not observed in the other curves, since in these cases the software program averaged the temperature measurements over one-hour intervdls.

Discussion and Conclusions

Considering only the standnoint of experiments conducted in MOTA, the most preferable mode of reactor shutdown is the scram, dropping both temperature and power simultaneously. Depending on tre experimental objective, the next best procedure would be either to maintain the target temperature as long as possible while the reactor power is slowly reduced or to allow the temperature to decline as a result of the reduction in reactor power. The implementation of the first of these latter two procedures for the large number of gas-gapped canisters in MOTA, however, is very difficult with existing hardware and software.

From the standpoint of experiments conducted at the higher irradiation temperatures, the least preferable procedure would be a sudden drop in temperature due to helium purging, followed by a slow decline in temperature of several hours duration before the power is reduced to a negligible level. Unfortunately, this was the procedure employed at the end of Cycle 10C. After purging, six hours was required for the power level to fall from 100 to 5%. This was equivalent to 3 effective full power hours of neutron irradiation, during which an additional 0.02 dpa was accumulated. An independent assessment by Sekimura, based on microstructural evolution during isothermal irradiation, yielded an estimate of 0.01 dpa.[2]

Note that in the 600°C capsule, there was an immediate drop of ~110°C upon helium purging, followed by a much more gradual decline over the next six hours. In the 520°C capsule, the initial drop was only ~50°C, followed by a less rapid decline. These different levels of temperature drop account in part for the atypical behavior shown in Figure 1, where more loops were formed at 600°C than at 520°C. Another relevant consideration involves the fact that radiation-induced microstructural densities increase at lower target irradiation temperatures, providing greater numbers of sinks for absorption of point defects and, therefore, decreasing the tendency toward nucleation of new dislocation loops as the temperature decreases.

Based on these two considerations, it is not surprising that small loops were oot found by Sekimura and Ishino after irradiation at ~420°C. A similar observaticn was made by Newkirk and Garner in Fe-15Cr-25Ni-xP alloys irradiated at 420°C.[4]

Since helium purging was not involved at the end of Cycles 10A and 10B, it is expected that the influence of temperature history in the first two cycles would be small since the irradiation during shutdown proceeded at temperatures closer to the target temccrature. It is also anticipated that any accumulated lower temperature microstructure would quickly be dissolved at the beginning of the next cycle. Sekimura and Ishino noted that the short term accumulation of small loops in Cycle 10C would not have influenced the void swelling or precipitation very much, but the addition of small loops would affect mechanical property measurements because of their associated hardening.[1]

It is surprising that exposure levels of only 0.01-0.02 dpa could cause significant amounts of microstructural alteration to a material which had already reached ~30 dpa. Kiritani and coworkers, however, note that "only several percent of exposure to neutrons at lower temperature was found to result in one hundred percent difference in the final defect structures in some cases, while it causes only a slight difference in others."[5,6] In Kiritani's studies, however, much lower displacement levels were employed compared to that of the FFTF studies. Thus, the relative amount of microstructural alteration was often much larger in those studies. The majority of the differences in Kiritani's studies also appear to have been caused by low temperature nucleation events at the beginning, rather than the end of the irradiation.

Concern has been expressed recently that the details of temperature history associated with typical reactor operation may dominate the overall response of a material during irradiation and possibly obscure the action of the variables thought to be under study.[5-7] Is it possible that similar microstructural alteration may have occurred in MOTA 1G and MOTA 2A, both irradiated in FFTF Cycle 11?

It appears from the temperature histories shown for Cycle 11 that similar behavior will not be observed. The shutdown procedure for the 11A and 11B cycles involved ramp-downs in temperature rather than helium purging. Thus, in experiments conducted in MOTA 1G and MOTA 2A, any resultiny lower temperature alteration of microstructure should have been small and was probably dissolved at the beginning of the next cycle. The scram associated with the Cycle 11C shuidown guaranteed that the accumulated displacement damage at lower temperatures was very small. Therefore, MOTA operation in Cycle 11 can be considered as having been conducted under the best conditions obtainable.

References

1. N. Sekimura and S. Ishino, Journal of Nuclear Materials, 179-181 (1991) 542-545

2. N. Sekimura, to be presented at the 16th International Symposium on Effects of Radiation on Materials, Denver, CO, June 22-24, 1992.

3. F. A. Garner, Fusion Reactor Materials Semiannual Prowess ReDort DOE/ER-0313/9, (April 1991) 50-57

4. J. W. Newkirk and F. A. Garner, to be presented at the 16th International Symposium on Effects of Radiation on Materials, Denver, CO, June 22-24, 1992.

5. M. Kiritani, Journal of Nuclear Materials, 160 (1988) 135-141.

6. M. Kiritani, T. Yoshiie, S. Kojima, Y. Satoh and K. Hamada, Journal of Nuclear Materials, 174 (1990) 327-351.

7. N. Yoshida, Journal of Nuclear Materials, 174 (1990) 220-228.

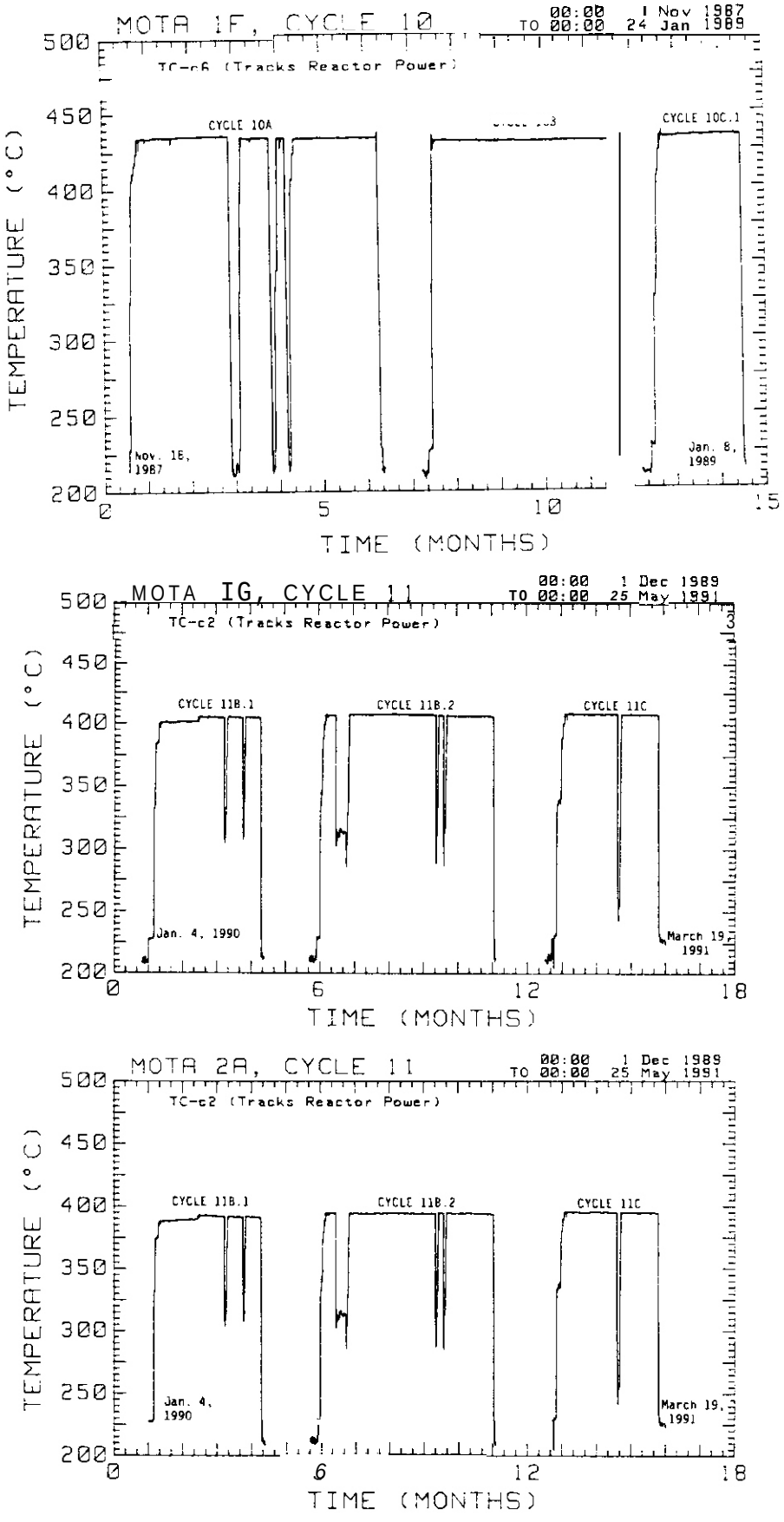

Fig. 3. Temperature plots for coolant thermocouples in MOTA 1F, MOTA 1G, and MOTA 2A

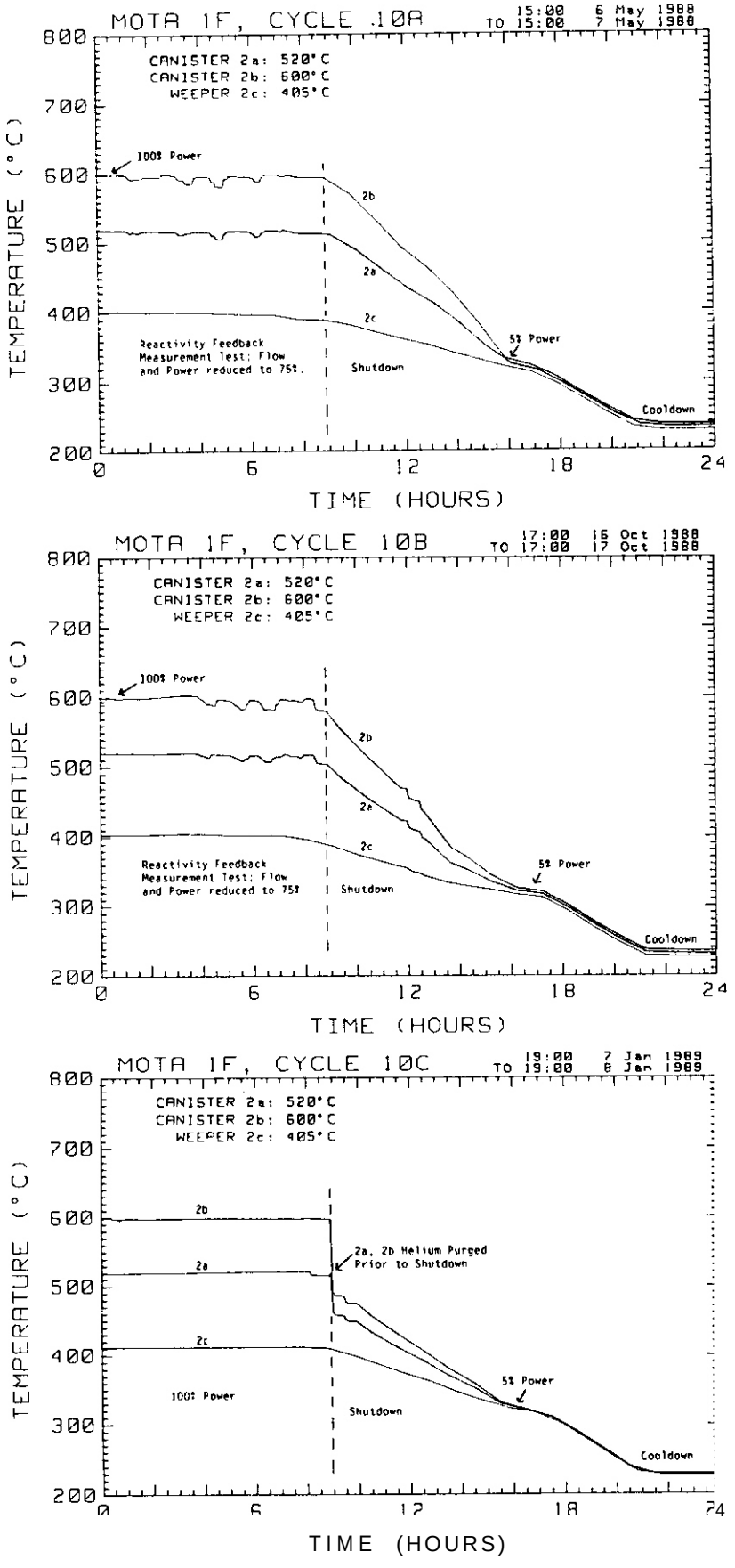

Figure 4. Shut-down temperature histories for MOTA IF during cycles 10A, 10B, 10C.

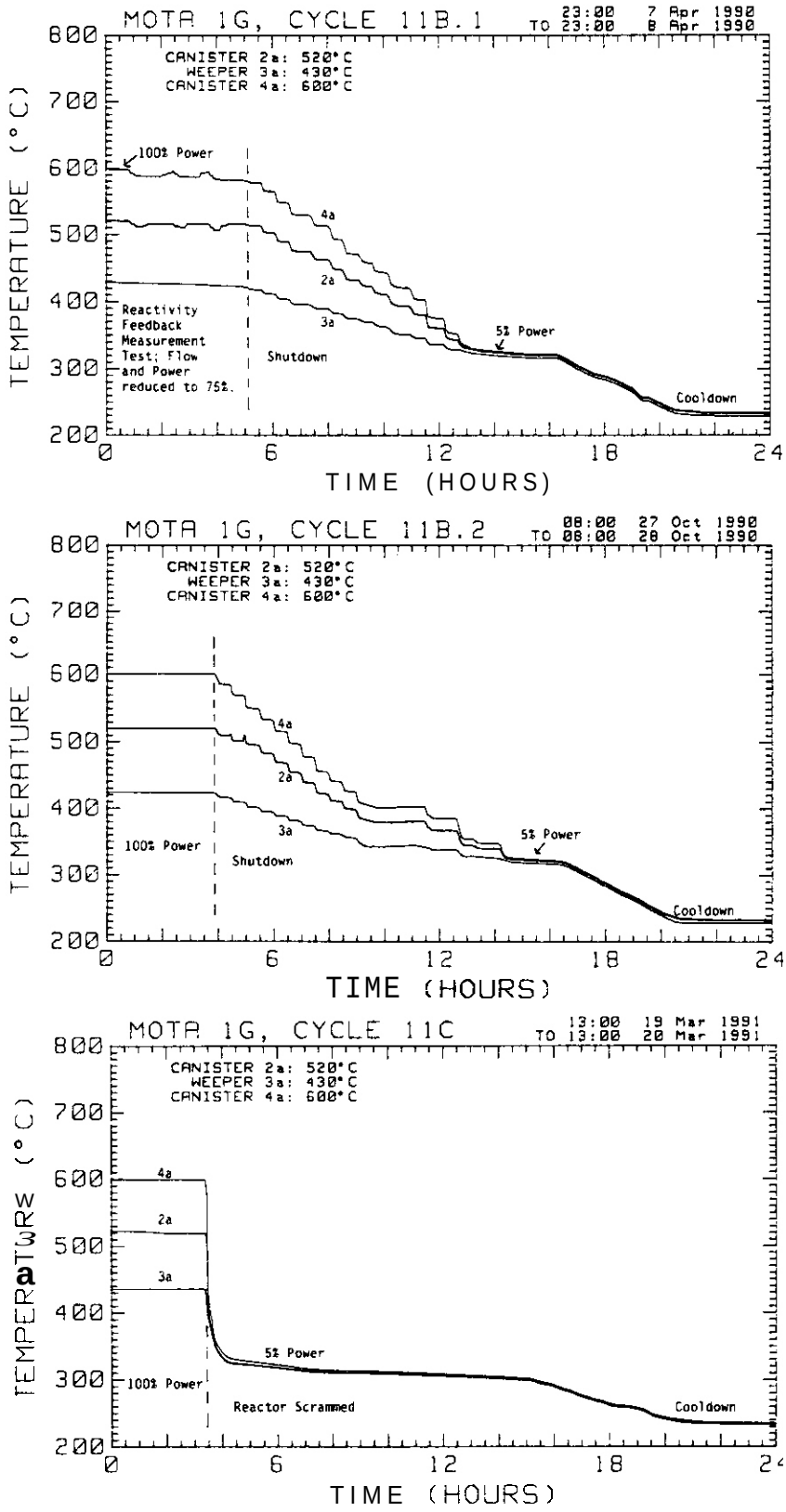

Figure 5. Shut-down temperature histories for MOTA 1G during cycles 118.1, 118.2 and 11C.

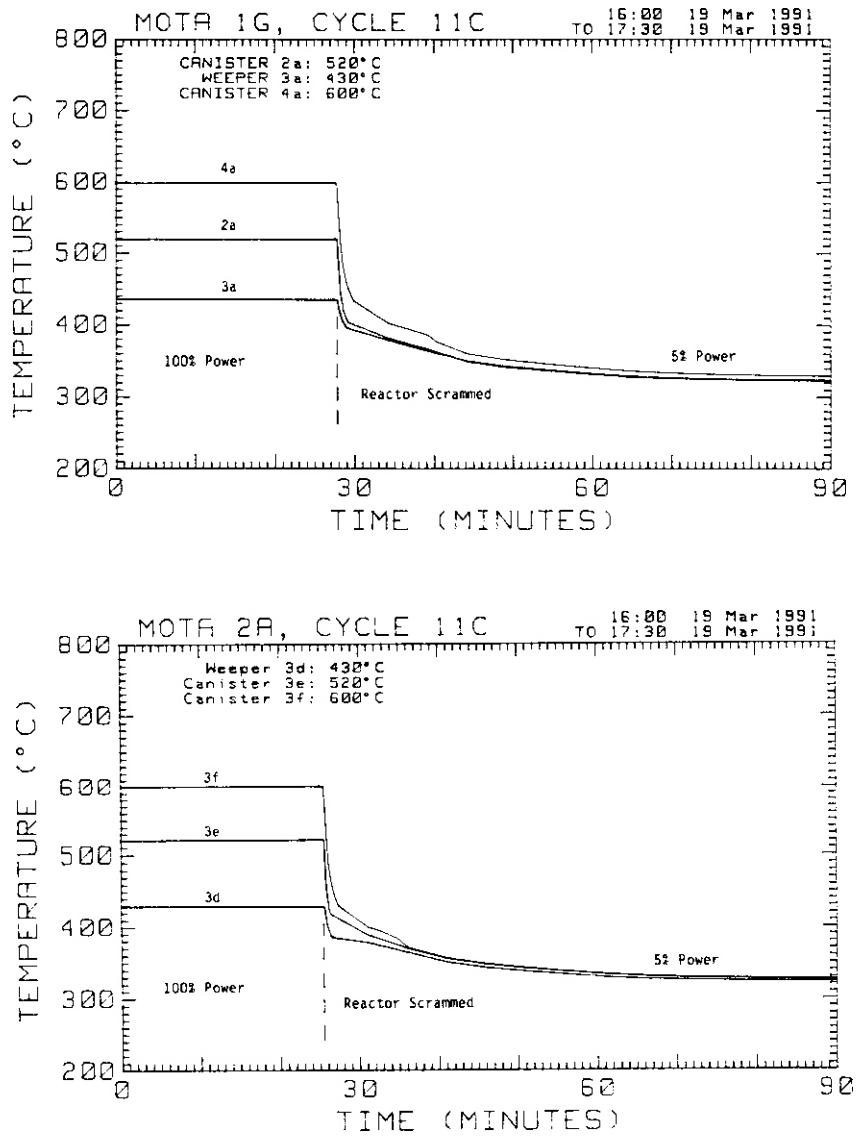

Figure 6. Expanded plots of temperature history for MOTA 1G and MOTA 2A, showing details of temperature history following scram at end of cycle 11C.

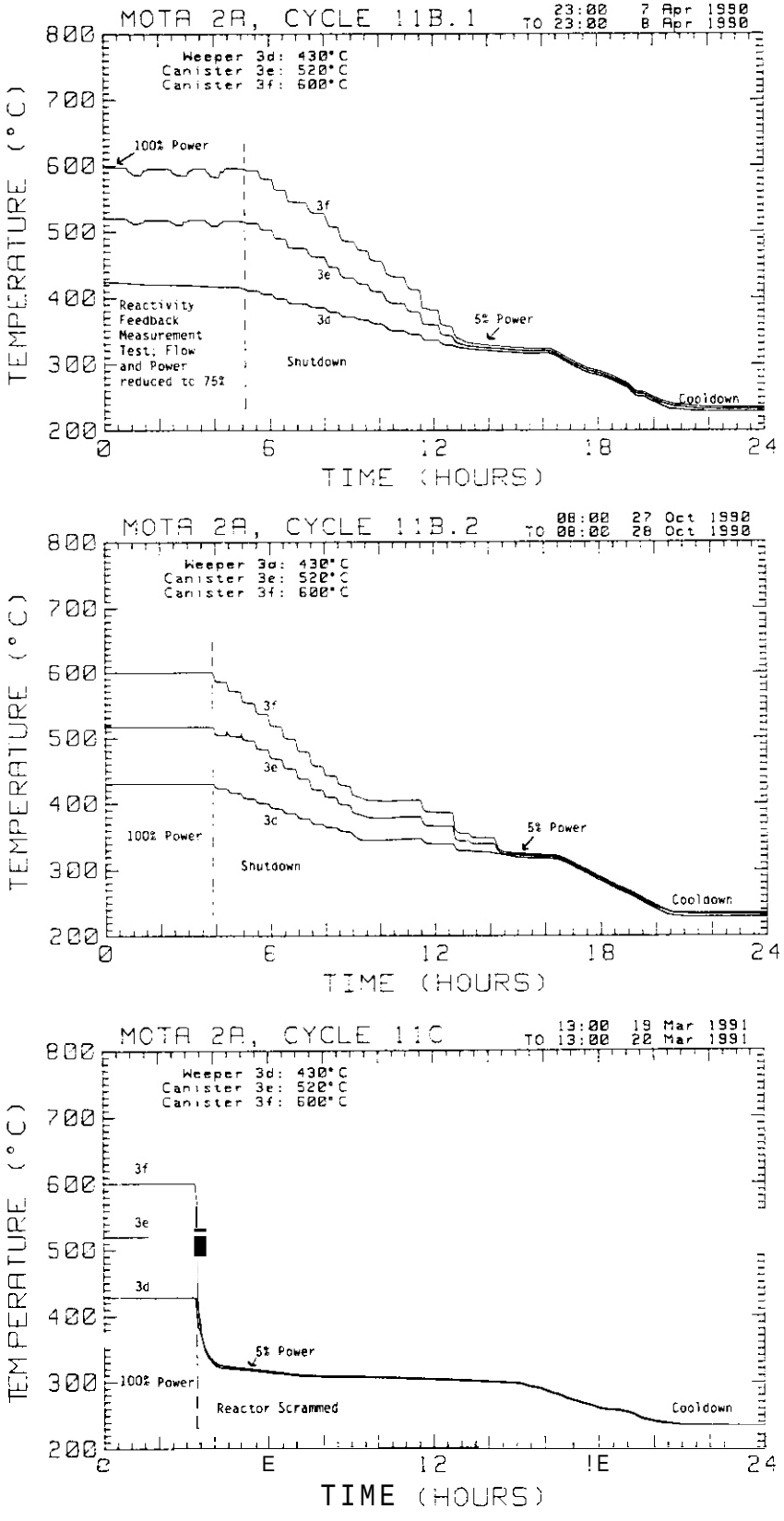

Figure 7. Shut-down temperature histories for **MOTA 2A** during cycles **11B.1, 11B.2 and 11C.**

FABRICATION AND OPERATION OF HFIR-MFE RB* SPECTRALLY TAILORED IRRADIATION CAPSULES

A. W. Longest, D. W. Heatherly, E. D. Clemmer (Oak Ridge National Laboratory), and J. E. Corum (Midwest Technical, Inc.).

OBJECTIVE

The objective of this work is to fabricate and operate irradiation capsules for irradiating magnetic fusion energy (MFE) first-wall materials in the High Flux Isotope Reactor (HFIR) removable beryllium (RB*) positions. Japanese and U.S. MFE specimens are being transferred to RB* positions following irradiation to 7.5 dpa at temperatures of 60, 200, 330, and 400°C in Oak Ridge Research Reactor (ORR) experiments ORR-MFE-6J and -7J.

SUMMARY

Fabrication and operation of four HFIR-MFE RB* capsules (60,200,330, and 400°C) to accommodate MFE specimens previously irradiated in spectrally tailored experiments in the ORR are proceeding satisfactorily. With the exception of the 60°C capsule, where the test specimens are in direct contact with the reactor cooling water, the specimen temperatures (monitored by 21 thermocouples) are controlled by varying the thermal conductance of a small gap region between the specimen holder and the containment tube.

Irradiation of the 60 and 330°C capsules was started on July 17, 1990. As of September 30, 1991, these two capsules had completed 12 cycles of their planned 28-cycle irradiation to a damage level of 20 displacements per atom (dpa). Fabrication of parts for the other two (200 and 400°C capsules) is complete. Assembly of the 200 and 400°C capsules is scheduled for completion in FY 1993; operation of these two capsules will follow the first two (60 and 330°C).

PROGRESS AND STATUS

Introduction

A series of spectrally tailored irradiation capsules are being fabricated and operated as part of the U.S./Japan collaborative program for testing MFE first-wall materials in mixed-spectrum fission reactors. The test specimens are being irradiated in the RB* facility' of the HFIR.

Four HFIR-MFE RB* capsules were designed to accommodate Japanese and U.S. MFE specimens previously irradiated to 7.5 dpa at temperatures of 60, 200, 330, and 400°C in the ORR in spectrally tailored experiments ORR-MFE-6J and -7J. Details of these ORR experiments, including descriptions of the test matrix, mechanical property specimens, and techniques of spectral tailoring, have been reported elsewhere.[2,3] Hafnium liners are being used in the HFIR-MFE RB* experiments to tailor the neutron spectrum to closely match the helium production-to-atom displacement ratio (14 appm/dpa) expected in a fusion reactor first wall.

The HFIR-MFE RB* capsules are being irradiated in pairs (first the 60 and 330°C capsules, then the 200 and 400°C capsules) to a damage level of 20 dpa.

60' C Capsule

The 60°C capsule, designated HFIR-MFE-60J-1, is an uninstrumented capsule with the test specimens in contact with the reactor cooling water. Capsule design, assembly, and details of the specimen loading were described previously.'

Irradiation of this capsule began July 17, 1990, at the start of HFIR cycle 289. As of September 30, 1991, 12 cycles of its planned 28-cycle irradiation to a damage level of 20 dpa had been completed. Specimen operating temperatures in this capsule are predicted to be within 10°C of 60°C.

330°C Capsule

The 330°C capsule, designated HFIR-MFE-330J-1, is an instrumented and singly contained capsule where the specimen temperatures are monitored by 21 thermocouples and controlled by adjusting the thermal conductance of a small gas gap region between the specimen holder outer sleeve and the containment tube. This capsule is cooled with 49-C reactor cooling water flowing downward over the containment tube surface. Capsule design, assembly, and details of the specimen loading were described previously.[5,6]

Irradiation of this capsule began on July 17, 1990, at the start of HFIR cycle 289. As of September 30, 1991, 12 cycles of its planned 28-cycle irradiation to a damage level of 20 dpa had been completed.

Typical thermal operating data for the 330J-1 experiment are shown in Figs. 1 through 7 for HFIR Cycle No. 299 and in Figs. 8 through 14 for HFIR Cycle No. 298. Two cycles are required to show pertinent thermal patterns because the capsule is rotated 180° at the end of each cycle to provide near-uniform neutron exposure to specimens at any given elevation; in Cycle No. 299 the capsule was at its first orientation and in Cycle No. 298 the capsule was 180° from its first orientation. Table 1 gives thermocouple junction locations in the capsule and the first orientation of the capsule with respect to the direction of the reactor core vertical centerline. Figs. 15 and 16 are vertical and horizontal sections through the capsule, respectively, and show the arrangement of test specimens and thermocouple assemblies in the aluminum alloy specimen holder. As indicated in Fig. 16, there are seven thermocouple assemblies in the specimen holder, each containing three thermocouple elements. These three-junction assemblies were formed by swaging a stainless steel tube containing three individual Type K stainless-steel-sheathed thermocouples to a final diameter of 1.04 mm. In addition, there are three single-junction thermocouples (TE-22, TE-23, and TE-24) above the specimen holder to measure temperature drop across the annular test piece of 10% dense DUOCEL aluminum shown in Fig. 15.

The data acquisition system being used with the 330J-1 capsule scans all the sensor signals every six seconds and determines the maximum, minimum, and average temperature indicated by the thermocouples in the specimen holder. The average temperature is used for capsule temperature control and is maintained within about 5°C of 325°C by manual adjustment of the composition, and hence thermal conductance, of the flowing helium-neon mixture in the control gas gap between the specimen holder sleeve and containment tube. From design calculations for the capsule, values for the maximum calculated temperature increase from the adjacent specimen holder to the specimen peak-temperature location are 20°C for the TEM specimens (all but 4°C is the temperature increase across the gas gaps on either side of the tube containing the TEM disks), 16°C for the rod tensile specimens, 16°C for the pressurized tube specimens, and 5°C for the flat tensile, crack growth, and grodzinski fatigue specimens (based on a 0.0127-mm helium gap between the flat specimens and holder). The maximum calculated temperature increase for the 1.04-mm-diameter thermocouple assemblies in the specimen holder is 3°C (based on a uniform 0.0635-mm helium gap between the thermocouple assemblies and the holder).

The average temperature is recorded every 6 seconds; a sample of all other operating data is recorded every minute. These raw data are further reduced to produce plots such as those shown in Figs. 1 through 14. The data reduction program reduces each selected parameter to 200 data points for the period being processed. Several modes of data processing are available. These are SAMPLE which gives the last sample in each interval, AVERAGE which gives the average of all samples within the interval, HIGH which gives the highest sample within the interval, and LOW which gives the lowest sample within the interval. In preparation of Figs. 1 through 14, the HIGH mode was used for maximum temperature, the LOW mode was used for minimum temperature, and the AVERAGE mode was used for all other parameters.

The operating data from the 330J-1 capsule are close to expectations with the minor exceptions that the helium-neon control gas mixture required is richer in neon than design calculations predicted and the lower end of the specimen holder operates about 15°C higher than the upper end (compared to predicted symmetry about the holder midplane). The temperature criterion for the experiment was to operate at specimen temperatures within 25°C of 330°C. Based on the temperature measurements to date and the design calculations relating measured temperatures to specimen temperatures, the specimen operating temperature range is close to the temperature criterion range of 305°C to 355°C. The TEM and rod tensile specimens in the lower end of the specimen holder may be operating as much as 15°C above the desired range during the latter portion of each HFIR fuel cycle (i.e., maximum of 370°C). However, if the average temperature were lower, some specimen temperatures would be below the desired range.

Only one thermocouple failure has occurred since the start of irradiation. TE-15 failed on October 1, 1990; thereafter, a total of 20 thermocouples instead of 21 have been included in the average temperature determination.

200 and 400°C Capsules

The 200 and 400°C capsule designs were described previously' and are basically the same as that of the 330°C capsule. The main differences in the three capsule designs are associated with (1) the number and spacing of the specimen holder slots and holes to accommodate the different specimen loadings, (2) the width of the temperature control gas gap region between the specimen holder outer sleeve and containment tube to obtain the desired specimen temperatures, and (3) the test piece included in the aluminum plug and holder above the test specimen holder to obtain extra information.

Fabrication of parts for both capsules is complete. Assembly of the capsules is scheduled for completion in FY 1993. Operation of these two capsules will follow the first two (60 and 330°C).

FUTURE WORK

Assembly of the 200 and 400°C capsules is scheduled to be completed in FY 1993.

REFERENCES

1. K. R. Tboms et al., "HFIR Irradiation Facilities Improvements • Completion of the HIFI Project," J. Nucl. Mater., 155-157 (1988) 1340-45.

2. J. L. Scott et al., pp. 12-20 in *ADIP* ***Semiann. Prog. Rep., March 31, 1985,*** DOE/ER-0045/14, U.S. DOE, Office of Fusion Energy.

3. J. L Scott et al., ***Second Annual Prog. Rep. on United States-Japan Collaborative Testing in the High Flux Isotope Reactor and the Oak Ridge Research Reactor,*** Sept. 30, 1985, ORNL/TM-10102.

4. A. W. Longest et al., "Design and Fabrication of HFIR-MFE RB* Spectrally Tailored Irradiation Capsules," in ***Fusion Reactor Materials Semiann. Prog. Rep., March 31, 1988,*** DOE/ER-0313/4, U.S. DOE, Office of Fusion Energy.

5. A. W. Longest et al., "Design and Fabrication of HFIR-MFE RB* Spectrally Tailored Irradiation Capsules," in ***Fusion Reactor Materials Semiann. Prog. Rep., Sept. 30, 1987,*** DOE/ER-0313/3, U.S. DOE, Office of Fusion Energy.

6. A. W. Longest et al., "Design and Fabrication of HFIR-MFE RB* Spectrally Tailored Irradiation Capsules," in ***Fusion Reactor Materials Semiann. Prog. Rep., Sept. 30, 1988,*** DOE/ER-0313/5, U.S. DOE, Office of Fusion Energy.

7. A. W. Longest et al., "Design and Fabrication of HFIR-MFE RB* Spectrally Tailored Irradiation Capsules," in ***Fusion Reactor Materials Semiann. Prog. Rep., March 31, 1989,*** DOE/ER-0313/6, U.S. DOE, Office of Fusion Energy.

Table 1. Thermocouple junction locations in the HFIR-MFE-33OJ-1 Irradiation Capsule

Thermocouple number	Junction location		
	Axial distance above reactor can midplane (cm)	Radial distance from capsule centerline (cm)	First orientation' (degrees clockwise from direction of reactor core vertical centerline)
TE-01	-10.8	0.478	0
TE-02	-0.25	0.478	0
TE-03	10.5	0.478	0
TE-04	-10.4	0.478	180
TE-05	0.18	0.478	180
TE-06	10.7	0.478	180
TE-10	-6.65	1.27	288
TE-11	241	1.27	288
TE-12	653	1.27	288
TE-16	-6.40	1.27	108
TE-17	-2.29	1.27	108
TE-18	6.68	1.27	108
TE-13	-14.1	1.27	0
TE-14	0.10	1.27	0
TE-15	14.3	1.27	0
TE-19	-13.9	1.27	180
TE-20	4.08	1.27	180
TE-21	13.9	1.27	180
TE-7	-246	0.795	252
TE-8	-0.10	0.795	252
TE-9	2.34	0.795	252
TE-22	19.5	0	Not applicable
TE-23	19.5	1.49	324
TE-24	19.5	1.49	144

* Capsule is rotated 180° at the end of each HFIR fuel cycle.

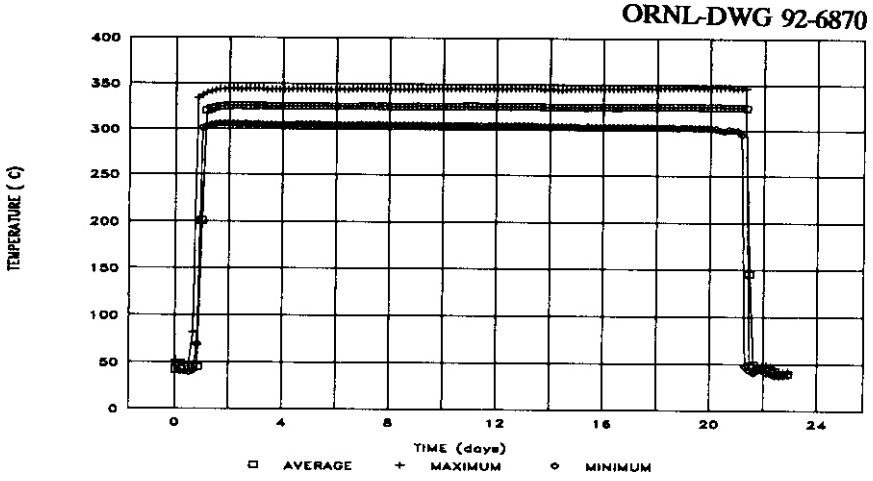

Fig. 1. Specimen holder temperatures in the HFIR-MFE-330J-1 capsule during HFIR Cycle 299. (TIME 0 = 0000 hours on July 25, 1991).

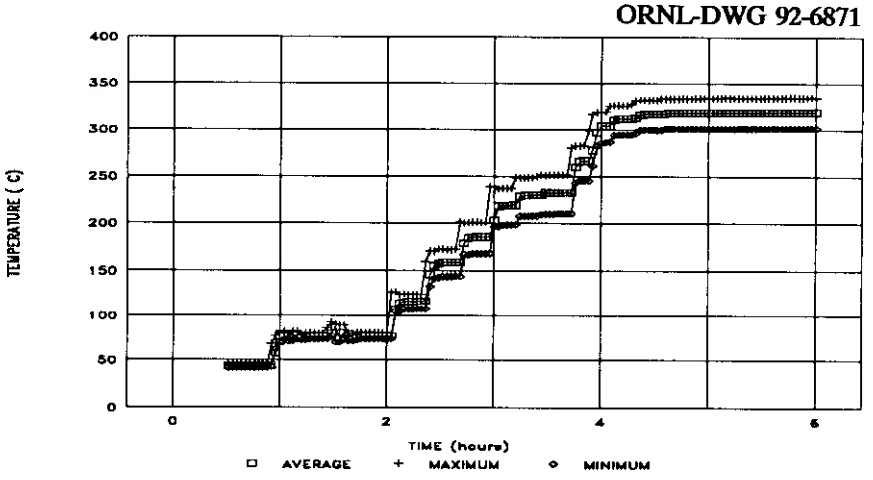

Fig. 2. Specimen holder temperatures in the HFIR-MFE-330J-1 capsule during HFIR Cycle 299 start-up on July 25.1991. (TIME 0 = 1900 hours on July 25.1991).

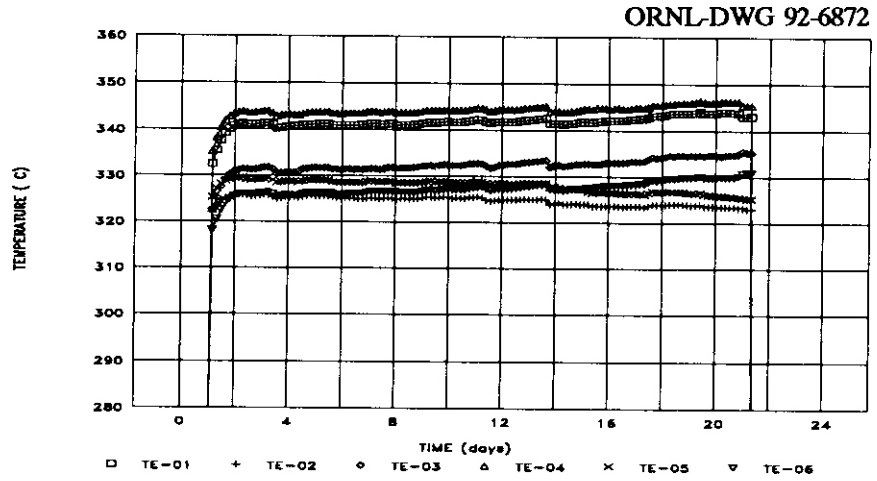

Fig. 3. Individual thermocouple readings in the HFIR-MFE-33OJ-1 capsule during HFIR Cycle 299. (TIME 0 = 0000 hours on July 25,1991).

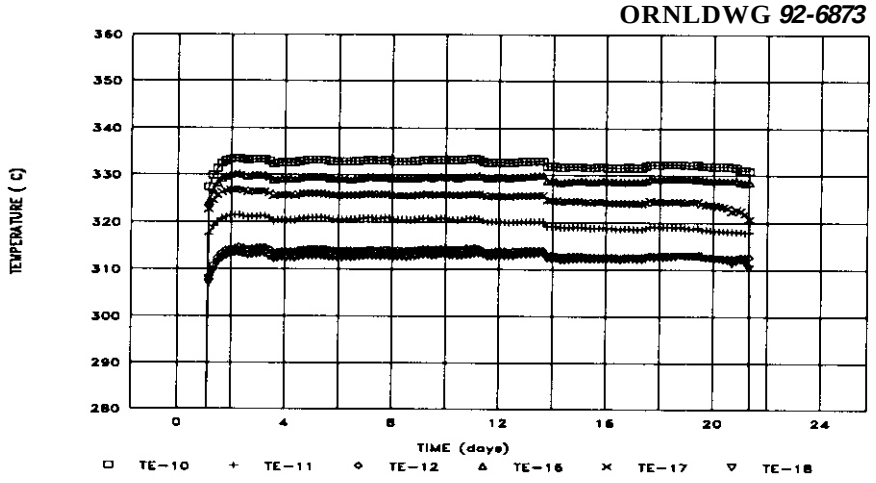

Fig. 4. Individual thermocouple readings in the HFIR-MFE-330J-1 capsule during HFIR Cycle 299. (TIME 0 = 0000 hours on July 25.1991).

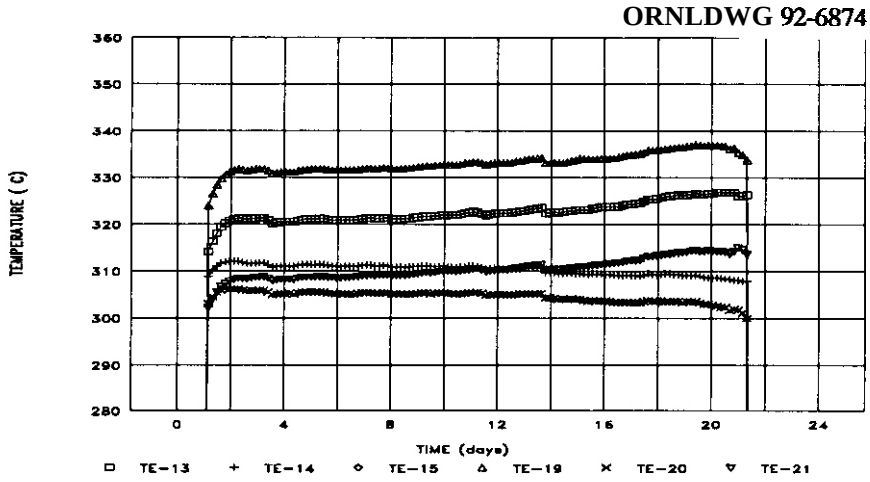

Fig. 5. Individual thermocouple readings in the HFIR–MFE–33OJ–1 capsule during HFIR Cycle 299. (TIME 0 = 0000 hours on July 25, l991).

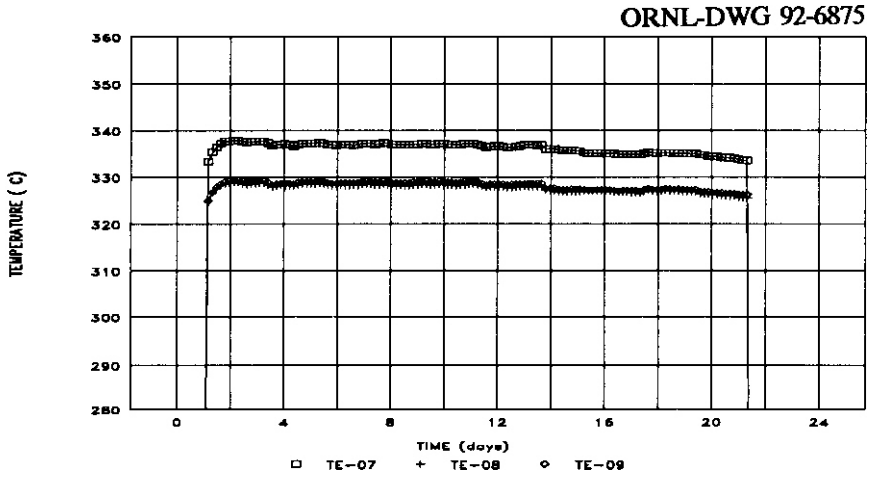

Fig. 6. Individual thermocouple readings in the HFIR–MFE–330J–1 capsule during HFIR Cycle 299. (TIME 0 = 0000 hours on July 25.1991).

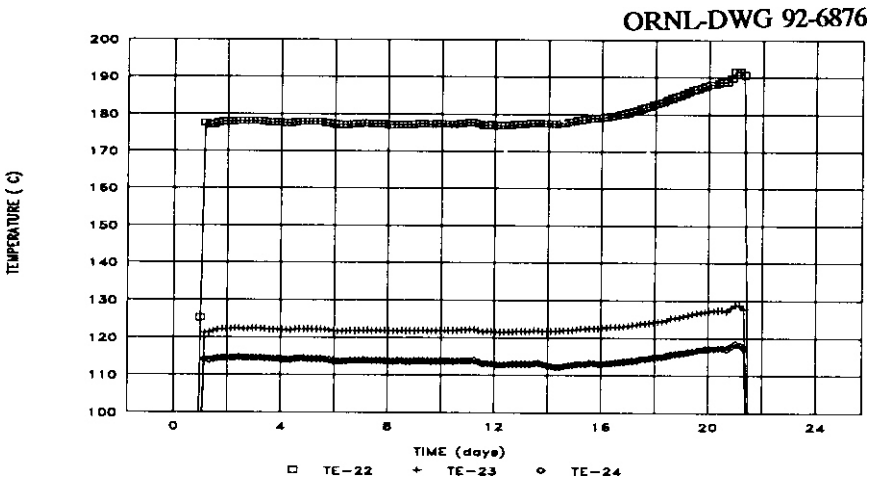

Fig. 7. Individual thermocouple readings in the HFIR-MFE-330J-1 capsule during HFIR Cycle 299. (TIME 0 = 0000 hours on July 25.1991).

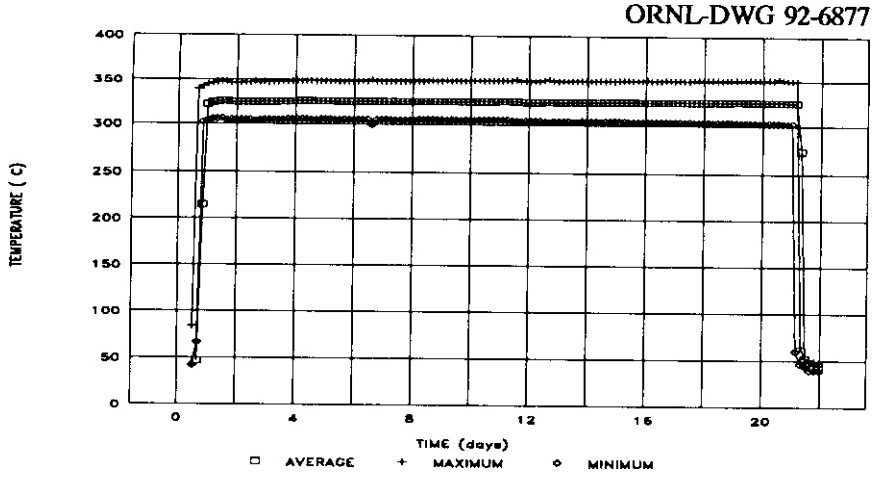

Fig. 8. Specimen holder temperatures in the HFIR-MFE-330J-1 capsule during HFIR Cycle 298. (TIME 0 = 0000 hours on June 20,1991).

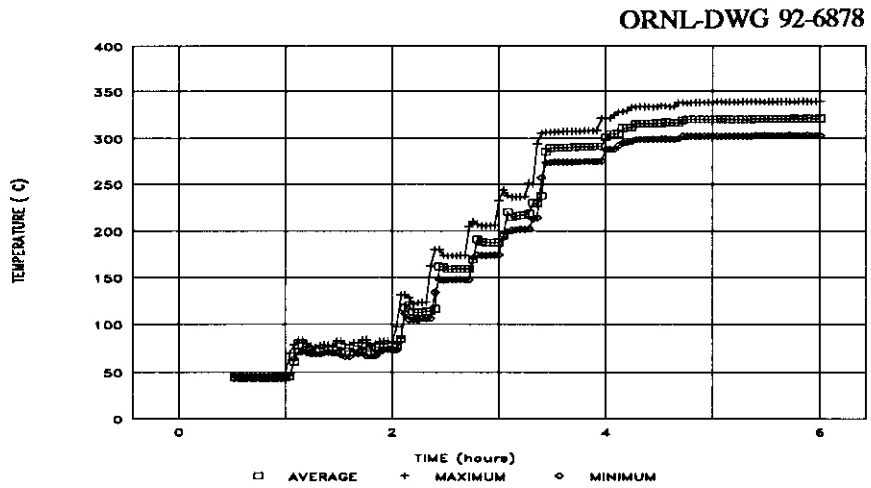

Fig. 9. Specimen holder temperatures in the HFIR–MFE–33OJ–1 capsule during HFIR Cycle 298 start–up on June 20,1991. (TIME 0 = 1500 hours on June 20,1991).

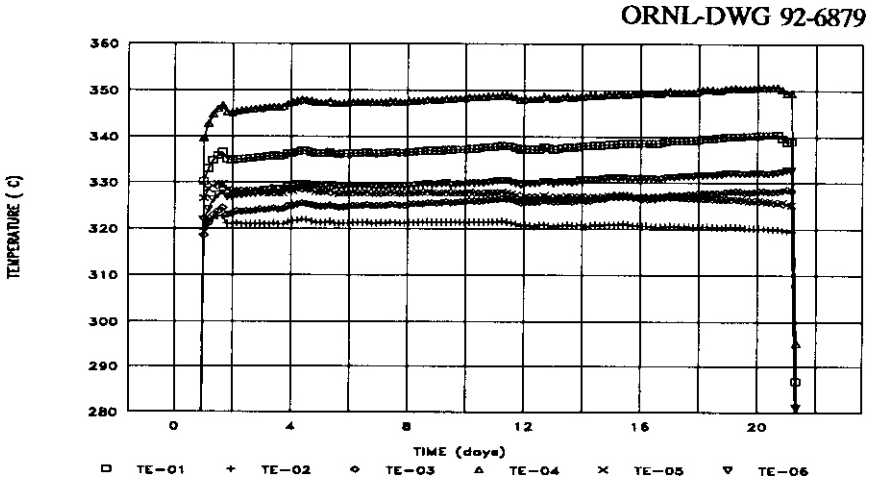

Fig. 10. Individual thermocouple readings in the HFIR–MFE–330J–1 capsule during HFIR Cycle 298. (TIME 0 = 0000 hours on June 20, 1991).

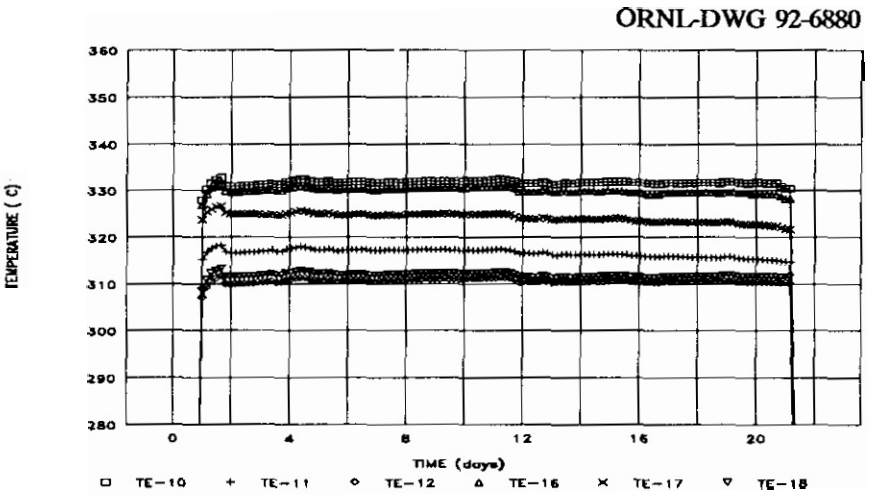

Fig. 11. Individual thermocouple readings in the HFIR-MFE-330J-1 capsule during HFIR Cycle 298. (TIME 0 = 0000 hours on June 20,1991).

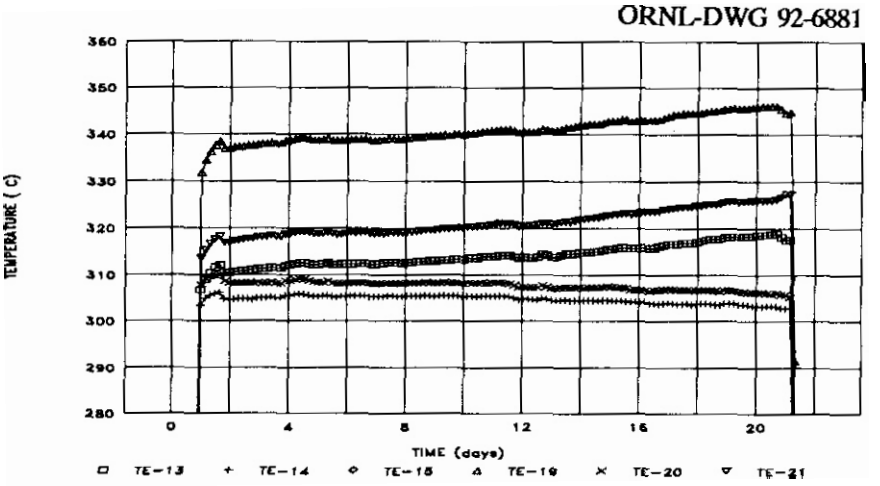

Fig. 12. Individual thermocouple readings in the HFIR-MFE-330J-1 capsule during HFIR Cycle 298. (TIME 0 = 0000 hours on June 20.1991).

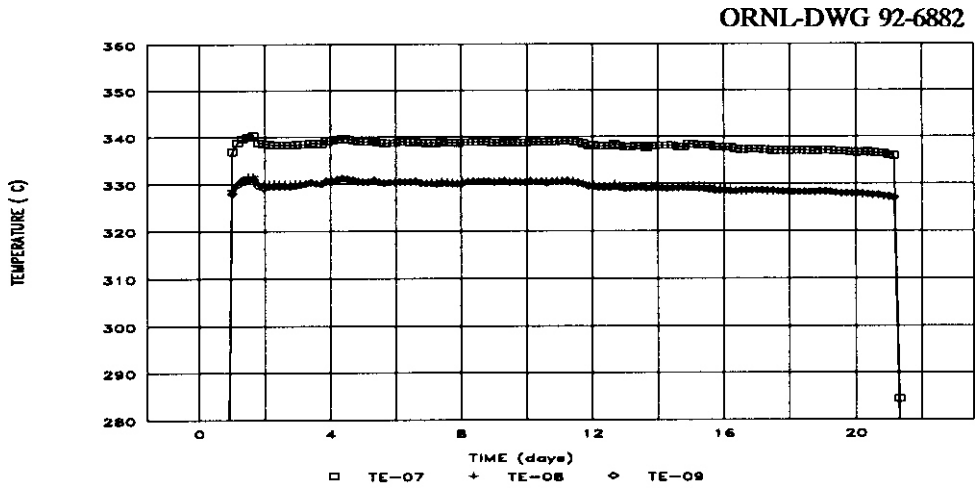

Fig. 13. Individual thermocouple readings in the HFIR-MFE-330J-1 capsule during HFIR Cycle 298. (TIME 0 = 0000 hours on June 20,1991).

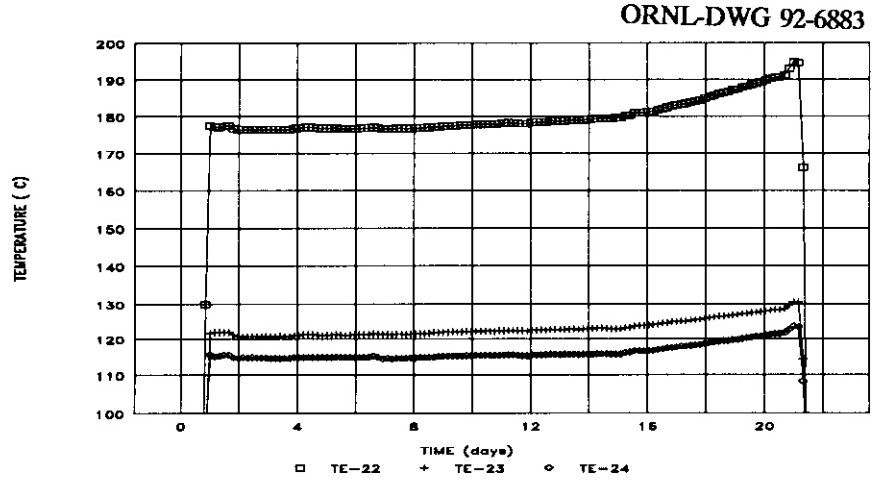

Fig. 14. Individual thermocouple readings in the HFIR-MFE-33OJ-I capsule during HFIR Cycle 298. (TIME 0 = 0000 hours on June 20,1991).

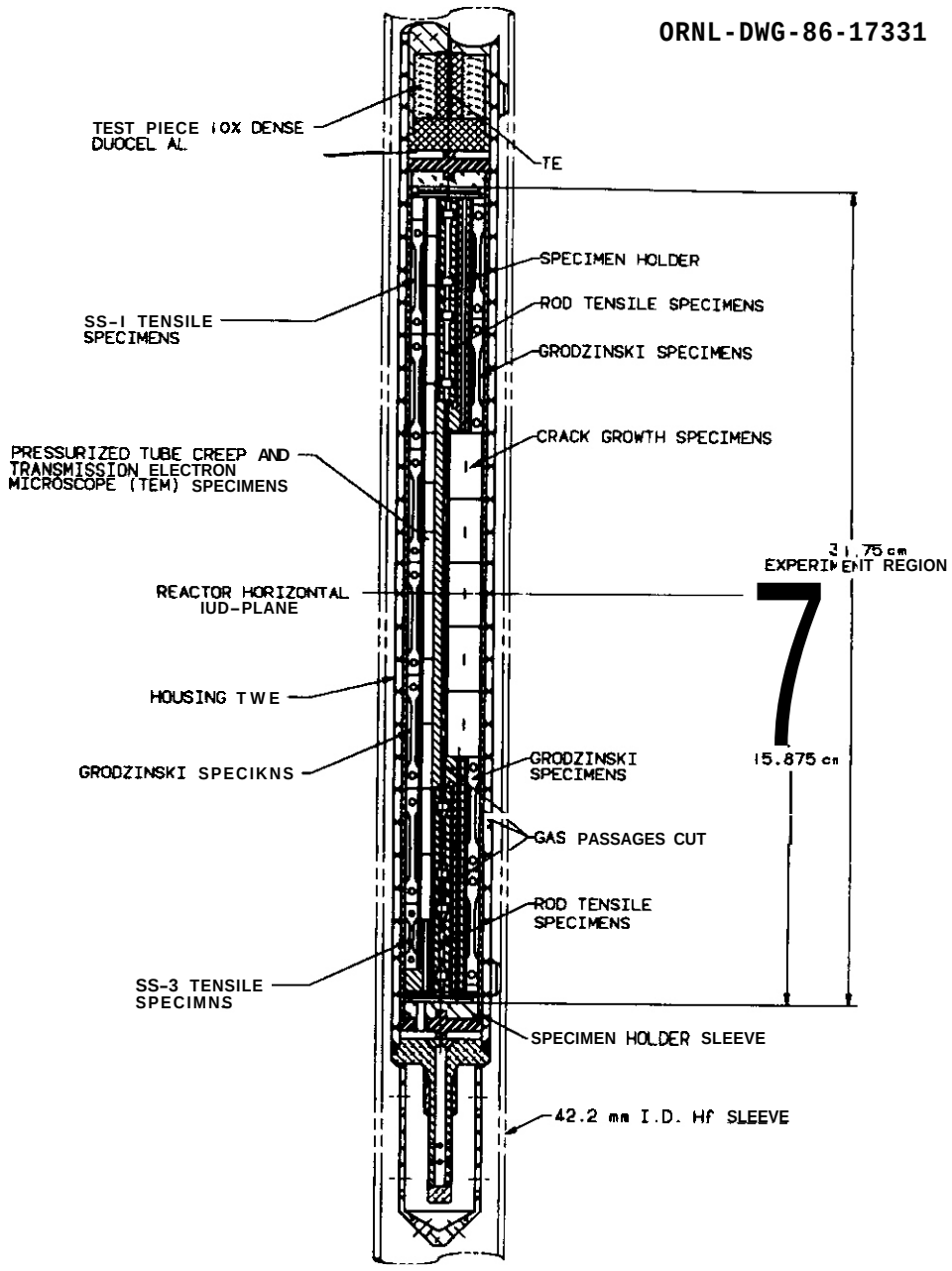

Fig. 15. Vertical section through the HFIR-MFE-33OJ-1 capsule.

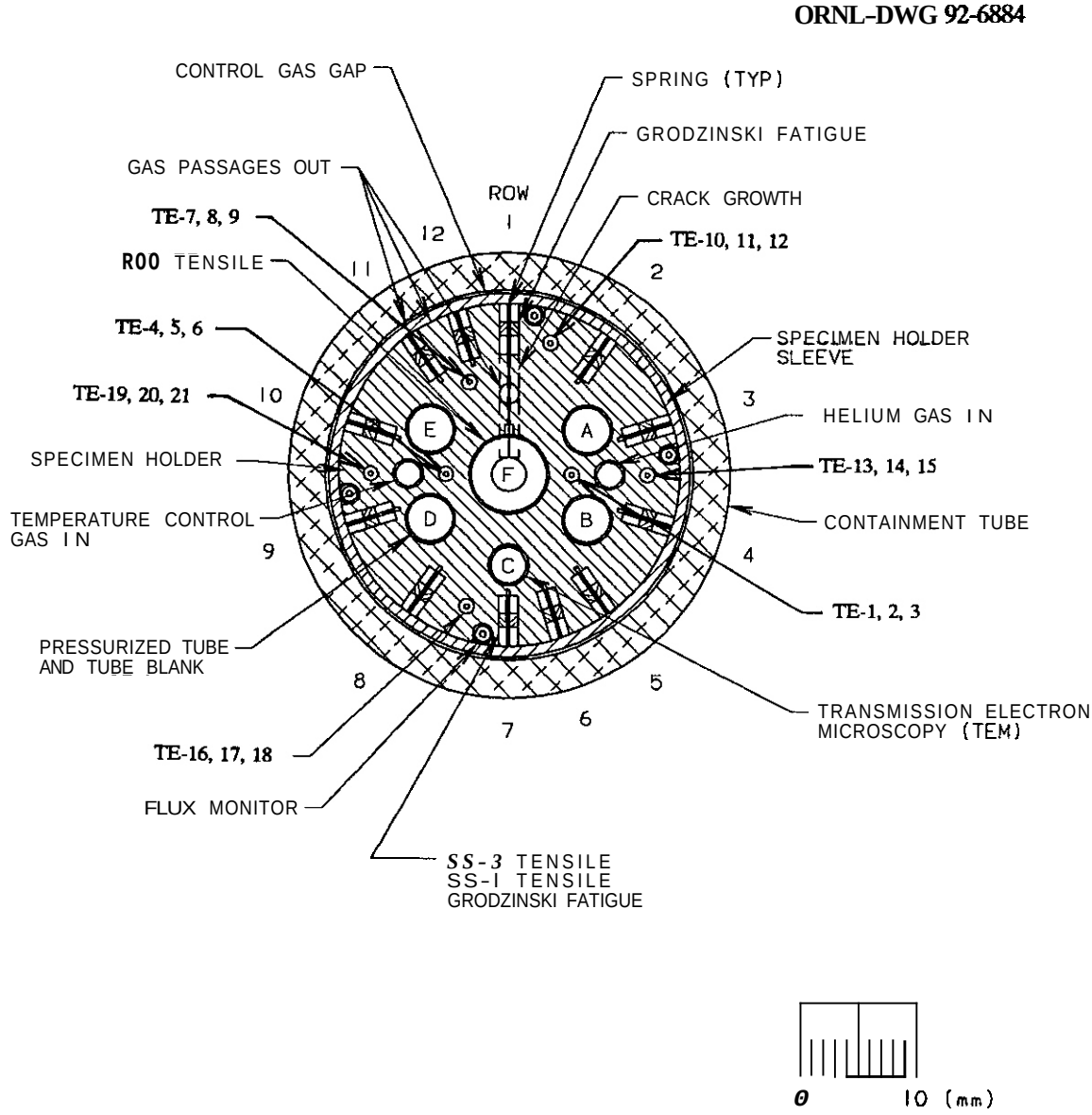

Fig. 16. Horizontal section through the HFIR-MFE-33OJ-1 capsule.

FABRICATION AND IRRADIATION OF HFIR-MFE-JP-17, -18, AND -19 TARGET IRRADIATION CAPSULES · A.W. Longest, D. W. Heatherly, J. E. Wolfe, K. R. Thoms (Oak Ridge National Laboratory), and J. E. Corum (Midwest Technical, Inc.).

OBJECTIVE

The objective of this work is to fabricate and irradiate capsules for testing magnetic fusion energy (MFE) reactor candidate first-wall materials in the High Flux Isotope Reactor (HFIR) target positions. Japanese and U.S. test specimens are being irradiated to determine fracture toughness of austenitic stainless steels and a few chromium femtic steels and high heat flux alloys after irradiation to 3 dpa at temperatures of 60-125 and 250-300°C.

SUMMARY

Fabrication and irradiation of three new uninstrumented HFIR target capsules for testing 12.5-mm-diameter stainless steel fracture toughness specimens to a damage level of approximately 3 displacements per atom (dpa) at temperatures of 60-125 and 250-300°C are proceeding satisfactorily. Two low temperature capsules of identical design, designated HFIR-MFE-JP-18 and HFIR-MFE-JP-19, each contain 32 fracture toughness specimens directly cooled by reactor cooling water. Irradiation of these two capsules is nearing completion. A single helium-filled elevated temperature capsule, designated HFIR-MFE-JP-17, will contain a stack of 86 fracture toughness specimens. Additional neutronic calculations were required for this experiment to insure that it will not cause unacceptable neutron flux shifting and hot spots in HFIR fuel regions. Irradiation of this capsule is scheduled to start in late November, 1991. Included in each capsule are companion transmission electron microscopy (TEM) and SS-3 tensile specimens for correlation of microstructural, tensile, and fracture toughness properties.

PROGRESS AND STATUS

Introduction

Three fracture-toughness-specimen irradiation capsules are being fabricated and irradiated as part of the U.S./Japan collaborative program for testing fusion reactor candidate first-wall materials in mixed-spectrum fission reactors. The test specimens are being irradiated in HFIR target capsules designed' for 60-125°C and 250-300°C specimen temperatures.

These capsules accommodate 12.5-mm diameter stainless steel Disk-Shaped Compact DC(T) specimens of standard proportions: also, companion TEM and SS-3 tensile specimens are accommodated to permit correlation of microstructural, tensile, and fracture toughness properties. The capsules are uninstrumented and are intended to provide early irradiation data on low-temperature fracture toughness properties of candidate first-wall alloys. Spectral tailoring of the neutron flux is deemed unnecessary for the planned 2-cycle irradiation to a damage level of approximately 3 dpa. In the HFIR target region, helium production-to-atom displacement ratio in austenitic stainless steels in a short irradiation of 1 to 2 cycles is reasonably close to the ratio (14 appm/dpa) expected in a fusion reactor first wall.

60-125°C Capsules

Two uninstrumented low-temperature capsules of identical design, designated HFIR-MFE-JP-18 and HFIR-MFE-JP-19, were fabricated and under irradiation by the end of the report period. Each capsule contains 31 12.5-mm-diameter fracture toughness specimens, either a dummy fracture toughness specimen holding TEM specimens or a blank stainless steel specimen in its place, and 8 SS-3 tensile specimens; details of the test specimen loadings are given in Table 1. In addition to test specimens, each capsule contains six small melt-materials capsules for temperature monitoring and eight dosimetry capsules for neutron exposure and damage determination. These capsules are of the shrouded type with the fracture toughness specimens directly cooled on their flat faces hy downward-flowing reactor cooling water. Capsules JP-18 and JP-19 are being irradiated in HFIR target positions B-1 and E-7, respectively. Predicted temperatures over the crack region of the fracture toughness specimens range from approximately 60-85°C near the ends of the 50-cm test length to 65-125°C near the middle. The crack region is defined as the region of the specimen between radii of 0.14 and 0.41 cm; the postirradiation-testing crack surface is expected to be bounded by these radii.

The first cycle of the planned two-cycle irradiation of capsules JP-18 and JP-19 was completed on September 17, 1991, and the second cycle was started on September 27, 1991. Exposure for the first cycle, HFIR Cycle No. 300, was 1724 MWd, or approximately 20.3 days at 85 MW reactor power.

Table 1. Test specimen loadings in HFIR target capsules JP-18 and JP-19

Specimen position no.	Specimen type	Distance from specimen centerline to reactor core midplane (cm)	Specimen Identification	
			Capsule JP-18	Capsule JP-19
Top				
1	Fracture toughness	25.2	FF5	FF7
2	Fracture toughness	23.7	FA3	FA6
3	Fracture toughness	22.1	FC17	FC3
4	Fracture toughness	20.6	FM11	FM13
5	Fracture toughness	19.1	FL15	FL6
6	Fracture toughness	17.6	FK7	FK3
7	Dummy fracture toughness holding TEM specimens	16.0	FL-34, FL-40, FL-41, FL-50 FK-43, FK-44, FK-35, FK-51 FA-31, FA-33, FA-35, FA-42 FH-36, FH-41, FH-50, FH-53 FA-55, FA-56, FA-70, FA-71 FA-82, FA-90, FA-92, FA-97 FM-50, FM-51, FM-52, FM-53 FC-27, FC-28, FC-34, FC-35 FD-19, FD-20, FD-21, FD-22 FF-29, FF-30, FF-31, FF-32 FE-22, FE-23, FE-24, FE-25 FG-50, FG-51, FG-52, FG-53 11 unmarked TEM specimens of alloy EC 316 LN	No TEM specimens. (A blank stainless steel disk was installed in position No. 7 instead of a dummy fracture toughness specimen).
8	Fracture toughness	14.5	FR11	FR2
9	Fracture toughness	13.0	FH1	PH9
10	Fracture toughness	11.5	FE14	FE5
11	Fracture toughness	9.95	FD8	FD9
12	Fracture toughness	8.42	FG8	FG7
13	Fracture toughness	6.90	FF9	FF17
14	Fracture toughness	5.37	FB4	FB7
15	Fracture toughness	3.85	FA8	FA7
16	Fracture toughness	2.33	FC12	FC18
Reactor core	SS-3 Tensile (total of 8)	0	FD6T, FD8T, FF7T, FF9T FE17T, FE20T, FH3T, FH1T	FA23T, FA24T, FB19T,FB21T FC28, FC29, FL20T, FL17T
17	Fracture toughness	2.33	FC16	FC22
18	Fracture toughness	3.85	FA21	FA11
19	Fracture toughness	5.37	FB16	FB11
20	Fracture toughness	6.90	FF6	FF15
21	Fracture toughness	8.42	FG5	PO9
a	Fracture toughness	9.95	FD12	FD3
23	Fracture toughness	11.5	FE8	FE15
24	Fracture toughness	13.0	FH8	FH12
25	Fracture toughness	14.5	FR13	FR4
26	Fracture toughness	16.0	FS1	FS2
27	Fracture toughness	17.6	FK2	FK14
28	Fracture toughness	19.1	FL3	FL12
29	Fracture toughness	20.6	FM3	FM10
30	Fracture toughness	22.1	FC6	FC23
11	Fracture toughness	23.7	FA16	FA17
32	Fracture toughness	25.2	FF16	FF2

250-300°C Capsule

Parts for a single uninstrumented helium-filled elevated temperature capsule, designated HFIR-MFE-JP-17, were fabricated during this report period. Start of assembly is awaiting the results of additional neutronics calculations currently being made by the ORNL Research Reactors Dinsion to insure that the relatively large amount of stainless steel in this target capsule will not cause unacceptable neutron **flux** shifting and hot spots in the reactor fuel regions.

Capsule JP-17 will contain a stack of ***86*** 12.5-mm-diameter fracture toughness specimens (total of real specimens plus one or more dummy specimens holding TEM specimens and a few blank specimens) and 12 SS-3 tensile specimens, all within a tight-fitting aluminum cladding tube. **A** few of the stainless steel fracture toughness specimens near the ends of the 50-cm test length may be replaced by copper alloy and carbon specimens, This capsule is of the shrouded type and will be cooled by reactor cooling water flowing downward between the cladding tube and shroud tube. Capsule JP-17 will be irradiated in one of the **six** HFIR peripheral target positions; these positions accommodate slightly larger capsules than do the interior target positions. Thermal design of the capsule was described in the preceding progress report'.

The planned two-cycle irradiation of capsule JP-17 **is** scheduled to start by the end of November 1991.

FUTURE WORK

Completion of assembly and start of irradiation of capsule JP-17 **is** scheduled for November 1991

REFERENCES

1. **A.** W. Longest et al., "Design and Fabrication of HFIR-MFE-JP Target Irradiation Capsule," Fusion Reactor Materials Semiannu. Pron. Rept., March 31. 1991, DOE/ER-0313/10, U.S. DOE Office of Fusion Energy.

AN ATTEMPT TO REDUCE RADIOACTIVITY FOR ENERGY-DISPERSIVE X-RAY ANALYSIS·

S. Hamada (Japan Atomic Energy Research Institute)

OBJECTIVE

To develop a specimen preparation technique which reduces the intensity of radioactivity of a neutron-irradiated materials for microchemical analysis by analytical electron microscope (AEM) with energy dispersive X-ray spectroscopy (EDXS).

SUMMARY

A composite specimen preparation technique for the AEM was developed using unirradiated materials. The technique reduced the mass of material from a dummy irradiated specimen by more than a factor of 100. A I-mm diam. disk was punched from a dummy irradiated 3-mm diam. transmission electron microscope (TEM) disk. The 1-mm disk was then pressed into a hole previously punched at the center of a second 3 mm diam. disk creating a composite disk. The composite disk was electropolished using a twin jet Tenupol until the thickness of the center of the composite was about 100 μm. Approximately 100 μm of nickel plating was then deposited on the surface of the thinned composite. Standard electropolishing by Tenupol unit was performed on the nickel-plated composite specimen and the composite specimen was examined by TEM.

PROGRESS AND STATUS

The observation and characterization of the microstructure and microchemistry which result from phase transformations and damage produced during irradiation play important roles in understanding the subsequent macroscopic material properties. Without such information one can not logically proceed with the systematic development of candidate alloys for the various nuclear energy applications.

Analytical electron microscopy is often employed to observe and characterize the morphology, crystallography and microchemistry of small regions of a specimen. However, it is difficult to apply AEM to irradiated materials because the gamma-radiation emitted from the specimen itself interferes with compositional analysis by EDXS.

Attempts to apply an AEM and EDXS to highly radioactive specimens have been made. These attempts can be divided into two categories: methods which reduce the intensity of radioactivity that reaches the X-ray detector by using a lead-shielded collimated X-ray detectors[1,2] and methods which reduce the volume of radioactive material.[3,4] The former method is not as generally applicable and requires modification of the microscope and EDXS system. Therefore, the philosophy of the latter method was adopted in this work. Two techniques have been previously applied to reduce the volume of material. One technique is to mechanically press a 1 mm diam. disk of radioactive material in to an annulus of unirradiated material and then electropolish the "composite" in a conventional manner.3 The disadvantage of this technque is that electropolishing tends to produce cavities during electropolishing at the interface between the disk and the annulus. Another technique is to bond the 1 mm diam. disk to a 3 nun diam. by electroplating with nickel which produces a stronger bond between the radioactive material and its substrate.4 The disadvantages of this techique are that the long electroplating time required to deposit a sufficient thickness of nickel-plating and dimpling in the irradiated material. In the present work, the disadvantages of each technique are overcome by combining both techniques to prepare samples with reduced radioactivity.

ExDerimental Results

Two unirradiated standard TEM specimens (3 mm diam. x 0.25 mm thick) type 316 stainless steel were used in this study. One specimen was treated as radioactive dummy while the other was assumed to be unirradiated. A 1 mm diam. disk was punched from the dummy radioactive 3 mm disk

using die punch and was pressed into a 1 nun diam. hole of the "unirradiated" annulus. Figure 1 shows the specimens used in this study and the resulting composite specimen. The punched 1 mm diam. disk did not exhibit bulging or bending except at the edges.

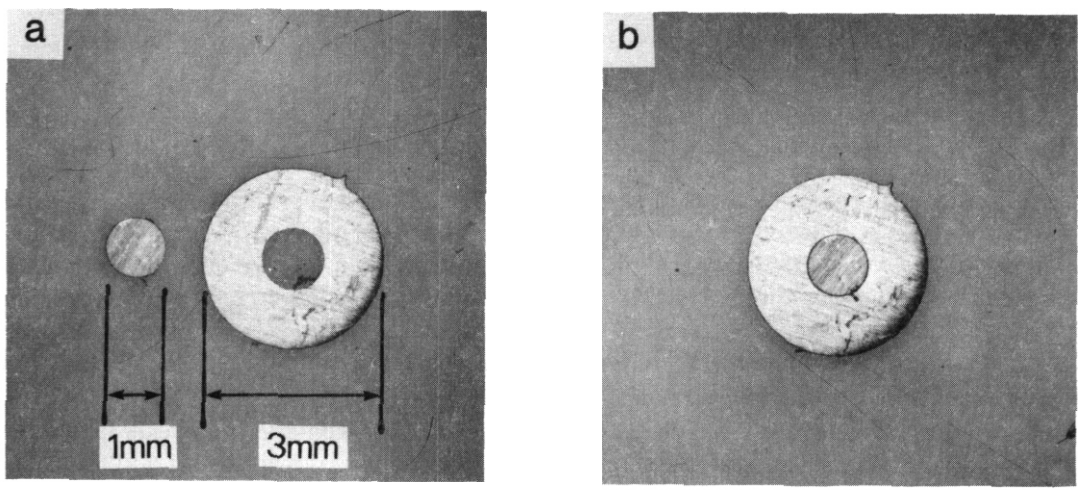

Fig. 1. Shape of the specimen used in this experiment. (a) 1mm diam disk specimen (left) and an annulus with 1 mm diam perforation (right); (h) composite disk.

The composite was electropolished with 5% perchrolic acid in acetic acid at 15°C with 70 V (200 mA) in a twin-jet Tenupol unit until the thickness of the center area of the composite was approximately 100 µm. A standard Tenupol 3 mm diam. specimen holder with 1 mm jet cathodes was used. Nickel plating was deposited on the partially polished composite to produce a stronger bond between the 1 nun diam. disk and annulus and to prevent cavitation of the disk/annulus junction during thinning. The thickness of the nickel plating deposited on the partially-thinned composite was approximately 100 µm. The nickel plating rate was estimated from weight change measurements to be about 1 µm per minute. Details of the nickel plating technique have been described elsewhere.5 After nickel plating for 120 minutes, the interface of the composite was thicker than that on the rest of the specimen as shown Fig. 2(a). A schematic cross-section of the nickel-plated thinned, composite disk is shown in Fig. 2(b). The nickel-plated composite specimen was then electropolished to perforation using a standard Tenupol unit using the same conditions as given above (Fig. 3).

In order to evaluate the degree of reduction of the intensity of radioactivity by this procedure, an ordinary TEM disk specimen (3 nun diam.) and a 1 mm diam. disk thinned by electro-polishing were weighed. The results indicated that this preparation technique could reduce the volume and, thus, intensity of radioactivity of a TEM specimen to below 1% of that of as-irradiated one. Further, as another application of this procedure, high resolution TEM observation of ferritic steels was also investigated. Conventional TEM of a ferritic steel will not usually permit either high-resolution observation or kinematical diffraction condition due to shift of electron-beam through the strong magnetic field in the ferritic steel. A special transmission electron microscope with an anti-magnet pole piece is often employed to reduce the influence of magnetic field through ferritic steels to image ferritic steels. However, high-resolution observation through such microscopes is difficult. To observe ferritic steels with higher resolution and to reduce the influence of magnetic field using high resolution TEM, it is also desirable to prepare a small volume specimens similar to radioactive material. Fig.4 shows a typical micrograph of a ferritic steel observed with high magnification and under kinematic conditions.

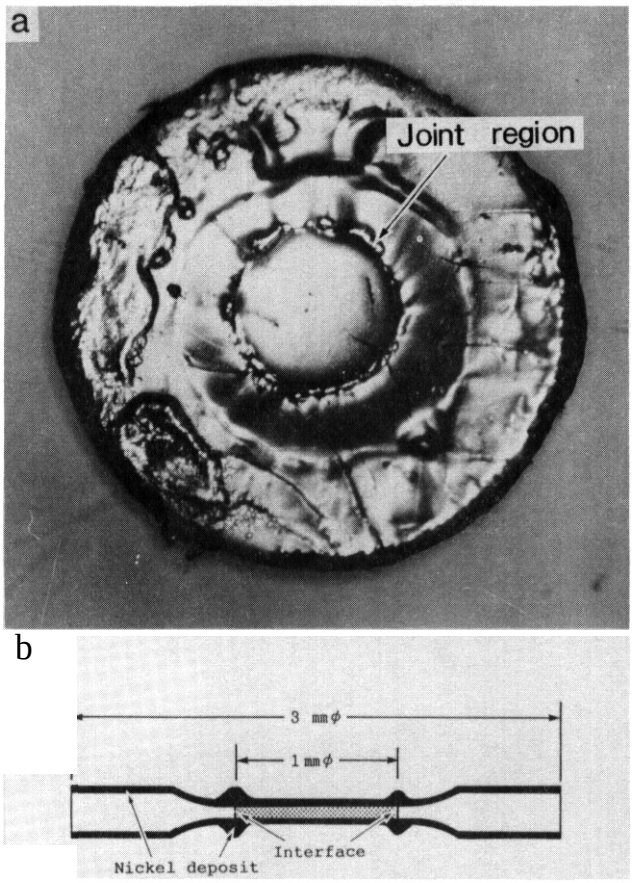

Fig. 2. (a) Surface of a nickel-plated composite after electropolishing; (h) schematic cross section of specimen shown in Fig. 2(a).

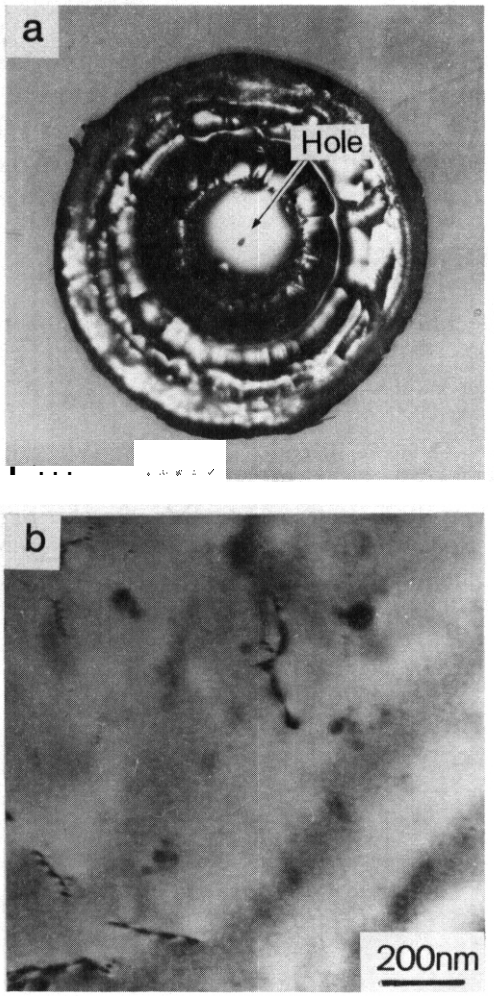

Fig. 3. Thinned TEM disk of solution-annealed type 316 stainless steel after final jet polishing. (a) TEM composite disk. (b) Microstructure observed in disk shown in (a).

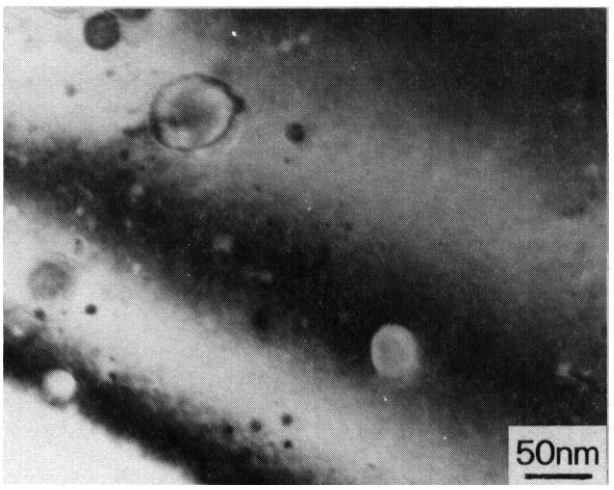

Fig. 4. (a) Typical micrograph of oxide dispersive steel (ODS) including fine oxide particles such as Y_2O_3 and TiO_2 (direct observation magnification 100,000×; tilt angle 20°).

Conclusion

A technique to reduce the intensity of radioactivity of a neutron-irradiated TEM specimen for energy dispersive X-ray analysis was developed. The TEM specimen preparation procedure developed may reduce the volume and. thus. the intensity of radioactive material in a TEM specimen to below 1% of that in the as-irradiated condition. This method may also allow high resolution observation of ferritic steel specimens in standard transmission electron microscopes.

FUTURE WORK

This technique will be applied to radioactive specimens.

References

1. **N.J.** Zaluzec, Introduction to Analytical Electron Microscopy **(PLENUMPRESS.** NEW YORK. 1979)pp.121.
2. K. Farrell, J. Bentley and D.N. Braski, Scripta Met. ,11(1977)243.
3. P.K.Rose and J. Rowe, J.of Material Science, 22(1987)3771.
4. S. Dumbill and W.C. Fuller. YKAEA Reoort AERE M 3640(1987).
5. S. Hamada. M. Tanaka and K. Shiraishi, J.Nucl.Mater. ,114(1983)338

2.0 DOSIMETRY, DAMAGE PARAMETERS AND ACTIVATION CALCULATIONS

HELIUM GENERATION RATES IN ISOTOPICALLY TAILORED FE-CR-NI ALLOYS IRRADIATED IN FFTF/MOTA L.R. Greenwood, F.A. Garner, Pacific Northwest Laboratory[a], and B.M. Oliver, Rockwell International.

OBJECTIVE

To investigate the effects of the neutron spectrum on mechanical property changes in metals

SUMMARY

Three Fe-Cr-Ni alloys have been doped with 0.4% ^{59}Ni for side-by-side irradiations of doped and undoped materials in order to determine the effects of fusion-relevant levels of helium production on microstructural development and mechanical properties. The alloys were irradiated in three successive cycles of the Materials Open Test Assembly (MOTA) located in the Fast Flux Test Facility (FFTF). Following irradiation, helium levels were measured by isotope dilution mass spectrometry. The highest level of helium achieved in doped alloys was 172 appm at 9.1 dpa for a helium(appm)-to-dpa ratio of 18.9. The overall pattern of predicted helium generation rates in doped and undoped alloys is in grod agreement with the helium measurements.

PROGRESS AND STATUS

Introduction

Fusion reactors will produce significant levels of helium in materials due to (n,α) reactions with 14 MeV neutrons. For iron-based engineering alloys, helium will be produced at a rate of about 10 appm per atomic displacement (dpa). Concern has been raised that these elevated helium levels will affect the evolution of microstructural damage and thereby affect mechanical properties. Irradiations in fast reactors generally produce helium at levels which are 10% or less than those of fusion levels. Consequently, techniques have been devised to elevate helium production to simulate fusion reactor conditions.

In the present experiment, Fe-Cr-Ni alloys were doped with 0.4% of ^{59}Ni [1] which has a high (n,α) cross section for low-energy neutrons. The addition of natural nickel is a well-known technique for elevating helium production in mixed-spectrum reactors due to the $^{58}Ni(n,\gamma)^{59}Ni(n,\alpha)$ sequential reaction[2]. However, unlike the present experiment, time is required for the burn-in of ^{59}Ni before helium production becomes significant. This delay in helium production in mixed-spectrum reactors may impact the experiment strongly, especially 'during the incubation phase of microstructural development.

In a recent series of papers on the use of ^{59}Ni isotopic doping, it has been shown that single-variable comparisons of the effect of helium at fusion-relevant generation rates do not support a significant role for helium in determining the tensile properties of simple austenitic alloys [3-6]. This is in contrast to the results of comparative irradiation studies conducted at significantly different displacement rates [7-9] or at helium generation rates significantly higher than that of anticipated fusion environments[8,9].

Experimental Measurements

Three alloys were prepared for the present irradiations, namely Fe-15Cr-25Ni, Fe-15Cr-25Ni-0.04P, and Fe-15Cr-45Ni. In each case, some of the alloy was doped with 1.98% ^{58}Ni and some was left undoped using only natural nickel[1]. The ^{59}Ni content was 1.58% for Fe-15Cr-25Ni and Fe-15Cr-25Ni-0.04P, and 0.88% for Fe-15Cr-45Ni. For the purposes of this study, the small addition of phosporous is insignificant and shall be ignored. The alloys were then irradiated in three successive experiments in the MOTA position of the FFTF. Samples were originally placed in five different levels of the MOTA-ID subassembly at temperatures between 365-600°C. This experiment lasted for 185.8 EFPD from August 17, 1985, to July 19, 1986, at a power level of 400 MW. After irradiation, these alloys and additional unirradiated alloys were inserted into MOTA-1E from September 10, 1986, to September 10, 1987, attaining 341.8 EFPD at 291 MW. Following this, two sets of alloys were additionally irradiated in MOTA-1F from November 18, 1987, to January 8, 1989, reaching 335.4 EFPD at 291 MW. Irradiations further continued in MOTA-1G; however, these samples were removed from the reactor on March 19, 1991, and their helium levels have not yet been analyzed. Details of these irradiations are discussed further in reference 10.

Following irradiation, samples of the various alloys were analyzed for their helium content at Rockwell International's Rocketdyne Division. The measurements were performed using a specialized gas mass spectrometer system [11]. Each sample was prepared by cutting two "quarter" specimens from each original transmission electron microscope (TEM) disk. The specimens were then acid-etched to remove the outer ~0.02

(a) Pacific Northwest Laboratory is operated for the U.S. Department of Energy by Battelle Memorial Institute under Contract DE-AC06-RLO 1830.

to 0.04 mm of surface to eliminate any corrections for alpha-recoil effects. Final specimen masses ranged from 2 to 3 mg.

Each of the helium analyses involved vaporizing the specimen in a resistance-heated graphite crucible in one of the mass spectrometer systems' high-temperature vacuum furnaces, and then measuring the ^4He released relative to a known quantity of added ^3He spike (isotope dilution method). The helium spikes were obtained by expanding and partitioning a known quantity of ^3He gas through a succession of accurately calfbrated volumes [12]. The mass sensitivity was determined by analyzing various combinations of ^3He and ^4He spikes. Mass discrimination for ^3He and ^4He was typically 1.5. Measured helium values ranged from $\sim 2 \times 10^{12}$ to $\sim 6 \times 10^{15}$ atoms.

The results of the helium measurements, in terms of helium concentration, are summarized in Table 1, which also lists the position in the reactor, dpa, and ^{59}Ni doping conditions. Conversion from total measured helium to helium concentration was based on the specimen mass and on atom concentration values determined for each alloy ($\sim 1.07 \times 10^{22}$ atoms/g). The helium concentration values in Table 1 represent average values for the duplicate analyses conducted on each sample. The uncertainty following each value represents the total estimated (1σ) uncertainty. Average reproducibility between the duplicate helium analyses was 0.9%.

The dpa calculations were performed with the SPECTER computer code[13]. Note that the quoted dpa values are alloy-dependent. For example, in the below-core basket, the Fe-15Cr-45Ni alloy received 9.1 dpa during cycles 1D and 1E while the Fe-15Cr-25Ni alloy received only 8.6 dpa. This difference is due to the higher dpa rate for nickel than iron. Both of these alloys have higher dpa rates than pure iron or stainless steel.

Helium Calculations

The production of helium from ^{58}Ni is determined by the following expression:

$$\frac{N(He)}{N_o(^{58}Ni)} = \frac{\sigma_\alpha [\sigma_T(1-e^{-\sigma_T\phi t}) - \sigma_\gamma(1-e^{-\sigma_T\phi t})]}{\sigma_T(\sigma_T-\sigma_\gamma)} \qquad (1)$$

where $N(He)$ = helium atoms produced at time t
$N_o(^{58}Ni)$ = initial number of ^{58}Ni atoms
σ_α = $^{59}Ni(n,\alpha)$ cross section
a = ^{59}Ni total absorption cross section
a_γ = $^{58}Ni(n,\gamma)$ cross section
ϕ = total neutron flux
t = irradiation time

Equation 1 applies to all irradiations with nickel, including the undoped alloy, and should be further multiplied by 0.683 to account for the abundance of ^{58}Ni. However, in fast reactors, the main source of helium is due to threshold (n,α) reactions with all isotopes of nickel, iron, and chromium. These threshold reactions are assumed to produce helium by a linear product of the cross section times the neutron fluence. Although one usually associates the $^{58}Ni(n,\gamma)^{59}Ni(n,\alpha)$ two-step reaction with thermal neutrons, the epithermal flux in fast reactors is large enough to produce significant levels of helium.

In the case of ^{59}Ni doping, equation 1 simplifies to the following equations:

$$N(^{59}Ni) = N_o(^{59}Ni)\, e^{-\sigma_T\phi t} \qquad (2)$$

$$N(He) = N_o(^{59}Ni)\, \frac{a_\alpha}{\sigma_T}(1-e^{-\sigma_T\phi t}) \qquad (3)$$

The first equation above incorporates the burn-up of ^{59}Ni, which was as high as 30% in the present irradiations. Neutron cross sections for the (n,α), (n,p), and (n,γ) reactions from ^{59}Ni and for the (n,γ) reaction from ^{58}Ni were taken from the ENDF/B-V evaluation[14]. The burn-up cross section was taken as the sum of the three reaction cross sections for ^{59}Ni. Previously, we have published data showing that these equations and neutron cross sections give excellent agreement with helium measurements in mixed-spectrum reactors[14]. Displacement damage calculations and helium production from natural nickel, chromium, and iron were provided by the SPECTER computer code.[14] There is also a small increase in displacement damage due to the energetic (340 keV) ^{56}Fe recoils from the $^{59}Ni(n,\alpha)$ reaction (i.e. additional dpa = helium(appm)/567) [2]. This dpa enhancement has been included in the calculations for both doped and undoped specimens; however, the maximum difference is only 0.2 dpa for any of the irradiated alloys.

In order to adequately calculate helium production for these experiments, it is essential to have measurements of the neutron fluence and energy spectra. Unfortunately, dosimetry data have not been completely analyzed for all of these irradiations. Hence, it was necessary to rely on neutron flux and spectral calculations to fully map the helium production in the MOTA; such calculated neutron spectra were available from cycle 9A [15]. Both fluence gradient and neutron spectral measurements were performed for

selected locations in the MOTA-1E and MOTA-IF experiments [16]. Comparison between the calculations and dosimetry measurements supports the validity of the calculations. Such comparisons show generally good agreement between dosimetry and calculations for in-core positions: however, the dosimetry measurements are consistently higher than calculations for above-core and below-core positions.

Thus it is not expected that the present calculations will give an exact fit to the helium data. Rather, the intent is to show that we can generally describe the data and more importantly predict the behavior of helium generation in doped and undoped alloys throughout the MOTA assembly.

Helium Production Calculations for FFTF/MOTA

Helium production calculations are illustrated in Figure 1 for Fe-15Cr-45Ni as a function of axial location in the MOTA assembly after completion of the MOTA-IE and MOTA-IF irradiations (677.2 EFPD at 291 MW). The bottom curve shows helium production for the undoped alloy and the top curve includes the enhanced helium from the ^{59}Ni-doped alloy. There is some additional helium even in the undoped alloy due to burn-in of ^{59}Ni from ^{58}Ni(n,γ). The undoped alloy helium production curve is similar in shape to that of the neutron fluence or dpa curves, although there is a bulge in the below-core region caused by the burn-in of ^{59}Ni. The helium production from the ^{59}Ni-doped alloy more clearly shows the effects of the changing neutron spectrum. Outside the FFTF core region (-45 to t45 cm) there is a rapid increase in epithermal neutrons, resulting in an increase in helium production. The maximum helium production occurs in the below core basket (-70 to -55 cm). The helium production curve is not axially symmetric due to differing distributions of steel supports and sodium coolant.

The peculiar axial dependence of the helium production from ^{59}Ni-doping enhances the variation of the He(appm)-to-dpa ratio as a function of axial location, as shown in Figure 2. In-core, the He/dpa ratio about doubles as a result of the doping. However, the ratio climbs to fusion-like values of 10-18 for out-of-core positions for the doped alloy. Note that the undoped alloy curve also shows a slight increase below core due to the buildup of ^{59}Ni from ^{58}Ni.

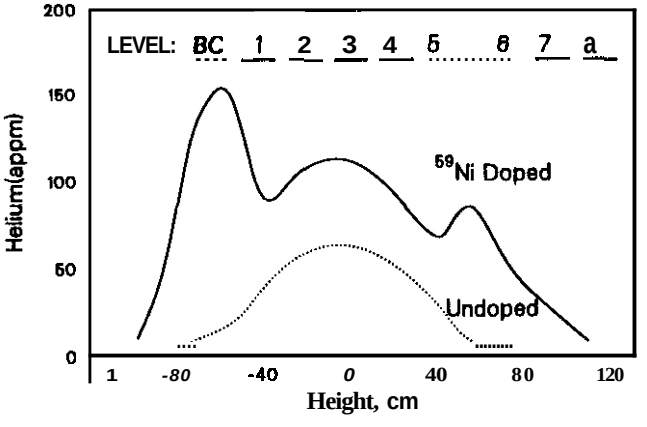

Figure 1. Helium production (appm) for both the ^{59}Ni-doped and uadoped Fe-15Cr-45Ni alloy as a function of height in the MOTA assembly after the 1E and 1F irradiation.

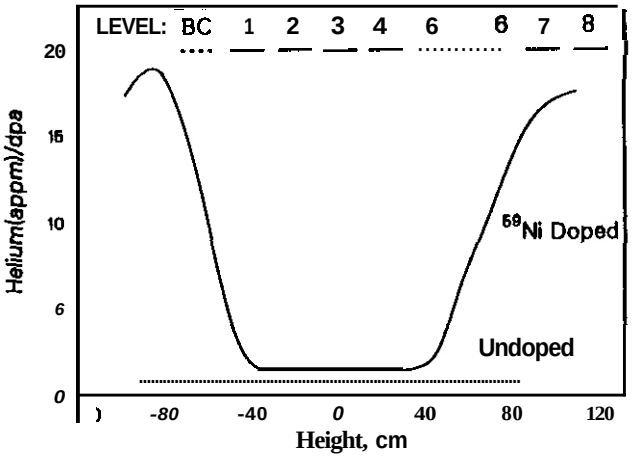

Figure 2. Helium(appm)-to-dpa ratios for both the ^{59}Ni-doped and undoped Fe-15Cr-45Ni alloy as a function of height in the MOTA assembly after the 1E and 1F irradiation.

Figure 3 shows the time dependence of the helium-to-dpa ratio at the midplane of the FFTF/MOTA in both the doped and undoped alloys. The small but steady increase in both ratios is due to the burn-in of ^{59}Ni, an effect that is often neglected when calculating helium generation in fast reactor experiments. It is also evident from Figure 3 that at midplane much higher ^{59}Ni doping levels would be needed to significantly increase helium production. Fusion-like He/dpa levels would require ^{59}Ni doping of 10-15%, which would be difficult to produce or handle. Fig
ure 4 shows the time-dependent helium production in the below-core basket of the MOTA. Because of the higher flux of epithermal neutrons, there is a clear decrease in the helium/dpa ratio for the doped alloy due to burnup of ^{59}Ni and a much sharper percentage increase in the ratio for the undoped alloy due to burn-in of ^{59}Ni.

Comoarison of Helium Measurements and Calculations

Helium measurements and calculations are compared in Table I. These data span four different reactor positions; two different alloys, both doped and undoped; and irradiations in various FFTF reactor cycles. Radial flux gradients were ignored for the present calculations: however, calculations show that the flux varies by about 8% across the MOTA subassembly [15]. We should also note that recent calculations indicate that the presence of various moderating materials or highly neutron absorbing materials in the MOTA can

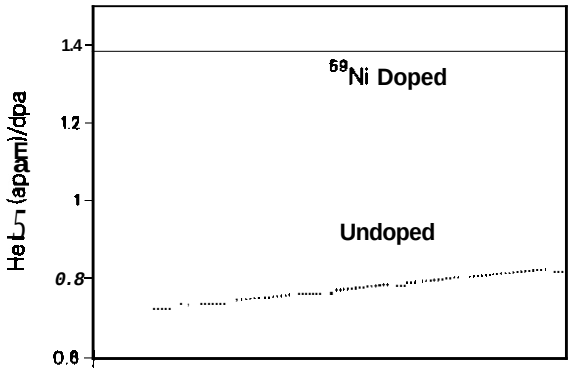

Figure 3. Helium/dpa ratio vs. dpa for both the ^{59}Ni-doped and undoped Fe-15Cr-45Ni alloy near the midplane (+2.6 cm) of the MOTA assembly.

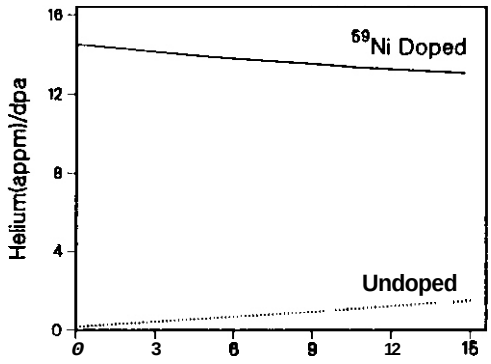

Figure 4. Helium/dpa ratio vs. dpa for both the ^{59}Ni-doped and undoped Fe-15Cr-45Ni alloy in the below core basket (-65.9 cm) of the MOTA assembly.

data [16,17,18] indeed shows that the calculated flux at -66 cm is low by about 20-30%. This difference is in good agreement with the C/M ratios near 0.75 for the below-core position. Similarly, dosimetry data at +123 cm is about 25-50% higher than calculated for level *8;* this would explain the low C/M ratios of 0.34-0.41 found for this position,

The present calculations and their agreement with the currently available helium data, support the model of helium production in both doped and undoped alloys and indicate that helium levels for the in-csre irradiation positions can be accurately predicted. However, at present, uncertainties in the neutron spectra limit our ability to predict helium production for out-of-core positions. Consequently, it is essential that accurate helium measurements be performed for these experiments so that we can properly account for helium effects and correlate property changes accordingly. Similarly, neutron dosimetry measurements must be pursued in order to fully define the energy spectrum in all positions of the MOTA. This will be particularly important for out-of-core positions that are finding increasing use for fusion materials irradiations.

FUTURE WORK

Work currently in progress for MOTA-2A includes complete neutron spectral measurements for all levels of the MOTA. Analysis of these data will provide a more complete picture of the uncertainties in the neutron energy spectra: such information will also be applicable to previous MOTA irradiations. Additional helium measurements are also planned for the MOTA-1G irradiation, which was concurrent with the MOTA-2A experiment.

REFERENCES

1) R. L. Simons, H. R. Brager, and W. Y. Matsumoto, J. Nucl. Mater., 141-143 (1986) 1057-1060.

2) L.R. Greenwood, J. Nucl. Mater., 115 (1983) 137-142.

3) M. L. Hamilton and F. A. Garner, these proceedings.

3) F. A. Garner, M. L. Hamilton, R. L. Simon and M. K. Maxon, J. Nucl. Mater., 179-181 (1991) 554-557.

5) J. F. Stubbins and F. A. Garner, J. Nucl. Mater., 179-181 (1991) 523-525.

6) H. Kawanishi, F. A. Garner and R. L. Simons, J. Nucl. Mater., 179-181 (1991) 511-514.

7) A. F. Rowcliffe, A. Hishinuma, M. L. Grossbeck and S. Jitsukawa, J. Nuci. Mater., 17Y-181 (1991) 125-129.

8) M. L. Hamilton, A. Okada and F. A. Garner, J. Nucl. Mater., 179-181 (1991) 558-562.

9) N. Sekimura, F. A. Garner and R. D. Griffin, these proceedings.

10) M. L. Hamilton, F. A. Garner, and B. M. Oliver, Fusion Reactor Materials Semiannual Progress Reuort, DOE/ER-0313/9 (1990) 61-68.

11) H. Farrar IV and B.M. Oliver, J. Vac. Sci. Technol. A4 (1986) 1740.

12) B. M. Oliver, J. G. Bradley, and H. Farrar IV, Geochim. Cosmochim. Acta 48 (1984) 1759.

13) L. R. Greenwood and R. K. Smither, ANL-FPP/TM-197 (1985).

14) L. R. Greenwood, D. W. Kneff, R. P. Skowronski, and F. M. Mann, J. Nucl. Mater. 122-123 (1984) 1002-1010.

15) R. L. Simons, Westinghouse Hanford Company, private communication (1990).

16) L. R. Greenwood, Fusion Reactor Materials Semiannual Progress Report, DOE/ER-0313/9 (1990) 31-36.

17) R. L. Simons, Damage Analysis and Fundamental Studies Ouarterly Progress Reuort, DOE/ER-0046/21 (1985) 10-14.

18) L. S. Kellogg, W. N. McElroy, and W. Y. Matsumoto, private communication (1989).

HELIUM PRODUCTION RATES IN THE LASREF FACILITY - W. F. Sommer, (Los Alamos National Laboratory), B. M. Oliver, (Rockwell International Corporation), and F. A. Garner, (Battelle, Pacific Northwest Laboratory*)

OBJECTIVE

The objective of this study is to determine the helium generation rates produced in the Los Alamos Spallation Radiation Effects Facility (LASREF).

SUMMARY

Foils of Cu, Lo, Fe and Ni were irradiated in LASREF. The flux was determined by measurement of the gamma ray intensities induced by transmutation. The induced helium levels were measured by an isotope dilution mass spectrometry method. For copper the helium/dpa ratio was found to be 11.1 appm/dpa, which is ~40% of the rate predicted by an earlier calculation.

PROGRESS AND STATUS

Introduction

A review of the Los Alamos Spallation Radiation Effects Facility (LASREF) was recently conducted by members of the U.S. fusion material, community to assess the feasibility of using LASREF to meet various program goals.[1] One action item that emerged from that meeting was a request that dosimetry and helium analysis be performed on a set of foils that had recently been irradiated in one of the rabbit tubes.

Experimental Details

The specimens were in the form of TEM disks (3 mm diameter and varying in thickness from ~0.05 to 0.13 mm) and were prepared from sheet foil of pure Cu, Co, Fe and Ni. These were irradiated in the second inboard rabbit tube in the beam stop region of the tos Alamos Meson Physics Facility. The foils were cut in half sections, one half to be used for measurement of neutron flux and spectra via measurement of gamma-ray energies and intensities and the other half to be sent to Rockwell International for determination of helium levels.

Prior to helium analysis, the specimens were etched to remove ~0.013 mm of surface material, cut in half and weighed. The etching was performed to ensure that only bulk material was analyzed, unaffected by surface losses of alpha particles or by gains by implantation from adjacent specimens.[2] The helium content was determined on duplicate !half-specimens by isotope-dilution mass spectrometry using a procedure described previously.[3,4] The full details of the current analysis are contained in reference 5.

Results and Discussion

The measured helium concentrations are shown in Table 1 and range from 0.097 appm fnr cobalt and 0.152 appm for nickel. Analysis of the gamma ray intensities vas used to prqvide input to the spectral fitting code STAY'SL.[6] This yielded an average total flux of 4.0 X 10^{12} n cm^{-} sec^{-1}. Table 2 presents some details of the neutron spectrum.

The damage level in copper was calculated to be 0 011 dpa, using energy-dependent displacement cross sections determincd by Wechsler and coworkers.[7] 'Displacement values for the other three elements have not yet been calculated. For copper, this yields a helium generation rate of 11.1 appm/dpa. This value is ~40% of the 0.31 appm and 28.2 appm/dpa values estimated earlier by Wechesler and coworkers for copper.

The helium generation rate found for copper in LASREF is much closer to that calculated for various fusion spectra than is that found in fast reactors where most radiation experiments on copper are conducted. In the STARFIRE spectra, the rate is 7.0 appm/dpa, while in EBR-II (row 7 midplane) and FFTF (MOTA midplane) it is 0.080 and 0.042 appm/dpa, respectively.[8]

FUTURE WORK

Foils from another irradiation experiment that spanned all four rabbit positions will be analyzed to obtain the displacement profile and helium generation profiles across the rabbit facility.

REFERENCES

1. D. G. Doran, Report of the LASREF Evaluation Committee, Pacific Northwest Laboratory Report PNL-SA 18584, July 1990.

* Operated for the U.S. Department of Energy by Bactelle Memorial Institute under Contract DE-AC06-76RLO 1830.

2. D. W. Kneff et al., "The Use of Helium Accumulation Neutron Dosimetry to Characterize the LAMPF Radiation Effects Facility Neutron Environment," Enclosure to Rockwell Letter 81ESG-985, February 3, 1981.

3. Harry Farrar IV and B. M. Oliver, "A Mass Spectrometer System to Determine Very Low Levels of Helium in Small Solid and Liquid Samples," J. Vac. Sci. Techno. A4, 1740 (1986).

4. B. M. Oliver, J. G. Bradley, and Harry Farrar IV, "Helium Concentration in the Earth's Lower Atmosphere, " Geochim. Cosmochim. Acta 48, 1759 (1984).

5. B. M. Oliver, Helium Analysis of LAMPF Foils, Rockwell International Report, 91RC06410, August 26, 1991.

6. F. G. Perey, Oak Ridge National Laboratory Report ORNL-TM-6062 (1977).

7. M. S. Wechsler, O. R. Davidson, L. R. Greenwood and W. F. Sommer, ASTM STP 870, (1985), pp. 1189-1198.

8. L. R. Greenwood, private communication of results of SPECTER code

Table 1

Specimen	Specimen Mass' (mg)	'He Measured (10^{12} atoms)	Helium Concentration (appm)	
			Measured	Averaged[c]
Fe-A	1.207	1.408	0.1082	0.110
-B	1.172	1.411	0.1117	±0.002
Ni-A	0.593	0.9327	0.1533	**0.152**
-B	0.622	0,9669	0.1513	±0.001
Cu-A	1.474	1.694	**0.1213**	0.122
-8	1.643	1.904	0.1223	±0.001
Co-A	0.313	0.3053	0.09544	0.097
-B	0.660	0.6616	0.09808	±0.002

tlux and Spectra for Rabbit 2 Experiment	
Energy, E	Integral Flux Above Energy E, $n/cm^{-2}\ s^{-1}$
E > 20 MeV	2.9×10^{11}
E > 0.1 MeV	2.1×10^{12}
Total	4.0×10^{12}

Neutron Activation Analysis of Monolithic Ceramics and Ceramic Composites- Lance L. Snead, Oak Ridge National Laboratory.

OBJECTIVE

The purpose of this work is to identify the impurity elements which dominate the neutron induced radioactivity in selected ceramics and ceramic composites.

SUMMARY

Several ceramics and ceramic composites of interest for fusion reactors have been irradiated and the isotopes responsible for the induced activity identified. Twenty six isotopes were positively identified and the activity of each measured. The two isotopes which have the combination of highest activity and the longest half life are ^{110m}Ag and ^{60}Co. The possible sources of the impurities are briefly discussed.

PROGRESS AND STATUS

Introduction

The neutron activation characteristics of pure ceramics make them very attractive for application in fusion reactors.[1-3] If such materials could be used to the exclusion of metallic alloys in fusion reactors, long term waste disposal benefits as well as ease of maintenance could be achieved. This is shown graphically in Fig. 1 a-d. Figure 1 a gives the induced activity for pure materials subjected to a STARFIRE first wall flux to a neutron wall loading of 1 MW/m^2. Figure 1 b gives the specific dose rate associated with these materials at a distance of 1 meter. It is apparent from Fig. l b that there is an advantage to utilizing materials which are made up of elements which age generally found in ceramic materials. Figure 1 c-d show the induced activities and dose rates for several ceramic compounds of interest for fusion applications as well as type 316 stainless steel.

Figure 1d includes both monolithic ceramic materials and some commercially available continuous fibers (Nicalon and Nextel) which would be used in ceramic matrix composites. Nicalon is primarily silicon carbide but has 20% SiO_2 and 10% excess carbon while Nextel is mainly Mullite with additions of B_2O_3. From Fig. 1d it is apparent that in a matter of minutes the dose rate associated with all but the alumina and Nextel fall orders of magnitude below the SS 316. The aluminum content in both the alumina and Nextel dominates the activity and within a matter of days the associated dose rate also falls well below the stainless.

Several design4 studies have proposed the use of the CVD SiC/Nicalon composite system for use as the major fusion reactor structural material. These materials are seen to perform extremely well. decaying to the point where actual hands-on maintenance could be employed within days of reactor shutdown. However, even if large ceramic components of fusion systems could be engineered, impurities inherent in the ceramics will dominate the activity. This negates the benefit of the low activity base material. It is the purpose of this work to identify the impurity isotopes occurring in present day ceramic materials so that their concentration can be reduced and the true activity levels associated with the application of ceramics in fusion reactors can be realized.

Experimental

Monolithic ceramic and ceramic composite samples were obtained from various sources. The monolithic ceramics were in the form of 3 mm discs and were irradiated in the ORR reactor. The composite materials had been fabricated for bend bars or brittle ring testing and had been irradiated either in the HFIR or FFTF reactors. A PGT High Purity germanium detector was used with a Nuclear Data counting system. The detection system was preset to 0.5 KeV/channel with an energy tolerance for data manipulation of 1 KeV. In order for an isotope to be positively identified all major lines with proper relative intensities had to be present above background. The major energy lines and intensities used for the isotope identification are given in Appendix A.

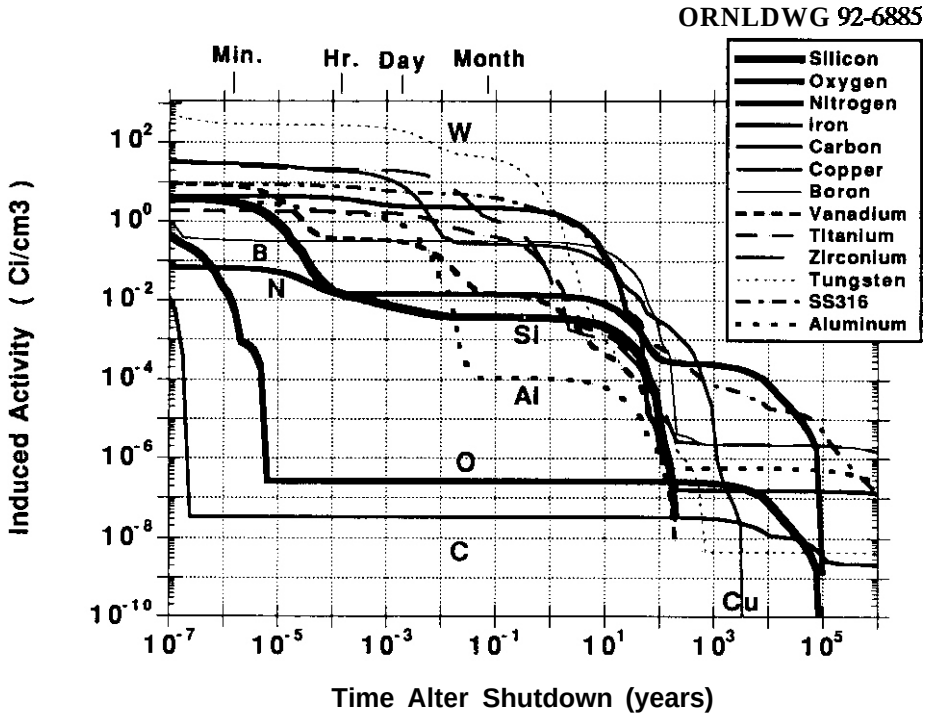

Figure Ia: Induced activity for pure materials subjected to 1 MW-Yr/m^2 Stariire first wall spectrum

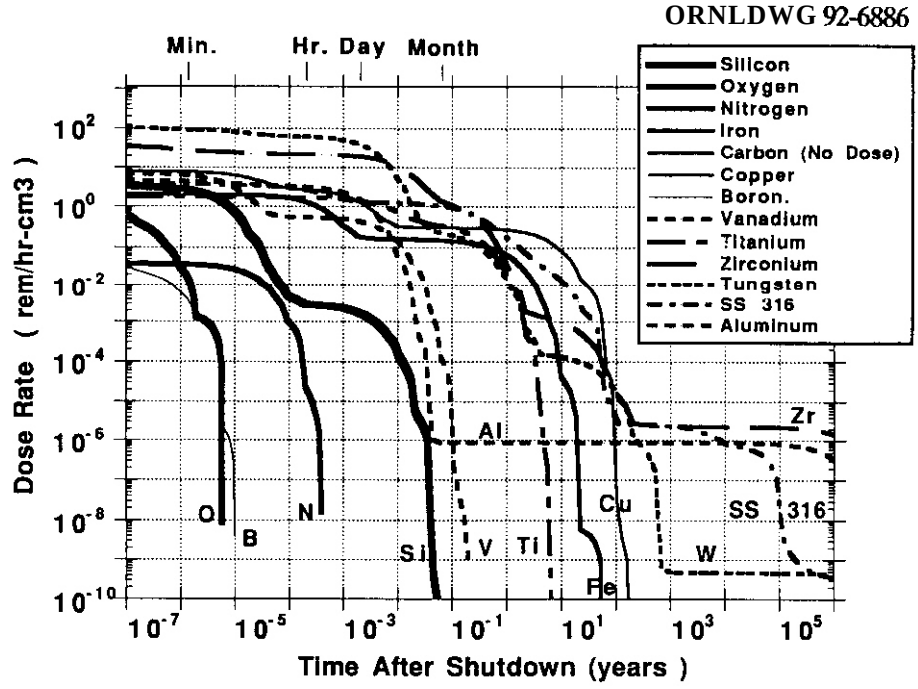

Figure Ib: **Dose** Rate for pure materials subjected to 1 MW-Yr/m^2 Starfire first wall spectrum.

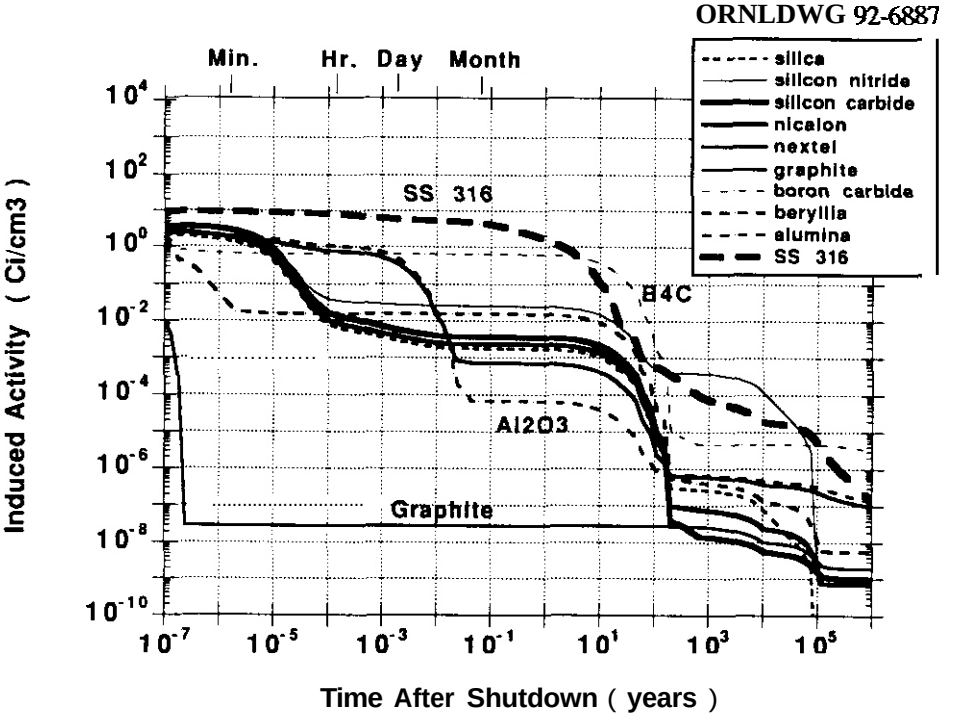

Figure 1c: Induced Activity for select compounds subjected to 1 MW-Yr/m^2 Starfire first wall spectrum.

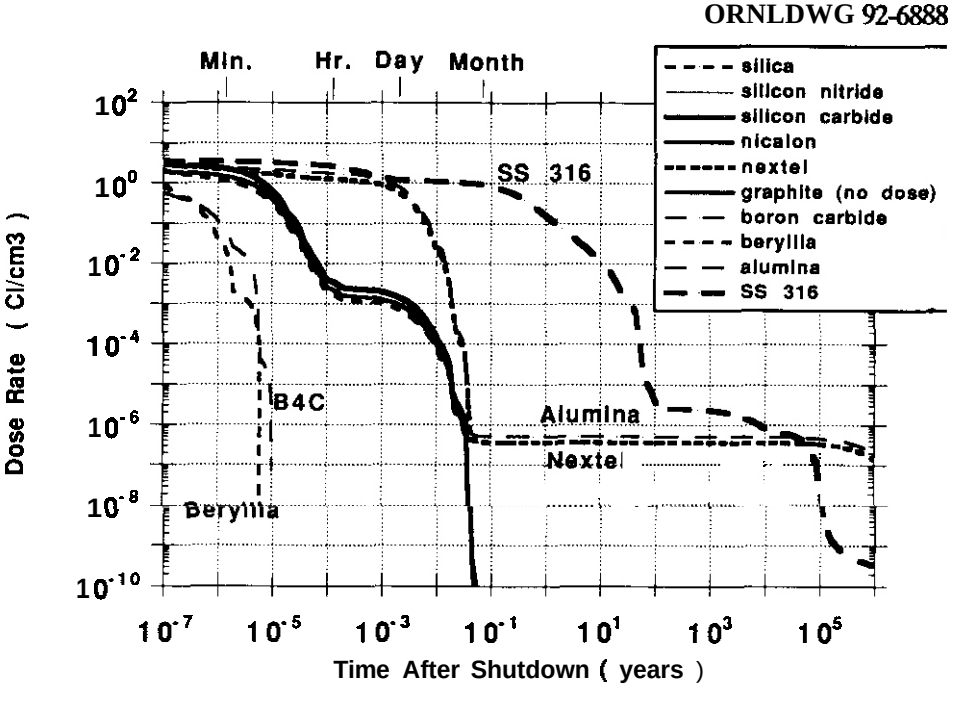

Figure 1d: Dose Rate for select compounds subjected to 1 MW-Yr/m^2 Starfire first wall spectrum.

Specific information corresponding to the samples is given Table 1. The counting times listed in this table correspond to the detector live time. **Note** that the samples histories do not permit a direct comparison of all the various materials. Direct comparison can only be made for the case of the ORR activated monolithic ceramics and the HFIR irradiated C/C composites as the irradiation and counting histories are the same.

Table 1: Ceramic Sample Specifics

Sample	Source	Fluence (dpa)	Removed (date)	Counted (date)	Volume (cc)	Count Time (sec)
COMPOSITES (HFIR Irradiated)						
SiC/Nicalon	ORNL	1	9/7/90	8/22/91	1.12	900
SiC/Nicalon	ORNL	3	6/15/91	8/22/91	1.34	900
SiC/Nicalon(FFTF)	GA	15		8/22/91	0.12	7200
C/C(Pitch)	NAMCO	1.5	9/7/91	8/22/91	1.208	5400
C/C(Pitch)	FMI	1.5	9/7/91	8/23/91	0.756	10800
C/C(PAN)	FMI	1.5	9/7/91	8/23/91	0.759	10800
CERAMICS (ORR Irradiated)						
SI3N4		7-8	12/86	9/26/91	7.2E-3	64800
AL2O3		7-8	12/86	9/25/91	5.7E-3	56700
MgAlO2		7-8	12/86	9/27/91	7.2E-3	26800
MgO-1%Ni		7-8	12/86	9/26/91	6.1E-2	14400
MgO-1%Li		7-8	12/86	10/9/91	7.2E-3	43200

Results and Discussion

Those isotopes which were positively identified for the ceramic composites and monolithic ceramics are given in Tables 2 and 3, respectively. From Table 2 it is seen that 26 different radioactive isotopes were identified. Appendix A gives the decay chain, decay energies and associated relative intensities for each of these isotopes. From this appendix it **is seen** that none of the identified isotopes were obtained by transmutation of the base ceramic material. The root of the induced activity is therefore an artifact of impurities in the raw materials used in the ceramic or a product of the manufacture of the composites. **As** an example, the most likely source of radioactivity from the silicon carbide composite is from impurities in the fibers or the reacting MTS (methyltrichlorosilane) gas which makes up the composite matrix. This gas is nominally 97% pure with polymers and other silanes making up the balance of impurities. **A** second gas which was used in processing was propylene which is used to deposit the fiber/matrix carbon interface. **No effort** has been made to measure or reduce any metallic impurities in these process gasses. The source of metallic impurities could also be from hardware associated with the weaving of the composite preform or the chemical vapor deposition chamber and gas handling system.

It can be speculated that the source of the majority of the impurities can be identified by grouping the elements into four categories. **The** first category would be those isotopes which have transmuted from Period IV elements, which also are the constituents of steels. These would be the isotopes: $^{50,60}Co$, ^{51}Cr, ^{59}Fe, ^{54}Mn. If the composites were contaminated during the weaving or composite processing these would be the most likely isotopes to be found. The second group are the rare earth isotopes: $^{141,143}Ce$, $^{154,155,156}Eu$, and ^{160}Tb. These isotopes are thought to originate from parent rare earths in the raw materials. It has previously been shown that the use of a halogen treatment5 purification process can greatly reduce the induced activity in C/C composites for identical composite processing. This indicates that these elements are present in the raw materials. The third group of elements are the daughters of strong carbide formers: ^{181}Hf, ^{46}Sc, ^{95}Nb, ^{95}Zr and ^{182}Ta. This group is also thought to originate from the raw material since strong carbide formers would be difficult to separate with conventional purification processes. The final group is simply the unstable daughter of the parent impurities identified. While several lines were identified fitting this category the only two isotopes which met the selection criteria were ^{125}Te which comes from the b decay of ^{125}Sb:

$$^{125}Sb \text{-- } \beta \text{ --> } ^{125}Te \text{ -- IT,}\gamma\text{--> } ^{125}Te(\text{Stable}).$$

and ^{95}Nb which comes from ^{95}Zr:

^{95}Zr-- β --> ^{95}Nb -- β --> ^{95}Mo (Stable)

Niobium can then belong to one or both of groups three and four. If naturally occurring ^{93}Nb (100% abundant) was present as a carbide in the base materials two capture reactions would be required to create the unstable Nb^{95} isotope. While it seems more likely for the ^{95}Nb to have occurred as a granddaughter of ^{95}Zr it can be seen from the FMI fabricated C/C pitch composite of Table 2 that ^{95}Nb has a relatively large activity in the absence of zirconium. This would indicate that the niobium has transmuted from the naturally occurring ^{93}Nb. The niobium activity is therefore attributed to both groups three and four.

Several other isotopes were identified which do not neatly fit into these categories. These include ^{110m}Ag, $^{131,133}Ba$, ^{109}Cd, ^{134}Cs, ^{192}Ir and ^{65}Zn. The ^{110m}Ag isotope was found in all but the General Atomics SiC/Nicalon composite irradiated in FFTF(MOTA). There are two isotopes which would occur if there were silver metal contamination, namely ^{108}Ag and ^{110}Ag, each with distinctive lines. The ^{108}Ag line was not found to be present above background in any of the samples so it is speculated that the ^{110}Ag isotope occurs from a neutron capture of the cadmium daughter ^{109}Ag:

^{109}Cd -- EC--> ^{109}Ag(Stable) -- n,γ-->^{110m}Ag-- β --> ^{110}Cd(Stable)

Table 3 gives the isotopes identified in ORR irradiated monolithic ceramics. These ceramics were irradiated as 3mm discs and were removed from the reactor in December of 1986. The short lived impurities which were identified for the composites of Table 2 could therefore not be identified due to the long time interval before counting. The major long lived impurity in these materials, as with the composites, is the ^{60}Co isotope which has a 5.26 yr half life. The Ni doped MgO not surprisingly showed a very high activity of ^{60}Co as compared to the undoped material. This is most likely due to the high cobalt impurity levels normally found in nickel.

Conclusion

This paper has described the induced activity in some ceramics of interest for fusion applications. The activity level is significantly higher than that which would be due to the base ceramic materials alone. The activity from these samples is dominated by impurities which are present in the raw materials or are derived from the mechanical processing of the ceramics. The two main isotopes of concern from a long term waste disposal issue are the ^{110m}Ag and ^{60}Co isotopes. These two isotopes have the combination of longest half-lives and highest activity of the isotopes found. While activity levels measured in these materials do not appear to pose a threat from a long term waste disposal perspective there would have to be a serious reduction in the shorter lived isotopes such as ^{51}Cr, ^{156}Eu, ^{46}Sc and ^{125}Sb before one could contemplate hands on maintenance of components removed from the reactor.

FUTURE WORK

Further work needs to be carried out to determine the sources of the contaminants measured in these materials. In the case of the composites, many continuous fibers (such as Nicaion, Pan and Pitch carbons) and the monolithic ceramics which constitute composite matrices are being irradiated in both FFTF and HFIR.[6,7] On the individual composite constituents are analyzed the sources can be narrowed. Once the sources are identified an effort can be made to reduce the impurity level due to these elements.

Due to the extreme difference in impurity cross sections between the spectrum that the samples in this study have seen and what would be seen in a fusion spectrum, it is clear that the induced activities would be quite different. In order to obtain the activity that the impurities would have for fusion reactor application one would have to calculate the impurity concentration from the induced activity measured in this paper and recalculate the activity for a fusion spectrum.

Table 2: Specific Activities of Ceramic Composites (μCi/cc)

Isotope	T 1/2	SiC/Nic ORNL 3dpa	SiC/Nic GA 15dpa	C/C(Pitch) NAMCO	C/C(PAN) FMI	C/C(Pitch FMI
AgllOM	249 y	3.27		1.82	0.053	0.158
Ba 131	11.2 d	3.16				
133	7.2 y	0.54				
Cd 109	62.3 d	1.69	18.9			0.159
Ce 141	32.5 d	1.99				
143	33.0 h					
Co 58	71.3 d	0.57		0.17	0.262	
60	5.26 y	10.70	10.66	1.65	2.06	2.08
Cr 51	27.7 d	224.03				
Cs 134	21 y			0.008	0.026	0.040
Eu 154	8.5 y		0.17	0.067	0.22	0.026
155	5.0 y			0.041	0.158	0.006
156	15.2 d	67.23				
Fe 59	44.5 d	11.7				
Hf 181	42.4 d	9.56				
Ir 192	74.0 d	0.37		2.54	0.317	0.132
Mn 54	312.2 d	0.89		0.66	0.026	0.265
Nb 95	35.1 d			3.46		1.165
Sb 124	60.2 d	12.15				
125	2.77 y		2.67			
Sc 46	83.8 d	30.97		71.11	27.30	8.70
Ta 182	114.5 d	74.70		0.25	33.86	11.19
Tb 160	72.4 d			2.57	0.30	0.18
Te 125	58 .0 d	73.66		4.41		
Zn 65	243.8 d	14.54	8.08	0.12		0.066
Zr 95	64.03 d	0.40		1.57	0.441	

Table 3: Specific Activities of Monolithic Composites (μCi/cc)

Isotope	Si3N4	A1203	MgAlO2	MgO-1%Ni	MgO-1%Li	MgO
Ba 133	0.116					
Co 60	2.26	2.14	55.08	511.3	612.6	8.86
Cs 134	4.11	0.954	2.08			
Eu 155	0.179					
Mn 54	7.44		21.31			
Zn 65	29.72		78.36			

REFERENCES

1. G. R. Hopkins and J. Chin, "SiC Matrix/SiC Fiber Composite: A High-Heat Flux, Low Activation, Structural Material", J. Nucl. Mat. 141-143 (1986) 148-151.

2. G. R. Hopkins and R. J. Price, "Fusion Reactor Design with Ceramics", Fusion Eng. and Design/Fusion 2 (1985) 111-143.

3. L. H. Rovner and G. R. Hopkins. "Ceramic Materials for Fusion", Nucl. Tech. Vol 29, June 1976. 274-302.

4. S. Grotz, et. al. The ARIES Tokamak Reactor Study. Tenth International Conference on Structural Mechanics in Reactor Technology (SMIRT.) Anaheim, California, August 1989.

5. T. Shakima et. al., "Induced radioactivity of commercial isotropic graphites for high heat flux tiles",J. Nucl. Mat. 179-181 (1991) 209-213.

6. S. J. Zinkle and L. L. Snead, "Irradiation of Conventionally and Isotopically tailored ceramics in HFIR", Fusion Reactor Materials Semiannual Report, DOE/ER-0313/10. pg. 314 - 316.

7. S. J. Zinkle and L. L. Snead, "Irradiation of Ceramics in FFTF", Fusion Reactor Materials Semiannual Report, DOE/ER-0313/10. pg. 317-319.

APPENDIX A : Decay data of identified isotopes

Element	E (KeV)	e m .	T1/2	DECAY CHAIN
Ag110M	657.7	94	249.8 y	Ag110M-- β --> Cd110(Stable)
	677.6	11.5		
	686.8	7		
	706.8	16		
	744.19	A		
	163.9	22.6		
	818.0	7.4		
	884.7	75.0		
	937.5	34.4		
	1384	26.1		
	1475	4.0		
	1505	13.9		
	1562	1.3		
Ba 131	123.7	54.0	11.6 D	Ba131--EC-->Cs131 --EC(no γ)-->Xe131(Stable)
	216.0	21.4		
	373.2	15.0		
	496.3	47.0		
	620.2	14.1		
Ba 133	79.6	11.0	7.2 y	Ba133M-- IT --> Ba133-- EC--> Cs133(Stable)
	81.0	55.0		
	276.4	12.0		
	303.1	30.6		
	356.3	100.0		
	348.1	14.2		
Ba 133M	75.9	17	38.9 h	
Cd 109	22.1	25.54	62.3 d	Cd109 -- EC--> Ag109(Stable)
Ce 141	145.5	49	32.5 d	Ce141-- β --> Pr141 (Stable)
143	57.4	12.0	33.0 h	Ce143-- β --> Pr143 -- β --> Nd143 (Stable)
Co 58	511.0	30.0	71.3 d	Co58 -- EC,β^+ --> Fe58 (Stable)
	810.6	99.4		
Co 60	1173	99.0	5.26 y	Co60 -- β^+ --> Ni60 (Stable)
	1332	100		
Cr 51	320.1	9.9	27.7 d	Cr51-- EC --> V51 (Stable)
Cs 134	569.4	16.0	2.1 y	Cs134 -- β --> Ba 134 (Stable)
	604.7	98.1		
	795.8	86.0		

Element E (KeV) e m . T1/2 DECAY CHAIN

Eu 154	123.1	40.0	8.5 y	Eu154 -- β --> Gd154 (Stable)
	243.0	6.6		
	723.3	19.1		
	873.2	11.3		
	996.3	10.7		
	1004.8	17.6		
	1274.8	33.6		
155	60.0	1.4	5.0 y	Eu155 -- β --> Gd 155 (Stable)
	86.5	33.5		
	105.3	22.4		
156	88.8	11.4	15.2 d	Eu156 -- β --> Gd156 (Stable)
	723.3	6.19		
	811.7	10.8		
	1065	5.5		
	1153	12.5		
	1242	7.4		
	1966	4.0		
	2097	4.1		
Fe 59	1291	44.0	44.5 d	Fe59-- β^+ --> Co59 (Stable)
Hf 181	133.0	41.0	42.4 d	Hf181-- β --> Ta181 (Stable)
	136.3	6.9		
	346.0	12.0		
	482.2	83.0		
Ir 192	205.8	3.3	74.0 d	Ir192 -- β --> Pt192 (Stable)
	308.4	30.6		
	316.5	85.8		
	374.4	7.7		
	468.0	50.5		
	604.4	8.9		
	612.4	5.4		
Mn 54	834	100	312.2 d	Mn54 -- EC --> Cr54 (Stable)
Nb 95	765.8	99.8	35.1 d	Nb 95-- β --> Mo 95 (Stable)
Sb 124	602.7	98.0	60.2 d	Sb124-- β --> Te124 (Stable)
	1691.0	48.3		
Sb 125	35.46	5.9	2.77 y	Sb125-- β --> Te125 -- IT --> Te 125(Stable)
	176.3	6.3		
	421.9	26.9		
	463.5	10.0		
	600.7	18.4		
	606.8	5.2		
	636.1	11.2		

Element	E (KeV)	emm.	T1/2	DECAY CHAIN
Sc 46	889.3	100	83.8 d	Sc46 -- β --> Ti46 (Stable)
	1121	100		
Ta 182	65.7	3.0	114.5 d	Ta182-- β --> W182 (Stable)
	67.8	44		
	84.7	2.8		
	100.1	15.1		
	152.4	1.7		
	222.1	8.4		
	229.3	4.1		
	264.0	3.9		
	1121	37		
	1189	17.5		
	1221	29.3		
	1231	12.4		

Tb 160	86.8 298.6 879..3 962.1 966.1 1178.1 1271.9	13.7 27.1 30.0 10.2 24.7 15.2 7.6	72.4 d	Tb160 -- β --> Dy160 (Stable)
Te 125	35.5	6.75	58.0 d	Te125 -- IT --> Te 125(Stable)
Zn 65	511 1115.5	2.8 50.6	243.8 d	Zn65-- EC,β^+ --> Cu65 (Stable)
Zr 95	724.2 756.8	43.6 54.8	64.03 d	Zr95-- β --> Nb95 -- β --> Mo95 (Stable)

3.0 MATERIALS ENGINEERING AND DESIGN REQUIREMENTS

MATERIALS HANDBOOK FOR FUSION ENERGY SYSTEMS - J. W. Davis (McDonnell Douglas Missile Systems Company)

OBJECTIVE

The primary objective is to provide a consistent and authoritative source of material property data for use by the fusion community in the design and analysis of fusion components and systems. The source of this data are contributions from the experimental programs funded by the Fusion Materials programs within D&T. As a result this activity serves as a bridge between the materials experimental programs and the design community by providing the results of fusion researchers in a form readily understood by the design community.

SUMMARY

The database effort during this period was directed towards three different program areas: 1) Material property support to ITER during the CDA phase, **2)** Continuation of the Material Handbook for Fusion Energy Systems, and 3) Development of the IEA International Fusion Material Handbook.

PROGRESS AND STATUS

ITER Materials Support

During the ITER Conceptual Design Activity (CDA), to assist in the design of the diverter, first wall and blanket structures, a Design Databook was created by the U.S. using information provided by the four participants (E.C., Japan, U.S., and U.S.S.R.) at the two ITER Materials workshops, which were held in Garching, Germany in 1988 and 1990. Information provided included both irradiated and unirradiated data on candidate diverter and first wall materials (carbon-carbon, pyrolytic graphite, pure copper, dispersion strengthened and alloyed copper, molybdenum and molybdenum alloys, niobium alloys, and vanadium alloys) along with data on the blanket structural material, annealed 316 stainless steel. Information was also presented on solid tritium breeding ceramics and neutron multipliers but this information was not converted into datapages because of time and budget constraints. Information on **all** of these materials can be found in the IAEA report "ITER Blanket, Shield and Material Data **Base,**" ITER Documentation Series No. 29, 1991.

Materials Handbook for Fusion Enerev Systems

As a result of shrinking material research budgets within the U.S. program, the flow of information to the materials handbook has been significantly reduced. However with the advent of the ITER program and the desire ,of each country to show their capabilities this situation is changing and information is beginning to **flow** into the U.S. Handbook. There is a lead time before this information is reviewed but in the interim 25 data pages covering the thermophysical and mechanical properties of annealed 316 stainless steel were incorporated into the Handbook. These datapages were developed in support of the ITER program and are marked accordingly. While they are called "INTERIM" datapages they have been reviewed by the structural materials group on the ITER program and approved for use in design on ITER. In addition to the ITER datapages, work is currently in progress to develop datapages on liquid lithium and on the irradiated fracture toughness of ferritic steel. A significant amount of thermophysical information has been provided which is currently being converted to an engineering format.

Originally the Handbook was structured to be available both in paper and electronic form. The electronic version was designed around the CTSS protocol on the NERSC network. This computer network will be changed from CTSS to UNICOS and **as a** result the controlling codes for access to the electronic version of the Handbook will have to he rewritten to be accepted by UNICOS. Work **is** in progress to accomplish, however the rate of progress will depend on which programs are incorporated into the system and rate at which they are put on the "C" and " F machines.

International Fusion Materials Handbook

In 1987 authorization to create an International Fusion Materials database was given by the International Energy Agency (IEA). The handbook was organized along the lines of the U.S. materials handbook with task groups responsible for developing datapages. Work has been progressing on the development of stainless steel and breeder datapages. Preliminary datapages have been prepared and submitted to the task group participants for review and comment prior to release. Release of the first draft of the handbook is anticipated in the second half of 1992.

SUMMARY AND CONCLUSIONS

The activities on the ITER Design Databook are currently on hiatus until the Engineering Design Activity (EDA) agreement is signed and further work is dependent upon the approval of the managing director of the ITER program. The U.S. Materials handbook is back on track with contributions beginning to come in. Work is progressing on converting the information received on the solid tritium breeding materials into engineering datapages. The International Fusion Materials Handbook got off to an uncertain start but is progressing. The prime difficulty was a large cumbersome organization which made receipt of datapages difficult. This activity is in the process of being streamlined which should increase both the publication rate and the response time.

4.0 FUNDAMENTAL MECHANICAL BEHAVIOR

THE INFLUENCE OF HELIUM ON MECHAHICAL PROPERTIES CF MODEL AUSTENITIC ALLOYS, DETERMINED USING ^{59}Ni ISOTOPIC TAILORING AND FAST REACTOR IRRADIATION - M. L. Hamilton and F. A. Garner, Pacific Northwest Laboratory*

OBJECTIVE

The objective of this study is to determine the influence of fusion-relevant helium generation rates on mechanical property changes induced by radiation.

SUMMARY

Tensile testing on model Fe-Cr-Ni alloys removed from four discharges cf the ^{59}Ni isotopic doping experiment in FFTF indicates that helium/dpa ratios typical of fusion reactors do not produce changes in the yield strength or elongation that are significantly different from those at much lower helium generation rates. It also appears that tensile properties approach a saturation level that is depenaent only on the final irradiation temperature, but not prior temperature history or thermomechanical starting condition.

OBJECTIVE AND STATUS

Introduction

Until recently it has been impossible to conduct experiments in which spectrum-related parameters such as helium/dpa ratio were varied without also accepting variations in other important parameters such as displacement rate or temperature history. A technique currently being used, however, allows the study of the influence of helium alone on density change, microstructural evolution and mechanical properties. This technique utilizes isotopic tailoring to vary the helium production rate without introducing changes in neutron spectrum or displacement rate.[1,2] It is possible to generate substantial variations in He/dpa ratio without varying any other important uarameter by using alloys between which the onlv difference is the presence or absence of ^{59}Ni, 'an isotope that does not occur naturally, and irradiating doped and undoped specimens side by side in the appropriate reactor spectra.'

A particular advantage of comparative isotopic doping experiments is that one need not be concerned with the details of temperature history, which are now known to heavily influence the outcome of some fission-fusion correlation experiments.[3] Since both doped and undoped specimens are irradiated side by side, the primary variable is only the helium/dpa ratio. The production rate of helium in doped specimens is also nearly, but not exactly, constant throughout the experiment, providing that no changes occur in the neutron environment. Small variations in helium production rate occur in both sets of alloys in response to burn-in or burn-out of ^{59}Ni.[4]

This paper presents data obtained from (miniature tensile specimens irradiated in an experiment conducted in the Fast Flux Test Facility (FFTF) utilizing the Materials Open Test Assembly (MOTA). A previous paper presented the results of the first discharge of this experiment.[5] The details of the helium measurements are included in another paper.[4]

Exuerimental Details

The alloys employed in this study were nominally Fe-15Cr-25Ni, Fe-15Cr-25Ni-0.04P and Fe-15Cr-45Ni (wt%) in both the cold worked and annealed conditions. These alloys were chosen to complement those used in several earlier studies, one in the Experimental Breeder Reactor-I1 (EBR-II), designated the AD-1 experiment,[6,7] and another conducted in the Oak Ridge Research Reactor, designated MFE-4.[7] The acquisition of the ^{59}Ni, the production of the ^{59}Ni-doped tensile specimens, and their irradiation conditions are described elsewhere.' Microscopy disks were also prepared and irradiated; the results of transmission electron microscopy (TEM) examination are described in detail in References 8-10. The miniature tensile specimens nominally measured 5.1, 1.0 and 0.25 mm in gauge length, width and thickness, respectively. They were tested at room temperature at a strain rate of 4.7×10^{-4} sec^{-1} in a horizontal test frame described in Reference I1. Yield strengths were determined at 0.2% offset More than one tensile specimen was tested for some conditions, but the majority of test conditions involved only a single specimen.

Figure 1 shows a schematic representation of the five irradiation sequences of the ^{59}Ni experiment, each defined by its target irradiation temperature and its location in FFTF/MOTA. The experiment was initiated in MOTA 1D, but a short temperature excursion referred to as an overtemperature event compromised the integrity of the test. A decision was made to run the MOTA in the helium-purged mode for the remainder of FFTF cycles 7 and 8 while a series of reactivity feedback tests were conducted. The majority of the MOTA canisters therefore operated at variable but lower temperatures until the end of MOTA 1D

*Operated for the U.S. Department of Energy by Battelle Memorial Institute under Contract. DE-AC06-/CRLO 1830.

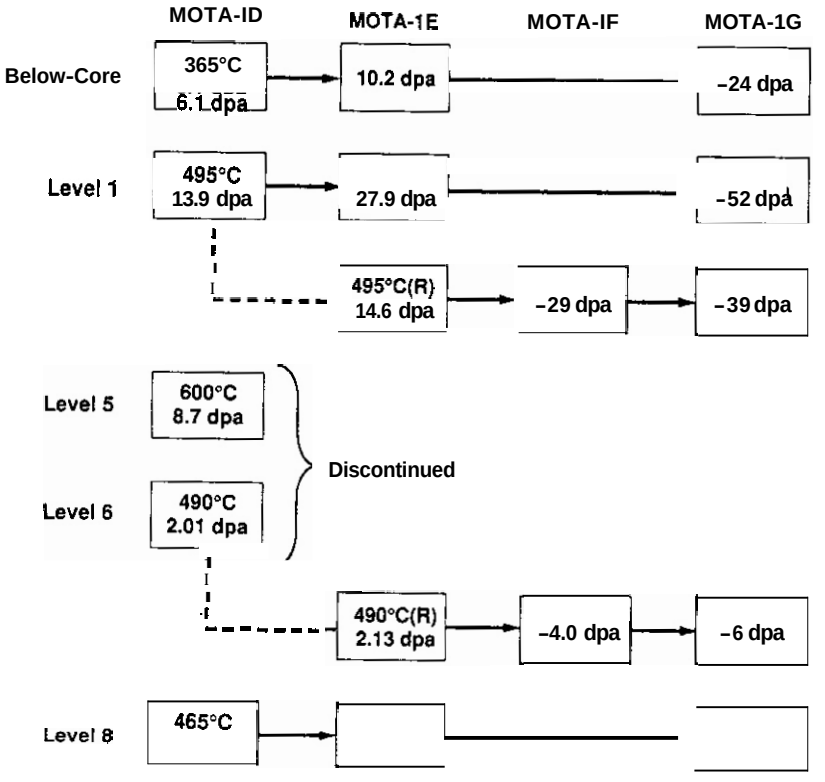

Fig. 1. Schematic representation of nominal irradiation sequences for the ^{59}Ni isotopic tailoring experiment. "**495°C** (R)" and "**490°C** (R)" refer to the sequences inserted as replacements for the original sequences at **495** and **490°C**. Damage levels given represent cumulative totals.

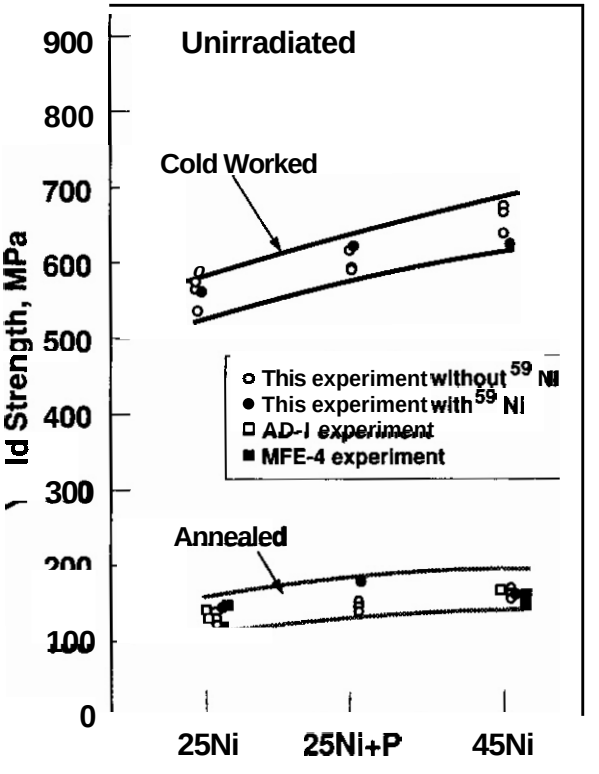

Fig. 2. Yield strength data on unirradiated specimens from both the FFTF/MOTA ^{59}Ni experiment and two related experiments conducted in other reactors using larger specimens.[11]

Two of the compromised experimental sequences show .in Figure 1 were restarted with duplicate specimens in MOTA 1E at the same temperatures, 490 and 495°C. The original 490 and 600°C sequences were not continued to higher radiation exposure due to the magnitude of the temperature excursion, during which these canisters experienced 553 and 806°C, respectively, for fifty minutes. The 495°C sequence also experienced an overtemperature, reaching 629°C for fifty minutes, but was continued in the irradiation sequence along with the replacement sequence at 495°C to allow an evaluation of temperature history effects. The sequences at 365 and 465°C did not experience a temperature excursion during MOTA 1D and continued irradiation as planned.

Results of Tensile Tests

Three tensile tests were conducted on unirradiated specimens for each undoped alloy in both the cold worked and the annealed conditions. Since the availability of doped specimens was rather limited, only one was tested for each combination of doped alloy and thermomechanical starting condition. Figure 2 shows that the range of yield strengths in the undoped specimens is not large and that the single doped specimen in each condition did not exhibit any significant difference in behavior. Also shown in Figure 2 are the yield strengths exhibited by the larger specimens of the unirradiated arnealed alloys that were irradiated in the AD-l and MFE-4 experiments,' demonstrating excellent agreement between the results from tensile specimens of different geometries in the three experiments.

Figures 3 through 7 show the yield strength and elungation data obtained at ail five temperature,;. The helium generation rates given are averages for Fe-15Cr-25Ni over the first two irradiation seqments. Helium measurements have not yet been completed for the last segment. ?he width of the error bars at zero dpa corresponds to the variability in the data shown in Figure 2 and provides a basis for determining whether variations observed between doped and undoped specimens are significant compared to tne scatter associated with the measurement technique. The most significant feature of the data shown in Figures 3 through 7 is the relative unimportance of isotopic doping at all test temperatures in determining the yield strength. Also significant is the tendency toward convergence of the data on aiinealed anc cold worked specimens to saturation levels that depend only on alloy composition and irradiation temperature. A similar convergence was observed previously in 316 stainless steel over a wide range of irradiation temperatures, with convergence levels sensitive to both temperature and displacement rate.[12,13]

At 495°C only annealed tensile specimens were irradiated and it is therefore not possible to confirm that convergence occurs at this temperature. TEM disks were irradiated at 495°C in both the annealed and cold worked conditions, however, and convergent microstructures appear to have developed.[8,10] The data at 495°C demonstrate another type of convergence, however. Note that the strengrh of the original specimens, i.e., those that were subjected to the overtemperature, initially reached a very high level and then fell to lower levels during the second and third irradiation sequences, while the specimens in the replacement sequence reached the same lower level of strength directly. Similar behavior is evident in the elongation data, with the lower irradiation temperatures associated with irradiation following the overtemperature giving rise to lower ductility levels that increased with subsequent irradiation at the originally intended higher irradiation temperature. Thus the microstructure and tensile properties converge at a level dependent more on the final irradiation temperature than on earlier temperature history.

The high strength levels that were reached originally did not arise from the temperature excursion itself, however, but from the prolonged irradiation at lower temperatures that followed the overtemperature event. The higher density of microstructure and the resulting higher strength and lower ductility that developed at the lower temperatures were then replaced by a microstructure and tensile properties more appropriate to the temperatures achieved in the second and third irradiation segments.

The influence of temperature history can also be seen in the 490°C irradiation, conducted above the core at higher helium/dpa levels and lower dpa rates. The behavior of the annealed alloys at 493°C is similar to that observed following in-core irradiation at 495°C.

Discussion

It appears that the helium generation rate in this experiment is of second order importance compared to the other variables studied. In the absence of variations in displacement rate, ihe influence of helium is minimal. A similar conclusion was reached by Mansur and Grossbeck[14] in a comparison of tensile data from EBR-II and the High Flux Isotope Reactor on the Japanese and U.S. versions of PCA, the Prime Candidat? Alloy of the fusion materials program. Although the displacement rates in the two reactors were comparable, the differences in helium generation rates in that comparison were even larger than in the current experiment.

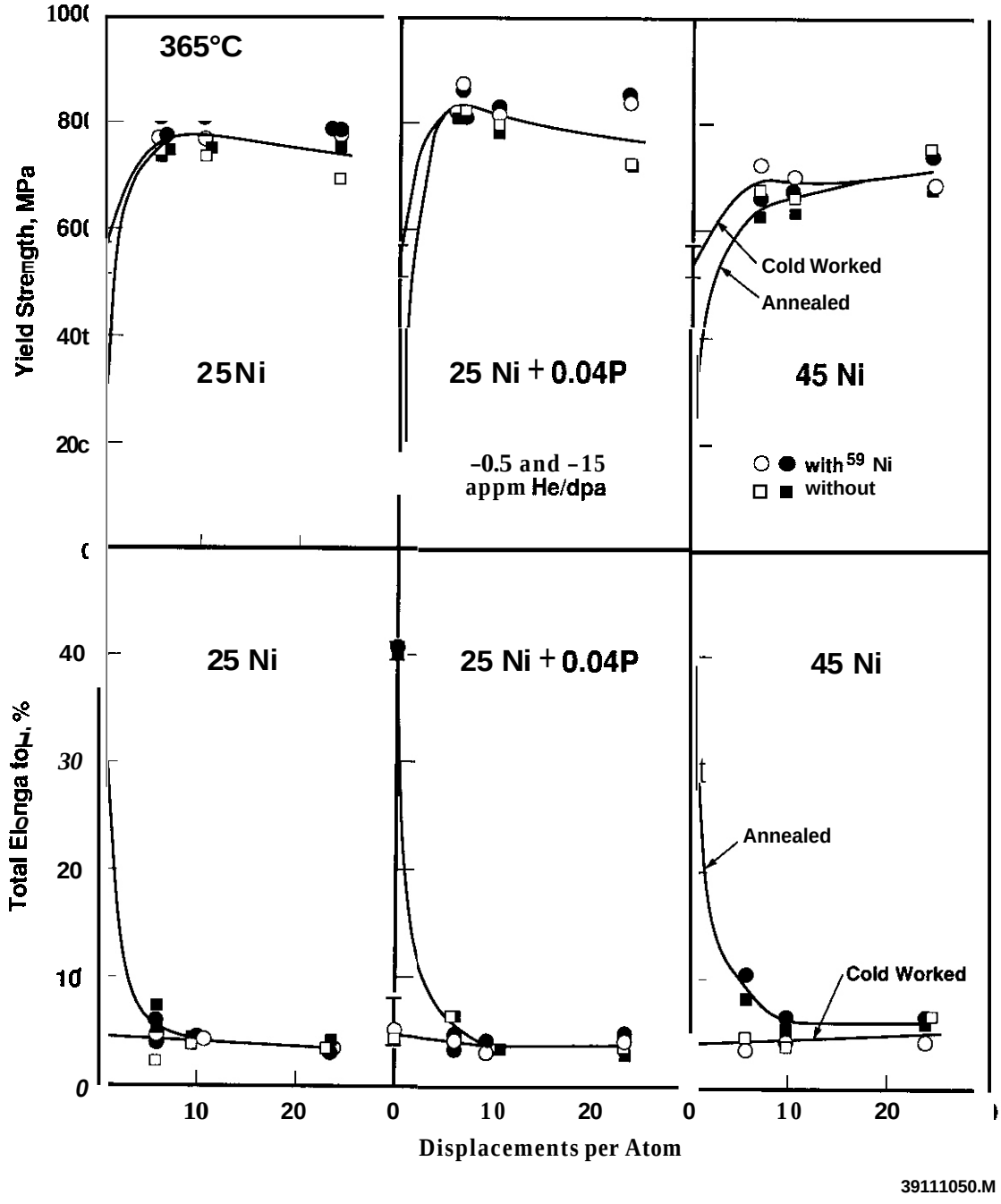

Fig. 3. Influence of thermomechanical starting state and isotopic doping on yield strength and elongation of three alloys irradiated below the core at *365°C.*

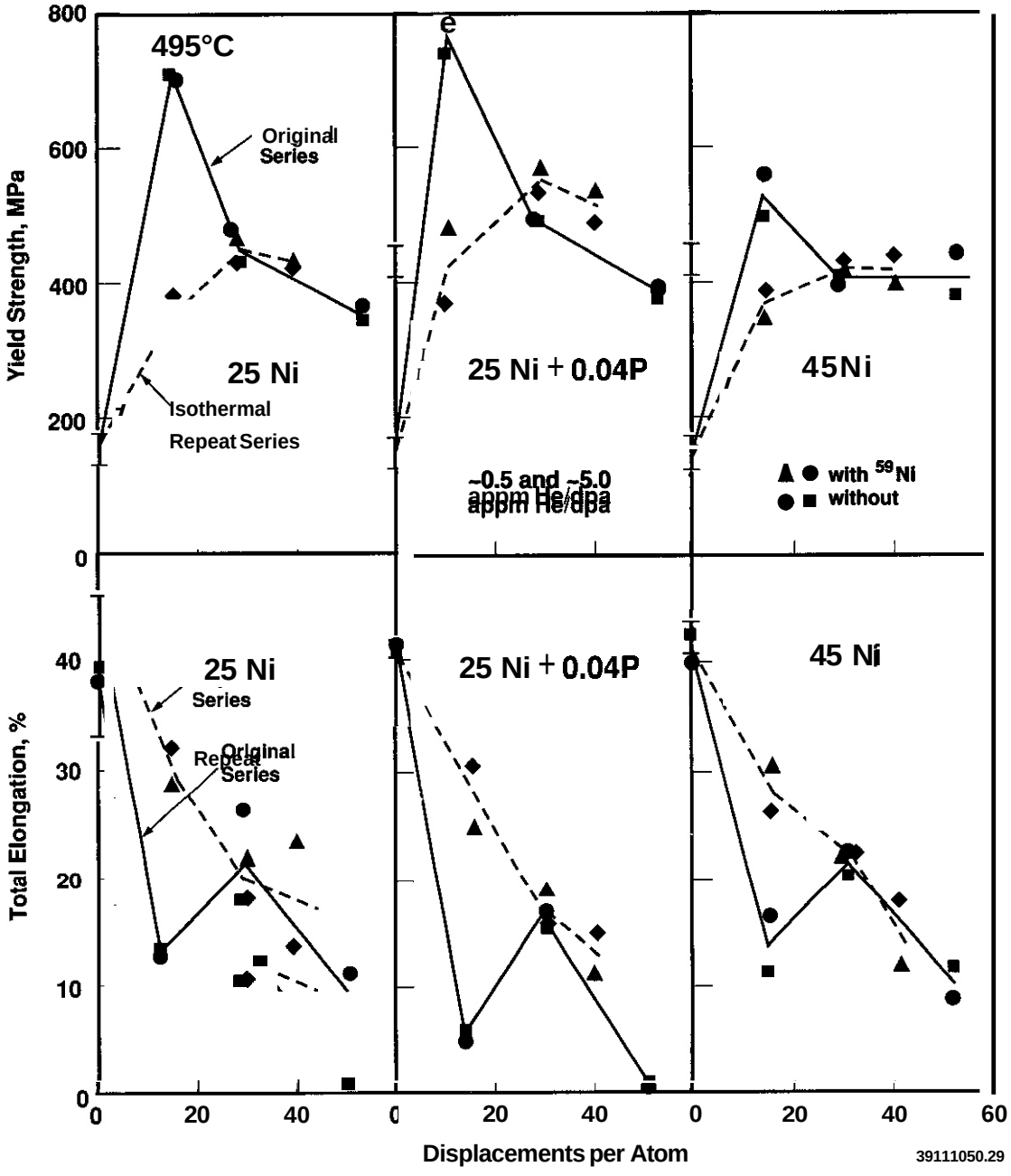

Fig. 4. Influence of isotopic doping and temperature history on the yield strength and elongation of annealed alloys following irradiation at the bottom of the core at 495°C. The dotted lines correspond to the isothermal repeat sequence.

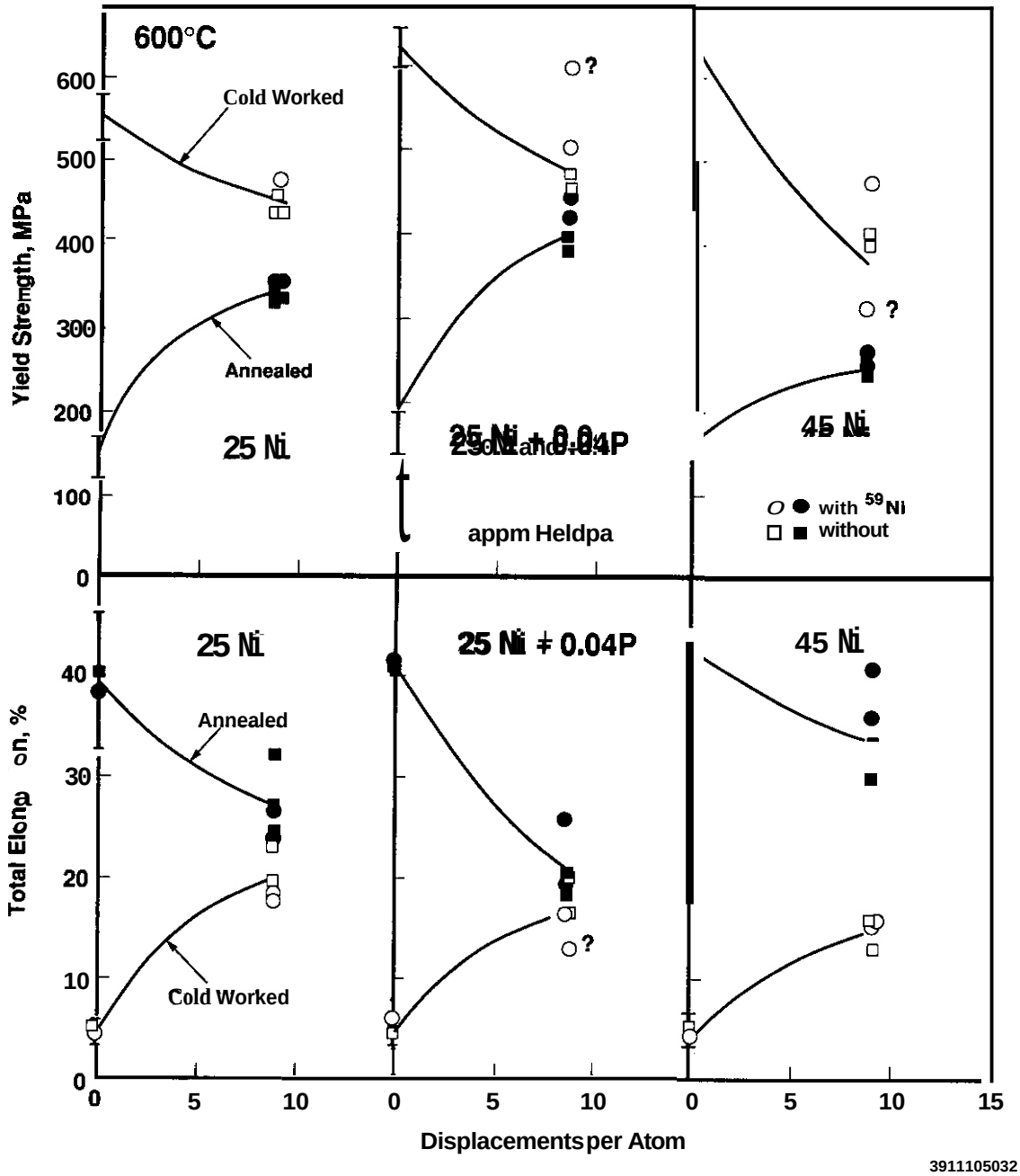

Fig. 5. Influence of isotopic doping and thermomechanical starting state on yield strength and elongation following irradiation at the top of the core at 600°C.

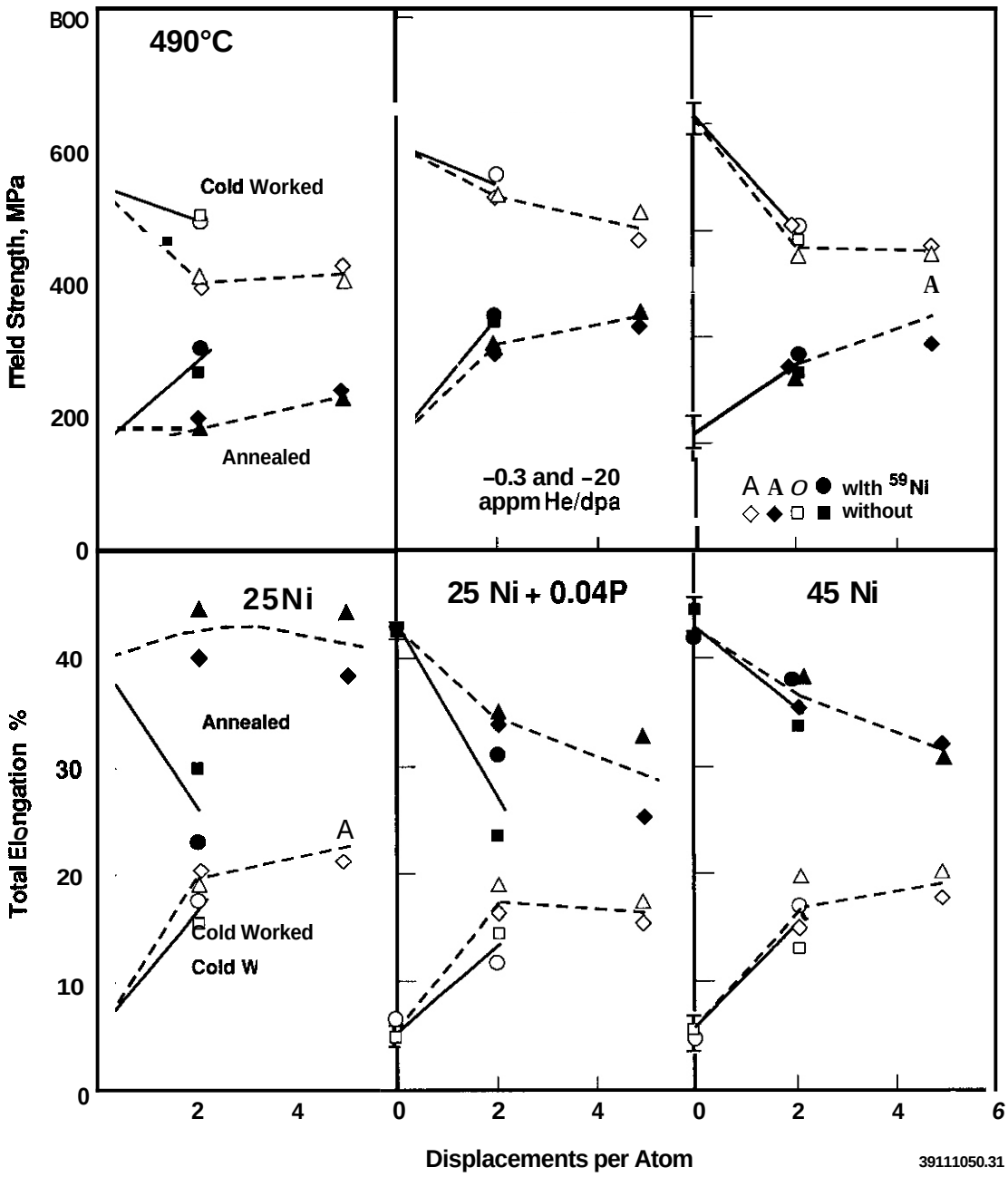

Fig. 6. **Influence of thermomechanical starting state, isotopic doping and temperature history** on **yield strength and elongation following irradiation above the core at 490°C. The dotted lines correspond to the isothermal repeat sequence.**

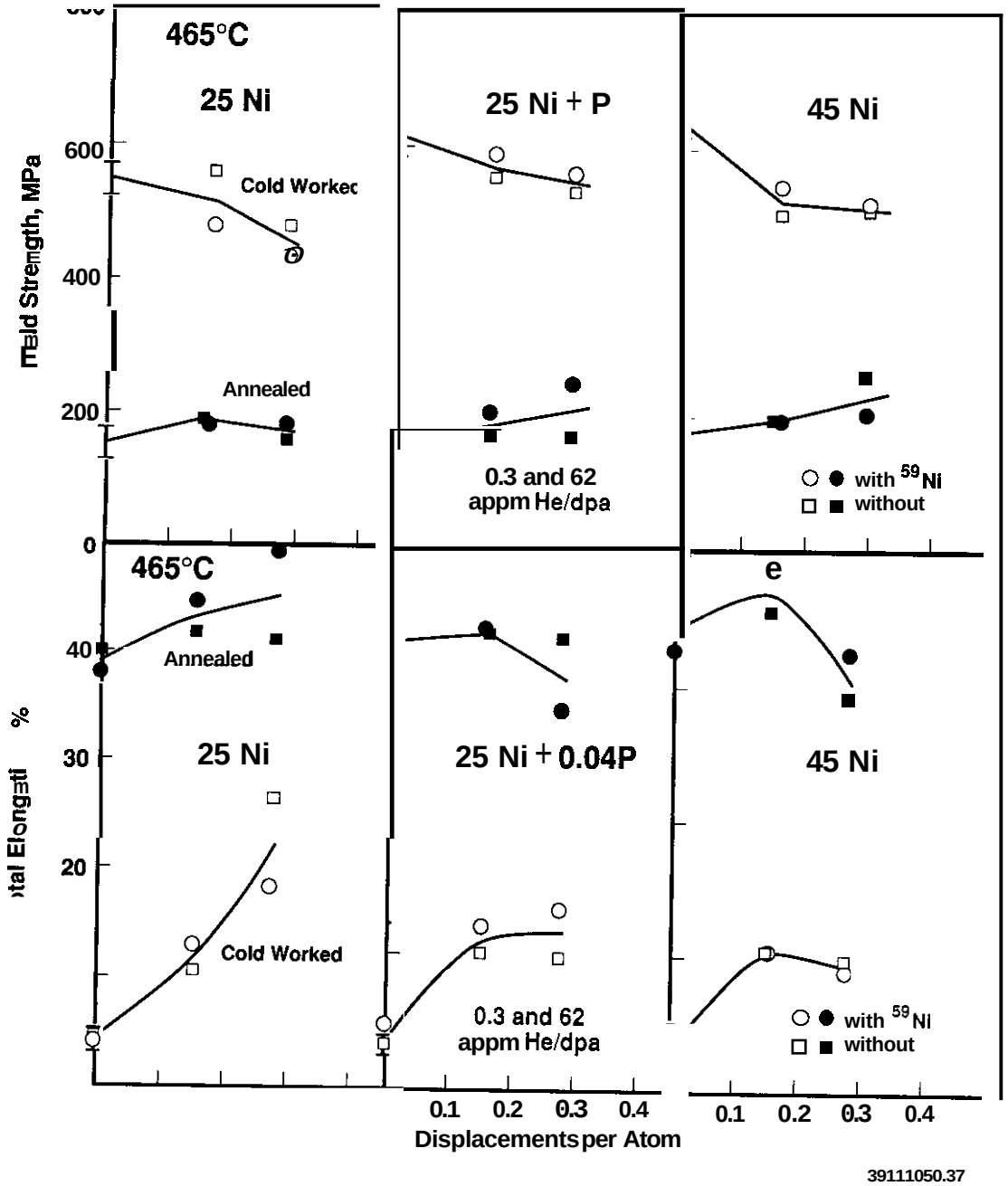

Fig. 7. Influence of thermomechanical starting state and isotopic doping on yield strength and elongation following irradiation above the core at 465°C.

CONCLUSIONS

When model Fe-Cr-Ni alloys are irradiated at constant displacement rate but at very different helium/dpa rates in the range 365 to 600°C, there is nu significant variation in their tensile properties as a function of helium. The impact of helium generation rafe is secondary to the influence of cold work, temperature, nickel level and phosphorus level. it appears that tensile properties converge to a saturation level that is dependent on irradiation temperature and composition but not on early temperature history or helium generation rati.

FUTURE WORK

Microscopy examination of high fluence specimen> will continue to confirm the development of convergent microstructures. Density change measurements will also continue.

REFERENCES

1. R. L. Simons, H. R. Brager and W. Y. Matsumoto, J. Nucl. Mater. 141-143 **(1986) 1057-1060.**

2. **G. R.** Odette, **J.** Nucl. Mater. 141-143 **(1986) 1011-1017.**

3. M. Kiritani, J. Nucl. Mater. **160 (1988)** 135-141.

4. L. R. Greenwood, F. A. Garner and 8. M. Oliver, this conference.

5. F. A. Garner, M. L. Hamilton, R. L. Simons and M. K. Maxon, J. Nucl. Mater. 179-181 **(1991)** 554-557

6. H. R. Rrager, F. A. Garner and M. L. Hamilton, J. Nucl. Mater. 133 & 134 **(1985)** 594-598.

7. M. L. Hamilton, A. Okada and F. A. Garner, J. Nucl. Mater. 179-181 **i.1991)** 558-562.

8. **J.** F. Stubbins and F. A. Garner, **J.** Nucl. Mater. 179-181 **(1991)** 573-525.

9. H. Kawanishi, F. A. Garner and R. L. Simons, J. Nucl. Mater. 179-181 **(1991)** 511-514.

10. J. F. Stubbins and F. A Garner, this conference.

11. N. F. Panayotou, S. D. Atkin, R. J. Puigh and 8. A. Chin, The Use of Small-scale Specimens for Testing Irradiated Material. ASTM STP **888,** W. R. Corwin and G. E. Lucas, Eds., American Society for Testing and Materials, Philadelphia, 1986, pp. 201-219.

12. F. A. Garner, M. L. Hamilton, **N.** F. Panayotou and G. D. Johnson, J. Nucl. Mater. **103 & 104 (1981)** 803-**808.**

13. F. A. Garner, H. L. Heinisch, R. L. Simons and F. M. Mann, Radiation Effects and Defects in Solids **113 (1990)** 229-255.

14. L. K. Mansur and M. L. Grossbeck, J. Nucl. Mater. 155-157 **(1988)** 130-147

5.0 RADIATION EFFECTS: MECHANISTIC STUDIES, THEORY AND MODELING

THE IMPACT OF SPECTRAL EFFECTS IN FAST REACTORS ON DATA ANALYSIS AND DEVELOPMENT OF FISSION-FUSION CORRELATIONS L.R. Greenwood, F.A. Garner, and H.L. Heinisch, Pacific Northwest Laboratory[a]

OBJECTIVE

The objective of this study is to examine the influence of neutron spectral differences on correlation of radiation effects data.

SUMMARY

Models describing the production of freely migrating defects (FMD) during neutron irradiations were applied to materials studies in fast reactors, where neutron spectral effects have been largely ignored. Calculations for the Experimental Breeder Reactor II (EBR-II) and the Fast Flux Test Facility (FFTF) show that effects of spectral differences between in-core and out-of-core positions are significantly larger on the basis of freely migrating defects than on the basis of dpa. As an example, data on swelling behavior measured both in-core and out-of-core in EBR-II show nearly a linear dependence on FMD production but not on dpa.

PROGRESS AND STATUS

Introduction

The development of radiation-resistant materials for fusion reactors relies on the correlation of test data obtained in a variety of neutron spectra, none of which are similar to those expected in fusion reactors. A successful correlation occurs when data are compared on the basis of a damage parameter that accounts for spectral differences. Displacements per atom (dpa) is a widely used and effective damage parameter, especially for neutron spectra in which a very large fraction of the damage is produced by high energy neutrons. As more is learned about the production of lattice defects in radiation damage events and the roles of defects in microstructural evolution, it is becoming clear that good correlations may require damage parameters based on more specific representations of defect production than is embodied in the dpa concept[1].

The embrittlement of fission reactor pressure vessels has been found to be substantially greater than predicted by tests conducted in-core and correlated with dpa as the exposure parameter[2]. Successful correlations of both in-core and pressure vessel data [3,4,5] have recently been developed, however, and are based on the significant contributions to residual damage produced by thermal neutrons, which comprise a very large fraction of the neutrons at the pressure vessel. The thermal neutron (n,γ) reaction produces energetic recoil atoms in iron near 400 eV, which are very efficient at producing mobile point defects. Correlations were achieved using energy-dependent production models of those defects that are assumed to be effective in changing the microstructure [4,5]. It should be noted that these were simple, preliminary models. The characterization of effective defects is still under investigation.

Another very promising concept, the production bias, incorporates the temperature dependence of interstitial and vacancy clusters against dissolution and has been used to describe differences in the temperature dependence of the swelling rates for electron and neutron irradiations[6].

In this paper we examine the potential influence of the neutron energy dependence of the production of effective defects in fast neutron test facilities. Generally, dpa is considered a good damage parameter for correlating fast reactor data obtained in-core. However, current use of out-of-core positions for spectral tailoring experiments requires that we assess the correlation of data from both in-core and out-of-core positions, where epithermal contributions to the spectrum become more important. Two current models of effective defect production are used to examine differences in the neutron spectral effects between in-core and out-of-core positions in both FFTF and EBR-II.

Effective Defect Production

Opa is a calculated quantity that indicates the potential for creating point defects in a material exposed to a particular radiation source. It is based on a simple model, first proposed by Kinchin and Pease and modified by Norgett et al. [7], for partitioning the damage energy (that part of the recoil energy that goes into displacing atoms) by the amount required to produce a stable Frenkel pair. At very low recoil energies a few, isolated stable Frenkel pairs are produced in each event, about equal to the number predicted by the Kinchin-Pease model. At high recoil energies a collision cascade occurs, in which the damage energy is deposited in a small volume of the lattice. As the cascade energy dissipates, most of the displaced atoms recombine, leaving only very few point defects per unit damage energy. A significant

(a) Pacific Northwest Laboratory is operated for the U.S. Department of Energy by Battelle Memorial Institute under Contract DE-AC06-ROL 1830.

fraction of the residual point defects are thought to be in clusters, whereas the remaining mobile defects are free to migrate away from the cascade region. The freely migrating defects and, depending on the temperature, those that dissociate from immobile clusters, are the point defects that effectively participate in microstructural changes.

Atomistic computer simulations [8] utilizing the binary collision cascade computer code MARLOWE [9] and stochastic annealing simulations yielded energy-dependent functions for the production of "freely migrating defects" in individual, isolated cascades at room temperature in Cu [10]. The freely migrating interstitial function from reference 8 was chosen as a test case and is referred to as Hmod.

The second test case was an energy dependent function for freely migrating defects proposed by Wiedersich [11]. The function was fitted to data extracted from solute segregation experiments on Ni-Si and Cu-Au alloys irradiated at temperatures of 650-900 K with heavy ions [12]. This function is referred to as Wmod. This model has had some success in describing materials effects for pressure vessel steel [4].

These preliminary models represent the scope of theoretical and experimental activities aimed at characterizing the production of the effective defects in radiation damage. Both models have serious shortcomings. Hmod is based on computer modeling of the physical processes in individual cascades in a pure metal; it does not include the effects of intercascade interactions or alloy compositions. The empirical Wmod function is fitted to data that are interpreted from the high damage rate experiments using rate theories that may not properly represent defect production in cascades.

Relative to calculated dpa, both Hmod and Wmod are near unity at low energies and drop steeply with increasing energy to constant values of a few percent (see Figure 1). The primary difference between the two functions is the magnitude of the constant value reached at high energies. Wmod clearly predicts more dramatic spectral effects than Hmod because of the lower number of freely migrating defects at higher recoil energies.

Calculational Method and Results

Calculations were simplified by making use of the SPECTER computer code [13] which contains energy-dependent atomic recoil distributions for 40 different elements for neutron energies up to 20 MeV. A computer program was written to integrate the freely migrating defect models over the primary recoil energy distributions at each of 100 neutron energies between 1.0 x 10^{-10} and 20 MeV. In this way, energy-dependent defect production cross sections were determined for each model. These cross sections were then added to the SPECTER cross section libraries so that defect production is calculated along with the standard dpa for any specified neutron energy spectrum and length of irradiation. The calculated cross sections are shown in Figure 2.

Defect calculations were performed as a function of axial location in rows 2 and 7 of EBR-II at Argonne National Laboratory, and for the Materials Open Test Assembly (MOTA) in FFTF at Hanford. Neutron spectra were taken from calculations for run 78C in EBR-II [14] and for run cycle 9A in FFTF [15]. In order to understand the effects of considering surviving defects as a damage parameter as opposed to dpa, the enhancement factor was determined for each axial location relative to midplane. The calculated dpa would thus have a value of 1.0 at all locations. Note that the enhancements are only relative since, as is clearly shown in Figures 1 and 2, both Hmod and Wmod predict significantly fewer defects than the calculated number of displacements (dpa) on an absolute scale. As can be seen in Figures 3 and 4, relative defect production in the new models is enhanced by factors of 2 to 3 in comparison to dpa. This is a significant difference if one is attempting to correlate material property changes observed in irradiations conducted at various axial positions. Note that significant effects are seen for the below-core basket region and above-core levels 6-8 for the MOTA assembly in FFTF, positions that are being used more frequently in current fusion materials experiments.

Comparisons with Materials Effects Data

Many radiation-induced property changes are sensitive not only to composition but also to a wide array of environmental variables. Void swelling, for instance, is strongly sensitive to temperature history, displacement rate, and applied stress, all of which exert their primary influence on the duration of the transient regime of swelling [16]. Temperature and displacement rate variations are frequently strongly coupled in many reactors, however, and displacement rate gradients are invariably accompanied by variations in neutron spectra [1]. This sometimes makes it difficult to separate the influence of each of these three variables. The potential impact of spectral variations in data analysis can be demonstrated using two published data sets.

Porter and Garner [17] examined the swelling of 1.5-m-long pressurized creep tubes constructed from annealed 3041 stainless steel that were irradiated in Row 7 of EBR-II to peak doses of ~80 dpa. Swelling was measured for ten one-inch sections from each pin; one at the core centerline, three just above the core bottom and six below the core bottom. The temperature varied from ~380 to ~400°C over this range and the displacement rate varied by a factor of ~4. As shown in Figure 5, swelling along the length of these pins exhibited a complex behavior in response to variations in temperature, displacement rate and possibly neutron spectra. If the Wmod enhancement factors calculated for Row 7 are used to normalize the data,

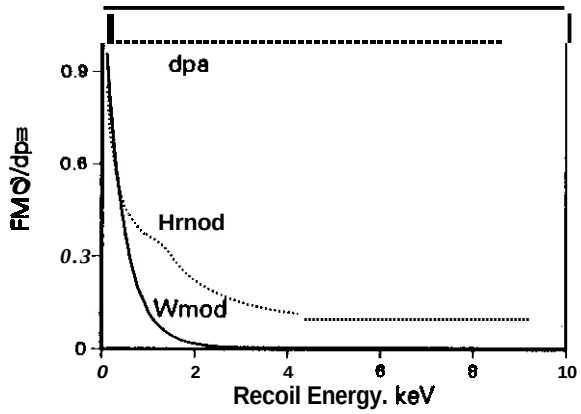

Fig. 1. Comparison of defect survivability fractions for the Hmod and Wmod models of freely migrating defects compared with the standard dpa model.

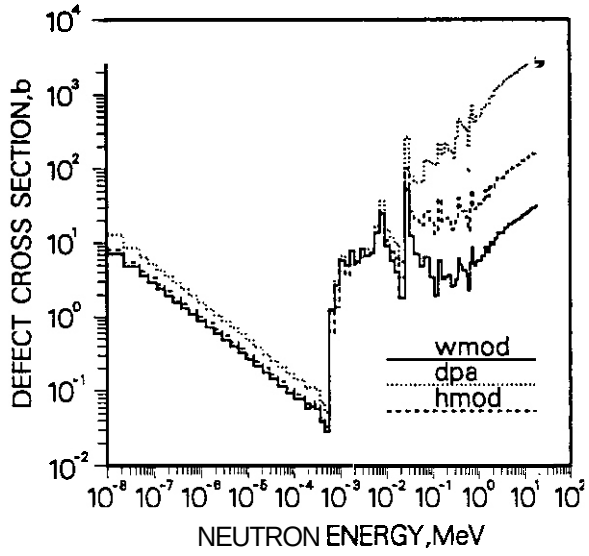

Fig. 2. Comparison of displacement damage cross sections for iron for the Hmod and Wmod models with that for the standard dpa model.

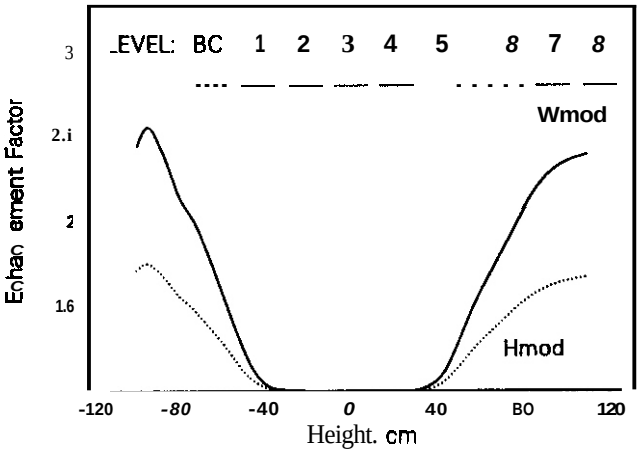

Fig. 3. Relative enhancements over the standard dpa model are shown for Hmod and Wmod as a function of axial location in the MOTA of FFTF.

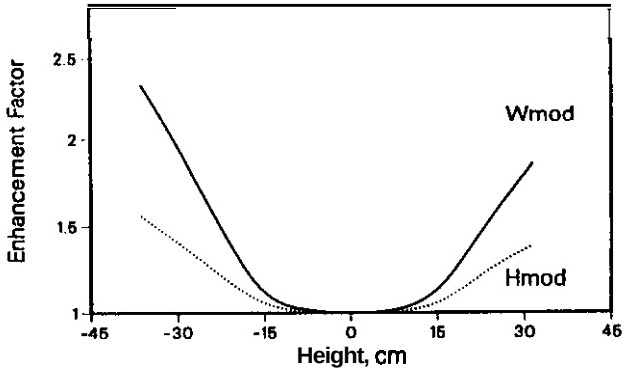

Fig. 4. Relative enhancements over the standard dpa model are shown for Hmod and Wmod as a function of axial location in row 7 of EBR-II.

however, much of the complexity disappears, particularly in the below-core region. Since the temperature difference is only 10°C in this region, it is evident that the apparent sensitivity tu displacement rate is much lower than previously assumed [16]. This is particularly true for highly stressed pins, where stress reduces the duration of the transient region and thereby its impact on the data analysis.
Swelling in the below-core region exhibits an almost linear dependence on FMD production. The maximum enhancement factor for this data set was calculated to be 2.0, using the Wmod model. Enhancement factors calculated with Hmod are smaller than with Wmod and hence are not as effective in linearizing the data. Wmod was similarly found to be more effective than Hmod in fitting pressure vessel steel data obtained in different irradiation facilities [4].

The impact of spectral enhancement factors is even easier to demonstrate for data sets where incubation-related phenomena are small, where the impact of temperature variations is minimal, and where a larger range of spectral variation is involved. Lewthwaite and Mosdale [18] provided such an opportunity when they reported an apparently strong inverse dependence of irradiation creep on displacement rate, as shown in Figure 6. Using weighted helical springs suspended in sodium-filled tubes, spanning both in-core and deep below-core positions in the Dounreay Fast Reactor (DFR), they observed enhancement in creep rates as large as a factor of four for displacement rates varying as much as a factor of 20. Lewthwaite and Mosedale concluded that there was "no unambiguous evidence" supporting a displacement flux effect on point defect recombination and suggested an alternative possibility involving "the inadequacy of the displaced atom concept" with its "incomplete description of events in energetic cascades." Although neutron spectral data were not available for the DFR reactor, the spectral effects are expected to be similar to those for EBR-II, as shown in Figure 4. It is interesting to note that the size of the spectral effects in Figure 6 is clearly comparable to that in Figure 4, which suggests that the apparent displacement rate effect may well be more readily explained by spectral differences, with dpa rate effects playing a secondary role.

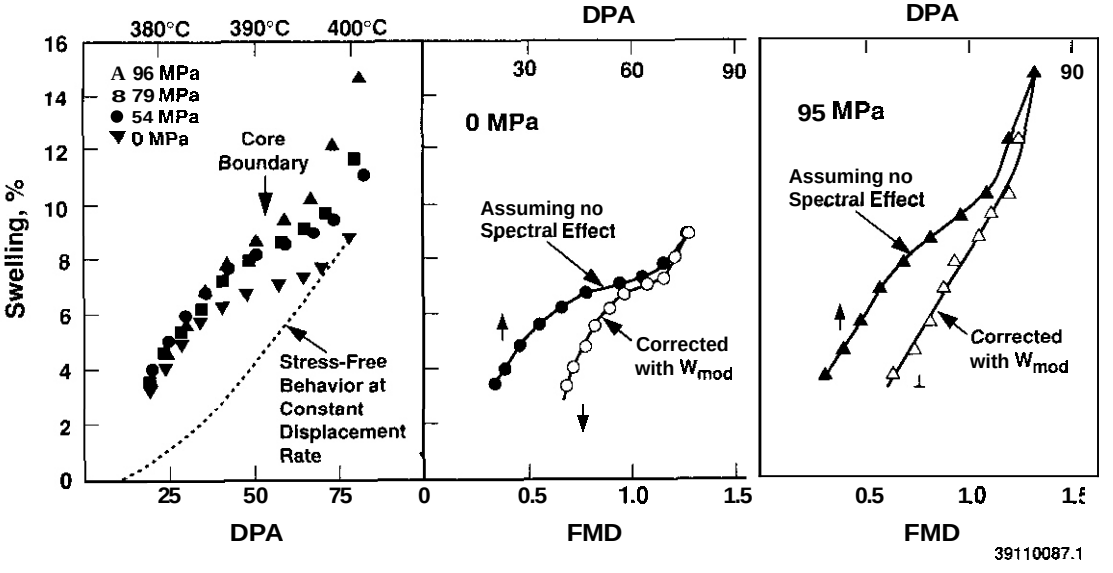

Figure 5. (a) Swelling variations observed along the length of four annealed 304L stainless steel tubes pressurized to different hoop stress levels and irradiated in EBR-II, plotted vs calculated displacement level. Effect of spectral effectiveness on these data is shown in (b) for a stress-free pin and (c) for a highly stressed pin, plotted vs FMD.

FUTURE WORK

Spectral effectiveness damage calculations are also being performed for other reactors. including the Oak Ridge Research Reactor and the High Flux Isotope Reactor, both at Oak Ridge National Laboratory. Besides pressure-vessel considerations mentioned previously, other data sets will be examined fur spectral effects. The calculations will also be used to predict the possible magnitude of spectral effects for various reactor positions.

CONCLUSION

Spectral effects have been shown to be significant for fast reactors, especially in the comparison of data between in-core and out-of-core positions. Although the models considered in this paper appear to have some success in analyzing swelling data, as well as explaining apparent differences in pressure vessel steel data mentioned previously, it should be stressed that these models are preliminary attempts to describe complex phenomena. More work is needed to develop physically-based models and to test them in various neutron spectra.

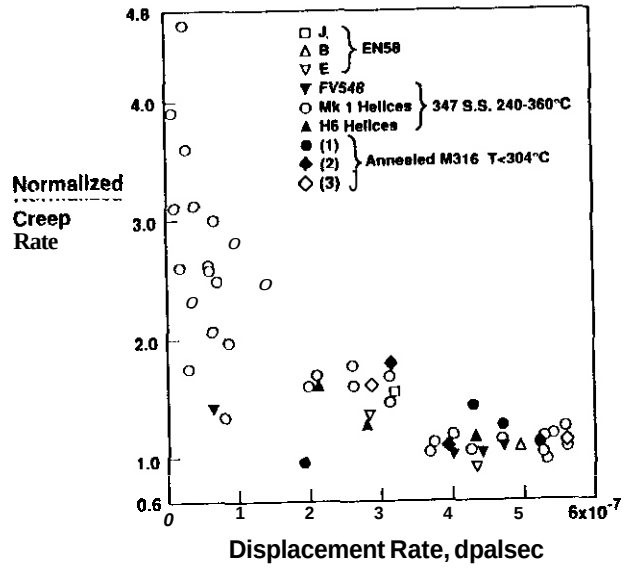

Figure 6. Enhancement of creep rates measured by Lewthwaite and Mosedale in various positions in and below the core of the DFR reactor relative to that measured at core center, implying a strong dependence on either displacement rate or neutron spectra.

REFERENCES

1. F. A. Garner, H. L. Heinisch, R. L. Simons, and F. M. Mann, Radiation Effects and Defects in Solids, Vol. 113 (1990) 229-255.

2. Evaluation of HFIR Pressure-Vessel Integrity Considering Radiation Embrittlement, ids. R. O. Cheverton, J. G. Merkle and R. K. Nanstad, ORNL/TM-10444 (1987).

3. L. K. Mansur and K. Farrell, J. Nucl. Mater., 170 (1990) 236.

4. C. A. Hrabal, Modified Damage Parameters Applied to a Typical Light-Water Reactor's Pressure Vessel Supports, ASTM-Euratom Symposium on Reactor Dosimetry, Strasbourg, France, August 1990.

5. H. L. Heinisch, J. Nucl. Mater., 178 (1991) 19.

6. C. H. Woo, B. N. Singh, and F. A. Garner, proceedings of ICFRM-5, to be published in J. Nucl. Mater.

7. M. J. Norgett, M. T. Robinson and I. M. Torrens, Nucl. Eng. Des., 33 **(1975)** 50.

8. H. L. Heinisch , J. Nucl. Mater., 117 (1983) 46.

9. M. T. Robinson and I. M. Torrens, Phvs. Rev. B9, (1974) 5008.

10. H. L. Heinisch and F. M. Mann, J. Nucl. Mater., 122-123 (1984) 1023

11. H. Wiedersich, J. Nucl. Mater., 179-181 (1991) 70

12. L. E. Rehn and P. R. Okamoto, Mater. Sci. Forum 15-18 (1987) 985.

13. L. R. Greenwood and R. K. Smither, SPECTER: Neutron Damage Calculations for Materials Irradiations, ANL/FPP-TM-197 (1985).

14. F. C. Franklin, E. R. Ebersole, and R. R. Heinrich, Analysis of EBR-II Low-Power Dosimetry Run 78C, ANL-77-76 (1977).

15. R. L. Simons, Westinghouse Hanford Company, private communication (1990)

16. F. A. Garner, J. Nucl. Mater., 122-123 (1984) 459-471.

17. D. L. Porter and F. A. Garner, ASTM STP 870, 1985, pp. 212-220.

18. G. W. Lewthwaite and D. Mosedale, J. Nucl. Mater., 90 (1980) 205-215.

Neutron-Induced Swelling of Binary Ni-A1 Alloys - M. A Mitchell, (University of Illinois) and F. A. Garner. (Pacific Northwest Laboratory)[a]

OBJECTIVE

The objective of this effort is to explore the response to irradiation of materials used in fission-?usion correlation experiments.

SUMMARY

Five Ni-Al binary alloys with aluminum levels of 1.1, 2.6, 4.2, 7.1 and 13.3 weight percent were irradiated at eight temperatures ranging from 400 to 650°C in the EBR-II fast reactor. The density changes induced during irradiation were found to be strongly dependent on both aluminum content and the irradiation temperature. Dynamic solute redistribution caused by radiation-induced segregation and the temperature-dependent formation of γ′ phase also appears to contribute significantly to the density changes.

PROGRESS AND STATUS

Introduction

Nickel and various nickel binary alloys are often employed in fundamental studies of radiation damage. These studies most often focus on segregation and phase stability [1,2] but are sometimes directed toward the influence of recoil spectra.[3,4,5] The employment of pure nickel in spectral recoil studies has recently been called into question, however, due to its tendency toward saturation of swelling, a process that can overshadow the effects of variables such as neutron spectra, displacement rate or helium/dpa ratio.[6] Nickel alloys present other complications, such as the tendency toward short-range order in Ni-Cr alloys during ion or neutron irradiation, a process that leads to increased energy requirements for dislocation movement.[7]

In one recent study, however, it was shown that phase instabilities routinely observed in ion irradiations of Ni-Si alloys do not occur under typical neutron irradiation conditions, probably as a consequence of the differences in displacement rate between neutron and ion irradiation experiments.[8] Not only do neutron irradiation experiments proceed at much lower displacement rates compared to those of ion irradiation studies, but neutron experiments are free of perturbations from surface effects and displacement rate gradients that are typical of ion experiments. Since the majority of the irradiation data for nickel binary alloys involves the use of charged particle irradiation, there is a need for neutron irradiation data for comparison before drawing conclusions concerning the influence of recoil spectra, transmutation or displacement rate.

Experimental Details

Ni-Al alloys with aluminum contents of 1.1, 2.6, 4.2, 7.1, and 13.3 weight percent were irradiated in three separate experiments in the EBR-II fast reactor. The alloys with the three lowest aluminum levels were solution annealed for one hour at 1093°C and air cooled. The Ni-7.1Al alloy was irradiated in two starting conditions: 1149°C/1hr/WQ and 1149°C/1hr/WQ+ 816°C/3.75hr/AC. The pure γ′ alloy Ni-13.3Al was also irradiated in two conditions: 1100°C/1hr/WQ and 1100°C/1hr/WQ+ 800°C/48hr/WQ. Tables 1 and 2, as well as Figure 1, describe the composition, starting condition and phase distribution of these alloys in more detail.

In each of the three experiments, eight irradiation temperatures were used, varying from 400(±5°C) to 650°C (±15°C), but each experiment reached different exposure levels. The first experiment, designated AA-IX, involved a single irradiation sequence of all alloys except Ni-13.3Al, reaching temperature-dependent exposures of 1.5 to 2.8 x 10^{22} n/cm^2, E > 0.1 MeV, which is equivalent to 8.2 to 14.3 dpa in pure nickel. The different exposure levels reflect axial differences in displacement rate, which ranged from 0.6×10^{-6} to 1.1×10^{-6} dpa/sec.

The second experiment, designated AA-VII, involved the four alloys employed in the first experiment, but proceeded in three separate irradiation vehicles. Peak exposures were reached of 5.5, 7.6, and i2.1 x 10^{22} n/cm^2 (27.5, 38.0, 60.5 dpa in pure nickel) at 650°C. At two temperatures (400 and 454°C). however, only those specimens from the first and third exposure levels were measured. The Ni-13.3Al alloy was included in only the third experiment, designated AA-XII, and reached exposures of 5.1 to 7.1 x 10^{22} n/cm^2 (25.5 to 35.5 dpa) in a single irradiation sequence.

---

[a] Operated for the U.S. Department of Energy by Battelle Memorial Institute under Contract DE-AC06-76RLO 1830.

Table 1. Description of Ni-Al Alloys

Alloy Desiqnation	Heat Number	Aluminum Content Wt.%	At.%	Phases	Measured Densitv, g cm^{-3}
E13	75376	1.1	2.4	γ	8.7351
E14	75358	2.6	5.4	γ	8.5540
E15	75359	4.2	8.7	γ	8.3564
E16	75360	7.1	14.3	γ + γ′	8.0507
E16*	75360	7.1	14.3	γ + γ′	8.0518
FE	--	13.3	25.0	γ′	7.5012
FF**	--	13.3	25.0	γ'	7.5088

* Aged at 816°C for 3.75 hours
** Aged at 800°C for 48 hours

Table 2. Chemical Analysis of Ni-Al Alloys

Alloy Desisnation	Ni	Al	Fe	Mn	cu	Cr	Mo	Si	Ti	Co	C	O	N
E13	Bal	1.1	0.53	0.005	0.015	0.21	N.D.	0.01	0.05	0.02	0.005	0.0013	0.0005
E14	Bal	2.6	0.35	0.005	0.015	0.15	N.D.	0.01	0.05	0.005	0.005	0.0011	0.0005
E15	Bal	4.2	0.20	N.D.	0.03	0.05	N.D.	0.02	0.01	0.004	0.005	0.0010	0.0005
E16	Bal	7.1	0.18	0.005	0.01	0.05	N.D.	N.D.	N.D.	0.005	0.004	0.0029	0.0008

[1]ND = not determined

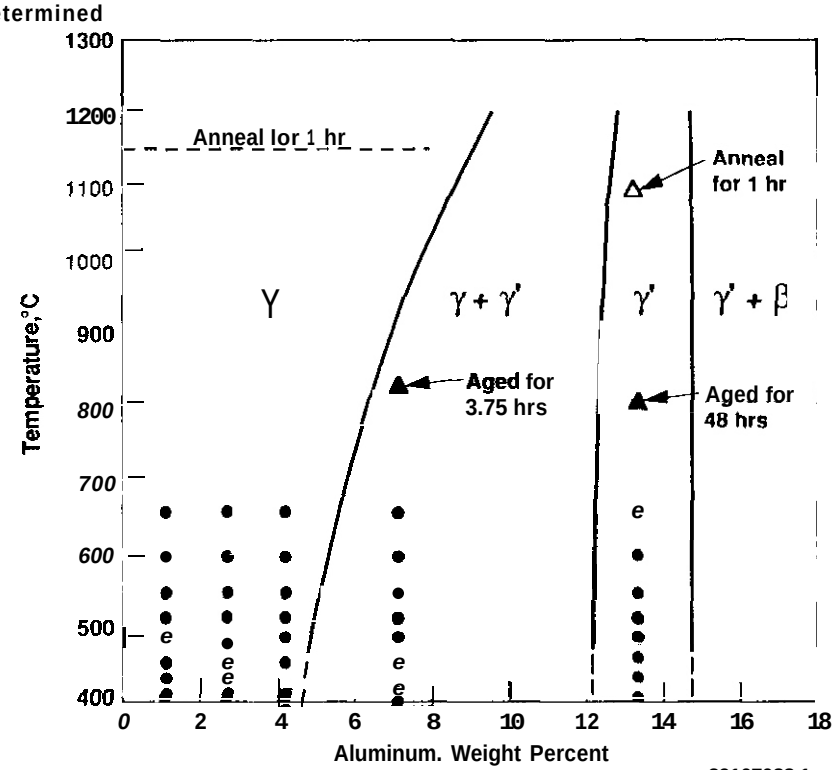

Fig. 1. Phase diagram for Ni-Al system showing relationship of phase stability with processing and irradiation conditions used in this study. The black circles denote the material and temperature conditions explored in this study.

The specimens were irradiated in the form of rods (3 mm diameter by 12.7 mm long) in the AA-IX experiment and in form of microscopy disks (3 mm diameter by 0.75 mm thick) in the other two experiments. The density of each specimen was determined before and after irradiation using an immersion density technique demonstrated to be accurate to ± 0.16%.[9]

Results

Figures 2-5 present a compilation of the density changes produced by the irradiation. The density change in most instances is the sum of void swelling and lattice parameter changes arising from various solute redistribution and precipitation processes. The latter contribution may be either positive or negative in sign.

It is clear in Figure 2 that progressive additions of aluminum decrease the swelling toward a saturation level at lower irradiation temperatures. At higher temperatures, however, there is a tendency to again increase in swelling at the higher aluminum levels. Typically, at intermediate temperatures the upswing starts in the range between 2.6 and 4.2 percent aluminum.

At a given displacement level, swelling yenerally decreases with increasing irradiation temperature, as shown in Figures 7 and 4. The crossover of the swelling curves at some temperatures in Figure 2 for the lowest two fluence levels appears to be a consequence of the different flux/temperature relationships employed in the AA-IX and AAVII experiments. It may also arise in part from the time-dependent and flux-dependent phase changes that occur during irradiation. Figure 3 shows that at 593 and 650°C densification can occur, reflecting a strong contribution from solute redistribution that overwhelms the contribution of void swelling.

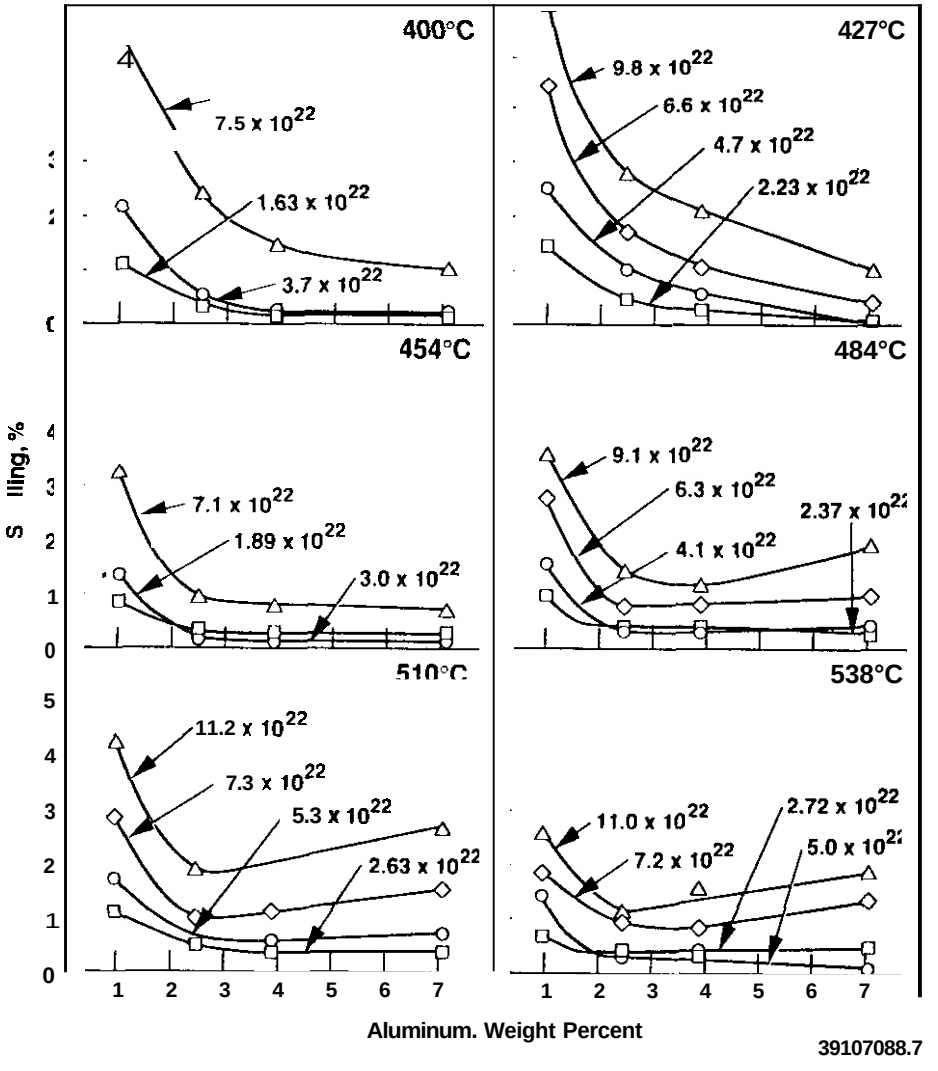

Fig. 2. Swelling of quenched Ni-AI alloys observed in EBR-II at 400-538°C as a function of aluminum content

Figure 4 shows that, except at the highest temperatures, the swelling of these alloys is relatively linear with neutron exposure and that the swelling rate is quite sensitive to irradiation temperature at the lowest aluminum level. As the aluminum level increases, however, the range of swelling rates becomes much smaller

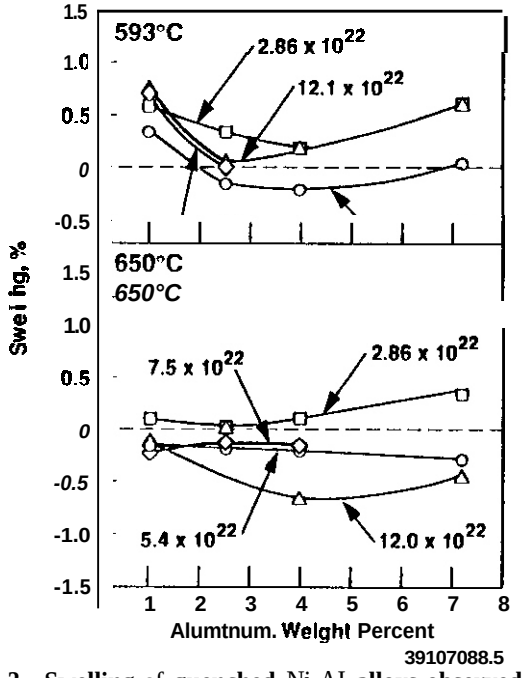

Fig. 3. Swelling of quenched Ni-Al alloys observed in EBR-II at 593 and 650°C as a function of aluminum content.

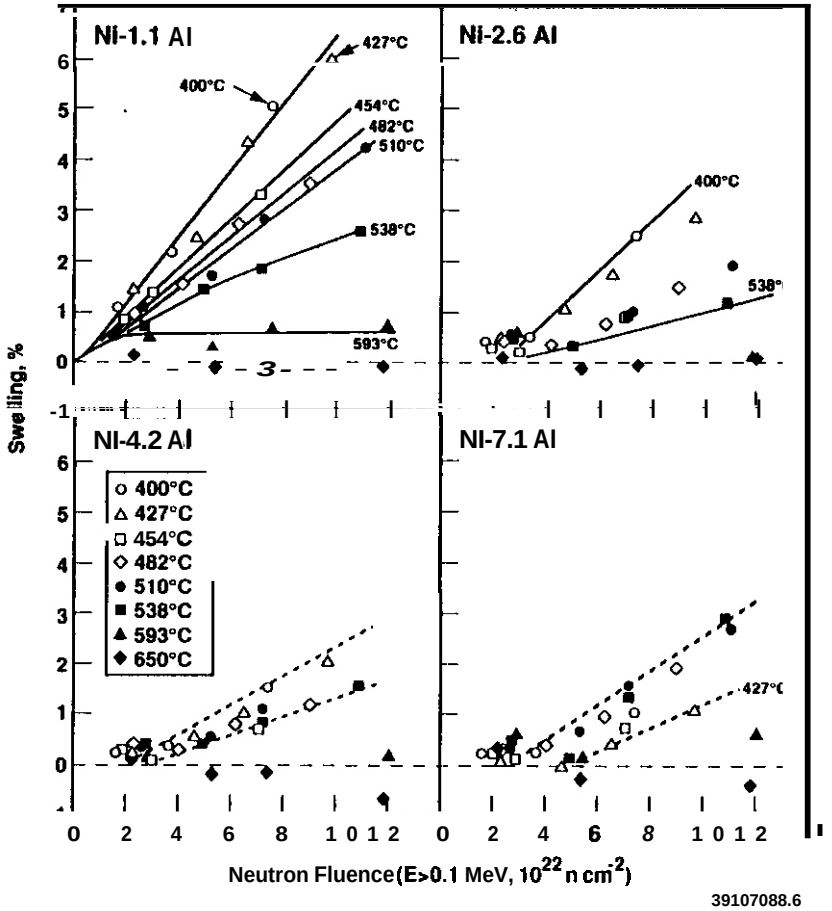

Fig. **4. Swelling of quenched Ni-Al alloys observed in EBR-II as a function of displacement level and irradiation temperature.**

From the behavior observed at the higher aluminum levels, note that the data from the AA-IX lower fluence experiment fall outside the response band of the data from the AA-VII experiment. This emphasizes again how temperature and flux relationships can influence the early evolution of these alloys.

Figure 5 shows how aging of the Ni-7.1Al alloy introduces differences in density changes as large as 0.5% compared to that *of* the unaged alloy. In general, the aged alloy exhibits less density change than does the unaged alloy, but there were some exceptions. No trend or pattern can be discerned in the exceptions that might provide some insight on the microstructural processes involved.

In the AA-XII experiment the Ni-13.3Al alloy did not exhibit significant swelling in either starting condition. In fact, most specimens exhibited substantial densification, as shown in Table 3.

Table 3. Density changes measured in Ni-13.3Al

Temperature °C	Neutron Fluence 10^{22}n/cm^2(E>0.1MeV)	Annealed	Annealed and Aged
400	5.1	-0.35	-0.12
427	6.2	-1.04	-0.41
454	4.8	-0.53	-0.44
482	6.0	-0.33	-0.51
510	6.9	+0.05	-0.42
538	6.E	4.04	t0.47
593	7.1	-0.65	-.013
649	7.1	+0.03	+0.31

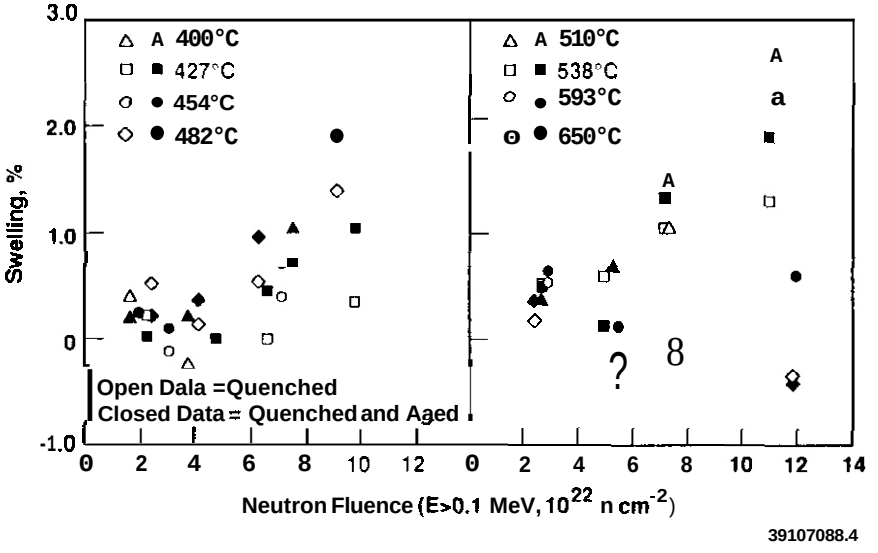

Figure 5.Comparison between swelling observed in Ni-7.1Al in the quenched and the quenched plus aged condition.

Discussion

The only previously published void swelling data on Ni-A1 binary alloys was generated using charged particle irradiation.[10-12] Aluminum additions in these studies were found to reduce swelling progressively. in agreement with the results of the current study. The explanations advanced in the ion bombardment studies for the effect of aluminum on swelling concerned the interaction of aluminum with the paint defects produced by irradiation. It is known, however, that substantial redistribution of aluminum occurs during irradiation as a direct result of such interactions.[1,2]

The substantial densification observed in the Ni-13.3Al over a wide temperature range and the lesser but still significant densification observed in Ni-7.1Al during irradiation at higher temperatures suggest that

solute redistribution occurs on a wide scale duriny irradiation at temperatures ≤650°C, even though aging at temperatures of 800-816°C for relatively short times did not cause significant changes in density.

As shown in Table 1, the difference in density between the aged and unaged starting conditions of Ni-7.1Al in the unirradiated condition is ~0.01%. This is insufficient to account for the differences observed in radiation-induced changes in densitv for the two conditions. A similar situation exists for the Ni-13.3Al alloy. As shown in Figure 6, the density of unirradiated alloys is a strong function of aluminum content but does not seem to be very sensitive to phase distribution or the heat treatments explored in this experiment

Therefore, the differences in density change exhibited by the different heat treatments of the Ni-7.1Al alloy probably represent the influence of the volume and distribution of γ′ on void swelling. As shown in Figure 7, there is a significant difference in the y' size distribution between the unaged and aged. condition before irradiation. The γ′ volume fraction increased substantially during aging, and thus the aluminum content of the matrix decreased considerably. Since the density of Ni-7.1Al does not change significantly with aging at 816°C, the partial molar volume of the aluminum at that temperature must be the same in both the γ and γ′ phases.

If we assume, however, that the γ′ distribution produced in Ni-7.1Al during irradiation at a given temperature is that dictated by the phase diagram, we would expect that the γ′ fraction will strongly increase as the irradiation temperature decreases, as shown in Table 4. Thus, the matrix at the lower irradiation temperatures should contain progressively lower levels of aluminum, approaching the matrix level of the Ni-4.2Al alloy. Additionally, if we assume that the rate of approach to equilibrium will increase with increasing irradiation temperature, and that the γ′ phase does not swell appreciably, as demonstrated in Table 3, then the rate of swelling may exhibit a minimum with aluminum content at intermediate irradiation temperatures as shown in Figure 2. It is well known that aluminum segregates sway from sinks during irradiation and that the segregation phenomenon usually peaks at intermediate irradiation temperatures [1,2].

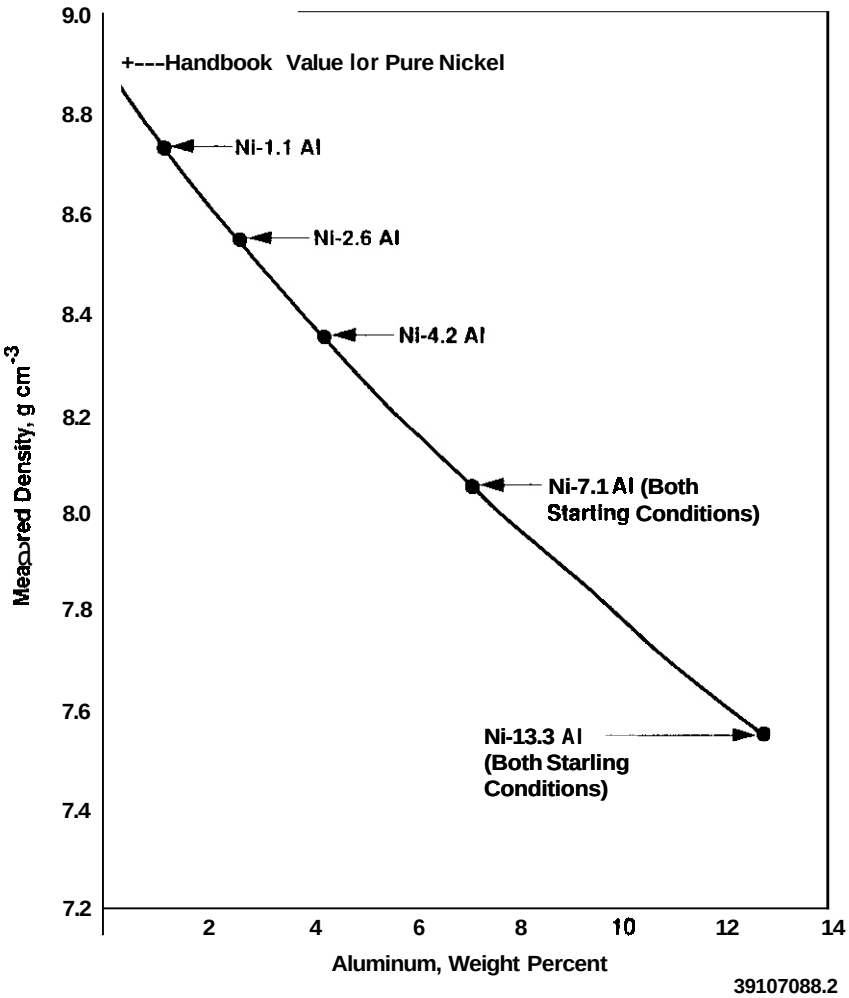

Fig. 6. Measured values of density in unirradiated Ni-AI alloys.

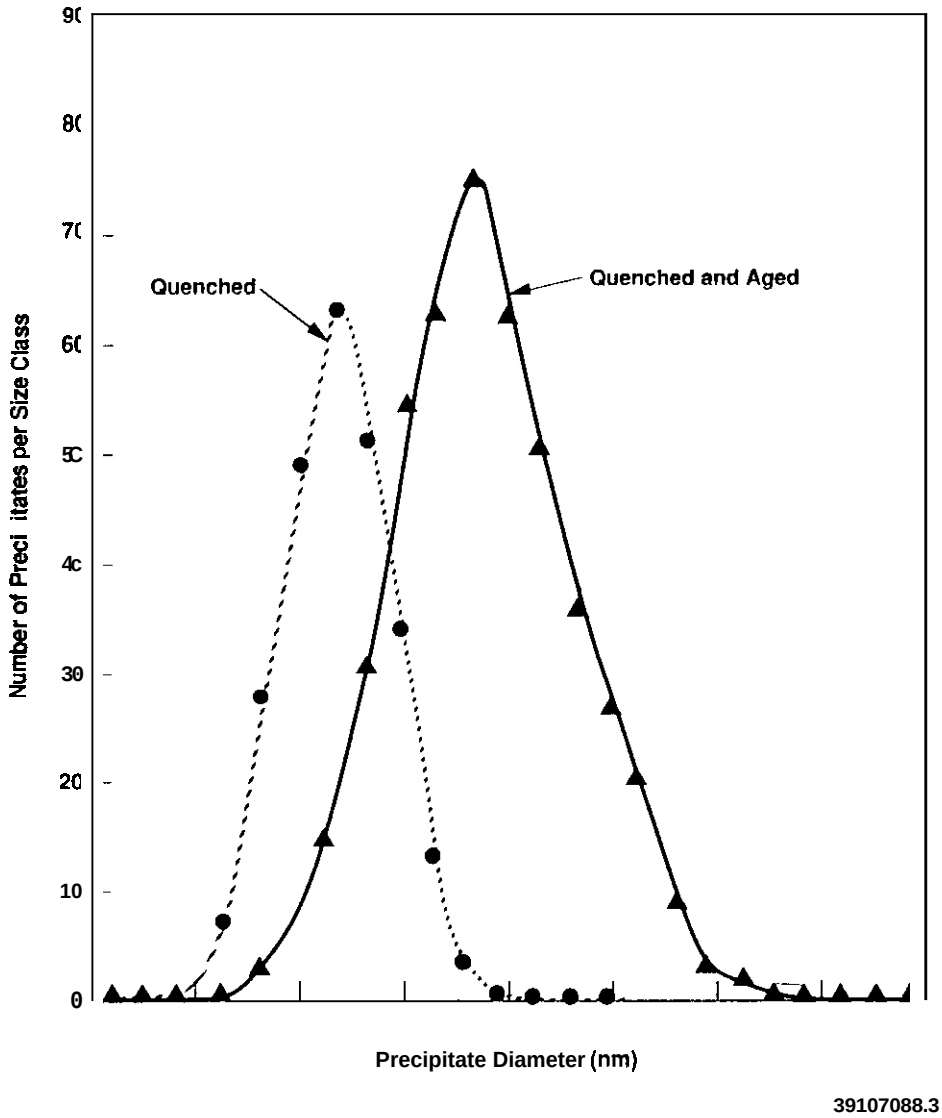

Fig. 7. Size distribution of γ' measured before irradiation on the two heat treatment conditions employed for the Ni-7.1Al alloy (unpublished data courtesy of M. K. Korenko of Westinghouse Hanford Company).

Table 4

Equilibrium Volume Percent of γ'
In Ni-7.1Al Calculated From the Phase Diagram

T (°C)	Equilibrium Volume Percent of γ'
440	31
540	28
640	23
740	18
816	11

There is also a possibility that the equilibrium distribution of γ' predicted by the phase diagram is not the same as that produced following irradiation. Nelson, Hudson and Mazey found that Ni 6.5Al(wt.%) underwent a significant alteration in solute and precipitate distribution during ion irradiation at temperatures comparable to those employed in this study.[13]

It is also possible that the response of swelling to increasing aluminum level may partially reflect the influence of aluminum in modifying the displacement rate. The calculation of the displacement rate for binary alloys involves some complexity and has not yet been evaluated for this study.

CONCLUSIONS

Ion irradiation data on nickel-binary alloys have been studied by others to yield information on phase stability under irradiation and also to study the influence of recoil spectra. Neutron data are necessary for comparison with ion data in order to determine the influence of surface effects, displacement rate gradients and differences in displacement rate. In a series of experiments conducted in EBR II the density changes induced in Ni-Al binary alloys by neutron irradiation were found to be strongly affected by the amount of aluminum in the alloy matrix, the irradiation temperature, and the redistribution of solute that occurs as a result of radiation-induced segregation and the formation of the γ' phase.

REFERENCES

1. L. E. Rehn and P. R. Okamoto, in Phase Transformations During Irradiation, Frank V. Nolfi, Jr., Applied Science Publications Ltd. 1983, pp. 247-290.

2. A. J. Ardell and K. Janghorban, pp. 291-329 in ref 1.

3. F. A. Garner, H. L. Heinisch, R. L. Simons and F. M. Mann, Radiation Effects and Defects in Solids, 113 (1990) 229-255.

4. F. A. Garner, Journal of Nuclear Materials 174 (1990) 229-239.

5. T. Muroga, H. Watanabe, M. Araki and N. Yoshida, Journal of Nuclear Materials, 155-157 (1988) 1290.

6. F. A. Garner, pp. 125-135, in Fusion Reactor Materials Semiannual Progress ReDort, DOE/ER-0313/8 (1990).

7. F. A. Garner, Journal of Nuclear Materials, 148 (1987) 288-293

8. H. Takahashi and F. A. Garner, "Response of Ni-Si and Ni-Al Alloys to Neutron Irradiation," in this report.

9. R. W. Powell, D. T. Peterson, M. I. Zimmerscheid and J. F. Bates, [illegible] (1981) 969, pp. 103 & 104.

10. R. S. Nelson "The Simulation of void Swelling - A Critical Assessment After Ten Years," Harwell Report AERE-R-8826, July 1977.

11. J. A. Hudson, S. Francis, D. J. Mazey and R. S. Nelson, pp. 326-333 in Effects of Radiation on Substructure and Mechanical Properties of Metals and Alloys. ASTM STP 529, American Society for Testing and Materials, 1973.

12. L. J. Chen and A. J. Ardell, Scripta Metallurgica, 10 (1976) pp. 1047-1050.

13. R. S. Nelson, J. A. Hudson and D. J. Mazey, Journal of Nuclear Materials, 44 (1972) pp. 318-330

PHASE SEPARATION IN FE-35Ni DURING THERMAL AGING AT 625°C - X. Ji and J. J. Hoyt, (Washington State University) and F. A. Garner, (Pacific Northwest Laboratory*)

OBJECTIVE

The objective of this effort is to determine the factors which control the microstructural and microchemical evolution of metals during neutron irradiation.

SUMMARY

It has been proposed in other studies that the spinodal-like decomposition process observed in sone helium effects studies may arise from a radiation-induced self-organization process involving segregation to helium bubbles. In this study phase separation in Fe-35Ni during thermal aging at 625°C has been investigated by means of X-ray diffraction, hardness and resistivity measurements. Line broadening of X-ray diffraction peaks demonstrates that this alloy is susceptible to thermal decomposition into two phases. Thus, helium and radiation-induced segregation are not prerequisites for decomposition to occur. However, the absence of appreciable concurrent changes in hardness or resistivity with aging time indicates that the phase separation reaction is very sluggish. Other experiments involving irradiation of Fe-35Ni and various Fe-Cr-35Ni alloys indicate that this phase separation can be accelerated substantially, however. An analysis of existing thermodynamic data has been used to demonstrate that an increased rate of spinodal decomposition can occur for the case of irradiated Fe-35Ni.

PROGRESS AND STATUS

Preface

Fe-Cr-Ni alloys of varying nickel level are currently employed in studies of the relative influence of helium and other variables on the evolution of microstructure and mechanical properties[1,2]. During the conduct of these studies it has been observed that a spinodal-like decomposition occurs in Fe-35Ni and various Fe-Cr-35Ni alloys during irradiation, contributing to the microstructural evolution[3-5] and also to changes in the mechanical properties arising from spinodal hardening.[6] Until recently, Separation of the relative contributions of this process and the effects of helium have proceeded on the assumptions that (!) radiation only accelerates or modifies the natural but sluggish tendency of Fe-35Ni alloys to decompose thermally, and (2) that the effects of helium and spinodal-like decomposition were not directly related.

Another school of thought proposes that there is no natural tendency to decompose and the formation of spinodal-like decomposition is a direct result of segregation to helium bubbles.[7,8] If this proposal is correct, helium bubbles must participate in some type of radiation-induced self-organization process in order to produce the long range crystallographic orientation of compositional modulation observed in the decomposed specimens investigated by Garner and coworkers.[4,5]

In order to investigate the validity of these two proposals, a series of thermal aging studies was initiated to ascertain whether decomposition could develop in the absence of irradiation. The following paper, submitted to Philosophical Magazine, presents the first results of these studiei.

INTRODUCTION

The Fe-Ni binary alloy system is very important from both a scientific and technological viewpoint. Alloys with compositions near Fe-35 at% Ni, known as invar alloys, exhibit a near zero thermal expansion coefficient over a substantial temperature range. This makes Fe-Ni alloys valuable in technological applications which demand a high degree of dimensional stability.

Russell and Garner[9] have proposed a high temperature miscibility gap between two coherent fcc phases γ_1 and γ_2 in the Fe-Ni system. The miscibility gap, which does not appear on the generally accepted version of the phase diagram,[10] is thought to explain several experimen a ly observed properties in this alloy system, including anomalies in the thermal expansion coefficient,[11] lattice parameter,[11] single crystal elastic constants,[12,13] electrical resistivity[14] and interdiffusion coefficient.[15] Thus, a detailed study of the proposed miscibility gap in Fe-Ni would provide significant insights into the observed physical properties of this important alloy system.

Further evidence for the existence of a miscibility gap was provided by Brager and Garner[16] who measured large amplitude fluctuations in Ni concentration in neutron irradiated Fe-Ni-Cr invar alloys. Additional observations of large scale decomposition at 510-725°C were later found in both ion and neutron irradiated

* Operated for the U.S. Department uf Energy by Battelle Memoria! institute under Contract DE-AC-05-76RLO 1830.

Fe-Ni and Fe-Cr-Ni alloys in the invar range.[3,4,5,17] Significant spinodal-like hardening was also observed in three Fe-Cr-35Ni alloys after irradiation at 425°C.[6] Garner and coworkers concluded that the irradiation served to enhance the kinetics of the alloy's natural tendency toward sluggish spinodal decomposition. Williams, Boothby and Titchmarsh[18] also observed concentration oscillations in an irradiated solute-modified Fe-15Cr-25Ni alloy but observed no decomposition in the unirradiated alloy after a very long heat treatment. The apparent contradiction between the behavior at 25 and 35% Ni led Murphy[7] to suggest that spinodal decomposition was unlikely in Fe-Cr-Ni alloys. She suggested that an irradiation-induced instability was the source of the observed concentration modulations.

To date, metallurgists and physicists have not universally accepted the idea of a thermally-induced miscibility gap at high temperature due to the absence of convincing microscopic or diffraction evidence of decomposition. The essentially equal scattering power of Fe and Ni for X-rays, as well as for electrons and neutrons, makes the usual diffraction techniques inapplicable, and the fine scale of thermally-induced decomposition is not observable by optical or electron microscopy. However, special experimental techniques can be employed to enhance the scattering contrast.

Wiedenmann, Wagner and Wollenberger[19,20] examined isotopically enriched Fe-34 at% Ni samples using small angle neutron scattering. Samples enriched in Ni^{62} serve to increase the scattering contrast. Their study confirmed the tendency for this alloy to decompose on a fine scale during thermal annealing for 5520 hrs (230 days) at 625°C and to develop large wavelength fluctuations in composition during proton irradiation at the same temperature. The authors also noted an increase in scattered intensity following 230 days of aging vs. 20 days of aging.

The high electrical resistivity measured in fcc 35Ni alloys is thought by some researchers to be caused by fine scale heterogeneities. Kachi and Asanol[21] determined from Mossbauer spectra measurements that at 4.2K this alloy is composed about equally of ferromagnetic and anti-ferromagnetic domains (γ_1 and γ_2 domains). The high resistivity was attributed to electron scattering at the interface between these domains. The existence of the domains in turn was attributed to concentration fluctuations which suggest the onset of a miscibility gap.

On the other hand, Simon, Lyon, Faudot, Rzepski, Dimitrov, Boulanger and Martin employed the technique of anomalous small angle X-ray scattering on thermally aged (≤500 hrs) Fe-Ni samples and found no evidence for spinodal decomposition. With the additional techniques of analytical transmission electron microscopy and thermal gravimetric analysis, they were able to place upper bounds on the amplitude of concentration fluctuations that could exist in their samples. The contradictory conclusions drawn by the aforementioned groups of scientists indicate that the existence of a high temperature thermally-induced miscibility gap in Fe-Ni is still very much in question.

Due to the difficulty of obtaining scattering data from thermally-aged specimens it is worthwhile to study by indirect means the spinodal decomposition process. Associated with modulations in composition is usually a locally varying lattice parameter. This spatial variation in strain will be manifested in a broadening of Bragg diffraction peaks. Precision lattice parameter measurements of Fe-20 at% Ni by Kachi and Asano[21] showed the expected line splitting that arises from the slightly different wavelengths of Cu $K\alpha_1$ and $K\alpha_2$ X-rays. Diffraction peaks for a Fe-30 at% Ni alloy were found by Kachi and Asano to broaden, however, without splitting. Their results suggest that at the higher Ni level the alloy might have decomposed into regions differing slightly in Ni content and, therefore, in lattice parameter.

A second indirect means used to study spinodal decomposition in Fe-Ni involves measurements of electrical resistivity vs. aging time. Schwartz and Plewes[23] used electrical resistivity to investigate the early stages of the spinodal decomposition process in a Cu-9Ni-6Sn alloy. The authors found that the percentage decrease in resistivity was proportional to A^2 where A is the amplitude of the three-dimensional compositional modulation. At 300°C, Schwartr et al. found a decrease in electrical resistivity of about 47% after just 20 hours of aging.

Changes in yield strength, or equivalently hardness, is yet another means of studying spinodal decomposition in systems which lack strong scattering contrast. Cahn[24] predicted that an alloy undergoing spinodal decomposition would exhibit an increase in yield strength and showed that the increase should be proportional to the product of the amolitude of compositional modulations and the modulation wavelenoth. Katb, Mori and Schwartz[25] later refined Cahn's treatments and demonstrated that the increase in yield strength is proportional only to the amplitude of composition 1 fluctuation. The Kato model was later confirmed in a study of Cu-Fe-Ni alloys by Butler and Thomas.?"")

The present study was conducted using the above techniques to investigate thermally-induced phase separation in Fe-35Ni at 625°C. Methods used include X-ray diffraction, hardness measurements and resistivity measurements. Furthermore, an analysis of existing thermodynamic data is presented. The thermodynamic calculations, combined with the results of this experiment, support the existence of a thermally-induced miscibility gap in the Fe-Ni system. In addition, the thermodynamic data, along with an expanded version of the aforementioned theory of Murphy,[7] are used to illustrate the enhanced kinetics of phase separation which occur due to irradiation.

EXPERIMENTAL PROCEUURE

The material used in this study was of nominal composition Fe-35 wt% Ni with low level of impurities, as shown in Table 1.

Table 1

Chemical Composition of Fe-Ni Alloy by Weight Percent

Fe	Ni	C	N	O	H
65	35	,003	<.0001	.0017	.0001

Two types of specimens were used. First, bars of dimension 57mm x 5mm x 5mm were prepared. Second, ground powder screened through at 44 μm sieve was employed. Both types of specimens were encapsulated together in quartz tubes under 175 torr argon atmosphere and then homogenized at 900°C for 48 hours before thermal aging at 625°C. After homogenization and aging, the quartz tubes were water quenched. Four different aging times (60, 120, 240, 480 hours) were chosen.

Fe-Ni alloys have very low resistances, usually on the order of milliohms. Low resistances, ohms to milliohms or microhms, are not measurable with the usual Ohmmeter or even Wheatstone Bridge devices due to bridge connecting leads, contact resistances and other problems. Therefore a Kelvin double bridge apparatus was used to make the resistivity measurements on the bar specimens, employing a constant 10 amperes current source with a voltage of about 2.6 volts. Resistivity tests proceeded at both room temperature and, in order to increase accuracy, low temperature. Low temperature testing was accomplished by placing the sample and its holder into 665 ml Pope Dewar Flask filled with liquid nitrogen (about -210°C).

After resistivity measurement, the bar specimens were then used to measure hardness using a standard Rockwell Hardness Tester (B scale). For each specimen, ten data points were taken and then averaged to determine the hardness value.

A Siemens D500 automated powder diffractometer was used for X-ray measurements at a power setting of 35 kv and 30 mA, using a monochromated Cu Ka incident beam.

RESULTS

X-ray Diffraction

The X-ray diffraction profiles of the Fe-35Ni alloy at different aging times are shown in Figure 1. The range of angular position 2θ varies from 85 degrees to 105 degrees. The as-quenched sample exhibits the expected distinctive splitting of the high angle (222) and (311) reflections usually observed from diffraction of $K\alpha_1$ and $K\alpha_2$ characteristic X-rays. The sharp diffraction peaks imply that this sample is homogeneous in concentration with the same lattice spacing everywhere. This result is consistent with the proposed Fe-Ni phase diagram by Russell and Garner.[9] At 900°C, this diagram specifies only one single γ phase.

The profiles of the aged specimens show that both peaks gradually broaden with increasing heat treatment time. Strong broadening was observed in the specimen aged 480 hours. No $K\alpha_2$ and $K\alpha_2$ separation can be seen in the intensity profiles of the (311) reflection. The broad diffraction peaks indicate decomposition into regions of differing lattice parameter. For the larger spacing, the corresponding diffraction line shifts to lower angle. On the other hand, the diffraction line corresponding to smaller spacing shifts to larger angle. The sum of these sharp lines, each slightly displaced from the other, causes the broadened diffraction line. This is consistent with the proposed phase diagram by Russell and Garner,[9] which predicts that during aging at 625°C, the γ phase decomposes into two coherent fcc phases γ_1 and γ_2. Although the (222) reflection is slightly broadened, the $K\alpha_1$ and $K\alpha_2$ diffraction peaks can still be resolved. The fact that the Ka doublet is still resolvable after 480 hours of aging indicates that phase separation in Fe-Ni is extremely sluggish under thermal conditions. The slow kinetics may be due to a low atomic mobility at 625°C and/or a low driving force. The much greater amplitude of compositional modulations observed in irradiated samples at similar temperatures and times may be explained at least in part, by the enhanced diffusion caused by irradiation.

Hardness

Shown in Figure 2 is the hardness response vs. aging time for the Fe-35Ni alloy. Clearly, within experimental error, there is no apparent change in hardness. Based on the X-ray diffraction results, this lack of response is not unexpected. First, the compositional fluctuations are not yet very pronounced due to the slow kinetics of decomposition. Kato et al.[25] concluded that the increment in yield stress due to

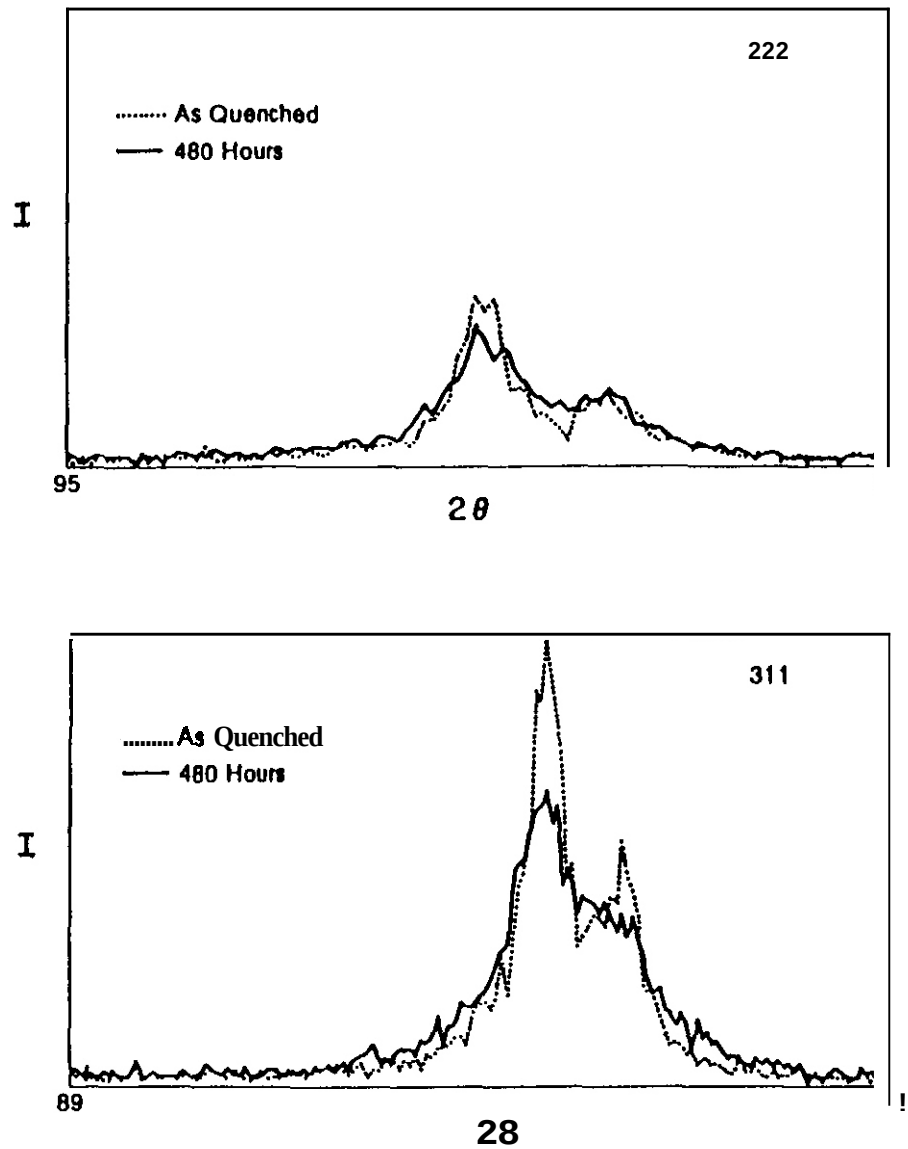

Figure 1. X-ray diffraction peaks in Fe-35Ni specimen as-quenched and aged 480 hours at 625°C

spinodal decomposition is proportional to the compositional amplitude. Since the amplitude of fluctuations measured in this study is quite small even at 480 hrs, the increment in yield stress or hardness is also small. Second, compared to X-ray line broadening measurements, hardness testing is in general much less sensitive to small scale decomposition.

According to Kato et al.,[25] the increment in yield stress is given by:

$$\frac{\Delta\sigma}{\sigma_0} = \left(\frac{1}{6}\right)^{1/2} \frac{A\eta Y}{\sigma_0} \qquad (1)$$

where σ_0 is the yield stress, $\eta = \left(\frac{1}{a}\right)\left(\frac{da}{dc}\right)$ describes the compositional variation of lattice parameter (a). For an isotropic material $Y = E/(1 - \nu)$ and η, determined from the work of Kachi et al.[21] is, 0.03.

Using eqn. (1), one can estimate an upper bound for the amplitude of concentration modulation present after aging for 480 hours at 625°C. Assume a value of $\Delta\sigma/\sigma_0$ equal to 0.1, that is, the maximum detectable change in hardness is 10%. Further assume a yield strength for Fe-35Ni of 350 MPa, a modulus of elasticity, E, equal to 150 GPa and a Poisson's ratio, ν, of 1/3. The amplitude of concentration fluctuations according to eq n. (1) is 0.01. This compares favorably with the results of Simon and coworkers.[22] In their study, magneto-thermogravimetric Curie temperature measurements indicated that aging in the temperature range 600-700°C did not produce concentration differences larger than 0.4 at.%.

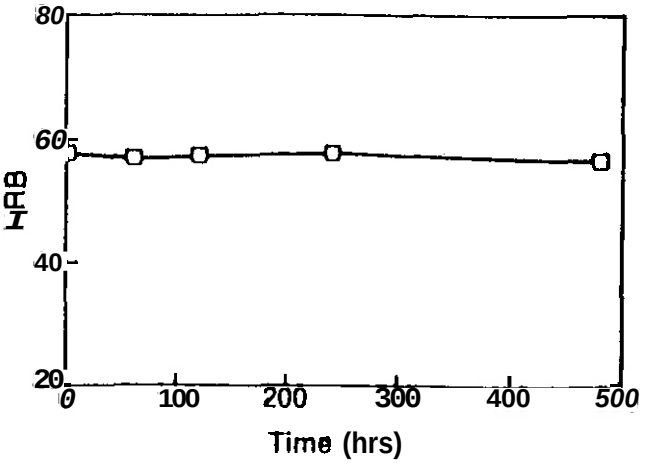

Fig. 2. Hardness versus aging time of Fe-35Ni specimen.

The experimental results of the present study suggest that the successful observation of high temperature phase separation in Fe-Ni depends on the experimental technique employed. Thus the differing conclusions drawn from the works of Simon et al.[22] and Wiedenmann et al.[19,20] may be explained in terms of the sensitivity of each experiment.

Resistivity

The resistivity measurements at both room temperature and low temperature are shown in Figure 3. No apparent changes in resistivity with aging time appear in this figure, once again signalling an extremely sluggish thermal transformation. According to the theory of Kolomets and Smirnov,[27] the change in resistivity due to spinodal decomposition is proportional to A^2, where A is the amplitude of the compositional modulation. Consequently, the change in resistivity at 625°C is too small at 480 hrs to be measured by this method.

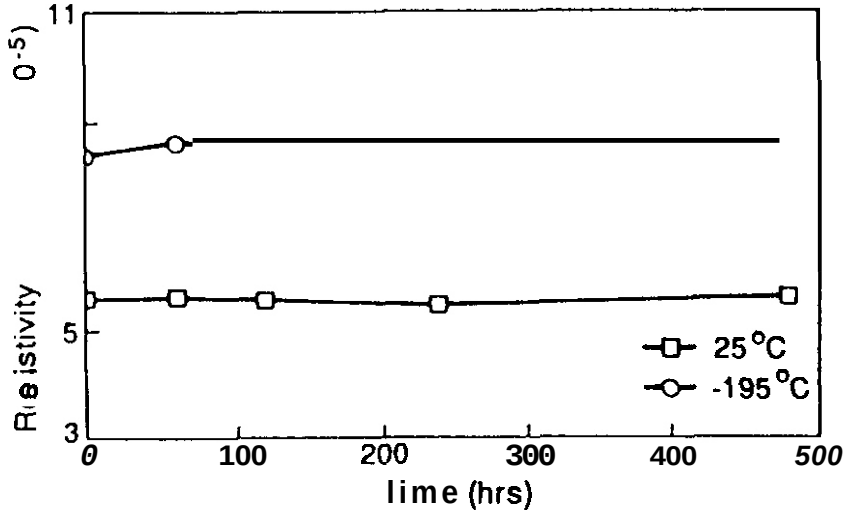

Fig. 3. Resistivity versus aging time of Fe-35 Ni specimen at room temperature and the temperature of liquid nitrogen.

DISCUSSION

In this section, we examine existing thermodynamic data on the Fe-Ni system in order to show that a miscibility gap at high temperatures is plausible and also to demonstrate the enhanced kinetics of spinodal decomposition under the influence of irradiation. Due to their technological importance, various thermodynamic properties of Fe-Ni alloys have been well investigated.[28-36] The Fe-Ni (fcc) system at high temperatures has been considered to form a continuous solid solution with negative values of mixing enthalpy AH. However, Kubaschewski, Geiger and Hack[37] have pointed out that AH has a region of negative curvature at about 20 at% Ni. Therefore, the alloy must split into two fcc phases in the equilibrium state at sufficiently low temperature, unless the splitting is suppressed by the mixing entropy effect. Values of AS and AH have been estimated by Kubaschewski and coworkers.[37]

In the following, the mixing free energy, $\Delta G = \Delta H - T\Delta S$, is calculated as a function of nickel content. If we neglect the temperature dependence of ΔH and ΔS, the calculated ΔG versus concentration curves are shown in Figure 4. The ΔG curve at lower temperatures exhibits two inflection points and has a common tangent in the Fe-rich region, suggesting the existence of a miscibility gap, as shown in Figure 5. The spinodal is the locus of points for which $d^2G/dX^2 = 0$. It can readily be found from the coefficients of a fourth order polynomial fit to the ΔG vs. concentration curves. The spinodal concentrations are then the roots of a second order polynomial.

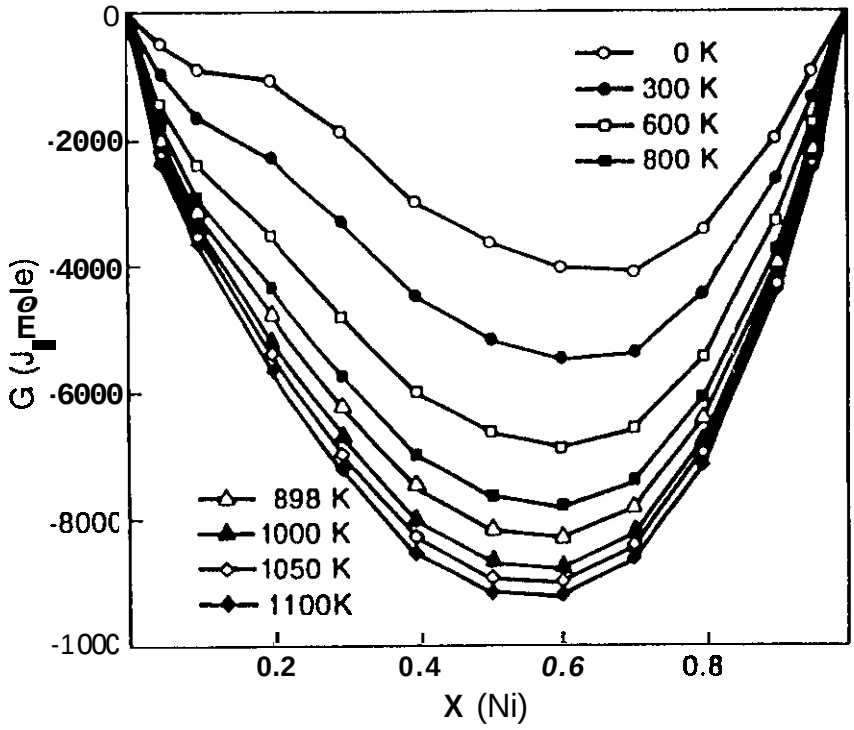

Fig. 4. Mixing **free energy versus X_{Ni}.**

Our estimated miscibility gap is plotted on the Fe-Ni phase diagram shown in Figure 5. The coherent spinodal is shown by the dashed curve. We find the critical point to be 28.1% Ni at 774°C. At 625°C, the spinodal concentrations are 23% Ni and 32% Ni and the miscibility gap boundaries are 21% Ni and 37% Ni. From the above computation it is interesting to note that the 35% Ni alloy lay inside the miscibility gap yet outside the spinodal decomposition region. Outside the spinodal the transformation must proceed by a process of nucleation and growth.

Tanji, Nakagawa, Saito, Nishimura and Nakatsuka[38] constructed free energy of mixing vs. composition curves and the phase diagram based on their isothermal EMF measurements and electrical resistivity data of Shirakawa.[39] The peak of the miscibility gap is at about 1300K and ~30% Ni. Their phase diagram is only qualitative and schematic, however.

Several earlier attempts have been made to predict the limits of the spinodal. According to Russell and Garner,[9,40] the gap limits are 28.5% Ni and 36.5% Ni at 625°C. In the study of Russell and Garner,[40] the experimental mixing enthalpy was reproduced by first taking the regular solution parabnlic enthalpy of mixing which gave $\Delta H = -5$KJ/mol at $X_{Ni} = 0.5$. Then a fourth order polynomial was added to insure a smooth composite curve and ideal mixing entropy was added to produce the curves for the free energy of mixing. Their miscibility gap and spinodal differ markedly from that which would be predicted using a regular solution model. In this approach, the miscibility gap does not broaden appreciably at lower temperature, as does the gap in a regular solution. At a given temperature, the miscibility gap and spinodal in Fe-Ni alloys lie at almost the same composition. The gap peak is at about 827°C and 35% Ni. They concluded that except near the center of the miscibility gap, an alloy would have to be cooled well below the phase boundary before spinodal decomposition could occur. Compared with their results, the gap in this study is wider and lower. And the critical point shifts toward the Ni-poor region.

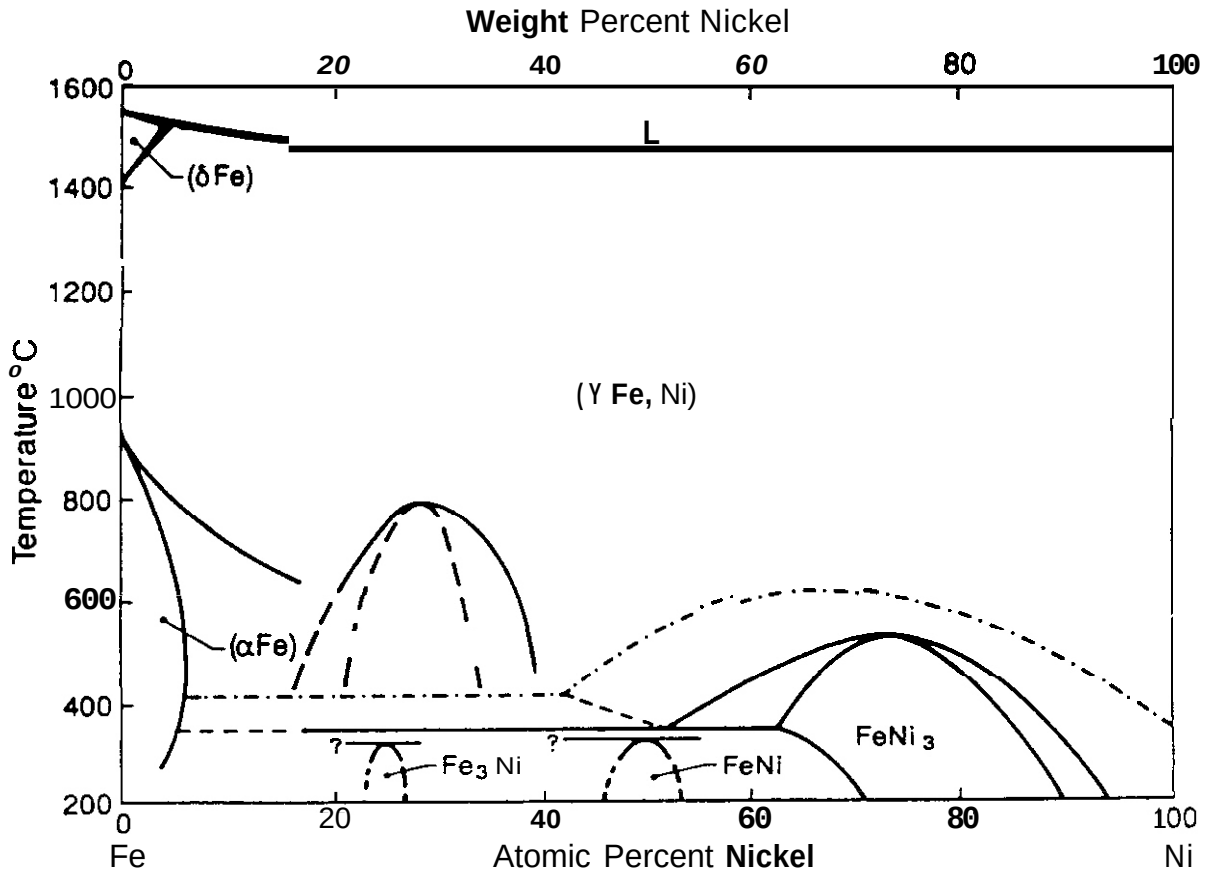

Fig. 5. Proposed Fe-Ni phase diagram showing a miscibility gap and spinodal.

Murphy[23] proposed that irradiation-induced decomposition might occur in the absence of a thermally induced driving force when interstitials exhibit a strong preference for exchanging with atoms of one element of the binary or ternary alloy. Murphy interpreted the compositional fluctuations observed in irradiated Fe-Ni-Cr-base alloys by this mechanism and suggested that spinodal decomposition may not be occurring. Both Russell and Garner and the current authors suspect that a mechanism such as that suggested by Murphy is expanding the miscibility gap during radiation.

Having developed a suitable free energy function for the Fe-Ni system, we are now in a position to examine the rate at which decomposition occurs in the thermal and neutron irradiated cases. Spinodal decomposition is characterized by the spontaneous growth with time of infinitesimally small amplitude compositional fluctuations. After long times, the decomposition process results in a system which is separated into two phases, i.e. regions of high and low solute concentration. In the theory of spinodal decomposition developed by Cahn,[24] the amplitude of concentration modulations is expressed in Fourier space with k representing the magnitude of the Fourier space vector. The quantity k is proportional to the reciprocal of the wavelength of fluctuations in real space. The compositional fluctuation with aging time can be expressed as a result of increases or decreases of the amplitude of each Fourier component:

$$A(kt) = A(k,0)\exp[G(k)\,t\,l, \qquad (2)$$

in which A(k, t) and A(k,0) are the amplitudes of the Fourier component of wave number k at time t and zero respectively, G(k) is an "amplification factor" defined by:

$$G(k) = -\left(\frac{M}{N_v}\right)k^2(f''+2\eta^2Y+2\kappa k^2), \qquad (3)$$

where M is the mobility of solute atoms, f is the Helmholtz free energy per unit volume, η is the fractional change in lattice parameter per unit change in composition, κ is the gradient energy coefficient, N_v is the number of atoms per unit volume and Y is a function of elastic constants.

Murphy[41] examined theoretically the growth or decay of solute concentration fluctuations for alloys during irradiation. Since linear stability theory was employed by Murphy, the form for the time dependent Fourier amplitudes is the same as that given in eqn. (2); only the amplification factor $G(k)$ is changed. For the irradiation case, $G(k)$ becomes:

$$G(k) = -(1+\beta)k^2\left(\frac{f_V d_{AV} d_{BV} C_V^\circ}{D_V} + \frac{f_I d_{AI} d_{BI} C_I^\circ}{D_I}\right) \tag{4}$$

$$-k^4 C_V^\circ C_I^\circ C_A^\circ C_B^\circ (1+\beta)\alpha C_V^\circ C_I^\circ \frac{(d_{BV} d_{AI} - d_{AV} d_{BI})^2}{D_I D_V F}$$

$$-k^4 C_V^\circ C_I^\circ C_A^\circ C_B^\circ \frac{(d_{AV} d_{BI} - d_{BV} d_{AI})}{F}\left(\frac{dK}{dC_B} - \frac{d\alpha}{dC_B} C_V^\circ C_I^\circ\right),$$

in which

$$\beta = \frac{C_B d(\ln\gamma_B)}{dC_B} = \frac{C_A d(\ln\gamma A)}{dC_A} \tag{5}$$

$$F = C_V^\circ C_I^\circ k^2 [k^2 D_I D_V + \alpha (D_I C_I^\circ + D_V C_V^\circ)], \tag{6}$$

where γ_i is the activity coefficient for the species i, C_i is the fractional concentration of, atoms of species i, D_I and D are interstitial and vacancy diffusion coefficients respectively, C_V, C, and C_i are the equilibrium concentration of vacancies, interstitials and species irrespectively, α is tie recombination coefficient, K is the production rate for vacancies and interstitials, d_V and d_{iI} are the partial mobilities for the migration of atoms of species i via vacancy and interstitial mechanisms, f_v and f, are the correlation factors for the diffusion of atoms in a homogeneous uniform lattice via the vacancy and interstitial mechanisms respectively.

It is important to note that in Murphy's theory a contribution due to gradient energy effects (see eqn. (3)) was not included, In order to illustrate the difference in the kinetics of spinodal decomposition for the thermal and irradiation cases, we will include such a term in the amplification factor.
Under typical neutron irradiation conditions, the recombination rate α and production rate K are very small, such that the second and third terms in eqn. (4) can be neglected. The second derivative of free energy f with respect to concentration is given by:

$$f'' = \frac{RT(1+\beta)}{(1-C_A)C_A},$$

where R is the gas constant and T is the absolute temperature

Substituting the last term of eqn. (3) dnd eqn. (7) into eqn. (4), $G(k)$ is given by:

$$G(k) = -k^2\left(\frac{f_V d_{AV} d_{BV} C_V}{D_V} + \frac{f_I d_{AI} d_{BI} C_I}{D_I}\right)\frac{(1-C_A)C_A}{RT}\left[f'' + 2\kappa k^2 \frac{A_w}{\rho}\right] \tag{8}$$

where A_w is the atomic weight and ρ is the density. Consider the Fe-30Ni alloy; the quantities d_{AV}, d f_v, D_V, $d_{,,}$, d_{m} f_I and D_I can be calculated from the table in Murphy's study [41]. From the thermodynamic estimates described above, the second derivative of free energy with respect to concentration of Ni at 898K

is calculated as -6.26 J/mole. The values of C_V° and C, depend on different circumstances. In the thermal case, $C_I^\circ = 0$ and $C_V^\circ = e^{-\frac{\Delta E_V^F}{KT}} = 2.96 \times 10^{-10}$. But in the irradiated case, C_I° and C_V° can be calculated by eqn. (7) and gqn. (6) employed in the study of Coghlan and Garner.[42] Under typical neutron irradiation conditions, $C_V = 3.23 \times 10^{-9}$ and $C_I = 1.39 \times 10^{-14}$ at 625°C with a displacement rate of 10^{-} dpa/s.

It remains to be seen how to best estimate the value of the gradient energy coefficient κ. Russell and Garner[40] attempted to evaluate κ based on the work of Cahn and Hilliard[43] using a regular solution model description of the thermodynamic properties of the Fe-Ni system. Their results indicated that κ is negative and they cited this as demonstrating the inadequacies of the regular solution model. In more recent years, κ has been related to the range of interaction of the system (i. e., nearest neighbor in the Ising model) and should be roughly the same in most binary alloy systems. In the present pork a value of κ equal to that stated by Rundman and Hilliard[44] for Al-Zn will be used, i.e., $\kappa = 1 \times 10^{-}$ erg/cm.

The amplification factor was calculated using the above approach for typical neutron conditions employed in the studies of Garner and coworkers.[4,5] The exponential of the amplification factor with respect to wave number curve is shown in Figure 6, showing that under irradiation the amplification factor is much larger than that of the thermal case in Fe-30Ni at 898K. Therefore the amplitudes of compositional fluctuations produced by long-term thermal annealing are much smaller than those produceo by irradiation at high displacement rate for comparable times and temperature. The results of figure 6 also explain why the specimen irradiated at 898K had much greater scattering intensity than exhibited by thermally aged specimens at 898K.[19]

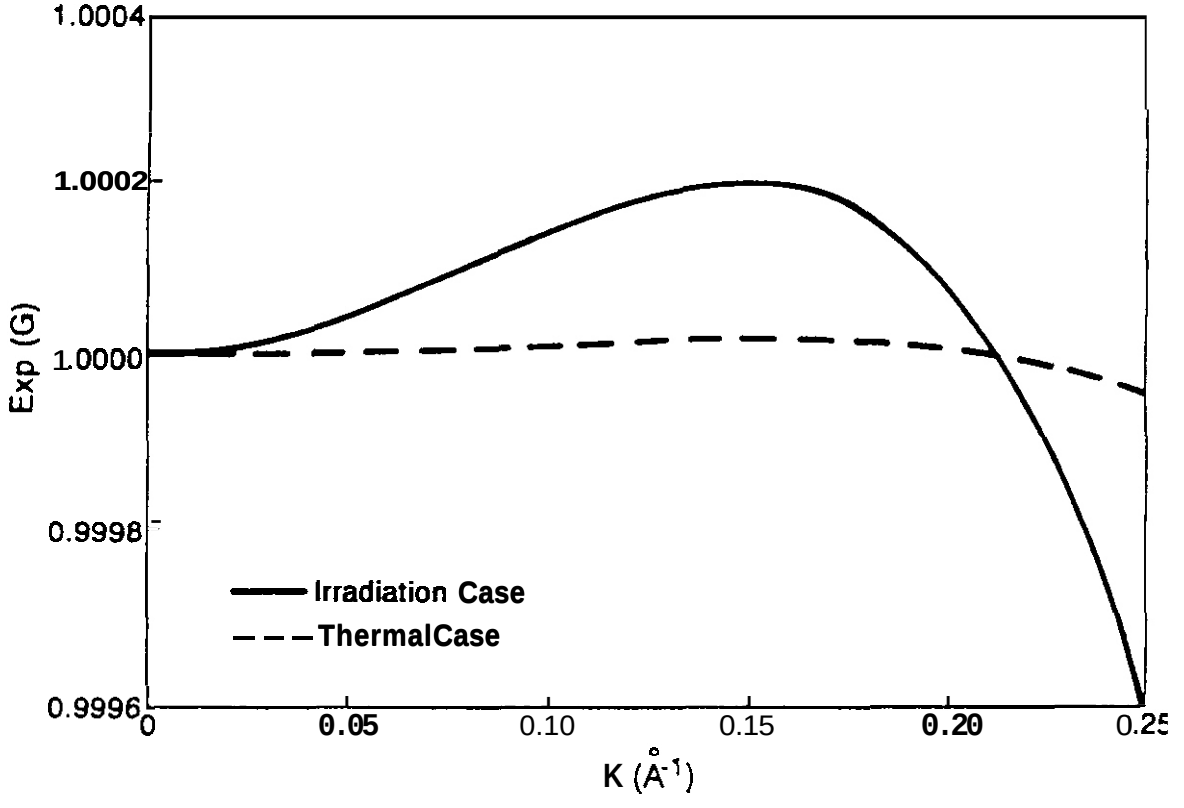

Fig. 6. Exponential of amplication factor versus wavenumber.

CONCLUSIONS

1. X-ray diffraction measurements of Fe-35Ni alloy exhibit line broadening with increasing aging time, which suggests the presence of a high temperature miscibility gap in this alloy.

2. The results of hardness and resistivity tests reveal that the kinetics of phase seoaration at high temperatures cannot be observed using such measurements. This suggests that thermal transformations in Fe-Ni alloys are very sluggish.

3. Previously published irradiation studies indicate that irradiation can dramatically enhance the rate of decomposition.

4. A thermodynamic analysis suggests that a coherent miscibility gap exists in the Fe-Ni system with a peak in the vicinity of 774°C and 28% Ni; this gap can be used to explain the experimental results presented in this paper. This analysis also demonstrates that radiation can significantly accelerate the decomposition.

FUTURE WORK

Aging continues at 625°C on the Fe-35Ni alloy. X-ray, resistivity and hardness measurements will be made for specimens aged for times greater than 480 hours.

REFERENCES

1. See papers by Garner and coworkers in J. Nucl. Mater., pp. 179-181 (1991) pp. 111-117, pp. 445-448, pp. 511-514, pp. 523-525, pp. 554-557, pp. 558-562.

2. M. L. Hamilton, F. A. Garner and 8. M. Oliver, Fusion Reactor Materials Semiannual Progress Report DOE/ER-0313/9, April 1991, pp. 61-68.

3. R. A. Dodd, F. A. Garner, J.-J. Kai, T. Lauritzen, and W. G. Johnston, 1987, Radiation-Induced Changes *in* Microstructure: 13th International Symposium (Part 1), ASTM STP 955, F. A. Garner, N. H. Packan and A. S. Kumar, Eds., ASTM, PA, p. 788.

4. F. A. Garner and J. M. McCarthy in Physical Metallurgy of Controlled Expansion Invar-Type Alloys, K. C. Russell and D. F. Smith, Eds., TMS-AIME, Warrendale PA (1990) p. 187.

5. F. A. Garner, H. R. Brager, and J. M. McCarthy, 1987, Radiation- Induced Changes in Microstructure: 13th International Symposium (Part 1), ASTM STP 955, F A. Garner, N. H. Packan and A. S. Kumar, Eds., ASTM, PA, p. 775.

6. H. R. Brager, and F. A. Garner, and M. L. Hamilton, 1985, J. Nucl. Mater., 133-134, p. 594.

7. S. M. Murphy, 1988, Phil. Mag. A, 58, p. 417

8. C. M. Shepherd, J. Nucl. Mater., 175 (1990) 170-176; also C. M. Shepherd and S. M. Murphy, J. Nucl Mater. 172 (1990) p. 143-150.

9. K. C. Russell and F. A. Garner, 1990, Metall. Trans. A, 21A, 5, pp. 1073-1082.

10. O. Kubaschewski, 1982, Iron Binary Phase Diagrams, Springer-Verlag, Berlin, p. 73.

11. A. I. Zakharov, 1989, Sov. Mater. Sci. Rev., 3, pp. 93-104.

12. G. Hausch and H. Warlimont, 1971, Phys. Lett., 36A, p. 415

13. H. Morita, H. Hiroyoshi, H. Fujimori and Y. Nakagawa, 1980, J. Magn. Magn. Mater., 15-18, p. 1197

14. Betteridge, W., 1984, Nickel and Its Alloys, Halsted Press, New York, p. 116

15. Nakagawa, Y., Tanji, Y., Morita, H., Hiroyoshi, H., and Fujimori, H., 1979, J. Magn. Magn. Mater., 10, p. 145.

16. H. R. Brager and F. A. Garner, 1985, Effects of Radiation on Materials, ASTM STP 870, F. A. Garner and J. S. Perrin, Eds., ASTM, Philadelphia, PA, 1985, pp. 139-150.

17. F. A. Garner, H. R. Brager, R. A. Dodd and T. Lauritzen, 1986, Nucl. Instr. and Meth. Phy. Res., 816, p. 244.

18. T. M. Williams, R. M. Boothby and J. M. Titchmarsh, 1987, Proc. BNES Canf. on Materials for Nuclear Reactor Core Applications, British Nuclear Energy Society, London, vol. 1, pp. 293-299.

19. A. Wiedermann, W. Wagner and H. Wollenberger, 1988, J. Less Common Metals, 45, pp. 47-53

20. A. Wiedenmann, W. Wagner and H. Wollenberger, 1989, Scripta Met., 23, p. 603.

21. S. Kachi and H. Asano, 1969, J. Phys. Soc. Japan, 27, p. 536.

22. J. P. Simon, O. Lyon, F. Faudot, J. Rzepski, O. Dimitrov, L. Boulanger and G. Martin, 1990, Physical Metallurgy of Controlled Expansion Invar-Type Alloys, edited by K. C. Russell and D. F. Smith, TMS-AIME, Warrendale, PA, pp. 51.

23. L. H. Schwartr and J. T. Plewes, 1974, Acta Metall., 22, p. 911.

24. J. W. Cahn, 1961, Acta Metall., 9, p. 795; 1963, Acta Metall., 11, p. 1275.

25. M. Kato, T. Mori and L. H. Schwartr, 1979, Acta Metall., 28, p. 285.

26. E. P. Butler and G. Thomas, 1970, Acta Metall., 18, p. 347.

27. I. D. Kolomets and A. A. Smirnov, 1962, Fiz. Met. Metall., 14, p. 3.

28. W. A. Dench, 1963, Trans. Faraday Soc., 59, p. 1279.

29. W. Steiner and O. Krisement, 1961, Arch. Eisenhüttenwesen, 32, p. 701.

30. O. Kubaschewski and L. E. Stuart, 1967, J. Chem. Engng. Data, 12, p. 418.

31. O. Kubaschewski and O. von Goldbeck, 1949, Trans. Faraday Soc., 45, p. 958.

32. R. A. Oriani, 1953, Acta Metall, 1, p. 448.

33. J. W. Spretnak, 1959, Trans MS AIME, 215, p. 185.

34. K. Ono, Y. Ueda, A. Yamaguchi and J. Moriyama, 1977, Trans Japan. Inst. Metals, 18, p. 610

35. C. Gatellier, D. Henriet and M. Olette, 1970, C. R. Acad. Sci., France, 271, p. 453.

36. 8. Predel and R. Mohs, 1970, Arch. Eisenhuttenwesen, 41, p. 143.

37. O. Kubaschewski, K.-H. Geiger and K. Hack, 1977, Z. Metallkd., 68, p. 337.

38. Y. Tanji, Y. Nakagawa, Y. Saito, K. Nishimura and K. Nakatsuka, 1979, Phys. Stat. Sol., A., 56, p. 513.

39. Y. Shirakawa, 1939, *Sci.* Repts., Tohoku Imp. Univ., 27, 485.

40. K. C. Russell and F. A. Garner, 1990, Physical Metallurgy of Controlled Expansion !:mar-Type Alloys, K. C. Russell and D. F. Smith, Eds., TMS-AIME, Warrendale, PA, p. 25.

41. S. M. Murphy, 1988, Phil. Mag. A, 58, p. 417.

42. W. A. Coghlan and F. A. Garner, 1987, Radiation-Induced Changes in Microstructure: 13th International Symposium (Part 1), ASTM STP 955, F. A. Garner, N. H. Packan and A. S. Kumar, Eds., ASTM, PA, p. *315.*

43. J. W. Cahn and J. E. Hilliard, 1958, J. Chem. Phys., 28, pp. 258-267.

44. K. B. Rundman and J. E. Hilliard, 1967, Acta Metall., 15, p. 1025.

PHOSPHIDE FORMATION IN NEUTRON-IRRADIATED Fe-15Cr-25Ni-P ALLOYS - H. Kinoshita, Hokkaido University and F. A. Garner, Pacific Northwest Laboratory*

OBJECTIVE

The objective of this study is to provide an understanding of the interactions of phosphorus and cold working on microstructural evolution in neutron irradiated alloys, and thereby assist in the interpretation of this alloy's performance in the ^{59}Ni isotopic tailoring experiment.

Summary

The results of microstructural examination of irradiation-induced phosphides formed in Fe-15Cr-25Ni-0.055P during the AA-14 experiment agree with trends observed in other studies conducted in both EBR-II and FFTF. The extent of phosphide formation in the annealed condition appears to be a well defined function of both phosphorus level and irradiation temperature. It also appears to be very sensitive to the presence of cold work.

PROGRESS AND STATUS

Introduction

In another report the influence of phosphorus on neutron-induced microstructural evolution of Fe-15Cr-25Ni was presented, focusing on two experiments, one conducted in EBR-II (AA-14 experiment) and another in FFTF.[1] Although the results of these studies[1,2] were in general agreement with the results of other studies,[3-5] there was one significantly new observation. It appeared that cold working tends to strongly modify and sometimes completely suppress the formation of nickel.rich phosphide precipitates compared to those that develop in annealed specimens.[1,2]

This report presents the results of a microstructural examination of the Fe-25.0Ni-15.2Cr-0.055P (wt%) alloy (designated E104) following irradiation to 14 dpa at 425, 500, and 600°C in the AA-14 experiment. This study was initiated to provide confirmation of phosphide behavior in response to cold working that was observed in the FFTF study. Details of the irradiation procedure, specimen preparation-and measurement are presented in reference 1. Only one specimen of each condition was available at a given temperature.

Results

Figure 1 presents the swelling inferred from density change measurements for both the annealed (1030°C/0.5 hr/water quench) and 30% cold worked conditions of alloy E33 (Fe-25.8Ni-14.8Cr (<0.005P)) and alloy E104 (Fe-25.0Ni-15.2Cr-0.055P). A density measurement is not available for E33 at 600°C. In addition, specimens were also irradiated in the 30% cold worked and aged (650°C/10 hr/water quench) condition. At 425°C the annealed condition densified 0.03%, compared to the 0.21% densification observed in the coid worked condition. Data at 500 and 600°C were not available for the aged alloy, however,

Figure 2 shows a comparison of the microstructures of the annealed and cold worked conditions at 14 dpa and 425°C, demonstrating both the influence of cold work in suppressing swelling and also the absence of phosphide formation in both conditions. These observations agree with those of other studies at comparable irradiation temperatures.

Figure 3 presents a comparison of the microstructures of the annealed and cold worked conditions at 14 dpa and 500°C. Needle-like phosphide precipitates of 200 nm length or greater at relatively high densities were observed in the annealed specimen. These nickel-rich phosphides also formed in the cold worked specimen but were smaller (≤100 nm) and at significantly lower density.

Figure 4 provides a comparison of the microstructures of the annealed and the cold-worked and aged condition at 600°C. (The cold worked specimen was destroyed during electropolishing). The annealed specimen possessed very large (≥500 nm) phosphide needles at much lower densities than observed at 500°C. The cold worked and aged specimen contained significantly less precipitation, with smaller (≤300 nm) needles at densities comparable to that of the annealed condition.

Discussion

In agreement with the results of the FFTF study, cold working in the AA-14 experiment was found to alter and retard the formation of phosphide precipitates. Since swelling was reduced by cold working in both the 425°C and 500°C specimens, this implies that phosphorus exerts it primary influence while in solution. This is also in agreement with results of earlier studies.[1-5]

*Operated by Battelle for the U.S. Department of Energy under Contract DE-AC06-76RLO 1830.

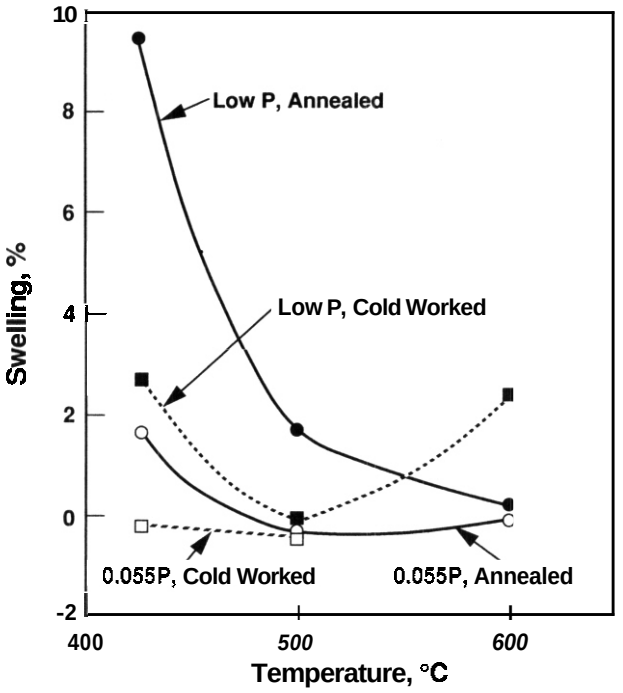

Fig. 1. Swelling observed in alloys E33 and E104 in the AA-14 experiment from EBR-II.

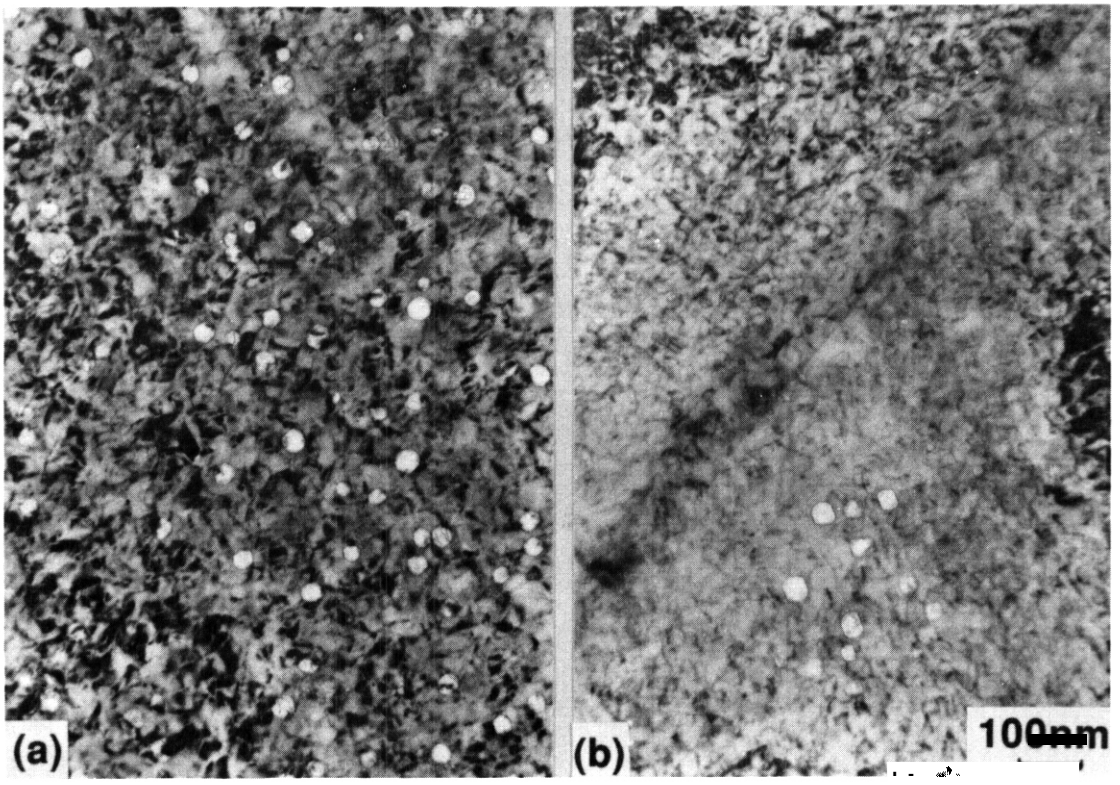

Fig. 2. Microstructures observed in the (a) annealed and (b) cold worked conditions of alloy E104 at 14 dpa and 425°C.

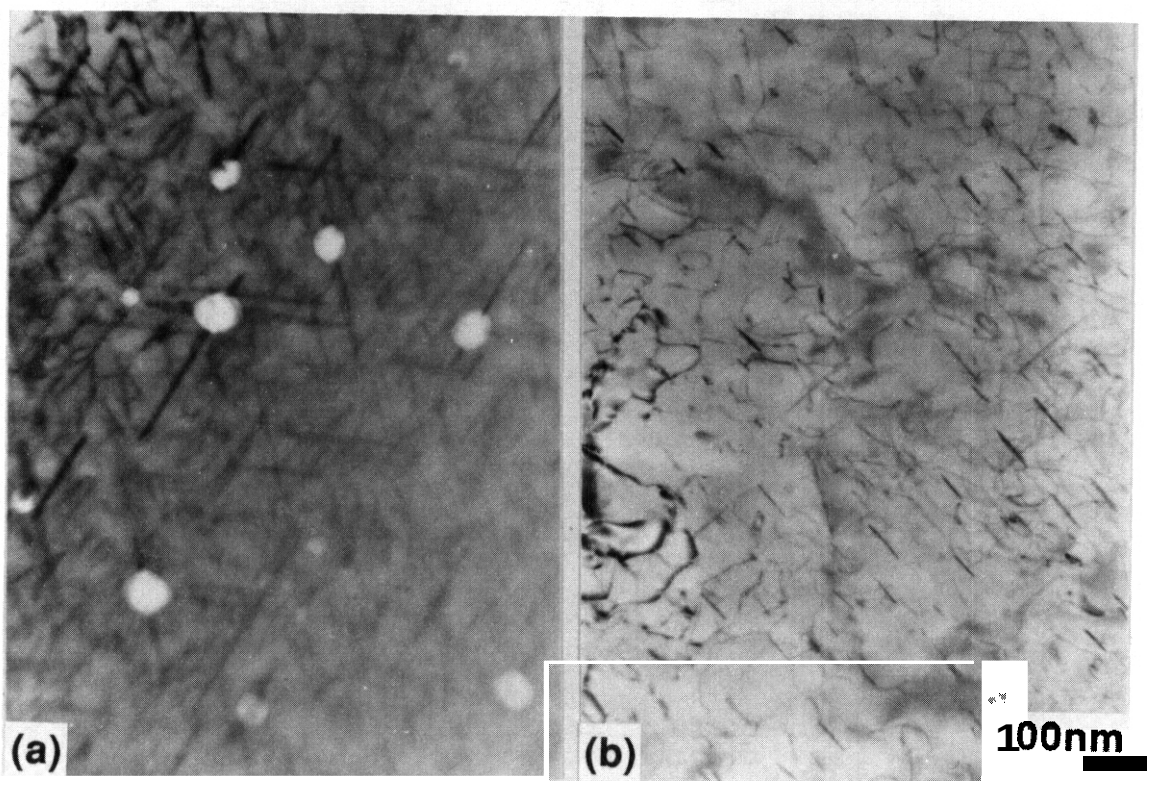

Fig. 3. Microstructures observed in the (a) annealed and (b) cold worked conditions of alloy E104 at 14 dpa and 500°C.

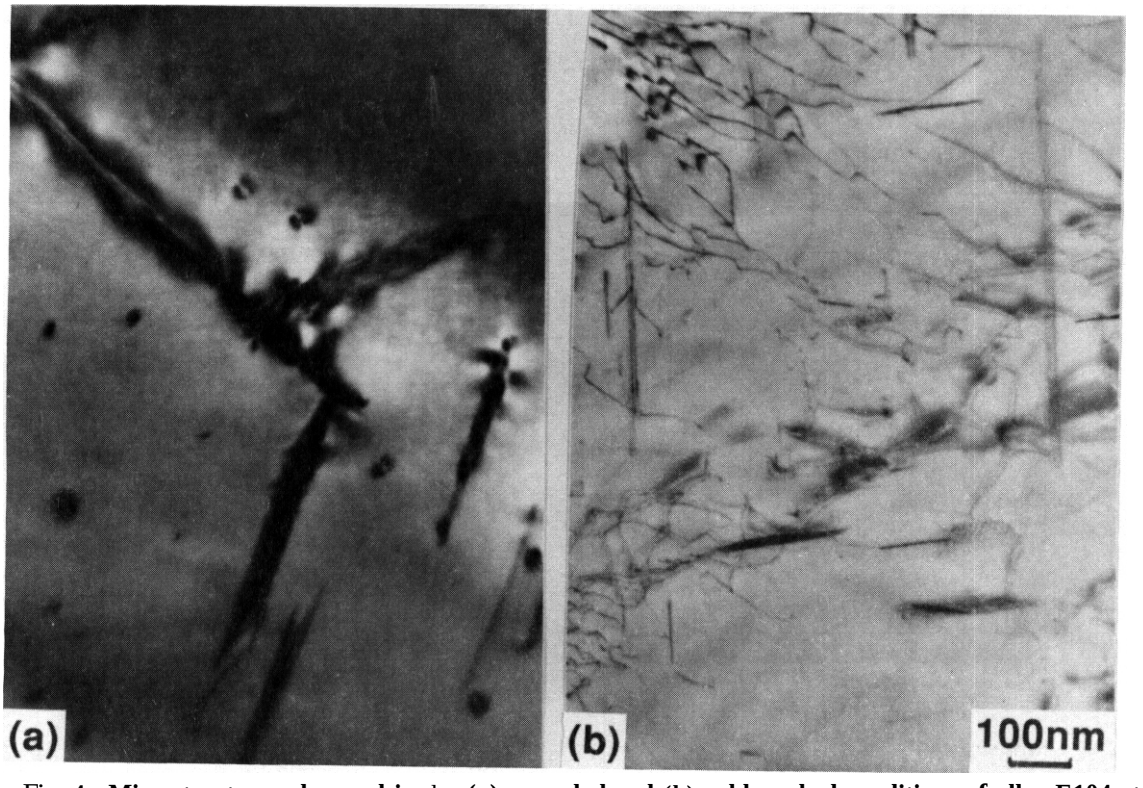

Fig. **4. Microstructures observed in** the **(a) annealed and (h) cold worked conditions of alloy E104 at 14 dpa and 600°C.**

Figure 5 provides a compilation of the available data on phosphide formation in neutron-irradiated Fe-15Cr-15Ni-P alloys in the annealed condition. Table 1 presents a compilation of the data sources and irradiation conditions used to construct this figure. It appears that phosphide formation in annealed Fe-15Cr-25Ni-P alloys is a very reproducible phenomenon, depending primarily on phosphorus level and irradiation temperature. Some dependence on displacement level must be involved, but insufficient data are available from the studies cited in this report to define this dependence.

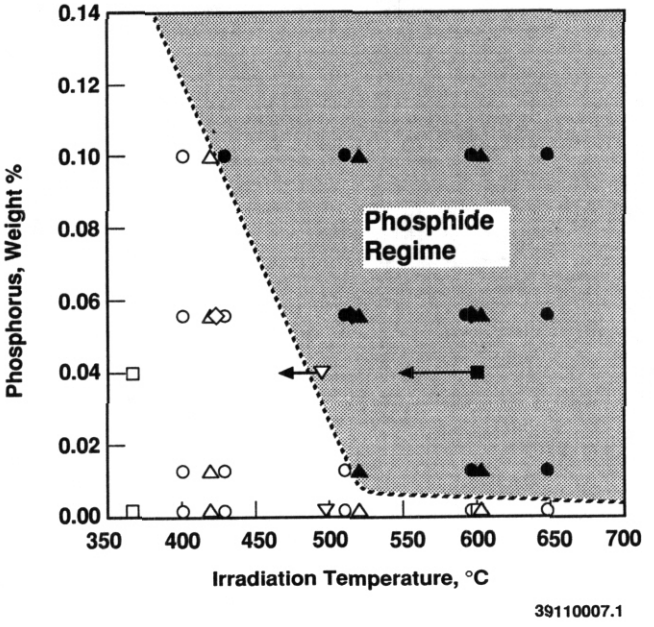

Figure 5. Compilation of data on phosphide formation in annealed Fe-15Cr-25Ni-P alloys from this study and others described in references 1-5. Open symbols denote absence of phosphide formation. Symbols with arrows involve irradiation temperatures that fell from their original levels in the middle of the irradiation.(6)

Table I Data Sources on Phosphide Formation Used to Construct Figure 5

Experiment Name	Reactor	Temperature °C	Displacement Level, dpa	Phosphorus Levels, wt%	Reference
AA-9	EBR-II	399, 427 510,593 649	8.2,11.2 13.2, 14.3 14.3	<0.005, 0.013 0.055, 0.10	3
AA-14	EBR-II	425,500, 600	14	<0.005, 0.055	This work
^{59}Ni Isotopic Tailoring Experiment	FFTF	495	14	≤0.005 0.04	4
^{59}Ni Isotopic Tailoring Experiment	FFTF	365, 600	5.2,8.8	<0.005 0.04	5
MOTA-1E	FFTF	420,500,600	~30	≤0.005, 0.013 0.055, 0.10	1,2

CONCLUSIONS

Nickel-rich phosphide precipitates form in neutron irradiated Fe-15Cr-25Ni-P alloys in the annealed condition in a very reproducible manner. Cold working appears to alter somewhat and suppress the formation of these precipitates, however.

ACKNOWLEDGMENTS

This work was sponsored by Monbusho, The Japanese Ministry for Science, Education and Culture and by the U.S. Department of Energy under contract DE-AC06-76RLO 1830 with Battelle Memorial Institute.

REFERENCES

1. F. A. Garner, K. Miyahara and J. W. Newkirk, submitted to J. Nucl. Mater. as part of the ICFRM-5 conference to be held in Clearwater, FL on Nov. 12-22.

2. J. W. Newkirk and F. A. Garner, to be presented at the 16th International Conference on Effects of Radiation on Materials, to be held in Denver, CO in June 1992.

3. T. Muroga, F. A. Garner and J. M. McCarthy, J. Nucl. Mater., 168 (1989) 109-120.

4. J. F. Stubbins and F. A. Garner, J. Nucl. Mater., 179-181 (1991) 523-525.

5. H. Kawanishi, F. A. Garner and R. L. Simons, J. Nucl. Mater., 179-181 (1991) 511-514

6. M. L. Hamilton, F. A. Garner and B. M. Oliver, Fusion Reactor Materials Semiannual Progress Report DOE/ER-0313/9, 1990, pp. 61-68.

Silicon's Role in Determining Swelling in Neutron-Irradiated Fe-Ni-Cr-Si Alloys - N. Sekimura, University of Tokyo, F. A. Garner, Pacific Northwest Laboratory*, J. W. Newkirk, University of Missouri

SUMMARY

Two silicon-modified alloy series, one based on Fe-15Cr-20Ni and another based on Fe-15Cr-25Ni were irradiated at target temperatures between 399 and 649°C in EBR-II. The influence of silicon on swelling is more complex than previously envisioned and indicates that silicon plays two or more competing roles while in solution. Radiation-induced formation of γ' (Ni_3Si) precipitates is dependent on silicon and nickel content, as well as temperature. Precipitation of γ' appears to play only a minor role in void formation.

OBJECTIVE

The objective of this study is to provide insight on the processes which contrcl the radiation-induced evolution of microstructure.

PROGRESS AND STATUS

Introduction

Until recently, silicon and phosphorus additions to austenitic stainless steels have beer perceived as acting only to delay the onset of void swelling during neutron or charged particle irradiation. Garner and Kumar have shown, however, that small additions of either of these elements strongly increased the neutron-induced swelling of austenitic Fe-Cr-Ni ternary alloys at relatively low irradiation temperatures.[1] Larger solute additions yielded a peak swelling level followed thereafter by a steep decline in swelling. Similar non-monotonic behavior was shown in reference 1 to have also been observed in several ion bombardment studies.[2,3]

It has been proposed by Garner and coworkers that this complex behavior indicates that two or more competing mechanisms are operating to control swelling and that the outcome of the competition is determined not only by the silicon or phosphorus level, but also by the action of both environmental variables such as temperatu,e and displacement rite, as well as material variables such as composition and thermomechanical treatment.[1,4,5,6] Because both of these elements form precipitaies during irradiation, the role of precipitation in controlling swelling needs to he understood. Microstructural analyses of phosphorus-bearing allovs have shown. however. that phosphorus exerts its orimary influence while in solution,[4,8,7] with both increases and decreases in swelling occurring without precipitation at lower irradiation temperatures. The same studies showed that phosphide precipitation occurred primarily at relatively high temperatures where non-monotonic behavior did not develop

This paper presents the results of microstructural studies conducted on Fe-15Cr-25Ni-Si specimens for which swelling values are shown in Figure 1, and also on Fe-15Cr-20Ni-Si alloys that were irradiated in another experiment. The 20% Ni alloys were chosen in recognition of the role played by nickel in coprecipitation with silicon, and were expected to yield less precipitation than at 25% Ni.

ExDerimental Details

The two sets of alloys, whose compositions are shown in Table 1, were irradiated in separate hut nominally identical irradiation vehicles, although slightly different irradiation temperatures were employed in each vehicle. The temperatures were not measured directlv but were calculated from knowledge of gamma heating rates. Uncertainties range from ± 5°C at 400°C and ± 25°C at 650°C. Each of these vehicles were placed in Row 2 of the Experimental Breeder Reactor II (EBR-II) at displacement rates that ranged tram 0.6 to 1.1 x 10^{-6} dpa/sec. The neutron spectra in EBR-II yields ~5 dpa for each 1.0 x 10^{26} n/m^2 (E>0.1 MeV).

The lowest amount of silicon added to the Fe-15Cr-20Ni alloy was 0.29 wt%, while in the Fe-15Cr-25Ni alloys the lowest was 0.14 wt%. The Fe-15Cr-25Ni-Si specimens were irradiated in static sodium in the form of rods (3 mm diameter by 12.7 mm long) in the annealed condition (1030°C/0.5 h/ air cool). These rods were sectioned after irradiation to produce ti.25 mm thick microscopy disks. The Fe-15Cr-20Ni-Si specimens were irradiated in the form of microscopy disks (3 mm by 0.25 mm thick) in three separate thermomechanical starting conditions: annealed (1030°C/30 min/water quench), 30% cold worked, and 30% cold worked followed by aging (650°C/10 hr/water quench).

The radiation-induced changes in density were measured by an immersion density technique known tr he accurate to ± 0.16% swelling. Specimen thinning and electron microscopy were accomplished using conventional procedures.

---

*Operated for the U.S. Department of Energy by Battelle Memorial Institute under Contract DE-AC06-76RLO 1830.

Table 1. Composition of Alloys, wt%

Designation	Fe	Ni	Cr	C	O	N	Si
AA-9 Experiment[1]							
E33	Bal	25.8	14.8	0.005	0.023	0.0028	≤0.02
E87	Bal	25.0	15.3	0.009	0.014	0.0022	0.14
E30	Bal	25.2	15.7	0.006	0.008	0.0017	0.39
E31	Bal	25.5	15.5	0.009	0.007	0.0020	0.70
E88	Bal	25.1	15.2	0.008	0.010	0.0025	0.90
AA-14 Experiment[2]							
G120	Bal	20.0	15.0	0.014	0.0080	0.0006	<0.01
G46	Bal	20.0	15.0	0.007	0.0095	0.0078	0.29
G34	Bal	20.0	15.0	0.009	0.0078	0.0013	0.69

Bal = balance.

(1) Alloys prepared by Hanford Engineering Development Laboratory

(2) Alloys prepared by General Electric Company at Schenectedy, NY

Results

Figures 1 and 2 present the swelling inferred from measured changes in density for these two alloy groups. The non-monotonic behavior is clearly evident in the 25% Ni alloys for temperatures in the range of 399 to 510°C. No data are shown for 593 and 649°C (both at 14.3 dpa), since swelling at all silicon levels was ≤ 0.10%, within the uncertainty of the measurement technique. It is important to note that if the data at 0.14% silicon were unavailable, one could conclude that swelling decreased monotonically with silicon. This is exactly the conclusion that would be drawn from most earlier studies as well as from the Fe-15Cr-20Ni-Si alloys of this study.

The swelling levels of the annealed condition in the 20% Ni alloy series were larger than those for the 25% Ni alloys at comparable doses and temperatures. The increased swelling is a direct consequence of nickel's role in extending the incubation period of swelling.[3] Cold worked alloys at 20% Ni swelled less than annealed alloys at all irradiation temperatures studied, and aged alloys reached intermediate values of swelling.

The increases in swelling between 0 and 0.14% silicon occurred without precipitation for all irradiation temperatures except 454 and 482°C, indicating that silicon exerts at least one of its roles while in solution

Although Muroga and coworkers[4] showed that the non- monotonic behavior of Fe-15Cr-25Ni-P alloys was mirrored in their void density, the situation for the Fe-15Cr-25Ni-Si alloys was somewhat more complex. figure 3 shows the dependence of void density and size on silicon content. The void densities at the lower irradiation temperatures decreased monotonically with silicon addition, and at higher temperatures there was some non-monotonic behavior but it was insufficient to produce non-monotonic swelling. Such behavior arose primarily from the dependence of the swelling incubation dose on silicnn and temperature. Thus, the void size dependence exhibits a rather complex behavior.

The only type of precipitate observed was the γ' phase based on Ni_2Si. As shown in Figure 4 there is an upper limit of temperature beyond which γ' does not develop for the silicon levels explored in this experiment. This is quite different from that of phosphide behavior, which exhibited a lower temperature limit but not an upper limit within the temperature range of the present experiments.[3] The γ' precipitates were nearly spherical in shape and appeared to be coherent with the matrix at lower silicon levels, but they developed irregular shapes at higher temperatures and higher silicon levels. Strain fields were also observed at precipitate surfaces at 510°C and 0.90% silicon, an indication of incoherency. At the 0.90% level, γ' also formed as thin intermittent plates at grain boundaries at 399 and 427°C. γ' was also observed on dislocation loops and void surfaces at lower irradiation temperature and higher silicon levels.

There was also a tendency for refinement of sire for the loop microstructure, especially at higher silicon levels. Refinement was also observed at 649°C, however.

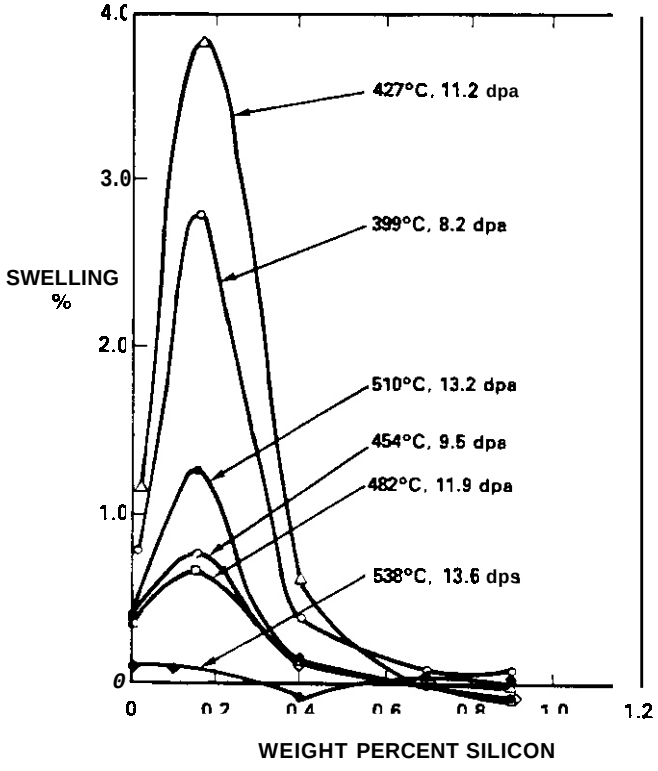

Figure 1. Influence of silicon on neutron-induced swelling of Fe-15Cr-25Ni-Si alloys in the AA-9 experiment.[11]

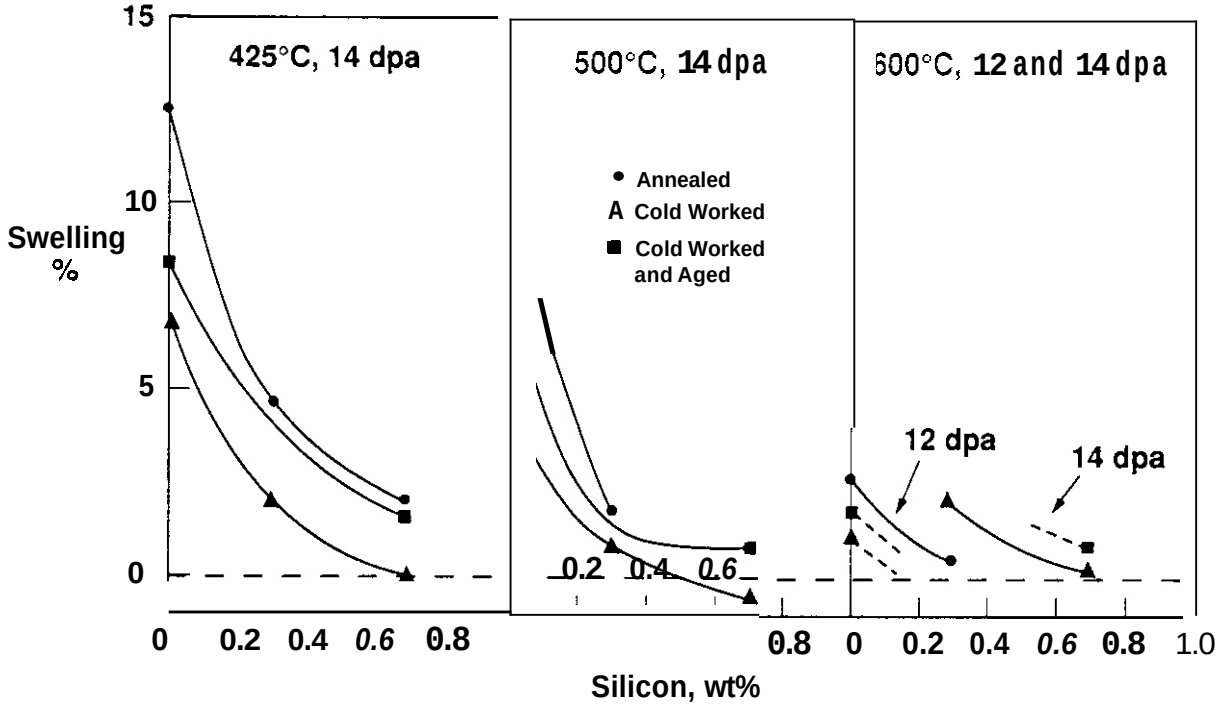

Figure 2. Influence of silicon and thermomechanical condition on neutron-induced swelling of Fe-15Cr-20Ni-Si alloys in the AA-14 experiment.

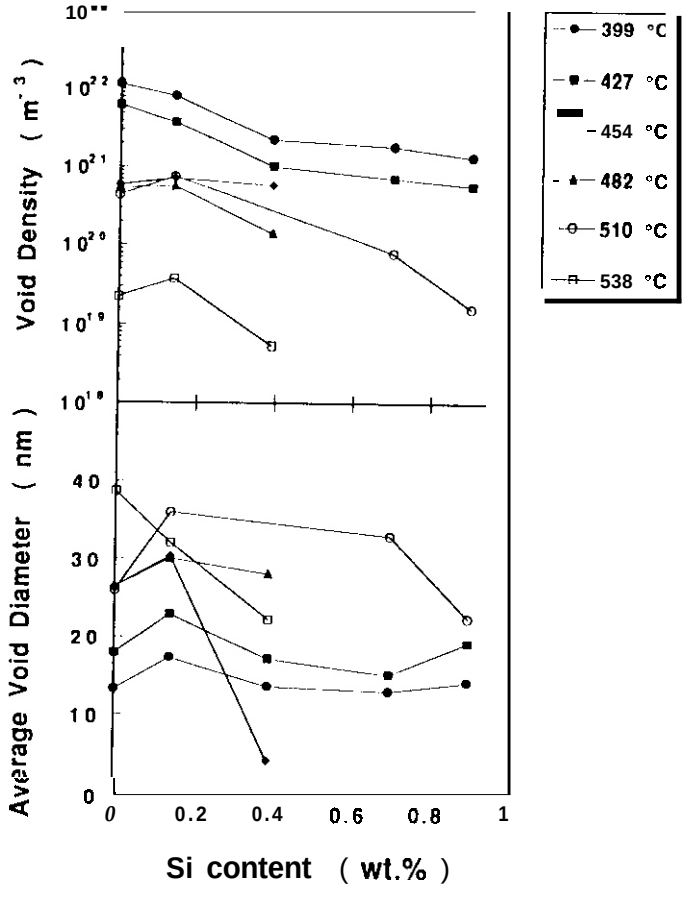

Figure 3. Void densities and sizes observed in Fe-15Cr-25Ni-Si alloys in the AA-9 experiment.

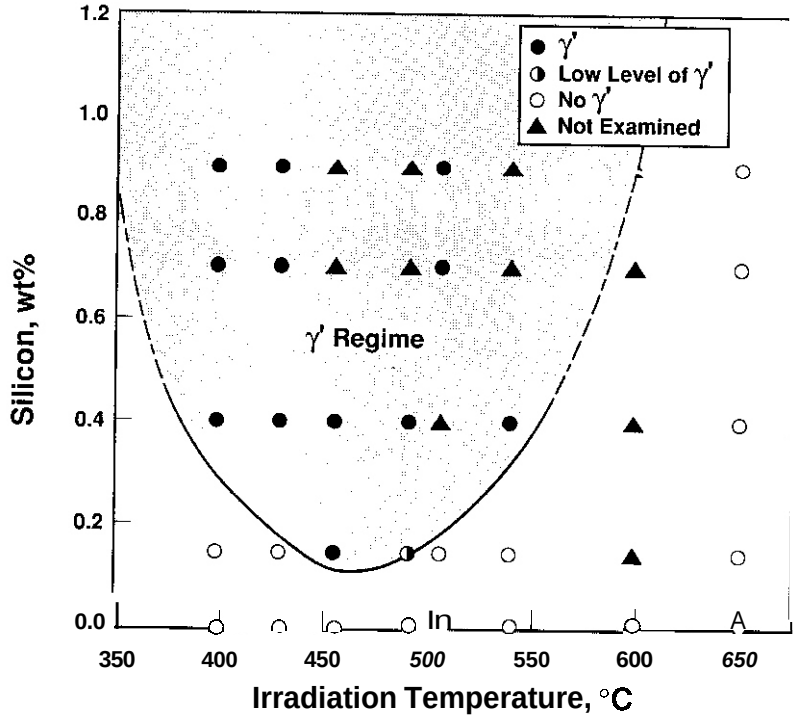

Figure 4. Dependence of γ' formation in Fe-15Cr-25Ni-Si on silicon level and irradiation temperature in the AA-9 experiment.

Microstructural analysis of the 20% Ni alloys determined that γ' precipitates formed at 425°C but not at 500 or 600°C. This result was not affected by either cold working or aging. This indicates once again that the primary influence of silicon must be exerted while in solution. The void distribution was not analyzed in detail but appeared to be a monotonically decreasing function of silicon content.

Discussion

Figure 5 demonstrates that studies to determine the role of solutes on microstructural evolution may overlook important phenomena by choosing compositional increments that are too large. Similar conclusions have recently been reached for titanium-modified stainless steels containing phosphorus[5] and for a range of steels containing molybdenum.[8]

Analysis of the 25% Ni alloy series is complicated by the variation in dpa level with irradiation temperature. The relative influence of temperature and silicon content can be discerned, however, by noting that the eventual steady-state swelling rate of this alloy is ~1.0%/dpa after a very abrupt end of the incubation period at ~10dpa.[9] Figure 6 demonstrates that the effect of temperature alone apnears to be monotonic in nature for the 0.14% Si alloy and does not exhibit the independence of temperature observed in the silicon-free alloy in the 400-510°C range.[4]

It has been proposed that silicon in solution can interact strongly with both interstitials and vacancies.[10] Watanabe and coworkers proposed a similar situation for phosphorus.[11] One consequence of interstitial binding is that at relatively low temperatures, loop nucleation was enhanced and loop microstructure was thus refined,[11] as observed in this study. This refinement is thought to hasten the development of the saturation dislocation microstructure that precedes steady state swelling, leading to earlier swelling compared to that of silicon-free alloys. Formation of γ' on loops may also help to stabilize them against unfaulting.

At higher silicon levels, silicon increases the effective vacancy diffusion coefficient, thus leading to a strong depression of void nucleation, especially at higher temperatures.[10,12] As silicon in solution is increased, this process will eventually overwhelm the effect of interstirial binding, leading to a peak in swelling at intermediate silicon levels

Radiation-induced segregation of silicon and nickel eventually leads to γ' formation, a process which adds additional complexity to the competition for point defects. Not only do the precipitate surfaces serve as additional neutral sinks for point defects that can contribute to suppression of swelling, but the removal of both silicon and nickel from the matrix influences the migration of point defects.[1]

CONCLUSIONS

Contrary to previously prevailing perceptions, small amounts of silicon often lead to strong increases in swelling as a result of a reduction in the duration of the transient regime. Larger levels of silicon then lead to increases in the transient duration, causing decreases in swelling. This complex behavior is thought to arise from competing roles of silicon while in solution. The role of y' precipitation on void swelling, if any, appears to be secondary.

Formation of the γ' phase in neutron-irradiated Fe-15Cr-Ni-Si alloys tends to increase with both silicon and nickel content. However, γ' forms only below some maximum temperature that appears to be dependent on nickel content. Void swelling also responds to silicon and nickel content is well as the irradiation temperature.

ACKNOWLEDGEMENTS

This work was supported by Monbusho, the Japanese Ministry of Education, Science, and Culture and the U.S. Department of Energy under Contract DE-AC06-76RLO 1830 and Contract DE-FG06-89ER-75522, the latter administered by the Northwest College and University Association for Science (Washington State University).

REFERENCES

1. F. A. Garner and A. S. Kuniar, ASTM STP 955, 1987, pp. 289-314

2. W. G. Johnston, T. Lauritren, J. H. Rosolowski and A. M. Turkalo, in Radiaticn Damage in Metals, American Society of Metals, *1976,* pp. 227-266.

3. G. R. Gessel and A. F. Rowcliffe, Proc. Inter. Conf. on Radiation Effects in Breeder Reactor Structural Materials, June 1977, pp. 431-442.

4. T. Muroga, F. A. Garner and J. M. McCarthy, J. Nucl. Mater., 168 (1989) 109-120

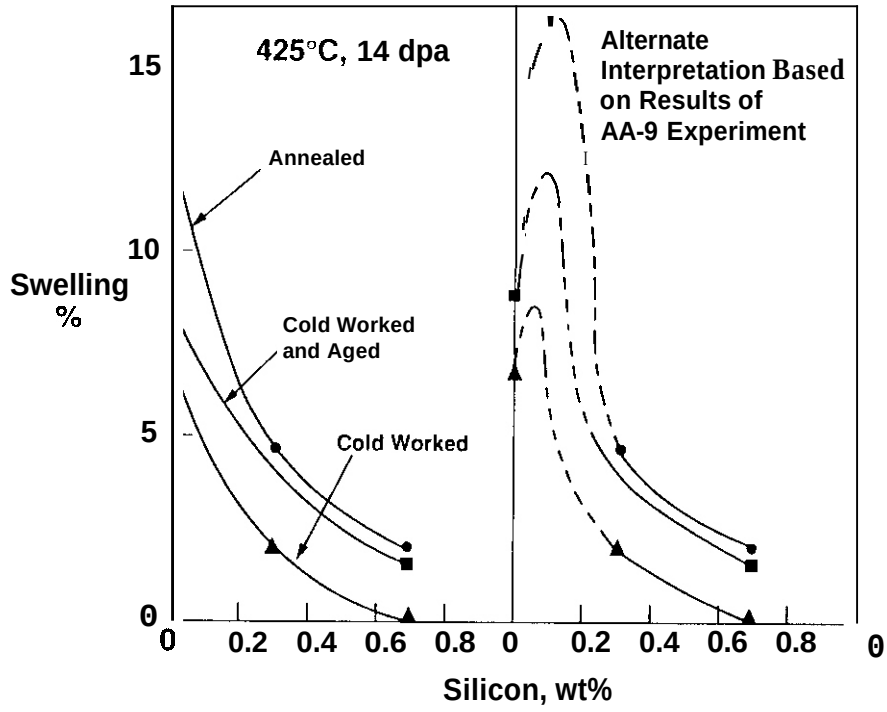

Figure 5. Alternative interpretations of swelling data on Fe-15Cr-20Ni-Si alloys from the AA-14 experiment.

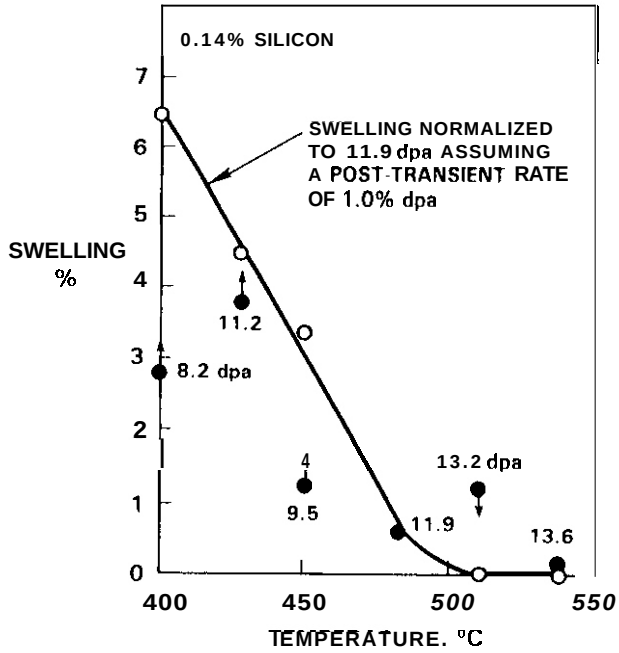

Figure 6. Swelling of Fe-15Cr-25Ni-0.14Si in the AA-9 experiment, normalized to 11.9 dpa, demonstrating the monotonic influence of irradiation temoerature.

5. F. A. Garner and M. A. Mitchell, in this semiannual report.

6. F. A. Garner, K. Miyahara and J. W. Newkirk, to be published in J. Nucl. Mater., proceedings of ICFRM 5.

7. H. Kinoshita and F. A. Garner, Fusion Reactor Materials Semiannual Report DOE/ER-0313/11, 1992, in press.

8. F. A. Garner, T. Lauritzen and M. A. Mitchell, submitted for presentation ai 16th Inter. Sym. on Effects of Radiation on Materials, Denver, CO, June 1992.

9. F. A. Garner and H. R. Brager, ASTM STP 870, (1985) pp. 187-201.

10. F. A. Garner and W. G. Wolfer, J. Nucl. Mater., 102 (1981) 143-150.

11. H. Watanabe, A. Aoki, T. Muroga and N. Yoshida, J. Nucl. Mater., 179-181 (1991) 529

12. B. Esmailradeh, A. Kumar and F. A. Garner, J. Nucl. Mater., 133 & 134 (1985), 590-593

ELECTRON IRRADIATION EXPERIMENTS IN SUPPORT OF FUSION MATERIALS DEVELOPMENT- D. S. Gelles (Pacific Northwest Laboratory*), S. Ohnuki and H. Takahashi (Hokkaido University), H. Matsui (Tohoku University) and Y. Kohno (University of Tokyo)

OBJECTIVE

The objective of this effort is to improve understanding of the effects of fast neutron irradiation on microstructural evolution by examining radiation damage response in a 1 MeV high voltage electron microscope.

SUMMARY

Microstructural evolution in response to 1 MeV irradiation has been investigated for tiiree simple ferritic alloys, pure beryllium, pure vanadium, and two siiaple vanadium alloys over a range of temperature; and doses. Microstructural evolution in Fe-3, -9, and -18Cr ferritic alloys is found to consist of crenulated, faulted a<100> loops and circular, unfaclted a/2 <111> loops at low temperatures, but with only unfaulted loops at high temperatures. The complex dislocation evolution is attributed to sigma phase precipitaults arising from chromium segregation to poini defect sinks. Beryllium is found to be resistant to electron damage; the only effect observed was enhanced dislocation mobility. Pure vanadium, V-5Fe, and V-1Ni microstructural response was complicated by precipitation on heating to 400°C and above, but dislocation evolution was investigated in the range of room temperature to 300°C and at 600°C. The three materials behaved similarly, except that pure vanadium showed more rapid dislocation evolution. This difference does not explain the enhanced swelling observed in vanadium alloys.

PROGRESS AND STATUS

Introduction

High voltage electron microscopy (HVEM) offers the unique advantage of continuous observation of microstructural evolution resulting from displacement damage so that the same features can be followed as a function of time in a given area of a specimen. All other techniques require that the specimen be examined between irradiation periods, and it is generally impossible to follow the same microstructural features with increasing dose. For example, microstructural evolution under neutron irradiation must be studied by comparing different specimens irradiated to different doses. Disadvantages of the HVEM technique are that the displacement damage does not duplicate 14 MeV neutron collision cascades, the damage rate is higher than that expected in a fusion device, and specimens are generally thinner so that surface effects can become iinportant. As a result, HVEM is not a major tool used in the design of fusion reactor materials, but it can supplement our understanding of irradiation damage response in materials. The present study therefore involved the use of HVEM to study microstructural evolution in several materials of interest to the fusion community.

The materials chosen for study were 1) simple Fe-Cr ferritic alloys, 2) pure beryllium, and 3) pure vanadium and two simple vanadium alloys (V-5Fe and V-1Ni). Martensitic stainless steels and vanadium alloys are candidate materials for a low activation first wall capable of withstanding high radiation damage levels, and beryllium will be required as a neutron multiplier in a fusion blanket and may be of use as a plasma interactive material.

Irradiation damage studies in ferritic alloys were intended to investigate two phenomena: dislocatian evolution and segregation effects on void shape. It has been shown that dislocation evolution in ferritic alloys is complex. involving formation of loops with both a/2 <111> and a<100> Burgers vectors. and growth and interaction of these loops to form a complex dislocation network.[1-4] However, it was not understood how the interactions occurred or what the consequences of such complex networks would be on dislocation motion, both during and following irradiation. Therefore, electron irradiation experiments were expected to reveal how the interacticn processes affected dislocation motion. It has also been shown that, void shape in ferritic alloys varies from octahedral to cubic to dodecahedral depending on the solutes present in the alloy. Because investigators have shown that irradiation induced segregation can be studied under controlled conditions in HVEM experiments,[5-7] we anticipated that segregation effects on void shape in ferritic alloys could be examined in detail during HVEM experiments.

Early irradiation experiments on pure beryllium had demonstrated only development of a/3 <11•0> type dislocations loops,[8-9] whereas recent experiments have shown that neutron irradiated beryllium ran develop small loops with Burgers vectors containing a non-basal component.[""] However, the contrast for such loops was very weak and could easily be overlooked. Therefore, it was felt that HVEM experiments designed to reveal these non-basal loops were needed to provide a clearer understanding of the dislocation evolutiun in beryllium.

---

*Operated for the U.S. Department of Energy by Battelle Memorial Institute under Contract DE-AC06-76RLO 1830.

Finally, recent results on neutron irradiated vanadium alloys containing iron[12-13] and nickel* have shown unexpectedly high void swelling. However, the mechanism by which this can occur is not yet completely understood. Therefore, it was expected that HVEM experiments could improve our understanding of this unexpected response.

ExDerimental Procedure

Specimens for irradiation were obtained in as-heat treated condition from various sources so that in each case the specimens were duplicates of conditions that had been neutron irradiated. Ferritic alloy specimens had previously been irradiated in the Experimental Breeder Reactor II (EBR-II) and/or the .Fast Flux Test Facility (FFTF),[1-3] pure beryllium specimens had previously been irradiated in FFTF,[4] pure[5] vanadium had previously been irradiated in the Japanese JOYO fast breeder reactor,[14] and vanadium alloys containing iron and nickel had previously been irradiated in FFTF.[12] Alloy compositions and heat treatments are described in the original reports.

Specimens were prepared for electron irradiation using standard electropolishing procedures in a Tenupol or Metal-Thin machine. The ferritic specimens were prepared in a solution of 5% perchloric acid in acetic acid at 55 V, 100 mA, and moderate pump speed. The beryllium was prepared using a solution of 10% nitric acid, 2% sulfuric acid, and 2% hydrochloric acid in ethylene glycol between 0 and 5°C at about 100 mA, but chemical polishing was required after perforation to remove a surface oxide (using a solution of 2% sulfuric acid and 2% hydrofluoric acid in water.) The vanadium specimens were prepared using a solution of 20% sulfuric acid in methanol at 10 V, 130 mA at moderate pump speed.

Electron irradiations were performed in the University of Hokkaido 1 MeV Hitachi 1300 electron microscope using a side entry, double tilting, heating stage. The University of Hokkaido microscope has been upgraded to provide a vacuum of 10^{-7} torr in the specimen chamber. Beam conditions were set at 1 MeV to provide a damage rate of 2×10^{-3} dpa/s or approximately 7 dpa per hour. This assumed a 35 barn cross section, the standard for iron used for the Hokkaido microscope, whereas electron irradiation experiments in the United States use 40 barns. No correction for beam heating is made for the irradiation temperatures reported. However, beam heating is expected to be on the order of 15°C.[15] Whenever possible, specimen orientations for ferritic and vanadium specimens were chosen near (011). However, in the case of beryllium, foil orientations were all near (00•1) and therefore it was impossible to orient the foil to obtain $\bar{g}$ = [00•1], so g = [10•1] was used. Following irradiation, specimens were examined in a JEOL 2000ES microscope, when practical, including the ferritic specimens. Compositional checks on precipitates were generally performed using S mode and employing a Link x-ray detector and analyzer.

Results

Fe-Cr Binary *Alloys*

Electron irradiations were performed on Fe-3Cr, -9Cr and -18Cr at temperatures between 350 and 500°C in order to investigate dislocation evolution. A summary of the irradiation experiments is given is Table 1. Initial experiments on Fe-9Cr revealed that dislocation evolution consisted primarily of crenulated faulted loops on {001} with a<001> Burgers vectors at lower temperatures (350, 400 and 450°C), but at 500°C the loops were more circular and unfaulted. A lower density of a/2 <111> unfaulted loops also developed in each of these cases. A check revealed that foil thickness did not alrer aislocation configuration, indicating tnat behavior was not a result of surface or environmental effects.

Examples of loop evolution in Fe-9Cr are provided in Figure 1. Figures la to ld show a specimen irradiated at 425°C to about 1 dpa for a foil near (110) using g = [110] so that two sets of the <001> loops are clearly visible and the third is in weak residual contrast when viewed on edge. For the loops in strong contrast, one set appears in inside contrast and the other in outside contrast, such that the inside contrast shows the loops to actually grow by formation of small faulted regions at first appearing as "sun bursts" or "flowers" and later defining a square shaped loop perimeter. Such shapes are characteristic of loop growth controlled by solute segregation, similar to pearlite and dendrite growth processes. Stereo examination revealed that all loops in inside contrast lie on one plane and all loops in outside contrast lie on the other plane, so all loops on a given plane have the same character, presumably interstitial. After a dose of about 1 dpa, sufficient image overlap has occurred to make interpretation very difficult. Figures le to 1h are included to show more clearly the development of loops with a/2 <111> Burgers vectors following irradiation at 350°C. In this case, an (001) orientation was selected so that two sets of a<100> loops appear on edge with the third out of contrast, but half the loops having a/2 <111> Burgers vectors will also appear in contrast between the on edge loops. Figures le to 1h reveal that the large a<100> loop images are composed of a number of short segments, and a lower density of a/2 <111> loops do evolve under irradiation.

The transition from faulted to unfaulted character for a<100> loops in Fe-9Cr is shown in Figure 2. Irradiations at 450 and 500°C to a dose of about 1 dpa can be compared for thick specimens under similar

*J. F. Stubbins, University of Illinois, unpublished work showing moderately high swelling in V-1Ni irradiated at 600°C to 15 dpa.

imaging conditions. The imaging conditions in Figures 2a and 2c use $\vec{g}$ = [110] near (113) so that two sets of a[100] loops can be seen highly tilted and therefore appearing in elongated configurations. The loops do not appear elliptical, but instead contain crenulations even at 500°C, again an indication of segregation-affected loop growth. However, although faulting is clearly evident at 450°C, no faulting is

Table 1. Summary of HVEM irradiation exoeriments

Material	Irradiation Conditions	Summary of Observations
Fe-3Cr	350°C to 1.2 dpa	Faulted crenulated a<100> loops often farm associated with retained dislocations, and unfaulted a/2 <111> loops also develop
	400°C to 1.3 dpa	Faulting is less obvious on a<100> loops and crenulations are coarser; unfaulted a/2 <111> loops are also present
Fe-9Cr	350°C to 1.6 dpa	a<100> loops form quickly and grow by Crenulation. and a/2 <111> loops nucleate in batches and grow more slowly
	400°C to 3.0 dpa 400°C to 1.3 dpa 400°C to 0.9 dpa	Similar to 350°C behavior except loop growth is more rapid
	425°C to 1.2 dpa	Similar to 400°C behavior
	425°C to 0.5 dpa dual beam 425°C to 3.5 dpa dual beam	Similar to single beam response. no voids identified
	450°C to 1.0 dpa	a<100> loops are still faulted but crenulations are less severe: a12 <111> loop nucleation is reduced but loops grow larger
	500°C to 0.9 dpa	a<100> loops are unfaulted but still crenulated: a12 <111> loops grow as large as a<100> loops
Fe-18Cr	350°C to 3.4 dpa	a<100> loops are more severely crenulated forming rafts of loops, a/2 <111> loops are on a very fine scale
	400°C to 2.5 dpa	Rafts of a<100> loops grow larger with rectangular outlines: a/2 <111> loops remain on a fine scale
	450°C to 2.6 dpa	a<100> faulted loops are larger and less crenulated: a/2 <111> loops are larger but can contain crenulations
	500°C to 2.0 dpa	a<100> loops are larger with rectangular outlines and less noticeable faulting: a/2 <111> dislocations eventually form a network
Be	100°C to 2.9 dpa	Dislocation tangle grows slowly by climb
	200°C further 2.9 dpa	Dislocation tangle is similar but climb is more rapid
	300°C further 2.4 dpa	Dislocation tangle is reduced. climb is more extensive and more rapid
	400°C further 1.8 dpa	Most dislocations have migrated away and motion is very rapid
Pure V	25°C to 1.0 dpa 25°C to 1.4 dpa	a/2 <111> loops nucleate and grow into a tangle with black spot contrast on steeply inclined segments during one of the two irradiation.: no Void swelling
	100°C to 1.3 dpa 100°C to 1.3 dpa	a12 <111> dislocation evolution similar; no void swelling
	200°C to 1.3 dpa 200°C to 1.4 dpa	a/2 <111> evolution more rapid developing into a tangle more quickly; strong contrast on steeply inclined segments again observed during one of the two irradiations; no void swelling
	300°C to 1.3 dpa 300°C to 1.3 dpa	a/2 <111> loop evolution less vapid with evidence of surface contamination and foil buckling; no void swelling
	600°C to 1.8 dpa 600°C to 2.4 dpa 600°C to 2.5 dpa	a/2 <111> dislocation tangle develops as precipitates in the irradiated region dissappear, no void swelling
V-5Fe	25°C to 1.3 dpa	Black spot damage to high denrity: no void swelling
	100°C to 1.3 dpa	Similar black spot damage; no void swelling
	200°C to 1.3 dpa	Dislocation structure coarser, developing into loops and eventually a dislocation tangle: no void swelling
	300°C to 1.3 dpa	a/2 <111> loop density lower and growth slower than at 200°C. no void swelling
	600°C to 0.1 dpa 600°C to 8.4 dpa	a/2 <111> dislocation tangle developed, no void swelling
V-1Ni	25°C to 1.3 dpa	Black spot damage to high density: no voir: swelling
	100°C to 1.3 dpa	Similar black spot damage; no void swelling
	200°C to 1.3 dpa	Black spot damage replaced by a12 <111> loop structure and eventually a dislocation tangle; no void swelling
	300°C to 1.3 dpa	Black spot damge grew into discernable loops; no void welling
	600°C to 0.5 dpa 600°C to 3.5 dpa 600°C to 2.4 dpa 600°C to 2.4 dpa	a/2 <111> dislocation tangle developed. no void swelling

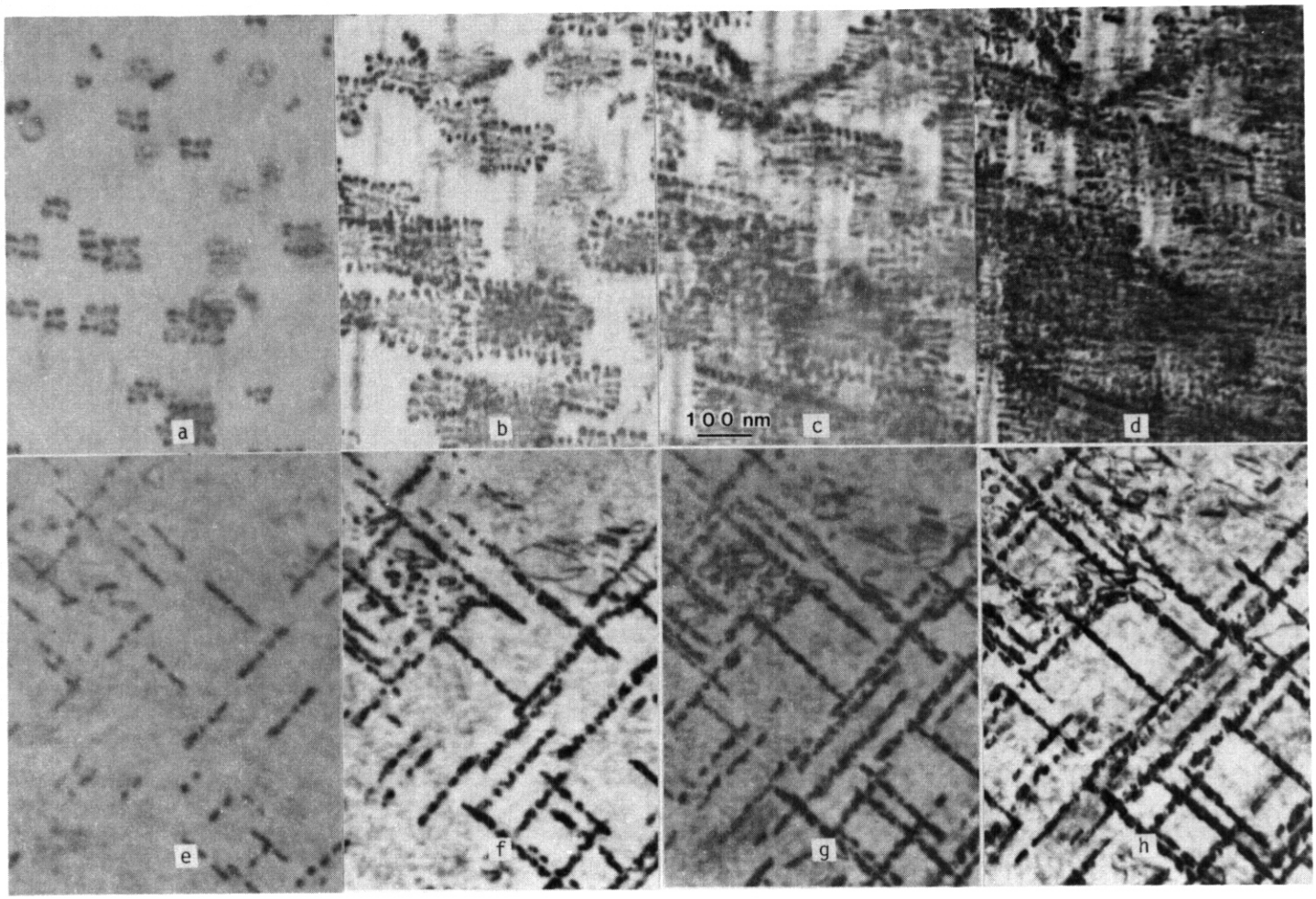

Figure 1. Growth of faulted loops in Fe-9Cr at 425°C as a function of dose using $\bar{g}$ = [1$\bar{1}$0] contrast for a foil near (110), (a) at 0.06 dpa, (b) 0.18 dpa, (c) 0.48 dpa and (d) at 1.2 dpa, and at 350°C using $\bar{g}$ = [011] contrast for a foil near (100), (e) at 0.05 dpa, (f) at 0.26 dpa, (g) at 0.71 dpa and (h) at 1.6 dpa.

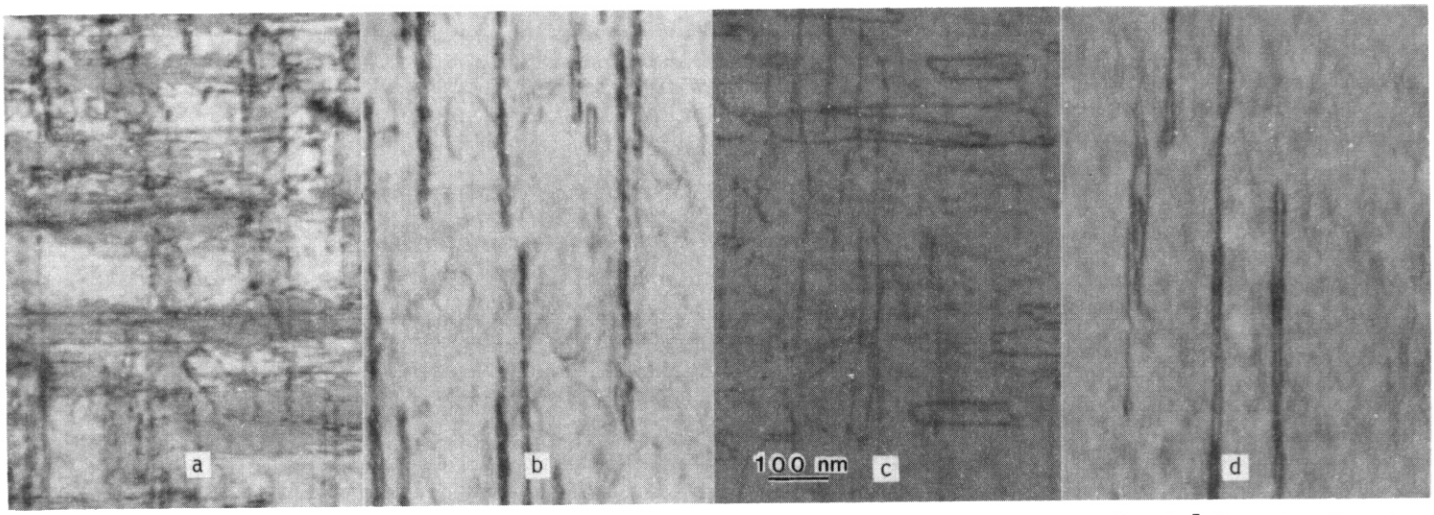

Figure 2. Faulted loops in Fe-9Cr following irradiation at 450°C to 1.0 dpa (a) in $\bar{g}$ = [1$\bar{1}$0] contrast and (b) in $\bar{g}$ = [002] contrast to reveal the presence of a/2 <111> loops, and unfaulted loops in Fe-9Cr irradiated at 500°C to 0.9 dpa (c) in $\bar{g}$ = [1$\bar{1}$0] contrast and (d) in $\bar{g}$ = [002] contrast.

present after irradiation at 500°C, and loop growth toward the surface tends to produce straight dislocation configurations. In Figures 2b and 2d, the imaging condition $\bar{g}$ = [200] near (001) is used so that only one set of a<100> loops appears on edge and all a/2 <111> dislocations should be visible in weaker contrast. These figures clearly indicate that a/2 <111> dislocations also form at higher temperatures.

It may be noted that faulted loops with a<100> Burgers vectors on (100) planes in body centered cubic crystal structures are unusual. Stacking faults with moderate stacking fault energy cannot be formed on (100) planes, so that the observation of faulted loops indicates that faulting is a result of precipitation in association with loop growth. The observation of crenulations, indicating that solute segregation is involved, further supports the expectation that precipitation is responsible for faulting. Such faulted loops in simple Fe-Cr ferritic alloys have often been observed.[16-21] Reference 17 explained the behavior as carbide precipitation. However, Figure 2 provides the example that at high enough irradiation temperatures, the faulted loops found in Fe-Cr alloys are replace by unfaulted crenulated loops; therefore, these precipitates, or precipifaults, as they are often called, become unstable at temperatures on the order of 500°C.

Irradiation of Fe-18Cr specimens produced results similar to those for Fe-9Cr except that faulted loop structures were formed at temperatures as high as 500°C and loop growth was slower. Irradiations were performed at 350, 400, 450 and 500'C in order to duplicate the experiments on Fe-9Cr. An example of response at 350°C is given in Figure 3. Figures 3a to 3d follow the same area at doses of 0.07, 0.2, 1.4, and 3.4 dpa in $\bar{g}$ = [1$\bar{1}$0] contrast for Figures 3a to 3c and in $\bar{g}$ = [002] in Figure 3d. Comparison of Figures 1 and 3 reveals that loop growth is significantly faster in the Fe-9Cr alloy.

Figure 4 shows loop development in Fe-18Cr as a function of irradiation temperdture using both **g** = [1$\bar{1}$0] and [002] image contrast in the same areas, in the same manner as shown in Figure 2. Figures 4a and 4b are for irradiation at 400°C, Figures 4c and 4d for 450°C and Figures 4e and 4f for 500'C. Comparison of Figures 2c and 4e clearly demonstrates that the transition to unfaulted loops occurs at lower temperatures for lower chromium levels. Note also that the size of a/2 <111> loops varies more rapidly with temperature than does the size of a<100> loops in Fe-18Cr.

Irradiation response in Fe-3Cr was found to be similar based on irradiations performed at 350 and 400°C, Figure 5 shows results of irradiation at 350°C. Figures 5a to 5c follow the same area at doses of 0.18, 0.49, and 1.3 dpa in $\bar{g}$ = [1$\bar{1}$0] contrast, and Figure-Sd shows the same area after 1.3 dpa in **g** = [002] contrast. A preexisting dislocation network is present before irradiation.[1,3] Following irradiation to 0.18. as shown in Figure 5a. loops form in association with the preexisting dislocations. but loops are crenulated and faulted. Loop growth continues with increasing dose, but as shown in Figure 5d, imaging in $\bar{g}$ = [002] reveals that a<001> dislocation contrast is segmented and that a/2 <111> dislocations are also present. Figure 6 provides similar comparison following irradiation at 400°C. Faulted loops may be present at both temperatures, but the $\bar{g}$ = [002] contrast image in Figure 6d appears to indicated a shift to unfaulted loop development; some loop segmentation can be seen but the structure resembles that shown in Figure 2d. Therefore, the trend that unfaulted loops can develop at lower temperatures while chromium content is reduced is further supported, but faulted loops can form at temperatures of 350 and 400°C even in Fe-3Cr.

Postirradiation examination was performed on all irradiated Fe-Cr alloys in order to better understand loop development and to identify the precipitate that was responsible for loop faulting. Dislocation contrast imaging experiments confirmed Burgers vector and dislocation character conclusions as described above. Both a<100> and a/2 <111> burgers vectors were present, and all a<100> loops on a given plane either showed inside or outside contrast, never both. This confirmed that they were probably all interstitial in character. Diffraction patterns of areas in specimens containing faulted loops were dominated by rel-rod effects due to the thin nature of the faulted loops. As a result, it was difficult to obtain accurate lattice spacing information for the precipitate. However, it is considered noteworthy that peaks in diffraction intensity due to the faulted loops tended to occur at ¼, ½ and ¾ of the distance between the 000 and 200 diffraction spots, and each of those diffraction features produced dark field images of the same

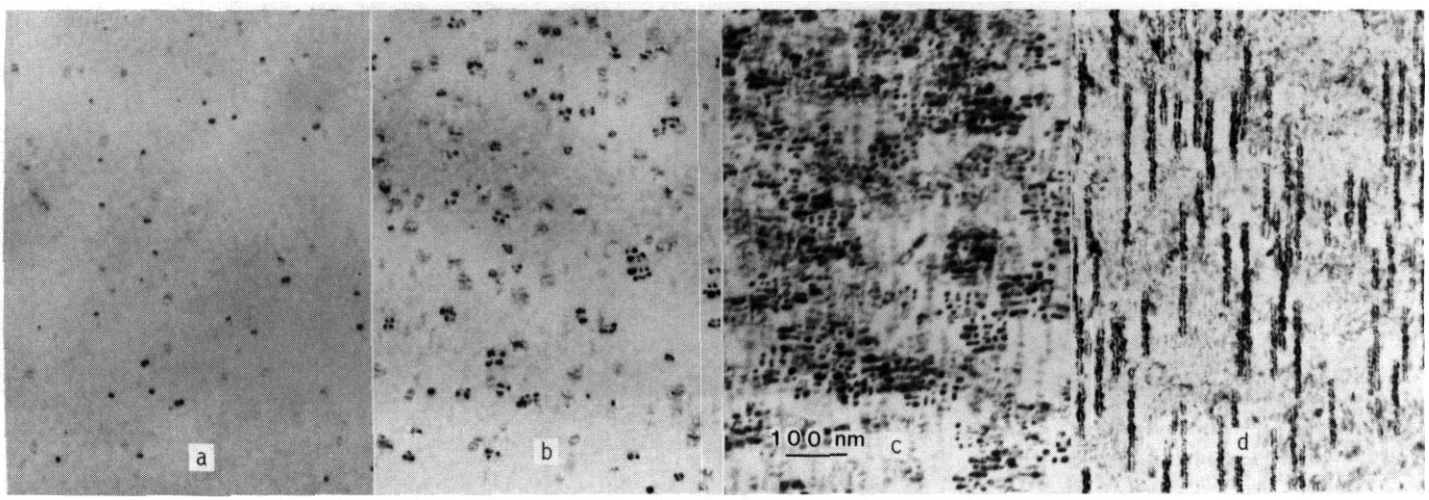

Figure 3. Growth of faulted loops in Fe-18Cr at 350°C as a function of dose in $\bar{g}$ = [1$\bar{1}$0] contrast, (a) at 0.07 dpa, (b) 0.20 dpa, (c) 1.4 dpa and in $\bar{g}$ = [002] contrast, (d) at 3.4 dpa.

faults. This could correspond to the 111 d-spacing for $M_{23}C_6$, or the 110 d-spacing for Fe-Cr sigma phase." Microchemical analysis of faulted loops within a Fe-9Cr foil were found to contain only a negligibly higher level of chromium than the surrounding matrix, even though the loops were oriented parallel to the electron beam, and the spot size was approaching 10 nm, in agreement with previous results.[18] However, it was noted that where etch pitting occurred on the edge of foils irradiated at high temperatures, the matrix appeared to have been eliminated, but the faulted features were retained, in effect producing an extraction replica.

Microchemical analysis of such features revealed the surprising result that both the precipitate and the surrounding region gave compositions of about 50% chromium, but in all cases the composition of the precipitate contained higher levels of chromium than those of the adjacent matrix, and in some cases, precipitate and adjacent matrix compositions were as different as 63% and 46% Cr. Therefore, chromium enrichment could be demonstrated at faulted loop features, albeit by a rather indirect method. Chromium enrichment due to radiation induced segregation (RIS) in ferritic steels is unusual; chromium is generally found to move away from point defect sinks in neutron irradiated ferritic alloys. Also, faulted loop formation in these materials is unusual following neutron irradiation; loops are usually unfaulted. The reason for both of these responses to electron irradiation are not yet understood.

A dual beam irradiation using I MeV electrons and He ions was performed on Fe-9Cr to provide a He/dpa ratio of 10, which is expected in a fusion environment. Irradiation was performed at 425°C corresponding to the peak swelling temperature both in fast flux reactors and electron irradiation studies.[1,4,23] Gislocation evolution was similar to that shown in Figure 1. However, following irradiation to 3.5 dpa, no evidence for void formation could be found. Based on this result, further efforts to study the effect of different solutes on void shape in electron-irradiated simple ferritic alloys were discontinued.

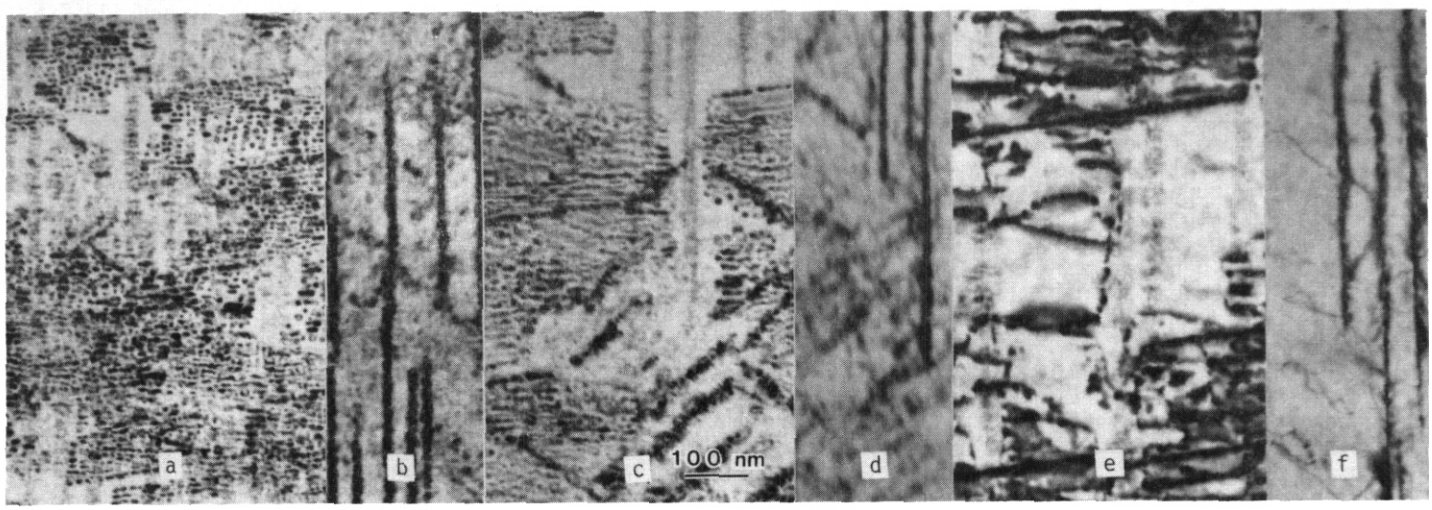

Figure 4. Comparison of irradiated microstructures in Fe-18Cr in $\bar{g}$ = {1$\bar{1}$0} and $\bar{g}$ = [002] contrast, respectively, as a function of irradiation temperature (a) to 1.3 dpa and (b) to 2.7 dpa at 400°C, (c) to 1.3 dpa and (d) to 2.6 dpa at 450°C, and (e) to 1.0 dpa and (f) to 2.0 dpa at 600°C.

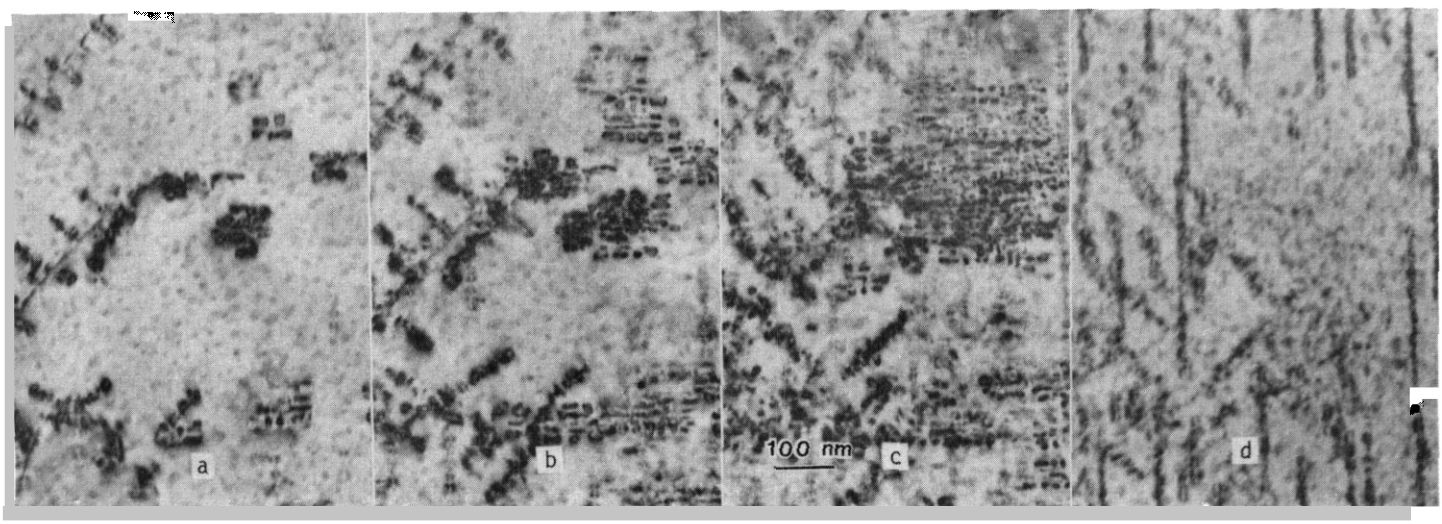

Figure 5. Dislocation evalution in Fe-3Cr irradiated at 350°C in **g** = {1$\bar{1}$0} contrast, (a) to 0.18 dpa, (b) to 0.49 dpa, (c) to 1.3 dpa, and in **g** = {002} contrast (d) to 1.3 dpa.

Beryllium

Specimens of commercial cast grade 99.7% pure beryllium were electron irradiated using 1 MeV electrons at temperatures from room temperature to 500°C. The irradiations are summarized in Table 1. No irradiations showed normal dislocation loop nucleation and growth behavior. Neither loops with a/3 <11•0> or a<00•1> were identified. However, it was possible to find dislocations already present in the specimen and determine the effect of irradiation on dislocation migration. The behavior observed can be summarized as follows: at room temperature and 100°C, climb of a/3 <11•0> dislocations was slow but discernable, whereas at 200 and 300°C, dislocation climb was quite rapid, and at 400°C and above, dislocation motion was *so* rapid that all dislocations present in the field of view rapidly disappeared, leaving little evidence of an effect of irradiation. An example is provided in Figure 7, showing a precipitate particle with an array of misfit-generated dislocations surrounding it. Figures 7a and 7b show the dislocation structure after irradiation at 120°C to about 1 and 3 dpa; Figures 7c and 7d show the same precipitate before and after irradiation to about 3 more dpa after the temperature was raised to 210°C; Figures 7e and 7f show a similar sequence at 290°C to another 2.4 dpa, and Figures 7g and 7h show similar conditions at 400°C for a further 1.8 dpa. The dislocation structure has disappeared at 400°C, and all that remains are surface tracks where the dislocations crossed the surfaces. Therefore, dislocation development appears to be quite different during electron and neutron irradiation. These electron irradiation results raise questions about the source of the dislocation damage observed in identical neutron irradiated specimens. Could the damage have been a result of lower temperature irradiation, for example during cool down, or could the structure that is associated with c type loops have originated from precipitate reactions or helium trapping?

Pure Vanadium. Y-5Fe and *V-1Ni*

Electron irradiation experiments in pure vanadium, V-5Fe, and V-1Ni provided several unexpected rerults. Significant electron irradiation damage was found in all compositions at low temperatures, even as low as room temperature, and precipitation occurred during specimen heating at temperatures of about 400°C. The precipitate was found everywhere, *so* it was not related to contamination from the beam, but only decorated foil surfaces. The same behavior was found in all alloys studied, *so* changes in composition had little effect on precipitate formation. Precipitation caused significant foil buckling. Furthermore, by 600°C, further precipitation ceased, and electron irradiation experiments were possible, and it was found that during subsequent irradiation, precipitates disappeared from the irradiated region. No void swelling could be identified. However, comparisons between dislocation evolution in pure vanadium and its high swelling alloys demonstrated that loop growth was more rapid in pure vanadium. These irradiation experiments are summarized in Table 1.

Examples of dislocation evolution in pure vanadium, V-5Fe, and V-1Ni at temperatures below the srart of surface precipitation are shown in Figures 8, 9 and 10, respectively. Dislocation development at room temperature, 100, 200, and 300°C is shown for each alloy after irradiation to doses as high as about 1 dpa using $\bar{g}$ = [200] contrast. The dislocation structures consist of loops of a/2 <111> Burgers vector, and no a<100> loops can be identified. The appearance of small black spot features in Figures 8b and 8i can be correlated with enhanced contrast at dislocation loops on the periphery of the irradiated region. The smaller non-overlapping loops near the edge of the irradiated region show black spot-like enhanced lobe contrast at the ends of loops where the dislocation line length is most steeply inclined and nearly parallel with the electron beam. However, the cause of such contrast is not yet understood.

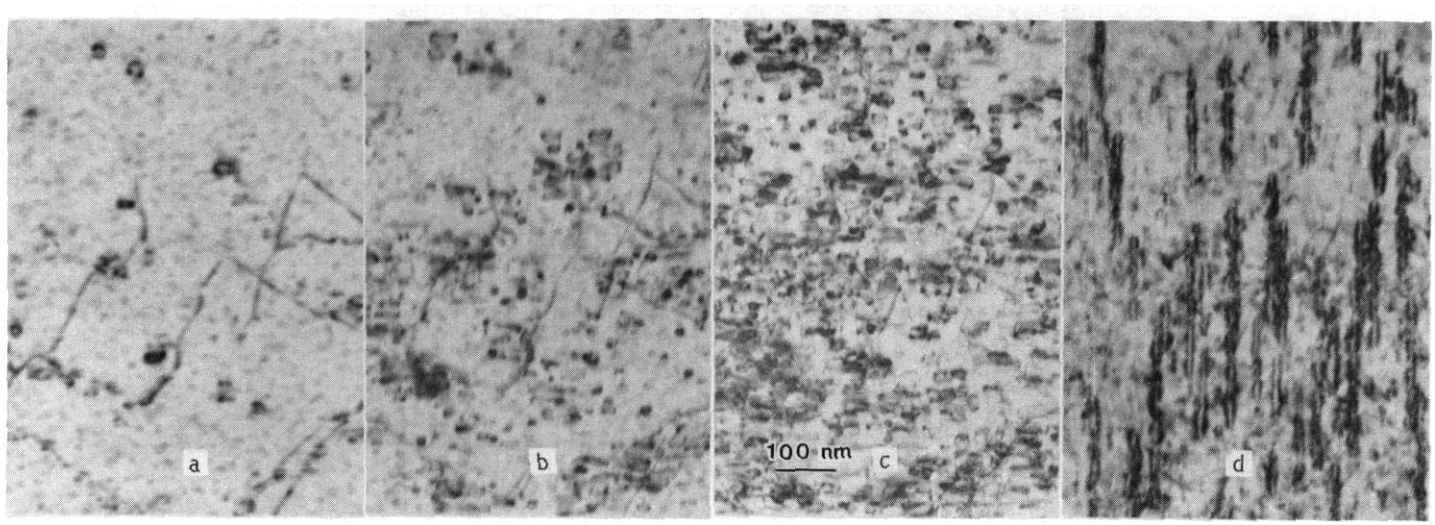

Figure 6. Dislocation evolution in Fe-3Cr irradiated at 400°C in $\mathbf{g}$ = [1$\bar{1}$0] contrast, (a) to 0.23 dpa, (b) to 0.52 dpa, (c) to 1.3 dpa, and in $\bar{g}$ = [002] contrast (d) to 1.3 doa.

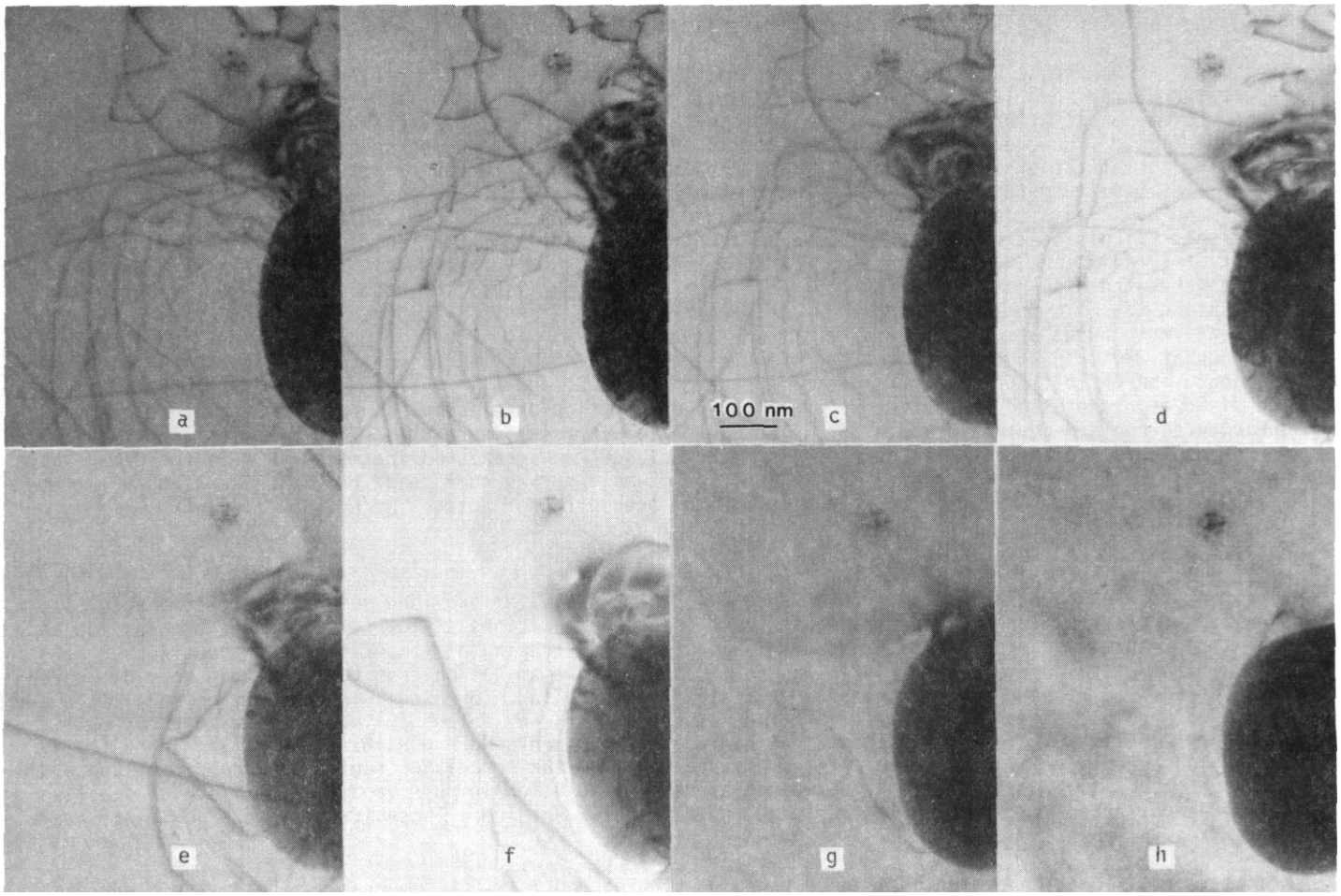

Figure 7. Dislocations around a precipitate particle in cast commercial grade beryllium after irradiation at 120°C to about 1.2 dpa in (a) and 3 dpa in (b), before and after irradiation to about 3 more dpa after the temperature was raised to 210°C, (c) and (d), before and after irradiation to another 2.4 dpa after the temperature was raised to 290°C, (e) and (f), and finally before and after irradiation at 400°C for a further 1.8 dpa, (g) and (h).

Comparisons of Figures 8, 9 and 10 show that at all temperatures, dislocation evolution is most rapid in pure vanadium, and the response is similar for the other two alloys, V-5Fe and V-1Ni. However, in all three cases, dislocation evolution is most rapid at 200°C, an unusual response indicating that the precipitation observed at higher temperatures probably affects low temperature response. Figure 11 provides comparison of all three materials following irradiation at 600°C after surface precipitation was complete. Again, **g** = [200] contrast is used, and no faulted or unfaulted a<100> dislocations can be identified. Therefore, electron irradiation experiments do not provide a straightforward explanation for enhanced swelling in V-5Fe and V-1Ni in comparison with pure vanadium.

Discussion

Several of the experimental results are worthy of further discussion. For ferritic alloys, further comments on faulted loop development are provided. Also, an apriori explanation for differences between electron and neutron irradiation is proposed. Fur beryl1ium, differences between the present and previous irradiation results are better defined. And for vanadium, the consequences of the irradiation results need further elaboration.

fe-Cr alloys

Electron irradiation of Fe-Cr alloys gives results similar to those observed previously. Buswell and Fisher[16] reported faulted loops in FV448, a commercial martensitic steel in the 12 Cr range, and attributed them to impurity absorption from the microscope vacuum. Suganuma and Kayano[17] found faulted loops in Fe-15Cr and attributed the crenulation phenomenon to Cr-(C,N) clusters that controlled loop growth, and faulting to chromium atom segregation around the small loops, which produced "a positive misfit" and showed "fringes like faulted defects." Takeyama and coworkers[11] found a<100> faulted loops in Fe-10Cr irradiated at 290 to 510°C. Although the investigators did not comment on the faulted nature of the loops, they were

able to show a slight chromium enrichment on the loops. Alexander wrote a Ph.D. Thesis" that included observations of the phenomenon, electron irradiating Fe-1, -5, -10 and -15Cr alloys over the temperature range 350 to 700°C. He did not differentiate between faulted and unfaulted configurations but did note that loop convolution was a function of temperature, microscope vacuum, and chromium content. Higher irradiation temperature, improved microscope vacuum, and lower chromium content all promoted less convolution. However, the temperature at which convolution ceased was only reduced by about 30°C between high and low chromium contents. Even a pure iron specimen showed convolution, although the trend with decreasing chromium content continued. Finally, Yoshida et al.[20] and Muroga et al.[21] found loops shaped like flower petals in Fe-10Cr and Fe-10Cr-1Ni following electron irradiation over the temperature range 300 to 500°C that were similar to the present results. (Faulting was not discussed.) Additions of nickel were found to decrease loop growth rates, and segregation to dislocations was found for chromium in Fe-10Cr, and nickel and chromium in Fe-10Cr-1Ni with nickel showing the greatest effect. Therefore, the present experiments only confirm observations over a wide range of compositions and temperatures. From the present results, it can be concluded that faulted loop formation is sensitive to composition and irradiation temperature such that unfaulted loops are found in Fe-9Cr above 450°C, in Fe-18Cr above 500°C, and in Fe-3Cr, probably above 400°C. Chromium enrichment at loops is also indicated. However, previous experiments demonstrate that interstitial content and microscope vacuum can also play a role.

Neutron irradiation response in Fe-Cr alloys differs from the electron irradiation experimental response in three ways: 1.) Void swelling is found after neutron irradiation but rarely after electron irradiation.[24-27] 2.) Loops are unfaulted after neutron irradiation but can be faulted after electron irradiation. 3.) After neutron irradiation, chromium depletion is found to occur at point defect sinks, whereas after electron irradiation, chromium enrichment is found. These differences are probably related. In general, it is argued that dissolved gases are needed for void nucleation. But an alternate argument can be presented. If segregation of chromium leads to faulted loop forniation as a result of precipifault growth, then dislocation evolution may be sufficiently retarded to prevent void swelling evolution. Kitajima et al.[26] argue that a critical dislocation density is required: 4x10' to 1x10^{10} cm^{-2}. Therefore, the fact that chromium segregation occurs during most electron irradiation experiments, but not during neutron irradiation, would lead to reduced dislocation evolution because of the retarding effects of solute segregation and would lead to a lower dislocation density, which should increase void swelling resistance.

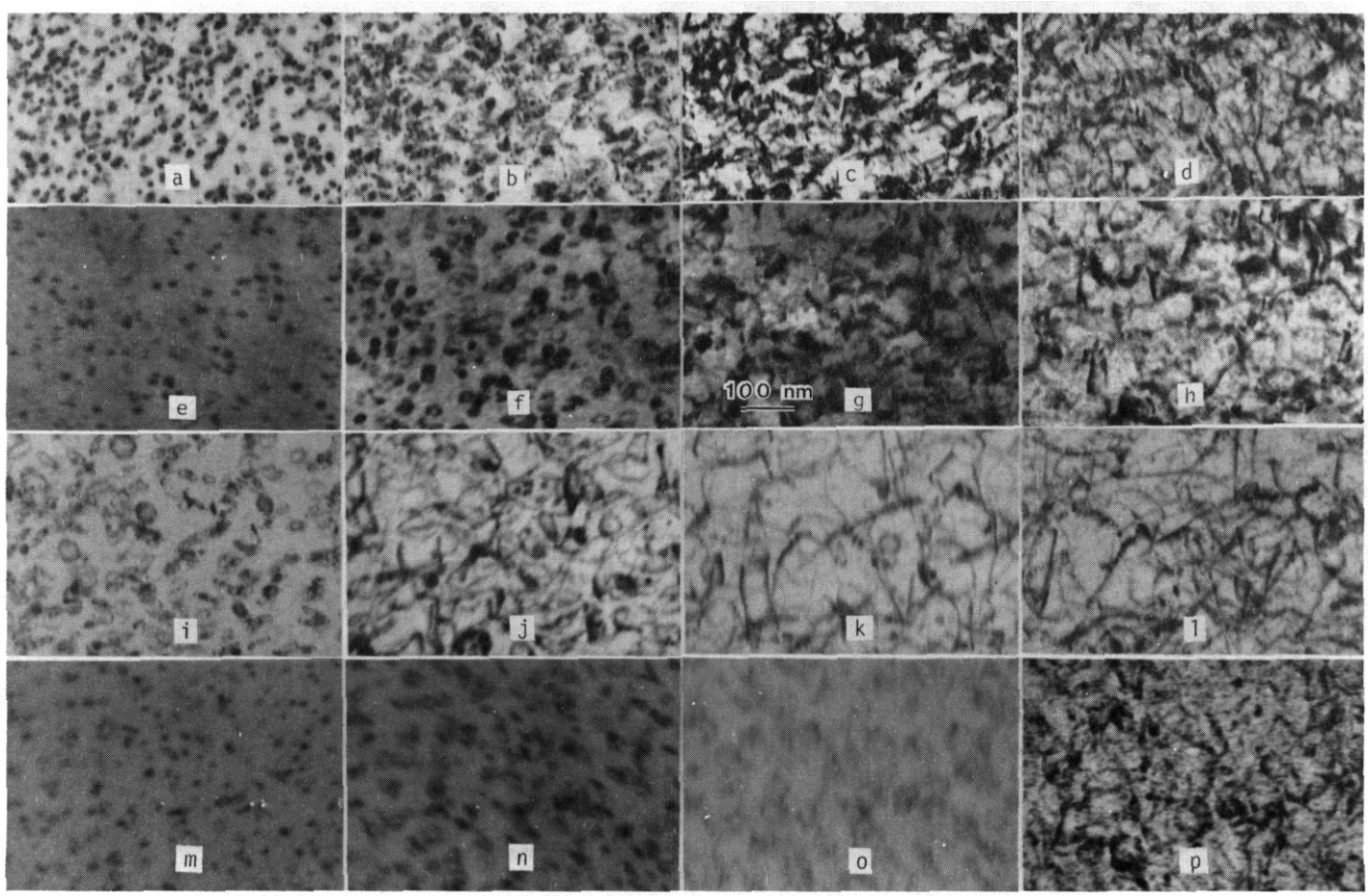

Figure 8. Dislocation evolution in pure vanadium as a function of temperature and dose. at 25°C to (a) 0.02 dpa, (b) 0.11, (c) 0.32 and (d) 0.95 dpa, at 100°C to (e) 0.07 dpa, (f) 0.20, (g) 0.66 dpa and (h) 1.3 dpa, at 200°C to (i) 0.06 dpa, (j) 0.19 dpa, (k) 0.51 dpa and (1) 1.3 dpa, and at 300°C to (m) G.06 dpa, (n) 0.19 dpa, (o) 0.50 dpa and (p) 1.3 dpa.

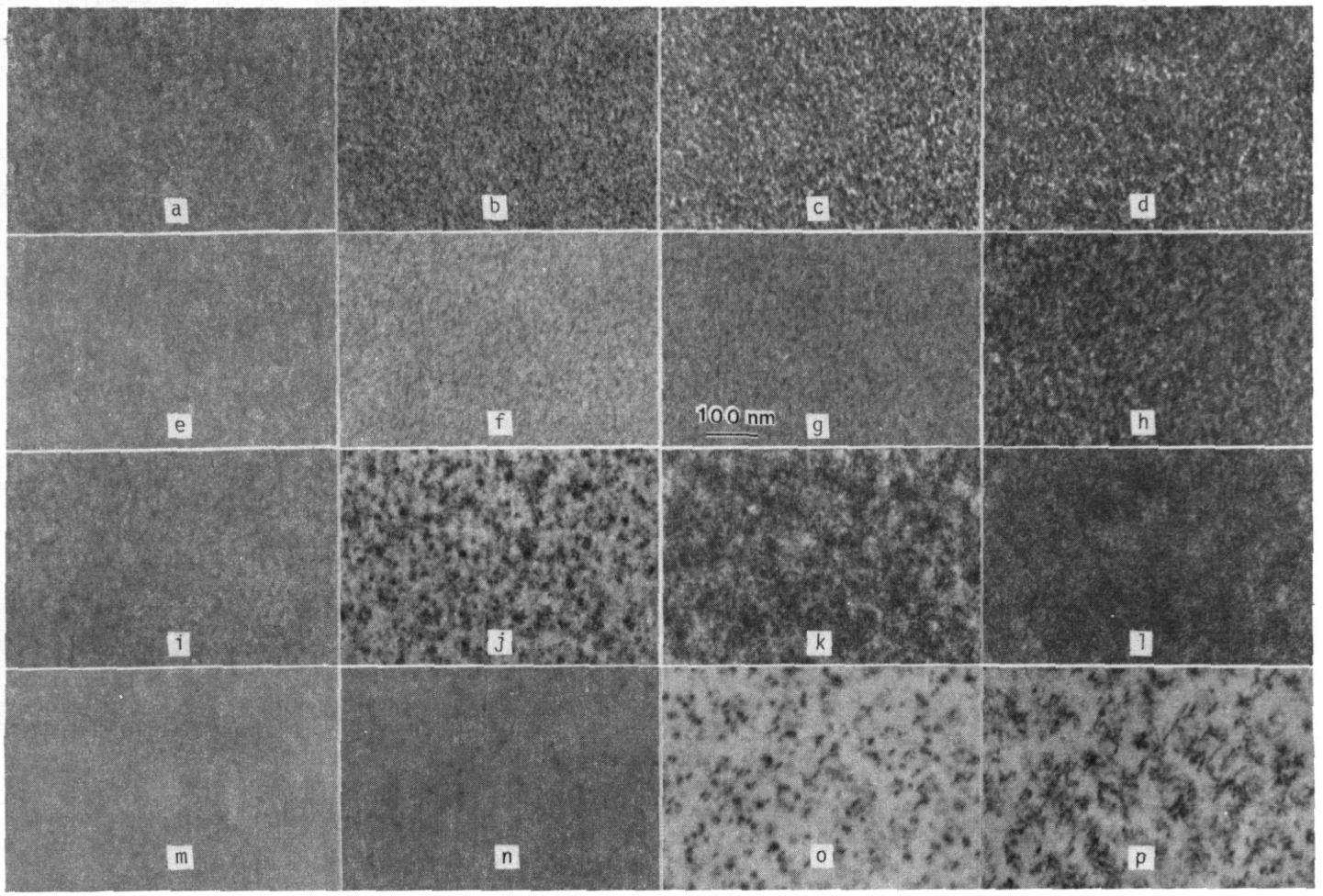

Figure 9. Dislocation evolution in V-5Fe as a function of temperature and dose. at 25°C to (a) 5.07 dpa, (b) 0.26, (c) 0.66 and (d) 1.3 dpa, at 100°C to *(e)* 0.07 dpa, (f) 0.27, (g) *0.66* dpa and (h) 1.3 dpa, at 200°C to (i) 0.07 dpa, (j) 0.26 dpa, (k) 0.66 dpa and (1) 1.3 dpa, and at 300°C to (m) 0.06 dpa, (n) 0.26 dpa, (o) 0.65 dpa and (p) 1.3 dpa.

It must be emphasized that the existence of a faulted loop on (100) planes with a Burgers vector of the type <100> for body centered cubic crystal structures can only produce stacking fault images due to phase contrast derived from the presence of a second phase. Planes cannot be stacked on the (001) plane to produce a stacking fault. Therefore, the observed faulted loops are precipifaults, and the unusual morphologies that have been observed are controlled by the arrival of the atomic species that contribute to the growth of the precipitate.

The question remains, what precipitate controls a<100> faulted loop development? The present results indicate that the precipitate controlling faulted loop growth is sigma, (FeCr). This cannot be based on rel-rod intensity peaks at ¼, ½ and ¾ of the distance between 000 and 200, but can be argued based on the apparent unfaulting temperature as a function of alloy chromium content. Figure 12 reproduces the Fe-Cr phase diagram and can be used to demonstrate that for Fe-18Cr, sigma can form at temperatures below 580°C. However, for Fe-9Cr, temperatures must be below 420°C, and for Fe-3Cr, temperature requirements on the order of 300°C can be estimated. Irradiation-induced segregation can overcome thermal equilibrium requirements. Therefore, observed unfaulting temperatures of greater than 500°C for Fe-18Cr, between 450 and 500°C for Fe-9Cr, and greater than 400°C for Fe-3Cr are reasonable estimates for formation temperatures for sigma in an electron irradiation environment where chromium is enriched at the loops. However, precipifaults may arise from other precipitation reactions. It is likely that when impurity absorption occurs during electron irradiation experiments, other precipitation reactions such as carbides, or carbo-nitrides may control faulted loop growth.

Beryllium

The electron irradiation experiments on beryllium in the present study provide results that are difficult to interpret. There has been only one other HVEM electron irradiation experiment on beryllium.[8] Carpenter and Fleck irradiated pure beryllium of nominal purity at 37°C using I MeV electrons and found after about 1 dpa that black spot damage formed as 10 nm clusters, and grew to 100 nm resolvable dislocation loops after 15 dpa. The loops tended to be aligned in rows in "end to end" orientations at a density of 10^{15} cm^{-3}. At 100°C, an incubation dose of ≈4 dpa was required before damage clusters were visible, and after 15 dpa,

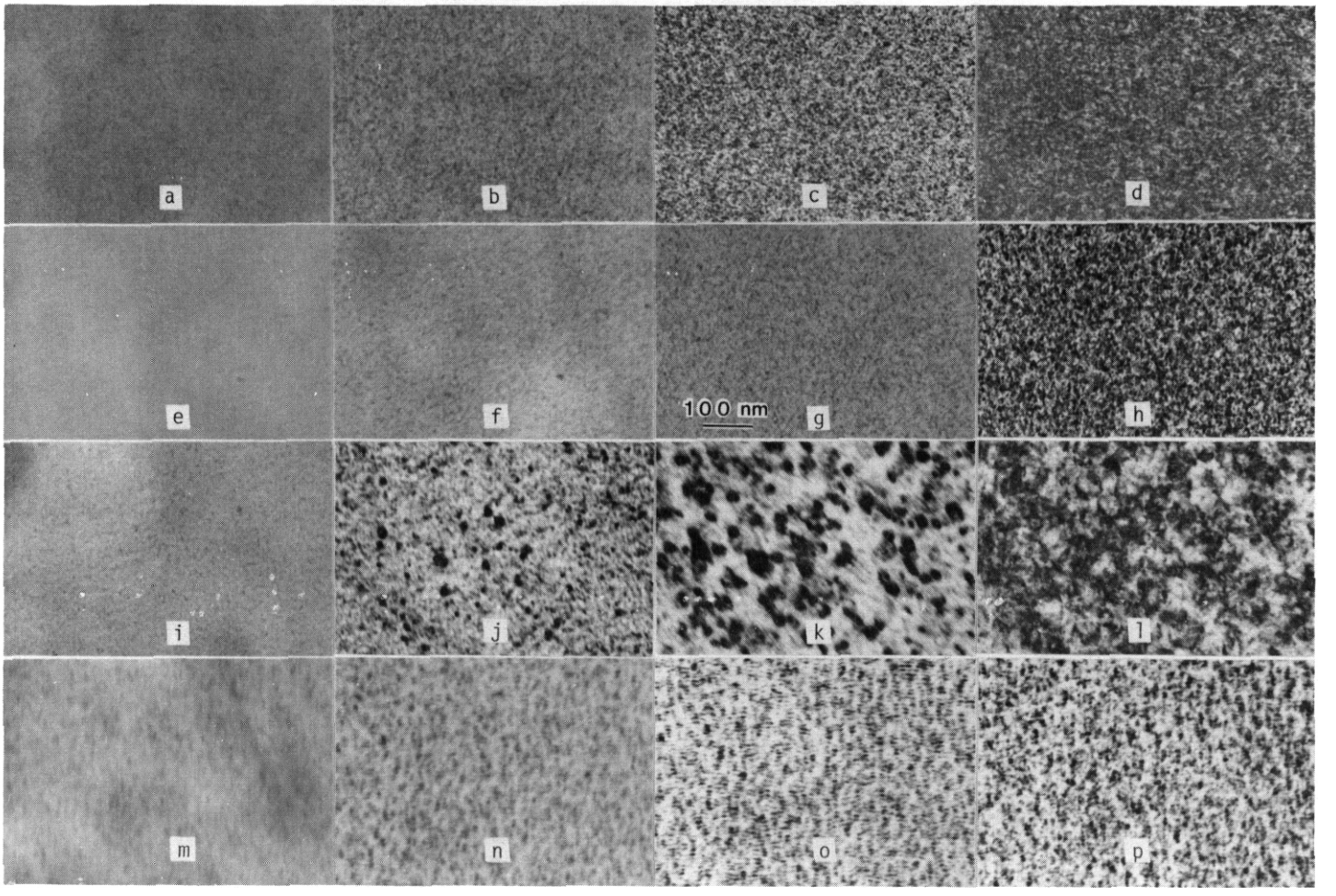

Figure 10. Dislocation evolution in V-1Ni as a function of temperature and dose, at 25°C to (a) 0.06 dpa, (b) 0.26, (c) 0.65 and (d) 1.3 dpa, at 100°C to (e) 0.06 dpa, (f) 0.25, (g) 0.63 dpa and (h) 1.3 dpa, at 200°C to (i) 0.07 dpa, (j) 0.27 dpa, (k) 0.66 dpa and (1) 1.3 dpa, and at 300°C to (m) 0.06 dpa. (n) 0.26 dpa, (o) 0.65 dpa and (p) 1.3 dpa.

loop diameters were as large as 120 nm at a density of 10^{15} cm^{-3}. Following irradiation at a temperature of 200°C, no dislocation loops formed but some dislocation motion was observed. This indicates that the present experiments were conducted either at temperatures that were too high or to doses that were too short. Unfortunately, in the present study no micrographs were recorded for irradiation at room temperature, and the dose achieved may have been too low to make dislocation evolution apparent on the microscope screen. Therefore, it is not possible to comment on the development of Burgers vectors with non-basal components based on the results of this work.

Vanadium

The electron irradiation experiments on pure vanadium and two vanadium alloys were intended to provide further understanding of the high swelling phenomenon found in the vanadium alloys. Although vanadium is a difficult material on which to perform electron irradiations because of its affinity for impurity pick-up, the present experiments have demonstrated that electron irradiation experiments are possible in a microscope with high vacuum capability.

The experiments were affected by impurity pick-up, but at temperatures below 300°C the effects were minimized sufficiently to provide satisfactory results. At 300°C and above, the results are complicated by precipitation. This was most apparent when precipitation occurred, but the 300°C irradiation condition has been included because loop growth at 300°C is slower than that at 200°C, a very unusual response, indicating that precipitation is affecting loop growth at 300°C. Additionally, electron energy loss analysis at PNL of an HVEM irradiated pure vanadium specimen showed that the precipitate was enriched in oxygen. Spectra were obtained from a surface precipitate and the nearby matrix, and a ratio of the two spectra clearly showed an oxygen edge overlapping the vanadium structure. The example is shown in Figure 13. Therefore, it is only reasonable to draw conclusions between pure vanadium and its alloys for irradiations at 200°C and below.

Dislocation evolution in the temperature range of room temperature to 200°C is found to be much more rapid in pure vanadium than in V-5Fe or V-1Ni. Such response is normal, as solute additions to pure materials

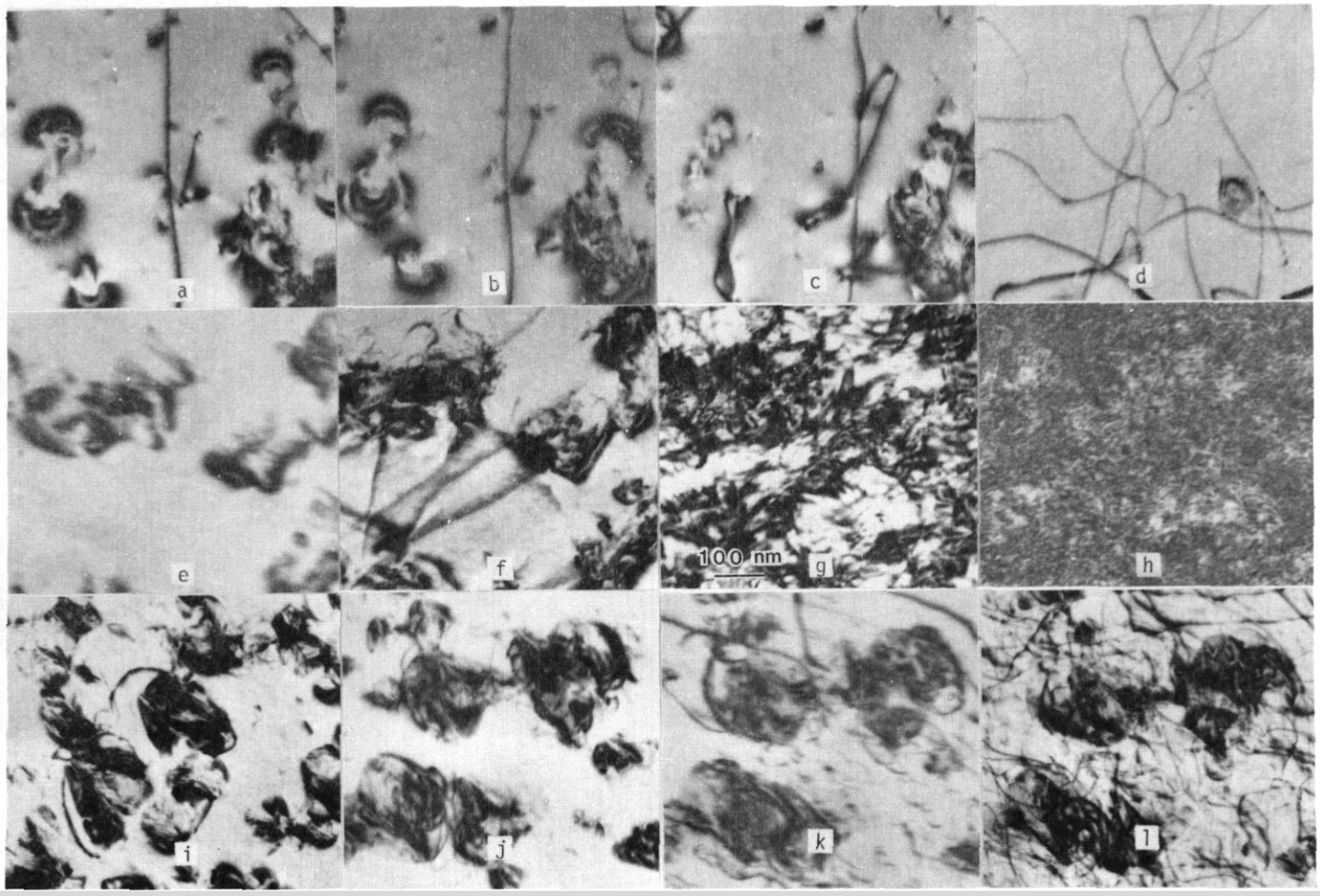

Figure 11. Dislocation evolution at 600°C in pure vanadium to (a) ≈0 dpa, (b) 0.12 dpa, (c) 0.48 and (d) 2.4 dpa, in V-5Fe to (e) ≈0 dpa, (f) 0.28 dpa, (g) 0.70 dpa and (h) 2.1 dpa, and in V-1Ni to (i) ≈0 dpa, (j) ≈0.60 dpa in a different area, to (k) ≈1.4 dpa and (l) ≈2.4 dpa.

are generally found to slow dislocation evolution. However, these results provide no clues as to why enhanced swelling is found in the alloys following neutron irradiation. Enhanced swelling should be accompanied by enhanced dislocation evolution. Therefore, high swelling is not simply a consequence of iron or nickel additions. A more complex explanation will be required. For example, segregation of solute to dislocations may be greater during neutron irradiation, and enhanced segregation may be necessary to alter dislocation dynamics. Or precipitation of ordered phases of vanadium involving iron or nickel may be necessary, and the high swelling response occurs in the ordered phases. Neither of these possibilities has been demonstrated.

CONCLUSIONS

Three classes of materials of interest to the fusion materials community have been irradiated using 1 MeV electrons in order to further characterize the effects of fast neutron irradiation on microstructural evolution.

Ferritic alloys, Fe-3Cr, -9Cr, and -18Cr, were found to develop a complex dislocation structure consisting of crenulated faulted a<100> loops and circular unfaulted a/2 <111> loops at lower temperatures, but at higher temperatures, the a<100> loops were unfaulted. The unfaulting transition temperature was found to increase with increasing chromium content. Complex dislocation evolution in the present experiments is attributed to precipifault growth controlled by solute segregation, and the controlling precipitate is identified as sigma phase formation resulting from chromium segregation.

Commercial cast grade beryllium was found to be resistant to HVEM irradiation damage over the temperdture range of room temperature to 400°C. The only observed effect of irradiation was enhanced dislocation mobility.

Pure vanadium and two vanadium alloys were found to develop a complex microstructural response as a function of temperature. Between room temperature and 300°C dislocation evolution dominated, but at 400°C a surface precipitate formed and stabilized. After heating to 600°C, further precipitation ceased and

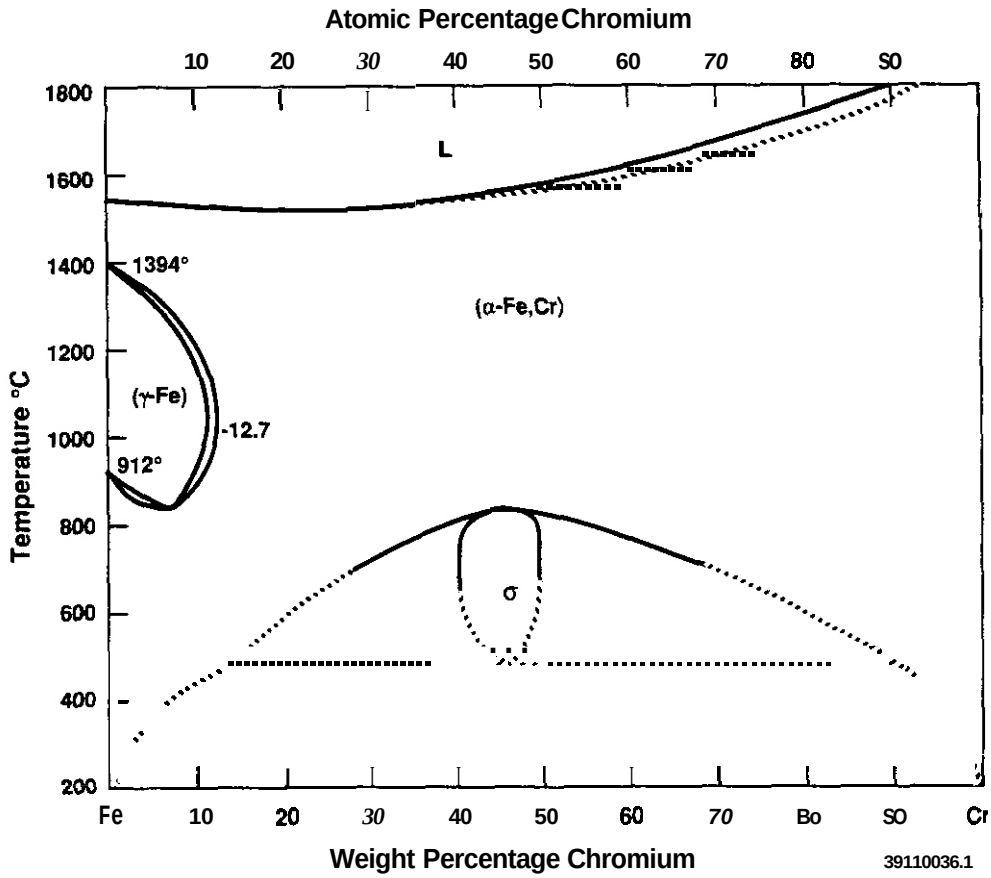

Fig. **12.** The Fe-Cr phase diagram showing **the** sigma-(o) phase boundaries.

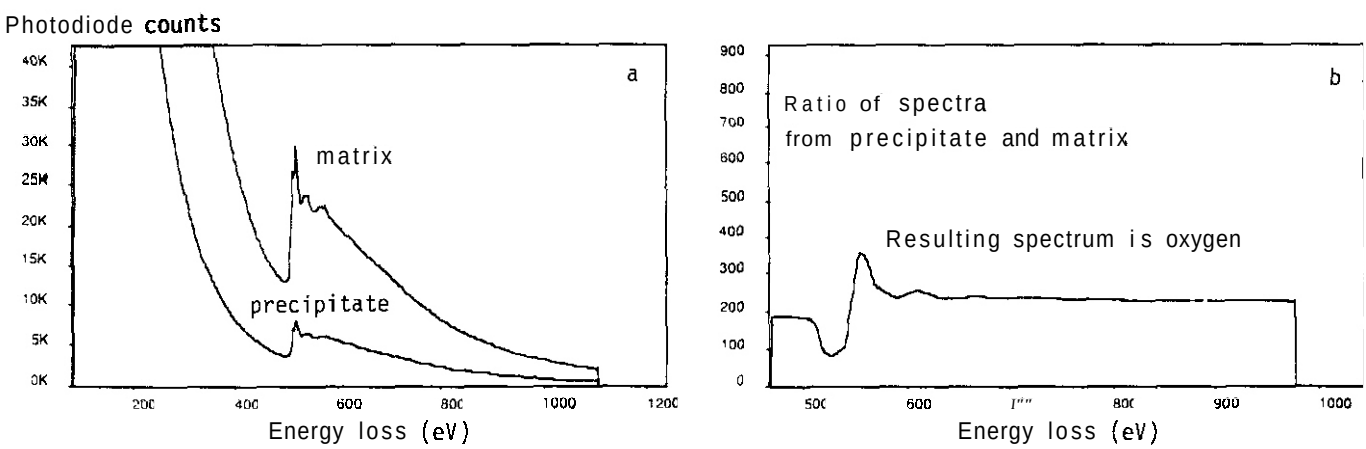

Figure 13. Parallel electron energy loss spectra from precipitate and matrix regions of a pure vanadium specimen following electron irradiation to temperatures as high as 600°C showing in (a) the individual spectra and in (b) the ratio of the two spectra revealing the presence of an overlapping oxygen edge.

electron irradiation again produced dislocation evolution. The three materials behaved similarly except that pure vanadium showed more rapid dislocation evolution. In light of the enhanced neutron induced swelling found in the alloys in comparison to pure vanadium, this difference indicates that alloying additions of iron and nickel to vanadium do not inherently provoke enhanced swelling; a more complex mechanism is **responsible.**

FUTURE WORK

This work has been completed

REFERENCES

1. D. S. Gelles, J. Nucl. Mater., 108-109 (1982) 515.

2. L. Horton, J. Bentley and K. Farrell, Ibid., 222.

3. O. S. Gelles, in Effects of Radiation on Materials, Vol. 1, ASTM STP 1046, N. H. Packan, R. E. Stoller and A. S. Kumar, Eds., (ASTM, Philadelphia, 1990) 73.

4. A. E. Ward and S. 8. Fisher, J. Nucl. Mater., 166 (1989) 227.

5. H. Takahashi, S. Ohnuki and T. Takeyama, J. Nucl. Mater, 103-104 (1981) 1415

6. S. Ohnuki, H. Takahashi and K. Nagasaki, Ibid, 155-157 (1988) 823.

7. H. Takahashi, S. Ohnuki, H. Kinoshita and F. A. Garner, in Reduced Activation Material, for Fusion Reactors, ASTM STP 1047, R. L. Klueh, D. S. Gelles, M. Gkada and N. H. Packan, Eds., (ASTM, Philadelphia, 1990) 93.

8. G. J. C. Carpenter and R. G. Fleck, in Beryllium 1977, (Royal Society, London,1977) 26/1

9. Y. Mishima, S. Ishino and S. Shiozawa, ibid reference 8, 25/1.

10. G. P. Walters, C. M. Van Der Walt and M. J. Makin, J. Nucl. Mater., 11 11964) 335

11. D. S. Gelles, in Fusion Reactor Materials Semiannual Progress Report for the period ending September 30, 1989, DOE/ER-0313/7, 299.

12. H. Matsui, Y. Kohno and D. S. Gelles, presented at the 15th ASTM on Radiation Effects in Materials, held June 1990 in Nashville, TN, to be published.

13. H. Matsui, presented at the JIM fall meeting, held September 1990 in Sendai, JIM 107, report 212, 256.

14. S. Ohnuki, H. Takahashi and H. Kinoshita, in Reduced Activation Materials for Fusion Reactors, R. L Klueh, D. S. Gelles, M. Okada and N. H. Packan, Eds., ASTM STP 1047, (ASTM, Philadelphia, 1990) 190.

15. F. A. Garner, L. E. Thomas and D. S. Gelles, in Exuerimental Methods for Charged-Particle Irradiations, CONF-750947 (1975) 51.

16. J. Buswell and S. B. Fisher, "Interstitial Loop Growth in Electron Irradiated FV448," CEGB Report RD/B/N4564, Berkeley Nuclear Laboratories, (May 1979).

i7. K. Suganuma and H. Kayano, Rad. Effects, 54 (1981) 81.

18. T. Takeyama, H. Takahashi and S. Ohnuki, in Bulletin of the Faculty of Engineering, Hokkaido University, 121 (1984) 85.

19. R. N. Alexander, "Radiation Damage in Ferritic Steels," Ph. D. Thesis, University of Birmingham, U.K., 1986. Alternatively, *see* R. N. Alexander, M. H. Loretta, C. A. English and E. A. Little, in Proc. EMAG '85, 395 or R. N. Alexander, M. H. Loretta, C. A. English and E. A. Little, in Materials for Nuclear Reactor Core Applications, Vol. 1, (BNES, London 1987) 161.

20. N. Yoshida, A. Yamaguchi, T. Muroga, Y. Miyamoto and K. Kitajima, J. Nucl. Mater., 155-157 (1988) 1232.

21. T. Muroga, A. Yamaguchi and N. Yoshida, in Effects of Radiation on Materials: 14th International Symposium, Vol. 1, ASTM STP 1046, N. H. Packan, R. E. Stolier and A. S. Kumar, Eds., (ASTM, Philadelphia, 1989) 396.

22. K. W. Andrews, D. J. Dyson and S. R. Keown, Intrepretation of Electron Diffraction Patterns, (2nd Ed., N.Y., Plenum Press, 1973).

23. D. S. Gelles and L. E. Thomas, unpublished results on HVEM irradiated HT-9, a commercial 12% Cr martensitic stainless steel.

24. E. A. tittle, Rad. Effects, 16 (1972) 135.

25. E. Kuramoto, K. Futagami and K. Kitajima, Proc. of Fifth Int. Conf. on High Voltage Electron Microscopy held in Kyoto, Japan (1977) 589.

26. K. Kitajima, K. Futagami and E. Kuramoto, J. Nucl. Mater.,85 & 86 (1979) 725

27. D. R. Arkell and T. M. Williams, J. Nucl. Mater., 74 (1978) 144.

SUMMARY OF FINAL REPORT ON THE DOE GRANT DE-FG03-84 ER52110 WITH UCLA ON "RADIATION EFFECTS ON STRUCTURAL MATERIALS," - N.M. Ghoniem, University of California, Los Angeles

OBJECTIVES

The objective of this effort is to summarize research efforts supported by DOE at UCLA during the period 1/1/84 through 1/31/90.

SUMMARY

Research efforts at UCLA on the effects of fusion neutron irradiation on structural materials covered a wide range of theoretical and materials engineering problems during the six year period supported by the DOE grant No. DE-FG03-84ER52110. In this brief report, highlights of research accomplishments are presented in the following areas:

(1) Atomic Displacements
(2) Microstructure Evolution
(3) Materials Engineering. Mechanics and Design
(4) Invention of Low-Activation Steels
(5) Research Motivated by Grant Support

PROGRESS AND STATUS

History and Objectives

A three-year research proposal entitled, "Radiation Effects on Structural Materials" was submitted to the Materials Branch of the Development and Technology Division of the Office of Fusion Energy in mid-1983. The project was subsequently approved for a three-year period starting in January 1984. The objectives of the proposed research were stated as the development of theoretical methodologies and insights in the following areas of radiation effects on structural materials for fusion applications:

1. Helium effects on the properties of austenitic and ferritic alloys;
2. Microstructure evolution under irradiation;
3. Radiation hardening of austenitic and ferritic alloy systems, and radiation embrittlement of ferritics;
4. Precipitation kinetics under irradiation, and in-reactor creep;
5. Development of design equations for critical materials properties.

The research was based on both mechanistic and phenomenological descriptions of basic radiation effects. Mechanistic approaches result in greater understanding of the basic underlying physical processes. On the other hand, phenomenological theories often lead to useful equations for data extrapolations and for design purposes. The following general achievements were expected from the proposed research

1. To discover fundamental radiation-damage phenomena and to gain new insights into the underlying physical mechanisms;
2. To suggest carefully planned experiments in order to unravel the action of important damage processes;
3. To extrapolate present-day experimental data to anticipated fusion conditions;
4. To develop design correlations for the improvement of blanket design concepts

A milestone chart of proposed research is shown in Figure I

This phase of our research was a balanced mix of fundamental radiation-damage studies and design-oriented investigations. Based on our success with this work, we proposed a continuation project for a subsequent three-year period (February I, 1987 - January 31, 1990). The emphasis of the continuation proposal was on the fundamental aspects of microstructure behavior under fusion irradiation conditions.

The proposed research covered a number of areas within the broad framework of radiation-damage theory. The overall objective was to develop and apply new theoretical methods in order to enhance the understanding of radiation-damage phenomena in a fusion environment. Specifically, we proposed a continuation of our work utilizing non-equilibrium statistical mechanical methods to describe microstructure evolution during irradiation.

The majority of approaches for analyzing microstructure evolution have been based on deterministic causal description that were provided by rate theory conservation equations. However. the existence of a large number of interacting entities. on the order of 10^{30} atoms in a typical engineering solid, implies that the system's degrees of freedom are much larger than can be represented by individual equations. Such a situation naturally leads to fluctuations around a reference state. In this work, we concentrated mainly on the role of these fluctuations on microstructural development and evolution. First, fluctuations around a "critical" state can determine the extent of embryonic cluster nucleation. Second, as the clustering System evolves, fluctuations determine the "dispersion" or "spread" around the average state.

The work we proposed as listed below addressed a number of related areas in radiation damage:

1. Numerical solution to the transient, two-dimensional Fokker-Planck equation for the self-consistent description of helium-filled cavity nucleation and growth;
2. Development of an analytical "moments" method for describing the evolution of probability density of interstitial loops;
3. Development of a new method to experimentally measure, for the first time, dislocation bias towards self-interstitials;
4. Monte Carlo numerical simulations of collision cascades in polyatomic media;

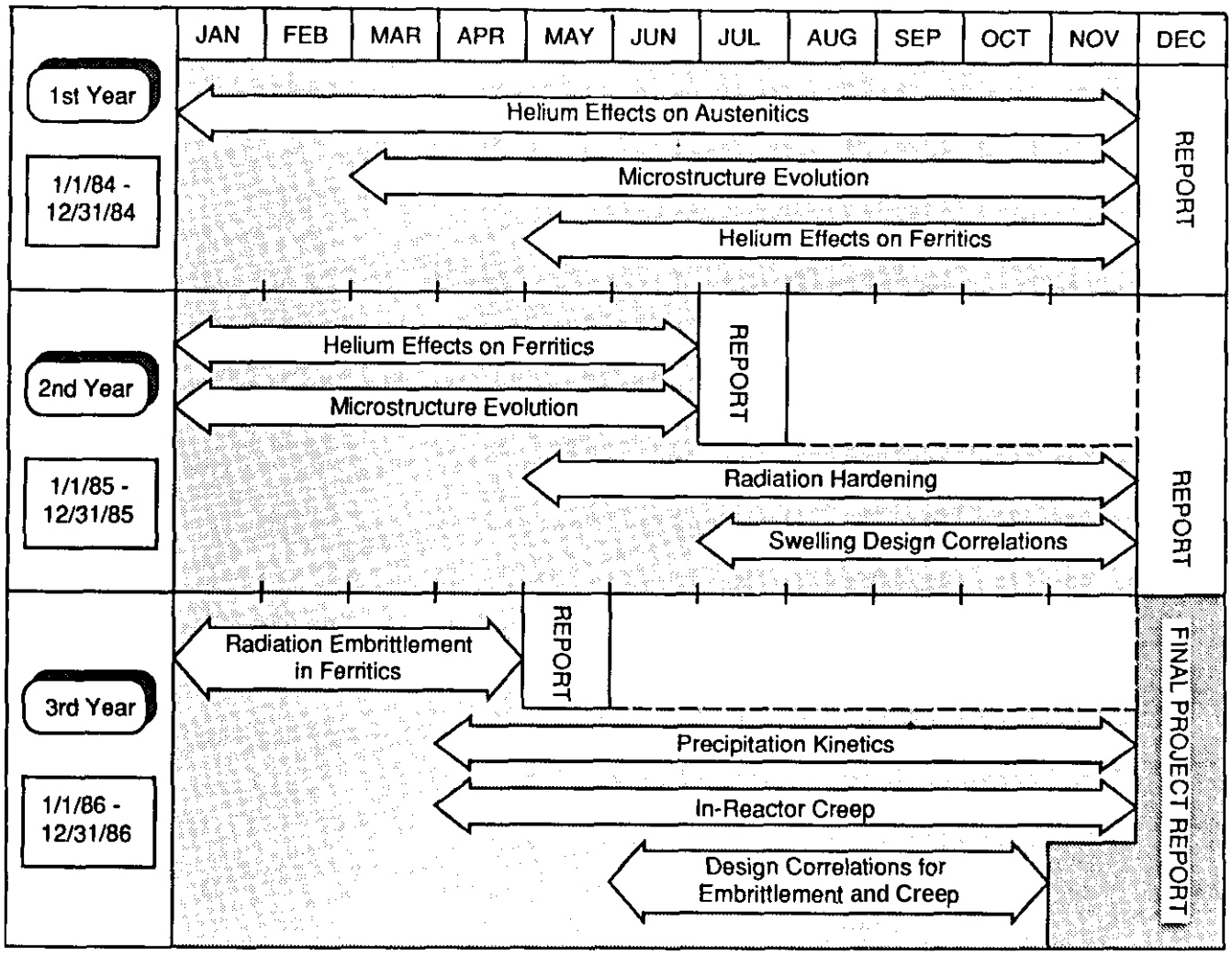

Fig. 1. Milestone chart for proposal on "Radiation Effects on Structural Materials"

5. Dislocation system self-organization and the relationship to in-rcacror creep;
6 Precipitate stability during irradiation

A milestone chart, as originally proposed, is shown in Fig 2. Research on collision cascades and dislocation creep seemed particularly promising. The Department of Energy agreed to grant UCLA a 'no-fund extension" of the project until November 1990.

Highlights oi Research Accomplishments

Research work sponsored hy the original grant and its continuation resulted in 3 considerable numher of publications that can he roughly grouped into five separate categories. Most of the published research (55 papers and numerous reports) was directly funded by the two granrs over the six-year period. A number of published papers. however, were not directly funded by the grants. although the work was essentially motivated by the general themes established under this DOE sponsorship. We will highlight in this section the salient achievements of our research work.

Atomic Dinolacement

The interaction of energetic ions with solids results in a number of interesting physical phenomena. A detailed understanding of such phenomena is required for the development of technological applications which are based upon ion-solid interaction mechanisms.

Utilizing the advanced state of knowledge on the interaction of energetic particles with solids, we concentrated on a number of key problems that are particularly important to fusion energy systems. First we developed an analytical theory compute the rates of precipitate dissolution by collision cascades [1,6]. Results of this work were used to outline the range of conditions (e.g., precipitate size, density, displacement rate, ion energy, and temperature) for which precipitate dissolution is important. The work was later correlated to experiments by the University of Tokyo group (Professor Ishino and co-workers). Further calculations were made later for the interaction of collision

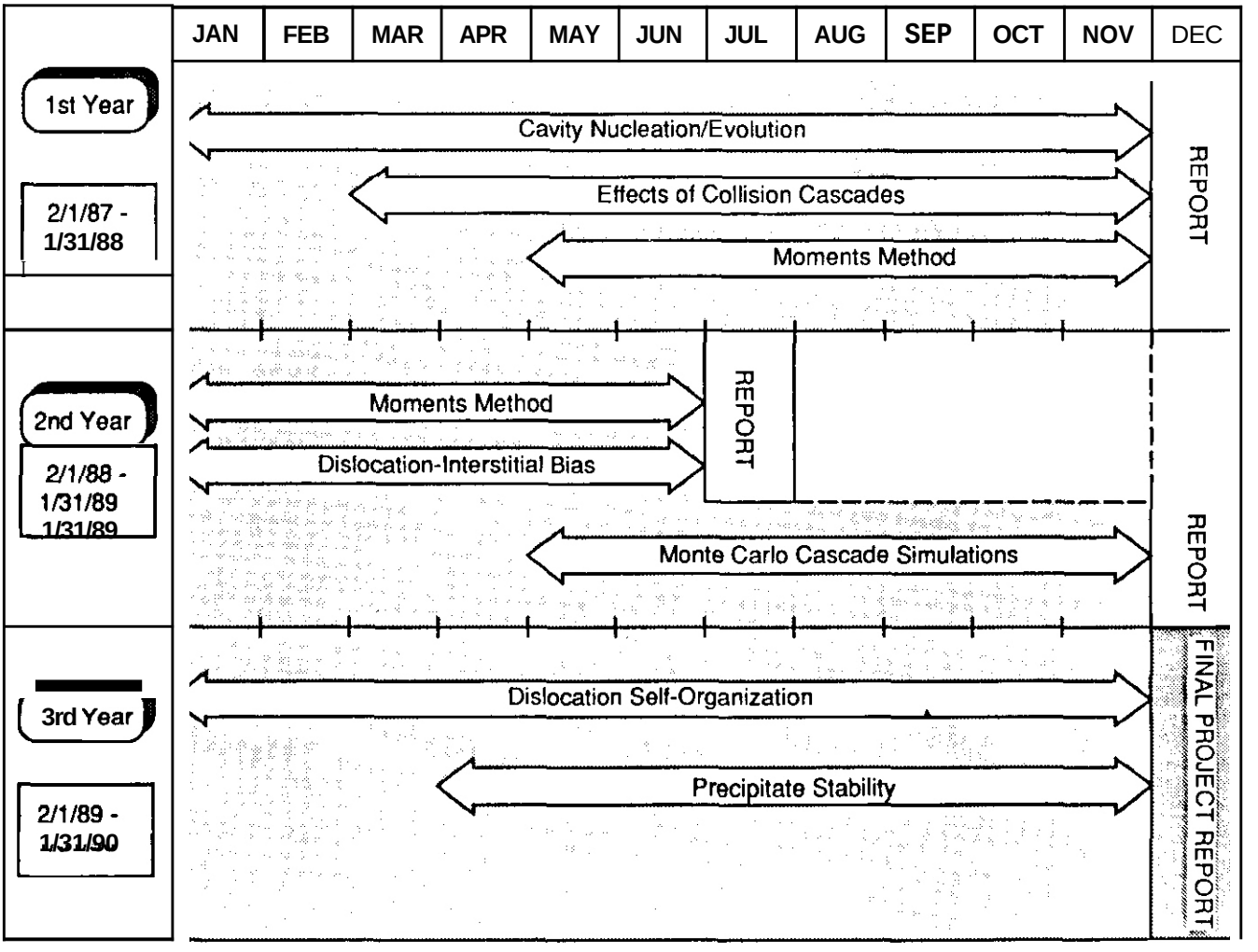

Fig. 2. Milestone chart for continuation proposal on "Statistical Theory of Radiation Effects"

cascades and precipitates [4]. Because the TRIM code was fairly limited in dealing efficiently with multi-layered and multi-component solids, we launched an effort to develop computational capabilities for ion-solid interaction problems, which resulted in two computer codes; TRIPOS (for the transport of ions in polyatomic solids) [3,4] and CASC-MD (for molecular dynamics simulations of cascades) [7-9]. While the binary collision approximation (BCA) was used in TRIPOS. full solution of the simultaneous equations of motion of atoms in the crystal *was* accomplished in CASC-MD. An efficient and accurate closed-form solution to the scattering integral **was** established for general interatomic potentials in Ref. [3]. Some of the major achievements of our work in the area of ion-solid interactions are described here.

Ion transport in solids is essentially controlled by the slowing down of energetic ions through collisions with background nuclei and their electrons. The energy losses for **ions** in collisions can be adequately treated by separating them into nuclear and electronic Parts. Because nuclear collisions cause significant energy and momentum losses, nuclear energy loss has to be individually treated; the binary collision approximation is generally adequate. Because of the mass disparity between electrons and ions. only a small amount of momentum and energy is transferred in electronic collisions. Therefore, energy **loss** due to electrons **on a** moving ion can be considered to be a continuous process and may be fully treated through the use of the continuous electron-stopping power approximation.

Various theories were developed for the treatment of ion nuclear and electronic energy losses. Although the Thomas-Fermi potential is the most sophisticated model for treating nuclear collisions. its use requires cumbersome numerical calculations. In our work. we used continuous power-law-potential fits to the Thomas-Fermi model. For very **low** ion energies, we used the Born-Mayer potential. The collision integral was analytically solved by using the moment approximation. and accordingly, the power-law cross section **was** derived. For electronic stopping, the Biersack-Haggmark model, which combines both the Lindhard-Scharff low-energyand the Bethe-Bloch high-energy models, was adequate.

Ion transport problems are generally treated by using either deterministic or probabilistic methods of analysis. The deterministic methods. however, can only deal with simplified problems. Applying the discrete ordinate multi-group treatment to ion transport is much more difficult than it is for neutron transport. The high anisotropy in nuclear collisions, recoil multiplication in slowing-down processes. and the need for group cross sections lead to considerable calculational difficulties. For our work, a probabilistic Monte Carlo method **was**

developed to treat ion transport in polyatomic multi-layer solids, It is capable of simulating cascade damage in both bulk and surface radiation damage analyses. This code has been shown to be superior in both computing speed and versatility when compared with other equivalent Monte Carlo codes, and simulation results agree with those from either experiments or other codes.

Cascade-Diffusion Theorv. In order to ascertain bulk radiation damage, TRIPOS is used to simulate displacement collision cascades. An immediate application of the results is for the treatment of stochastic diffusion of point defects in the so-called cascade-diffusion theory.

Our study shows that the 6-function cascade model used in earlier investigations by different authors yields singular point-defect concentration fluctuations. Therefore. non-zero cascade size has to be included in order to avoid this singularity which is unphysical. With the consideration of cascade strength and size, our results from the homogeneous cascade model show that the point-defect concentration fluctuations can be smaller by a factor of **5** than those from the point-cascade model. For high-energy collision cascades, our results show that the fluctuations from the uniform tree subcascade models are 2 to 3 times higher than those from the homogeneous cascade model. However, the results from both subcascade models are a factor of 2 to 3 times smaller than those from the point-cascade model (see Ref. (15)).

Precipitate Dissolution. Precipitate dissolution is a mechanism which degrades material physical properties, particularly the creep strength, during irradiation. We nuemrically simulated this dissolution by using TRIPOS. A collision cascade induced by a 14-MeV fusion neutron was able to totally destroy some of the small precipitates with a diameter of 15 Å or less but only 10% of the larger precipitates (**30-A**diam) were destroyed by the same collision cascade. The average dissolution rate for 30-A-diam precipitates has a maximum of **1%** for an optimized separation of 100 Å (see Refs. [1,6]).

Recent experimental work [N. Sekimura, T. Zama, H. Kawanishi and S. Ishino, "Precipitate Stability in Austenitic Stainless Steels During Heavy Ion Irradiation," presented at 2nd Intl. Conf. on Fusion Reactor Mater. (Chicago, IL, April 1986)] at the University of Tokyo shows that precipitates greater than 200 Å are not dissolved for irradiation doses up to 100 displacements per atom by fusion collision cascades. Our work has also been extended by Muroga *et al.* [T. Muroga and K. Kitajima, "Computer Simulation of Precipitate Recoil Re-Solution by Energetic Collision Cascades," presented al 13th Intl. Symp. on Effects of Radiation on Mater. (Seattle, WA, June 1986)] at Kyushu University to explain the incubation dose phenomenon in the swelling of fusion reactor materials. We have also observed the preferential dissolution (sputtering) effect for the Monte Carlo-type precipitates.

A cascade slowing-down theory based on coupled diffusion equations was developed to determine the average dissolution rate of precipitates. Hard-sphere collisions and no electronic stopping were assumed. A Neumann series expansion was used to solve for the coupled diffusion equations and the results were similar to the "escape zone" concept proposed for the fission gas-bubble re-solution effects. Planar and spherical precipitate models were shown to yield similar results. An empirical formula to determine the dissolution parameter as a function of precipitate size and PKA energy was also derived (see Refs. [1, 4 and 6]).

Surface Sputtering Analysis. The TRlPOS code was applied to the analysis of surface radiation-damage problems with sputtering of surface atoms as the main emphasis. The sputtering yield calculations from TRIPOS consistent with either experimental results or theoretical predictions from other codes. and analog TRIPOS code was a factor of 3 to 10 times faster than TRIM. Importance sampling techniques such as particle splitting and Russian roulette were used, which further enhanced the TRlPOS simulation speed by an extra factor of 3.

For light ions on gold, copper, and tantalum surfaces, TRlPOS results showed good agreement with results from experiments and/or TRIM. For helium ions on graphite and titanium surfaces, it was found that neither TRIM nor TRIPOS predictions were in perfect agreement with experimental results if unadjusted surface binding energies were used. However, good agreements from TRIPOS were obtained by adjusting the surface binding energies, indicating probably that other atomic surface phenomena can be dominant for these two surfaces in addition to the collisional effect (see Ref. [4]).

Preferential Sputtering and Associated Surface Evolution Phenomena. Surface evolution and preferential sputtering of compounds and alloys under ion bombardment was finally investigated. Results from earlier theoretical works using the EVOLVE and TRIDYN codes differed.

Results from TRIPOS were similar to those from TRIDYN, where an ion mixing zone resulting from light ion implantation was observed. However, for the case of 2-keV Ar on laminated AuPt, the results from TRIPOS show a 20-A-thick altered layer, whiic those from EVOLVE show a 40-A-thick layer. The disagreement is attributed to possible problems in the EVOLVE code for treating high-Z recoils. TRIPOS showed that these recoils generally remain at their point of generation while EVOLVE shows that these recoils travel a significant distance from their point of generation. On the other hand, simulations from TRIPOS show good agreement with the results from TRIDYN for 5-keV Ar on LuFe.

TRIPOS was also used to simulate the experiment of 150-eV ^{3}He on Cu-3%Au (G.L. Nelson and R. Bastasz, *J. Vac. Sci.* Tech.. 20 (1982) 498)]. Good agreement with experimental results was obtained. Far fusion reactor first-wall and limiter coatings made of TiC, an enrichment of titanium atoms in the surface region is predicted by TRIPOS simulations. This result is in qualitative agreement with experimental observations.

Modeling of the surface seems to have an important influence on the results of theoretical studies and a major effort is needed to couple our analyses with theories predicting the surface topography, chemistry. and other surface atomic clustering processes. Such effort will yield valuable information on this important topic.

Cascades in Polvatomic Ceramics. The understanding of radiation damage phenomena in polyatomic ceramic materials is still at an early stage as compared to that in metallic structural alloys. The binary collision approximation was used in a Monte Carlo study of high-energy collision-cascade creation in $MgAl_2O_4$. The study focussed on two aspects of cascade generation: cascade morphology and cascade stoichiometry. In the high-energy regime, typical fusion neutron cascades showed a tree-like morphology. To a large degree, instantaneous recombination occurs in the "stem " part of the cascade because of the closer separation of vacancy-interstitial pairs. Following this recombination phase, fusion neutron cascades tended to result in Frenkel pairs distributed on the "branches" of the tree in a zone extending

over 100 to *200* nm. The stoichiometry of displacements within the cascade was found to be substantially different from bulk stoichiometry. and was dependent upon the energy and type of primary knock-on atom (PKA) (see Ref. [5]).

Molecular Dynamics of Cascades and Sputtering. An empirical. composite interatomic potential was developed to describe interaction of energetic particles by pair potentials at high energies and many-body potentials at low energies. Molecular-dynamics (MD) studies of low-energy collision cascades were performed. The displacement threshold surface in copper was investigated and compared to experimental data. Our computer simulations showed good agreement with the experimental results of King and Benedek at 10 K.

The study of the collisional phase of low-energy cascade evolution showed the following: (1) The development of a replacement collision sequence (RCS). which leads to stable Frenkel pairs, is completed in about 0.1 ps. (2) The initial propagation of a RCS is much faster than the longitudinal elastic (sound) wave in copper and is even faster than the initial PKA speed, showing that cascades Propagate through collective atomic motions. (3) The close agreement of our MD results with the experinental data on the displacement threshold surface indicates the usefulness of this composite potential for the simulation of low-energy ion-solid interactions (see ref. (8)).

The interaction between low-energy copper atoms and an atomically smooth [100] surface was investigated using an MD computational method. A newly formulated interatomic potential, which empirically combines the Ziegler universal potential at high energy and the embedded-atom many-body potential at low energies, was utilized in the study of near-surface cascade dynamics. The analysis included surface atom sputtering. and reflection and penetration of incident copper atoms. It was shown that the sputtering yields of low-energy Cu atoms on a [100} Cu surface are in general agreement with experiments and with other MD calculations using only pair potentials. It was shown in this work, however. that while pure pair-potential MD simulations show no reflection and Monte Carlo calculations give unrealistically large values, our analysis demonstrated the physical transition from reflection to adsorption as the incident atom energy is lowered. Detailed mechanisms of sputtering, penetration, and reflection of atoms with energies in the range of 10-1000 eV were given.

Microstructure Evolution

It is now well-established that the mechanical and physical properties of materials can be controlled by changing the basic microstructure. Irradiation introduces atomic displacements, heat, and new transmuted atoms. Complex microstructural changes take place in irradiated materials. It is, therefore, central to the development of alloys for fusion conditions that an understanding of the basic mechanisms which govern microstructural evolution of structural materials during irradiation is established. The following is a brief summary of our work in this area.

Pulsed irradiation fluxes can cause alterations in the development of irradiated microstructures when compared to those resulting from steady irradiation. Theoretical analysis of irradiation damage development and examination of pulsed ion-irradiated microstructures have indicated conditions for expected effects from pulsing on fusion reactor materials. In pure metals, high instantaneous damage rates and pulse annealing periods comparable to defect relaxation times can cause significant pulsing effects. In addition, irradiation-affected phases in alloys are altered by pulsed irradiation compared to steady irradiation [10].

Theoretical and experimental evaluations of pulsed flux effects on radiation damage indicate that pulse compression for inertial confinement frequency and phase stability for magnetic fusion are important pulsed effects issues. Pulse compression, (*i.e.*, brief periods of high damage rate) increased mutual recombination of point defecu and increased the interstitial clustering kinetics. On the other hand, pulse annealing periods allowed recovery of nonequilibrium defect states, irradiation microstructures. and radiation-modified phase changes. Pulsed-irradiation compared to steady-irradiation experiments conducted at constant instantaneous damage rates have shown significant differences in irradiation response for alloys containing unstable phases. Stable alloys were generally insensitive to pulsed flux effects except at high temperature. Pulsing theories have shown that greater pulsing effects are expected for heavy ion-irradiation damage rates than for magnetic-fusion damage rates, and for low dose microstructures than for high dose microstructures.

One of the major uncertainties in understanding cavity nucleation and growth is the degree of stability of helium-vacancy clusters (HVCs) in an irradiation field. Such stability is a complex function of irradiation variables (damage rates, helium production rates, and fluence), as well as material parameters (sink density, temperature, and defect parameters). The goal of investigating the stability of HVCs is to understand and consequently to model cavity size distributions. Our research first investigated helium-vacancy binding energies, which were then used in analyzing the stability of HVCs under irradiation. The stability studies established the critical HVC size, *i.e.*, the helium:vacancy ratio that ensures growth under specified irradiation conditions. Using these models it is possible to understand the cavity size distribution of various simulation facilities. The fine cavity-size distribution seen in many high flux isotope reactor experiments can be explained by the favorable irradiation conditions, which lead to "spontaneous" nucleation of HVCs. In experimental breeder reactor-II experiments, on the other hand, the conditions for Spontaneous nucleation of HVCs are not met, and nucleation is "delayed," and occurs by stochastic fluctuations [11].

Using a rate theory model, Ghoniem, Alhajji, and Kaletta [14] developed a solution to the problem of the rate of helium absorption at grain boundaries. In fusion reactor conditions, helium is expected to be uniformly generated inside the grains of structural materials. With the simultaneity of displacement damage production, helium atoms can be trapped in vacancies or vacancy clusters, inhibiting the migration of helium.

In this work [14], we showed reasonable agreement with available data on matrix helium-filled cavity nucleation and growth. This investigation demonstrated the effects of several physical mechanisms that are significant in interpreting experiments and furthering theory development. The following points were concluded:

1. The injection of helium gas into the solid, either by nuclear reactions or by implantation, cannot be separated from the question of vacancy mobility. It was shown that large helium concentrations lead to the immobilization of a large fraction of vacancies, leading to a "constrained" model of cavity growth provided that the cavities or clusters are immobile.

2. Helium gas re-solution due to the interaction of displacement damage with gas-filled cavities is a process of prime importance to cavity re-nucleation. At high re-solution rates, "dynamic nucleation" is a continuous process throughout irradiation.

3. Theoretical models and experiments are both needed to determine the effects of re-solution

4. The external source of helium injection can be less important compared to internal helium sources to gas re-solution effects on gas arrival rates at grain boundaries.

5. During early irradiation, helium gas is trapped in small vacancy clusters. A large fraction of gas migrates to grain boundaries until matrix cavity nucleation is complete. When this is achieved, the majority of introduced gas resides in matrix bubbles, and a small percentage still arrives at grain boundaries.

Heavy ion irradiation accelerates the production of displacement damage in irradiated materials. Bullough and Ghoniem [13] developed exact analytical solutions to the time-dependent equations of point-defect diffusion to spherical cavities. In their work, they showed that the effective cavity sink strength increased with dose rate. Therefore. care must be exercised in high displacement-damage simulations, or microstructural sink strengths will be underestimated.

Collision cascade size and shape effects on point-defect diffusion during irradiation were studied in Ref. [15]. In contrast to the point cascade model of the cascade-diffusion theory of Mansur *el al.*, where cascades are mathematically modeled as δ-functions, we represent cascades as spheres and spherical shells. The dimensions of the vacancy cascade sphere, or the interstitial cascade shell correspond to the energy of the PKA. Subcascades are also studied at high PKA energies. It is shown that the 6-function representation of collision cascades overestimates the rms value of the magnitude of point defect fluctuation by a factor of 2 to 5, for large size cascades typical of fusion reactor conditions.

Our results showed that fluctuations in point-defect concentrations are sharply reduced as compared to those of the point cascade model if the cascade size effect is taken into account. For larger size cascades, the spherical cascade model predicts a lower magnitude of fluctuation in point-defect concentration. However, for cases where the damage rate is fixed and cascade strength and size are increasing, the decrease in point- defect concentration fluctuations is partly due to the homogeneous distribution of point defects within the cascade. Tree-like point-defect distributions in large cascades can be approximated either by a linear subcascade model or by a homogeneous subcascade model. These two models depict extreme configurations observed in Monte Carlo simulations of defect structures in large cascades. Defect concentration fluctuations based on these two subcascade models fell in between those based on the point and homogeneous cascade models. For the same conditions, the point-defect model gives a sharp increase in the magnitude of the defect concentration fluctuation, while the homogeneous cascade model actually predicts a decrease in the magnitude of this fluctuation. The actual behavior of the concentration fluctuation is expected to fell in between the results from the two subcascade models. For an anticipated fusion-reactor neutron spectrum, cascades tend to have sizes that correspond to defect concentration fluctuations around the plateau region for the subcascade models.

Modeling cavity nucleation at grain boundaries in structural alloys under the combined influence of helium and stress was the primary objective of our work in Ref. [16]. The role of stress in cavity nucleation was analyzed by using an extension of classical theory, taking into account grain boundary sliding to describe stress concentration buildup and relaxation at particles and triple-point junctions. Helium clustering in the matrix is modeled using rate theory. The helium flux to grain boundaries is determined applying sink strength theory which takes into account the various competing clustering mechanisms in the matrix. Helium clustering on grain boundaries was also theoretically investigated using rate theory. The work agrees with experimental observations showing that irradiation results in grain- boundary bubble densities that are orders of magnitude larger than cavity populations observed in conventional creep experiments. It is shown that even if the total injected helium is as little as one part per million, it can result in grain-boundary bubble densities on the order of 10^{13} m^{-2}. Such cavity population exceeds typical grain-boundary cavity densities associated with creep experiments. Grain-boundary bubble densities are shown to reach steady state for injected helium amounts an the order of 10 parts per million.

Our time-dependent extension to classical nucleation theory has shown that, in the absence of irradiation, grain-boundary sliding is the driving force for grain-boundary cavity nucleation. When sliding is resisted by triple-point junctions or by hard particles at grain interfaces, sufficiently localized stresses are set up and immediately relaxed by diffusion or dislocation creep. The ensuing nucleation pulse was shown to be sensitive to the cavity shape and to the boundary inclination to the applied stress. Stress-induced cavity nucleation can, therefore, be statistical and dependent on the stochastic nature of sliding, and the distribution of irregularities on boundaries normal to the applied stress. It was concluded that, with a cavity shape factor on the order of 0.01 and surface normal to inclinations of only 15 to 20 degrees to the applied stress, a small number of such nucleation pulses is required to saturate all available nucleation sites. It was also shown that stress-induced nucleation is very rapid and that cavity life is spent mainly in the growth regime.

Under irradiation, the introduction of helium from nuclear reactions causes a dynamic helium flux to grain boundaries. This atomic helium flux drives another mode of grain-boundary cavity nucleation; helium-vacancy clustering. The rate theory of helium clustering showed that this mode of cavity nucleation is much stronger than the stress-induced mode. With as little helium as 1 appm total, helium-nucleated grain- boundary cavity densities on the order of 10^{13} m^{-2} may result. This work and experiments on grain-boundary cavitation by helium are in basic agreement. The effective helium migration energy on the grain-boundary for such an agreement is on the order of the self-diffusion energy. Calculated grain-boundary bubble densities in the presence of irradiation are several orders of magnitude greater than cavity densities in the absence of irradiation. These quasi-steady-state densities are reached rather quickly at helium contents on the order of 10 appm. Our model also shows that, consistent with experiments, the saturation cavity density increases with increasing helium implantation rate.

An important parameter in the rate theory of swelling is the dislocation-loop bias factor, Z_i^1, which is a measure of the rate of interstitial atom absorption relative to vacancy absorption at interstitial loops. The Fokker-Planck (F-P) equation was used to describe interstitial loop evolution. with a kinetic nucleation current boundary condition at di-interstitial atomic clusters. The majority of loop

nucleation is shown to be finished after one milli-dpa, which allows the shape of the loop distribution function to be governed mainly by the drift (F) and dispersion (D) functions in the F-P equation. Since collision cascades contribute significantly to D, their effects must be suppressed by using low-energy ions or high-energy electrons to produce spatially homogeneous atomic displacements. Under these conditions. both F and D are shown to be proportional to the square root of the number of atoms in a loop. The proportionality parameters depend on material and irradiation conditions and are linearly proportional to Z_i^1. The ratio, F/D, which resembles the Peclet number in fluid flow, can be used in a unique way to determine Z_i^1 without the usual complications of uncertainties in material and irradiation conditions. This is shown to constitute an internal variable measurement of the bias factor.

The moments solution to the F-P equation, with transient nucleation conditions, can be effectively used to measure the interstitial-loop bias factor. Z_i^1. To take advantage of this solution, a number of experimental conditions must be satisfied. These conditions are: (1) Irradiation doses beyond a short transient period of $\sim$ 0.001 dpa and before loop unfaulting at several dpa's; (2) Sample temperatures low enough such that vacancy emission from loops does not significantly contribute to their growth (*i.e.*, below 450 - 500°C for Ni at a dose rate of $\geq 10^{-4}$ dpa/s); (3) The use of low-energy ions or high-energy electrons to minimize the effects of collision cascades on the fluctuations in loop sizes during their growth.

Comparison between the current theory and experiments showed that a combination of the parameters Z_i^1, E_{2i}^b, E_i^M, and D_c/D_s can produce all observed features of interstitial loop evolution in ion-irradiated nickel. The best set of these parameters was found to be $Z_i^1 = 2$, $E_{2i}^b = 1.19$ eV, $E_i^M = 0.55$ eV, and $D_c/D_s = 60$.

The dynamical evolution of a 1-D dislocation pile-up was numerically studied in Ref. [18]. By extending particle methods of computational statistical mechanics, criteria for accurate numerical simulation of the pile-up evolution were established. A combination of explicit integration of the equations of motion and dislocation 'freezing' after 40 position oscillations gave a maximum error of 5% in the trajectory of the leading dislocation. Explicit integration preserves spatially oscillatory behavior and was shown to give accurate results. The evolution of the dislocation distribution function showed small density wave formation during the compression phase of the pile-up. Our work on the dynamics of dislocation pile-ups impacts the understanding of the development of localized plastic deformation ahead of cracks in ductile materials. This approach will be pursued for other micromechanical applications where continuum mechanics is incapable of treating localized plasticity.

The formation of inhomogeneous distributions of vacancy loops in irradiated materials was studied [19] in the framework of a dynamical model based on the rate theory of radiation damage. Dislocation structures are associated with dynamical instabilities due to the competition between defect motion and interactions. The dependence of the critical wavelength of the microstructures on material variables, such as the displacement-damage rate, network-dislocation density, or temperature, was obtained. The postbifurcation analysis was performed in the weakly nonlinear regime where the selection and stability properties of 3-D Structures were investigated.

The occurrence of pattern-forming instabilities seems natural for defect populations in irradiated metals and alloys. It mainly results from the different mobilities and bias in the migration of point defects to line defects, such as vacancy loops or network dislocations. We showed that structures with different symmetries may be simultaneously stable beyond the primary bifurcation. For example, when the diffusion and interactions of point defects are isotropic. the maxima of the vacancy loop density may correspond to either bcc lattices or planar arrays. Hence, these structures could be in nonparallel orientations, *i.e.*, with a structure different from the structure of the host lattice. On increasing further the displacement-damage rate, bcc lattices become unstable and a first-order-like transition should occur to planar structures. In the case of anisotropic interstitial diffusion, planar structures should be the rule. Hence, since the symmetry of the defect structures is a crucial issue in irradiated material, our analysis shows that a careful study of the post-bifurcation regime is needed to test the relevance of particular kinetic models to the interpretation of experimental observations.

Atomic clustering into circular planar disks is an important process responsible for interstitial-loop formation in the bulk of irradiated materials. and the evolution of atomic planes during thin-film growth. We developed a stochastic theory for the formation of planar-atomic clusters by atomic diffusion [20]. The theory accounts for transient coupling between master equations representing small-size atomic clusters and an F-P equation for larger ones. The F-P equation was solved self-consistently, together with the master equations by the moments method. Equations for the rates of change of atomic species and for the nucleation rate of atomic clusters were simultaneously solved with appropriate equations for the average size and various moments of the distribution function. An application of the theory was given by comparing the results of calculations with experimental data on interstitial-loop formation in ion-irradiated nickel,

The nucleation phase of interstitial loops was shown to be very fast, and the transient period for loop formation is finished in about 0.001 dpa. The effects of three point-defect parameters on loop density and average size was studied by comparing theoretical calculations to experiments. An increase in the loop bias factor, Z_i^1, was found to increase the average loop size but had a very small effect on the total loop density. An increase in the di-interstitial binding energy, E_{2i}^b, increased the loop density and reduced the average diameter in a significant way. For nickel, a value of $E_{2i}^b = 1.19$ eV reproduced available experimental data. The value of the effective self-interstitial migration energy had a dramatic effect on the total loop density and the loop average size. A value of $E_i^{me} = 0.55$ consistency with experimental data. This is an indication that interstitial migration is hindered by atomic traps.

The distribution function of circular-planar atomic clusters, when displayed as a function of the loop diameter. is non-Gaussian. The deviation from Gaussian behavior is caused by several factors. First. the continuous nucleation of small-size clusters introduces a component of small-size clusters. Second, if the dispersion and drift functions are size dependent, higher-order additional terms are introduced as correlations to the Gaussian distribution function. Third, the assumption that the stochastic process of atomic additions to a cluster results in an instantaneous circular disk produces a transformation of the stochastic process from size space to diameter space. This transformation introduces another distortion to the distribution function.

Applying the theory to interstitial-loop formation revealed several simplifying features that are consistent with experiments. The high mobility of single interstitials and large binding energy of a di-interstitial cluster result in rapid termination of the nucleation process and, hence, nucleation-relateddistortions to the distribution functionare nearlynonexistent. A consequenceof cluster growth by diffusional

accretion of single atoms or by addition of small numbers of multiple atoms from cascades is a distribution function that is nearly Gaussian in size space. Higher-order non-Gaussian corrections to the moments of the distribution function tend rapidly to zero for large <x> (or long times). This is a result of the growth law used for individual atomic clusters. Viewed from a different perspective, in the limit of large <x> and assuming no other growth mechanism to dominate (*e.g.*, coalescence), the thermodynamic limit is attained where the ratio of the system variance lo the average size tends to zero in accordance with the law of large numbers,

Atomic agglomeration into interstitial loops under irradiation is affected by collision cascades. Comparisons of theoretical calculations and experiments indicated that the stochastic fluctuations in loop sizes caused by the net absorption of single interstitial atoms are not adequate to explain the wide dispersion in the distribution function. To be consistent with experimental observations. additional fluctuations because of cascades must be included.

Time evolution of non-equilibrium systems, where the probability density is described by a continuum F-P equation, is a central area of interest in stochastic processes. In our work (Ref. [21]), numerical solution of a 2-D F-P equation describing the growth of HVCs in metals under irradiation is given. First, nucleation rates and regions of stability of HVCs in the appropriate phase space for fission and fusion devices were established. This was accomplished by solving a detailed set of cluster kinetic rate equations. A nodal line analysis was used to map spontaneous and stochastic nucleation regimes in the helium-vacancy (h-v) phase space. Growth trajectories of HVCs were then used to evaluate the average HVC size and helium content during the growth phase of HVCs in typical growth instability regions.

The growth phase of HVCs was modeled by a continuum 2-0. time-dependent F-P equation. Growth trajectories were used to define a finite solution space in the h-v phase space. A highly efficient *dynamic remeshing* scheme was developed to solve the F-P equation. As a demonstration, typical HFIR irradiation conditions were chosen. Good agreement between the computed size distributions and those measured experimentally were obtained.

In Ref. [22], the evolution of helium-filled cavities during neutron irradiation was analyzed in terms of the stochastic theory of atomic clustering. The conventional separation of nucleation and growth was replaced by a self-consistent evolution model. Starting from kinetic rate (master) equations for the clustering of helium and vacancies, helium mobility, HVC stability, and cavity nucleation and growth were all included in the model. Under typical fusion irradiation conditions (cascade damage and high helium-to-dpa ratios), the following is suggested: (1) Helium mobility decreases with the evolution of the microstructure. At quasi-steady state, it is mainly controlled by interstitial replacement of thermal desorption. (2) Gas re-solution from cavities by cascades increases nucleation at high fluences. (3) The cavity size distribution is broadened because of cascade-induced fluctuations. (4) The majority of helium-filled cavities are in a non-equilibrium thermodynamic state.

In Ref. [23], new concepts were reviewed which replace the conventional separation of microstructure evolution analysis into nucleation and growth. Classical nucleation theory is inadequate under fusion conditions (high helium-to-dpa ratios) and the usual "mean field" approximation of microstructural growth cannot account for cascade effects. A comprehensive theory of microstructure evolution under fusion conditions was formulated based on non-equilibrium statistical mechanics. Dynamic re-solution of helium gas in cavities was shown to cause continuous nucleation of helium-filled cavities. Microstructure evolution (*e.g.*, dislocation loops and cavities) was modeled by kinetic rate equations for small sire features and by F-P equations for sizes larger than few atomic dimensions. Semi-analytical and numerical methods were developed for the analysis of microstructure evolution and the results were compared to experiments. The problem of spatial self-organization of microstructures under irradiation was described in terms of newly developed Ginzburg-Landau-type equation and the results were also compared to experiments.

Materials Engineering, Mechanics, and Design

Research at UCLA on materials engineering, mechanics, and design has been motivated primarily by conceptual design studies. In this regard, the thrust of our work has been on extrapolation of materials data to the operating environment of a fusion reactor. Strong contributions from design studies have been made. The results of this area of research are therefore both fundamental and applied. A brief summary of research performed at UCLA in this area in given below.

In this paper. Rei. [24], we presented the results of our analysis of data provided by SANDVIK Steel Research Center for the high temperature properties of HI-9. We developed design equations for use in inelastic structural mechanics applications for the most important thermal creep parameters. Empirical correlations for creep rupture time and the complete description of elongation *versus* time were presented. A phenomenological description of steady-state creep was also developed. It was found that dislocation creep can explain the measured data.

The sensitivity of lifetime predictions for fusion-reactor blanket Structures was investigated in Ref. [25] by applying the Monte Carlo numerical technique. A structural computer code, stress analysis including radiation effects (STAIRE), developed for the analysis of mirror fusion blankets, was developed and used as a deterministic model for the prediction of the lifetime of semicircular coolant tubes. Uncertainties in material variables were treated as probabilistic inputs to the STAIRE code and output distributions were obtained.

Irradiation creep rates were shown to be sufficient for relaxation of swelling-induced stresses under most conditions. In the absence of high stresses, the creep limit seems lo be life-limiting, although this depends on the design-dependent swelling rate. In the case of the Mirror Advanced Reactor Study (MARS) blanket design, a lifetime of several hundred displacements per atom was shown to be highly probable.

The effects of radiation on the structural performance of fusion reactor structures is recognized as a major issue for the development of fusion reactor technology. Neutron irradiation changes the mechanical Properties of structural components resulting in a general degradation of these properties. In addition to the mechanical loads (pressure and weight) and the thermal strains, non-uniform inelastic strain fields are induced by radiation swelling and creep in fusion structures. In Ref. [26], we described a new computer code, STAIRE,

(stress analysis including radiation effects). This code is based on standard beam theory for pipe-bends. The theory was modified in two areas: (1) consideration of the pipes' cross-section deformation as the radius of curvature changes; and (2) inclusion of inelastic radiation and thermal strains (swelling and creep). An efficient analytical/numerical approach was developed for the solution of indeterminate beam problems. As an application of the method, the stress distribution and deflections of toroidal blanket pipes in MARS were evaluated. Swelling strains were identified as a major source of stress and deformation in the proposed blanket design, and possible Solutions to the problem were outlined.

Several methods for developing design correlations for ferritic steels were discussed in Ref. [27]. Equations describing swelling, embrittlement, and irradiation creep were reviewed. We developed design equations for use in elastic structural-mechanics applications for the most important thermal-creep parameters. Empirical correlations for creep rupture time and the complete description of elongation *versus* time were presented. A phenomenological description of steady-state creep was also developed.

Creep processes. due to irradiation and thermal fields, have generally been assumed to relax stresses resulting from the loading of structural components. However, in order to determine failure modes and mechanisms, a global inelastic structural analysis is required. We developed the STAIRE computer code to meet this need. This code is based on a modified beam theory for the self-consistent determination of stresses and deflections in beams of circular cross section. The work was applied to the lifetime analysis of the MARS blanket modules. The objective of the work in Ref. [28] was to assess the global (3-D) impact of both irradiation and thermal creep strains on the stress resulting from thermal and swelling strains.

A pin-type fusion reactor blanketed using γ-$LiAlO_2$ solid tritium breeder was designed [29]. Tritium transport and diffusive inventory were modeled utilizing the DIFFUSE code. Two approaches were used to obtain Characteristic $LiAlO_2$ grain temperatures. DIFFUSE provides intragranular diffusive inventories which scale up to blanket size and the results compared well with a numerical analysis, giving a steady-state blanket tritium inventory of 13 g.

Start-up transient inventories were modeled using DIFFUSE for both full and restricted coolant flow. Full flow gave rapid inventory buildup while restricted flow prevented this buildup. Inventories after shutdown were modeled and it was found that reduced cooling had little effect on removing tritium but preheating rapidly purged inventory.

DIFFUSE provided parametric modeling of solid breeder density, radiation, and surface effects. Massive inventory and marginal tritium release resulted from 100% dense pins. Only large trapping energies and concentrations increased inventory significantly. Diatomic surface recombination was only significant at high temperatures

Our theoretical model, presented in Ref. [30], described high-temperature helium embrittlement as a sequence of four steps. First. helium clustering in the matrix was described by the conventional rate theory. This was coupled to rate equations for the transport of single helium atoms to grain boundaries in the second phase. The third step was concerned with the influence of helium and stress on the nucleation of cavities at grain boundaries. with particular emphasis on the role that precipitates and triple-point junctions play in the nucleation process. Finally, various growth modes of grain boundary cavities which lead to fracture by inter-linkage of equally spaced grain-boundary cavities were investigated [30]. A description of this comprehensive model was given, with emphasis on the growth and inter-linkage of grain boundary cavities under the effects of irradiation and applied stress. A comparison between the model predictions and recent experimental creep rupture data was given. The model proposed a new explanation of the creep rupture behavior of martensitic steels as opposed to austenitic steels. Vacancy source limitation at grain boundaries resulting from dislocation interactions was identified as the primary reason for the retarded growth of grain-boundary cavities in martensitics.

Mechanical interaction between the solid breeder material and its cladding during power cycles is an important consideration in the design of solid breeder blankets. The analysis presented in Ref. [31] gives a design tool for material choices and lifetime prediction for breeder pins. The UCLA solid-breeder blanket design was evaluated and operating conditions were suggested. The material model for the pellet included linear thermoelastic behavior and swelling. The cladding was assumed to be thin and to exhibit swelling and creep. Two alternate breeder/cladding material pairs were analyzed (Li_2O/2.25 Cr-1Mo and $LiAlO_2$/9-C). While high swelling excludes the Li_2O/2.25Cr-1Mo design, it was found that in the $LiAlO_{22}$/9-C case, compatibility of thermal expansion between the breeder and the cladding (as well as low swelling of the breeder) resulted in less than 0.5% total plastic strain after one year of operation.

The bowing of circular-solid breeder pins was studied using standard beam theory in Ref. [32]. Deformations caused by thermal gradients. swelling gradients, and gravitational forces were included in the investigation and swelling was found to cause the most severe pin bowing. The bowing of beryllium multiplier rods was found to be insignificant when swelling is not considered. In all cases, it was found that adding internal supports can reduce the rod deflections to acceptable levels without increasing the stresses beyond design limits.

The formation of dislocation cells and subgrain structure is of great significance to understanding high-temperature deformation of many solids. Experimental observations on dislocation patterns, and cellular structures in particular, were reviewed in Ref. [33]. The basic features of such structures were discussed, and the conditions allowing dislocation patterning behavior were described. Theoretical formulations that attempt to model this phenomenon were reviewed, with emphasis on recent dynamical computer simulations [34].

Singular thermal stress fields in bonded viscoelastic quarter planes were studied with
the use of viscoelastic analogy [35]. The order of the singularity was shown to depend on the material properties, indicating that it will vary with time in viscoelastic materials. This was studied in detail for Maxwell materials, and it was shown that the order of singularity generally increased with time, This evolution of the singularity can, for certain combinations of material properfies. lead to initial increases in the stress levels near the edge of the interface before relaxation occurs.

Solutions for thermal stress singularities in finite bonded strips were sought in Ref. [36] by using an eigenfunction expansion in the neighborhood of singularity. The coefficients in the resulting series were determined by satisfying the boundary conditions on surfaces far removed from the singularity either pointwise or in an integrated sense. The latter of these techniques was found to be more reliable. The

accuracy of the solution was checked by comparing it to a semianalytical solution for thermal stresses in bonded quarter plane, which was derived by using the Millin transformation. It was shown that the eigenfunction approach provides accurate solutions for the leading term in the series, thus capturing the essence of the thermal stress fields near the edge of the interface. The far-field solutions. however, are found to feature excessive inaccuracies. which are attributed to numerical errors.

A relevant design data base is needed for structural components in near-term and commercial fusion devices. A high-flux, high-fluence fusion-neutron test facility is required for testing the failure mechanisms and lifetime-limiting features for first-wall, blanket, and high-heat-flux components. In Ref. [37], we described the key aspects of the fusion environment that influence the response of structural and high-heat-flux components. In addition to test capabilities for fundamental radiation-effects phenomena, *e.g.*, swelling, creep, embrittlement, and hardening, it was shown that the facility must provide an adequate range of conditions for accelerated tests in order to study the limitations on component lifetime due to the interaction between such fundamental phenomena. In high-heat-flux components, testing the failure mechanisms of duplex structures was shown to require maintenance of an appropriate temperature gradient in the 14-MeV neutron field. Thermal stresses were shown to cause component Failure, particularly when the degradation in the thermal conductivity and mechanical properties by irradiation were considered. Several factors were discussed for assessment of the failure modes of the first-wall and blanket structures: displacement-damage dose and dose rate, the amount of helium gas generated, the magnitude of irradiation and thermal creep, prototypical temperature and temperature-gradient distributions, module geometry, and external mechanical constraints.

A simple dislocation model for creep in engineering materials was constructed [38] in order to predict high temperature deformation under arbitrary time-dependent stress and temperature histories. The model also has the advantage of being compatible with the rate theory of radiation damage, which allows radiation effects to be included. The basis of the model was the generation and immobilization of dislocations at subgrain boundaries, the recovery of the static dislocations at the boundaries, the dynamics of nucleation and growth of subgrains, and the evolution of the dislocation density of the boundaries. The effects of solutes and hardening precipitates were included. Example calculations were given for the martensitic steel, HT-9.

A new methodology in computational micromechanics, dislocation dynamics (DD) was introduced in Ref. [39]. Dislocation dynamics was developed to examine the dynamic behavior of dislocation distributions in solid materials. Under conditions of externally applied stress, dislocations exhibit glide with a velocity proportional to the power of the applied stress and climb motion with a velocity that is a function of the applied stress and temperature. These motions result from long-range force fields comprising both externally applied stress and long-range interactions between individual dislocations. Short-range reactions were represented as discrete events. The DD methodology was to be differentiated from particle methods in Statistical mechanics (*e.g.*, molecular dynamics and the Monte Carlo method) in two respects. First, DD was developed to study the dynamical behavior of "defects" in the solid. Second. the small number of dislocations allows for a complete dynamical representation of the evolution of dislocations in the material medium without the requirement of statistical averaging. The purpose of the DD methodology was to bridge the gap between experimentally observed phenomena and theoretical descriptions of dislocation aggregates, Particularly the evolution of self-organized dislocation structures under temperature, stress, and irradiation conditions.

The dynamic organization of dislocations into spatially heterogeneous substructures was demonstrated by applying the principles of dislocation dynamics that were outlined in Ref. [39]. This work was continued in Ref. [40], where it was shown that the formation of persistent slip bands is a consequence of the competition between dipole formation and annihilation of dislocations of opposite Burgers vectors in the absence of temperature-enhanced climb recovery under cyclic stress conditions. Planar arrays, which were also uniaxial structures, were shown to arise from enhanced dislocation multiplication and the formation of stable dipole configurations along a slip Plane at lower temperatures where climb was unimportant. Biaxial dislocation systems experience additional degrees of freedom compared with uniaxial systems because of available motion along additional slip systems. It was demonstrated that for a system of orthogonal slip directions at high temperatures in which climb and glide motion were competitive, dislocation cellular structures formed as a result of immobile dipole and junction formation and by the internal elastic strain energy minimization caused by long-range self-shielding. It was shown that the internal elastic strain energy is reduced by the self-organization process. However, the short-range nonlinear processes (*i.e.*, dipole and junction formation) were shown not to allow absolute elastic energy minimization.

Thermal and swelling stress fields in bonded structures were sought in Ref. [41] by using a model consisting of two thin, rectangular strips perfectly bonded along one surface, Existing results for stresses in the bulk, based on beam theory. were presented and their limitations were discussed. Plane elasticity was used to derive general solutions for the stress fields near the edge of the structure, in many cases yielding logarithmic or algebraic singularities. Methods far coupling these general edge fields to the Stresses in the bulk were discussed, and the techniques were applied to the materials and loading conditions relevant to fusion Components. The impact of swelling and creep on both the order of the singularity and on its intensity was shown.

The sensitivity of lifetime predictions of fusion structures with limited materials data base was studied in Ref. [42]

In Ref. [43], we presented an engineering analysis for the design of the first wall/blanket system for the TITAN reverse-field-pivot conceptual fusion reactor. The geometry of the first wall was dictated by the surface heat flux, the coolant temperature, and the maximum allowable structure temperature. We found that a reasonable design could be found up to 4 MW/m^2 heat-flux wall load.

The thickness of the blanketed tubes was determined by the internal heat generation rate, a minimum coolant bulk temperature set by the requirement on thermal efficiency, as well as the temperature limit on the structure. The radius of the tubes was given by the required structure fraction.

The aspect ratio of the rectangular channel design was determined by the pressure Stress concentration at the corners. The wall thickness was limited by the heat generation rate and fluid bulk temperature. These two constraints defined the allowable range of designs. Further analysis addressed the effect of poloidally varying coolant temperature and the effect of the irradiation environment.

Naughton, Ghoniem, and Lin [44] developed a micromechanical model for the effects of irradiation on fatigue crack initiation. The model was able to explain the ductility-dominated low-cycle fatigue regime, as well as the strength-dominated high-cycle fatigue regime.

In Ref. [43], Ghoniem and Amodeo developed a method for computer simulation of the behavior of individual dislocations. The equations of motion of individual dislocations were simultaneously solved by using extensions of dynamical particle-simulation methods [i.e., molecular dynamics, Langevin dynamics, and the Monte Carlo methods]. The evolution of 1- and 2-D patterns was illustrated by computer simulation of dislocation dynamics. In 1-D patterns, criteria for accurate numerical simulation of dislocation pile-up evolution were established. The potential for using specialized numerical and computational techniques to reduce the demands on existing computers was discussed. The work was completed in Ref. [46], where a rapid algorithm for dislocation dynamics calculations was developed.

Research on Low-Activation Steels

In 1983. the idea of developing a low-activation Steel for fusion applications emerged at UCLA. We then contacted the Department of Energy requesting support for its development. However. funding limits and priorities did not allow dedicated support for this idea. Since our research on radiation effects and fusion malerials has mainly been funded by the grants outlined in this report, we were fortunate to be able to pool the available resources and develop the first known low-activation steel in the world, UCVS-I. A patent on this steel, and on several others which were developed in collaboration with Hanford Engineering Development Laboratory, was granted on November 11. 1986 (U.S. Patent No. 4622067). We summarize our efforts on ferritic alloys in fusion applications below.

Proposed fusion reactors may enjoy significant advantages regarding public safety and waste disposal over current fission reactors. Neutron activation of the structural materials can be minimized by the appropriate choice of alloys. Unfortunately, commercially developed alloys for high-temperature applications become activated with neutron absorption, leading to sometimes very long decay chains. The work reported in Ref. [47] discussed the results of a new "low activation" ferritic alloy, UCVS-1, developed at UCLA. This alloy, which contains vanadium instead of molybdenum for high-temperature strength, showed very promising combinations of strength, ductility. and low long-term radioactive products. It was shown in this paper [47] that the strength and ductility of UCVS-I are comparable to 2-1/4 Cb-1 Mo up to 400°C, achieving significant advantages with regard to safety and radioactive waste disposal.

The patent disclosure (Ref. [48]) relates to ferritic alloys, and specifically to development of low-activation bainitic and martensitic stainless steels. The United States Government has rights in this invention pursuant to Contract No. DEAC06-76FF02170 between the United States Department of Energy and Westinghouse Electric Corporation.

Ferritic alloys are required far structural usage in the development of commercial fusion systems, where the residual fuel and wastes will themselves have negligible residual radioactivity. For purposes of this disclosure, "low activation" shall be defined as a radiation level below 1 Ci/m^3 after waste disposal and burial for 100 years.

Low activation characteristics have not been vital in the development of structural materials for use with nuclear fission reactors, since the high levels of long-term radioactivity that persist in the spent fuel generated by a fission system far overshadow the amount of radioactivity in the surrounding structure. Most research and development with respect to long-term radioactive levels has been directed to the fuel components rather than to the machine structure.

The invention of this steel is a result of a study designed to develop bainitic and martensitic stainless Steels with low-activation characteristics for structural applications in fusion reactors. The objective was to identify low-activation ferritic alloys, and specifically low-activation bainitic and martensitic stainless steels, which had strength properties capable of being utilized in fusion reactor structural components.

To achieve the objectives, the ferritic alloy having a bainitic or martensitic microstructure consists primarily of chromium (2.0 to 13.0% by weight), vanadium, tungsten and/or tantalum (0.3 to 1.5% by weight), carbon (0.075 to 0.30% by weight), manganese (0.I to 15.0% by weight). and silicon (0.05 to 1.00% by weight). The remainder of the alloy is iron. The resulting alloy is characterized by low-activation properties and is devoid of subversive amounts of elements that materially interfere with this characteristic, In general. other elemental additions to the alloy should total less than 0.5% of its total weight. The alloy content of nitrogen, niobium, molybdenum, nickel, and copper should be maintained below maximum total weight percentages which have been developed theoretically from known characteristics of these elements when exposed to nuclear particle bombardment as follows: nitrogen, less than 0.33% by weight; niobium, less than 0.000029% by weight; molybdenum, less than 0.003% by weight; nickel, less than 0.9% by weight; and copper, less than 0.12% percent by weight. If any one of these elements is present at the prescribed limit, none of the others may be present.

Ferritic/martensitic alloys are being developed for structural applications in fusion reactors. Within the ferritic/martensitic class of alloys, compositional and heat treatment variations are performed to optimize alloy properties for specific applications. The environmental conditions in fusion reactors pose a new challenge for ferritic/martensitic alloy optimization. Examples of the unique features of fusion designs include high surface- heat loads, magneto-forces, liquid-metal coolants, neutron radiation effects, etc.

Reference [49] summarizes information relevant to the selection of alloy types to fusion applications. Four types of alloys were considered: HT-9, 2-1/4 Cb-1 Mo, Nb-stabilized 2-1/4 Cb-1 Mo. and the low-activation vanadium alloy UCVS-I. The important metallurgical variables and heat treatments influencing various structural phases (ferritic, bainitic. and martensitic) are discussed. Relevant mechanical property data is summarized to illustrate the definition of possible ranges of operating temperatures of these alloys for fusion applications. Since liquid metals, such as Li or LiPb, were considered to be candidate coolants and tritium breeders, we presented an assessment for liquid-metal compatibility with ferritic/martensitic steels. Radiological properties for both accident and radioactive waste disposal were then presented with emphasis on some of the unique possibilities with this class.

The Mirror Advanced Reactor Study (MARS)developed a high temperature blanket for thealternative applications of high efficiency electricity production or process heat for synthetic fuel production. The blanket had two radial zones. The choice of material for the metallic structure was a critical factor in the design. We selected HT-9 ferritic steel because of its excellent physical and mechanical properties; resistance to neutron-induced void swelling and helium embrittlement, and compatibility with lead-lithium. The MARS reactor

was designed for a 5-MW/m^2 wall loading and experienced a first a wall damage rate of 69 dpm/full power years. Thus, we required a combination of design flexibility and material properties that would allow reliable operation to over 200 dpa. Through the use of HT-9, we were able to design a high performance blanket for a tandem mirror reactor that appears capable of long life operation (see Ref. [50]).

Our research on ferritic/martensitic alloys is summarized in Ref. [51]. The relevant design data are presented in a manner which defines the operation design windows for this class of alloys.

Research Motivated by Grant Support

The experience that we gained in developing theories and models for microstructural evolution has been helpful in a closely related area of research; that is the study of surface atomic clustering. Although no direct support *was* obtained from the grants reported here, collaborative efforts with Dr. Charles Stone (supported by DOE Magnetic Fusion Energy Technology fellowship), and Dr. Martin Vicanek (supported by a NATO grant) resulted in the publication of four papers (Ref. 52-55). For these papers, we developed **rigorous** models of surface atomic clustering under conditions of bombardment by thermal or energetic particles. The work is important to a number of applications, among which is the re-deposition process of surface atoms in the environment of a plasma edge (as in divertors or limiters).

Participation by Graduate Students, Post-Doctoral Fellows snd Visiting Scientists

During the six year period covered by the grant (January 1984 through January 1990), one Masters and eight Ph.D. degrees were completed under the supervision of Professor N. M. Ghoniem. Two of the earned Ph.D. degrees were not supported by the grant, two others were partially supported, and one postdoctoral fellow was partially supported for approximately three years after earning his Ph.D. All Ph.D. and **M.S.** graduates. with the exception of **one,** are either U.S. citizens or permanent residents of the United States. Two of the former Ph.D. students hold academic positions; one is an associate professor and the second is an assistant professor. Other former students hold technical positions in national labs, universities, or **are** employed in the private Sector. **A** brief description of former graduate Students and of our distinguished visiting scholars is given below.

Ph.D. Degrees

1. Jamal Alhajji: "Theoretical Modeling of the High Temperature Helium Embrirtlement in Structural Alloys," lune 1985; Associate Professor of Mechanical Engineering, University of Kuwait.

2. Shahram Sharafat: "Theory of Helium Transport, Clustering and Cavity Evolution in Structural Materials Under Irradiation," March 1986; Development Engineer, University of California, Los Angeles.

3. Philip Shang-Chlh **Chou:** "A Monte Carlo Approach to Ion Transport in Solids and Its Applications in Bulk and Surface Damage Analysis," June 1986; Research Engineer, Taiwan.

4. James P. Blanchard "Analysis of Singular Stress Fields in Duplex Fusion Components." June 1988; Assistant Professor of Nuclear Engineering, University of Wisconsin; recipient of an NSF Presidential **Young** Investigator Award, 1990-1995.

5. Robert Amodeo: "Dynamic Simulation of Dislocation Pattern Formation in Metals During High Temperature Monotonic and Cyclic Deformation," June 1988; Research Engineer. Xerad, Inc., Santa Monica, CA.

6. Rodger Martin: "Simulation of Charge Generation and Transport in Semiconductors Under Energetic Particle Bombardment," March 1990; Research Scientist, Oak Ridge National Laboratory, Oak Ridge, TN.

7. George Orient: "Analysis of Steady-State Propagating Cracks in Creeping Metals," (co-advisor, Prof. Russ Westmann), April 1990; Research Engineer, Rockwell Science Center, Los Angeles.

8. Charles Stone: "Modeling Thin-Film Formation by Energetic Atom Deposition," March 1991; Research Scientist, General Atomics, La Jolla, CA.

M.S. Student

1. Timothy Naughton: "Micromechanics of Fatigue Crack Initiation Under Irradiation," (co- advisor, Professor T. H. Lin), 1986; Research Engineer, Edwards Air Force Base, Mojave Desert, California.

Visiting Scientists

1. Dr. Isabil Abril: Physics Department, University of Alicante, Spain, 1988; Atomic collisions in solids.

2. Dr. Christian Abromeit: Hahn-Meitner Institute, Berlin, Germany, 1989; Radiation stability of alloys.

3. Dr. Daniel Walgraef: University of Brussels, Belgium, 1987-1990; Spatial ordering of microstructures.

4. Dr. John Gittus: Director General, British Atomic Forum. United Kingdom, University of California Regents Lecturer, 1989; Dislocation creep.

List of Publications

Research publications supported by the grant have mainly been the result of M.S. or Ph.D. dissertation work for students supervised by N. M. Ghoniem, or the result of joint collaborations betweem N.M. Ghoniem, post-doctoral fellows, and visitors to UCLA. The work is published in firs,-rate refereed journais or proceedings of technical meetings. The publications are listed here under five coherent categories, as summarized in section 2.

Published Research of "Atomic Displacements"

1. P. S. Chou and N. M. Ghoniem, "An Approximate Analytical Calculation of Precipitate Dissolution Rate Using a Slowing Down-Diffusion Theory for Charged Particles," *Nucl. Instr. and Meth.,* B9:209-217, 1985.

2. P. S. Chou and N. M. Ghoniem. "Collisional Aspects of Preferential Sputtering Using the Monte Carlo Method," *J. Nucl. Mater.,* 141-143:216-220, 1986.

3. I. P. Blanchard, N. M. Ghoniem, and S. P. Chou, "An Approximate Solution to the Scattering Integral for General Interatomic Potentials," *J. Appl.* Phys., 61:3120-3123, 1987.

4. P. Chou and N. M. Ghoniem, "Applications of the Monte Carlo Code TRIPOS to Surface and Bulk Ion Transport Problems," *Nucl. Instr. Meth. Phyr. Res..* B28:175-184, 1987.

5. N. M. Ghoniem and S. P. Chou, "Binary Collision Monte Carlo Simulations of Cascades in Polyatomic Ceramics," *J. Nucl.* Maler., 155-157:1263-1267, 1988.

6. S. P. Chou and N. M. Ghoniem, "On Precipitate Dissolution Using the Cascade Slowing-Down Theory," *Nucl. Instr. Meth. Phys. Res.,* B42:145-148, 1989.

7. S. P. Chou and N. M. Ghoniem. "The Effects of Many-Body Interactions on Point-Defect Generation," *J. Nucl. Mater.,* 176, 1990.

8. S. P. Chou and N. M. Ghoniem, "Molecular Dynamics of Collision Cascades with Composite Pair/Many-Body Potentials," *Phys.* Rev., B43(4):2490, 1990.

9. S. P. Chou and N. M. Ghoniem, "Molecular Dynamics Simulations of Low-Energy Copper-Atom Interaction with Copper Surfaces," *J. Maler. Research,* accepted.

Published Research on "Microstructure Evolution"

10. E. P. Simonen, N. M. Ghoniem, and N. H. Packan, "Pulsed Flux Effects on Radiation Damage," *J. Nucl. Maler..* 122&123:391-401, 1984.

11. S. Sharafat and N. M. Ghoniem, "Stability of Helium-Vacancy Clusters During Irradiation," *J. Nucl. Mater.,* 122&123:531-536, 1984.

12. N. M. Ghoniem, "Helium Migration and Its Influence on Cavity Formation in Irradiated Materials," Res *Mechanics,* 10287-294, 1984.

13. R. Bullough and N. M. Ghoniem, "The Effect of Void Surface Motion on the Void Sink Strength for Point Defects," J. *Nucl.* Maler., 12747-55. 1985.

14. N. M. Ghoniem, J. N. Alhajji, and D. Kalleta, "The Effect of Helium Clustering on Its Transport to Grain Boundaries," *J. Nucl. Mater.,* 136:192-206, 1985.

15. P. Chou and N. M. Ghoniem, "On the Stochastic Theory of Point Defect Diffusion During Irradiation: Cascade Size and Shape Effects," *J. Nucl. Mater.,* 137:63-72, 1985.

16. I. N. AI-Hajji and N. M. Ghoniem. "Nucleation of Grain Boundary Cavities Under the Combined Influence of Helium and Applied Stress." *Acta Metall.,* 35:1067-1075, 1987.

17. N. M. Ghoniem, "Determination of the Bias Factor by the Moments Solution to the Fokker-Planck Equation," *J. Nucl. Maler.,* 155-157:1123-1127, 1988.

18. N. M. Ghoniem and R. Amodeo. "Computer Simulation of Dislocation Pattern Formation," *Solid State* Phenomena, 3&4:377-388, 1988.

19. D. Walgraef and N. M. Ghoniem, "Spatial Instabilities and Dislocation Loop Ordering in Irradiated Materials," *Phys. Rev.,* B39:8867-8872. 1989.

20. N. M. Ghoniem, "Stochastic Theory of Diffusional Planar Atomic Clustering and Its Application to Dislocation Loops." Phys. *Rev..* B39:11810-11819, 1989.

21. S. Sharafat and N. M. Ghoniem, "Nan-Equilibrium Agglomeration of Helium-Vacancy Clusters in Irradiated Materials," *Radial. EJJ. snd Def. Solids,* 113:331-358, 1990.

22. N. M. Ghoniem, "Nucleation and Growth Theory of Cavity Evolution Under Conditions of Cascade Damage and High Helium Generation." *J. Nucl. Mater.,* 174168-177, 1990.

23. N. M. Ghoniem, "Theory of Microstructure Evolution Under Fusion Neutron Irradiation," J. *Nucl. Mater.,* 179. 1990.

Published Research on "Materials Engineering, Mechanics and Design"

24. R. J. Amodeo and N. M. Ghoniem, "Constitutive Design Equations for Thermal Creep Deformation of HT-9," *J. Nucl. Mater.*, 122&123:91-95, 1984.

25. J. P. Blanchard and N. M. Ghoniem, "The Influence of Irradiation and Thermal Creep on Stress Redistribution in Fusion Blankets," *J. Nucl. Mater.*, 122&123:101-105, 1984.

26. J. P. Blanchard and N. M. Ghoniem, "Inelastic Structural Analysis of the MARS Tandem Mirror Fusion Reactor," *Nucl. Eng. Des./Fusion*, 2:19-27, 1985.

27. R. S. Amodeo and N. M. Ghoniem, "Development of Design Equations for Ferritic Alloys in Fusion Reactors," *Nucl. Eng. Des./Fusion*, 2:97-110, 1985.

28. J. P. Blanchard and N. M. Ghoniem, "The Influence of Uncertainties in Material Properties, and the Effects of Dimensional Scaling on the Prediction of Fusion Structure Lifetimes," *Nucl. Eng. Des./Fusion*, 4:67-74, 1986.

29. R. Martin and N. M. Ghoniem, "Modeling of Tritium Transport in a Fusion Reactor Pin-Type Solid Breeder Blanket Using the DIFFUSE Code," *J. Nucl. Maler.*, 141-143:244-248, 1986.

30. J. N. AI-Hajji and N. M. Ghoniem, "Comprehensive Modeling of Creep Fracture by Grain Boundary Cavitation in Irradiated Structural Alloys," *J. Nucl. Maler.*, 141-143536-539, 1986.

31. G. E. Orient and N. M. Ghoniem, "A Model for the Mechanical Interaction Between Solid Breeder and Cladding Materials," Fusion *Technol.*, 101617-1622, 1986.

32. J. P. Blanchard and N. M. Ghoniem. "The Bowing of Solid Breeder Rods in a Pin-Type Fusion Reactor," *Fusion Technol.*. 101623-1627, 1986.

33. R. J. Amodeo and N. M. Ghoniem, "A Review of Experimental Observations and Theoretical Models of Dislocation Cells and Subgrains," *Res Mechanica*, 23:137-160, 1988.

34. R. J. Amodeo and N. M. Ghoniem, "Dynamical Computer Simulation of the Evolution of a One-Dimensional Dislocation Pileup," *Int. J. Engng. Sci.*, 26:653-662, 1988.

35. J. P. Blanchard and N. M. Ghoniem, "Relaxation of Thermal Stress Singularities in Bonded Viscoelastic Quarter Planes, *J. Appl. Mechanics*, 56:756-762, 1989.

36. J. P. Blanchard and N. M. Ghoniem, "An Eigenfunction Approach to Singular Thermal Stresses in Bonded Strips." *J. Thermal Slresses.* 12:501-527, 1989.

37. N. M. Ghoniem and J. B. Whitley, "Fusion Neutron Test Facility Requirements for Interactive Effects in Structural and High-Heat-Flux Components," *J. Fusion Energy*, 8:157-167, 1989.

38. N. M. Ghoniem, J. R. Matthews, and R. J. Amodeo, "A Dislocation Model for Creep in Engineering Materials," *Res Mechanica*, 29:197-219, 1990.

39. R. J. Amodeo and N. M. Ghoniem, "Dislocation Dynamics: Part I—A Proposed Methodology for Deformation Micromechanics," *Phys. Rev.*, B41:6958-6967, 1990.

40. R. J. Amodeo and N. M. Ghoniem, "Dislocation Dynamics: Part II—Applications to the Formation of Persistent Slip Bands, Planar Arrays, and Dislocation Cells," *Phys. Rev.*, B41:6968-6976, 1990.

41. J. P. Blanchard and N. M. Ghoniem. "Analysis of Singular Stress Fields in Duplex Fusion Components," *J.* Nucl. *Mater.*, 175:54-70, 1990.

42. J. P. Blanchard and N. M. Ghoniem, "Senstivity Analysis for Lifetime Prediction of Fusion Structures," *Trans., 8th Int. Conf. on Structural Mechanics in Reacror Technology (SMiRT-8)* (Brussels, Belgium, August 1985) N4/5:85-89.

43. G. Orient, J. P. Blanchard, and N. M. Ghoniem, "Thermostructural Design of the First Wall/Blanket for the TITAN-RFP Fusion Reactor," *Structural Mechanics in Reactor Technology. [Trans. 9th Int. Conf. (SMiRT-9)* Lausanne. 1987] F. H. Wittmann, Ed. (A. A. Balkema, Rotterdam, 1987) p. 169.

44. T. D. Naughton, N. M. Ghoniem, and T. H. Lin, "Radiation Effects on the Micromechanical Aspects of Fatigue-Crack Initiation," *Effects of Radiation on Materials*, 13th Int. Symp., pt. II, ASTM-STP-956 (American Society for Testing Materials, 1987) pp. 223-238.

45. N. M. Ghoniem and R. J. Amodeo, "Computer Simulation of Dislocation Pattern Formation," *Proc.,* Int. Conf. on Nonlinear Phenomena in Materials Science (Aussois, France. Sept. 1987) pp. 1-12.

46. R. J. Amodeo and N. M. Ghoniem, "Rapid Algorithms for Dislocation Dynamics in Micromechanical calculations." *Proc.,* TMS Fall Meeting, (New Orleans, LA, Nov. 1991).

Published Research on "Low-Activation Steels"

47. N. M. Ghoniem, A. Shabaik, and M. Z. Youssef, "Development of a Low Activation Vanadium Steel for Fusion Applications," Proc., Topical Conf. on Ferritic Alloys for Use in Nuclear Energy Technology (Snowbird, Utah, June 1983).

48. D. S. Gelles, N. M. Ghoniem, and R. W. Powell, "Low-Activation Steels for Fusion Reactor Applications," *US. Patent No. 4,622,067*, November 11, 1986.

49. N. M. Ghoniem, J. Blink, and N. Hoffman, "Selection of Alloy Steel Type for Fusion Power Plant Applications in the 350-500°C Range," Proc., Topical Conf. on Ferritic Alloys for Use in Nuclear Energy Technology (Snowbird. Utah, lune 1983).

50. J. D. Gordon, J. K. Garner, N. M. Ghoniem, and J. F. Parmer, "Ferritic Steel Applications in the MARS High Temperature Blanket," *Proc.,* Topical Conf. on Ferritic Alloys for Use in Nuclear Energy Technology (Snowbird, Utah. lune 1983).

51. N. M. Ghoniem. "Development of Radiation-Resistant, Low-Activation Ferritic Alloys for Fusion Applications," *J. Fusion Energy,* accepted.

Published Research Motivated bv Grant Suooort

52. C. A. Stone and N. M. Ghoniem, "Modeling the Early Stages of Thin Film Formation by Energetic Atom Deposition," *Metall. Trans.,* 20A:2609-2617, 1989.

53. C. A. Stone and N. M. Ghoniem. "The Effects of Cluster Sire-Dependent Aggregation on Thin Film Formation," Vacuum. 41:1111-1113, 1990.

54. M. Vicanek and N. M. Ghoniem. "The Effects of Mobility Coalescence On the Evolution of Surface Atomic Clusters," *Thin Solid Films*, accepted.

55. M. Vicanek and N. M. Ghoniem. "Two Group approach to the Kinetics of Particle Cluster Aggregation. *J.* Comp. *Phys.,* accepted.

6.0 DEVELOPMENT OF STRUCTURAL ALLOYS

6.1 Ferritic Stainless Steels

EFFECT OF IRRADIATION IN HFIR ON TENSILE PROPERTIES OF Cr-Mo STEELS -- R. L. Klueh and P. J. Maziasz (Oak Ridge National Laboratory)

OBJECTIVE

The goal is the evaluation of the tensile behavior of irradiated ferritic steels and to relate changes to irradiation damage and transmutation helium.

SUMMARY

Tensile specimens of tempered martensitic 9Cr-1MoVNb and 12Cr-1MoVW steels with and without additions of 2% Ni were irradiated in the High Flux Isotope Reactor (HFIR) at 400 and 600°C to displacement damage levels of up to 72 dpa. Nickel was added to the steels to produce transmutation helium, and up to 700 appm He was produced in the steels with 2% Ni. Irradiation at 400°C caused an increase in strength and decrease in ductility, while irradiation at 600°C caused a decrease in strength and an increase in ductility. Results at 400°C were similar to data from previous tests on steel irradiated to ≈11 dpa (up to 110 appm He), where it was concluded that helium caused a strength increase in addition to the hardening caused by displacement damage alone. The present results indicate that the helium-enhanced strengthening at 400°C saturates with increasing helium concentration, similar to the saturation (at a lower strength level) with displacement-damage dose found in the absence of helium.

PROGRESS AND STATUS

Introduction

An important requirement for a structural material for fusion reactor applications is resistance to irradiation damage by high-energy neutrons. Ferritic steels are highly resistant to void swelling during irradiation in fast reactors and, for that reason are candidate materials for fusion applications. However, in addition to displacement damage caused by the high-energy neutrons (14.1 MeV) produced during the deuterium-tritium fusion reaction, large amounts of transmutation helium will also be generated. Because no adequate source of deuterium-tritium fusion neutrons exists, it is necessary to simulate the effects of such irradiation.

For alloys that contain nickel, it is possible to generate helium and displacement-damage effects simultaneously in a mixed-spectrum fission reactor, such as the High Flux Isotope Reactor (HFIR). Fast neutrons of the mixed spectrum cause displacement damage, and helium is produced by thermal neutrons in the following two-step reaction: $^{58}Ni(n,\gamma)^{59}Ni$ followed by $^{59}Ni(n,\alpha)^{56}Fe$. About 68% of natural nickel is ^{58}Ni.

This technique has been used extensively to study helium effects in austenitic stainless steels, which contain high concentrations of nickel. Because the 9Cr-1MoVNb steel (nominally 9%Cr-1%Mo-0.25%V-0.07%Nb-0.1%C. compositions in wt %) and 12Cr-1MoVW steel (nominally 12%Cr-1%Mo-0.25%V-0.5%W-0.2%C) being considered for fusion structural applications normally contain only about 0.1 to 0.2 and 0.5% Ni. respectively, irradiation in HFIR produces much less helium than a fusion reactor would. However, if the nickel content is increased to about 2%, these martensitic steels then have approximately the same ratio of helium to displacement damage during irradiation in HFIR that the original, unmodified alloys will attain in a tokamak-type fusion reactor first wall.

Nickel-doped steels were used to investigate the effect of helium on the tensile properties of 9Cr-1MoVNb and 12Cr-1MoVW steels.' Tensile specimens of these steels and the steels with 1 and 2% Ni (9Cr-1MoVNb-2Ni, 12Cr-1MoVW-1Ni, and 12Cr-1MoVW-2Ni) were irradiated to ≈11 dpa in HFIR at 300, 400, and 500°C. The results indicated that helium affected the tensile behavior. A helium effect was also indicated by comparing the changes in mechanical properties observed after irradiation in HFIR at 400°C with those obtained after irradiation to ≈16 dpa in EBR-II (Experimental Breeder Reactor) at 390°C (< 1 appm He formed during irradiation in EBR-II).'

Tensile specimens of 9Cr-1MoVNb, 9Cr-1MoVNb-2Ni, 12Cr-1MoVW, and 12Cr-1MoVW-2Ni steels have now been irradiated up to ≈72 dpa in HFIR. This paper will present and discuss the results of those irradiations.

Experimental procedure

Electroslag remelted heats of 9Cr-1MoVNb (0.1% Ni) and 12Cr-1MoVW (0.5% Ni) steels and these steels with 2% Ni, designated 9Cr-1MoVNb-2Ni and 12Cr-1MoVW-2Ni, were irradiated in HFIR. Chemical compositions of the alloys are given in Table 1. These are the same heats of steel used in the previous experiment.'

Table 1. Composition of 9Cr-1MoVNb and 12Cr-1MoVW heats of steel

Element	Concentration (wt %); balance iron			
	9Cr-1MoVNb		12Cr-1MoVW	
	0% Ni	2% Ni	0% Ni	2% Ni
C	0.09	0.064	0.21	0.20
Mn	0.36	0.36	0.50	0.49
P	0.008	0.008	0.011	0.011
S	0.004	0.004	0.004	0.004
Si	0.08	0.08	0.18	0.14
Ni	0.11	2.17	0.43	2.27
Cr	8.62	8.57	11.55	11.71
Mo	0.98	0.58	0.93	1.02
V	0.209	0.222	0.27	0.31
Nb	0.063	0.066	0.018	0.015
Ti	0.002	0.002	0.003	0.003
Co	0.013	0.015	0.017	0.021
C"	0.03	0.04	0.05	0.05
Al	0.013	0.015	0.030	0.028
B	t0.001	t0.001	<0.001	<0.001
W	0.01	0.01	0.54	0.54
As	<0.001	t0.001	<0.001	<0.002
Sn	0.003	0.003	0.002	a.002
Zr	t0.001	<0.001	t0.001	<0.001
N	0.050	0.053	0.020	0.017
O	0.007	0.006	0.005	0.007

Miniature cylindrical tensile specimens with a reduced section of 2-mm-diam by 18.3-mm long were machined from 6.35-mm-diam rods. The rods were normalized-and-tempered prior to machining the Specimens. The normalizing treatment for the 9Cr steels was 0.5 h at 1040°C and for the 12Cr steels 0.5 h at 1050°C, after which they were cooled in flowing helium. The 9Cr-1MoVNb was tempered 1 h at 760°C: the 12Cr-1MoVW was tempered 2.5 h at 780°C. The 9Cr-1MoVNb-2Ni and 12Cr-1MoVW-2Ni steels were tempered 5 h at 700°C. Tempered martensite microstructures were obtained by these heat treatments. Details on heat treatment and on microstructural characterization in the unirradiated condition have been published.[2]

For each experiment, eleven specimens were arranged along the capsule axis with each specimen surrounded by an aluminum holder. Each holder was sized to maintain a gas gap around the specimen gage section. The specified temperature was achieved by adjusting the thickness of the gas gap between the specimen and holder in order to provide resistance to the radial flow of heat produced in the specimen by nuclear heating. The specimen holders were contained in a 0.62-m-long aluminum tube that was surrounded by a shroud to provide a high reactor coolant velocity.

The capsules were irradiated in a HFIR peripheral-target position with a different peak thermal-neutron fluence and fast fluence (> 0.1 MeV) for each experiment. Fluence values were determined from five to eight dosimetry packets placed at various heights within the irradiation capsule. Atom displacement rates (dpa) and helium concentrations (at. ppm) were calculated from the dosimetry analysis. Since the flux in HFIR is a maximum at the centerline of the reactor and decreases rapidly with distance from that position, only specimens at the center position along the length of the capsule received the peak fluence (a capsule containing TEM disks was in the position directly in the center of each capsule). Therefore, displacement damage of each specimen varied, depending on its height in the capsule relative to the reactor midplane. Helium concentration of the specimens also depended on the specimen position in the capsule and on the nickel concentration of the alloy. Irradiation temperatures were calculated to be approximately 400 and 600°C.

Tensile specimens were irradiated in capsules in four irradiation experiments: HFIR-CTR-49, HFIR-CTR-50, HFIR-CTR-55, and HFIR-CTR-56 (they will be referred to as CTR-49, etc.). CTR-49 and -50 were to be irradiated to fluences of about 50 and 100 dpa. respectively, and CTR-55 and -56 were to be duplicates of CTR-49 and -50, respectively. Capsule CTR-49 and -55 reached their goal fluence. However, the other *two* experiments were still in progress when HFIR was shut down due to questions concerning the structural integrity of the reactor pressure vessel. When it was decided to operate HFIR at 85% of maximum power when restarted, CTR-50 and -56 were discontinued, because the fixed heat-transfer geometry would produce lower irradiation temperatures at the reduced power level.

Tensile tests were conducted in a vacuum on a 44-kN capacity Instron universal testing machine using a nominal strain rate of 4.6×10^{-4}/s. In addition to testing materials in the irradiated condition, normalized-and-tempered specimens and normalized-and-tempered specimens that had been thermally aged for up to ≈27,000 h at 400 and 600°C were also tested. Tests on the irradiated or aged specimens were at the irradiation or aging temperatures, respectively.

Results

Tensile properties for normalized-and-tempered, thermally aged, and irradiated specimens are given in Table 2 for 9Cr-1MoVNb and 9Cr-1MoVNb-2Ni steels and Table 3 for 12Cr-1MoVW and 12Cr-1MoVW-2Ni steels. These tables indicate that displacement damage and helium concentration varied from 37 to 72 dpa and 30 to 719 appm He, respectively. The 9Cr-1MoVNb contained the least helium (30 appm He), and the steels with 2% Ni contained the most (up to 719 appm).

Table 2. Tensile properties of normalized-and-tempered, thermally aged, and irradiated 9Cr-1MoVNb and 9Cr-1MoVNb-2Ni steels

Experimental Conditions[a]	Irradiation dpa	Irradiation appm He	Test Temperature (°C)	Strength (MPa) Yield	Strength (MPa) Tensile	Elongation (%) Uniform	Elongation (%) Total
			9Cr-1MoVNb				
N&T			400	754	848	2.4	8.1
Aged 400°C							
2 500 h			400	735	828	2.5	8.1
5 000 h			400	729	821	2.4	8.0
14 000 h			400	718	820	2.4	7.8
27 000 h			400	729	828	2.5	7.9
Irrd., 400°C	43	36	400	881	916	0.9	5.8
	60	49	400	865	898	0.7	5.6
	37	30	400	998	1018	0.3	4.7
	38	32	400	1004	1027	0.4	4.9
N&T			600	707	785	1.6	8.9
Aged 600°C							
2 500 h			600	633	690	1.4	7.4
5 000 h			600	622	680	1.3	7.4
14 000 h			600	535	574	1.3	8.1
27 000 h			600	542	593	1.4	7.8
Irrd., 600°C	43	36	600	385	405	0.8	10.7
	60	49	600	399	425	1.3	10.8
	37	30	600	181	192	0.6	12.7
	38	32	600	371	389	0.8	15.3
			9Cr-1MoVNb-2Ni				
N&T			400	683	804	2.1	1.8
Aged 400°C							
2 500 h			400	704	784	3.3	8.9
5 000 h			400	744	818	3.5	9.1
14 000 h			400	690	765	2.9	8.2
27 000 h			400	680	756	3.0	8.4
Irrd., 400°C	37	381	400	1118	1193	0.8	1.7
	52	522	400	1162	1184	0.4	3.9
	45	445	400	940	957	0.4	1.9
	46	477	400	938	968	0.6	4.1
N&T			600	647	744	1.5	6.9
Aged 600°C							
2 500 h			600	517	573	1.6	9.1
5 000 h			600	512	587	1.6	8.5
14 000 h			600	485	532	1.6	9.1
27 000 h			600	474	525	1.7	8.8
Irrd., 600°C	37	381	600	461	536	1.7	9.8
	52	522	600	428	450	1.1	8.8
	45	445	600	360	380	0.9	10.6
	46	477	600	381	400	n.8	8.8

[a]N&T = normalized and tempered; Irrd. = irradiated.

Table 3. Tensile properties of normalized-and-tempered, thermally aged, and irradiated 12Cr-1MoVW and 12Cr-1MoVW-2Ni steels

Experimental Conditions[a]	Irradiation dpa	Irradiation appm He	Test Temperature (°C)	Strength (MPa) Yield	Strength (MPa) Tensile	Elongation (%) Uniform	Elongation (%) Total
			12Cr-1MoVW				
N&T			400	786	964	2.4	5.6
Aged 400°C							
2 500 h			400	760	908	7.1	7.9
5 000 h			400	771	901	6.9	7.6
14 000 h			400	753	894	6.8	7.5
27 000 h			400	779	912	6.8	7.5
Irrd., 400°C	52	121	400	1101	1166	1.0	2.3
	72	161	400	1083	1110	0.6	2.3
	49	112	400	1030	1075	0.9	3.4
	51	120	400	1064	1099	0.8	3.1
N&T			600	738	917	2.4	5.6
Aged 600°C							
2 500 h			600	528	592	1.9	11.0
5 000 h			600	501	570	1.1	11.1
14 000 h			600	514	583	2.1	11.0
27 000 h			600	500	587	2.4	10.0
Irrd., 600°C	52	121	600	438	474	1.3	6.4
	72	161	600	473	522	1.6	6.8
	49	112	600	350	400	1.6	5.6
	51	120	600	385	415	1.3	6.8
			12Cr-1MoVW-2Ni				
N&T			400	755	883	3.1	8.1
Aged 400°C							
2 500 h			400	714	861	3.8	8.4
5 000 h			400	704	854	3.4	7.9
14 000 h			400	696	852	3.1	7.2
27 000 h			400	703	855	3.1	7.4
Irrd., 400°C	49	532	400	1104	1153	1.1	3.6
	70	719	400	1013	1052	0.7	2.9
	53	552	400	1056	1105	1.0	3.2
	55	589	400	1043	1089	0.6	2.2
N&T			600	626	743	2.3	7.4
Aged 600°C							
2 500 h			600	603	690	1.6	9.1
5 000 h			600	566	641	1.5	9.6
14 000 h			600	568	643	1.6	8.5
27 000 h			600	549	630	2.0	9.0
Irrd., 600°C	49	532	600	494	608	2.9	8.2
	70	719	600	495	580	2.3	11.2
	53	552	600	409	451	1.3	14.8
	55	589	600	422	471	1.6	10.7

[a]N&T = normalized and tempered; Irrd. = irradiated.

Figure 1 shows yield stress behavior for the four irradiated specimens for each heat of steel. Although there was a variation of displacement damage and helium concentration for the four specimens of a given steel irradiated in the four capsules, there was little variation in strength for a given steel at either 400 [Fig. 1(a)] or 600°C [Fig. 1(b)]. Specimens irradiated in CTR-50 received the highest fluence. but Fig. 1 gives no indication that the strength of these specimens was any different from the strength of specimens irradiated to lower fluences at either 400 or 600°C.

Examination of the yield stress data indicates that on average there was little difference between 9Cr-1MoVNb and 9Cr-1MoVNb-2Ni and between 12Cr-1MoVW and 12Cr-1MoVW-2Ni steels at 400 or 600°C. There was also little difference between the 9Cr and 12Cr steels. A comparison of the ultimate tensile strengths for the four steels shows that irradiation had a relative effect similar to that observed for yield stress (Tables 2 and 3).

Total elongations for the irradiated steels are shown in Fig. 2. As was true for strength, there was little difference in elongation for specimens of a given steel irradiated in the different capsules to different fluences. At 400°C [Fig. 2(a)], the 9Cr-1MoVNb and 9Cr-1MoVNb-2Ni steels have fairly similar values, as do the 12Cr-1MoVW and 12Cr-1MoVW-2Ni steels.

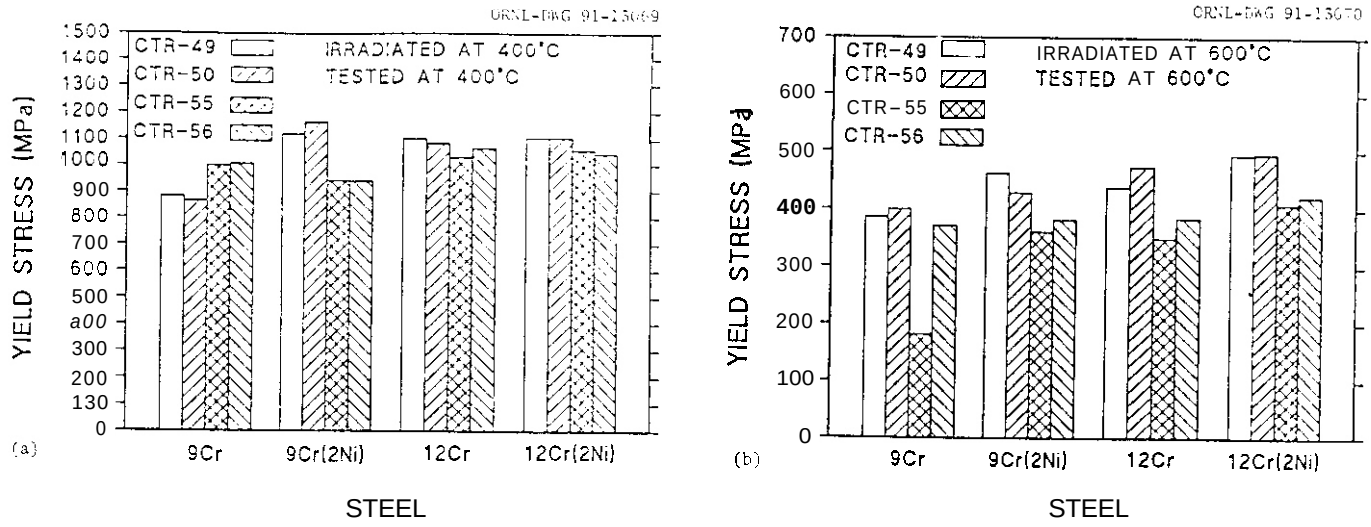

Fig. 1. Yield stress of 9Cr-1MoVNb. 9Cr-1MoVNb-2Ni, 12Cr-1MoVW, and 12Cr-1MoVW-2Ni steels irradiated in four capsules (CTR-49. -50, -55, and -56) to 37-72 dpa at (a) 400°C and (b) 600°C.

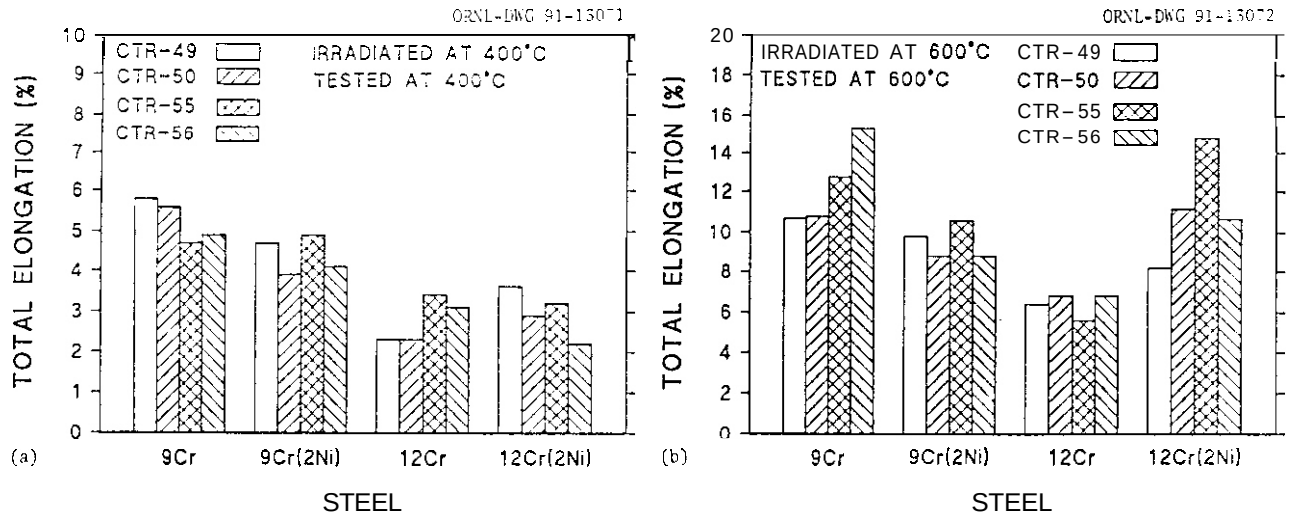

Fig. 2. Total elongation of 9Cr-1MoVNb, 9Cr-1MoVNb-2Ni, 12Cr-1MoVW, and 12Cr-1MoVW-2Ni steels irradiated in four capsules (CTR-49, -50, -55, and -56) to 37 to 72 dpa at (a) 400°C and (b) 600°C.

A somewhat greater difference was observed at 600°C [Fig. 2(b)], where the average elongation of the 9Cr-1MoVNb was slightly greater than that of 9Cr-1MoVNb-2Ni, and the elongation of the 12Cr-1MoVW-2Ni was slightly greater than that of 12Cr-1MoVW. Relative changes for uniform elongation were similar to those observed for total elongation (Tables 2 and 3).

Figures 3 and 4 show the effect of thermal aging on yield stress after aging for up to 27,000 h at 400 and 600°C. None of the steels showed a significant change after aging at 400°C (Fig. 3). while at 600°C (Fig. 4), the strength decreased initially and then remained relatively constant with increased aging time. Although not shown. thermal aging had a similar effect on ultimate tensile strength. Thermal aging at 400°C had little effect on uniform and total elongation. Aging at 600°C caused a slight increase in total elongation. but uniform elongation remained relatively unchanged (Tables 2 and 3).

Yield stress values for irradiated specimens are also shown in Figs. 3 and 4. For all steels, irradiation caused hardening relative to the unaged and aged specimens at 400°C and caused softening at 600°C.

The center of each irradiation capsule contained a packet of transmission electron microscopy (TEM) specimens at 400°C. Because they were at the reactor midplane, they received the highest fluence available in the reactor experiment. Specimens from CTR-50, the capsule irradiated to the highest fluence, were thinned and examined after irradiation to 75 dpa and up to 760 appm He. Photomicrographs are shown of 9Cr-1MoVNb (73 dpa, 60 appm He) and 9Cr-1MoVNb-2Ni

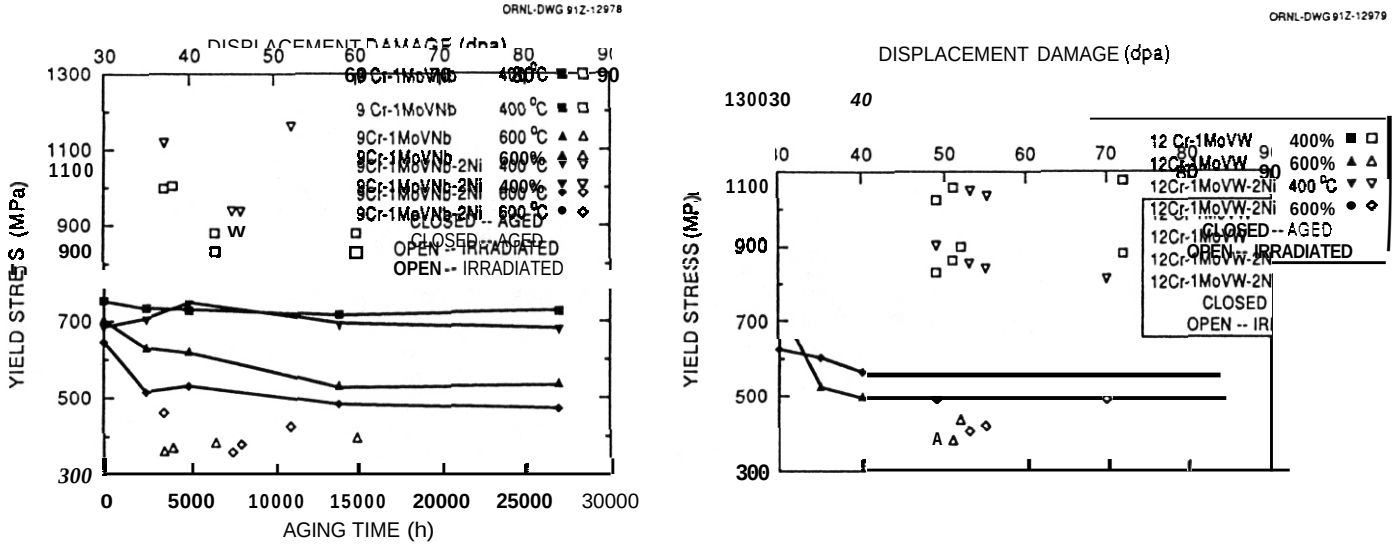

Fig. 3. Yield stress vs. aging time and yield stress vs. displacement damage for 9Cr-1MoVNb and 9Cr-1MoVNb-2Ni steels thermally aged and irradiated at 400 and 600°C.

(75 dpa. 725 appm He) in Fig. 5 and of 12Cr-1MoVW (73 dpa, 165 appm He) and 12Cr-1MoVW-2Ni (74 dpa, 760 appm He) in Fig. 6. Only a preliminary discussion of the results as related to the tensile behavior will be presented here. A more detailed characterization of the microstructures will be presented elsewhere.

All of the steels irradiated at 400°C contained a significantly higher radiation-induced dislocation density than found after tempering; they also contained complicated precipitate structures that showed effects of irradiation as well. For both the 9Cr and 12Cr steels, the grain and subgrain boundary features of the microstructure for a given type of steel (9Cr or 12Cr) were similar with and without a nickel addition. The 9Cr-1MoVNb and 9Cr-1MoVNb-2Ni steels basically had equiaxed prior-austenite grain boundary structures decorated by $M_{23}C_6$ precipitates (Fig. 5). After irradiation. however, there was little evidence of the intragranular lath subgrain structure that is characteristic of normalized-and-tempered steel and which remains virtually unchanged when the steel is thermally aged at 400°C (ref. **3)**. By contrast, the irradiated 12Cr-1MoVW and 12Cr-1MoVW-2Ni steels retained most of their characteristic as-tempered martensitic lath structure after similar irradiation

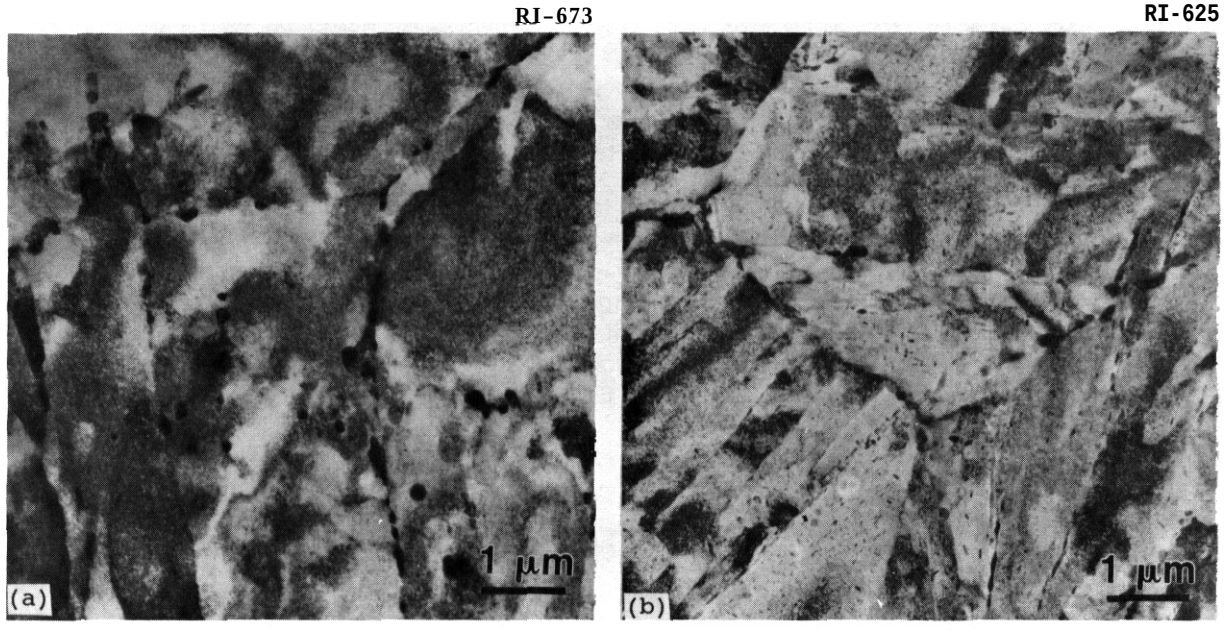

Fig. 5. Microstructure of irradiated (a) 9Cr-1MoVNb (73 dpa, 60 appm He) and (b) 9Cr-1MoVNb-2Ni (75 dpa, 725 appm).

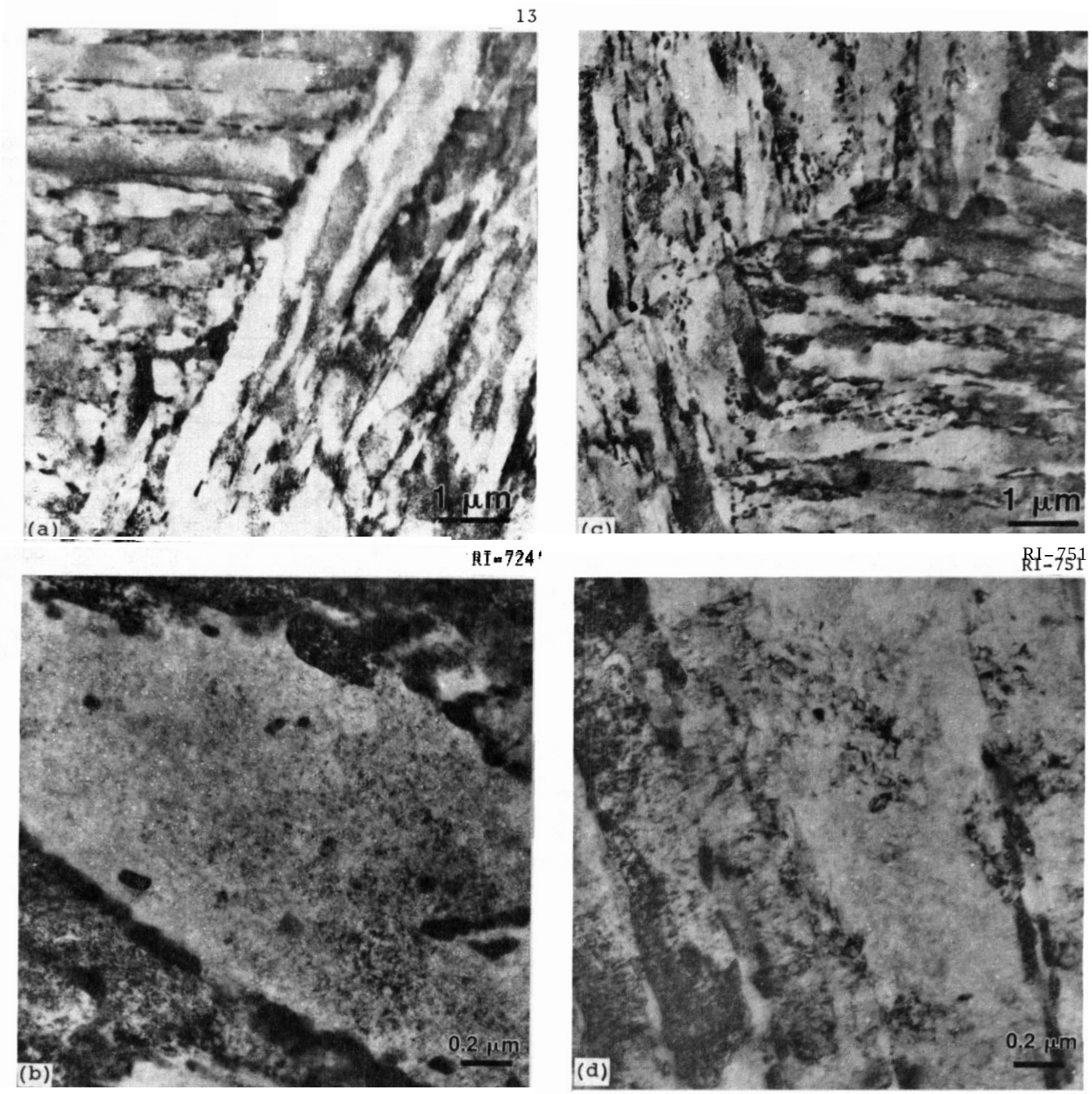

Fig. 6. Microstructure of irradiated (a) and (b) 12Cr-1MoVW (73 dpa, 165 appm He) and (c) and (d) 12Cr-1MoVW-2Ni (74 dpa, 760 appm He). Photomicrographs in (b) and (d) are at higher magnification and show cavities.

at 400°C (Fig. 6). In the 12Cr steels, both the prior-austenite grain boundaries and lath sub-boundaries were heavily outlined by $M_{23}C_6$ (or a mixture of $M_{23}C_6$ and M_6C precipitates).' The 12Cr steels also had high concentrations of radiation-produced dislocations within the laths and subgrains, similar to those seen in the 9Cr steels. All of the steels contained cavities, which were mixtures of larger bias-driven voids and very small subcritical bubbles. The density of cavities was much higher in the steels with 2% Ni. Some small cavities are visible in Fig. 6 for the 12 Cr steels. Microstructure will be analyzed in more detail, including swelling, in forthcoming papers.

Discussion

Previous work demonstrated that helium contributed to the strength increases observed when the nickel-doped and undoped 9Cr-1MoVNb and 12Cr-1MoVW steels were irradiated in HFIR.[1] In those studies, it was shown that the nickel itself did not affect the behavior. Results from the present work support those previous conclusions. In addition, the present high-fluence results show that hardening caused by helium saturates with increasing fluence. Hardening caused by helium is superimposed upon the hardening caused by displacement damage. Hardening due to displacement damage alone is known to saturate with fluence for various alloys,[5] and such saturation has been demonstrated for 9Cr-1MoVNb and 12Cr-1MoVW steels irradiated in EBR-II.[6]

The saturation of hardening with fluence caused by displacement damage from fast reactor irradiation, where little helium forms, is attributed to a saturation in the concentration of dislocation loops formed by self-interstitials generated by the displacement damage--although the loops still continue to grow.[7] Under any given set of irradiation conditions, a steady-state defect Concentration is expected. Steady state implies that the number of excess defects at any point in time equals the number of those created by irradiation minus those that annihilate through natural recombination and those incorporated in sinks (loops and network dislocations).[5,7]

Mechanisms by which helium can affect strength have been postulated, beyond the simple strengthening effect caused directly by helium atoms in interstitial or substitutional positions.[1] For example, helium can stabilize higher order vacancy clusters (di- or tri-vacancy clusters) that can form when the helium and vacancies are mobile.[9,10] Stabilization of such clusters can interfere with Frenkel pair recombination, which can either cause more self-interstitials to be present at any instant, or can cause more self-interstitials to migrate and cluster to form ond grow loops.[11] More large vacancy clusters and more loops would both cause additional hardening relative to helium-free irradiation to the same displacement damage level; such hardening should be proportional to the helium buildup. Because excess self-interstitials caused by helium are mobile and difficult to retain in the matrix, either more loop nucleation and/or growth would occur relative to irradiation where a low helium:dpa ratio is produced (i.e. in a fast reactor). There is evidence that helium refines the scale of loop nucleation and prolongs loop stability to higher fluences.[11] Such processes that produce more loops would logically give rise to more strengthening than that caused by displacement damage alone. and the strengthening would be expected to saturate when the dislocation microstructure stabilizes.

Previous work indicated that helium affects the hardening of 9Cr-1MoVNb and 12Cr-1MoVW steels irradiated in HFIR at 400°C to 8-11 dpa.[1] This conclusion was reached by comparing results obtained on steels with 1 and 2% Ni to those without any nickel additions. A similar conclusion was reached by comparing the HFIR results at 400°C with data from specimens irradiated to ≈16 dpa in EBR-II at 390°C,[12] where again essentially no helium was produced.

Data for the post-irradiation yield stress and the change in yield stress caused by the irradiation for the present and previous HFIR experiments at 400°C and the EBR-II experiment at 390°C are shown in Table 4. Also shown is the helium concentration for each specimen. This table shows the difference between the steels irradiated in HFIR (8-11 dpa)[1] and EBR-II[12] that was taken as evidence for a helium effect. When data from the present HFIR investigation (37-72 dpa) are compared with the previous HFIR data, it appears that an increase in yield stress has occurred for 9Cr-1MoVNb and 12Cr-1MoVW steels irradiated in the present HFIR experiment relative to the previous experiment. However, no further hardening occurred in the steels with 2% Ni during the present experiment. After the current high-dose irradiation, there was no difference between the yield stress of the 12Cr-1MoVW and 12Cr-1MoVW-2Ni steels, but there was a difference between the 9Cr-1MoVNb and 9Cr-1MoVNbPNi steels. These observations can be interpreted to mean that the strength of the 9Cr and 12Cr standard steels approaches that for the respective steel with 2% Ni.

All these results imply that a saturation in hardening occurs with increasing helium concentration, and saturation occurs when a level of ~80 appm He is achieved. This follows from the observation that the 9Cr-1MoVNb-2Ni and 12Cr-1MoVW-2Ni contained ~80 appm He after the 8 to 11 dpa experiment,[1] and there was no further increase in yield stress during the present experiment (37-72 dpa and 450 to 600 appm He). After the present experiment, the 12Cr-1MoVW steel contained over 80 appm He, and the yield stress had increased to become equivalent to that for 12Cr-1MoVW-2Ni steel. Finally, the yield stress of the 9Cr-1MoVNb steel after the present experiment did not equal that for 9Cr-1MoVNb-2Ni. However, the 9Cr-1MoVNb contained only 37 appm He, which is less than the concentration required for saturation.

Table 4 indicates a substantial difference between the strength of specimens irradiated in HFIR and those irradiated in EBR-II to 16 dpa. Irradiation hardening has been shown to saturate for 9Cr-1MoVNb and 12Cr-1MoVW steels by about 10 dpa in EBR-II.[6] Steels with and without the nickel additions also show no difference in their yield stress when irradiated in EBR-II (Table 4), which indicates that these steels saturate at the same strength level during EBR-II irradiation. A common saturation strength for the undoped and doped steels in HFIR and in EBR-II indicates that nickel itself is not having a chemical effect on strength. This supports the validity of using nickel doping to study helium effects.

Table 4. Comparison of yield stress after irradiation in HFIR at 400°C to 8 to 11 dpa and 37 to 72 dpa and irradiation in EBR-II at 390°C to ~16 dpa[a]

	9Cr-1MoVNb			9Cr-1MoVNb-2Ni			12Cr-1MoVW			12Cr-1MoVW-2Ni		
	He (appm)	YS	ΔYS[b]	He (appm)	YS	ΔYS	He (appm)	YS	AYS	He (appm)	YS	ΔYS
HFIR (8–11 dpa)	7	881	274	77	1098	370	15	929	359	80	1056	263
HFIR (37–72 dpa)	37	937	209	456	1039	354	129	1070	301	598	1062	350
EBR-II (~16 dpa)	t3	687	93	t3	729	24	<3	794	249	t3	808	38

[a]Data for 8–11 dpa Were taken from ref. 1; only one specimen was tested; data for 37–72 dpa from the present experiment are an average value from four Specimens. Data for EBR-II were taken from ref. 4, and only one specimen was tested.

[b]ΔYS is the change in yield stress during irradiation relative to control specimen.

From these observations we conclude that irradiation hardening saturates with fluence when hardening is due to displacement damage alone (EBR-II irradiation). and that it saturates at a higher strength level when both displacement damage and helium are produced (HFIR irradiation). Saturation of the hardening caused by helium is expected if the hardening is due to helium atoms themselves or due to an excess of interstitial atoms caused by helium-vacancy cluster formation and a barrier to vacancy-interstitial recombination.' Strength would also saturate if small bubbles were causing the hsrdening.

Previous results for irradiation in both HFIR' and EBR-II[12] indicated that hardening occurred at temperatures up to about 400°C, but not at 450°C or higher. At 500 and 550°C, radiation-enhanced softening relative to the softening caused by aging was observed.[1,6,12] Similarly, softening was observed for specimens irradiated at 600°C in the present study. The loss of strength was accompanied by an increase in total elongation, indicating a normal relationship between ductility and strength and no indication of elevated-temperature helium embrittlement.

Charpy specimens of the undoped and nickel-doped steels irradiated in HFIR at 400°C indicated that helium enhanced the irradiation-induced increase in ductile-brittle transition temperature (DBTT) and decrease in upper-shelf energy.[7,11] This followed from comparing results for specimens irradiated in HFIR and in EBR-II. After irradiation in EBR-II, where essentially no helium was produced, the shift in DBTT saturated with fluence after irradiation to 13 dpa.[15] These saturation values from EBR-II did not apply for 9Cr-1MoVNb and 12Cr-1MoVW steels irradiated to 40 dpa in HFIR, where up to 100 appm He was generated.[7] Furthermore, irradiating the nickel-doped steels in HFIR caused a shift in DBTT that increased with increasing helium concentration. One possible explanation for such an observation on the Charpy behavior was that toughness was reduced by the enhanced hardening caused by helium.[7] Observations on the saturation of hardening from the present experiment do not support that conclusion, because indications are that hardening saturated with fluence well before 40 dpa. This implies that the radiation-induced fracture behavior is due to more than just hardening; such behavior could be related to radiation-induced changes that promote intergranular failure. This needs to be verified.

The microstructures of the steels irradiated at 400°C to 73 to 75 dpa (Figs. 5 and 6) were consistent with previous TEM observations made after irradiation to ≈40 dpa in HFIR.[16] In those studies, the as-tempered substructure of the 9Cr-1MoVNb and 9Cr-1MoVNb-2Ni steels was observed to be unstable during irradiation relative to the 12Cr-1MoVW and 12Cr-1MoVW-2Ni steels. Subgrain coarsening and recovery have apparently continued in the high-fluence irradiation experiment. until most of this microstructure has disappeared (Fig. 5). However, despite the instability of the intragranular substructure, including many of the associated carbide precipitate particles, both the prior-austenite grain boundaries and the intergranular carbide precipitates in the 9Cr steels remain quite stable during irradiation. Consistently, both the intragranular substructure and their associated carbide precipitates in the 12Cr-1MoVW [Fig. 6(a)] and 12Cr-1MoVW-2Ni [Fig. 6(b)] steels remain quite stable during irradiation at 400°C. possibly because the amount of precipitate in the 12Cr steels is greater than in the 9Cr steels. The 12Cr steels contain over twice as much carbide precipitate in the as-tempered condition,[7] because their carbon content is twice that of the 9Cr steels.

Despite the differences in substructure stability and in the amount of precipitate in the 9Cr and 12Cr steels, their hardening behavior at 400°C is similar. This is because the hardening is caused primarily by the dislocation loops and network dislocations generated by irradiation, along with any network dislocations that remain from the tempered martensite. The dislocation component of the microstructure generally builds to a steady-state concentration, which explains why hardening saturates with fluence. There may be minor effects of fine precipitates or bubbles that are also present in the microstructure, but the major cause of hardening appears to be the dislocations.

TEM specimens were not irradiated at 600°C in these experiments. However, previous observations on specimens irradiated in HFIR to ≈40 dpa showed that there was no loop generation or radiation-induced network formation for irradiations at 500 to 600°C.[16] In fact, there was very little difference in the overall appearance of the microstructure of the irradiated specimens compared to those same steels in the normalized-and-tempered condition.[16] The tensile behavior at

600°C indicates that the overall changes in dislocation and precipitate structure during irradiation are producing an effect similar to that observed after thermal aging at 600°C, although it appears that irradiation accelerates the aging process. This is not unexpected, given that irradiation can enhance diffusion.

Summary and conclusions

Standard 9Cr-1MoVNb and 12Cr-1MoVW steels and these steels containing 2% Ni were irradiated in HFIR to 72 dpa at 400 and 600°C. Tensile specimens were tested at the irradiation temperature, and the results were compared with the as-heat-treated (normalized-and-tempered) and thermally aged specimens. Irradiation of nickel-containing steels in the mixed-neutron spectrum of HFIR resulted in the formation of transmutation helium. Up to 700 appm He formed in the steel with 2% Ni. The observations and conclusions can be summarized as follows:

1. Thermal aging to 27,000 h at 400°C had little effect on the strength and ductility of the steels. Aging to 27,000 h at 600°C resulted in a loss of strength and a slight increase in ductility.
2. When irradiated at 400°C, all the steels showed an increase in strength and a decrease in ductility relative to the steels in the normalized-and-tempered and the aged condition. However, there was linle difference between the strength of the steels with and without nickel.
3. The increase in strength caused by irradiation at 400°C saturated with increasing fluence. At saturation, the strength for a steel irradiated in HFIR. where transmutation helium formed, is higher than for a steel irradiated in EBR-II. where very little helium formed.
4. Irradiation at 600°C resulted in a loss of strength and an increase in ductility relative to the normalized-and-tempered steel. The loss in strength was greater than that observed for steels thermally aged in the absence of irradiation.

Acknowledaments

We gratefully acknowledge Dr. L. H. Greenwood for his analysis of the dosimetry specimens in the capsules and his calculations of helium concentrations; L. T. Gibson and N. H. Rouse for carrying out the experimental work; M. L. Grossbeck and J. A. Horton for reviewing the manuscript; and Frances Scarboro for preparing the manuscript.

References

1. H. L. Klueh and J. M. Vitek, J. Nucl Mater. 150 (1987) 272.
2. R. L. Klueh. J. M. Vitek. and M. L. Grossbeck, in: Effects of Irradiation on Materials: Eleventh International Symposium. ASTM-STP 782, Eds. H. R. Brager and J. S. Perrin (American Society for Testing and Materials, Philadelphia, 1982) p. 648.
3. P. J. Maziasz and R. L. Klueh. in: Effects of Irradiation on Materials: Fifteenth International Symposium, ASTM-STP 782. Eds. R. E. Stoller and D. S. Gelles (American Society for Testing and Materials, Philadelphia) to be published.
4. P. J. Maziasz and R. L. Klueh, in: Effects of Irradiation on Materials: Fourteenth International Symposium, ASTM-STP 1046, Eds. N. H. Packan. R. E. Stoller and A. S. Kumar (American Society for Testing and Materials, Philadelphia, 1989) p. 35.
5. E. E. Bloom, in: Radiation Damage in Metals. Eds. N. L. Peterson and S. D. Harkness (American Society for Metals, Metals Park, Ohio, 1976) p. 295.
6. R. L. Klueh and J. M. Vitek. J. Nucl. Mater. 182 (1991) 230.
7. P. G. Shewmon. in: Fundamental Aspects of Structural Alloy Design, Eds. R. I. Jaffee and B. A. Wilcox (Plenum Press, New York, 1977) p. 173.
8. L. M. Brown, A. Kelly, and R. M. Mayer, Phil. Mag. 19 (1969) 721.
9. L. K. Mansur. E. H. Lee, P. J. Maziasz. and A. F. Rowcliffe, J. Nucl. Mater. 141-143 (1986) 633.
10. N. M. Ghoneim. S. Sharafat. and L. K. Mansur. Point Defects and Defect Intemctions in Metals, J. Takamura, M. Doyama. and M. Kiriani, Eds. (University of Tokyo Press, Tokyo, 1982) p. 865.
11. P. J. Maziasz. Effects of Helium Content on Microstructural Development in Type 316 Stainless Steel Under Neutron Irradiation, Oak Ridge National Laboratory, ORNL-6121 (1985).
12. R. L. Klueh, P. J. Maziasz, and J. M. Vitek. J. Nucl. Mater. 141-143 (1986) 960.
13. J. M. Vitek. W. R. Corwin, R. L. Klueh, and J. R. Hawthorne. J. Nucl Mater. 141-143 (1986) 948.
14. R. L. Klueh and D. J. Alexander, J. Nucl Mater. 179-181 (1991) 733.
15. W. L. Hu and D. S. Gelles, in: Influence of Radiation on Material Properties: Thirteenth International Symposium (Part II), ASTM STP 956, F. A. Garner, C. H. Henager, Jr., and N. Igata, Eds. (American Society for Testing and Materials, Philadelphia, 1987) p. 83.
16. P. J. Maziasz. R. L. Klueh, and J. M. Vitek. J. Nucl Mater. 141-143 (1986) 929.
17. J. M. Vitek and R. L. Klueh, Met. Trans. A. 14A (1983) 1047.

6.2 Austenitic Stainless Steels

TEMPERATURE DEPENDENCE OF THE DISLOCATION MICROSTRUCTURE OF PCA AUSTENITIC STAINLESS STEEL IRRADIATED IN ORR SPECTRALLY-TAILORED EXPERIMENTS -P.J. Maziasz (Oak Ridge National Laboratory)

OBJECTIVE

Microstructural analysis of neutron irradiated austenitic stainless steels and correlation with changes in mechanical properties.

SUMMARY

Specimens of solution-annealed (SA) and 25% cold-worked (CW) PCA austenitic stainless steel were irradiated in ORR in spectrally-tailored experiments specially designed to produce fusion-relevant Heldpa ratios (12-16 appm He/dpa). SA and CW PCA were irradiated at 330 and 400°C to 13 dpa while only CW PCA was irradiated at 60, 200, 330 and 400°C to 7.4 dpa. While cavities and fine MC precipitates were only detectable at 330 and 400°C. dislocations were a major component of the radiation-induced microstructure at 60-400°C. The mixtures of "black-dot" loops, larger Frank loops, and network that comprised the total dislocation structure were very dependent on irradiation temperature. Both SA and CW PCA contained Frank loops and network dislocations at 330 and 400°C. Frank loop concentrations were maximum at 330°C and dislocation evolution with dose was most evident at 400°C. At 60 and 200°C, the microstructure was dominated by very dense dispersions of (1-3 nm diam.) "black-dot" loops. Some Frank loops were observed at 200°C, but almost none were found at 60°C. Surprisingly, there was significant radiation-induced recovery of the as-cold-worked dislocation network in CW PCA at ail irradiation temperatures. There appears to be a distinguishable transition in the nature of the radiation-induced microstructure between *200* and 330°C.

PROGRESS AND STATUS

introduction

Spectral-tailoring to control the Heldpa ratio in irradiated steels has been a major thrust of the overall fission reactor irradiation efforts of the U.S. Fusion Materials Program (FMP) since about 1980 [1-3]. Spectral-tailoring was achieved in the Oak Ridge Research Reactor (ORR) by periodically changing the materials that surround the experimental subassembly in the reactor core to alter the ratio of fast to thermal neutron fluxes, thereby altering ratio of helium generation to displacement damage production in Ni-bearing like type 316 and the fusion prime-candidate austenitic (PCA) stainless steel. These experiments have produced a variety of new data on radiation-induced property changes in austenitic stainless steels that are particularly relevant to near-term fusion devices like the International Thermonuclear Experimental Reactor (ITER) [4-6]. Such data from ORR experiments include: a.) He/dpa dependant void swelling that appears maximum at the fusion Heldpa ratio [3], b.) irradiation-creep rates at 400-500°C that increase with Heldpa ratio [2] and, that are greater at 60°C than at 200400°C [7], c.) high radiation-induced hardening and low uniform elongation at 60-330°C [8], and d.) radiation-induced sensitivity to aqueous electrochemical attack after irradiation at 200-400°C, but not at 60°C [9,10]. The purpose of this work is to characterize the microstructure of SA and CW PCA specimens irradiated in ORR spectrally-tailored experiments at 60 to 400°C to doses of 7.4 and 13 dpa, and to relate microstructure to the irradiated mechanical properties.

Exoerimental

Standard TEM disks (3 mm diameter, 0.25 mm thick) of the PCA steel were irradiated in either the 25% cold-worked (CW) or the solution-annealed (SA) (0.5h at 1100°C) condition. The PCA (K-280 heat) is a 14Cr-16Ni-2Mn-2Mo-0.25Ti-0.05C (wt.%) austenitic stainless steel. Disks of both SA and CW PCA were irradiated in the spectrally-tailored ORR-MFE-4 experiment (U.S. FMP) at 330 and 400°C to 13 dpa and 230 appm He, but only CW PCA disks were irradiated in the ORR-MFE-6J/7J experiment (U.S.-Japan Collaborative Program [11]) at 60, 200. 330 and 400°C to 7.4 dpa and 130 appm He. The radioactive specimens were thinned in a remotized Tenupole automatic electropolishing unit. Microstructural analysis was performed on a JEM 2000FX analytical electron microscope (AEM) (LaB_6, 200KV), using standard techniques to obtain quantitative microstructural data.

Results

A. Analvsis of the Total Microstructure

Cavities. precipitates and dislocations were ail present in the microstructures of SA and CW PCA specimens irradiated at 330 and 400°C. More detailed quantitative microstructurai data and immersion-density swelling date from these specimens can be found elsewhere [12]. No cavities or precipitates were detectable in the CW PCA specimens irradiated at 60 and 200°C. Swelling in SA and CW specimens irradiated to 13 dpa at 330°C was about 0.2%. and was due entirely to the very high ($>2.5\times10^{23}$ m^{-3})

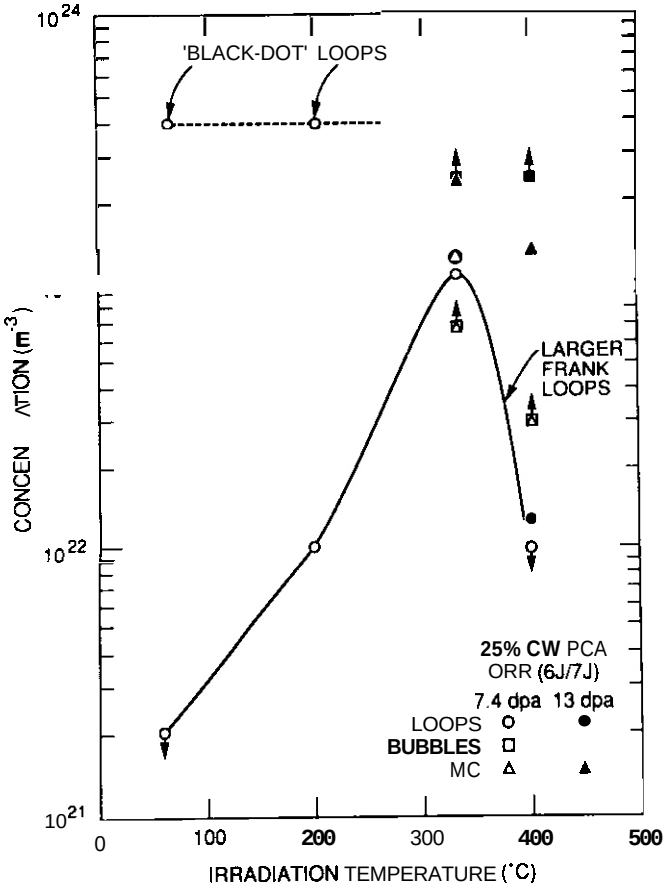

Fig. 1. Temperature dependence of the concentrations of various microstructural components in 25% CW PCA irradiated in ORR MFE 6J/7J (7.4 dpa) and MFE-4 (13 dpa).

B. Analysis of the Dislocation Microstructure

Quantitative calculations of contributions from "black-do?' loops, larger Frank loops, and network dislocations to the total dislocation concentrration for each specimen are given in Table 1.

B.1 -- 60°C

Very high (4 x 10^{23} m^{-3}) concentrations of (1.4-3 nm diam) "black-dot" loops were the dominant feature of CW PCA irradiated to 7.4 dpa (Figs. 1 and 2). This specimen contained virtually no larger Frank loops (Fig. 3). and the concentration of network dislocations was over ten times lower than that found in as-cold-worked material (Table 1 and Fig. 4). indicating significant recovery during irradiation. Previous, more detailed work on similar microstructures found in SA 316 irradiated in HFIR at 55°C proved that such "black-dot" defects were indeed all loops [13]. The 2½ D imaging technique [focus changes in weak-beam dark field (WBDF)] imaging mode [14] furthermore indicates that all of the "black-dot' loops in ORR-irradiated CW PCA were the same in nature (either all vacancy or all interstitial loops), as had been observed in HFIR-irradiated SA 316.

B.2 -- 200°C

Dense populations of "black-do? loops were again observed in CW PCA, identical to those found at 60°C (Figs 1 and 2). However, at this temperature, there was a marked increase in nucleation and growth of larger Frank interstitial loops (Fig 3), coupled with a slight decline in the network dislocations remaining after irradiation (Fig. 4, Table 1). Together, these different components still add up to about the Same total dislocation Concentration, mainly because the contribution of the "blackdor' loops dominates this number.

Table 1. Summary of Concentration Data for US-PCA Irradiated in Spectrally Tailored Experiments ORR-MFE-4A and -4B and -6J and -7J

Alloy/ Condition	Irradiation Conditions		Dislocation Concentration (Ω m/m^3)				Number Density of Large Loops (m^{-3})
	Temperature (°C)	Dose (dpa)	Network	"Black-Dot" Loops	Larger Frank Loops (line length/m^3)	Total	
SA-PCA	As-annealed		4×10^{12}	None	None	$\leq 5 \times 10^{12}$	
SA-PCA	400	13	1.8×10^{15}	None	1×10^{15} (25 nm)[a]	~3 $\times 10^{15}$	1.3×10^{22}
SA-PCA	330	13	9×10^{14}	None	3.1×10^{15} (16.5 nm)[a]	~4 $\times 10^{15}$	6.0×10^{22}
25% W-PCA	As-cold worked		$\geq 5 \times 10^{15}$	None	None	$\geq 5 \times 10^{12}$	0
25% CW-PCA	400	13	1.1×10^{15}	None	8.4×10^{14} (21 nm)[a]	~2 $\times 10^{15}$	1.3×10^{22}
25% W-PCA	400	7.4	2×10^{14}	None	9×10^{14} (29 nm)[a]	1.1×10^{15}	9.9×10^{21}
25% W-PCA	330	13	$<9 \times 10^{14}$	None	4.7×10^{15} (12.4 nm)[a]	4.7–5.6 $\times 10^{15}$	1.2×10^{23}
25% CW-PCA	330	7.4	4.5×10^{14}	None	3.1×10^{15} (9 nm)[a]	3.5×10^{15}	1.1×10^{23}
25% CW-PCA	200	7.4	2.6×10^{14}	2.8×10^{15} (2.2 nm)[a]	5×10^{14} (16.5 nm)[a]	~3.6 $\times 10^{15}$	9.6×10^{21}
25% W-PCA	60	7.4	3.4×10^{14}	2.8×10^{15} (2.2 nm)[a]	$<1 \times 10^{14}$ (16.5 nm)[a]	~3.1 $\times 10^{15}$	1.9×10^{21}

[a]Average diameter of loops in this size class.

B.3 - 330°C

The CW PCA irradiated to 7.4 dpa contained about ten times more Frank loops than found at 200°C (Fig. 1), with many smaller loops so that the average size is less than found at 200°C (Fig. 3, Table 1). The concentration of network dislocations at 330°C was about double that found at 200°C, but radiation-induced network recovery was still substantial (Fig. 4, Table 1). The total dislocation content was slightly higher than at 200°C, and was dominated by the contribution from the Frank loops. No "blackdot" loops were found at this temperature. The bright dots visible in WBDF (Fig. 2) were strain images from tiny MC precipitates and helium bubbles that were definitely resolvable in the bright-field (BF) imaging mode [12]. As dose increased to 13 dpa, Frank loop nucleation and growth both increased, concurrent with a significant increase in the network dislocation concentration, so that the total dislocation content also increased with dose (Fig. 5, Table 1). This suggests that et 13 dpa, loops were now evolving (growing and unfaulting) io produce network dislocations during irradiation,

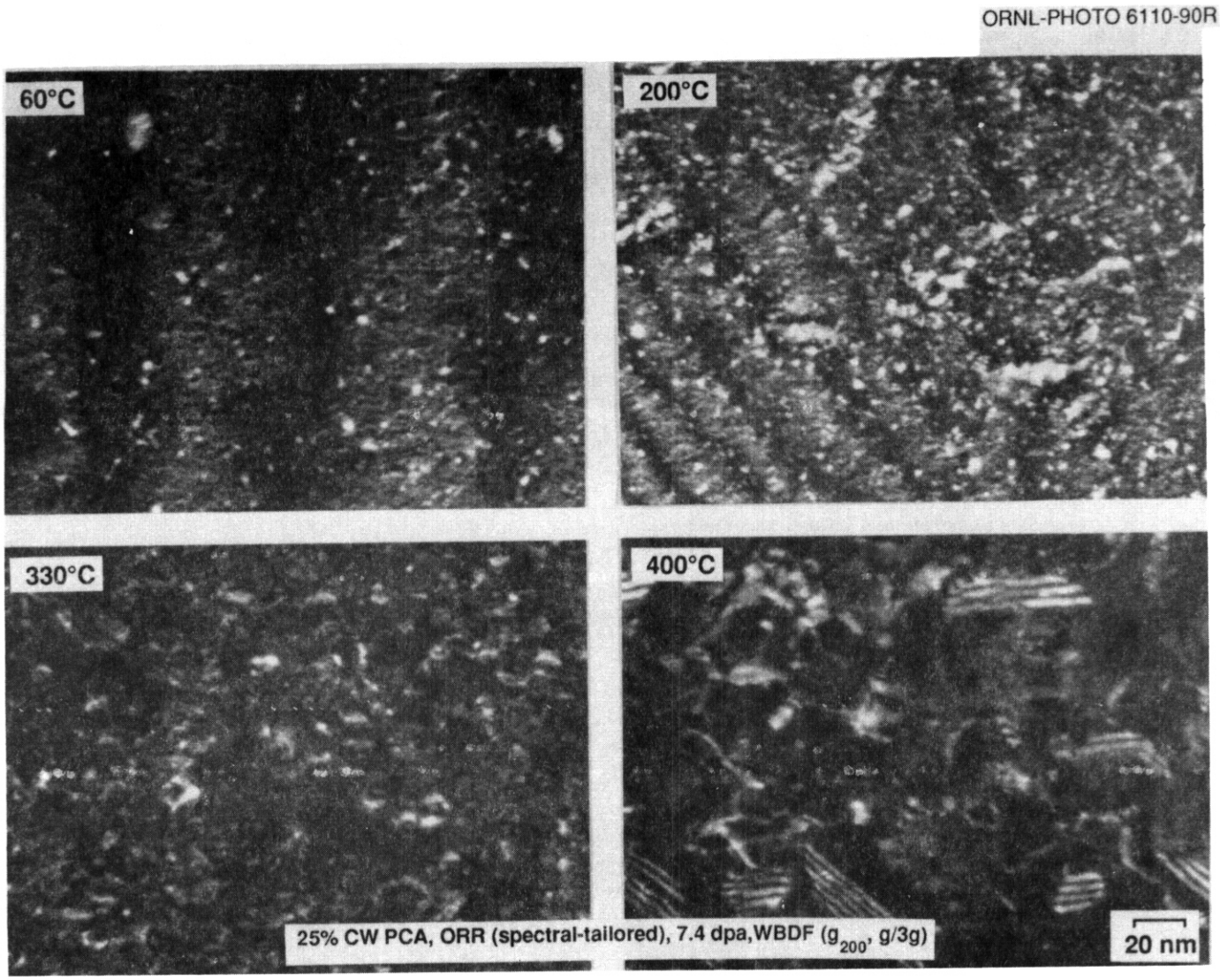

Fig. 2 Weak-beam dark-field (WBDF) TEM imaging of the dislocation microstructure of 25% CW PCA irradiated at 60-400°C (conditions indicated). Small bright dots at 60 and 200°C are strain images of tiny "black-dot" loops, whereas similar features at 330°C are tiny helium bubbles and MC precipitates.

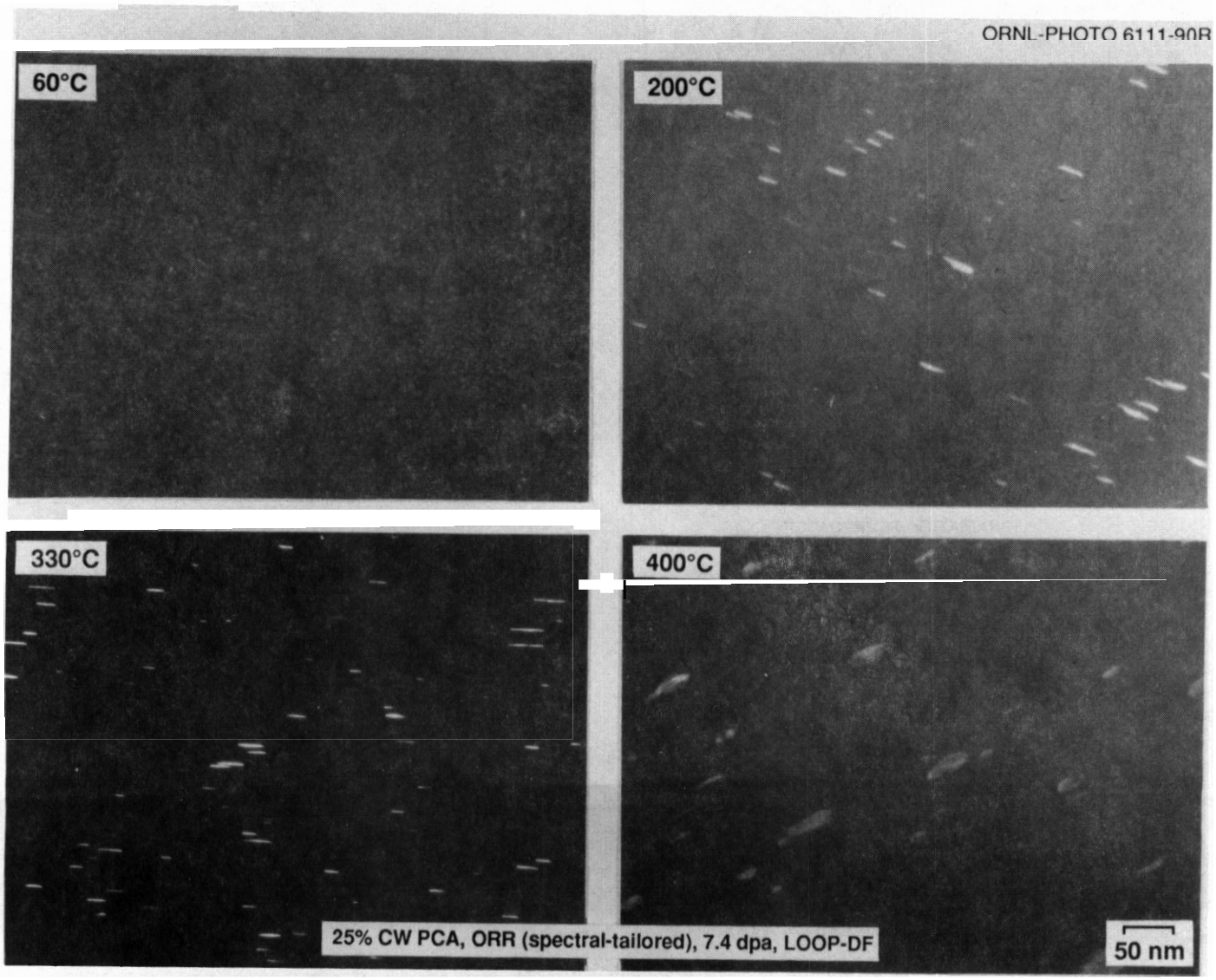

Fig. 3 Dark-field TEM using the <111> satellite streaks around g_{200} reflections to image the fault plane of larger Frank interstitial loops in 25% CW PCA irradiated at 60-400°C (conditions indicated).

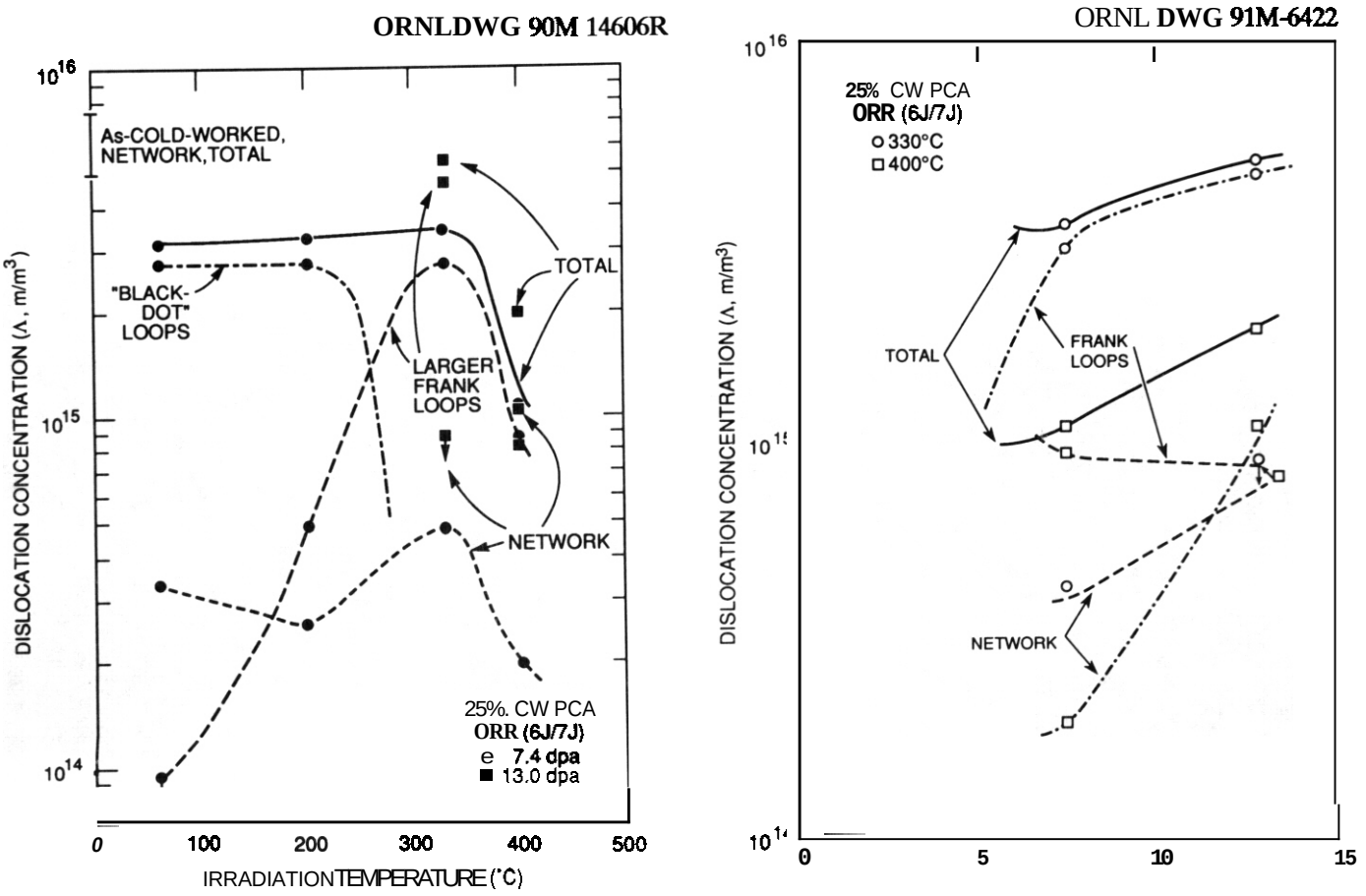

Fig 4. Temperature dependence of the dislocation concentration from various components of the dislocation microstructure in 25% CW PCA irradiated in ORR MFE 6J/7J (7.4 dpa) and MFE 4 (13 dpa).

SA PCA irradiated to 13 dpa had a dislocation Structure similar to that found in CW PCA at the same dose. The Frank loop Structure was coarser and there were more network dislocations than found in the CW PCA. This observation strongly indicates that loop evolution during irradiation at 330°C is producing network dislocations, because the SA PCA had virtually no network dislocations prior to irradiation (Table 1).

B.4 -- 400°C

All components of the microstructure of ORR irradiated CW PCA were coarser at 400°C than at the lower irradiation temperatures, particularly the Frank loop structure (Figs. 2 and 3). and the dislocation microstructure at 400°C evolved more with dose from 7.4 to 13 dpa than it did at 330°C (Fig. 5). After 7.4 dpa, the CW PCA contained far fewer and much larger loops at 400°C than were found at 330°C. This indicates that loop nucleation was a maximum at 330°C, and that loop growth is increasing with temperature above 330°C. Both the network and total dislocation concentrations fall significantly at 400°C compared to 330°C (Fig. 5). As dose increased from 7.4 to 13 dpa, loop nucleation increased, but average loop size decreased with dose because there were more smaller loops and the size of the largest loops declined (from 62 nm to 37 nm diam. [11]). There was, however, nearly a ten-fold increase in the network dislocation content of CW PCA, and the total dislocation content doubled with dose. Again these changes indicate that loop evolution was producing network dislocations at 400°C, as found at 330°C. Despite the increase in radiation-induced dislocation content with dose, there are still fewer dislocations after 13 dpa than there were in the as-cold-worked material.

There were more and larger Frank loops, and more network dislocations in SA PCA irradiated at 400°C to 13 dpa than in CW PCA. Therefore, the total dislocation content in the SA PCA was about three times greater than that found in CW PCA after irradiation to 13 dpa (Table 1). AS at 330°C, this clearly proves that loop evolution is the major source of radialion-induced dislocation network generation at 400°C.

Discussion

The data from these spectrally-tailored ORR experiments are unique in terms of their systematic temperaturedependence (temperatures were measured and controlled), isothermal dose-dependencies (330 and 400°C) and fusion-relevant He/dpa ratio, ail achieved for the same PCA alloy. The most important aspects of this radiation-induced dislocation behavior for comparison to previous fission-reactor data on 300-series austenitic stainless steels irradiated at 450°C and below are: a.) the strong temperature dependence of Frank loop nucleation in the CW PCA. b.) the degree of radiation-induced recovery of the as-cold-worked dislocation network at lower temperatures until evolution of the Frank loop structure begins to generate new network dislocations at higher temperatures, and c.) the transition in nature of the overall microstructure developed during irradiation between 200 and 330°C.

The absence of large Frank loops and recovery of the initial network dislocations have both been observed before in CW 316 and CW 316+Ti irradiated in HFIR at 55°C [15,16]. The degree of dislocation network recovery. however, is greater for Cw PCA irradiated in ORR. The abundant nucleation of large Frank loops in SA 316, SA 316+Ti and SA 347 irradiated in HFIR at 55°C makes their absence in the cold-worked materials more striking and somewhat puzzling. At very low doses (0.0010.03 dpa), only "black-dot" interstitial loops are observed in SA 316 irradiated at 90°C in RTNS-II (14 MeV neutrons) or in a fission reactor (<2-3 MeV neutrons) [17]. The "black-dot" loops in these lowdose specimens were positively identified as interstitial loops. The absence of large Frank loops and the recovery of the network in CW Steels both make sense if the network dislocations are initially dominant sinks for interstitials (with the corresponding vacancies being immobile), so that those dislocations climb and annihilate.

Previous microstructural observations at various irradiation temperatures support the idea of lower and higher temperature regimes of microstructural development [18-22], but this work shows the clearest evidence for a transition in temperature between such regimes. The evolution of bubbles, precipitates and/or voids with dose, and evolution of Frank loops into a radiation-produced dislocation network appear to be the distinguishing features of the "higher-temperature" regime. By contrast, "black-dot" loops and their persistence to higher doses appear to be characteristic of the "lower-temperature"regime. Small defect clusters mixed with larger Frank loops have been reported in CW 316 steel [18] and a CW high-purity Fe-Cr-Nl-Mo alloy [19] irradiated in a previous spectrally-tailored ORR experiment (MFE-2) at 250, 290 and 450°C to 3-5 dpa. The small defects, however, were not identified, and at 450°C (in the CW 316) may well have been tiny helium bubbles visible in WBDF. but not detectable in BF in the electron microscopes used in 1982[17]. High-dose, mixed-spectrumfission-reactor microstructural data on various austenitic stainless steels (type 348. type 316 and PCA or JPCA) includes positive identification of fine helium bubbles and/or precipitates at 300-350°C after 33-55 dpa, and no positive identificationof other small defects as "blackdot" dislocation loops [20-22]. Previous work also definitely identified "black-do? loop damage in SA and CW austenitic stainless steels (316, 316+Ti and 347) irradiated in HFIR at 55°C to 1-11 dpa [20,21]. Fine helium bubbles and MC precipitates found in CW and SA PCA irradiated ORR at 330°C were ciearly distinguishable from the "black-dot" loops identified at 60 and 200°C, particularly with the help of 2½D imaging [12]. The very lowdose RTNS-II data showing "black-dot" damage at 290°C is consistent with the low-temperature microstructure regime being below 330°C, but at such low doses, one does not really know the loop growth characteristics.

This paper is too short to completely correlate these microstructures with radiation-induced property change data, but several trends can be noted that point to the importance of changes observed the dislocation structure with temperature. Radiation-induced hardening and reductions in total elongalion with irradiation temperature follow the temperature dependence observed for nucleation and growth of the Frank loops, with hardening being maximum at 330°C where the maximum number of such loops is observed [6,8]. Maximum sensitivity to electrochemical attack was observed after irradiation at 400°C and has been related to strong effects of radiation-induced segregation (RIS) of solutes [5,9,10]. Such behavior would at least be consistent with of the overall coarsening of the microstructure from 330 to 400°C, and the more rapid evolution of the dislocation structure with dose, because both Frank loop evolution and RIS development strongly reflect the behavior of interstitials at these temperatures (13]. More work is definitely needed to better connect microstructural evolution with properties changes. The degree and nature of the changes observed at these temperatures and fluences argue for smaller temperature increments and lower doses in future experiments.

Conclusions

1. CW PCA irradiated in spectrally-tailored ORR experiments lo 7.4-13 dpa shows recovery of initial dislocation network at 60-400°C, "blackdot" loops only at 60 and 200°C, and very temperature dependent formation of larger Frank loops, (none at 60°C and a maximum at 330°C).
2. Comparison of SA and CW PCA irradiated at 330 and 400°C indicates that growth and unfauiting of Frank loops produces the network dislocations observed at 13 dpa. and suggests that network recovery is necessary in the CW material before Frank loops nucleate and grow.
3. There is a transition between the low- and high-temperature regimes of radiation-induced microstructural evolution between 200 and 330°C in ORR.

References

1. M.L. Grossbeck and K.R Thorns, ADIP Quart. Prog. Rep. DOE/ER-0045/3, US-DOE (June, 1980) p. 10.

2. M.L. Grossbeck and J.A. Horak, J. Nucl. Mater., 155157 (1988) 1001.

3. R.E. Stoller, P.J. Maziasz, A.F. Rowciiffe and M.P. Tanaka, J. Nucl. Mater., 155-157 (1988) 1328.

4. A.F. Rowcliffe, A. Hishinuma, M.L. Grossbeck and S. Jitsukawa, J. Nucl. Mater. 179-181 (1991) 125.

5. J.L. Boutard. J. Nucl. Mater. 179-181 (1991) 1179.

8. P.J. Maziasz, et al., Fusion Technol., 19 (1991) 1571.

7. M.L. Grossbeck. L.K. Mansur and M.P. Tanaka, Effects of Radiation on Materials: 14th International Symposium, ASTM STP 1046, vol. II, Philadelphia, PA (1990) p. 537.

8. M.L Grossbeck. et al., FRM Semiannu. Prog. Rept., DOE/ER-0313/6, (March 1989) p. 259.

9. T. Inazumi, G.E.C. Bell, E.A. Kenik, and K. Kiuchi, Corrosion 48 (1990) 786.

10. T. Inazumi and G.E.C. Bell, FRM Semiannu. Prog. Rept., DOE/ER-0313/8, (March 1990) p. 272

11. J.L. Scott, et al., J. Nucl. Mater., 141-143 (1986) 996.

12. P.J. Maziasz, FRM Semiannu. Prog. Rept.. DOE/ER-0313/10, (July 1991) p. 99.

13. P.J. Maziasz, Ph.D. Thesis, Oak Ridge National Laboratory Report, ORNL-6121 (Nov., 1985).

14. J.B. Mitchell and W.L. Bell, Acta. Met. 24 (1976) 147.

15. F.W. Wiffen and P.J. Maziasz. J. Nucl. Mater. 103&104 (1981) 821.

16. P.J. Maziasz, Am. Nucl Soc. Trans. 39 (1981) 433.

17. H.L. Heinisch, T. Muroga and M. Kiritani, FRM Semiannu. Prog. Rept., DOE/ER-0313/8 (March, 1990) p. 51.

18. P.J. Maziasz. ADIP Semiannu. Prog. Rept., DOE/ER-0045/9, (Sept., 1982) p. 78.

19. H.R. Erager and F.A. Garner, Effects of Radiation on Materials: Eleventh Conference, ASTM STP 782. Philadelphia, PA (1982) p. 152.

20. M.P. Tanaka, S. Hamada, A. Hishinuma and P.J. Maziasz. J. Nucl. Mater. 155-157 (1988) 801.

21. S. Hamada, et al., Effects of Radiation on Materials: 14th Internat. Symp., ASTM STP 1046, vol. I (1989) p. 172.

22. L.E. Thomas and J.M. Beeston. J. Nucl. Mater., 107 (1982) 159.

LOW-TEMPERATURE TENSILE BEHAVIOR OF IRRADIATED AUSTENITIC STAINLESS STEELS - A. Hishinuma, S. Jitsukawa (Japan Atomic Energy Research Institute) and M.L. Grossbeck (Oak Ridge National Laboratory)

OBJECTIVE

The objective of this work is to define the tensile properties of 316 type steels irradiated in the low-temperature regime, below 773 K.

SUMMARY

The low-temperature tensile properties of type 316 stainless steel (3316) and Japanese Primary Candidate Alloy (JPCA) irradiated in spectrally tailored Oak Ridge Research Reactor (ORR) and in High Flux Isotope Reactor (HFIR) capsules are summarized. The yield and tensile strengths in the ORR-irradiated specimens were found to increase with increasing irradiation temperatures up to 330°C followed by a decrease with increasing temperature. This strength maximum was accompanied by an elongation minimum. Similar trend curves were observed in the HFIR-irradiated specimens, although the temperature of peak strength was shifted higher. The behavior can he understood roughly in terms of microstructural development of dislocation loops and recovery of network dislocations during irradiation. The temperature of peak strength seems to depend on irradiation conditions such as He:dpa ratio and irradiation dose rate.

PROGRESS AND STATUS

Introduction

Low-temperature properties of type 316 austenitic stainless steels, such as mechanical properties and corrosion susceptibility during and after neutron irradiation, are currently a concern in relation to future fusion devices. Type 316 austenitic stainless steel was chosen primarily as the first wall and blanket structural material for the next machines such as the International Thermonuclear Experimental Reactor (ITER). However, there have been few data obtained up to now because of both difficulties of irradiation and lack of interest in such properties at ITER operating conditions, especially at temperatures below 500°C.

For the present study, data on tensile properties of type 316 stainless steel and PCA irradiated at temperatures below 500°C to relatively **low** doses are summarized.

Exoerimental Procedure

Alloys investigated were type 316 stainless steel in annealed (J316-SA) and 20% cold-worked conditions (J316-CW) and the prime candidate alloy in annealed (JPCA-SA) and 15% cold-worked (JPCA-CW) conditions. Sheet specimens (SS-I type) with gauge sections of 20.3 mm in length, 0.762 mm in thickness and 0.025 mm in width, and sub-mini round bar tensile specimens with gauge sections 18.3 mm in length and 2.03 mm in diameter were made. Detailed dimensions of the tensile specimens are shown elsewhere.'

The specimens were irradiated in the spectrally tailored ORR capsules to get an atomic displacement level of about 7 dpa and helium levels of about 100 appm. The radiation temperatures were 60,200,330 and 400°C. The details of spectral tailoring and temperature control procedures can be seen elsewhere? The HFIR irradiation was also carried out at temperatures ranging from 300 to 500°C to doses of 22 and 27 dpa with 1600 and 2000 appm He, respectively.

Specimens were tested on an Instron universal testing machine at elevated temperatures at pressures in the 10^{-4} Pa range. A strain rate of 4.2 x 10^{-4} s^{-1} was used. Detailed conditions are also given elsewhere.'

Results and Discussion

Results of the tensile tests of J316 and JPCA are summarized in Table 1. lrradiation conditions are shown, where displacement damage and helium production rates were calculated based on reports of L. R. Greenwood and D. V. Steidl.[3,4] Yield strength (YS), ultimate tensile strengtl, (UTS) and total elongation (TE) of J316 and JPCA irradiated in the ORR are shown graphically in Figs. 1 and 2 (ref. 5), respectively. Similar temperature dependence of YS, UTS and TE in both J316 and JPCA can be seen. YS and UTS for SA specimens increased with increasing test and irradiation temperature up to 330°C, where the maximum of each strength property was observed. The strength for CW specimens had a similar trend in

Table 1. Tensile properties of Spectrally tailored ORR- and HFIR-irradiated J316 and JPCA

Irradiation Test Temperature	Materials/ material condition	Damage (dpa/ appm He)	Strength, MPa Yield	Ultimate	Elongation, % Uniform	Total
	ORR Spectrally Tailored Irradiation (Sheet)					
60/RT	J316/SA	6.9175	703	752	24.5	29.9
60/RT	J316/SA	6.9175	690	745	27.6	32.5
60/RT	J316/20CW	6.9/75	834	855	0.64	8.5
60/RT	J316/20CW	6.9/75	855	883	0.63	7.5
2001200	J316/SA	6.9175	745	745	0.2	4.0
2001200	J316/SA	6.9/75	758	765	0.2	5.9
2001200	J316/20CW	6.9175	793	821	0.64	4.4
2001200	J316/20CW	6.9175	841	869	0.48	3.3
2001200	J316/20CW	6.9175	821	862	0.63	3.4
3301330	J316/SA	7.41102	848	855	0.29	3.1
3301330	J316/SA	7.41102	869	869	0.31	2.9
3301330	J316/20CW	7.41102	862	876	0.44	2.3
3301330	J316/20CW	7.41102	993	1007	0.34	2.0
4001400	J316/SA	7.41102	595	677	4.6	7.0
4001400	J316/SA	7.41102	650	717	4.3	6.8
4001400	J316/20CW	7.41102	415	457	1.0	2.8
4001400	J316/20CW	7.41102	800	848	1.6	3.4
60/RT	JPCA/15 CW	6.9186	876	889	0.38	8.1
60/RT	JPCA/15 CW	6.9186	862	869	0.44	7.3
60/RT	JPCA/25 CW	6.9186	910	924	0.44	4.5
60/RT	JPCA/25 CW	6.9186	917	931	0.44	4.5
2001200	JPCAISA	6.9186	714	717	0.35	11.3
2001200	JPCAISA	6.9186	696	703	0.31	11.1
2001200	JPCA/15 CW	6.9186	827	855	0.51	3.6
2001200	JPCA/15 CW	6.9/86	807	814	0.31	3.4
3301330	JPCAISA	7.4/118	821	821	0.23	2.5
3301330	JPCAISA	7.4/118	800	807	0.38	3.2
3301330	JPCA/15 CW	7.41118	876	889	0.38	2.3
3301330	JPCA/15 CW	7.41118	938	945	0.38	2.2
3301330	JPCA/15CW Rod	7.41118	931	945	0.42	5.3
3301330	JPCA/15CW Rod	7.41118	958	958	0.31	5.4
4001400	JPCAISA	7.41118	505	652	10.5	12.9
4001400	JPCAISA	7.41118	549	667	2.5	10.5
6001400	JPCA/15CW	7.41118	855	896	0.59	2.9
4001400	JPCA/15CW	7.41118	827	841	0.38	1.9
	HFIR Irradiation (Rod)					
3001300	JPCA/SA	2711973	770	789	2.43	9.93
3001300	JPCA/15 CW	2711973	775	798	1.0	6.6
3001300	JPCA/15 CW	2711973	747	780	1.7	7.27
4001400	JPCAISA	2211585	878	888	0.38	6.4
4001400	JPCAISA	2211585	896	910	0.44	6.0
4001400	JPCAICW	2211585	952	972	0.42	5.5
4001400	JPCAICW	2211585	859	974	1.4	6.3
5001500	JPCAISA	2712008	650	732	4.7	8.2
5001500	JPCAISA	2712008	631	724	7.2	11.7
5001500	JPCAICW	2712008	678	765	7.1	11.4
5001500	JPCAICW	2712008	624	713	6.3	10.2

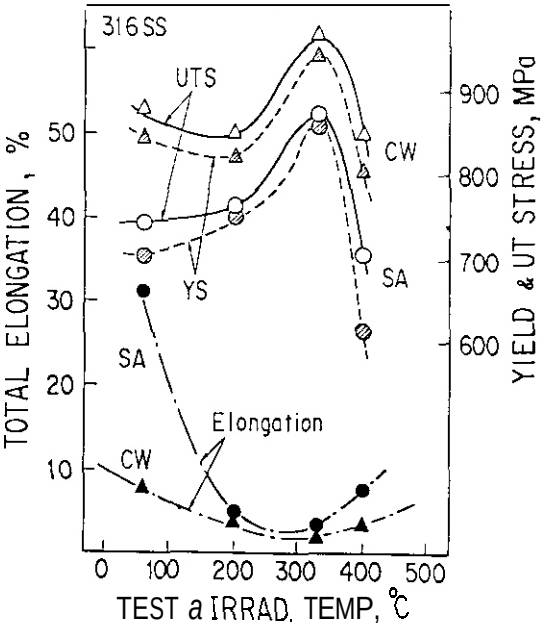

Fig. 1. Temperature dependence of yield and ultimate strength and total elongation of J316 irradiated in the Spectrally tailored ORR.

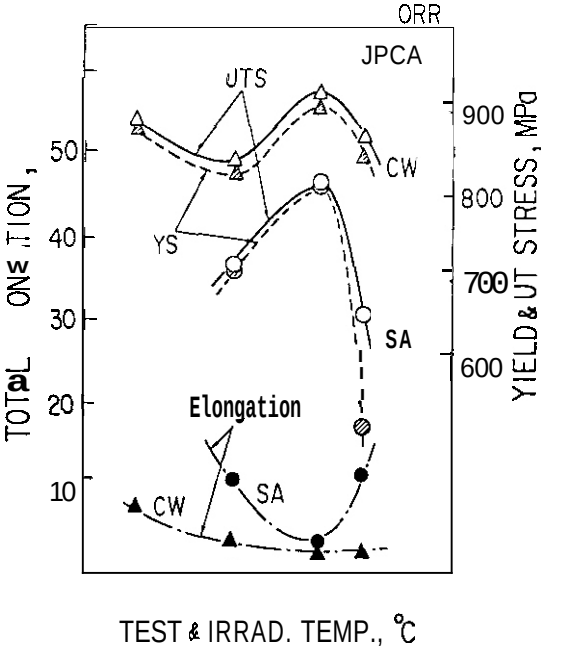

Fig. 2. Temperature dependence of yield and ultimate strength and total elongation of JPCA irradiated in the spectrally tailored ORR.

temperature dependence although a shallow relative minimum was seen around 200°C. Corresponding to the maximum strength, an elongation minimum was observed around 330°C. Similar tensile properties were reported[6] in 20% cold-worked type 316 stainless steels irradiated in ORR to about **5** dpa without spectral tailoring, where the temperature and magnitude of the strength maximum were nearly equal, respectively, to that of previous specimens irradiated to *I* dpa. This inverse temperature dependence of irradiation hardening observed at temperatures below 330°C **is** expected to he closely related to the microstructural development. Compared to the microstructural data reported by P.J. Maziasz on USPCA-CW,' the strength behavior of JPCA-CW can he explained by the temperature dependence of network dislocation density, not by black dot loops or Frank loops. While in JPCA-SA, Frank loops produced during irradiation may he a dominant factor for the strength (although it is very difficult to understand the temperature dependence). The loop concentration increases with increasing irradiation temperature. The behavior is similar to that observed in an electrochemical potentiokinetic reactivation (EPR) experiment: where 60°C irradiated JPCA did not show any sensitization compared to unirradiated specimens. Specimens irradiated at 200, 330, and 400°C showed vigorous irradiation-induced sensitization.

Figure 3 shows tensile properties of JPCA irradiated in the HFIR, where similar temperature dependencies of **YS,** UTS and TE are shown? In this case the strength maximum and the elongation minimum were observed at a temperature of about 400°C. Compared with the data from ORR-irradiated specimens, the maximum in strength was shifted higher in temperature by about 100°C. The difference could he explained by the He:dpa ratio or by the rather large difference in atomic displacement level. **A** difference in He:dpa ratio has resulted in a large difference in swelling response between spectrally tailored ORR and HFIR irradiations, depending on the balance of positive and negative effects of helium on nucleation and the growth rate of voids? In the case of hardening, helium also has positive and negative effects on microstructural development during irradiation. Helium and/or helium bubbles could act as effective vacancy bias sinks, especially in the temperature regime below SOOT, to enhance dislocation loop formation. The higher temperature of the peak in strength resulting from HFIR irradiation (large He:dpa ratio) could be explained by the above effect. This may **also** depend on irradiation dose rate or on the difference in dose itself, but this will not he explored further here. It is also noted that these data were obtained from bar-type specimens, which usually show higher strength and elongation compared to **SS-I** type sheet specimens, as seen, for example, in Table 1.

The elongation **loss** at around 330 to 400°C in 316 type austenitic stainless steels described above was very similar to that of unirradiated 316-CW, obtained from slow strain rate tensile tests (SSRT) **as** shown in Fig.4 (ref. 10). In this case it has been pointed out that transformation to a phase such as α'-martensite during cold working and/or the SSRT was the cause of the elongation minimum at around 350°C (ref. 11). It should he noted that type 316 stainless steel and types similar to it generally have poor phase stability. ***As*** a result, magnetization in such unstable steels is highly likely under high energy neutron irradiation'' or under heavy cold rolling.

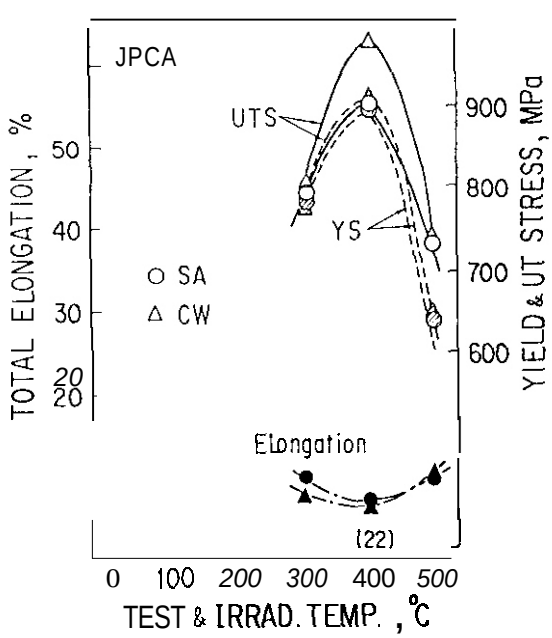

Fig. 3. Temperature dependence of **yield and ultimate strength and total elongation** of **JPCA irradiated in** HFIR.

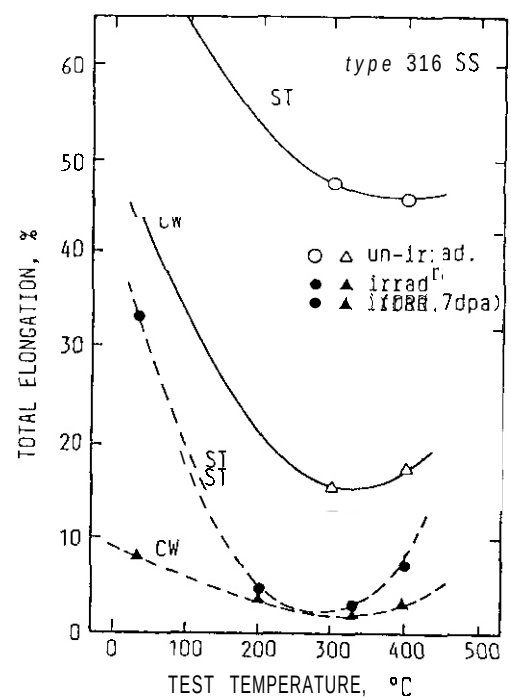

Fig. 4. Comparison of **temperature dependence** of **total elongation of 5316 after ORR irradiation and SSRT (slow strain rate test) elongation** of **unirradiated ones. strain rate = 8.3×10^{-6}/s.**

CONCLUSIONS

Tensile properties of both cold-worked and annealed type 316 stainless steels irradiated in spectrally tailored ORR capsules and in the HFIR at temperatures ranging from ambient to 500°C were examined. The main characteristics are as follows:

(1) The yield and ultimate tensile strengths of annealed specimens increase with increasing irradiation and test temperatures from ambient to around 300°C, followed by a decrease with increasing temperature.

(2) Both YS and UTS of cold-worked specimens have a temperature dependence similar to annealed specimens accompanied by a minimum around 200°C.

(3) An elongation minimum corresponding to the strength maximum was observed in both SA and CW alloys.

(4) Although the situation is complicated by differences in displacement rate and total dose, the above characteristics did not appear to depend upon neutron spectrum. The strength maximum and the elongation minimum were observed at a higher temperature in the HFIR than in spectrally tailored ORR irradiations. This could be explained by a helium effect characterized by the difference in the He:dpa ratio.

FUTURE WORK

Microstrutural analyses on irradiated specimens at low temperatures focusing on black dot?., dislocation loops and phase transformations will continue.

REFERENCES

1. M. P. Tanaka, P. J. Maziasz, A. Hishinuma and S. Hamada, J. Nucl. Mater. 141-143 (1986) 943.
2. J. L. Scott et al., ADIP Ouart. Proe. Rept. Seot. 30. 1985, DOE/ER-0045/15, p. 12.
3. L. R. Greenwood, Fusion Reactor Materials Semiann. Proe. Rept., DOEER-031316 (1989), p. 23; L. R. Greenwood and D. V. Steidl, Fusion Reactor Materials Semiann. Proe. Reot., DOE/ER-0313/8 (1990), p. 34.
4. M. L. Grossbeck, T. Sawai, S. Jitsukawa and L. T. Gibson, Fusion Reactor Materials Semiann. Proe. Revt., DOE/ER-0313/6 (1989), p. 259.
5. A. Hishinuma and S. Jitsukawa, J. Nucl. Mater. 169 (1989) 241.
6. R. L. Klueh and P. J. Maziasz, ASTM STP 956, 1987, pp. 207.
7. P. J. Maziasz, private communication (February 1991).
8. T. Inazumi and G.E.C. Bell, Fusion Reactor Materials Semiann. Proe. Reat., DOE/ER-0313/8 (1990), p. 272.
9. R. E. Stoller and G. R. Odette, ASTM STP 782, ASTM(1982) p. 275.
10. T. Ishiyama, K. Kiuchi and A. Hishinuma, 16th Symposium on Fusion Technology, 3-7 September, 1990.
11. K. Kiuchi, M. Kiuchi and T. Kondo, J. Nucl. Mater. 179-181 (1991) 481-84.
12. For example, J. T. Stanley and L. E. Hendrickson, J. Nucl. Mater. 80 (1979) 69.

THE EFFECT OF HELIUM ON MICROSTRUCTURAL EVOLUTION AND MECHANICAL PROPERTIES OF AUSTENITIC STEELS AS DETERMINED BY SPECTRAL TAILORING EXPERIMENTS - N. Sekimura, University of Tokyo, F. A. Garner, Pacific Northwest Laboratory*, and R. D. Griffin, University of Wisconsin-Madison

OBJECTIVE

The objective of this study is to determine the relative influence of helium generation rate and other important material and environmental variables on neutron-induced microstructural evolution.

SUMMARY

Fe-15Cr-XNi alloys irradiated at both low (0.66 to 1.2) and very high (27 to 58) helium/dpa levels exhibit significantly different levels of strengthening due to an unprecedented refinement of cavity microstructure at the very high helium levels. When compounded with the nickel dependence of helium generation, the cavity distribution for some irradiation conditions and alloy compositions can be driven below the critical radius for bubble-to-void conversion, leading to a delay in swelling. The critical radius also appears to be dependent on the nickel level. The refinement may not have resulted from the high helium levels alone, however, but also may have been influenced by differences in displacement rate and temperature history in the two experiments.

PROGRESS AND STATUS

Introduction

A variety of experiments are underway to assess the interactive influence of helium generation rate and other important variables on the radiation-induced evolution of both microstructure and mechanical properties of simple metals and Fe-Cr-Ni austenitic alloys. One of these involves a comparison of the response of a series of Fe-15Cr-XNi and Fe-YCr-35Ni alloys in two reactors, EBR-II and ORR. The details of these experiments were published earlier by Hamilton, Okada and Garner.[1] They showed that significant differences in both swelling and mechanical properties developed between the EBR-II and ORR specimens [1]. While the swelling values at higher irradiation temperatures were comparable, and exhibited the expected dependence on composition and temperature, swelling was suppressed in ORR at lower temperatures and lower nickel levels, as shown in Figure 1. Even though the swelling was less in the ORR specimens, the radiation-induced changes in yield strength were much larger in ORR than in EBR-II, as shown in Figure 2.

Exuerimental Details

The AD-1 experiment was conducted to doses of 9.5 to 11.3 dpa in EBR-II at relatively low helium/dpa ratios typical of fast reactors. The ratios range from 0.66 to 1.2 appm/dpa for nickel levels of 25 to 45%. The MFE-4 experiment was conducted at a lower displacement rate in ORR to doses of 12.2 to 14.3 dpa at calculated helium/dpa ratios ranging from 27 to 58 appm/dpa[2]. A recent measurement on the 34.5% Ni alloy from the ORR experiment shows that the actual helium levels compare well with the calculated values, being only 4-8% lower[3]. For a given irradiation temperature the displacement level was relatively independent of nickel content in EBR-II, but this was not the case in ORR, where the $^{58}Ni(n,\gamma)^{59}Ni(n,\alpha)^{56}Fe$ reaction that produces the large helium levels in this reactor also makes a measurable contribution to the displacement rate (see Table 1).

The microstructural origins of the behavior shown in Figures 1 and 2 were sought using transmission electron microscopy. This paper presents the results of the annealed Fe-15Cr-XNi (x = 20 to 45) alloys only. Analysis of the interactive effects of helium generation rate with cold working and chromium variations is still in progress and will be published later.

Results

The analysis effort has concentrated on specimens irradiated at 330, 400 and 500°C in ORR and at 395°C in EBR-II. The EBR-II microstructural data at 450°C were reported in an earlier paper.[4] A comparison is shown in Figure 3 of the swelling at 500°C in ORR as determined by both immersion density and microscopy, showing relatively good agreement. No precipitates were observed in any alloy. As can be seen in Figure 4 the major difference between the two sets of irradiations is reflected in the cavity density. Whereas the EBR-II cavity densities exhibit the usual trends, decreasing both with irradiation temperature and nickel content, the densities reached in ORR not only increase with nickel content but reach levels that are two to three orders of magnitude larger than in EBR-II. Cavity densities are in excess of 10^{23} m^{-3} at 400°C and they are even larger at 330°C. These are some of the largest ever observed in reactor irradiation studies. The cavity densities at 400°C increase with nickel level, but show saturation at higher nickel contents.

---

* Operated for the U.S. Department of Energy by Battelle Memorial Institute under Contract DE-AC06-76RLO 1830.

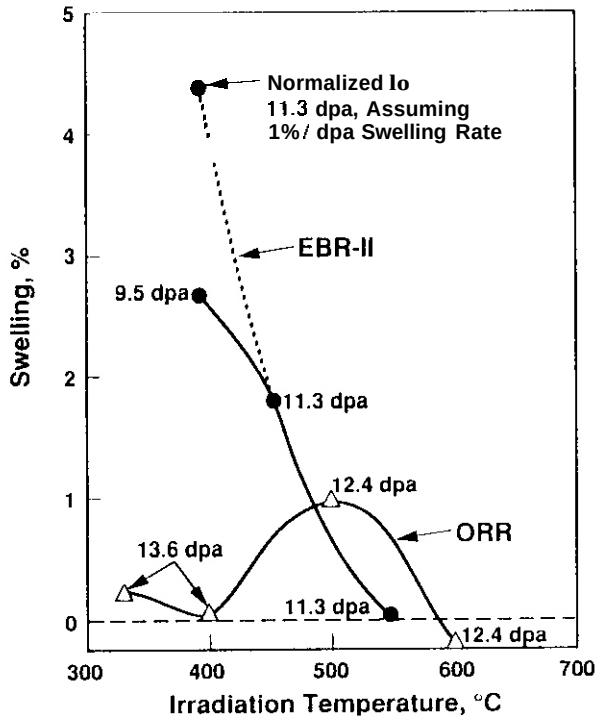

Figure 1. Comparison of swelling behavior of Fe-14.9Cr-24.4Ni in ORR and EBR-II reactors, showing strong suppression in ORR at lower irradiation temperatures' (displacement levels are shown beside each datum.) Similar behavior was observed at other nickel levels.

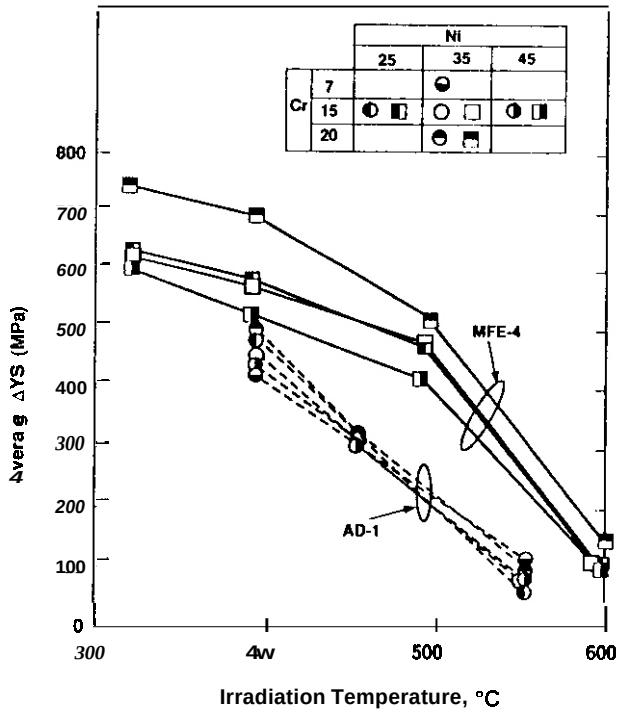

Figure 2. Comparison of radiation-induced changes in yield strengths of Fe-15Cr-XNi and Fe-YCr-35Ni alloys irradiated in the AD-1 experiment in EBR-II and the MFE-4 experiment in ORR.

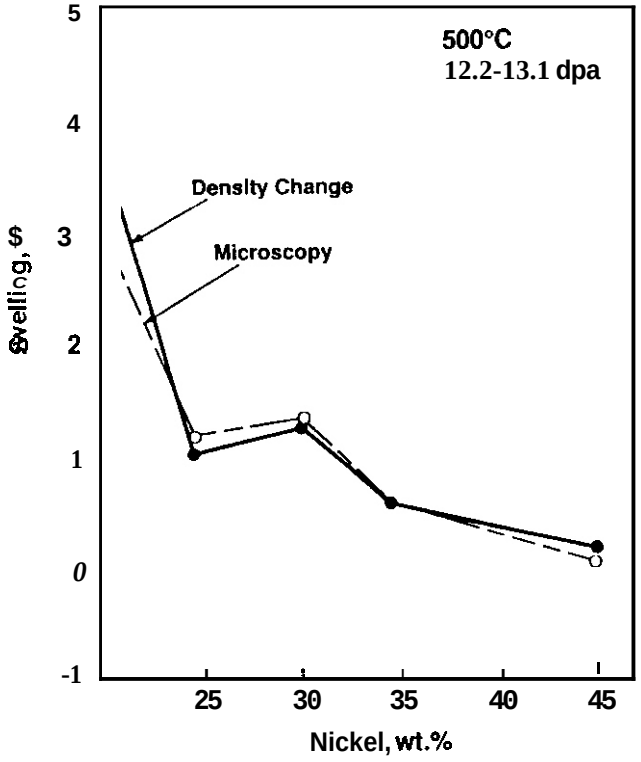

Figure 3. Excellent agreement between two different types of measurement of swelling in Fe-15Cr-XNi alloys irradiated at 500°C in ORR.

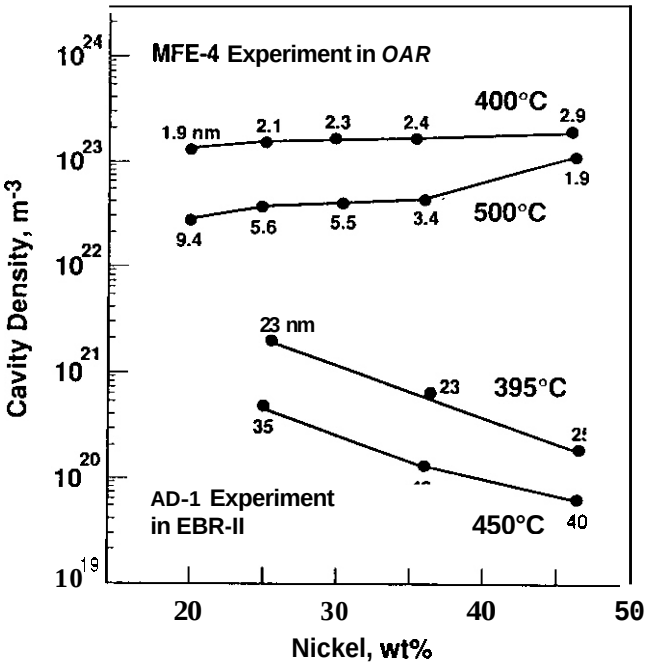

Figure 4. Cavity densities observed in the Fe-15Cr-XNi alloys irradiated in EBR-II and ORR. Mean cavity sizes are shown in nm.

Table 1
Displacement and Helium Levels[a] in the
MFE-4 Experiment in ORR

	330 and 400°C			500 and 600°C		
Composition. wt%	dpa	He. appm	appm/dpa	dpa	He. appm	appm/dpa
Fe-19.7Ni-14.7Cr	13.4	371	27.7	12.2	332	27.2
Fe-24.4Ni-14.9Cr	13.6	463	34.0	12.4	414	33.4
Fe-30.1Ni-15.1Cr	13.8	555	40.2	12.6	495	39.3
Fe-34.5Ni-15.1Cr	14.0	647[b]	46.2	12.7	573[b]	45.1
Fe-45.3Ni-15.0Cr	14.3	832	58.2	13.1	740	56.5

(a) These values were calculated using dosimetry calculations and measurements provided in Reference 2 for individual elements.

(b) Measured values of helium at 34.5 Ni and 330, 400, 500 and 600°C were 4-8% lower, at 597 ± 4, 611 ± 7, 533 ± 3 and 552 ± 7 respectively.

The width of the size distribution of the cavities in the ORR experiment at 500°C was observed to become progressively smaller as the nickel content increased, as shown in Figure 5. This contrasts with the behavior observed in EBR-II, where cavities are in general larger but whose sizes are relatively independent of nickel content at a given irradiation temperature.

In contrast to the behavior observed at 500°C, the cavity sizes at 330 and 400°C are very small, but increase with nickel content as shown in Figure 6. Note that the cavity sizes for the most part do not change significantly between 330 and 400°C.

Figure 7 compares loop densities as a function of nickel content from the 500°C ORR specimens with those of another comparable experiment conducted in EBR-II[5]. The dislocation structure in the ORR experiment was dominated by a high density of loops at all nickel levels, while the EBR-II experiment contained mostly tangled dislocation segments, especially at lower nickel levels.

Discussion

In the range of 400-500°C the swelling of Fe-Cr-Ni ternaries in EBR-II is known to exhibit a transient regime of ~10 dpa prior to swelling at a rate of ~1%/dpa.[6] If this trend also pertains to swelling at the lower displacement rate of ORR then these alloys would have accumulated 280-580 appm helium prior to reaching the 10 dpa level. The large decrease in swelling at lower temperatures at all nickel levels relative to that in EBR-II may reflect the impact of the very large and almost unprecedented density of cavities arising from the high helium levels.

The swelling in ORR at 500°C increases with declining nickel content as the cavity density decreases from the 10^{23} to the 10^{22} m^{-3} level, but at this temperature in EBR-II it is known that swelling also increases as the nickel level falls.[6] Note in Figure 1 that swelling levels in the 24.4Ni alloy at 500°C were comparable in the two reactors. Thus the behavior observed at 500°C reflects a lesser impact of the helium-induced refinement, while still responding to the nickel's influence on swelling via its effect on vacancy diffusivity and dislocation bias.[7-9]

It is significant that the cavity sizes at 45% Ni and 500°C, as well as at all nickel levels at 330 and 400°C, are small enough that most of them are probably helium bubbles rather than voids. At these sizes, the cavities may have been driven below the critical radius for bubble-to-void conversion.[10] Cavity densities and sizes increased with nickel content at these temperatures, but were not proportional to either the nickel level or the helium content. This suggests that the critical cavity radius for bubble-to-void conversion increases with nickel content. This experimental evidence is consistent with the results of other studies, in which a variety of nickel-dependent mechanisms of swelling behavior were proposed.[5,7-9,11] The extensive refinement of the cavity microstructure is probably the major reason for the much larger level of strengthening observed in the tensile tests on specimens irradiated in ORR. The microstructural results indicate that, at all irradiation temperatures studied, the refinement of cavities (along with a smaller refinement of loop microstructure) is sufficient to account for the higher levels of strengthening observed in the ORR experiment.

It is tempting at this point to attribute the observed refinement in ORR solely to the higher helium levels, but there appears to be other contributing factors. Hamilton and Garner have recently irradiated the 25 and 45% Ni alloys in FFTF using ^{59}Ni isotopic doping to study the effect of helium in a truly single variable manner[12,13]. In the absence of displacement rate variations, a helium/dpa ratio of ~15 appm/dpa yielded no significant variations in swelling or tensile properties at 365°C. Yet in the ORR experiment a helium/dpa ratio roughly twice this level (34 appm/dpa for the 24.4Ni alloy) caused near-total suppression of swelling at 330 and 400°C. This change in behavior is too abrupt to explain confidently in terms of helium only, and would require invoking some very sensitive threshold behavior in which a factor of only two increase could provoke such an exaggerated response.

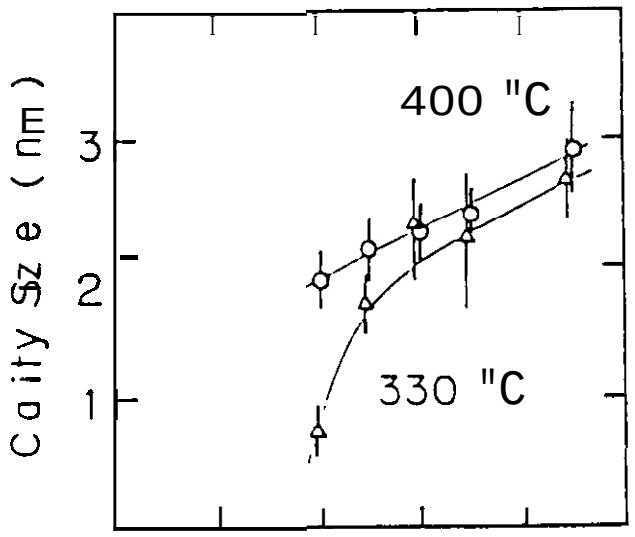

Figure 5. Cavity sizes observed in Fe-15Cr-XNi alloys irradiated in ORR at 330 and 400°C.

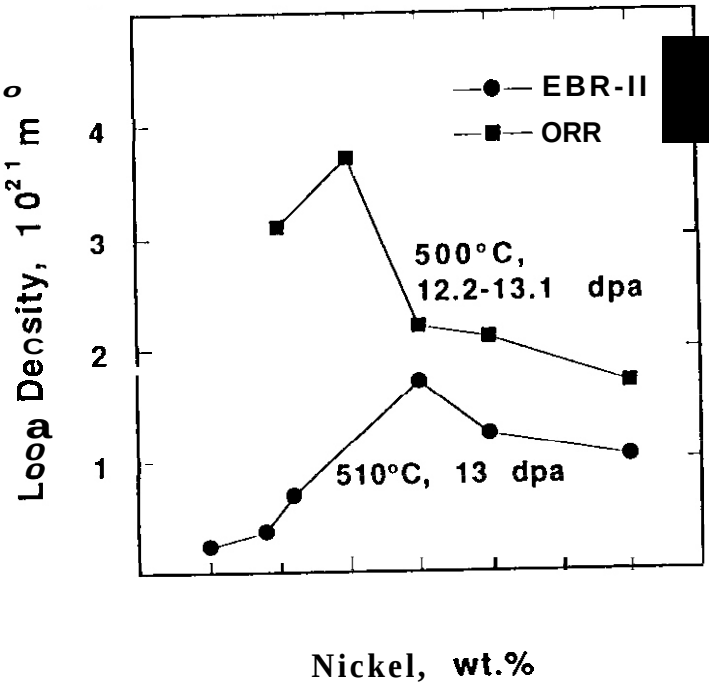

Figure 7. Comparison of loop densities observed at ~500°C in the MFE-4/ORR experiment ana in the AA-7/EBR-II experiment.[5]

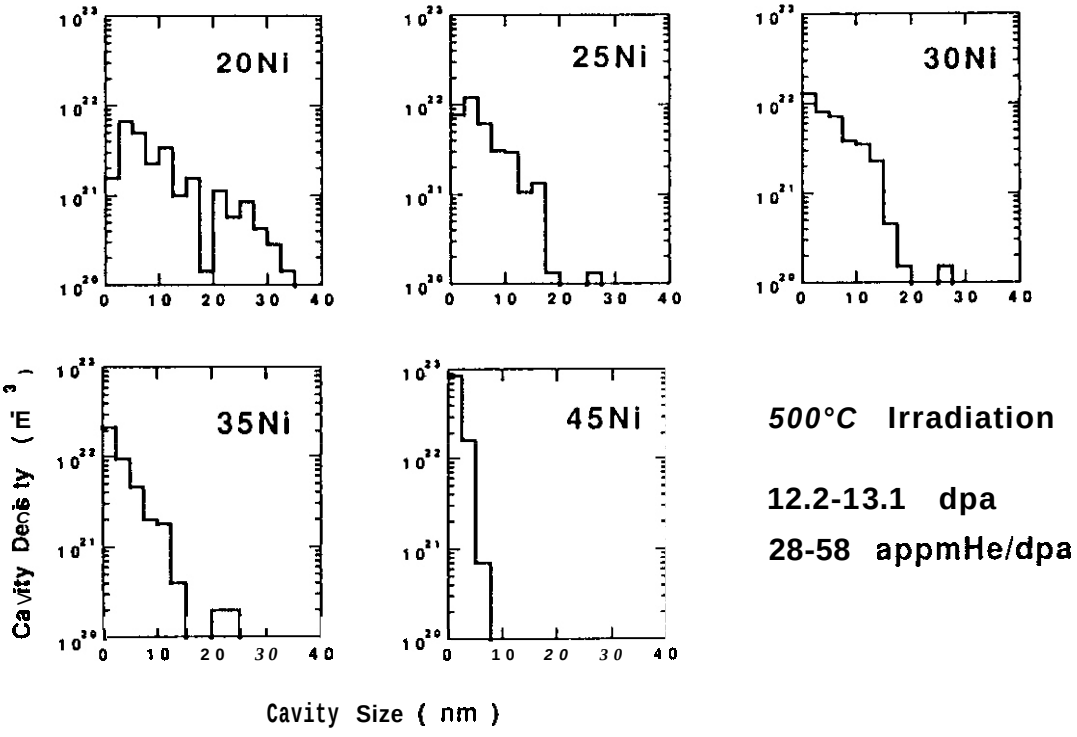

Figure 6. Cavity size distributions observed in Fe-15Cr-XNi alloys irradiated in ORR at 500°C.

However, there are two important differences between the manner in which the ORR and EBR-II experiments were conducted. First, the ORR experiment proceeded at roughly an order of magnitude lower displacement rate and microstructural development and its macroscopic consequences are known to be very sensitive to displacement rate [14]. If the lower displacement rate and higher helium generation rate in ORR retard the growth and infaulting of loops at lower nickel levels, as shown in Figure 7, this could cause the lower swelling observed. At higher nickel levels, however, it appears that the higher helium production rate is the main reason for loop refinement.

More recently, however, it has been shown that details of temperature history in fission reactors can have a very large impact on microstructural evolution, especially when irradiation proceeds, even for very brief periods, at lower temperatures [15-19]. The ORR reactor had a low inlet temperature and a high gamma heating rate, and thus irradiation temperatures were closely tied to reactor power level. One facet of ORR operation was the automatic step-down of the power level periodically for periods of 10-30 min, resulting in periodic temperature decreases on the order of 100-150°C. Garner, Sekimura and their coworkers recently showed experimentally that only 0.01 dpa accumulated under such conditions can cause a significant refinement of microstructure.[18,19] It may be possible that helium bubble nucleation at higher nickel levels is particularly sensitive to refinement under such conditions.

CONCLUSIONS

Comparison of microstructures developed in Fe-Cr-XNi alloys irradiated in EBR-II and ORR shows that very large amounts of helium can significantly strengthen alloys via their effect on refinement of cavity microstructure. In addition, this refinement may have as one of its consequences a reduction of individual cavity sizes below the critical radius of bubble-to-void conversion for some alloys and irradiation conditions. It also was found that the critical radius appears to increase with nickel content. However, there also appears to be a possibility that the refinement in ORR was assisted by significant differences in displacement rate and temperature history compared to that found in EBR-II.

ACKNOWLEDGMENTS

The ORR portion of this work was sponsored by the Japan/U.S. FFTF-MOTA Collaboration of U.S. Department Of Energy and Monbusho, the Japanese Ministry for Education, Science and Culture. The AD-1 portion was conducted under the auspices of the Northwest College and University Association for Science at Pacific Northwest Laboratory.

FUTURE WORK

Microscopy examination will continue, concentrating on the effects of chromium variations and cold work Examanation will also proceed for specimens irradiated at 600°C.

REFERENCES

1. M. L. Hamilton, A. Okada and F. A. Garner, J. Nucl. Mater., 179-181 (1991) 558-562.

2. L. R. Greenwood, in Fusion Reactor Materials Semiannual Prowess Report DOE/ER-0313/6 (1989) pp. 29-35.

3. F. A. Garner and B. M.Oliver, in Fusion Reactor Materials Semiannual Prowess Report, DOE/ER-0313/9, (1991) pp. 58-60.

4. H. R. Brager, F. A. Garner and M. L. Hamilton, J. Nucl. Mater., 133 and 134 (1985) 594-598.

5. T. Muroga, F. A. Garner and S. Ohnuki, J. Nucl. Mater., 179-181 (1991) 546-549.

6. F. A. Garner and H. R. Brager, ASTM STP 870, 1985, pp. 187-201.

7. F. A. Garner and A. S. Kumar, ASTM STP 955, pp. 289-314.

8. J. J. Hoyt and F. A. Garner, J. Nucl. Mater. 179-181 (1991) 1096-1099.

9. W. A. Coghlan and F. A. Garner, ASTM STP 870 (1985) 289.

10. G. R. Odette, et al., J. Nucl Mater., 85 and 86 (1979) 533-545, also 103 and 104 (1981) 1361-1366 and also 122 and 123 (1984) 514-519.

11. E. H. Lee and L. K. Mansur, Philos. Mag. A52 (1985) 493.

12. F. A. Garner, M. L. Hamilton, R. L. Simons and M. K. Maxon, J. Nucl. Mater., (1991) 554-557.

13. M. L. Hamilton and F. A. Garner, this conference.

14. F. A. Garner, H. L. Heinisch, R. L. Simons and F. M. Mann, Rad. Eff. Def. Sol., 113 (1990) 229-255.

15. M. Kiritani, J. Nucl. Mater., 160 (1988) 135-141.

16. M. Kiritani, T. Yoshiie, S. Kojima, Y. Satoh and K. Hamada, J. Nucl. Mater., 174 (1990) 327-351.

17. N. Yoshida, J. Nucl. Mater., 174 (1990) 220-228.

18. N. Sekimura and S. Ishino, J. Nucl. Mater., 179-181 (1991) 542-545.

19. F. A. Garner, A. M. Ermi, N. Sekimura and J. W. Newkirk, Fusion Reactor Materials Semiannual Prowess ReDort DOE/ER-0313/11 (1992) in press.

THE COMPLEX ROLE OF PHOSPHORUS IN THE NEUTRON-INDUCED SWELLING OF TITANIUM-MODIFIED AUSTENITIC STAINLESS STEELS - F. A. Garner, Pacific Northwest Laboratory and M. A. Mitchell, University of Illinois

OBJECTIVE

The objective of this study is to determine the factors that control the microstructural evolution of structural materials during irradiation.

SUMMARY

At very low levels (<0.02 wt%), phosphorus additions to austenitic stainless steels often cause a substantial increase in void swelling. This phenomenon occurs in both simple model alloys and more complex solute-modified alloys typical of materials being considered for breeder reactor or fusion reactor service. This effect is observed in both annealed and cold-worked steels. At levels above 0.02% phosphorus, there is a reversal in behavior and swelling declines. This non-monotonic behavior tends to occur at lower irradiation temperatures in relatively simple alloys, but often persists to much higher temperatures in more complex titanium-modified alloys employed in the fusion and breeder reactor programs.

PROGRESS AND STATUS

Introduction

Until recently, it was thought that increasing levels of phosphorus addition to austenitic stainless steels always resulted in monotonic reductions in neutron-induced swelling at temperatures and displacement rates typical of fast breeder or fusion reactor environments.[1-4] Several recent studies, however, have shown that at temperatures below ~500°C, the swelling of Fe-25Ni-15Cr(wt%) exhibits a non-monotonic response to phosphorus addition, first strongly increasing in swelling in the range of 0<P<0.02 wt% and then declining steeply thereafter, as shown in Figures 1 and 2. The range between 0 and 0.04% phosphorus has not been studied in most other irradiation studies and a steep peak in swelling with phosphorus was not detected. At higher irradiation temperatures, a peak does not occur in the swelling of Fe-25Ni-15Cr.

Garner and coworkers have proposed that this complex behavior indicates that two or more competing mechanisms are operating to control swelling and that the outcome of the competition is determined not only by the phosphorus level but also by the action of both environmental variables such as temperature and displacement rate, as well as material variables such as composition and thermomechanical treatment[5-8].

The behavior observed in Fe-25Ni-15Cr may not be typical of steels being considered for breeder reactor or fusion service, however. Such steels are lower in nickel level and contain significant levels of other solutes known to affect void swelling, particularly Mo, Ti, Si, and C. Although phosphorus additions are also used to reduce swelling in these steels, very little attention has been paid to the range between 0.0 and 0.04%P. Figures 3 and 4 present some previously published data on titanium-modified steels that appear to confirm that a simple monotonic reduction in swelling with phosphorus level occurs at both relatively high and relatively law irradiation temperatures. Although Figure 4 contains data at ~0.02% phosphorus, Figure 3 does not; however, and an intermediate peak in swelling might exist.

The data sets in Figures 3 and 4 were derived from the MV-III material variables experiment, for which only a portion of the results have been published[1,2,9]. One of the variables studied in this experiment was that of phosphorus content, and many alloys contained phosphorus variations in the range between 0.0 and 0.08%. The objective of this study is to determine whether the non-monotonic behavior observed in simple Fe-25Ni-15Cr alloys also occurs in more complex titanium-modified alloys currently being employed in fusion or breeder reactor materials research.

Exoerimental Efforts

The MV-III experiment involved 150 heats of modified AISI 316 stainless steels, all of which contained approximately 14 weight percent (wt%) nickel and silicon levels greater than or equal to 0.7 wt%. Each was designated by a heat number starting with the letter A followed by a one-to-three digit number. Many of these compositional variations on AISI 316 existed in more than one thermomechanical condition and were irradiated at as many as six temperatures. This experiment thus involved over two thousand combinations of material/irradiation conditions. There were two major and several minor categories of specimens. The largest portion of the experiment comprised alloys having variations in a number of major solute elements (Ti, Si, P, Zr, Cr, C, Mo), with each element having at least two and sometimes as many as five different concentration levels. One of the other categories of allovs was used to exolore the influence of minor trace impurities. In this series, alloys designated as "high purity" were hade from high purity ingredients and had a nominal alloy composition of Fe-16Cr-14Ni-2.5Mo-2.0Mn-0.8Si-0.2Ti-0.04C-0.01Zr. The

*Operated for the U.S. Department of Energy by Battelle Memorial Institute under Contract DE-AC06-76RLO 1830.

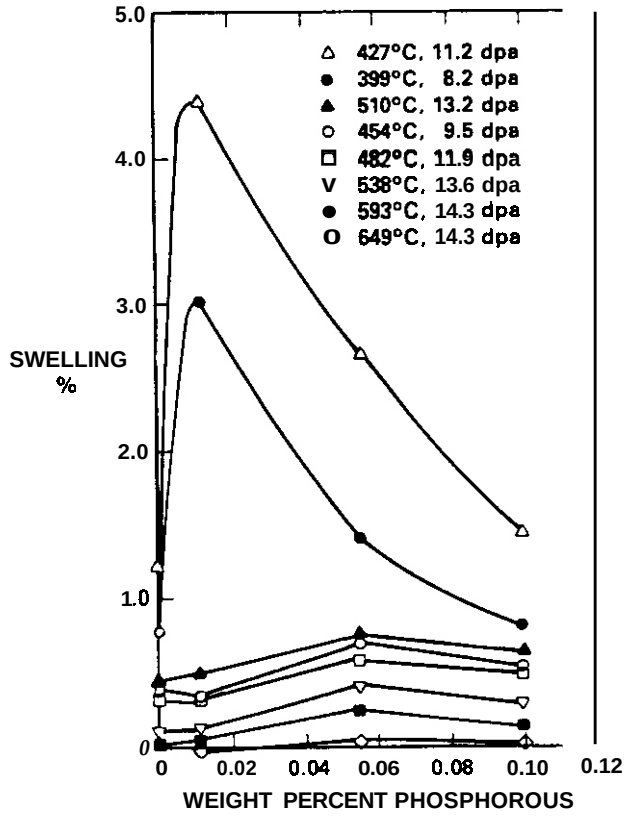

Figure 1. Influence of phosphorus on neutron-induced swelling of solution-annealed Fe-25Ni-15Cr at various combinations of temperature and displacement damage after irradiation in EBR-II[5].

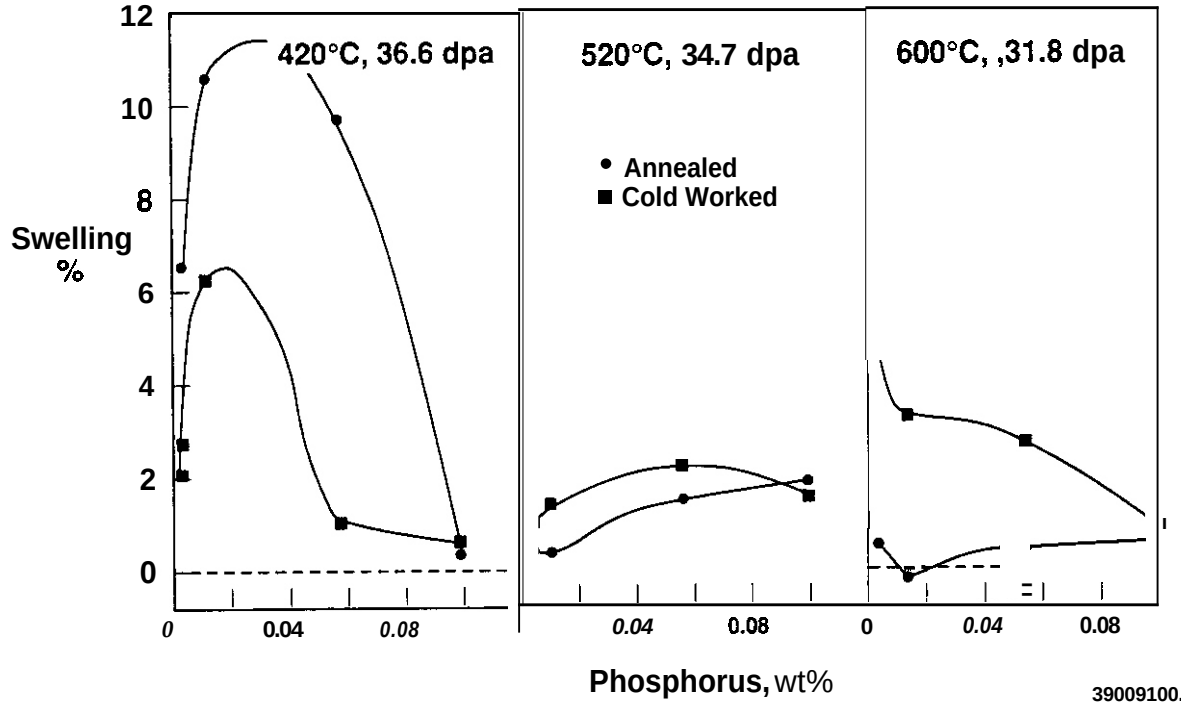

Figure 2. Influence of phosphorus and cold work on neutron-induced swelling of Fe-25Ni-15Cr under various conditions following irradiation in FFTF.[6]

"trace" impurity alloys had the same base composition but contained small and typical amounts (0.01 to 0.05 wt%) of ten minor elements (Al, As, Co, Cu, N, Nb, Sn, Ta, V and W) normally found in AISI 316. At these levels, phosphorus is also considered to be a trace element but it had already been included as a major solute in the more extensive alloy series at levels ranging from 0.01 to 0.08 wt%. The data shown in Figure 3 and 4 are derived from the high purity and trace alloy series. Note that no appreciable difference in swelling arises from variations in either trace elements or zirconium.

The specimens were prepared in the form of microscopy disks (3 mm diameter by 0.3 mm thick) and were contained in sodium filled subcapsules. The irradiation was conducted in Row 2 of the EBR-II fast reactor at displacement rates ranging from 0.6 to 1.1 x 10^{-6} dpa/s. Each 1.0 x 10^{22} n/cm^2 (E>0.1 MeV) in this reactor produced approximately 5 dpa of displacement damage. Displacement levels as large as 75 dpa were reached at some irradiation temperatures. After removal and cleaning, the radiation-induced changes in density were measured using an immersion density technique accurate to ±0.16% swelling. Due to the large size of the specimen matrix and limited Funding, however, only selected subsets of the specimens were chosen for density measurement.

The MV-III swelling data library was reviewed to provide groups of alloys that varied primarily in phosphorus content. Small variations in minor elenients such as Zr that were demonstrated in the MV-III experiment to have little influence on swelling were ignored while defining these groups. Since not all specimens were measured at the termination of the experiment, the comparisons for each alloy group are not always derived from the same combinations of starting condition, temperature, and fluence. Overall, however, the results are quite illuminating.

Results

In data subsets where alloys in the middle of the 0.0-0.04% P range were not prepared or not measured, the swelling appears to decrease in the usual monotonic behavior, as shown in Figures 5 and 6. Note, however, that in the A116/A174 comparison that two relatively low swelling conditions appear to increase in swelling. Based on the results observed in other alloy groups, this is thought to be the consequence of an intermediate peak in swelling that was not detected.

Figure 7 shows a much more detailed comparison for another alloy group, indicating very steep intermediate peaks at or below 0.02% P for both annealed and cold worked alloys. As implied by the dotted lines in Figure 7 it is very difficult to determine how pronounced the peaks should be drawn without data in the 0.0-0.02% range. The data subsets shown in Figures 7-9 confirm that such intermediate peaks in swelling are very common, although under some conditions, especially for the cold worked starting state, only monotonic behavior is observed. Note, however, that non-monotonic behavior is observed over the entire temperature range examined in this study, while it did not occur above ~500°C in the less complex Fe-25Ni-15Cr-xP alloys.

Discussion

If each datum defining a peak in swelling at ~0.02% were to be discarded, it would appear in almost every case that swelling decreased monotonically with phosphorus content. The replacement of this previously prevailing perception with that of non-monotonic behavior leads to a number of interesting conclusions.

First, the steepness of the swelling response at the lowest phosphorus levels implies that apparently negligible phosphorus differences in "pure" alloys cannot be confidently neglected. This probably accounts in part for the variability in the onset of swellinq often observed by different researchers working on nominally identical alloys. Trace elements such as-phosphorus were not always measured in many earlier experiments. Since phosphorus levels are difficult to control precisely at very low levels for large industrial heats, it may not be prudent to specify relatively low phosphorus levels in defining the composition of a steel for fusion or breeder reactor service. This may result in variability in swelling from heat to heat.

Second, the steep increase of swelling occurs at temperatures and phosphorus levels for which phosphide precipitation does not occur in either simple alloys[7,8,10,11] or complex alloys such as the ones used in this study.[12,13] Thus, the role of phosphorus to increase swelling must be exerted while it is in solution. It has also been shown. however. that the subseauent decline in swellina of Fe-25Ni-15Cr for P>0.02% at lower irradiation temperatures also occurs without precipitation.[7,8] This suggests that two or more solute-related mechanisms are in competition to produce the non-monotonic behavior. Precipitation-related mechanisms may assert themselves following phosphide formation at higher temperatures and phosphorus levels, as discussed by Lee and coworkers,[14-17] and this would then add to the complexity of the competition.

Third, there may be a strong consequence to the changing level of phosphprus remaining in solution during and after phosphide formation. Whereas the studies by tee and coworkers [14-17] tended to emphasize only the physical aspect of precipitate interaction with point defects and helium atoms, the formation of phosphides will reduce the matrix phosphorus level from the suppression side of the swelling peak to the enhancement side. Perhaps void formation does not begin until phosphide formation is nearly complete and the phosphorus level is <<0.02%.

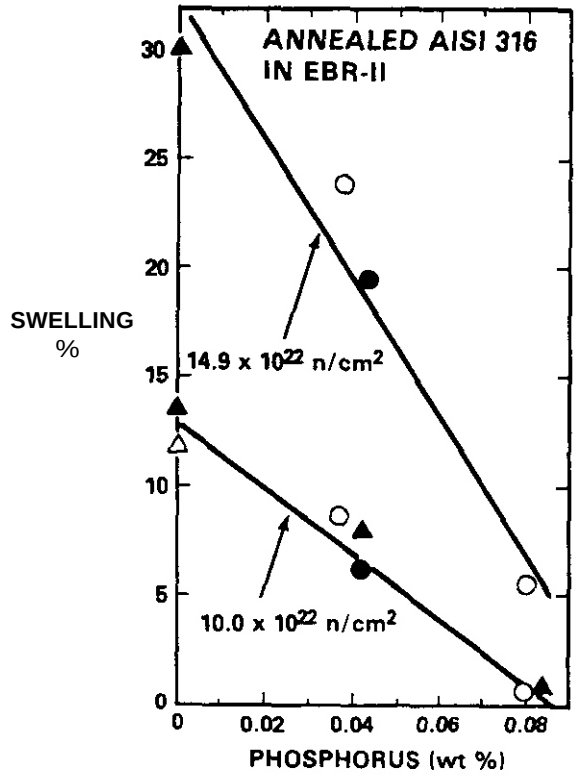

Fig. 3. The relative influence of phosphorus, zirconium, and trace impurities on the swelling of annealed "high purity" Fe-16Cr-14Ni-2.5Mo-2.0Mn-0.8Si-0.2Ti-0.04C alloys after irradiation to 50 and 75 dpa at 540°C. The open circles denote alloys with 0.1 wt % Zr, and the closed circles denote 0.01 wt % Zr.[2]

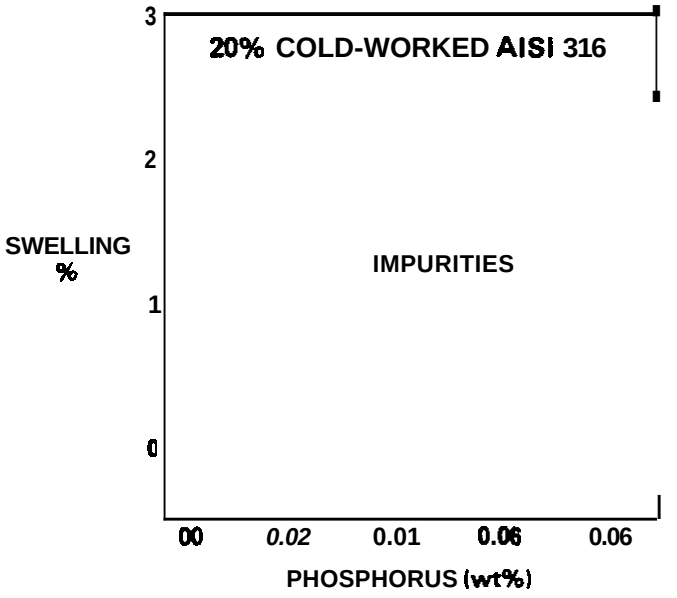

Fig. 4. Swelling at 425°C and 55 dpa (11.0×10^{22} n cm^{-2}, E >0.1 MeV) of the same alloys shown in Fig. 3 but in the cold worked condition, with one additional alloy at –0.02% P.[2]

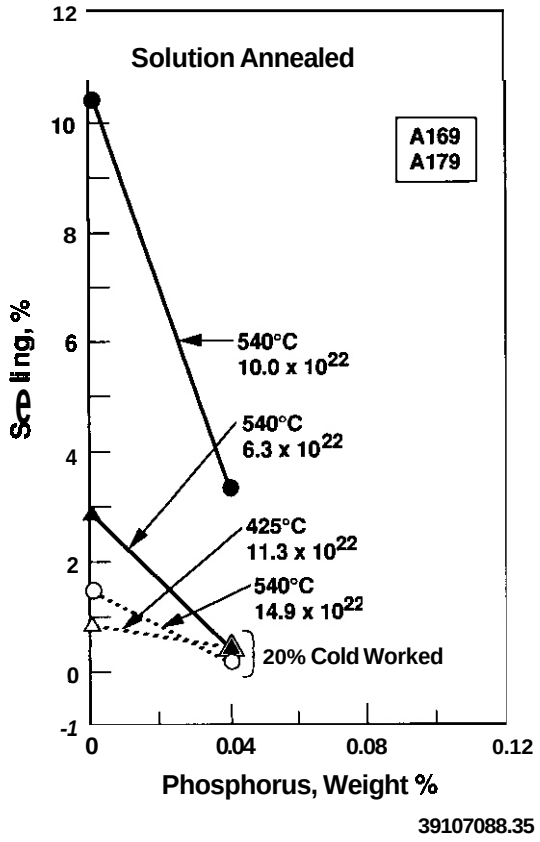

Fig. 5. "Apparently" monotonic decrease of swelling for Fe-14.8Cr-13.8Ni-2.5Mo-2.0Mn-1.55Si-0.2Ti-0.04C alloys observed with phosphorus content in the MV-III experiment. Alloy designations shown in the inset are listed in order of increasing phosphorus level.

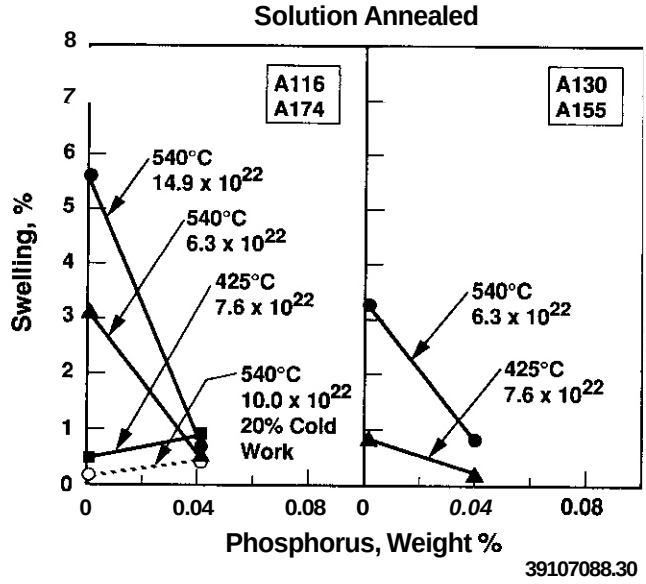

Fig. 6. "Mostly" monotonic decrease of swelling observed for (a) Fe-10.5Cr-13.8Ni-2.4Mo-2.0Mn-0.7Si-0.2Ti-0.04C and (b) Fe-16.3Cr-13.7Ni-2.4Mo-2.0Mn-0.8Si-0.2Ti-0.04C alloys with phosphorus content in the MV-III experiment.

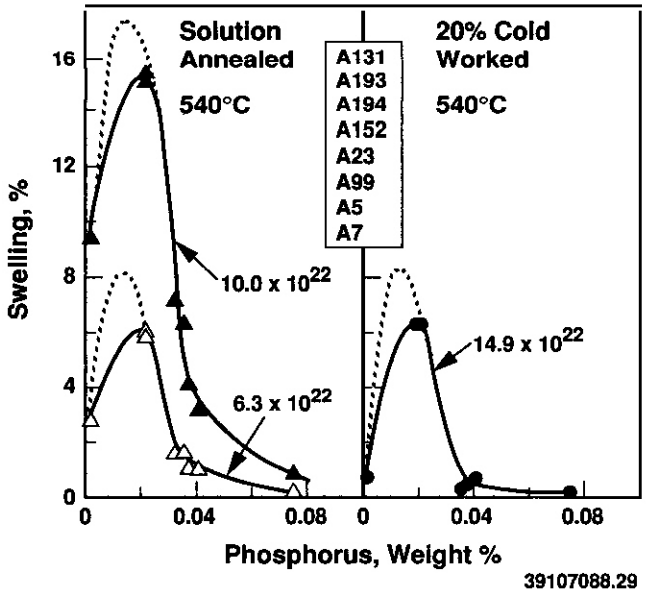

Fig. 7. Non-monotonic swelling behavior of Fe-16.2Cr-13.8Ni-2.5Mo-2.0Mn-1.5Si-0.2Ti-0.4C alloys with phosphorus content in the MV-III experiment.

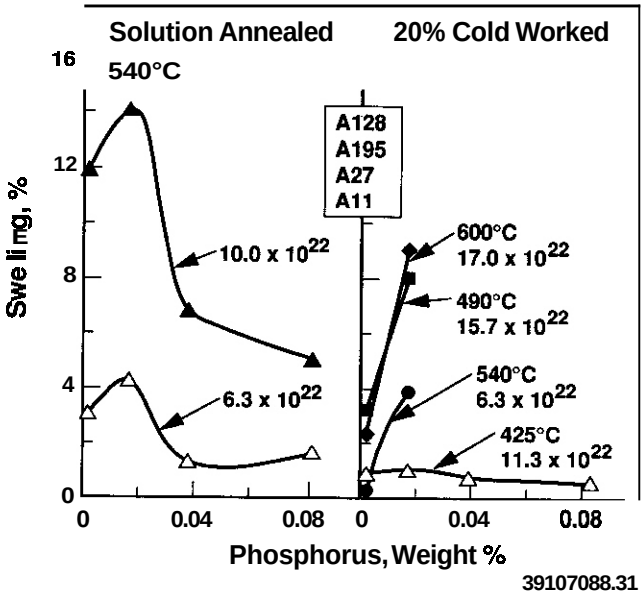

Fig. 8. Swelling of Fe-16.2Cr-13.7Ni-2.5Mo-2.0Mn-0.7Si-0.1Ti-0.04C alloys observed in the MV-III experiment.

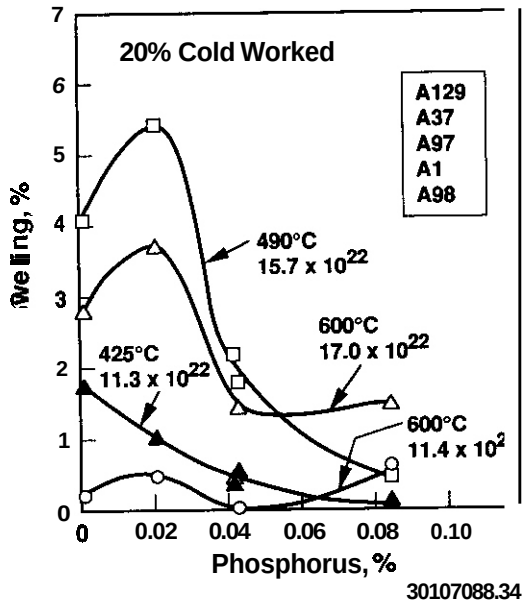

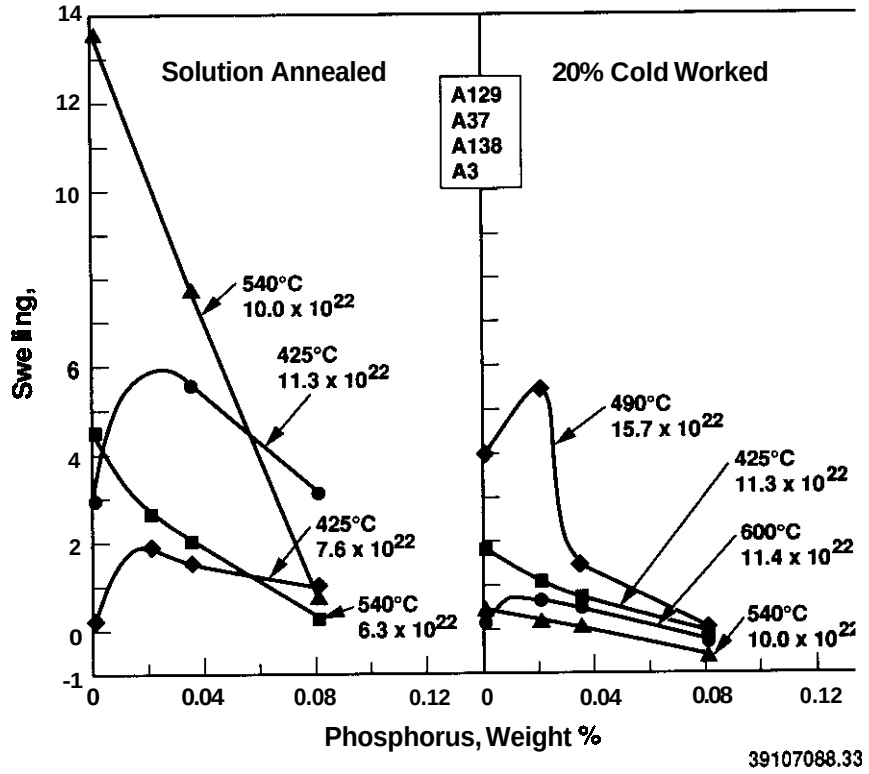

Figure 9. Swelling of Fe-16.3Cr-13.6Ni-2.5Mo-2.0Mn-0.7Si-0.2Ti-0.04C alloys observed in the MV-II! experiment.

Fourth, the formation of phosphides has been demonstrated to be strongly enhanced by the presence of elements such as titanium and silicon.[15,17,18] Thus, it is not surprising to observe that the action of phosphorus changes with alloy content. One consequence of this interaction is that the non-monotonic behavior appears to extend to much higher temperatures in the solute modified alloys than was observed in the unmodified higher nickel alloys shown in Figures 1 and 2.

Finally, the temperature dependence of phosphorus influence in solute-free alloys suggests that in charged particle irradiation studies conducted at higher temperatures (to compensate for increases in displacement rate), one may not observe the non-monotonic behavior. Lee and Packan, for instance, did not observe such behavior in ion bombardment studies of Fe-13.7Cr-16.5Ni with 0.0, 0.01 and 0.05 wt% phosphorus.[17]. Garner and Kumar[5] have also noted that the temperature and nickel dependence of phosphorus solubility must be taken into account when comparing neutron and charged particle studies.

It was demonstrated earlier in the MV-III experiment that the various roles of phosphorus manifest themselve in these titanium-modified alloys only as changes in the duration of the transient regime of swelling."' There is much microstructural and microchemical evidence, however, that shows that phosphorus is a very active element at all stages of the microstructural evolution. Evidence has been published to demonstrate strong binding of phosphorus with interstitials, thereby influencing the rate of Frank loop nucleation[17,18,19] and solute segregation.[20] Evidence is also available on the influence on the rate of dislocation recovery[3,17] and binding with vacancies,[21,22] thereby affecting void growth[1,2,23] and solute segregation.[19] In addition, there are precipitate-related mechanisms such as changes in matrix composition,[1,3] collection of helium in subcritical cavity nuclei,[15-17] and the precipitate-collector effect on radiation-induced point defects.[24-26] Due to the complexity of the many potential roles of phosphorus, it is not surprising that under a given set of material and environmental conditions, one subset or another of the mechanisms might dominate the behavior in a given experiment, while another set oi conditions might produce a different outcome. Garner and Kumar have presented a review of charged particle data on phosphorous effects that demonstrates further the variability of swelling in response to both phosphorus level and environmental differences.[5] They also note that silicon additions yield a similar non-monotonic swelling behavior. Garner, Lauritzen and Mitchell have also shown that molybdenum influences swelling in a similar manner.[27]

CONCLUSIONS

At very low levels (<0.02%), phosphorus additions to austenitic steels often cause a substantial increase in void swelling. This phenomenon occurs in both simple model alloys and more complex alloys typical of titanium-modified austenitic steels being considered for breeder reactor or fusion reactor service. This effect is observed in both annealed and cold-worked steels. At levels above ~0.02% phosphorus, there is a reversal in behavior and swelling declines. This non-monotonic behavior tends to occur at lower irradiation temperatures but often persists to much higher temperatures in more complex alloys. The variability of swelling in response to phosphorus level and other important variables suggests that a number of microchemical and microstructural mechanisms are competing to control the onset of void swelling.

FUTURE WORK

No further effort is planned.

REFERENCES

1. F. A. Garner and H. R. Brager, J. Nucl. Mater. 133-134 (1985) 511

2. F. A. Garner and H. R. Brager, J. Nucl. Mater. 155-157 (1988) 833.

3. M. Itoh, S. Onose and S. Yuhara, in Radiation-Induced Changes in Microstructure: 13th Inter. Symp. (Part 1) ASTM STP 955, F. A. Garner, N. H. Packan and P. S. Kunar, Eds., American Society for Testing and Materials, Philadelphia, 1987, p. 114.

4. J. F. Bates, R. W. Powell and E. R. Gilbert in Effects of Radidtion on Materials: Tenth Conference, ASTM STP 725, D. Kramer, H. R. Brager and J. S. Perrin, Eds., American Society tor Testing and Materials, 1981, pp. 713-734.

5. F. A. Garner and A. S. Kumar, in Radiation-Induced Changes in Microstructure: 13th Inter. Symp. (Part 1) ASTM STP 955, F. A. Garner, N. H. Packan and A. S. Kumar, Eds., American Society for Testing and Materials, Philadelphia, 1987, pp. 289-314.

6. F. A. Garner in Fusion Reactor Materials Semiannual Progress Report DOE/ER-0313/9, 1990, pp. 50-57.

7. T. Muroga, F. A. Garner and J. M. McCarthy, J. Nucl. Mater. 168 (1989) 109.

8. F. A. Garner, K. Miyahara and J. W. Newkirk, to be presented at the Fifth Internatidnal Conference on Fusion Reactor Materials, Clearwater, FL, Nov 1992.

9. F. A. Garner, H. R. Brager and R. J. Puigh, J. Nucl. Mater. 133-134 (1985) 535.

10. H. Kawanishi, F. A. Garner and R. L. Simons, J. Nucl. Mater. 179-181 (1991) 511

11. J. F. Stubbins and F. A. Garner, J. Nucl. Mater. 179-181 (1991) 523.

12. E. H. Lee, P. J. Maziasz and A. F. Rowcliffe, in Phase Stability During Irradiation, J. R Holland, L. K. Mansur and D. I. Potter, Eds., TMS-AIME, 1981, p. 219.

13. W. J. S. Yang in Radiation-Induced Changes in Microstructure: 13th Inter. Symp. (Part 1) ASTM STP 955, F. A. Garner, N. H. Packan and A. S. Kumar, eds., American Society for Testing and Materials,. Philadelphia, 1987, p. 888.

14. E. H. Lee, L. K. Mansur and A. F. Rowcliffe, J. Nucl. Mater. 122-123 (1984) 299.

15. E. H. Lee and L. K. Mansur, J. Nucl. Mater. 141-143(1986)695.

16. E. H. Lee and L. K. Mansur, Phil. Mag., in press.

17. E. H. Lee and N. H. Packan, in Effects of Radiation on Materials: 14th Inter. Symp. Vol. I, ASTM STP 1046, N. H. Packan, R. E. Stoller and A. S. Kumar, Eds., American Society for Testing and Materials, Philadelphia, 1988, pp. 133-146.

18. H. Watanabe, A. Aoki, T. Muroga and N. Yoshida, J. Nucl. Mater. 179-181 (1991) 529.

19. H. Watanabe, A. Aoki, H. Murakami, T. Muroga and N. Yoshida, J. Nucl. Mater. 155-157 (1988) 815

20. S. M. Murphy and J. M. Perks, J. Nucl. Mater. 171(1990)360.

21. A. F. Rowcliffe and R. B. Nicholson, Acta Met. 20(1972)143.

22. A. Azarian and K. Kheloufi, J. Nucl. Mater. 97(1981)25.

23. W. A. Coghlan and f. A. Garner in Radiation-Induced Changes in Microstructure: 13th Inter. Symp. (Part 1) ASTM STP 955, F. A. Garner, N. H. Fackan and A. S. Kumar, Eds., American Societv For Testing and Materials, Philadelphia, 1987, pp. 315-329.

24. L. K. Mansur, Phil. Mag. A44 (1981) 867

25. E. H. Lee, A. F. Rowcliffe and L. K. Mansur, J. Nucl. Mater. 103-104 (1981) 1403

26. A. D. Brailsford and L. K. Mansur, J. Nucl. Mater. 103-104 (1981) 1403.

27. F. A. Garner, T. Lauritzen and M. A. Mitchell, to be published in the proceedings of the 16th ASTM International Symposium on Cffects of Radiation on Materials, Denver, CO, June 22-24, 1991.

The Strong Influence of Temper Annealing Coriditions on the Neutron-Induced Swelling of Ccld Worked Austenitic Steels - F. A. Garner, (Pacific Northwest Laboratory*), J. F. Bates, (Westinghouse Hanford Company) and M. A. Mitchell, (University of Illinois)

Objective

The objective of this study is to define the variables that control the radiation-induced evolution of microstructure and mechanical properties in structural metals.

Summary

Although cold working is known to strongly influence neutron-induced swelling of austenitic stainless steels, it also appears that the annealing temperature employed before cold working has an equally large effect. Two irradiation studies conducted on AISI 316 stainless steel indicate that increasing the temperature of the intermediate temper anneal leads in general to a shortening of the transient regime of swelling. The evidence is consistent with the influence of both annealing temperature and irradiation temperature on carbide formation and its subsequent influence on the microchemical evolution and swelling of the steel.

STATUS AND PROGRESS

Introduction

The development of fission-fusion correlations cannot be successful unless the property change of interest is first well understood in the fission environment before attempting to model the influence of perturbations arising from differences in neutron spectra. While some significant progress has been made in understanding the radiation-induced swelling behavior of simple Fe-Cr-Ni model austenitic alloys,[1-7] there are still a number of areas in which the response of more complex structural alloys is not well understood.

For Fe-Cr-Ni ternary alloys it now appears to he relatively easy to understand the compositional and temperature sensitivity of the swelling incubation period, as well as its relatively abrupt termination, and the insensitivity to many variables of the steady-state swelling rate at ~1%/dpa. In more complex alloys, however, the transition between the incubation and steady-state swelling regimes can he quite protracted. Whereas many steels quickly reach the 1%/dpa swelling rate, others approach it very slowly, with 1%/dpa reached only at very high swelling levels.[2,8]

Simple models based on void and dislocation microstructure alone are not capable of describing such prolonged transition behavior in typical structural steels. An excellent example of this problem is shown in Figures 1-4. Brown and coworkers me ured the swelling of cold worked M316 fuel cladding as a function of temperature and displacement damage.?? As shown in Figure 1 this alloy did not reach the 1%/dpa swelling rate during this experiment and displayed a protracted transient regime that was very sensitive to irradiation temperature and neutron flux. Brown and coworkers also measured the microstructural densities at several damage levels. Note in Figure 2 that the dislocation density saturated relatively early in the irradiation at a temperature-dependent level that did not change significantly with further irradiation. Only the void characteristics changed significantly between the different dpa levels, as shown in Figure 3. When the measured swelling rates were matched against those predicted by Cawthorne using rate theory and the measured sink strengths (Figure 4),[10] it was apparent that there were significant differences in both magnitude and temperature dependence.

In particular, Figure 4 does not show the proportionality between swelling rate and the sink strength term $(a, \alpha_d)/(\alpha_v+\alpha_d)^2$, required by simple swelling theory. The dislocation sink Strengdislocation line length, and the void sink strength is $4\pi rC$ where r is the mean void radius and C the void concentration. It is considered by the current authors, however, to be particularly significant that the microstructural-based prediction exhibits the relative temperature independence of swelling rate on temperature that has been observed in experimental studies. This implies that there is another transient procers superimposed on that involving the microstructural sinks alone. This unidentified process apparently has its own temperature dependence and contributes strongly to controlling the instantaneous rate of void swelling.

It is obvious, therefore, that some other non-microstructural variable must be involved. One of the major candidate mechanisms invoked to explain the inability of simple microstructural-based models to fully explain the kinetics of void swelling has been the sluggish compositional evolution of the matrix, as various elements are removed from the matrix via precipitation or segregation.[1,4,11-15] Such models usually concentrate on resultant changes in matrix concentration of elements known to be very active in suppressing swelling, e.g., nickel, silicon, and phosphorus. There is another element, however, whoce role in swelling is usually thought not to be as strong as these other elements, but which is known to control much of the

---

*Operated for the U.S. Department of Energy by Battelle Memorial Institute under Contract DE-AC06-76RLO 1830.

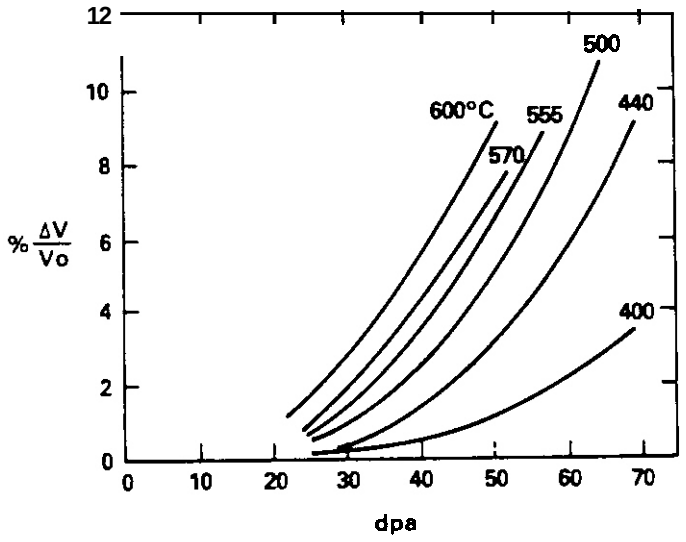

Fig. 1. Swelling vs. dose profiles reported by Brown and coworkers' derived from density measurements on six 20% cold worked M316 fuel pins.

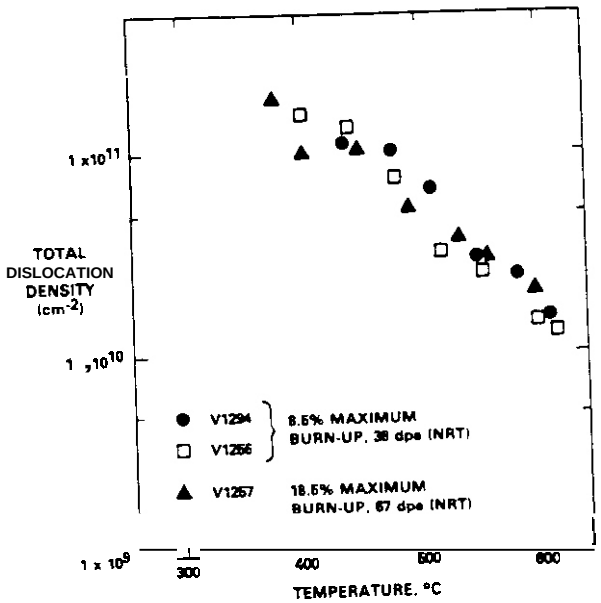

Fig. 2. Total dislocation density vs. temperature and displacement level, derived from microscopy measurements on three 20% cold worked M316 fuel pins.'

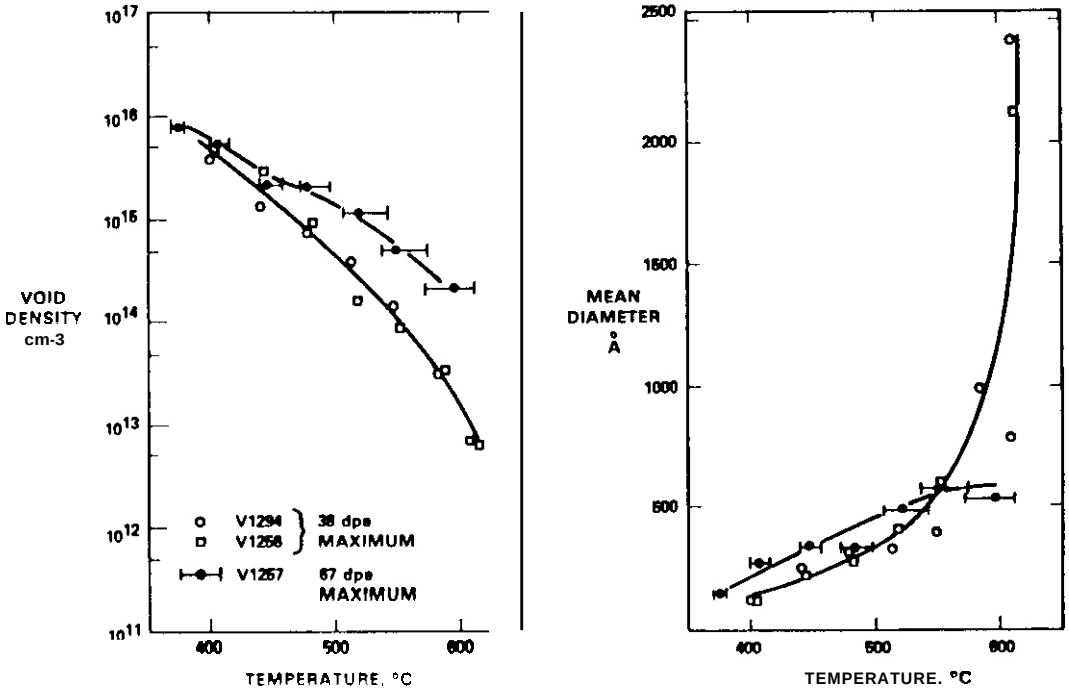

Fig. 3. Void characteristics observed in three 20% cold worked M316 fuel pins?

behavior of such steels in nonradiation environments. This element is carbon,[16] and its chemical activity is influenced not only by its concentration but also by its distribution and interaction with other solutes.

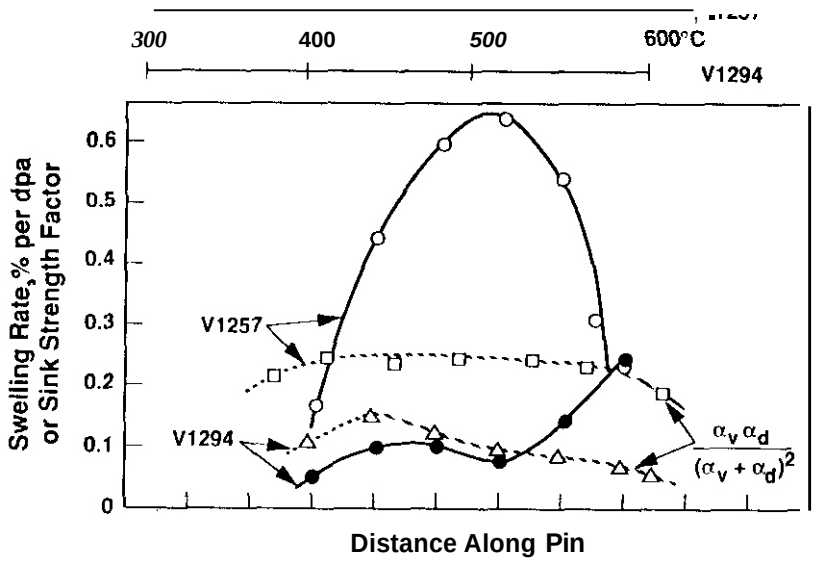

Fig. **4. Comparison of measured swelling rates (solid lines) with those predicted (dotted lines) by Cawthorne based on rate theory and measured microstructural parameters." The parameters α_v and α_d are the sink strengths for voids and dislocations, respectively. The end-of-life irradiation temperatures are shown above the figure.**

The distribution of carbon and other minor elements is probably influenced somewhat by both the mode of deformation and the resultant dislocation density, as well as the temperature history prior to irradiation. Although cold working to produce high densities of dislocations is known to decrease swelling in solute-modified steels, not much is known about its interactions during irradiation with elements such as carbon. Both the carbon level and cold work lev 1 are known to strongly influence the rate of microchemical evolution in nonradiation environments.[17] In general, however, the method of producing cold work in the laboratory varies from that employed in industry. One major difference lies in the annealing treatment experienced by such steels prior to cold working. Since the production of a given cold worked component in industry often involves multiple stages of reduction, this in turn requires multiple intermediate anneals. These are also referred to as temper anneals.

While the influence of cold work level on swelling has been studied by many researchers, the effect of intermediate annealing conditions on swelling has not been previously characterized. This report presents the results of two experiments directed toward the influence of annealing conditions on neutron-induced void swelling of AISI 316 stainless steel.

Exuerimental Details

RS-I Experiment

In the first experiment, designated RS-1, heat 81611 of AISI Type 316 stainless steel was one of a number of heats employed. It was a first core heat of steel for the Fast Flux Test Facility (FFTF) and its composition is given in Table 1. It was melted as a vacuum induction melt followed by vacuum arc remelting, using electrolytic grades of nickel, chromium, iron and manganese, metallic silicon and molybdenum, and electrolytic carbon. A 35.6 cm electrode was poured, remelted as a 40.6 cm ingot, air-cooled, heated to 1204-1260°C for 6-10 hours and pressed to 25.4 cm square billets. The billets were re-cogged to 12.7 cm, heated to 1204-1260°C and hot rolled to 3.8 cm diameter. The bars were then annealed at 1066°C, water quenched, cold drawn to 3.5 cm diameter and centerless ground to size. Fabrication into tubing was accomplished by gun-drilling short sections of finished bar and using a 9-step cold reduction sequence at Carpenter Steel. The final tube dimensions were 0.584 cm outer diameter with an 0.038 cm wall thickness.

Five different annealing temperatures in the range 1010 to 1121°C were employed before the last reduction step on various batches of this tubing, with the annealing conducted while passing through a 3-m-long

furnace at a feed rate of 2.03 cm/sec. The time spent at the target annealing temperature was approximately one minute. Two other specimen conditions were also chosen, with tubes annealed at either 1066 or 1121°C, but using a somewhat slower feed rate of 1.52 cm/sec.

One-inch sections of these tubes were sectioned axially to produce half-tubes and then marked with a code for identification. These were irradiated under static sodium in Row 2 of EBR-II in three separate B7a pins. In each pin, an identical specimen inventory was included in each of nine subcapsules maintained at one of nine target temperatures between 370 and 650°C. Temperatures were achieved by the use of gamma heating, maintaining an inert gas gap between the subcapsule outer wall and the inner wall of the B7a pins. Temperatures were calculated rather than measured. The uncertainty in temperature increases with irradiation temperature, and arises primarily from uncertainties in the local gamma flux, nominally thought to be ± 15%.

The initial temperatures published earlier for other portions of the RS-1 experiment [8] were found by later analysis to have been overestimated and also to have fallen slowly throughout the long history of this experiment due to the progressive insertion of other nonfueled experiments in Row 2.[18] This displaced some of the power generation and the associated gamma heating toward the outer rows, and gradually lowered the temperature experienced in each subcapsule. These temperatures were recalculated in this study for each reactor run by making detailed analyses of the run-to-run gamma heating levels as reported by the EBR-II operating staff: Table 2 presents the recalculated estimate; of the temperatures for the original and reconstituted subcapsules. Note that the largest difference occurs for the 650°C target temperature; this capsule attained only 572°C initially and spent the latter half of its residence in reactor at 549°C.

After each pin reached its first target fluence, the specimens were removed, cleaned, and then measurements made of their density. The uncertainty associated with the density measurement for specimens of this size is relatively small at ±0.05%. With the exception of one B7a pin (B119), the specimens from two of the pins were then reconstituted into new subcapsules to maintain the appropriate gas gap for further irradiation. The contents one B7a pin (B121) were reconstituted once, while the contents of the other pin (B120) were reconstituted twice. Following each discharge from reactor, the void swelling in volume percent was calculated from pre- and post-irradiation density measurements.

MV-III Exoeriment

The MV-III experiment was a much larger experiment also conducted in Row 2 of EBR-II. It explored the response to irradiation of a large range of compositional variations and starting states of titanium-modified 316 stainless steels. This experiment has been described in detail elsewhere, focusing on the titanium-modified steels.[14] 'Also included as reference heats in MV-II were several unmodified 316 stainless steels, however, designated FFTF' Core 1 and Core 4 steels. The Core 1 steel (heat CN-13) is essentially identical to the heat used in the RS-l study. Both the Core 1 and Core 4 heats were produced to the same specification, however. The measured compositions of these heats are shown in Table 1.

Some of the variables studied were the influence of annealing treatment, cold work, and aging on void swelling during irradiation of these two steels at 540°C. The specimens were microscopy disks (3 mm diameter by 0.3 mm thick) and were punched from rolled sheet. The thermomechanical conditions employed are shown in Table 3. The annealing conditions chosen were quite different from those of commercial practice and were selected to provide large grains for microscopy. This involved annealing temperatures (1150°C for 15 min and 1300°C for 5 min) higher than those employed in the RS-1 experiment. Annealing proceeded in argon-filled quartz tubes that were air cooled afterward. Note also that in the MV-III experiment, the annealing was performed on specimens that were not subsequently cold worked before irradiation.

Table 3. Starting Conditions Employed in the MV-III Experiment

SN	= 40% CW + 1150°C/15 min/AC + 40% CW + 1150°C/15 min/AC
NB	= SN + 650°C/1 hr/AC
NR	= 40% CW + 1300°C/5 min/AC + 40% CW + 1300°C/5 min/AC
S	= 40% CW + 1150°C/15 min/AC + 20% CW

AC = air cool, CW = cold work

Results

The swelling measured at all temperatures from RS-I specimens irradiated in the low fluence pin B119 were small (≤0.5%) and exhibited no consistent trends. These values will not be reported here. Figures 5-7 present the swelling results obtained from pins B120 and B121 (and their various reconstitutions) of the RS-I experiment for the cold worked FFTF Core 1 steel. The reader is cautioned to note the large differences in scale on each of these figures.

[1] FFTF is the Fast Flux Test Facility in Aichland, WA.

[2] The original target temperature was 600°C. The recalculated estimate is ~540°C

Table 1. Composition (Weight Percent) of 316 Steels Used in the RS-1 and MV-III Exoeriments

	Heat Designation		
Element	81611	Core 1	Core 4
Carbon	0.049	0.047	0.056
Manganese	0.161	1.77	1.53
Silicon	0.55	0.57	0.54
Phosphorus	0.003	0.004	0.002
Sulfur	0.006	0.006	0.005
Chromium	17.5	17.4	17.7
Nickel	13.7	13.7	13.7
Molybdenum	2.31	2.34	2.82
Copper	0.01	0.01	0.02
Boron	<0.0005	<0.0005	<0.0005
Cobalt	0.015	0.005	0.01
Aluminum	<0.005	0.005	0.01
Vanadium	0.02	0.02	0.01
Niobium	<0.005	0.005	0.01
Tantalum	<0.015	0 015	0.01
Arsenic	<0.005	10.005	<0.005
Nitrogen	0.004	0.004	0.002
Oxygen	not measured	0.002	0.002

Table 2. Estimated Temperatures in the RS-I Exoeriment

Target Temperature, °C	B-1i9[1]	B120/B121	B120a/B121a[2]	B120b[2]
371	376	37R	377	371
400	399	397	394	394
433	424	421	416	416
467	454	446	439	440
500	475	470	459	459
533	497	489	477	478
567	522	516	500	499
600	545	537	519	519
650	580	572	550	549

(1) Pin Designation
(2) B120a and B120b are successive reconstitutions of B120.

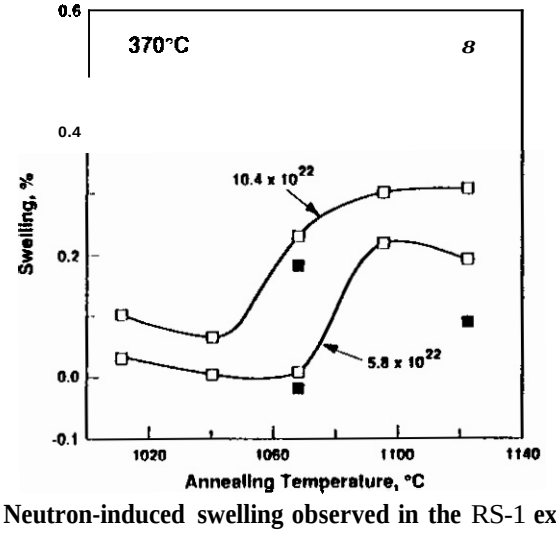

Fig. 5. Neutron-induced swelling observed in the RS-1 experiment for 20% cold worked AISI 316 stainless steel irradiated at ~370°C as a function of annealing temperature. Open symbols denote furnace feed rates of 2.03 cm/s; solid symbols denote 1.52 cm/s. Neutron fluences given in n/cm^2 (E > 0.1 MeV).

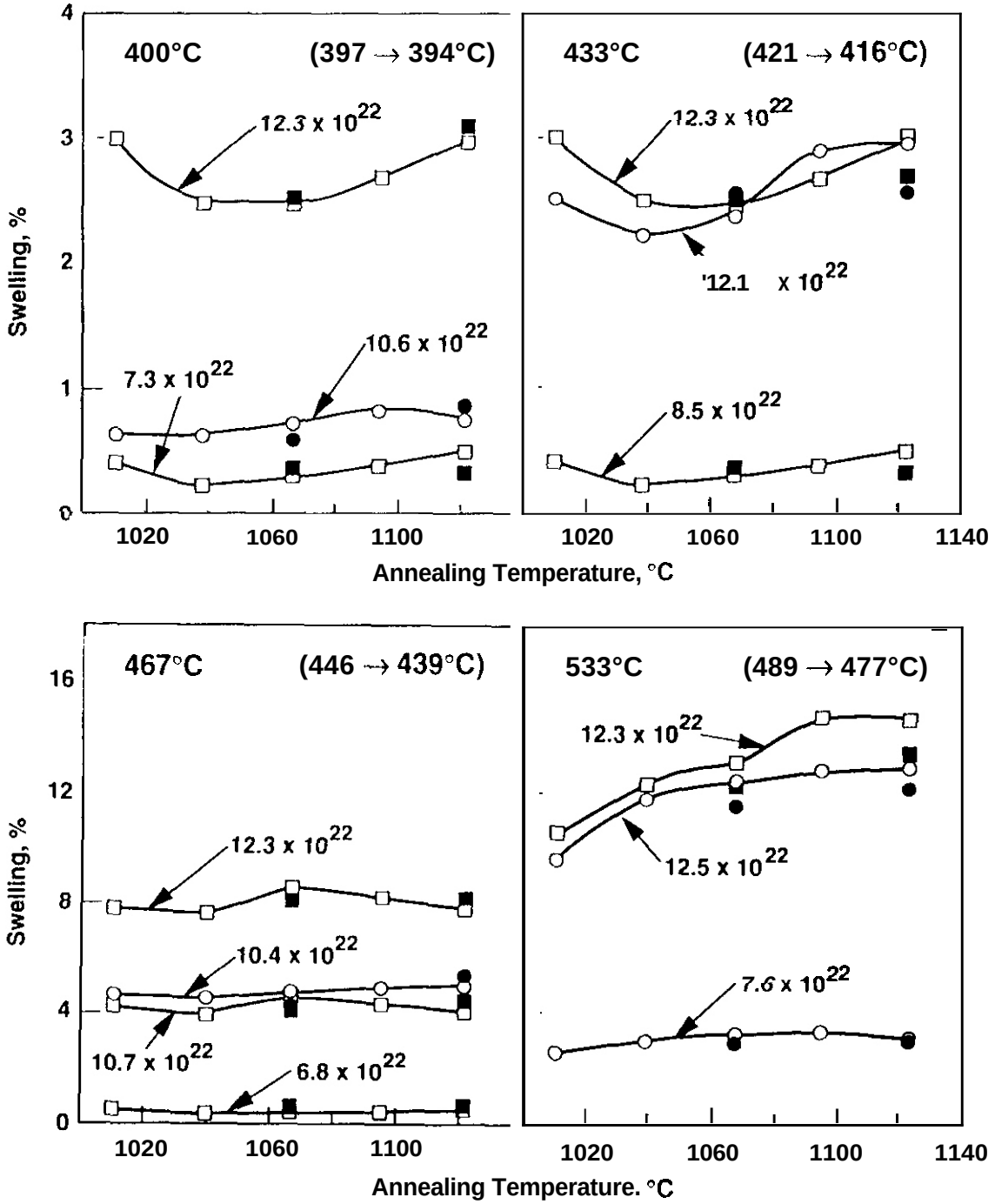

Fig. **6.** Neutron-induced swelling observed in the **RS-1** experiment for **20%** cold worked AISI **316** stainless steel irradiated at target temperatures of **400, 433, 467,** and **533°C as** a function of annealing temperature. The actual temperatures achieved varied with time and the range **is** shown in parentheses.

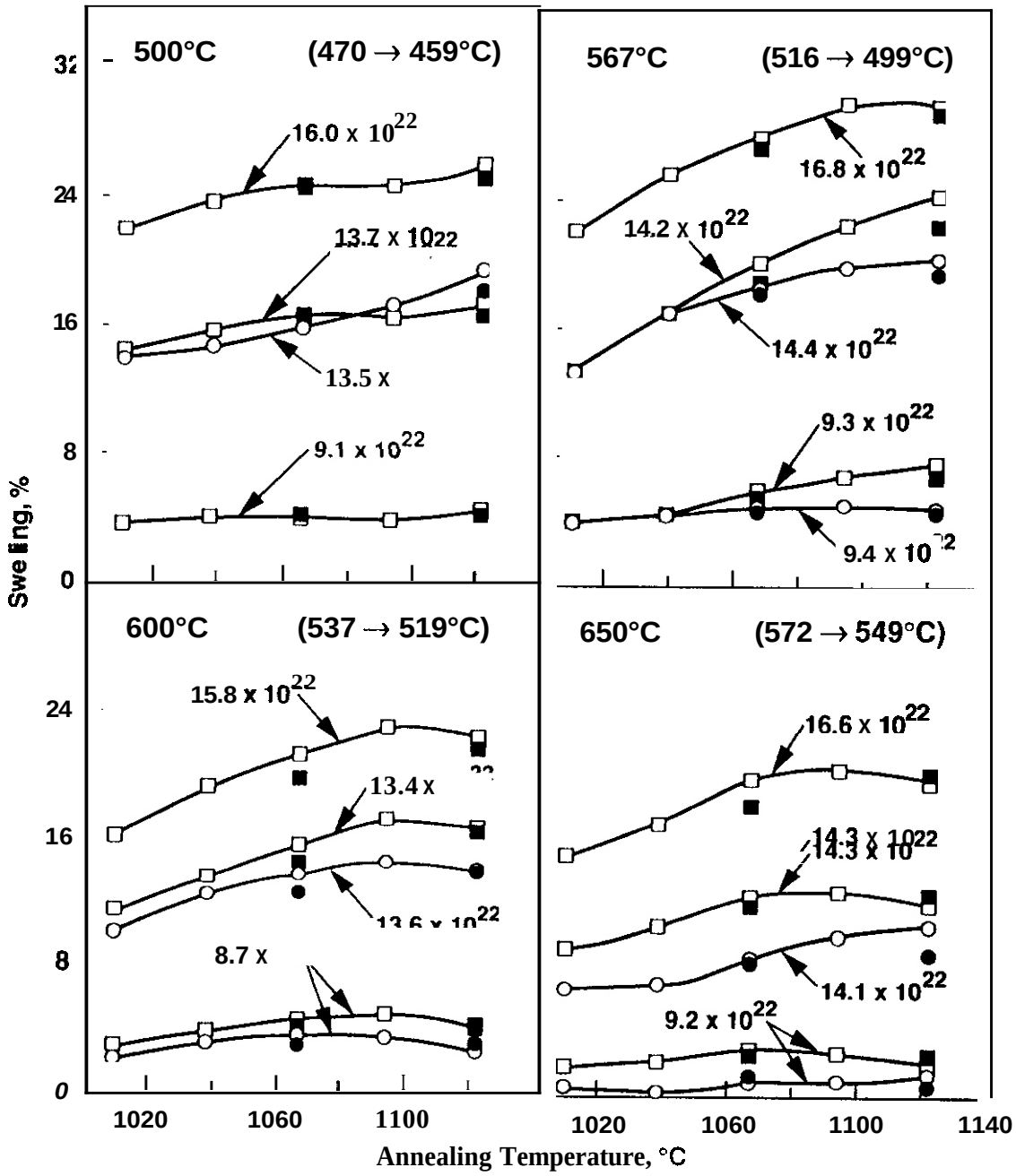

Fig. 7. Neutron-induced swelling observed in the RS-1 experiment for 20% cold-worked AISI 316 stainless steel irradiated at target temperatures of 500, 567, 600, and 650°C.

At target temperatures below ~500°C there were persistent but relatively minor variations in swelling, both as a function of annealing temperature and furnace feed rate, although the feed rate difference aoes not appear to be significant. Some variations between the results obtained at a given temperature in two essentially identical subcapsules (B120 and B121) were also observed, reflecting the sensitivity of void swelling to relatively small and unidentified details of temperature and flux history in the two pins.

At target temperatures of 500°C and above, however, the effect of annealing temperature becomes much more pronounced, 'with differences in swelling as large as 8-12%. This difference appears to develop rather slowly at first but to be maintained with further irradiation, thus manifesting itself both in the duration of the transient regime of swelling and in the degree of curvature observed during the transient regime. At the higher irradiation temperatures, the swelling appears to peak with annealing temperature and to begin to decline thereafter with increasing annealing temperature. The effect of furnace feed rate varies somewhat with both annealing and irradiatioc temperature, but appears to be a variabl? of second order importanre. At a target temperature of 650°C, ?he influence of annealing temperatur? appears to be declining compared to that observed in the range 500-600°C.

As shown in Figure 8, the trend toward declining swelling at the higher annealing temperatures is confirined in the MV-III experiment at 540°C, providing that one assumes this variable to operate in a similar way on both annealed and cold worked 316 steels,. (This dssumption was showri to correct in titanium-modified steels, as will be discussed later.)

Figure 9 shows that the 1300°C annealing treatment produces a change in the incubation period of swelling that is comparable to that obtained by cold working the 1150°C annealed steel. Aging the 1150°C annealed steel at 650°C prior to irradiation also delays swelling, but not as strongly. All starting conditions appear to approach the 1%/dpa swelling rate typical of 316 stainless steels employed in the U.S. fast reactor program.

Discussion

The manner in which the RS-I and MV-III experiments were conducted did not allow a microstructural examination, either before or after irradiation, that would help to identify the mechanisms involved in producing the observed differences in swelling.

It is possible that the RS-1 results can be explained simply in terms of residual cold work retained from the previous reduction step. In effect, the lower annealing temperatures may produce a higher net level of cold work following the last reduction. Thus, the observed differences reflect only a difference in cold work level. It is tempting, huwever, to concentrate on the role of carbon and other minor solutes in the MV-III experiment to the exclusion of other as yet unidentified processes. Although the 1300°C anneal in the MV-III experiment would be expected to reduce the dislocation density and thus accelerate tne onset of swelling, its effect on swelling is opposite and comparable to that of cold work. The 650°C aging treatment should slightly reduce the dislocation density, as showri in earlier studies by Brager and Garner[13], and also accelerate the growth of carbides. But once again, swelling is reduced by aging rather than enhanred. These observations tend to discount a strong dominant role of dislocatirn density alone, and point toward some role involving the availability and action of carbon and possibly other minor solutes in the matrix. Examples of such solutes could be sulphur and boron, precipitates (sulphides, borides) of which dissolve only at very high temperatures.

The irradiation temperature range where a large effect of annealing temperature on swelling is observed in the RS-I experiment corresponds to the temperature regime where $M_{23}C_6$ carbides form in relatively short times during thermal a ing [18] At higher temperatures (700-800°C), carbide nuclei form in minutes or less in cold worked steels.'" 'Thus $M_{23}C_6$ nuclei may be formed during the cooldown period following the temper anneal. If wE assume that hiuher annealinu temperatures more fullv homouenize the distribution of carbon and other solutes, and also prolong somewhat the cooling period, then more $M_{23}C_6$ nuclei may be formed following annealing at higher temperatures. However, such a proposal would not explain the subsequent turndown in swelling at the highest annealing temperature observed in both the RS-1 and MV-III experiments.

In the RS-1 experiment it would be expected that higher annealing temperatures would lead to a greater degree of recovery prior to cold working, as well as a more complete solutioniring of the carbon. Whatever processes dominate, they must occur very quickly, however, in order to account for the relative insensitivity of swelling to the furnace feed rate.

The cladding for the FFTF fast reactor was procured using ROT Standard M-3-28T, which specifies both process and product quality.[19] This standard requires a minimum final annealing temperature of 1038°C and is largely based on the avoidance of recrystallization during reactor operation[20]. For steels produced tc this standard it appears to be prudent not to exceed this minimum by any significant amount. It may not be prudent, however, to assume that all austenitic steels will exhibit the same behavior with annealing temperature. in reviewing the results of similar studies on a variety ot titanium-modified steels irradiated in the MV-III experiment, some steels were found to follow the pattern of decreased swelling with increasing annealing temperature, but others exhibited the opposite swelling behavior. Whatever the behavior observed, however, it was the same in both the annealed and cold-worked conditions, confirming the assumption made in the previous section.

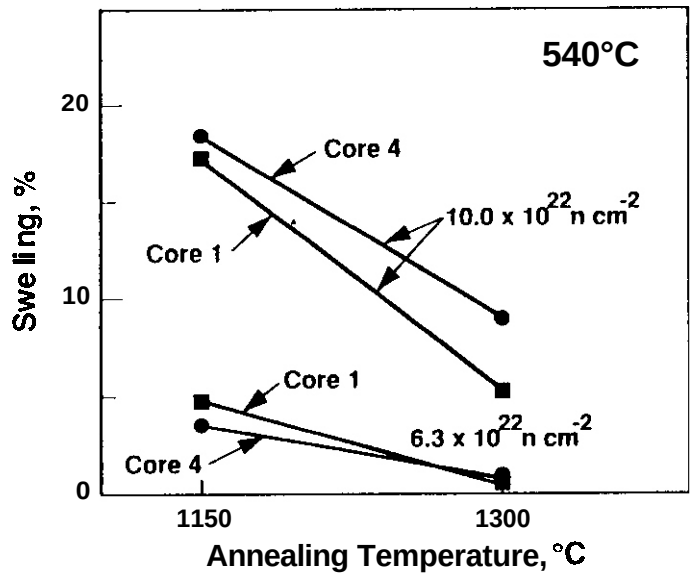

Fig. 8. Neutron-induced swelling observed in the MV-III experiment for two heats of annealed AISI 316 stainless steel irradiated at 540°C.

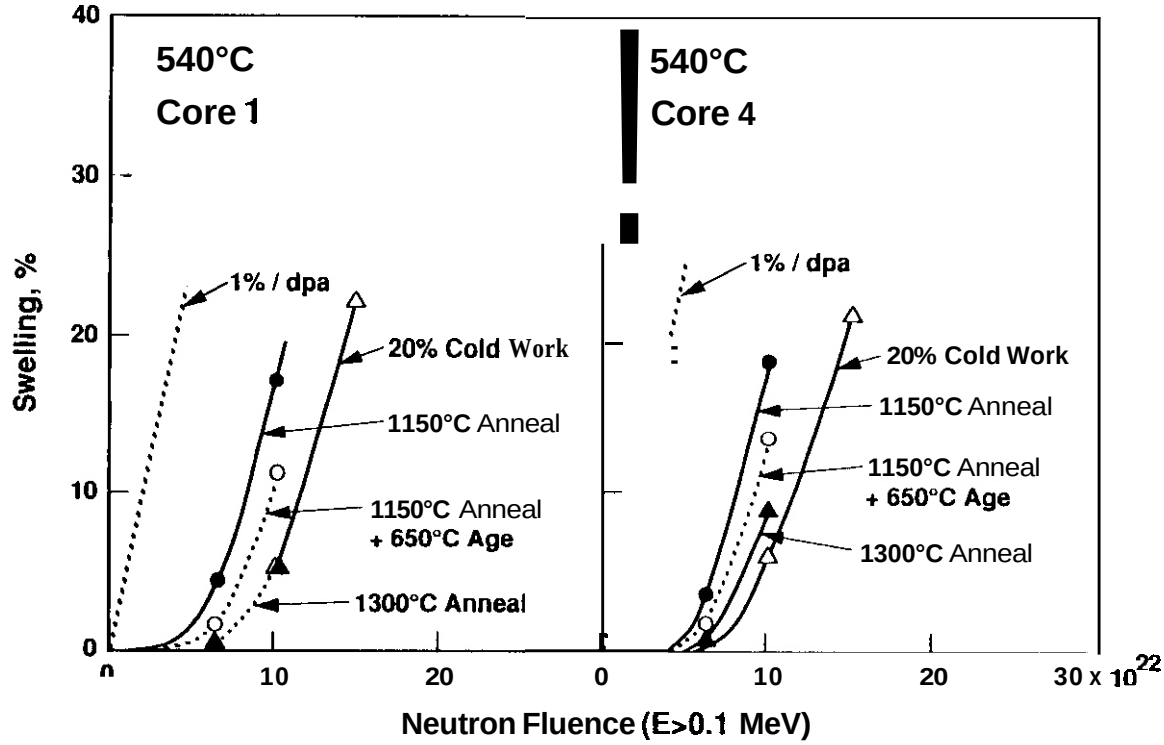

Fig. 9. Swelling vs. displacement level for two AISI 316 stainless steels irradiated at 540°C in various thermomechanical starting states.

While it is not possible at this time to predict for a given heat of steel how it will respond to differences in temper annealing conditions, it appears safe to state that the intermediate annealing temperature is an important variable, controlling in part the onset of void swelling of austenitic stainless steels. The impact of the annealing temperature on swelling of both annealed and cold worked steels can be as large as that of the cold work level.

Conclusions

The furnace temperature employed for temper anneals prior to cold working of AISI 316 stainless steel appears to have as strong an influence on void swelling as does the cold working itself. Altnough there is no microstructural evidence available to support this proposal, the parametric sensitivity of swelling observed in these experiments suggests that the distribution of carbon is strongly involved, whether it be in solution, in association with dislocations, or distributed as $M_{23}C_6$ precipitates.

Acknowledgements

This work was supported by the U.S. Department of Energy Under Contracts DE-AC06-76RLO 1830 and DE-AC06 76FF02170. M. A. Mitchell's participation was sponsored by the Northwest College and University Association for Science under U.S. Department of Energy grant DE-FG06-89ER-75522.

References

1. F. A. Garner and W. G. Wolfer, J. Nucl. Mater., 122-123(1984)201-206

2. F. A. Garner, J. Nucl, Mater. 122-123(1984)459-471.

3. F. A. Garner and H. R. Brager, in Effects of Radiation Materials: Twelfth International Symposium, ASTM STP 870, F. A. Garner and J. S. Perrin, Eds., American Society for Testing and Materials, 1985, 187-201.

4. F. A. Garner and A. S. Kumar, in Radiation Induced Changes in Microstructure: 13th liiternational Symposium (Part 1), ASTM STP 955, F. A. Garner, N. H. Packan and A. S. Kumar, Eds., American Society for Testing and Materials, 1987, 289-314.

5. W. A. Coghlan and F. A. Garner, ibid. ref. 4, 315-329

6. T. Muroga, F. A. Garner and S. Ohnuki, J. Nucl. Mater. 179-181(1991)546-549.

7. J. J. Hoyt and F. A. Garner, J. Nucl. Mater., 179-181(1991)1096-1099; and in updated form in Fusion Reactor Materials Semiannual Progress Report DOE/ER-0313/9, April 1991. 81-86.

8. F. A. Garner, in Optimizing Materials for Nuclear Applications, F. A. Garner, D. S. Gelles and F. W. Wiffen, Eds., The Metallurgical Society, 1985, 111-139.

9. C. Brown, R. M. Sharpe, E. J. Fulton and C. Cawthorne, in Dimensional Stabilitv and Mechanical Behavior of Irradiated Metals and Allovs, British Nuclear Energy Society, 1983, 63-67.

10. C. Cawthorne in Proceedings UK/US Fast Reactor Exchange Meeting on Cladding and Duct Materials, Nov. 1979, pp. 155-161, and letter to F. A. Garner, March 1, 1983.

11. F. A. Garner, in Phase Stability During Irradiation, J. R. Holland, L. K. Mansur and D. I. Potter, Eds., The Metallurgical Society, 1981, 165-189.

12. H. R. Brager and F. A. Garner, J. Nucl. Mater. 73(1978)9-19.

13. H. R. Brager and F. A. Garner, in Effects of Radiation on Structural Materials, ASTM STP *683*, J.A Sprague and D. Kramer, Eds., American Society for Testing and Materials, 1979, 207-232.

14. F. A. Garner and H. R. Brager, J. Nucl. Mater., 133-134, (1'385) 511-515; 155-157(1988)833-83.

15. T. Muroga, F. A. Garner and J. M. McCarthy, J. Nucl. Mater. 168(1989)109-120

16. J. F. Bates, R. W. Powell and E. R. Gilbert, in Effects of Radiation on Materials: Tenth Lonierence, ASTM STP 725, D. Kramer, H. R. Brager and J. S. Perrin, Eds., American Society for Testing of Materials, 1981, 713-734.

17. B. Weiss and R. Stickler, Met. Trans. 3(1972)851-866.

18. R. W. Clark, A. S. Kumar and F. A. Garner, J. Nucl. Mater., 155-157(1988) 845-849.

19. RDT Standard, "Austenitic Stainless Steel and Superalloy Tubing for BRP Core Components," Nov. 1977.

20. M. M. Paxton, R. L. Knecht, J. J. Holmes, IERSM Semiannual Progress Report, HEDL TME 74-51, Hanford Engineering Development Laboratory, 1974.

IRRADIATION CREEP AND CREEP RUPTURE OF TITANIUM-MODIFIED AUSTENITIC STAINLESS STEEL: AND THEIR DEPENDENCE ON COLD WORK LEVEL - F. A. Garner and M. L. Hamilton, (Pacific Northwest Laboratory*), C. R. Eiholzer, (Westinghouse Hanford Company), M. B. Toloczko, (University of California at Berkeley) and A. S. Xumar, (University of Missouri-Rolla)

OBJECTIVE

The objective of this effort is to provide insight into the factors that control the creep response of structural steels during neutron irradiation.

SUMMARY

A titanium-modified austenitic type stainless steel was tested at three cold work leveir to determine its creep and creep rupture properties under both thermal aging and neutron irradiation conditions. Both the thermal and irradiation creep behavior exhibit a complex non-monotonic relationship with cold work level that reflects the competition between a number of stress-sensitive and temperature-dependent microstructural processes. Increasing the degree of cold work to 30% from the conventional 20% level was detrimental to its performance, especially for applications above 550°C. The 20% cold work level is preferable to the 10% level, in terms of both in-reactor creep rupture response and initial strength.

PROGRESS AND STATUS

Introduction

The development of austenitic steels for fusion or breeder reactor service requires choosing not only the optimum composition but also the optimum processing history. Stainless steels are usually specified to be in the cold worked condition, both to provide sufficient strength and to resist void swelling. Cold working to progressively higher levels is known to lead to a continuous but diminishing reduction in swell' g.[1] Since the irradiation creep rate is known to be proportional to the concurrent swelling rate,"' it appears reasonable to assume that the creep rate should also be reduced at higher cold work levels. In fact, however, other factors come into play when irradiation and stress act on the steel simultaneously at elevated temperatures. Thus, the creep rate and creep rupture life may not be monotonic functions of the cold work level. The objective of this study is to provide some insight into the relationship between cold work and creep for the titanium-modified austenitic alloys employed in ths U.S. fusion and breeder reactor materials programs.

ExDerimental Procedure

The interplay between the various factors that influence the response of the cold worked alloy was investigated in a series of thermal and irradiation experiments involving either creep or creep rupture behavior. Thin walled gas-pressurized tubes 2.24 cm long with outer and inner diameters of 4.57 and 4.17 mm, respectively, were used. The tubes were constructed from a titanium-modified steel (*09* production heat 83508) and prepared in each of the 10%, 20% and 30% cold work levels. Larger tubes with outer and inner diameters of 5.84 and 5.08 mm and 2.82 cm long were also prepared at the 20% cold work level.

Two types of thermal control tests were performed. In the first type of test, end caps of 316 stainless steel were gas-tungsten-arc welded to one end of each tube and a gas inlet tube was welded to the other end. This configuration was used to conduct stress rupture tests at constant pressure in static argon gas at temperatures ranging from 538 to 760°C and hoop stresses ranging from 20 to 400 MPa. Failure of these constant pressure tests was detected by a sudden rise of retort pressure. Strains were measured only after specimen failure.

In the second type of thermal control test, both ends of the tubes were fitted with D9 end caps by electron beam welding and the tube was then pressurized with helium gas, after which the inlet hole in the top end cap was sealed with a laser beam. These tubes were heated at temperatures ranging from 550 to 750°C for times as long as 8,000 hours. The tubes were removed periodically and their diameters measured using a non-contacting laser system.[3] This type of test approximates a constant stress in the tube wall. As the tube expands in diameter, the effect of wall thinning on increasing the hoop stress balances out the decrease due to the drop in gas pressure. This is in contrast to the situation in the constant pressure tubes used in the stress rupture experiments, where the stress level in the tube wall rises slightly as the tube expands.

In-reactor tests using the sealed pressurized tube specimens were also conducted at temperatures between 400 and 667°C. Some of the tubes irradiated at temperatures of 575°C and above contained a unique isotopic

---

*Operated for the U.S. Department of Energy by Battelle Memorial Institute under Contract DE-AC06-76RLO 1830.

mixture of krypton and xenon tag gases added to the helium fill gas. These tag gas mixtures were included only in tubes at the 10% and 20% cold work levels. At the 20% level only the larger tube size contained the tag gas, even though both size tubes were irradiated in the experiment.

After sealing the tubes, the preirradiation diameter were measured at room temperature and the specimens were loaded into the Materials Open Test Assembly (MOTA), which was then placed into the Fast Flux Test Facility (FFTF). The specimens were actively maintained within ±5°C of their target temperature during irradiation.

When a gas tagged tube failed during a reactor cycle, the event was detected by spectrographic analysis of reactor cover gas samples and the failure time was recorded.[4] All tubes were removed from MOTA at the end of each irradiation sequence and their diameters were measured regardless of whether they had failed or not. Tubes that had not failed were returned for the next irradiation sequence.

As will be discussed in the next section, the 30% cold worked tubes in the first several irradiation sequences were found to exhibit much larger strains at the higher irradiation temperatures, and also to develop larger levels of instability in thermai aging studies. In addition, an expanded emphasis on ferritic steels required a reduction in MOTA volume reserved for austenitic alloys. A decision was, therefore, made to remove the 30% cold worked tubes from MOTA at the end of the second irradiation cycle. The 10% and 20% cold worked tubes were returned for a third cycle and reached a peak neutron fluence of 1.7 x 10^{23} n/cm^2 (E > 0.1 MeV).

Hardness measurements were performed on cross sections of the tubing in the as-received state and also on thermally aged specimens (650, 704, 760°C) for times as lonq as 3,000 hours.

Results: Stress Rupture

Figure la summarizes the overall behavior of the stress rupture data for 10% and 20% cold worked tubes, both of which were 4.57 mm in outer diameter. The actual data are plotted in Figures lb and lc as a function of the Larson Miller Parameter (LMP) to facilitate comparisons between the thermal and the in-reactor rupture data, which were derived in slightly different but overlapping temperature ranges.

The LMP is determined here as T[13.5 + log(t_r)], where T is the temperature in Kelvin and t_r is the time to irupture in hours. Note that the 10% cold worked condition exhibits slightly better thermal stress rupture behavior than the 20% cold work condition. The difference in the slope of the lines describing the 10 and 20% conditions suggests that the latter recovers more quickly than the former, a conclusion that is consistent with the results of earlier studies on AISI 304 and 316 stainless steel.[5]

Also shown in Figures lb and lc are comparisons between the thermal control and in-reactor data.[6] The in-reactor stress rupture lifetimes are significantly shorter than the corresponding thermal control data for rupture times greater than ~2,000 hours, although as reported earlier,[3] the rupture times are comparable below ~2,000 hours. For irradiation temperatures greater than 605°C, the limited in-reactor data suggest that the 20% cold worked condition exhibits slightly better stress rupture behavior than the 10% condition.

Results: Creep Rupture

The thermal creep studies shown in Figures 2 and 3 indicate that increasing the cold work level at 550°C causes thermal creep to decrease at all stress levels investigated. The same behavior is observed at low stress levels at 605°C, but the role of cold work reverses between 109 and 152 MPa at 605°C, and higher levels of creep occur with increasing cold work. At temperatures above 605°C increasing levels of cold work always increased thermal creep.

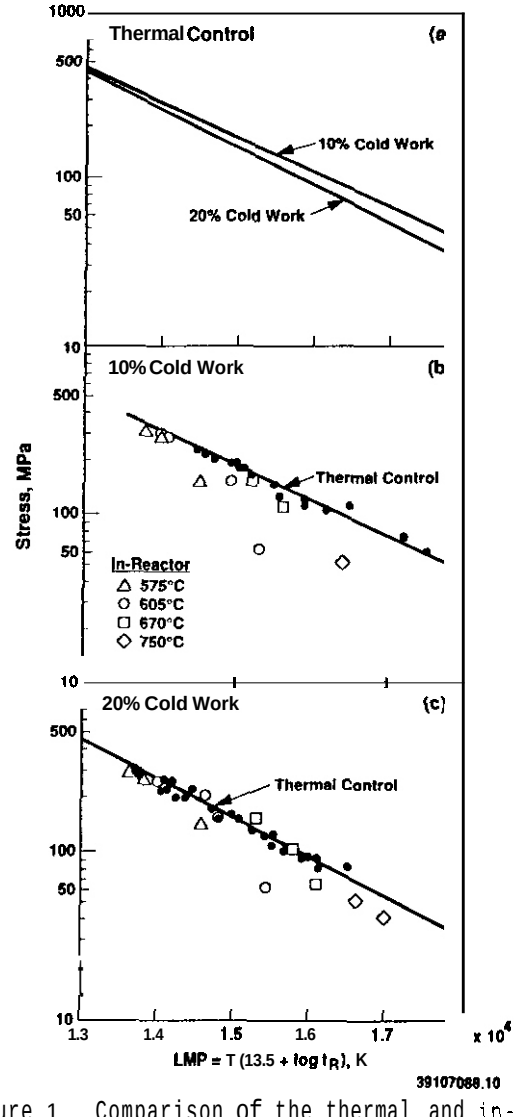

Figure 1. Comparison of the thermal and in-reactor stress rupture behavior of 10% and 20% cold worked D9.

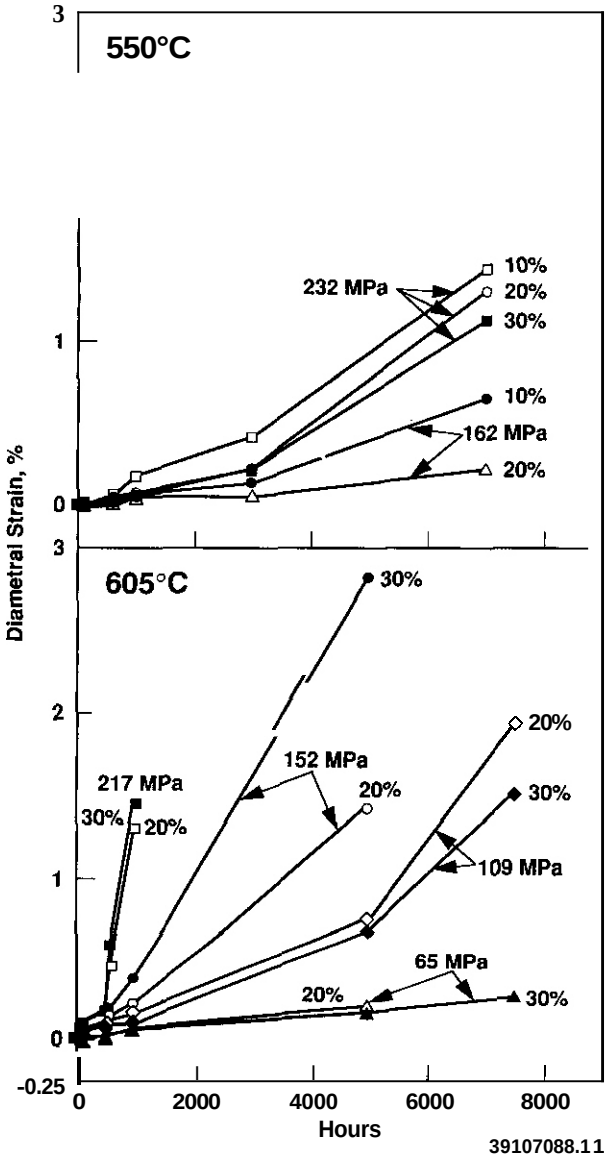

Figure 2. Thermal creep observed at 550 and 650°C for various cold work levels.

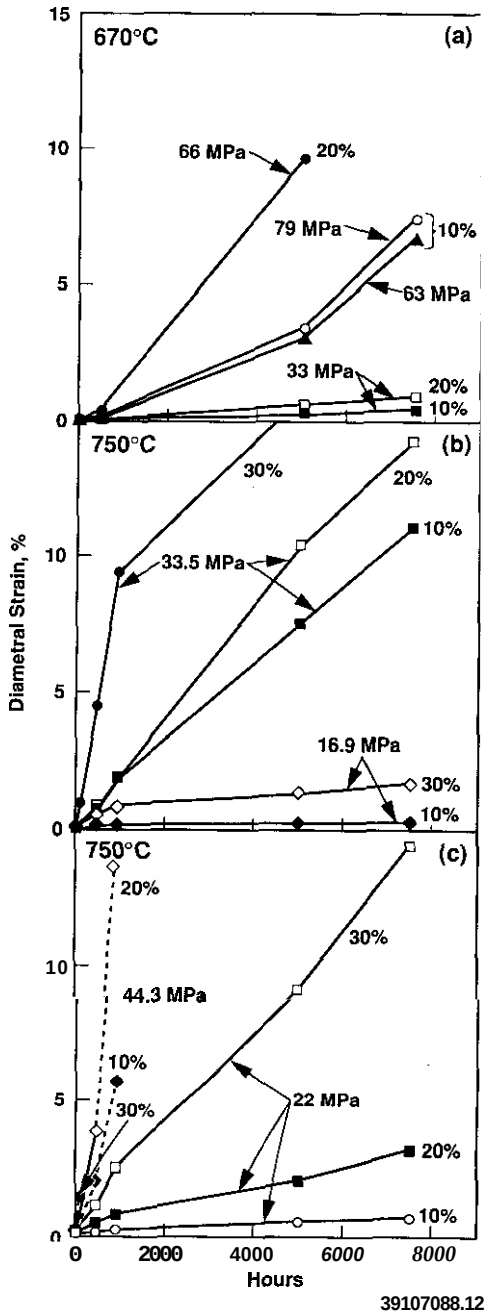

Figure 3. Thermal creep observed at 670 and 750°C for various cold work levels.

The in-reactor experiments were conducted not only at temperatures comparable to those of the thermal studies but also at lower temperatures, where thermal creep is negligible but irradiation creep and swelling are important. As shown in Figure 4, the effect of cold work level on the total strain at 400°C is second order in importance compared to the influence of stress level. There is, however, a reversal in the influence of cold work level on the total strain between 60 and 100 MPa. This reversal is also evident in the stress-normalized creep curves that are shown in Figures 5a-5c. Figure 5d demonstrates that cold work at 400°C is also expressed in its influence on the upper and lower boundaries of the normalized creep curves, first expanding the range of normaliied creep strain with stress level at the 20% cold work level, and then raising both the upper and lower limits of the response at the 30% level. The non-monotonic variability in the normalized strains at a given cold work level for such relatively low irradiation temperatures represents primarily the influence of stress in accelerating the development of void swelling.

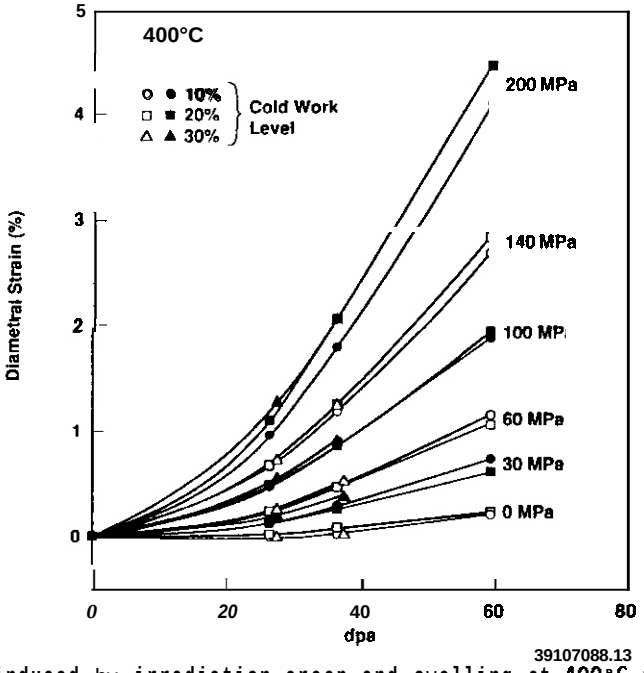

Figure 4. Deformation induced by irradiation creep and swelling at 400°C for threee cold work levels Open and closed data points are identical and are used only to differentiate closely spaced data.

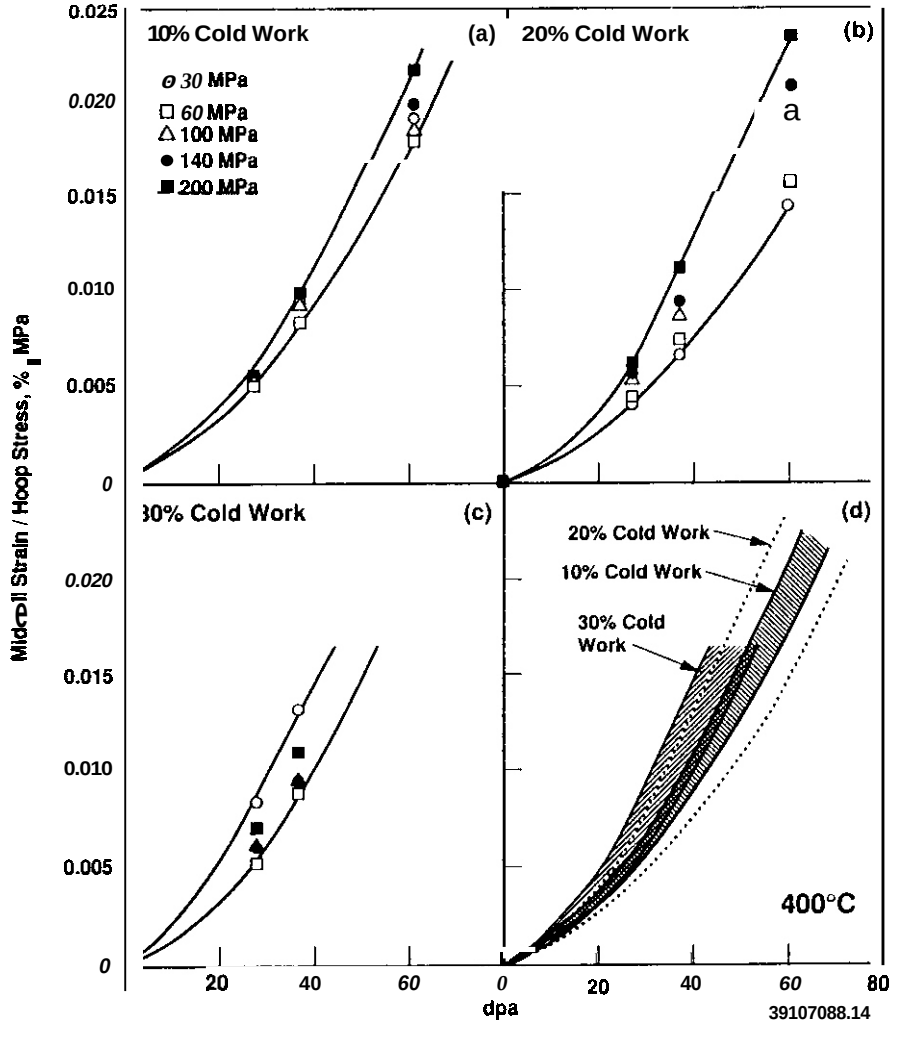

Figure 5. Normalized creep strains for pressurized tubes irradiated at 400°C. This treatment assumes that swelling is not affected by stress.

Diametral strains are shown in Figures 6-8 for irradiation temperatures above 400°C. The rate of irradiation-induced diametral straining generally increases with cold work level at 495, 550 and 600°C, although reversals in behavior are often observed in both swelling and creep at relatively low stress levels. The impact of 30% cold work in significantly accelerating the creep rate becomes particularly obvious at 600°C. A similar reversal and acceleration were observed at 605°C in the thermal creep experiment (Figure 2). At 667°C, however, such reversals in behavior were not observed, and increasing cold work levels always accelerated creep, as shown in Figure 9. Figures 10-13 show the influence of cold work level on the normalized creep strains for irradiation temperatures above 400°C. Note that the impact of cold work differences becomes more pronounced with increased irradiation temperature. In particular, the tendency toward separation of the response band of different cold work levels increases with irradiation temperature, as demonstrated most strongly in Figure 13.

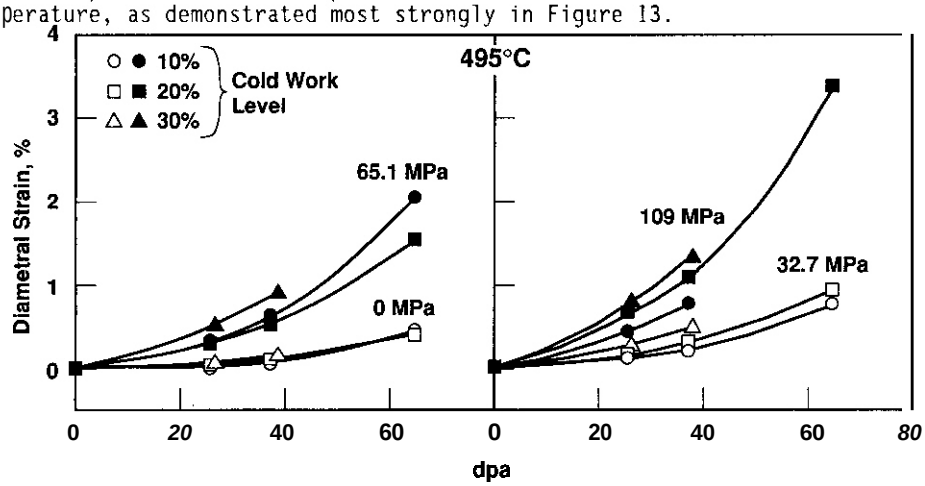

Figure 6. Diametral strains observed in tubes irradiated at 495°C.

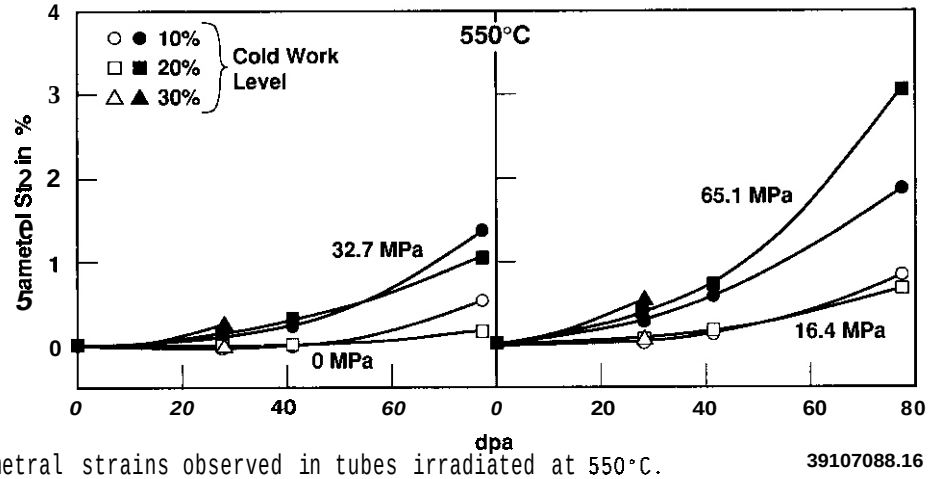

Figure 7. Diametral strains observed in tubes irradiated at 550°C.

39107088.16

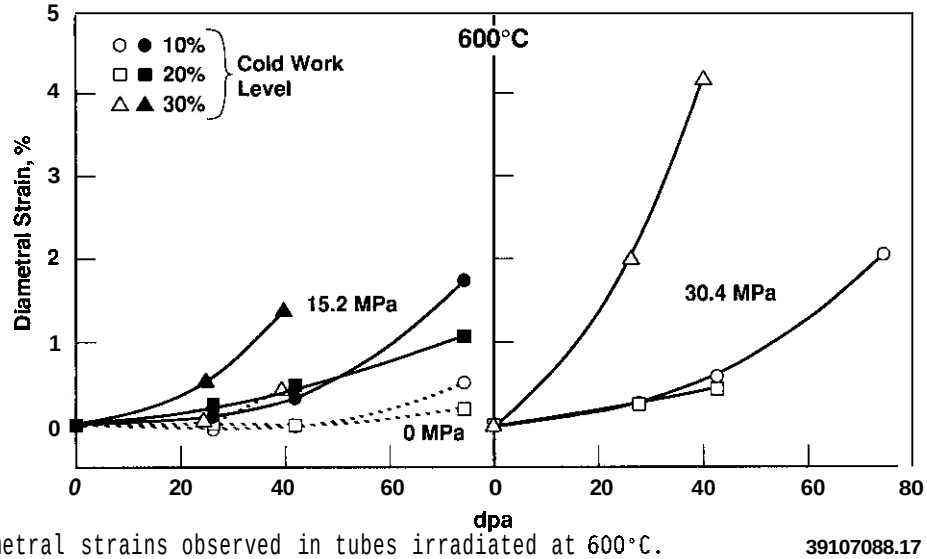

Figure 8. Diametral strains observed in tubes irradiated at 600°C.

39107088.17

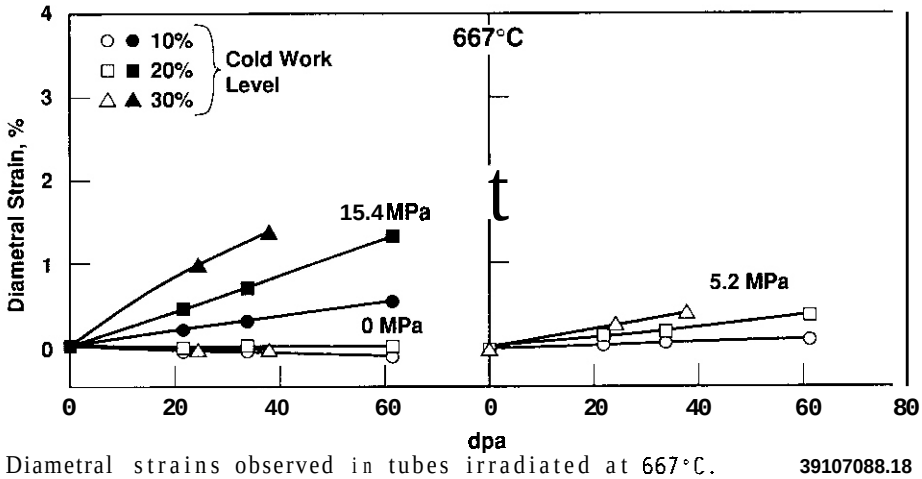

Figure 9. Diametral strains observed in tubes irradiated at 667°C. 39107088.18

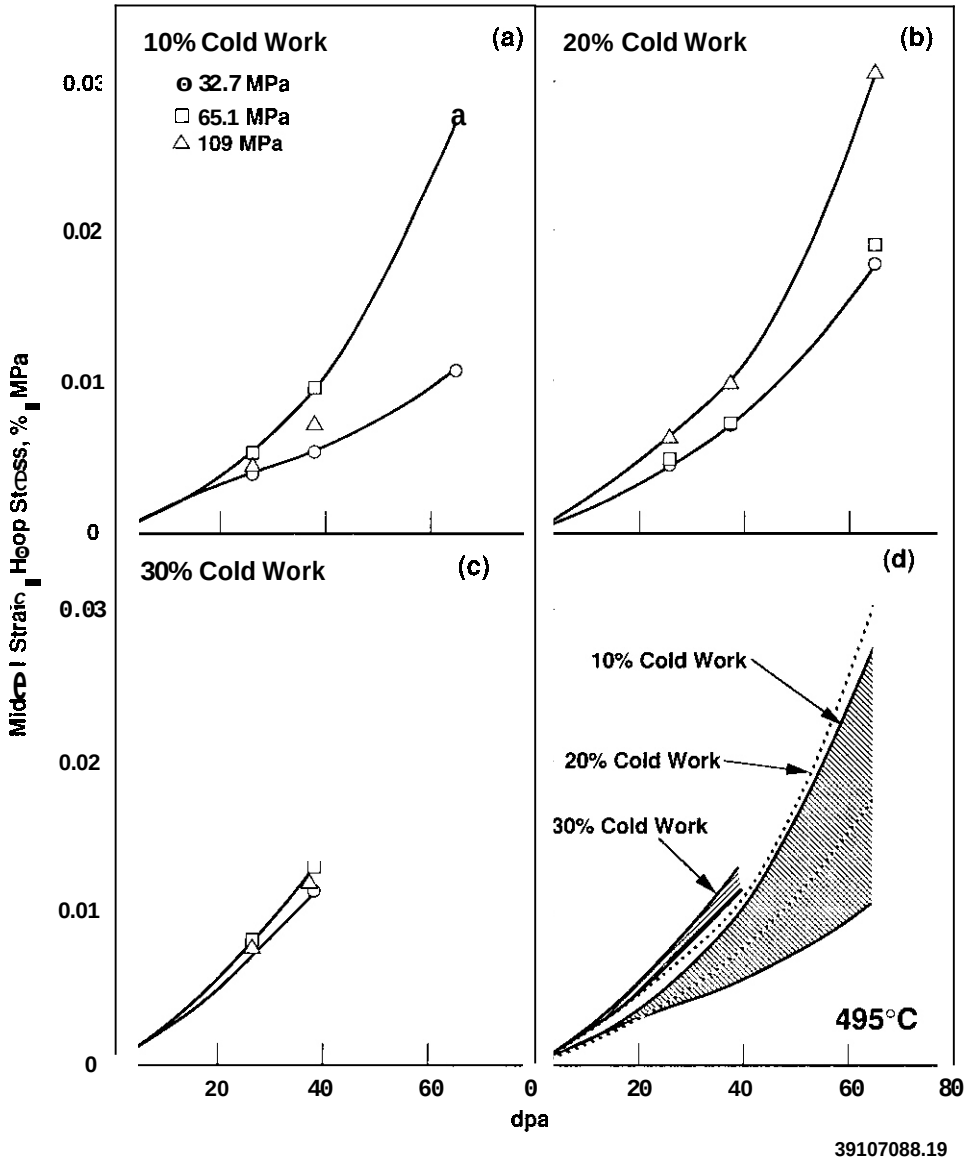

39107088.19

Figure 10. Normalized creep strains for pressurized tubes irradiated at 495°C

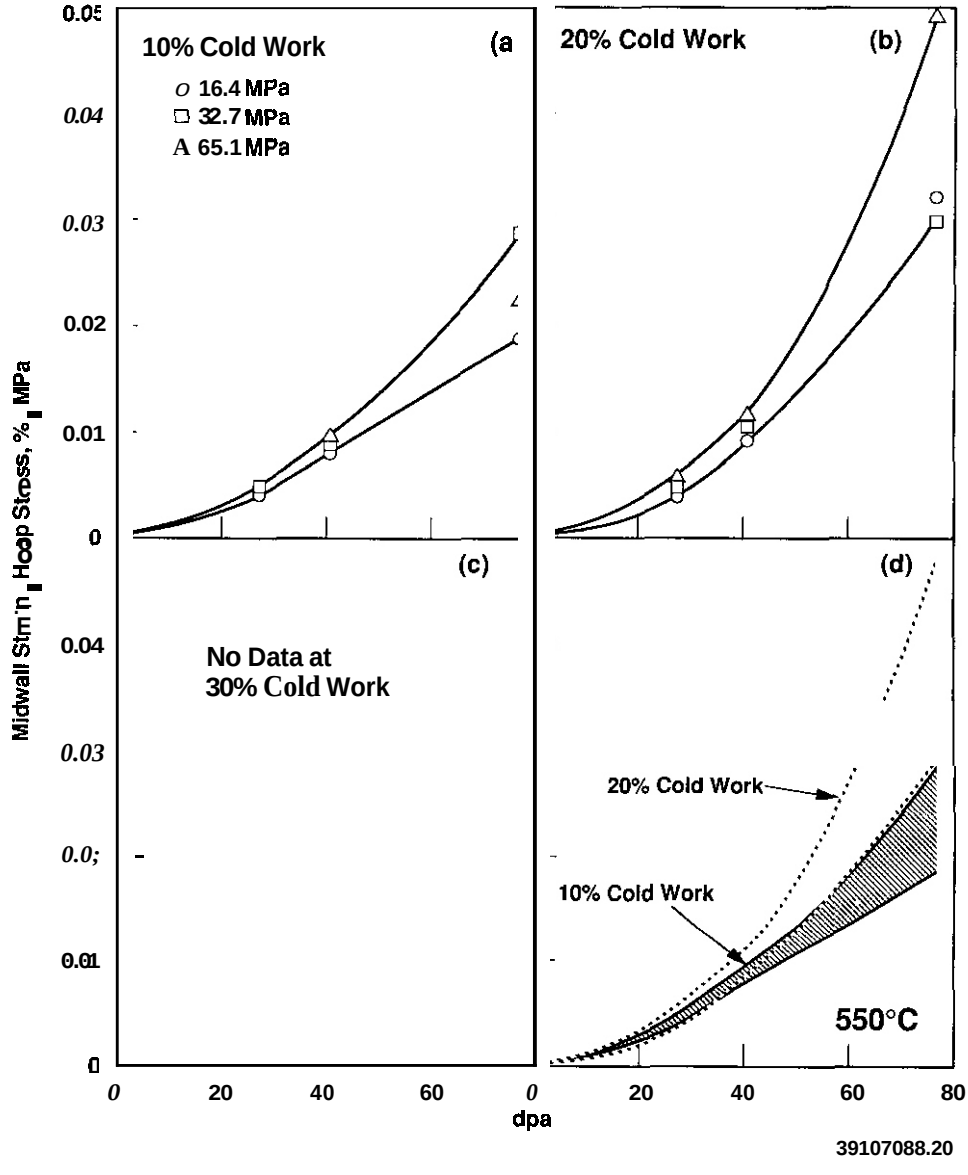

Figure 11. Normalized creep strains for pressurized tubes irradiated at 550°C.

Results: Hardness Measurements

As shown in Figure 14, 30% cold work always leads to an eventual decline in hardness during aging relative to the hardness of the 10 and 20% cold work levels. The abruptness of this decline increases with increasing aging temperature. A similar but less pronounced trend is observed when comparing the 20% and 10% cold work levels. The drop in hardness is a direct measure of the degree of recovery experienced by the steel. A simil r result has recently been published by Venkadesan and coworkers on an Indian version of this same steel.[7] Using smaller increments in cold work level than were employed in this study, they concluded that while the initial strength of the steel increased with cold work, levels greater than 17.5% led to a decline of the steel's properties during high temperature exposure. A similar conclusion was reached by Paxton for AISI 316 stainless steel.[8]

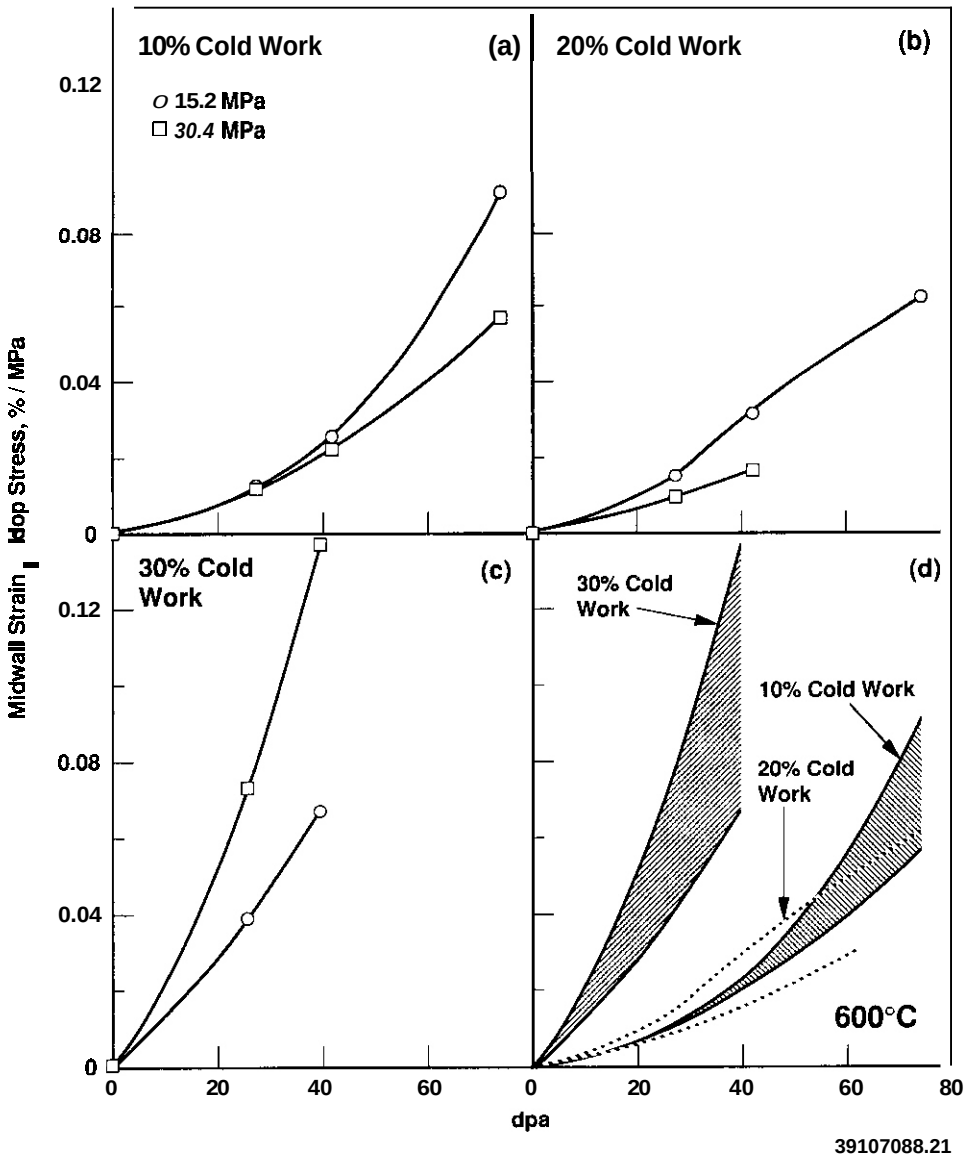

Fig. 12. Normalized creep strains for pressurized tubes irradiated at ***600°C.***

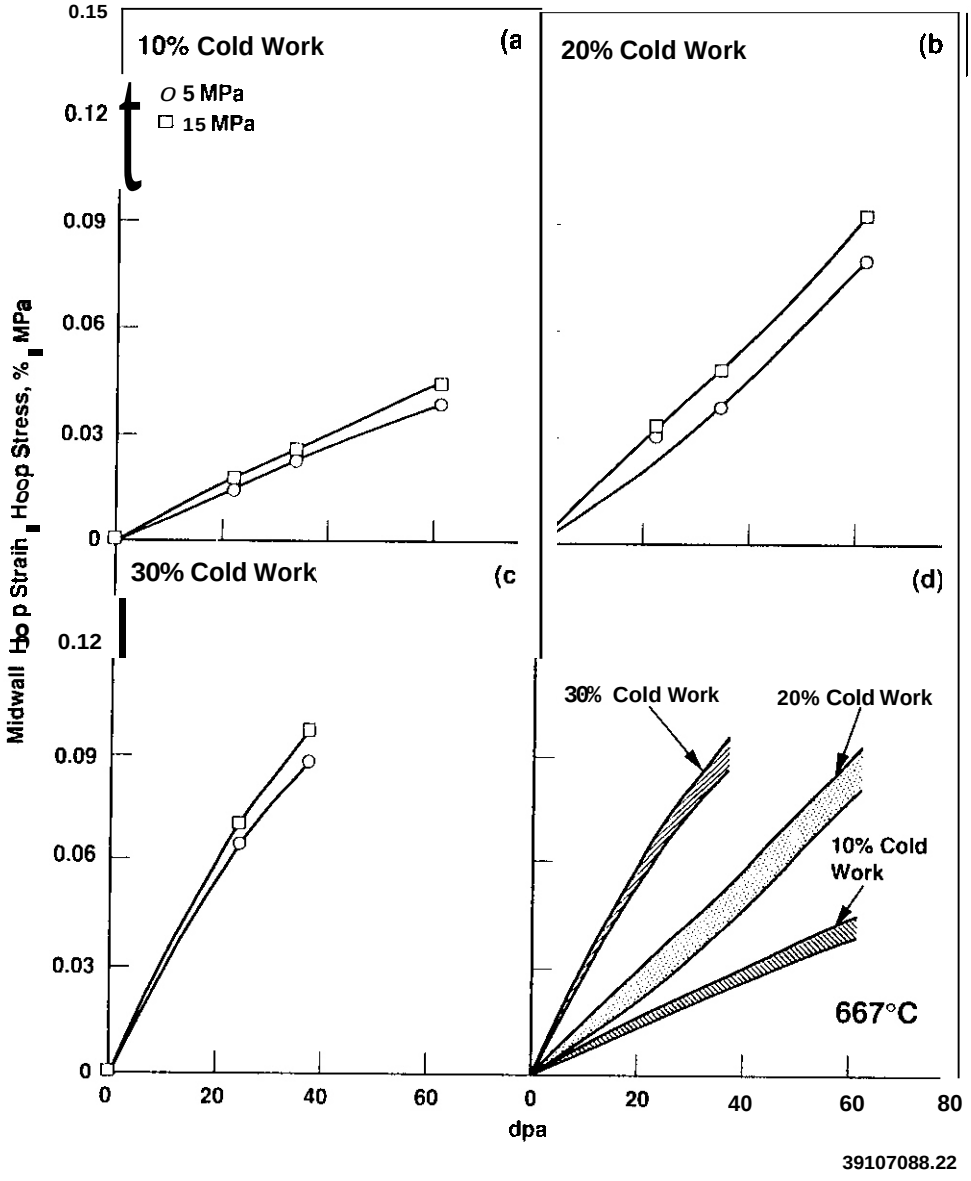

Fig. 13. Normalized creep strains for pressurized tubes irradiated at 667°C.

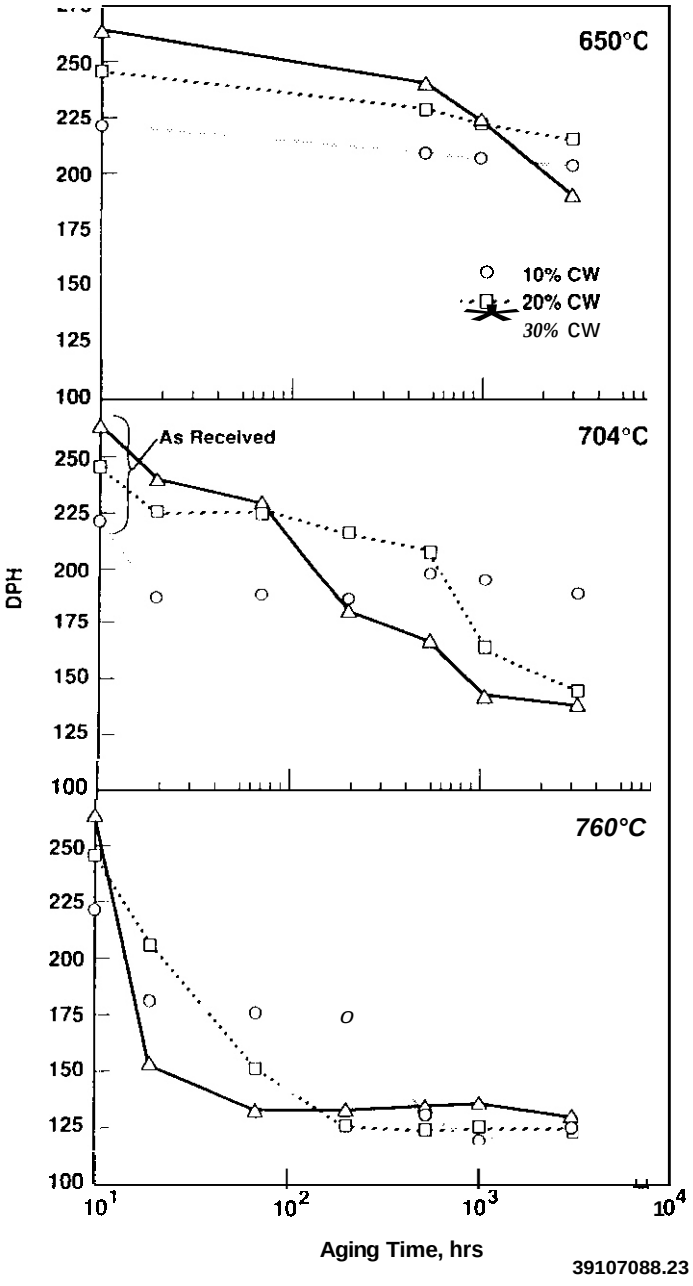

Fig. 14. Hardness following thermal aging as a function of initial cold work level

Discussion

The progressive influence of increasing cold work level on energy stored in a deformed material can be measured in terms of non-uniform lattice strain, as shown by Challenger and Lauritzen when they investigated the influence of cold work level on irradiation-induced swelling.[9] The lattice strain increases strongly from 0% to 20% cold work, as shown in Figure 15, but increases only an additional ~25% in the 20% to 30% cold work range, and very little more thereafter. With aging, the non-uniform lattice strain decreases somewhat; the largest and strongest changes occur at higher cold work levels, as demonstrated in Figure 15.

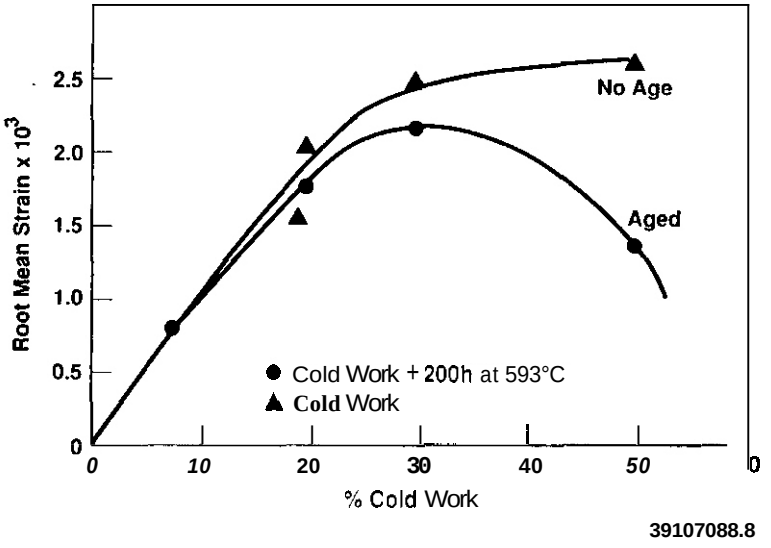

Fig. 15. Root mean Strain as a function of cold work level and thermal aging for AISI 316, as measured by Challenger and Lauritzen using x-ray line broadening.'

One would expect that the release of stored energy would be facilitated by the application of stress and that some temperature-dependent threshold stress would exist above which an accelerated release of stored energy would occur. This would be manifested as reversals in creep behavior with increasing stress level and was indeed observed in the high temperature irradiation and thermal creep studies presented in this paper. Similar observations in various steels have been made by other researchers, but the optimum cold work level depends on both the composition and irradiation environment.[5,10,11] In AISI 304, for example, the optimum cold work level was found to be only 10%.[10] This lightly alloyed steel is relatively weak compared to AISI 316 and other common stainless steels and does not offer as much resistance to recovery processes. The reversals with stress and the associated o timum cold work levels of other modified 316 steels have been found to vary with service temperature,[11] a finding consistent with the conclusions of this study.

The observed reversals during irradiation arise not only from thermally assisted processes, but also from other competing mechanisms. The release of stored energy and its associated effect on recovery provides the opportunity for some phases, particularly intermetallics, to form on moving grain fronts.[12,13] These phases often involve dimensional changes that contribute to the apparent creep strains.[14] It is known, however, that these phases are not only stress-sensitive in their rate of formation[15,16] but also subject to changes in composition arising from radiation-induced segregation.[17]

Another mechanism probably contributing to reversals in creep response arises from the conflicting roles of cold work in delaying void formation in stress-free materials[9,18,19] and the role of stress in promoting recovery of heavily cold worked material, a development which should promote void swelling. The onset of swelling is also known to be accelerated by stress even in the absence of cold work.[20-22] Additional complications involve the relationship between swelling and irradiation creep Irradiation creep is also known to be proportional to the rate of swelling. Thus stress-enhanced swelling leads to an acceleratior of creep.[23-25] Even before the onset of void swelling. the short-term transient regime of creep is known to be dependent on the stress state and initial cold work level.[26] In the absence of recovery, the transient ceases when the dislocation density has relaxed to its equilibrium level.

CONCLUSIONS

Based on the complexity of the competition between the various stress-sensitive and temperature-dependent processes discussed in the preceding section, it is not surprising that both thermal and irradiation creep exhibit nun-monotonic behavior with respect to stress, temperature and cold work level. It is szfe to state based on these studies, however, that increasing the cold work level of titanium-modified 316 from the conventional 20% level to 30% would be detrimental to its performance, especially at irridiation temperatures above 550°C. The driving force for the degradation of performance at the hiqher cold work level arises from the large level of non-uniform lattice strain induced during cold working and its release at high temperatures and stress levels.

The higher strength of 20% cold worked steel compared to that at 10% is not significantly offset by the differences in creep response. If it can be assumed that the response of this steel is typical of the alloy class, the 20% cold work level appears to be the optimum choice for the titanium-modified austenitic stainless steels employed in the U.S. fusion and breeder reactor materials programs.

REFERENCES

1. H. R. Brager and F. A. Garner, in Effects of Radiation on Structural Materials, ASTM STP 683, J.A. Sprague and D. Kramer, Eds., American Society for Testing and Materials, 1979, pp. 207-232.

2. F. A. Garner., Journal of Nuclear Materials, 122-123 (1984) 459-471

3. E. R. Gilbert and 3. A. Chin, in Effects of Radiation on Materials: Tenth Conference. ASTM STP 725, D. Kramer, H. R. Brager and J. S. Perrin, Eds. American Society for Testing and Materials, 1981, pp. 665-679.

4. R. J. Puigh and R. E. Schenter, in Effects of Radiation on Materials: Twelfth International Symposium, ASTM STP 870, F. A. Garner and J. S. Perrin, Eds., American Society for Testing and Materials, 1985, pp. 795-802.

5. R. A. Moen and D. R. Duncan, Hanford Engineering Development Laboratory Report, HEDL-TI-76005, March 1976.

6. R. J. Puigh and M. L. Hamilton, in influence of Radiation on Materials Properties: Thirteenth International Symposium (Part II), ASTM STP 956, F. A. Garner, C. H. Henager, Jr., and N. Igata, Eds., American Society for Testing and Materials, 1987. pp. 22-29.

7. S. Venkadesan, A. K. Bhaduri and P. Rodriguez, pp. 249-254 in Fast Reactor Core and Fuel Structurai Behavior, BNES, London, June 1990, pp. 249-254.

8. M. M Paxton, Hanford Ensineering Develooment Laboratory Report, HEDL-TME-74-11, February 1974

9. K. D. Challenger and T. Lauritzen, in Properties of Reactor Structural Materials After Neutron or Particle irradiation, ASTM STP 570, C. J. Barodi and F. R. Shobers. Eds., 1975, pp. 388-403.

10. L. Bernard, E. Campo and S. Quarantra, in Mechanical Behavior and Nuclear Applications of Stainless Steel at Elevated Temperatures, The Metals Society, London, May 1981, pp. 88-93.

11. Y. Kondo, T. Yukitoshi, K. Yoshikawa, N. Nagai, S. Ohta, M. Fujiwara, S. Yoshida, C. Tanaka, K. Uematsu and K. Suzuki, in Radiation Effects in Breeder Reactor Structural Materials, M. L. Bleiberg and J. W. Bennett, Eds., The Metallurgical Society, New York, June 1977, pp. 253-267.

12. B. Weiss and R. Stickler, Metallurgical Transactions, 3 (1972), pp. 851-866.

13. F. A. Garner, F. Abe and T. Noda, Journal of Nuclear Materials, 155-157 (1988), pp. 870-876.

14. R. J. Puigh, A. J. Lovell and F. A. Garner, Journal of Nuclear Materials, 122 & 123 (1984) 242-245.

15. F. A. Garner, in Damage Analysis and Fundamental Studies Quarterly Progress Report, DOE/ER-0046/5, May 1981, pp. 198-218.

16. K. C. Russell and F. A. Garner, in Damage Analysis and Fundamental Studies Quarterly Progress Report, DOE/ER-0046/7, November 1981, pp. 180-197.

17. W. J. S. Yang, in Radiation-Induced Chanses in Microstructure, ASTM STP 955, F. A. Garner, N.H Packan and A. S. Kumar, Eds., American Society for Testing and Materials, 1987, pp. 628-646.

18. H. R. Brager and F. A. Garner, in Effects of Radiation on Structural Materials, ASTM STP 683, J. A Sprague and D. Kramer, Eds., American Society for Testing and Materials, 1979, pp. 207-232.

19. H. R. Brager, Journal of Nuclear Materials, 57, (1975), 103.

20. F. A. Garner, E. R. Gilbert and D. L. Porter, in Ref. 3, pp. 680-697

21. T. Lauritzen, S. Vaidyanathan, W. L. Bell and W. J. S. Yang, in Radiation-Induced Changes in Microstructure, 13th International Symposium [Part I), ASTM STP 955, F. A. Garner, N. H. Packan and A. S. Kumar, Eds., American Society for Testing and Materials, 1987, pp. 101-103.

22. D. L. Porter, M. L. Takata and E. L. Wood, Journal of Nuclear Materials, 116, (1983). pp. 272-276.

23. F. A. Garner and R. J. Puigh, Journal of Nuclear Materiais, 179-181 (1991), pp. 577-580.

24. D. L. Porter, G. D. Hudman and F. A. Garner, Journal of Nuclear Materials. 179-181 (1991), pp 581-584.

25. F. A. Garner and D. L. Porter, Journal of Nuclear Materials, 155-157 (1988), pp. 1006-1011.

26. M. B. Toloczko, F. A. Garner and C. R. Eiholzer, "Determination of Creep-Swelling Coupling Coefficients for Irradiated Stainless Steels", Fusion Reaction Materials Semiannual Progress Reuort. DOE/ER-0313/9, 1991.

27. E. R. Gilbert and 8. A. Chin, Nuclear Technology, 52 (1981) 273-283

DETERMINATION OF THE CREEP COMPLIANCE AND CREEP-SWELLING COUPLING COEFFICIENT FOR NEUTRON IRRADIATED TITANIUM-MODIFIED STAINLESS STEELS AT ~400°C - M. B. Toloczko, University of California at Berkeley, F. A. Garner, Pacific Northwest Laboratory,(a) and C. R. Eiholzer, Westinghouse Hanford Company

OBJECTIVE

The objective of this effort is to provide irradiation creep data and design correlations for application to fusion and breeder reactor design.

SUMMARY

Irradiation creep data from FFTF-MOTA at ~400°C were analyzed for nine 20% cold-worked titanium-modified type 316 stainless steels, each of which exhibits a different duration for the transient regime of swelling. One of these steels was the fusion prime candidate alloy designated PCA. The others were various developmental breeder reactor heats. The analysis was based on the assumption that the $B_o + DS$ creep model applies to these steels at this temperature. This assumption was found to be valid. A creep-swelling coupling coefficient of $D \approx 0.6 \times 10^{-2}$ MPa^{-1} was found for all steels that had developed a significant level of swelling. This result is in excellent agreement with the results of earlier studies conducted in EBR-II using annealed AISI 304L and also 10% and 20% cold-worked AISI 316 stainless steels. There appears to be some enhancement of swelling by stress, contradicting an important assumption in the analysis and leading to an apparent but misleading nonlinearity of creep with respect to stress.

PROGRESS AND STATUS

Introduction

In a number of recent reports the creep-swelling relationship has been investigated for annealed AISI 304L[1] and various thermomechanical treatments of AISI 316 stainless steel.[2-6] These studies were conducted in EBR-II and showed a remarkable consistency in results, indicating that irradiation creep at most temperatures of interest could be described as consisting of several minor-contributions (precipitation-related dimensional changes and transient relaxation of cold-work-induced dislocations) and two major contributions.[6] The major contributions were associated with the creep compliance, B_o, a quantity unrelated to void swelling, and a swelling-driven creep component. Although swelling itself is very sensitive to a large variety of material and environmental variables, the instantaneous creep rate appears to be proportional only to the applied stress and the instantaneous swelling rate. As discussed in other publications,[7-11] the instantaneous creep rate can be written in the form

$$B = \bar{\epsilon}/\bar{\sigma} = B_o + D\dot{S}, \quad (1)$$

where $\bar{\epsilon}/\bar{\sigma}$ is the effective strain rate per unit stress, $\bar{\sigma}$ is the effective stress = $(\sqrt{3}/2)\,\sigma_{hoop}$, B_o is the creep compliance, D is the creep-swelling coupling coefficient and $\dot{S}$ is the instantaneous volumetric swelling rate. This equation applies primarily to annealed material that does not develop any significant phase-related strains or density changes. 316 stainless steels are known to exhibit density changes, however, arising from carbide precipitation[12] and formation of intermetallic phases.[13] If the material is cold-worked, another short-lived transient term is sometimes required to describe the relaxation of the dislocation density to its equilibrium level.

ExDerimental Details

In this study, the fusion prime candidate alloy (PCA heat K280) and eight other titanium-modified type 316 steels from the breeder reactor program were irradiated in FFTF/MOTA. For three of the alloys, 2.24-cm-long helium-pressurized tubes were used with outer and inner diameters of 4.57 mm and 4.17 mm, respectively. The other six alloys had tubes that were somewhat larger, with a length of 2.82 cm, and 5.84 and 5.08 mm outer and inner diameters. The difference in size alone does not influence the creep results.[12] The compositions of these steels are shown in Table 1. The specimens were removed periodically from the reactor and their diameters measured at five equidistant positions using a noncontacting laser system.[14] The three middle measurements were averaged to calculate the diametral strain. During any one irradiation interval the temperature is actively controlled within ±5°C. The tubes for any one alloy were placed side-by-side in

(a) Pacific Northwest Laboratory is operated for the U.S. Department of Energy by Battelle Memorial Institute under Contract DE-AC06-76RLO 1830.

Table 1. Composition (wt%) of Stainless Steels Used in this Study

Heal	Fe	Ni	Cr	Mo	Mn	Si	C	P	Ta	Zr
K280	BAL	16.63	14.31	1.95	1.83	0.52	0.048	0.014	--	--
83508'	BAL	15.77	13.70	1.65	2.03	0.80	0.039	<0.005	<0.01	<0.01
A094*	BAL	15.64	13.34	2.21	1.52	0.81	0.038	0.040	--	--
A095*	BAL	15.59	13.58	1.81	1.62	0.82	0.038	0.038	--	--
C38	BAL	15.60	13.66	1.82	2.20	0.82	0.048	0.032	<0.010	--
C39	BAL	15.59	13.59	1.82	2.19	0.78	0.048	0.088	<0.008	--
C40	BAL	15.60	13.63	1.81	2.20	0.81	0.044	0.088	<0.008	--
C42	BAL	15.79	13.62	1.81	2.30	0.81	0.049	0.030	<0.010	--
C44	BAL	20.08	13.64	1.80	2.30	0.83	0.046	0.032	<0.016	--

Continued:

Heat	S	V	Nb	Ti	Co	Cu	Al	B	N
K280	0.025	0.04	0.02	0.31	0.04	0.02	**0.05**	0.001	0.008
83508'	0.003	0.01	--	0.34	'0.01	<0.01	<0.01	0.0005	0.004
A094*	0.009	0.020	--	0.28	0.05	0.02	<0.01	0.0041	0.006
A095*	0.008	0.011	--	0.28	0.04	0.02	<0.01	0.0047	0.003
C38	0.004	0.03	<0.010	0.27	0.03	0.02	0.03	0.0033	0.002
C39	0.004	0.03	<0.008	0.27	0.03	0.02	0.03	0.0029	0.005
C40	0.006	0.02	<0.008	0.27	0.03	0.01	0.03	0.0064	0.006
C42	0.005	0.02	<0.010	0.26	0.03	<0.01	0.03	0.0062	0.002
C44	0.005	0.02	<0.016	0.26	0.03	0.02	0.03	0.0061	0.004

* These heats have a tube size of 5.84mm OD x 5.08mm ID x 28.2mm in Length. All others are 4.57mm OD x 4.17mm ID x 22.4mm in Length.

MOTA although different alloy sets experienced slightly different temperatures and neutron fluxes. For each group of tubes there were small cycle-to-cycle variations in temperature and neutron flux that arose as the group of tubes were placed at somewhat different reactor levels following each MOTA reconstitution (see Table 2). Preliminary results for PCA and one of the breeder reactor alloys have been reported previously.[11,12]

Results and Discussion

Figure 1 shows for three alloys the total diametral strains for nominally identical tubes irradiated side-by-side for a number of consecutive FFTF irradiation cycles at ~400°C. The data for the other six alloys are very similar, varying only the duration of the transient regime of deformation. The separate tubes of each alloy varied only in their internal gas pressure, which yielded hoop stresses ranging from 0 to 300 MPa. Note that these data are plotted against the neutron exposures expressed in units of dpa. An earlier report contained the data for PCA as a function of neutron fluence for energies greater than 0.1 MeV.[15] Both the neutron fluence and dpa values for the first several irradiation segments have been revised recently. The revised values are reported in Table 2.

The diameter changes of the zero stress tubes represent primarily the contribution of void swelling, but there may also be some secondary contribution from precipitation-related strains. The strains of the stressed tubes include additional contributions from irradiation creep and possibly the stress-enhanced portion of swelling, since applied stresses are known to accelerate the onset of swelling.[16-18] Figure 2 shows the diametral strains of the stress free tubes for all nine alloys, indicating that the transient regime of swelling varies somewhat with composition, fabrication history, and irradiation conditions.

In order for the creep data to fit the B_o t DS model, it is necessary for creep to be proportional to the first power of stress and to increase directly in proportion to the instantaneous swelling rate. If we calculate the midwall creep strains and divide them by the stress level, the validity of these assumptions can be checked. First, the creep strains are separated by subtracting the zero stress swelling strains. Figure 3 presents a comparison of the stress-normalized midwall strains for three steels. The latter figure shows that each of the steels exhibits accelerated creep rates that coincide with the onset of accelerated swelling, but that the stress-normalized creep strains do not appear to be completely linear with applied stress. However, this appearance is probably misleading, with the slight but steady increase in normalized creep strain with increasing stress arising from the somewhat incorrect assumption that swelling is not affected by stress. (Similar trends were observed in the other six steels.) In general, increasing the stress level progressively shortens the incubation period of swelling in cold-worked austenitic steels.[16-18] It appears in this study that there is also a small but persistent effect of stress on the incubation period of swelling.

Table 2. Irradiation History of Each Heat

	MOTA - 1A	MOTA - 1B	MOTA-1C	MOTA - 1D	MOTA - 1E	MOTA - 1F
K280 (PCA)						
Canister/Basket	1D3	1D5	1F5	1F5	1F5	1F1
Temp, °C	405	401	396	386	384	386
Φ_t, x10^{22} n/cm^2 (E>0 1MeV)	4 6	6 6	11 9	15 4	19 2	24 8
Cumulative dpa	20 4	29 3	50 2	65 3	81 1	106 8
83508 (D9 Reference)						
Canister/Basket	2F1	2F2	2F2	2F4	absent	absent
Temp.. °C	427	431	420	404		
Φ_t, x10^{22} n/cm^2 (E>0.1MeV)	6.0	9.2	16.7	21.9		
Cumulative dpa	27.8	42.6	77.2	101.2		
A094 (D9I - 2)						
Canister/Basket	absent	2F4	2F4	2F2	2F1	2F4
Temp, °C		431	420	410	410	410
Φ_t, x10^{22} n/cm^2 (E>0 1MeV)		3 1	10 3	15 7	23 7	30 6
Cumulative dpa		14 1	47 2	72 2	109 2	141 2
A095 (D9I - 1)						
Canister/Basket	absent	2F3	2F3	2F1	2F3	2F4
Temp., °C		431	420	410	410	410
Φ_t, x10^{22} n/cm^2 (E>0.1MeV)		3.1	10.5	16.0	23.4	30.3
Cumulative dpa		14.5	48.4	73.9	108.1	140.1
C38 (D9 B/P - 1)						
Canister/Basket	absent	1D2	1F5/1F4	1F2	1F2	1F6
Temp., °C		401	396	386	384	386
Φ_t, x10^{22} n/cm^2 (E>0.1MeV)		2.6	7 7	12 1	17 4	20.6
Cumulative dpa		11.5	32.4	52.3	76.5	89.8
C39 (D9 B/P - 2)						
Canister/Basket	absent	1D3	1F3	1F2	1F2	1F6
Temp., °C		401	396	386	384	386
Φ_t, x10^{22} n/cm^2 (E>0.1MeV)		2.4	8 0	12.4	17 7	20.9
Cumulative dpa		10.6	35.5	55.4	79.6	92.9
C40 (D9 B/P - 3)						
Canister/Basket	absent	1D3	1F3	1F3	1F3	1F6
Temp.. °C		401	396	386	384	386
Φ_t, x10^{22} n/cm^2 (E>0.1MeV)		2.4	8.0	12.2	17.0	20.2
Cumulative dpa		10.6	35.5	54.1	75.7	89.0
C42 (D9 B/P - 4)						
Canister/Basket	absent	2F4	2F4	2F5	2F3	2F3
Temp °C		431	420	404	414	405
Φ_t, x10^{22} n/cm^2 (E>0 1MeV)		3 1	10 3	15 4	22 8	30 1
Cumulative dpa		14 1	47 2	70 5	104 7	138 5
C44 (D9 B/P - 5)						
Canister/Basket	absent	1D3	1F3	1F2	1F2	1F6
Temp., °C		401	396	386	384	386
Φ_t, x10^{22} n/cm^2 (E>0.1MeV)		2.4	8.0	12.4	17.7	20.9
Cumulative dpa		10.6	35.5	55.4	79.6	92.9

The PCA (heat K280) alloy at the somewhat lower displacement rate and irradiation temperature is clearly swelling and creeping at rates comparable to that of the 83508 allay at a slightly higher displacement rate and temperature, but the onset of accelerated strain rate occurs with a delay of ~10 dpa relative to that of 83508. This delay cannot be attributed to compositional differences alone, but probably arises in part from both compositional and environmental differences (displacement rate and temperature). It may also reflect some differences in production methods associated with the two types of tubes.[12] Compared to the behavior of PCA and heat 83508, the A095 heat exhibits an even longer transient in both creep and swelling.

If both the small effect of stress on swelling and the possibility of precipitation-related strains are ignored, one can calculate a first order estimate of the B_o and D coefficients, using a least-squares fitting procedure. There are limitations to this approach, however, that are associated with the swelling level and the effect of stress. When swelling is low it is difficult to distinguish between and separate

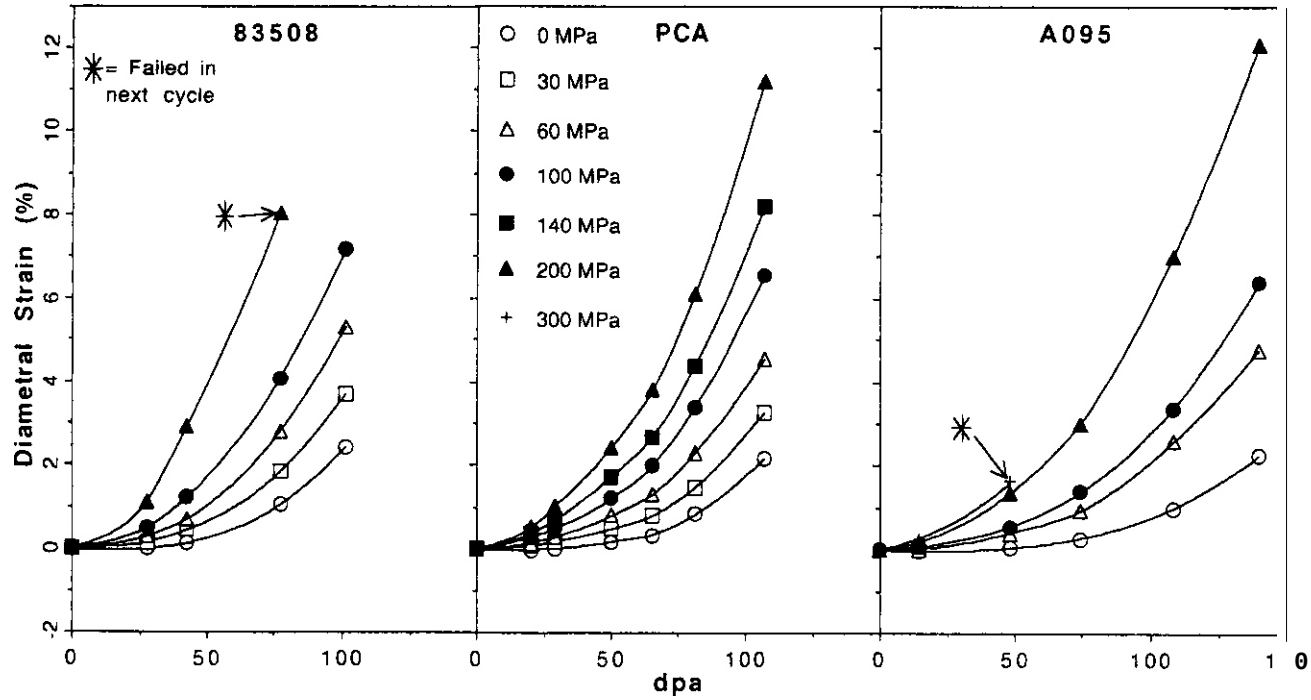

Fig. 1. Creep and swelling strains observed in pressurized tubes made from three titanium-modified stainless Steels that were irradiated in FFTF/MOTA at ~400°C.

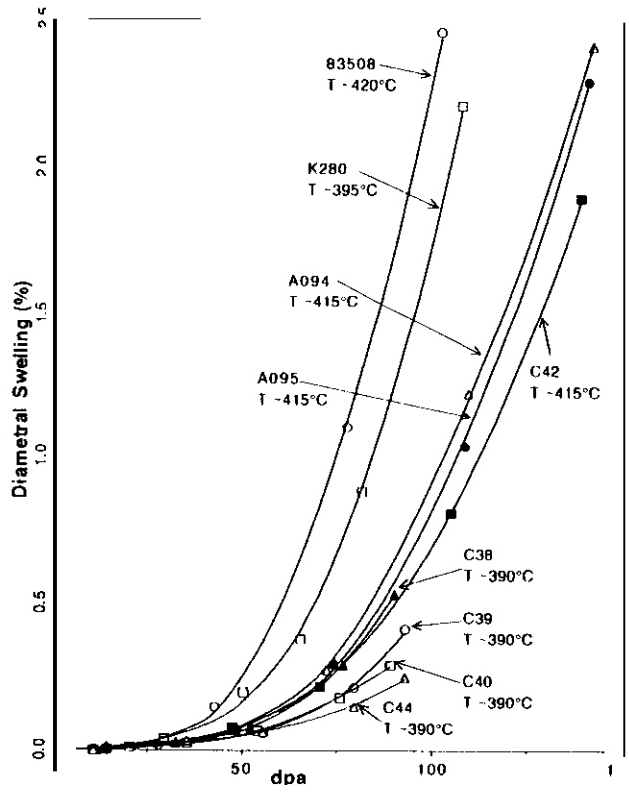

Fig. 2. Diametral strains resulting from void swelling at ~400°C in irradiated stress-free tubes constructed from nine titanium-modified stainless steels.

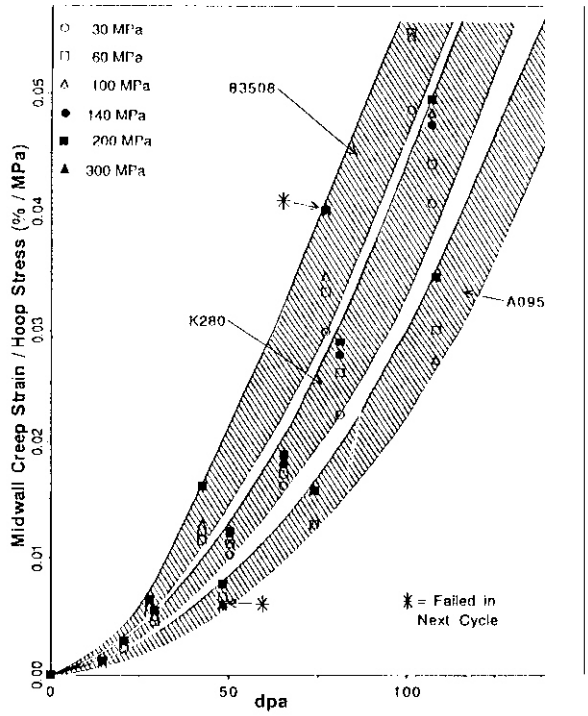

Fig. 3. Stress-normalized midwall creep strains observed at ~400°C in three heats of titanium-modified stainless steels. Note that the creep strains develop in the same sequence as does the swelling of the various heats. The slight increase in normalized creep strains with stress level is thought to reflect the stress enhancement of swelling rather than a nonlinearity of creep rate with stress.

the B_o and DS contributions, especially when precipitation-related strains occur early in the irradiation. As swelling increases, the relative contribution of the non-swelling-related strains decreases and better estimates of the creep-swelling coupling coefficient become possible. If stress accelerates swelling it will appear that the B_o contribution is larger than it actually is.

The initial step of the first order estimation procedure is to fit the stress-free linear swelling strain (S_L) curve (Figure 2) with an equation of the form

$$S_L = \frac{a}{c} \log \left[\frac{(b + e^{-cx})}{(1 + b)\, e^{-cx}} \right], \tag{2}$$

where x is the dose in dpa, a is the steady-state swelling strain rate, b is the incubation parameter and c is a parameter controlling the rate of curvature between the incubation and steady-state regimes.

The second step is to fit each creep strain curve in Figure 3 with an equation of the form

$$\varepsilon = qx + \frac{r}{c} \log \left[\frac{(b + e^{-cx})}{(1 + b)\, e^{-cx}} \right]. \tag{3}$$

Note that it is assumed that the incubation and curvature parameters are identical for both creep and swelling. This is a reasonable assumption if the B_o + DS model is correct. The degree of fit to the creep strain curves appears to confirm the validity of this assumption.

Upon integrating equation (1) with respect to x

$$\bar{\epsilon}/\bar{\sigma} = B_o X + DS + K. \tag{4}$$

where $S \approx 3S_L$ for small S_L. The parameter K = 0, since $\epsilon(0) = 0$ and $S(0) = 0$. When expressed in terms of midwall strain and hoop stress, σ_H, equation (4) becomes

$$\epsilon/\sigma_H = 3/4 \, [B_o x + DS]. \tag{5}$$

Substituting equations (2) and (3) into equation (5) yields

$$\frac{qx}{\sigma_H} + \frac{r}{c\sigma_H} \log \left[\frac{(b + e^{-cx})}{(1 + b)\, e^{-cx}} \right] = \frac{3}{4} B_o x + \frac{9Da}{4c} \log \left[\frac{(b + e^{-cx})}{(1 + b)\, e^{-cx}} \right]. \tag{6}$$

Solving for B_o and D gives

$$B_o = \frac{4q}{3\sigma_H} \text{ and } D = \frac{4r}{9a\sigma_H}. \tag{7}$$

The least-squares fitting routines used to determine q, r, a, b and c starts from an initial graphical estimate of these values. Table 3 lists the first-order estimates of B_o and D calculated for each stress level and each alloy. For the PCA alloy, the coefficients were found to be -2×10^{-6} MPa^{-1} dpa^{-1} and -0.6×10^{-2} MPa^{-1}. The average values of these coefficients are also shown in table 3 and Figure 4 for all nine alloys. It appears that the values of D converge to 0.6×10^{-2} when the swelling level is sufficiently large, although significant variation can occur in the B_o term at convergence. The value of 0.6×10^{-2} MPa^{-1} for D in these titanium-modified steels agrees with that observed in the low titanium stainless steels (AISI 304 and AISI 316) at ~400°C, but the B_o values found in this study for the low titanium steels are somewhat higher than the usually assumed value of -1×10^{-6} MPa^{-1} dpa^{-1}. The larger values of B_o found in the titanium-modified steels are thought to be a possible consequence of lower levels of densification compared to the larger level of precipitate-related densification that occurs in low titanium steels where the carbon is not bound up in titanium carbides.[11]

Table 3. Calculated Values of the Creep Compliance, B_o, and the Creep-Swelling Coupling Coefficient, D

	Stress level	B_o, x10^{-6} MPa^{-1}d a-1	D, x10^{-2} MPa^{-1}		Stress level	B_o, x10^{-6} MPa^{-1}d a-1	D, x10^{-2} MPa^{-1}
		2.8	0.63		100		1.19
	100	3.3	0.57		200	1.3	1.15
	200	3.7	0.75		Avg	1.2	1.13
	Avg	3.2	0.60				
K280	30	2 1	0 50	C39	60	1 1	1 4 1
	60	2 2	0 57		100	1 2	1 3 7
	100	2.3	0.64		200	1 4	1 4 5
	140	2.4	0.60		Avg	1 2	1 4 1
	200	2.4	0.64				
	Avg	2 3	0 59				
A094	60	1 4	0 41	C40	60	1 1	1 5 5
	100	1 4	0 40		100	1 0	1 74
	200	1.1	1.05		200	0 9	1 8 6
	Avg	1.3	0.62		Avg	1 0	1 7 2
A095	60	1.5	0.66	C44	60	0 8	2 41
	100	1.4	0.65		100	0 8	2 63
	200	1.8	0.75		200	0 6	2 99
	Avg	1.6	0 69		Avg	0 7	2 68
C42	60	1.4	0.40				
	100	1.6	0.56				
	200	1.6	0.73				
	Avg	1 5	0 56				

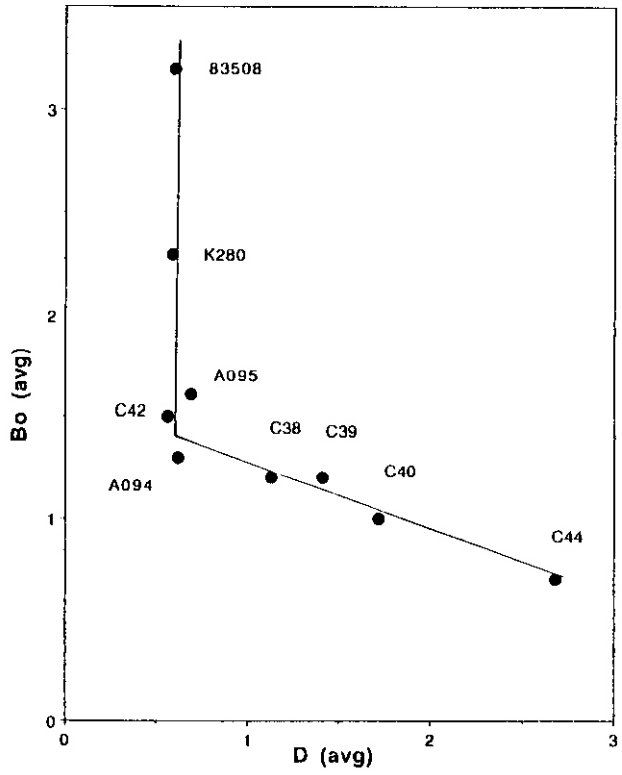

Figure 4. Calculated values of average creep compliance, B_o(avg), and average creep-swelling coupling coefficient, D(avg), for each alloy. Two regimes of behavior are observed. The data on the left hand vertical line describe alloys that exhibited a significant level of swelling. The other line describes irradiations in which the calculated value of B_o declines as the swelling level decreases. The lower derived values of B_o for these low swelling heats are accompanied by corresponding overestimates of the D coefficient.

Analysis of Data at Higher Temperatures

Both thermal creep and irradiation creep data from FFTF-MOTA are available for most of these steels at temperatures above 400°C. However, it is difficult to extract meaningful values of B_o and D from these higher temperature data. An overtemperature event in MOTA-10 for tubes irradiated at temperatures greater than 450°C resulted in a programmatic decision to terminate the irradiation of many of the high temperature tubes. At the lower fluence levels reached by these high temperature tubes, the swelling strains of titanium-modified steels were usually too low to provide separable estimates of the B_o and DS contributions.

In additirn, thermal creep becomes a large contributor to the strain at the higher temperatures and tends to obscure the OS contribution to the total strain rate. An attempt is currently being made to derive estimates of B_o and D from other high temperature data sets that reached higher swelling levels in irradiation experiments conducted in both FFTF and EBR-II. The results of this analysis will be reported elsewhere.(19)

CONCLUSIONS

Based on the results of this and other studies on various austenitic stainless steels irradiated at ~400°C in either EBR-II or FFTF, it appears that the B_o t DS model of irradiation creep is valid for application as a design equation. This model can be applied to both PCA and austenitic steels in general, providing the effect of stress on swelling is relatively small. At ~400°C the value of D in the 300 series of steels appears to be -0.6×10^{-2} MPa^{-1}, relatively independent of both composition and thermomechanical condition. Unfortunately, the data on titanium-modified steels available from FFTF at higher irradiation temperatures are insufficient at present to establish the temperature dependence of the creep-swelling coefficient.

ACKNOWLEDGEMENTS

M. B. Tolocrko gratefully acknowledges support from the U.S. Department of Energy, Division of University and Industry Programs, Office of Energy Research, as a Science and Engineering Research Semester program participant at Pacific Northwest Laboratory.

REFERENCES

1. D. L. Porter, F. A. Garner and G. D. Hudman, "Irradiation Creep and Swelling of Annealed 304L Stainless Steel at ~390°C and High Neutron Fluence," Fusion Reactor Materials Semiannual Prowess Report DOE/ER-0313/7 (1989) 133-139.

2. F. A. Garner, D. L. Porter and B. J. Makenas, J. Nucl. Mater. 148 (1987) 279-287.

3. D. L. Porter and F. A. Garner in Influence of Radiation of Material Properties, ASTM STP 956, Eds F. A. Garner. C. H. Henager, Jr. and N. Igata (1987) 11-21.

4. F. A. Garner and O. L. Porter, J. Nucl. Mater. 155-157 (1988) 1006-1013.

5. D. L. Porter and F. A. Garner, J. Nucl. Mater. 159 (1988) 114-121.

6. R. W. Clark, A. S. Kumar and F. A. Garner, J. Nucl. Mater. 155-157 (1988) 845-849.

7. F. A. Garner, J. Nucl. Mater. 122-123 (1984) 459-471.

8. F. A. Garner and D. S. Gelles, J. Nucl. Mater. 159 (1988) 286-309

9. K. Ehrlich, J. Nucl. Mater. 100 (1981) 149

10. F. A. Garner, W. V. Cummings, J. F. Bates and E. R. Gilbert, "Densification-Induced Strains in 20% Cold-Worked 316 Stainless Steel During Neutron Irradiation," HEDL-TME 78-9, Hanford Engineering Development Laboratory, June 1978.

11. R. J. Puigh, A. J. Lovell and F. A. Garner, J. Nucl. Mater. 122-123 (1988) 242-245.

12. F. A. Garner, R. J. Puigh, M. L. Hamilton, M. B. Toloczko and A. S. Kumar in this semiannual report

13. E. R. Gilbert and B. A. Chin in Effects of Radiation on Materials, Tenth Conference, ASTM STP 725, Eds. D. Kramer, H. R. Brager and J. S. Perrin, American Society for Testing and Materials, Philadelphia, (1981) 665-679.

14. M. B. Toloczko, F. A. Garner and C. R. Eiholzer, "Determination of Creep-Swelling Coupling Coefficients for Irradiated Stainless Steels," Fusion Reactor Materials Semiannual Progress Report DOE/ER-0313/9 (1991) 160-166.

15. F. A. Garner and R. J. Puigh, "Irradiation Creep of PCA Observed in FFTF/MOTA," Fusion Reactor Materials Semiannual Progress ReDort DOE/ER-0313/7 (1989) 140-144.

16. F. A. Garner, E. R. Gilbert and D. L. Porter, in Ref. 13 pp. 680-697

17. T. Lauritzen, S. Vaidyanathan, W. L. Bell and W. J. S. Yang in Radiation-Induced Chanues in Microstructure, 13th International Symposium (Part I) ASTM STP 955, F. A. Garner, N. H. Packan and A. S Kumar, Eds., American Society for Testing and Materials, Philadelphia, 1987, pp. 101-103.

18. D. L. Porter, M. L. Takata and E. L. Wood, J. Nucl. Mater. 116 (1983) 272-276

19. F. A. Garner and M. B. Tolozcko, in this semiannual reoort.

6.3 Refractory Metal Alloys

IRRADIATION-INDUCED PRECIPITATES IN VANADIUM ALLOYS CONTAINING TITANIUM

H. M. Chung. L. J. Nowicki. and D. L. Smith (Argonne National Laboratory)

OBJECTIVE

The microstructure. mechanical properties, and density of vanadium-base alloys are profoundly modified during neutron irradiation. The objective of this work is to characterize irradiation-induced precipitation in several candidate vanadium alloys containing titanium after irradiation in the Fast Flux Test Facility Materials Open Test Assembly (FFTF/MOTA) and to correlate the results with the swelling and mechanical properties of the alloys. thereby providing insight for development of an optimized alloy.

SUMMARY

The microstructures of V-Ti, V-Cr-Ti, and V-Ti-Si alloys were characterized by transmission electron microscopy (TEM) after neutron irradiation in the FFTF at 420 and 600°C to fluences up to 114 dpa. Two types of irradiation-induced precipitates were identified, i.e., Ti_2O and $Ti_5(Si,P)_3$. Blocky Ti(O,N,C) precipitatcs. which form by thermal processes during ingot fabrication, also were observed in all unirradiated and irradiated specimens. Irradiation-induced precipitation of spherical (<15 nm in diameter) $Ti_5(Si,P)_3$ phase was associatcd with superior resistance to void swelling. In specimens with negligible swelling, $Ti_5(Si,P)_3$ precipitation was significant. Irradiation-induced precipitation of the Ti_2O phase. a phase with needlelike morphology and approximately <20 nm thick and <200 nm long, was more pronounced in high-oxygen specimens irradiated at 600°C. It seems that ductility is significantly reduced when the precipitation of Ti_2O and $Ti_5(Si,P)_3$ is pronounced. These observations indicate that initial composition: fabrication processes; actual solute compositions of Ti, O, N, C, P, and Si after fabrication: O, N. and C uptake during service: and irradiation-induced precipitation are interrelated and are important factors to consider in developing an optimized alloy,

INTRODUCTION

The swelling behavior[1-5] and mechanical properties[6-10] of vanadium-base alloys (V-Ti, V-Cr. V-Cr-Ti, and V-Ti-Si). irradiated by fast neutrons at 420. 520, and 600°C in FFTF/MOTA was reported earlier. Density measurements showed that irradiation-induced swelling of vanadium-based alloys can be effectively inhibited by addition of >5 wt.% Ti in the alloy. For example, swelling of V-base alloys containing >5 wt.% Ti was <1%, in comparison with swelling as high as 3-4% for V. V-14Cr, V-15Cr-1Ti, and V-3Ti-1Si alloys upon irradiation at 420°C up to 114 dpa.[1] The superior resistance to void swelling of several high-Ti alloy specimens was associated in a previous investigation[5] with irradiation-induced formation of high-density precipitates that are spherical in morphology and approximately <15 nm in diameter. It was suggested in the study that the large interface area between the precipitates and matrix could serve as an effective sink to vacancies, thereby inhibiting void nucleation and growth. However. the very fine spherical precipitates could not be identified in the study.

In a similar effort to provide an understanding of significant ductility degradation of several promising alloys of the V-13.5Cr-5Ti type. Gelles et al.[11] investigated microstructural evolution of the alloys following irradiation at 600°C in FFTF/MOTA. They observed that specimen microstructure was characterized by two types of precipitates that formed in high density. i.e., (1) fine needlelike precipitates approximately <20 nm thick and <200 nm long and (2) spherical precipitates <15 nm in diameter, Based on its morphology. the latter appears to be same type of precipitate as those reported in Ref. 5 and correlated to the superior swelling resistance of some high-Ti alloys. The former type of precipitate was also reported by Loomis and Smith7 and by Ohnuki et al.[12] in some high-Ti alloys irradiated at 600°C. However, neither precipitate could he identified.

Impact tests were also conducted by Cannon et al.[10] on the V-13.5Cr-5Ti alloys. which exhibited significant degradation of ductility in tensile tests after irradiation at 600°C. The ductile-brittle transition temperature (DBTT) and the temperaturc of transition from transgranular-cleavage to ductile-rupture failure were estimated to be >400°C, indicating a significant degradation of fracture toughness. Hamilton and Loomis[9] considered hydrogen-induced embrittlement and an unfavorable precipitate development during irradiation as thc most likely causes of the ductility and toughness degradation. However, impact behavior was essentially similar after hydrogen removal. indicating that hydrogen-induced embrittlement was not the cause of the degradation.[9]

Thus. it seems evident from these investigations that the swelling and mechanical properties of V-Ti alloys are profoundly influenced by the two types of precipitates. i.e., the very fine spherical (referred to as Type 1 in Ref. 5) and the needlelike precipitates (referred to as Type II). The purpose of this investigation is to identify the two types of precipitates and thereby provide insight for development of optimized V-Ti alloy that will exhibit superior mechanical properties and resistance to void swelling.

MATERIALS AND PROCEDURES

Procedures for preparation of alloy specimens in this investigation have been described in earlier reports.[4,5] Chemical compositions of as-fabricated alloys are given in Table 1. The alloys were irradiated in the FFTF/MOTA at 420 and 600°C to neutron fluences (E > 0.1 MeV) ranging from 3×10^{22} n· cm^{-2} (17 dpa) to 1.9×10^{23} n· cm^{-2} (114 dpa). The specimens were sealed inside Li^7-filled TZM/Mo capsules during irradiation to prevent contamination by O. N. and C impurities dissolved in the sodium coolant of the FFTF.

Irradiated speamens of V-Ti, V-Cr-Ti, and V-Ti-Si alloys were selected and jet-thinned for TEM in a solution of 15% sulfuric acid-72% methanol-13% butyl cellosolve maintained at -5°C. TEM was conducted with a JEOL 100CX-II scanning transmission electron microscope (STEM) operating at 100 keV. Vanadium reflections were used as a standard in each selected-area diffraction (SAD) pattern to calculate reciprocal lattice spacings of the precipitates. In most cases, precipitate reflections were extremely weak and were easy to miss on the screen. It was best to detect the weak precipitate reflections by examining SAD patterns produced with a 22-cm camera length and an attached binocular. Dark-field images were obtained from as many precipitate reflections as possible in each SAD. SADs corresponding to several zone axes were obtained by tilting and transposing the specimen and were indexed to identify the crystallographic structure of the precipitate phase.

RESULTS

Primary Thermal Precipitation - Ti(O,N,C) Phase

All of the specimens of unirradiated or irradiated V-Ti, V-Cr-Ti, and V-Ti-Si alloys contained relatively large, blocky precipitates 100-1500 nm in diameter. Analyses of dark-field images and SAD patterns showed that these precipitates are of *fcc* structure with a lattice constant of ~0.42 nm. An example of an indexed SAD is shown in Fig. 1. The diffraction characteristics were consistent with the structure of TiO or TiN (both *fcc*, NaCl-type structure). Lattice constants of TiO and TiN have been reported as 0.418 to 0.424 nm and 0.422 to 0.425 nm, respectively, in the literature (see Table 2). TiC is also isostructural with TiO and TiN, with a similar lattice constant of 0.431 to 0.433 nm. Therefore, it appears that O, N, and C can dissolve in the structure simultaneously.

Examination of several TEM specimens from various alloys indicated a wide range of sizes and volume fractions, and a somewhat different morphology of the Ti(C,N,C) phase. In general, heats containing high oxygen (e.g., BL-12,O 1670 wt. ppm; BL-24, 1190 wt. ppm; and BL-34, 990 wt. ppm) developed more of this type of precipitate. This is shown in Fig. 2, which shows bright- or dark-field images of the phase obtained from eight alloys. On this basis, it is believed that O is the primary impurity dissolved in the phase. In a previous investigation, impurity composition of the same phase was analyzed by electron energy loss spectroscopy (EELS) on unirradiated specimens containing relatively low O and relatively high N.[13] The results indicated that N and C were primary impurities and that O was a secondary impurity. However, as pointed out by the authors, O quantification by EELS is very difficultin the presence of V and Ti because of the overlapping K and L edges. Thus, it is believed that the phase is a Ti(O,N,C)-type precipitate with a different degree of impurity composition in each heat of the alloy. However, O seems to be the major impurity that promotes the precipitation by a thermally driven process during fabrication. Ti(O,N,C) precipitates were not observed in V or V-Cr alloys. All of the Type-A, -III, and -V precipitates reported in Ref. 5, Type-I11 reported in Ref. 6, and the "blocky" precipitates reported in Ref. 11 are Ti(O,N,C) phase, which formed primarily by a thermal process. No evidence of precipitation of the higher-oxide TiO_2 was observed.

Secondary Thermal Precipitation - TiP Phase

In some high-Ti alloys (e.g., BL-15, 20.3 wt.% Ti), minor precipitates were observed. This type of precipitate was usually observed on or near grain boundaries and was referred to as Type IV in Ref. 5. An example of an indexed SAD pattern and dark-field morphology of this type of precipitate is shown in Fig. 3. The phase was identified as TiP, an *hcp* structure with lattice constants a = 0.3487 to 0.3513 nm and c = 1.165 to 1.175 nm (Table 2).

Table 1. Composition of Vanadium Alloys Irradiated in FFTF/MOTA

ANL ID	Nominal Composition (wt.%)	Concentration (wt. ppm) O	N	C	Si
BL-19	V	1101	161	360	----
BL-20	V	570	110	120	325
BL-36	V	810	86	250	e50
BL-51	V	570	49	56	370
BL-35	V-9.5Cr	340	45	120	e50
BL-4	V-10.0Cr	530	76	240	e50
BL-5	V-14.1Cr	330	69	200	<50
BL-50	V-1.0Ti	230	130	235	1050
BL-52	V-3.1Ti	210	310	300	500
BL-11	V-4.9Ti	1820	530	470	220
BL-46	V-4.6Ti	305	53	85	160
BL-34	V-8.6Ti	990	180	420	290
BL-12	V-9.8Ti	1670	390	450	245
BL-13	V-14.4Ti	1580	370	440	205
BL-15	V-17.7Ti	830	160	380	480
BL-16	V-20.4Ti	390	530	210	480
BL-10	V-7.2Cr-14.5Ti	1110	250	400	400
BL-43	V-9.2Cr-4.9Ti	230	31	100	340
BL-21	V-13.7Cr-4.8Ti	340	510	180	1150
BL-22	V-13.4Cr-5.1Ti	300	52	150	56
BL-23	V-12.9Cr-5.9Ti	400	490	280	1230
BL-25	V-14.4Cr-0.3Ti	390	64	120	<50
BL-26	V-14.1Cr-1.0Ti	560	86	140	e50
BL-24	V-13.5Cr-5.2Ti	1190	360	500	390
BL-40	V-10.9Cr-5.0Ti	470	80	90	270
BL-41	V-14.5Cr-5.0Ti	450	120	93	390
BL-43	V-9.2Cr-4.9Ti	230	31	100	340
BL-44	V-9.9Cr-9.2Ti	300	87	150	270
BL-47	V-4.1Cr-4.3Ti	350	220	200	870
BL-49	V-7.9Cr-5.7Ti	400	150	127	360
BL-42	V-3.1Ti-0.5Si	580	190	140	5400
BL-27	V-3.1Ti-0.3Si	210	310	310	2500
BL-45	V-2.5Ti-1.0Si	345	125	90	9900

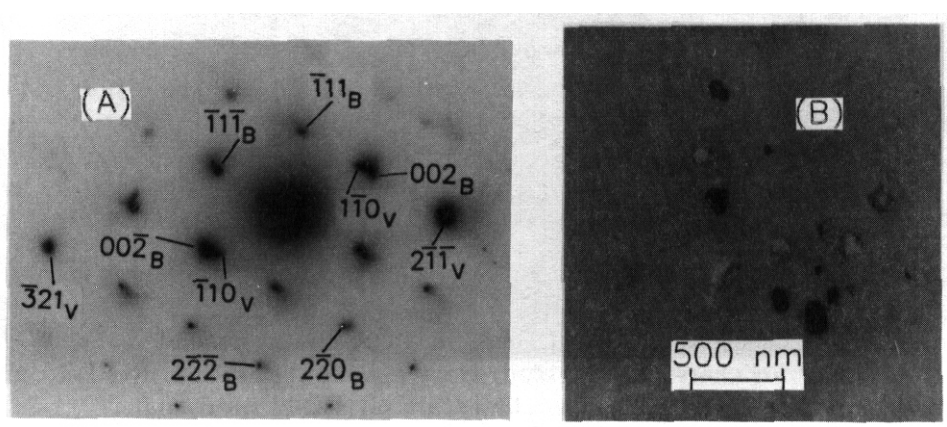

Fig. 1. Example of indexed SAD pattern (A) showing thermal precipitation of Ti(O,N,C) in V-3.1Ti-0.3Si (BL-27) irradiated at 420°C to 114 dpa. Dark-field morphology produced from the $<\bar{1}11>_{Ti(O,N,C)}$ reflection in (A) is shown in (B) in reverse contrast. Subscripts V and B in (A) denote vanadium and Ti(O,N,C), respectively.

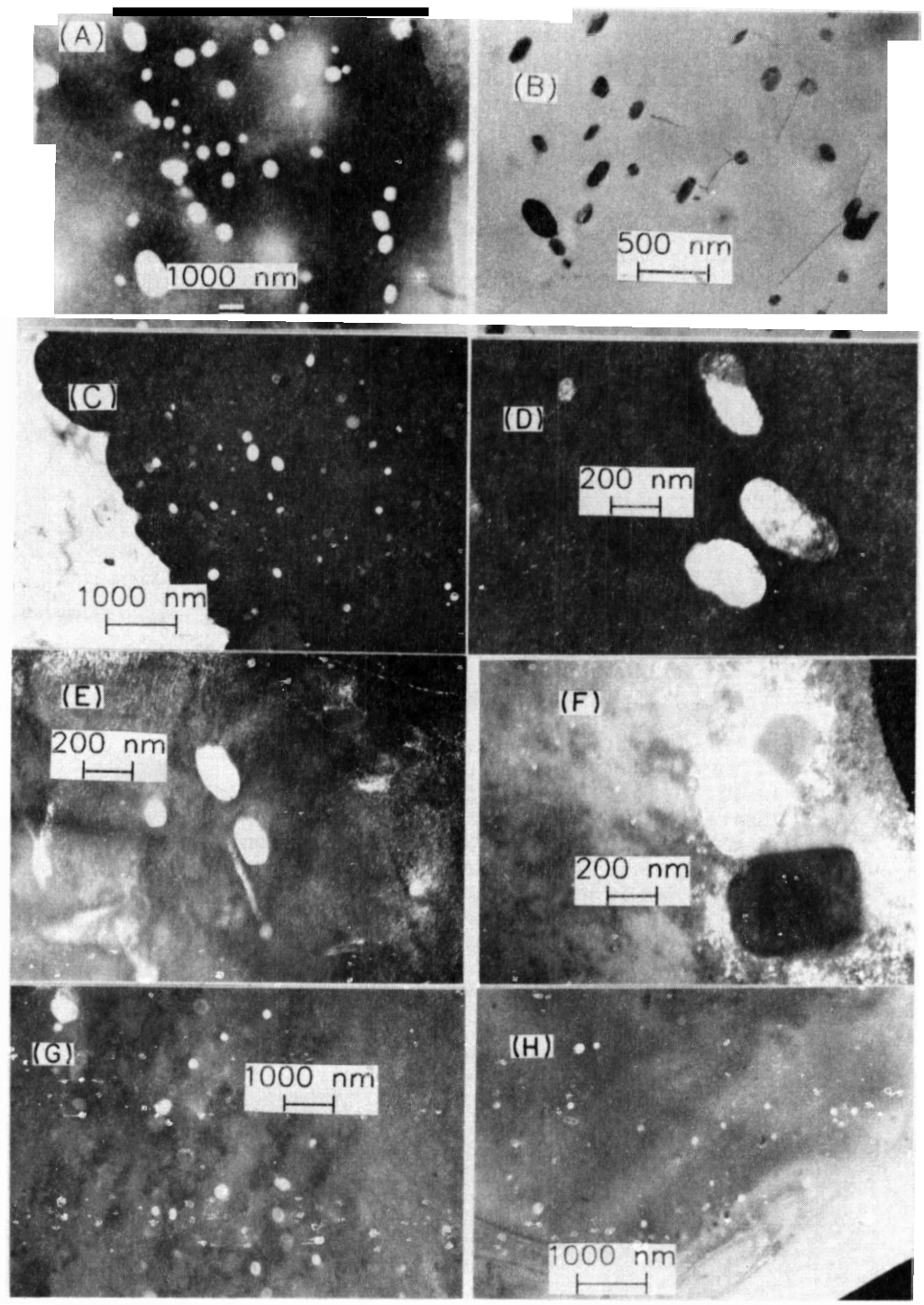

Fig. 2. Bright- or dark-field morphologies of Ti(O,N,C) observed in (A) BL-24, irradiated at 600°C to 17 dpa; (B) BL-34, unirradiated; (C) BL-12, unirradiated; (D) BL-15, irradiated at 420°C to 46 dpa; (E) BL-10, unirradiated; (F) BL-16, irradiated at 420°C to 114 dpa; (G) BL-27, unirradiated; and (H) BL-42, unirradiated.

Table 2. Summary of Crystal Structures and Lattice Constants of Ti Compounds Reported in Literature

Compound	Crystal Structure	Lattice Constants (in A)
TiC	fcc, NaCl-type	a = 4.313 to 4.330
TiC_2	cubic	a = 3.13
Ti_2H, TiH, TiH_2	fcc, CaF_2-type	a = 4.440
TiH_2	tetragonal	a = 4.42 to 4.45. c = 4.18 to 4.35
Ti_3N, e-phase	tetragonal	a = 4.92 to 4.94, c = 5.16
Ti_2N	tetragonal	a = 4.941, c = 3.037
TIN	fcc, NaCl-type	a = 4.22 to 4.25
Ti_3O	hcp. ordered Ti_2O	a = 5.141. c = 9.533
Ti_2O	hcp	a = 2.959. c = 4.683
Ti_3O_2, S-phase	tetragonal	a = 3.20. c = 5.12 or a = 5.344, c = 6.658
	hcp	a = 4.991. c = 2.879
TiO	fcc, NaCl-type	a = 4.182 to 4.243
TiO_2, rutile	tetragonal	a = 4.954. c = 2.958
TiO_2, anatase	tetragonal	a = 3.777. c = 9.501
TiO_2, brookite	orthorhomblc	a = 9.25.b = 5.45. c = 5.15
Ti_2O_3	rhombohedral	a = 5.433. a = 56°34'
	hcp	a = 5.149. c = 13.642
Ti_3O_5	monocllnlc	a = 9.75.b = 3.80. c = 9.44
	orthorhomhlc	a = 3.75,b = 9.48.c = 9.73
Ti_5O_9	trlcllnlc	
Ti_6O_{11}	triclinic	
Ti_7O_{13}	triclinic	
Ti_8O_{15}	triclinic	
Ti_9O_{17}	trlcllnlc	
Ti_3P	tetragonal	a = 9.956, c = 4.988
Ti_5P_3	hcp, Mn_5Si_3-type	a = 7.234.c = 5.090
TIP	hcp	a = 3.487 to 3.513 c = 11.65 to 11.75
TiP_2	orthorhombic, $PbCl_2$-type	a = 6.18.b = 8.25. c = 3.34
Ti_3Si	tetragonal	a = 10.39.c = 5.17
Ti_5Si_3	hcp. Mn_5Si_3-type	a = 7.463.c = 5.165
$TiSi_2$	orthorhomblc. C54-type	a = 8.25.h = 4.78.c = 8.54
	orthorhomhlc. $ZrSi_2$-type	a = 3.62.b = 13.76.c = 3.60
TiS_3	monoclinic	a = 4.973.b = 3.433. c = 8.714.β = 97.74'
TiS_2	hcp. CdI_2-type	a = 3.408 to 3.413 c = 5.691 to 5.701
Ti_2S_3	hcp. WC-type	a = 3.295.c = 3.190
	hcp	a = 3.422 to 3.442. c = 11.442 to 11.430
Ti_3S_4	monocllnlc	a = 5.98.b = 3.44.c = 10.14 β = 95°40'
Ti_4S_5	hcp	a = 3.424, c = 26.493
TiS	hcp, NiAs-type	a = 3.299.c = 6.380
Ti_6S	hcp	a = 2.966.c = 14.495

It seems that P atoms segregate thermally to grain boundaries during fabrication of ingots and that phosphides are formed preferentially on or near grain boundaries. Minor precipitates of $Ti_{1.7}P$, TiC, and a number of types of sulfides were also reported in unirradiated alloys in a previous investigation.[13]

Irradiation-Induced Precipitation - Ti20 Phase

The short needlelike precipitates (<20 nm in diameter and <200 nm in length), previously referred to as Type II in Refs. 5 and 6, were observed primarily in specimens of V-Ti (e.g., V-10Ti and V-20Ti) and V-Cr-Ti (e.g., V-15Cr-5Ti) containing high Ti after irradiation at 600°C. In a similar specimen irradiated at 420°C, precipitation of this type was negligible. Analyses of SAD and dark-field images showed that the precipitates are Ti20 phase, an *hcp* structure with lattice constants a = 0.2959 nm and c = 0.4683 nm. No other phase listed in Table 2 was compatible with the observed diffraction characteristics. Examples of indexed SAD and dark-field images,

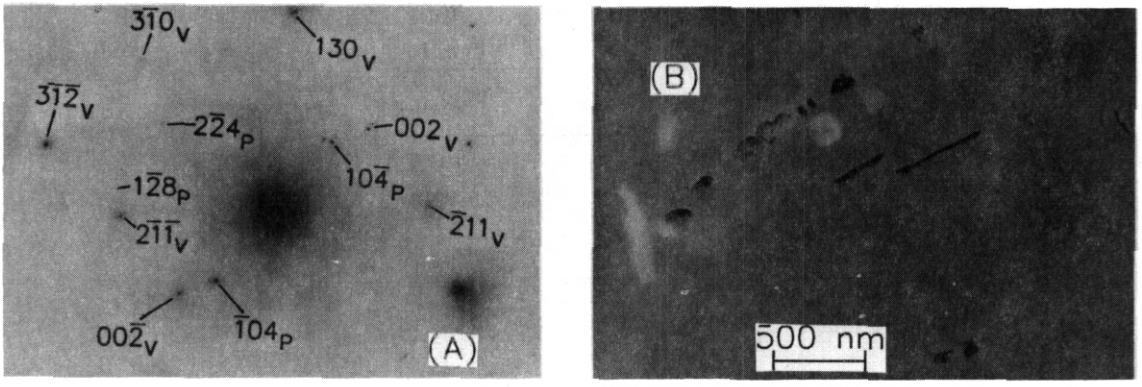

Fig. 3. Example of indexed SAD pattern (A) showing thermal precipitation of TiP on and near grain boundary in V-17.7Ti (BL-15) irradiated at 600°C to 84 dpa. Dark-field morphology produced from the $< \bar{1}04 >_{TiP}$ reflection in (A) is shown in (B) in reverse contrast. Subscripts V and P in (A) denote vanadium and TiP, respectively.

shown in Fig. 4, were obtained from a specimen of V-20Ti (BL-15) irradiated to 84 dpa at **600°C.** In the ***SAD*** of Fig. 4A, reflections from two grains of V matrix and Ti_2O are visible, as are reflections from the thermally formed precipitates of Ti(O,N,C) and TiP. In the SAD, $[110]_{Ti_2O}$ (d-spacing = 0.149 nm) is nearly parallel to $[002]_V$ (d-spacing = 0.151 nm). The dark-field images produced from $<002>_V$ reciprocal lattice **rods** and reported in Ref. 11 probably correspond to those from $<110>_{Ti_2O}$. In Fig. 4B, needlelike Ti_2O precipitates are relatively denuded near a grain boundary where a number of large TiP precipitates are located. Apparently, Ti **solutes** near the grain boundary had been "used up" to form the TiP precipitates during fabrication; as a consequence, sufficient Ti atoms were not available to permit Ti_2O precipitation during irradiation.

Irradiation-Induced Precipitation - $Ti_5(Si,P)_3$ Phase

Both V-18Ti (BL-15) and V-20Ti (BL-16) specimens irradiated at 420°C to 46 and 114 dpa, respectively, were characterized by profuse precipitation of a very fine (3-15 nm) spherical phase. This phase was also observed in high density in V-20Ti (BL-16) specimens after irradiation at 600°C to 17 dpa. However, the precipitates were not observed in V-3Ti-0.3Si (BL-27) after irradiation at 420°C to 114 dpa despite the high-Si content. The fine spherical precipitates were referred to as Type I in previous reports.[5,6] From bright-field imaging alone, it was difficult to either observe the precipitates or discern them from "black-dot" defects, which are of similar size and exhibit similar contrast. Therefore, it was necessary to search for and identify precipitate reflections in SAD patterns and to obtain dark-field images to determine the precipitate size and distribution.

Figure 5 shows examples of an indexed SAD pattern and dark-field images obtained from V-20Ti alloys irradiated at 420°C. The SAD pattern, obtained from the bright-field of Fig. 5A [from a specimen of BG15 (V-17.7Ti, Si 480 wt. ppm)] after irradiation at 420°C to 46 dpa, contains five rows of very weak reflections of the Type I precipitates that are parallel to the row of [110] of vanadium matrix (see indexed pattern, **Fig.** 5C). The two outermost rows of the weak precipitate reflections (Fig. 5C) are not visible in the printed SAD pattern (Fig. 5B), but could be identified from the original negative and in the slightly tilted SAD pattern. The patterns of the precipitate reflections could be indexed on the basis of the Ti_5Si_3 phase, an *hcp* Mn_5Si_3-type structure with lattice constants a = 0.7463 nm and c = 0.5165 nm (Table 2). A total of five zone axes were obtained and could be indexed consistently on the base of Ti_5Si_3. No other Ti-base phases listed in Table 2 were compatible with the diffraction characteristics of this type of precipitate. Ti_5P_3 is also isostructural with Ti_5Si_3, with similar lattice constants of a = 0.7234 nm and c = 0.5090 nm (Table 2). Therefore, it is expected that P atoms replace some Si atoms in the precipitate. In Fig. 5C, $< 01\bar{1} >_V$ (d-spacing = 0.2150 nm) is parallel to $<300>_{Ti_5(Si,P)_3}$ (d-spacing = 0.2154 nm). Figure 5D shows a dark-field image produced from $< 1\bar{3}\bar{1} >_{Ti_5(Si,P)_3}$ reflection in Fig. 5C. In this figure, a small number of voids in dark contrast, denoted with arrows, and a large number of the $Ti_5(Si,P)_3$ precipitates in white contrast are visible. An example of similar dark-field images is also shown in Fig. **6,** which was obtained from a BL-16 (V-20.4Ti, Si 480 wt. ppm) specimen irradiated at 420°C to 114 dpa.

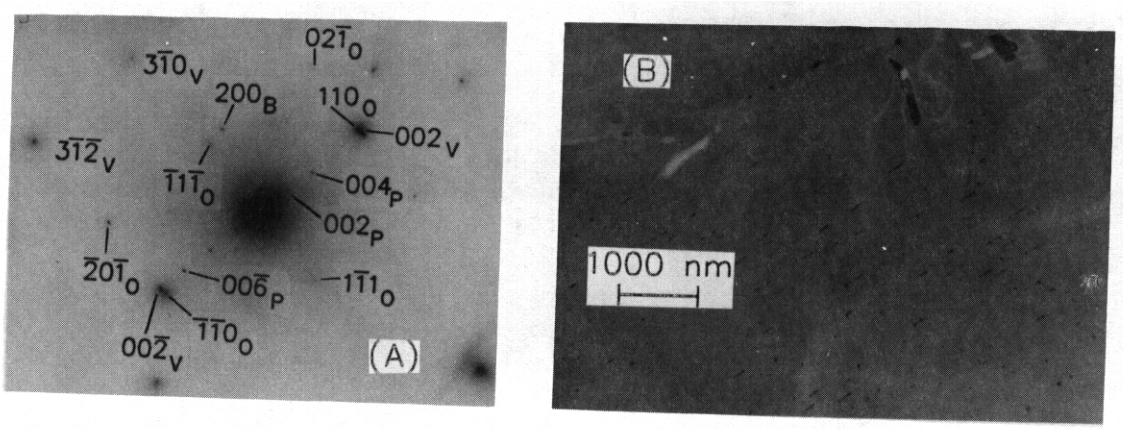

Fig. 4. Example of indexed SAD pattern (A) showing irradiation-induced precipitation of Ti_2O in V-17.7Ti (BL-15) irradiated at 600°C to 84 dpa. Dark-field morphology produced from the $< \bar{1}1\bar{1} >_{Ti_2O}$ reflection in (A) is shown in (B) in reverse contrast. Subscripts V, B, O, and P in (A) denote vanadium, Ti(O,N,C), Ti_2O, and TiP, respectively.

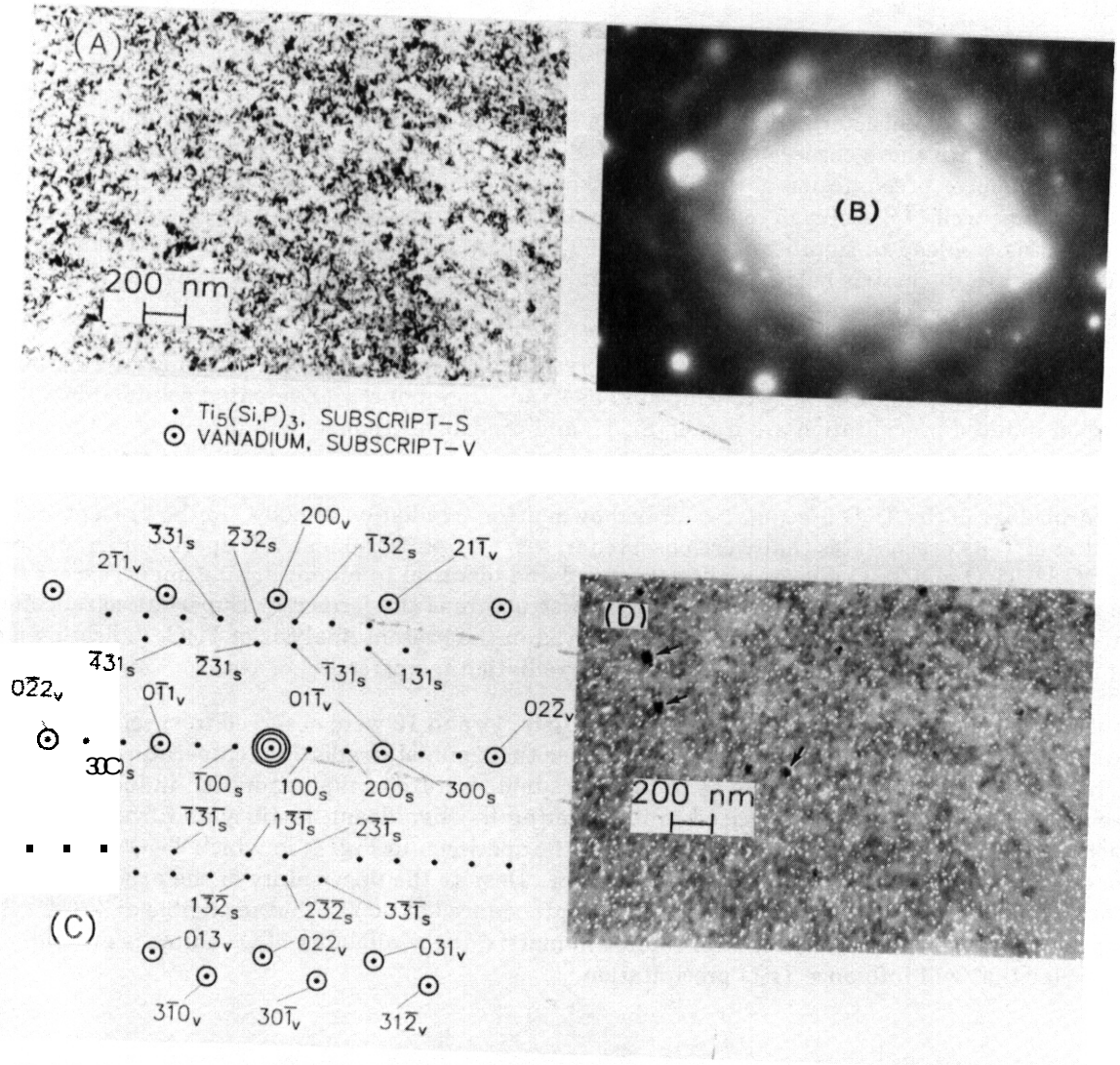

Fig. 5. Bright-field image (A), SAD pattern (B) and indexed pattern of (B) (C) showing irradiation-induced precipitation of $Ti_5(Si,P)_3$ in V-17.7Ti (BL-15) irradiated at 420°C to 46 dpa. Dark-field morphology produced from the $< 1\bar{3}\bar{1} >_{Ti_5(Si,P)_3}$ reflection in (C) is shown in (D). Subscripts V and S in (C) denote vanadium and $Ti_5(Si,P)_3$, respectively. A few voids are denoted with arrows in (D).

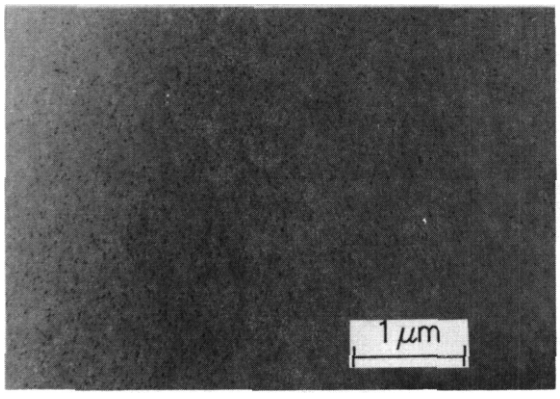

Fig. 6. Reverse-contrast dark-field image of $Ti_5(Si,P)_3$ precipitates observed in V-20.4Ti (BL-16) irradiated at 420°C to 114 dpa.

In Fig. 7, an indexed SAD pattern and dark-field image obtained from BG24 (V-13.5Cr-5.2Ti, Si 390 wt. ppm) after irradiation at 600°C to 17 dpa, and similar to those of Fig. 5, are shown. In Fig. 7A, $<1\bar{3}0>_{Ti_5(Si,P)_3}$ (d-spacing = 0.244 nm) is nearly parallel to c il 0 >v (d-spacing = 0.215 nm). The precipitate size shown in Fig. 7B seems to be somewhat larger than that of Figs. 5D or 6 (i.e., 15 vs. 10 nm), probably reflecting the influence of the higher irradiation temperature (i.e., 600 vs. 420°C).

DISCUSSION

Precipitation Characteristics

The results of TEM characterization of thermally formed precipitates [namely, Ti(O,N,C) and TiP] are generally consistent with those observed in unirradiated alloys,[13] except that O is believed to be the major impurity that influences precipitation of the Ti(O,N,C) phase. An important observation is that O, N, P, and probably C and S as well,[13] dissolve in ingots and tie up Ti solutes via precipitate formation during fabrication. In some cases, this can lead to significant depletion of Ti solutes in the vanadium matrix, thereby reducing the effective Ti content in the matrix below the level that inhibits void swelling. There is no evidence, however, that Si contributes to thermal precipitation.

Fine precipitates of Ti_2O and $Ti_5(Si,P)_3$ were observed in alloys only after some irradiation treatment. Therefore, both of the precipitates were concluded to be irradiation-induced. Evidently, solute atoms that control the irradiation-induced precipitation are free O, Si, Ti, and probably P that remain dissolved in the matrix after fabrication.

The morphology of the Ti_2O precipitates formed by neutron irradiation at 600°C in the present study is similar to that of Ti_3O precipitates that were observed in a V-14.1 at.%Cr-6.6 at.%Ti specimen irradiated by V++ ions at 677°C.[14] Ti_2O and Ti_3O phases are isostructural and identical in atomic arrangement, except that O vacancies in the latter are distributed orderly in a superstructure of the former.[15] Superlattice reflections characteristic of the O vacancy ordering were not observed in the present analysis of Ti_2O, indicating a salient feature of ion and neutron irradiation, or the effect of irradiation temperature, or both.

The needle- or plateletlike precipitates reported in Refs. 11 and 12 were observed in specimens known to have experienced temperature excursions of 156 to 206°C above the nominal irradiation temperature of 600°C for ~50 min. Therefore, some ambiguity remains as to the exact temperature of the irradiation-induced precipitation in those specimens, and care must be exercised in interpreting the significant ductility and fracture-toughness degradation observed in these specimens. In contrast, the specimen in Fig. 4, in which Ti_2O precipitates were identified, did not undergo such a temperature excursion. Despite the uncertainty of the exact irradiation temperature, it was evident that Ti_2O precipitation was pronounced at >600°C but negligible at 420°C. Beside the irradiation temperature and availability of Ti solutes in matrix, the availability of O solutes is evidently an important factor that will influence Ti_2O precipitation.

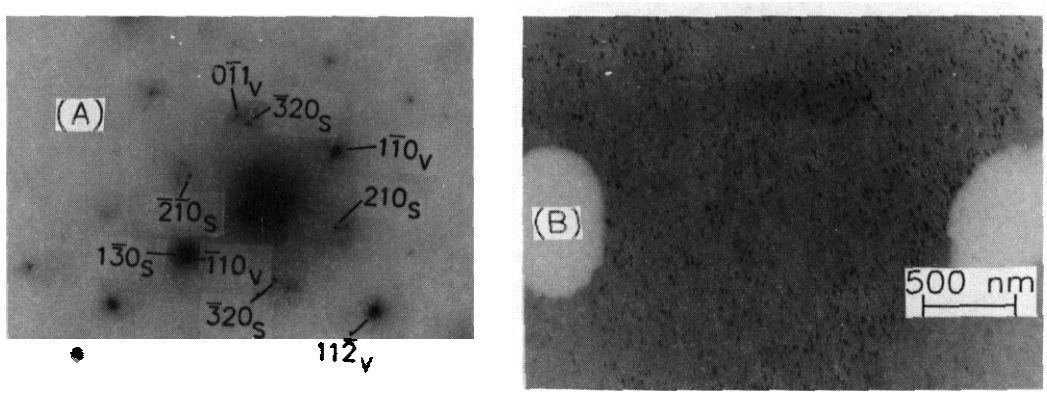

Fig. 7. Example of indexed SAD pattern (A) showing irradiation-induced precipitation of $Ti_5(Si,P)_3$ in V-13.5Cr-5.2Ti (BL-24) irradiated at 600°C to 17 dpa. Dark-field morphology produced from the $<\bar{3}20>_{Ti_5(Si,P)_3}$ reflection in (A) is shown in (B) in reverse contrast. Subscripts V and S in (A) denote vanadium and $Ti_5(Si,P)_3$, respectively.

In contrast to the strong influence of irradiation temperature on the precipitation of Ti_2O, precipitation of $Ti_5(Si,P)_3$ does not seem to be sensitive to irradiation between 420 and 600°C. Precipitation of the phase appears to be more sensitive to availability of Ti, Si, and probably P solutes in the matrix. Absence of $Ti_5(Si,P)_3$ precipitates in the Si-rich BL-27 (V-3.1Ti-0.3Si) specimens, irradiated at 420°C to 114 dpa, is most likely due to matrix depletion of Ti solutes by thermal precipitation of Ti(O,N,C).

Correlation with Swelling Behavior

Void swelling and density change were relatively significant in BL-27 (e.g., 3 % after irradiation at 420°C to 77 dpa) compared to those of high-Ti alloys (e.g., <0.8 % for BL-15 and BL-16) irradiated under similar conditions.* An example of significant void swelling in a specimen of BL-27, which contained negligible $Ti_5(Si,P)_3$ precipitates, is shown in Fig. 8. If sufficient Ti (e.g., 77 wt.%) were added and O, N, and C contents were minimized in the alloy, a significant amount of $Ti_5(Si,P)_3$ precipitate would form; as a result, void swelling would be negligible for a similar irradiation condition.

Even if Ti content is sufficiently high (i.e., >5 wt.%), precipitation of $Ti_5(Si,P)_3$ is expected to be negligible, and hence, swelling is expected to be significant if Si content is very low in the specimen. An example of this effect appears to have been manifested in the swelling of four alloys of V-13.5Cr-5Ti type, i.e., BL-21 (1150 wt. ppm Si), BL-23 (1230 Si), BL-24 (390 Si), and BL-22 (56 Si).[11] Swelling of BL-22 containing very low Si was significantly higher than swelling of the other alloys containing relatively high Si after irradiation at 420, 520, and 600°C up to 31 dpa. i.e., 1.56 to 2.39 vs. 0.0 to 1.4%.

Copious amounts of $Ti_5(Si,P)_3$ were observed in BL-15 irradiated at 420°C to 46 dpa (Fig. 5D), BL-16 irradiated at 420°C to 114 dpa (Fig. 6), and BL-24 irradiated at 600°C to 17 dpa (Fig. 7B). Void swelling in these specimens was negligible and the average density change was relatively small, i.e., 0.5, 0.4, and 0.14%, respectively.4 Thus, it seems that void swelling, and to a large extent density change, can be correlated with the number density of the $Ti_5(Si,P)_3$ precipitate. That is, the higher the precipitate density, the lower the void swelling. This could be attributed to the large interface area generated between the matrix and high-density precipitates of $Ti_5(Si,P)_3$, which acts as an efficient sink for vacancies and thereby inhibits nucleation and growth of voids. According to this model, the kinetics of void formation would be strongly influenced by the rates of vacancy formation, vacancy diffusion, and $Ti_5(Si,P)_3$ precipitation. Apparently, the rate of $Ti_5(Si,P)_3$ precipitation, e.g., at 420°C irradiation, would be slower than the rate of vacancy formation and may require some incubation time. In this situation, void swelling may be significant at an earlier stage, but diminishes at a later stage as a large number of $Ti_5(Si,P)_3$ precipitates form, resulting in a threshold fluence at which swelling reaches a maximum and subsequently decreases.4

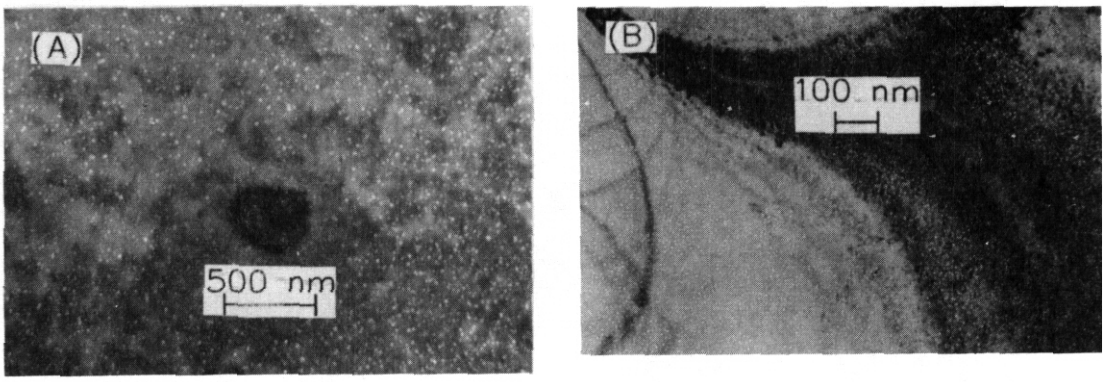

Fig. 8. Examples of significant void swelling observed in (A) V-3Ti-0.3Si (BL-27) and (B) V (BL-20) in absence of fine precipitates after irradiation at 420°C to 114 dpa.

Correlation with Mechanical Properties

Significant precipitation of spherical $Ti_5(Si,P)_3$ and needlelike Ti_2O is believed to be detrimental to material ductility and fracture toughness, as discussed relative to earlier findings.[11] The two alloys of V-13.5Cr-5Ti type (i.e., BG23 and BL-24), in which densities of irradiation-induced precipitates were high (Fig. 7 and Ref. 11), exhibited relatively low ductility after irradiation at 420,520, and 600°C in comparison with V-7.5Cr-15Ti, V-20Ti, and V-3Ti-0.3Si alloys.[6] The two alloys and the BL-21 for which fracture toughness was reported to be minimal[10] contained either relatively high O (as high as 1190 wt. ppm) or high Si (up to 1230 wt. ppm). Therefore, these three alloys of the V-13.5Cr-5Ti type seem to be conducive to significant precipitation of Ti_2O or $Ti_5(Si,P)_3$ or both during irradiation; as a consequence, they are susceptible to significant degradation of ductility and fracture toughness. However, it is difficult to determine which type of irradiation-induced precipitation, i.e., Ti_2O or $Ti_5(Si,P)_3$, is more detrimental to mechanical properties.

The specimens characterized in this study (Figs. 4-7) and in Ref. 11 (Figs. 3-6) still exhibited a significant level of total elongation, i.e., in excess of 10%.[6] Tensile elongations in most of V, V-Ti, V-Cr-Ti, and V-Ti-Si alloys measured after irradiation at 420,520, and 600°C were >9 % except in V-13.5Cr-5Ti alloys irradiated at 420°C.[6] Only in the high-Cr alloys irradiated at the low temperature have total elongations of <5 % been measured. This seems to indicate that in addition to the effects of irradiation damage and precipitation of Ti_2O or $Ti_5(Si,P)_3$, another type of irradiation-induced process may contribute to degradation of mechanical properties of V-Cr-Ti alloys containing Cr>10 wt.% and irradiated at 420°C [e.g., irradiation-induced formation of Cr (precursor of Cr-rich α' phase) or Cr-C clusters (precursor of $M_{23}C_6$-type phase)].

CONCLUSIONS

1. Primary and secondary precipitates that form via thermal processes during fabrication of vanadium-base alloys containing Ti are Ti(O,N,C) and TiP, respectively. The thermal precipitation influences the solute contents of Ti, O, and P atoms that remain in the matrix, which influence irradiation-induced precipitation during neutron irradiation at 420-600°C.

2. Two types of very fine irradiation-induced precipitates have been identified, i.e., needlelike Ti_2O (<20 nm thick and <200 nm long) and spherical $Ti_5(Si,P)_3$ (<15 nm in diameter). Precipitation of the latter can be significant at irradiation temperatures of 420 to 600°C, while the former seems to be more pronounced at higher temperatures. Besides the irradiation temperature, the actual concentration of Ti, O, Si, and probably P atoms that are not bound to thermal precipitates seem to be important in the formation of the irradiation-induced precipitates.

3. Significant precipitation of the Ti_2O and the $Ti_5(Si,P)_3$ phases seems to be a major factor in the degraded ductility and fracture toughness after irradiation. Void swelling and density change seem to be influenced primarily by number density of the fine $Ti_5(Si,P)_3$ precipitates. A higher number density of the precipitates is conducive to a lower swelling during irradiation. This is believed to be due to the large interface area between the matrix and the high-density precipitates of $Ti_5(Si,P)_3$, which acts as an efficient sink for vacancies thereby inhibits nucleation and growth of voids.

4. Minimizing Ti_2O precipitation and optimizing $Ti_5(Si,P)_3$ precipitation could be important in inhibiting swelling and at the same time ensuring acceptable mechanical properties of vanadium-base alloys containing Ti. This seems to involve controls of not only the relative but also the absolute contents of Ti and Si and the impurity elements O and N, and probably C, P, and S as well. Besides the precipitation of Ti_2O and the $Ti_5(Si,P)_3$, V-Cr-Ti alloys containing >10 wt.% Cr may be susceptible to an unidentified irradiation-induced process at 420°C, e.g., Cr or Cr-C clustering, which can lead to further degradation of mechanical properties. In this respect, it is desirable to limit Cr content in V-Cr-Ti alloys, e.g., to <6 wt.%.

FUTURE WORK

Effects of alloying elements (Ti, Cr, and Si), impurity content (O, N, C, Si, and P), volume fraction of Ti(O,N,C), irradiation temperature, and fluence on number density and distribution of the irradiation-induced precipitates will be determined quantitatively. The number density of $Ti_5(Si,P)_3$ precipitates will be correlated with size and density of voids. Similar correlation will be also obtained between ductility and $Ti_5(Si,P)_3$ and Ti_2O precipitates.

ACKNOWLEDGMENTS

The authors are grateful to B. A. Loomis for helpful discussions and for making the irradiated specimens available for microstructural characterization.

REFERENCES

1. B. A. Loomis and D. L. Smith, "Swelling of Neutron-Irradiated Vanadium Alloys," Fusion Reactor Materials Semiannual Progress Report for Period Ending March 31, 1989, DOE/ER-0313/6, Oak Ridge National Laboratory, Oak Ridge, TN, August 1989, pp. 339-345.

2. B. A. Loomis and D. L. Smith, "Relationship of Microstructure and Tensile Properties for Neutron-Irradiated Vanadium Alloys," Fusion Reactor Materials Semiannual Progress Report for Period Ending March 31, 1990, DOE/ER-0313/8, Oak Ridge National Laboratory, Oak Ridge, TN, August 1990, pp. 225-235.

3. B. A. Loomis, D. L. Smith, and F. A. Garner, "Swelling of Neutron-Irradiated Vanadium Alloys," in Proc. 4th Intl. Conf. on Fusion Reactor Materials, December 4-8, 1989, Kyoto, Japan.

4. B. A. Loomis, K. Abe, L. J. Nowicki, H. Chung, and D. L. Smith, "Swelling Dependence of Neutron-Irradiated Vanadium Alloys on Temperature, Neutron Fluence, and Thermomechanical Treatment," Fusion Reactor Materials Semiannual Progress Report for Period Ending September 30, 1990, DOE/ER-0313/9, Oak Ridge National Laboratory, Oak Ridge, TN, in press.

5. H. M. Chung, B. A. Loomis, and K. Abe, "Correlation of Microstructure and Swelling Behavior of Vanadium Alloys Irradiated in FFTF/MOTA at 420°C," Fusion Reactor Materials Semiannual Progress Report for Period Ending March 31, 1991, DOE/ER-0313/10, Oak Ridge National Laboratory, Oak Ridge, TN, pp. 135-144.

6. B. A. Loomis and D. L. Smith, "Tensile Properties for Neutron-Irradiated Vanadium Alloys," Fusion Reactor Materials Semiannual Progress Report for Period Ending September 30, 1989, DOE/ER-0313/7, Oak Ridge National Laboratory, Oak Ridge, TN, pp. 203-209.

7. B. A. Loomis and D. L. Smith, "Relationship of Microstructure and Tensile Properties for Neutron-Irradiated Vanadium Alloys," Proc. Fifteenth International Symposium on the Effects of Radiation on Materials, Nashville, TN, June 17-21, 1990, in press.

8. B. A. Loomis, L. J. Nowicki, and D. L. Smith, "Tensile Properties of Vanadium and Vanadium-Base Alloys," Fusion Reactor Materials Semiannual Progress Report for Period Ending March 31, 1991, DOE/ER-0313/10, Oak Ridge National Laboratory, Oak Ridge, TN, July 1991, pp. 145-155.

9. M. L. Hamilton and B. A. Loomis, "Impact Behavior of Irradiated V-15Cr-5Ti Following Hydrogen Removal," Fusion Reactor Materials Semiannual Progress Report for Period Ending September 30, 1990, DOE/ER-0313/7, Oak Ridge National Laboratory, Oak Ridge, TN, pp. 190-192.

10. N. S. Cannon, M. L. Hamilton, A. M. Ermi, D. S. Gelles, and W. L. Hu,"Influence of Neutron Irradiation on the Charpy Impact Properties of V-15Cr-5Ti," J. Nucl. Mater. 155-157,1988, pp. 987-991.

11. D. S. Gelles, S. Ohnuki, B. A. Loomis, H. Takahashi, and F. A. Garner, "Microstructural Explanation for Irradiation Embrittlement for V-15Cr-5Ti," Fusion Reactor Materials Semiannual Progress Report for Period Ending September 30,1989, DOE/ER-0313/7, Oak Ridge National Laboratory, Oak Ridge, TN, pp. 193-202.

12. S. Ohnuki, D. S. Gelles, B. A. Loomis, F. A. Garner, and H. Takahashi, "Microstructural Examination of Simple Vanadium Alloys Irradiated in the FFTF/MOTA," Fusion Reactor Materials Semiannual Progress Report for Period Ending September 30,1989, DOE/ER-0313/7, Oak Ridge National Laboratory, Oak Ridge, TN, pp. 177-189.

13. T. Schober and D. N. Braski, "The Microstructure of Selected Annealed Vanadium-Base Alloys," Met. Trans. A 20,1989, pp. 1927-1932.

14. B. A. Loomis, B. J. Kestel, and S. B. Gerber, "Solute Segregation and Microstructural Evolution in Ion-Irradiated Vanadium-Base Alloys," Proc. 13th Intl. Conf. on Radiation-Induced Changes in Microstructure, ASTM STP 955, Part I, Philadelphia, 1987, pp. 730-742.

15. B. Holmberg, "Disorder and Order in Solid Solutions of Oxygen in a-Titanium," Acta Chem Scandinavica 16,1962, pp. 1245-1250.

THE EFFECT OF HYDROGEN, CHROMIUM, TITANIUM, AND SILICON ON THE DUCTILE-BRITTLE TRANSITION TEMPERATURE OF VANADIUM AND VANADIUM-BASE ALLOYS* - B. A. Loomis, L. J. Nowicki, and D. L. Smith (Argonne National Laboratory).

OBJECTIVE

The objective of this research is to determine the composition of a vanadium-base alloy with the optimal combination of mechanical properties. corrosion resistance, fabricability, and weldability for use as a structural material in the environment of a magnetic fusion reactor.

SUMMARY

Ductile-brittle transition temperatures (DBTTs) were determined for dehydrogenated and hydrogenated unalloyed V and V-1Ti, V-10Ti, and V-7Cr-5Ti alloys from Charpy-impact tests. These DBTT data complement the data previously reported by Loomis et al.[1,2] on Charpy impact testing of V-3Ti-1Si, V-5Ti, V-5Cr-5Ti, V-10Cr-5Ti, V-20Ti, V-10Cr-10Ti, V-15Cr-5Ti, V-15Ti-7.5Cr, and Vanstar-7 alloys. The present experimental results show that V alloys with Ti additions (0-20 wt.%) have a minimum DBTT (≈-250°C) in an alloy containing ≈5 wt.% Ti, that addition of up to 15 wt% Cr to V-5Ti alloy results in a substantial increase (90-160°C) of the DBTT, and that Si additions (0.25-1.0 wt.%) to V-3Ti alloy result in a significant increase (≈60°C) in DBTT. In addition, the current results show that the presence of 400-1200 appm H in unalloyed V and V alloys causes a significant increase (60-250°C) in DBTT. The DBTT of V-5Ti, V-5Cr-5Ti, V-7Cr-5Ti, and V-10Ti alloys is least affected by H. The DBTT dependence of these materials on H, Cr, Ti, and Si concentration is presented in the form of tables, graphs, and parametric equations.

PROGRESS AND STATUS

Introduction

The V-15Cr-5Ti alloy has been considered to be a reference alloy for the evaluation of vanadium-base alloys as structural material for a fusion reactor, based on this alloy's generally attractive mechanical, corrosion, and irradiation performance. However, recent data obtained from Charpy impact tests and tensile tests on this alloy with and without neutron irradiation show that this alloy will be unacceptable as structural material for a fusion reactor because of its high DBTT (>250°C).[1-4] Loomis et al. have shown from Charpy-impact *tests* on unirradiated and irradiated vanadium alloys that a vanadium-base alloy containing Cr and/or Ti and Si alloying additions and intended for use as a structural material in a fusion reactor should contain 3-9 wt.% total alloying addition for maximum resistance to hydrogen- and/or irradiation-induced embrittlement.' In this report, we present additional data on the DBTTs for vanadium-base alloys that tend to confirm the requirement for a 3-9 wt.% combined Cr and/or Ti alloying addition.

Materials and Procedures

Unalloyed vanadium and vanadium-base alloys with the nominal compositions of V-1Ti, V-10Ti, and V-7Cr-5Ti were obtained in sheet form with a 50% thickness reduction, i.e., cold work, resulting in a nominal thickness of 3.8 mm. The compositions of these materials and previously tested vanadium alloys are listed in Table 1.[1,2]

Miniature Charpy-impact specimens were prepared for a determination of the temperature dependence of fracture behavior in the dehydrogenated and hydrogenated V and V alloys. The Charpy specimens had overall dimensions of 3.30 x 3.30 x 25.4 mm and a notch depth of 0.61 mm. Specimens were prepared with the notch orientation perpendicular to the rolling direction maintained during thickness reduction. Dehydrogenated Charpy-test specimens in the fully recrystallized condition were prepared from the 50% cold-worked materials by annealing for 1 h in a vacuum of 2 x 10^{-5} Pa.

The V and V-1Ti alloy specimens were annealed at 1025°C. Annealing temperature for the V-10Ti and V-7Cr-5Ti specimens was 1100°C. In the case of the previously tested alloy specimens, the V-Cr-Ti specimens and the Vanstar-7 specimens were annealed at 1125°C. The V-20Ti and V-3Ti-Si alloy specimens were annealed at 1100 and 1050°C, respectively. These annealing conditions for the cold-worked materials resulted in average recrystallized grain diameters in the range of 0.02-0.04 mm. Hydrogen was introduced into Charpy specimens of the alloys by annealing the cold-worked specimens at the previously mentioned temperatures in argon-filled quartz tubes for 1 h and subsequently quenching the tubes and their contents, without rupture, in water. The hydrogen concentration in the specimens was adjusted by surface-finishing the specimens prior to the anneal in the quartz tubes?

*Work supported by the Office of Fusion Energy, U.S. Department of Energy, under Contract W-31-109-Eng-38.

Table 1. Compositions of vanadium and vanadium-base alloys.

Nominal Composition	ANL I.D.	Concentration (wt.%)			Concentration (ppm)			
		Cr	Ti	Fe	O	N	C	Si
V	BL 51				570	49	56	370
V-1Ti	BL 50		1.0		230	130	235	1050
V-3Ti-0.5Si	BL 42	-	3.1	0.02	580	190	140	5400
V-3Ti-1Si	BL 45	-	2.5	0.01	345	125	90	9900
V-5Ti	BL 46		4.6		300	53	85	160
V-10Ti	BL 12		9.8	0.63	1670	390	450	245
v-2oTi	BL 15		17.7	0.04	830	160	380	480
V-5Cr-5Ti	BL 47	4.1	4.3		350	220	200	870
V-7Cr-5Ti	BL 49	7.9	5.7		400	150	127	360
V-10Cr-5Ti	BL 43	9.2	4.9	0.02	230	31	100	340
V-15Cr-5Ti	BL 24	13.5	5.2	0.05	1190	360	500	390
V-15Cr-5Ti	BL 41	14.5	5.0	0.02	330	96	120	400
V-10Cr-10Ti	BL 44	9.9	9.2	0.04	300	87	150	270
V-7.5Cr-15Ti	BL 10	7.2	14.5	0.09	1110	250	400	400
Vanstar-7[a]	BL 28	9.7		3.50	280	520	640	

[a]Alloy contains 1.3% Zr.

Hydrogen concentration in the Charpy specimens was determined from the total partial pressure of hydrogen that was evolved on heating a specimen at 15°C/min from 25°C to 1000°C. This procedure is discussed in more detail in Ref. 5. In the case of the Charpy specimens annealed in vacuum (i.e., dehydrogenated), the hydrogen concentration was determined to be <30 appm. Hydrogen concentration in the specimens annealed in quartz tubes (i.e., hydrogenated) ranged from 400 to 1200 appm.

The Charpy-impact tests were performed with an instrumented Dynatup Drop Weight Impact Test machine. Impact velocity and load for these tests were 2.56 m/sec and 14.995 kg, respectively. Energy absorption was determined from applied load-time data that were acquired during the impact. These data were analyzed and plotted with a GRC Model 730-I data acquisition and analysis system. Specimen temperature at the instant of impact was determined from a thermocouple that was spot-welded near the notch. Specimen temperatures during the Charpy tests were limited to -190 to 250°C. A curve for the energy absorbed during impact versus test temperature for V and V alloy specimens was fitted with a hyperbolic tangent equation to determine the curve inflection point: this curve point was used to define the DBTT.

The microstructures of annealed Charpy specimens, the appearance of fracture surfaces of tested specimens, and the temperature dependence of energy absorbed during the impact tests on the V alloys can be found in Refs. 1 and 2.

Experimental Results

The DBTTs for dehydrogenated (<30 appm H) and hydrogenated (400-1200 appm H) V and V-base alloys are presented in Table 2.

1. Dependence of DBTT on Ti concentration

The DBTT dependence of dehydrogenated (i.e., <30 appm H) and hydrogenated (i.e., 400-1200 appm H) V-Ti alloys on Ti concentration is shown in Fig. 1. The DBTTs of unalloyed V (-150°C for dehydrogenated V and -10°C for hydrogenated V) decrease as Ti concentration increases to ≈5 wt.%, to yield the alloys with the minimum DBTTs, i.e., ≤-250°C for dehydrogenated alloy and ≤-160°C for hydrogenated alloy. DBTTs for V-Ti alloys (dehydrogenated and hydrogenated) increase as Ti concentration increases from ≈5 to ≈20 wt.%. The DBTT values of a dehydrogenated and hydrogenated V-20Ti alloy were -40°C and 55°C, respectively.

As shown in Fig. 1, the presence of 500-900 appm H in binary V-(0-20)Ti alloys causes a significant DBTT increase (60-200°C) in the dehydrogenated alloy. The differences between the DBTTs of dehydrogenated and hydrogenated unalloyed V and binary V-Ti alloys suggest that V-Ti alloys containing ≤5 wt.% Ti may be more susceptible to hydrogen embrittlement (see Fig. 1).

Table 2. DBTT of V and V alloys

Nominal Composition	ANL I.D.	Hydrogen (appm)	DBTT (°C)
V	BL 51	<30	-150
		700	-10
V-1Ti	BL 50	<30	-225[a]
		650	-25
V-3Ti-0.5Si	BL 42	<30	-125
		520	-140
		970	-170
V-3Ti-1Si	BL 45	<30	-170
		994	-25
v-51i	BL 46	<30	-250"
		050	-160
V-10Ti	BL 12	<30	-190[a]
		600	-130
V-20Ti	BL 15	<30	-40
		580	+55
V-5Cr-5Ti	BL 47	<30	-225"
		1200	-125
V-7Cr-5Ti	BL 49	<30	-05
		600	-5
V-10Cr-5Ti	BL 43	<30	-60
		670	+50
V-15Cr-5Ti	BL 24	<30	-10
		590	+130
V-15Cr-5Ti	BL 41	<30	-10
		620	+135
V-10Cr-10Ti	BL 44	<30	+10
		1180	+155
V-7.5Cr-15Ti	BL 10	<30	+25
		400	+250
Vanstar-7	BL 28	<30	-65
		500	-25

[a] Lowest test temperature was -190°C. DBTT was estimated from the temperature for test temperatures above -190°C.

2. Dependence of DBTT on Cr concentration

The DBTT dependence of dehydrogenated and hydrogenated V-Cr-5Ti alloys on Cr concentration is shown in Fig. 2. The DBTTs of the dehydrogenated and hydrogenated V-5Ti alloy (viz., -250°C and -160°C. respectively) increase as the Cr concentration in this alloy rises to at least 15 wt.%. DBBT values of the dehydrogenated and hydrogenated V-15Cr-5Ti alloy (BL 41) were -10°C and 135°C, respectively.

As shown in Fig. 2, the presence of 500-1200 appm H in V-Cr-5Ti alloys causes a significant DBTT increase (60-145°C) in the dehydrogenated alloy. The differences between the DBTTs of dehydrogenated and hydrogenated V-Cr-5Ti alloys suggest that V-Cr-5Ti alloys containing <10 wt.% Cr may be less susceptible to hydrogen ernbrittlement (see Fig. 2).

3. Dependence of DBTT on Si concentration

The DBTTs for the V-3Ti-0.5Si (BL 42) and V-3Ti-1Si (BL 45) alloys are presented in Table 2 and in Fig. 1 (unfilled symbols). Although DBTTs of a V-31i alloy were not determined in this study, values for the dehydrogenated and hydrogenated alloys are estimated to be -250°C and -120°C, respectively, from Fig. 1 and the parametric equations pre-

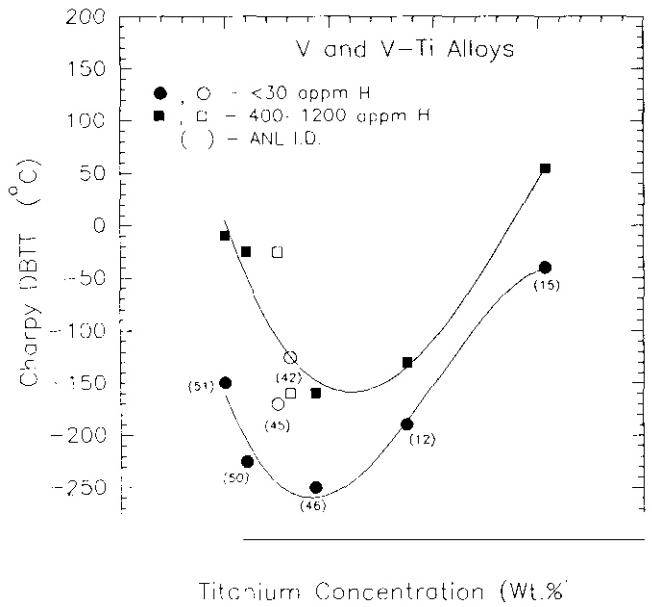

Fig. 1. V and V-Ti alloy dependence of DBTT on Ti concentration (●, ■ = V and V-Ti alloys; ○, □ = V-3Ti-Si alloys; ——— = curve fit).

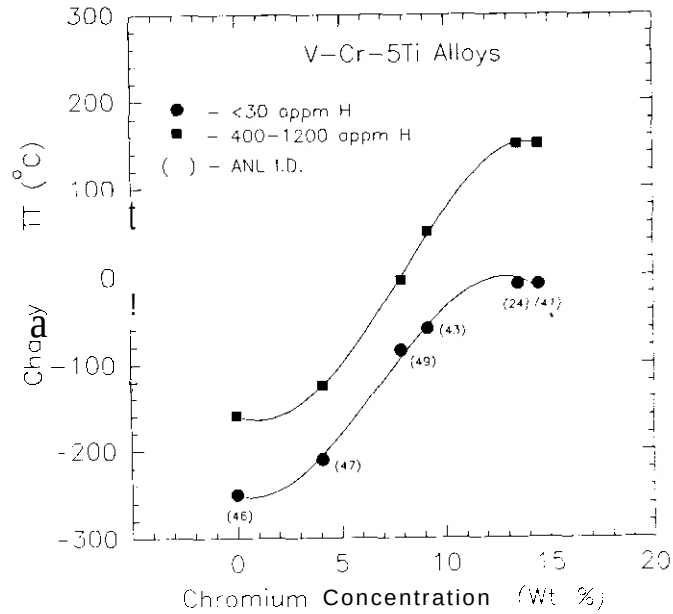

Fig. 2. V-Cr-5Ti alloy dependence on Cr concentration (——— = curve fit).

sented in Sec. 5. Therefore, it may be concluded that the addition of 5400-9900 ppm Si to a V-3Ti alloy results in an 80-125°C increase of DBBT in the dehydrogenated V-3Ti alloy. In the case of a hydrogenated V-3Ti alloy, the addition of 5400 ppm Si is estimated to result in a 20-50°C decrease of DBTT, whereas addition of 9900 ppm Si is estimated to result in a 95°C DBTT increase.

4. Dependence of DBTT on combined Cr and Ti concentration

The DBTT dependence of V and V-base alloys on combined Cr and Ti concentration, i.e., $C_{Cr} + (C_{Ti})^{0.95}$, is shown in Fig. 3. For the Vanstar-7 alloy, the Fe and Zr concentrations are treated as Cr and Ti concentrations, respectively. The DBTT dependence on combined Cr and Ti concentration is similar to that on Ti concentration shown in Fig. 1, i.e., the minimum DBTT for dehydrogenated and hydrogenated V-base alloys is seen when the combined Cr and Ti concentration is ≈5 wt.%.

The differences between DBTTs of dehydrogenated and hydrogenated unalloyed V and V-base alloys show that V-base alloys containing <15 W.% combined Cr and Ti concentration are less susceptible to hydrogen embrittlement.

5. Parametric equations

The DBTT dependence on concentration of alloying addition, i.e., C_{Ti}, C_{Cr}, and C_{Cr+Ti}, in dehydrogenated and hydrogenated unalloyed V and V-base alloys is formulated by the equations below (and shown graphically in Figs. 1-3).

V and V-Ti allovs (Fig. 1):

Dehydrogenated--
DBTT (°C) = -161.8521 - 52.1842 C_{Ti} + 7.9699 C_{Ti}^2 - 0.2641 C_{Ti}^3

Hydrogenated--
DBTT (°C) = 4.9477 - 59.5405 C_{Ti} + 6.1862 C_{Ti}^2 - 0.1356 C_{Ti}^3

V-Cr-5Ti alloys (Fig. 2):

Dehydrogenated--
DBTT (°C) = -251.0253 - 7.3711 C_{Cr} + 5.6421 C_{Cr}^2 - 0.2767 C_{Cr}^3

Hydrogenated–
DBTT (°C) = -159.9195 - 9.5031 C_{Cr} + 4.7791 C_{Cr}^2 - 0.0706 C_{Cr}^3 - 0.0078 C_{Cr}^4

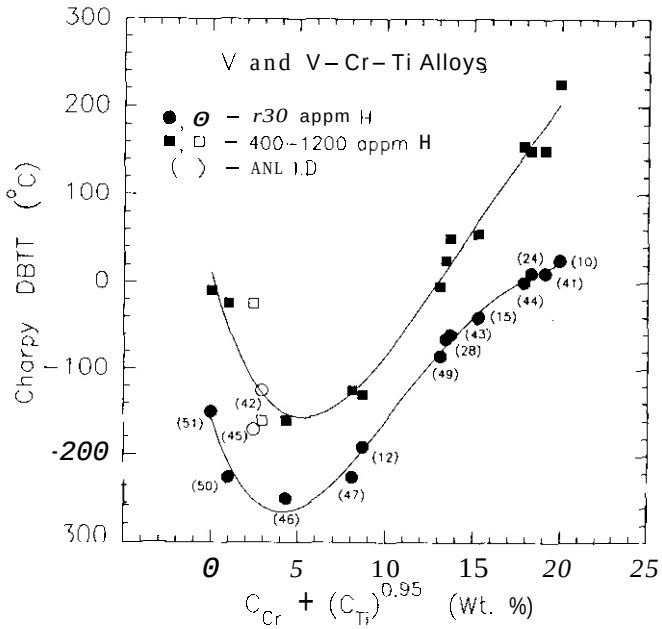

Fig. 3. V and V-base alloy dependence of DBTT on combined Cr and Ti concentration (●, ■ = V, V-Ti, V-Ti-Cr alloys; ○, □ = V-3Ti-Si alloys; ——— curve fit).

V-Cr-li allovs (Fig. 3):

Dehydrogenated--

$$DBTT\ (°C) = -158.8231\ 59.4804\ C_{Cr+Ti} + 9.9704\ C_{Cr+Ti}^{2} - 0.3962\ C_{Cr+Ti}^{3} + 0.0059\ C_{Cr+Ti}^{4}.$$ [Note: $C_{Ti} = (C_{Ti})^{0.95}$]

Hydrogenated--

$$DBTT\ (°C) = 9.5465 - 72.4629\ C_{Cr+Ti} + 9.6801\ C_{Cr+Ti}^{2} - 0.3962\ C_{Cr+Ti}^{3} + 0.0059\ C_{Cr+Ti}^{4}$$

DISCUSSION OF RESULTS

The results of this experimental study on V-Cr-Ti alloys utilizing Charpy-impact loading (2.56 m/s) show that the DBTT of these alloys is lowest (-250°C) when the combined Cr and Ti concentration in the alloy is ≈5 wt.%. Also, the DBTT of hydrogenated (400-1200 appm) V-Cr-Ti alloys is lowest (-160°C) when the the combined Cr and Ti concentration in the alloys is ≈5 wt.%. The microstructures of the dehydrogenated unalloyed V and V-Cr-Ti alloys after impact loading were observed optically, but to date we have been unable to detect a microstructural feature that would account for a minimum DBTT at ≈5 wt.% alloy concentration. Regarding DBTTs for V-Ti alloys, we note that the tensile properties of V-(0-20)Ti alloys at 600°c are also significantly altered when Ti concentration is ≈5 wt.% (see Figs. 7 and 15 in Ref. 6). Therefore, the minimum DBTT at ≈5 wt.% alloy concentration, under Charpy impact loading, of V-Cr-Ti alloys is tentatively attributed to *a* change in deformation mechanism.

CONCLUSIONS

1. A vanadium alloy containing Cr and/or Ti and intended for use as structural material in a fusion reactor should contain 3-9 wt.% total alloying addition to obtain a structure with the least susceptibility to hydrogen embrittlement and/or fracture on impact loading.

2. The presence of 5400-9900 ppm Si in V-Cr-Ti alloys causes a significant increase (≈100°C) of the intrinsic DBTT in such alloys.

3. V-base alloys containing <15 wt.% combined Cr and Ti concentration are less susceptible to hydrogen embrittlement.

FUTURE WORK

The microstructures of fractured Charpy specimens will be examined by optical and transmission electron microscopy to determine the significance of the ≈5 wt.% addition in determining Charpy-impact and tensile properties of V-Ti-Cr alloys.

REFERENCES

1. B. A. Loomis. B. J. Kestal. B. D. Edwards, and D. L. Smith, "Temperature Dependence of the Fracture Behavior and the DBTT for Dehydrogenated and Hydrogenated Vanadium-Base Alloys." in: Fusion Reactor Materials, Semiannual Progress Report for Period Ending September 30, 1988. DOE/ER-0313/5, U.S. Department of Energy, Office of Fusion Energy, pp. 242-255.

2. B. A. Loomis, and D. L. Smith, "Response of Unirradiated and Neutron-Irradiated Vanadium Alloys to Charpy-Impact Loading." J. Nucl. Mater., 179-181, Part A (1991). pp. 783-786.

3. N. S. Cannon, M. L. Hamilton, A. M. Ermi, D. S. Gelles. and W. L. Hu, "Influence of Neutron Irradiation on the Charpy Impact Properties of V-15Cr-5Ti," in: Fusion Reactor Materials, Semiannual Progress Report for Period Ending September 30, 1987, DOE/ER-0313/3, U.S. Department of Energy, Office of Fusion Energy, pp. 239-245.

4. D. N. Braski. "The Tensile Properties of Several Vanadium Alloys after Irradiation to 90 DPA in FFTF," in: Fusion Reactor Materials, Semiannual Progress Report for Period Ending September 30, 1987, DOE/ER-0313/3, U.S. Department of Energy, Office of Fusion Energy, pp. 235-238.

5. B. A. Loomis. A. B. Hull. O. K. Chopra, and D. L. Smith, "Hydrogen Concentration Distribution in Vanadium-Base Alloys after Surface Preparation and Exposure to Liquid Lithium." in: Fusion Reactor Materials, Semiannual Progress Report for Period Ending March 31, 1988, DOE/ER-0313/4, U.S. Department of Energy, Office of Fusion Energy, pp. 160-167.

6. B. A. Loomis. L. J. Nowicki. and D. L. Smith. "Tensile Properties of Vanadium and Vanadium-Base Alloys," in: Fusion Reactor Materials, Semiannual Progress Report for Period Ending March 31, 1991, DOE-ER/0313/10, U.S. Department of Energy, Office of Fusion Energy, pp. 145-155.

High Swelling Rates Observed in Neutron-Irradiated V-Cr and V-Si Binary Alloys · F. A. Garner ana D. S. Gelles, Pacific Northwest Laboratory*, H. Takahashi, S. Ohnuki and H. Kinoshita, Hokkaido University, B. A. Loomis, Argonne National Laboratory

OBJECTIVE

The objective of this effort is to determine the factors which control void swelling in vanadium-base alloys.

SUMMARY

Additions of 5 to 14 wt% chromium to vanadium lead to very large swelling rates during neutron irradiation of the binary alloys, with swelling increasing strongly at higher irradiation temperatures. Addition of 2 wt% silicon to vanadium also leads to very large swelling rates, but swelling decreases with increasing irradiation temperature. Addition of 1 wt% zirconium does not yield high swelling rates, however.

PROGRESS AND STATUS

Introduction

It was recently shown by Matsui and coworkers that V-5 at% Fe could reach very large levels of void swelling during irradiation in either the FFTF or JOYO fast reactors, especially at 600°C, the highest irradiation temperature studied.[1-3] Swelling was also accelerated at lower irradiation temperatures, but to a lesser extent. These data cast doubt on the prevailing assumption that the bcc lattice structure automatically confers immunity against the ~1%/dpa swelling rates observed in fcc metals.[4] The swelling rates observed by Matsui and coworkers were at least twice that level.

Loomis, Smith and Garner also found that vanadium-chromium binaries (with small amounts of aluminum) irradiated in FFTF Cycles 7-9 also exhibited substantially enhanced neutron-induced swelling at 600°C,[5] although the early temperature history of that particular irradiation was very complex. Vanadium with chromium additions in the range 9-14 wt% exhibited irradiation-induced density decreases of 38.9 to 42.4% at 77 dpa, corresponding to 63.6-73.6% volumetric swelling, as shown in Figure 1. These aata implied that the post-transient swelling rates were on the order of 1%/dpa or more. There was also some indication that the swelling at intermediate chromium levels (-5%) might be even higher, as illustrated in Figure 2, and comparable to that observed in V-5Fe.

Studies by Ohnuki and coworkers conducted on V-Cr alloys irradiated to lower displacement levels have confirmed that chromium additions indeed accelerate the void swelling phenomenon in vanadium.[6,7] In addition, silicon additions have also been observed recently to accelerate the swelling of vanadium.[2]

This paper presents a few additional details from the irradiations conducted by Loomis and coworkers in FFTF Cycles 7-9, as well as the results of a new study conducted in FFTF Cycle 11.

Experiment Details

Both of these studies were conducted in the Materials Open Test Assembly (MOTA) in different reactor cycles. Under normal operating conditions, MOTA canisters are actively controlled within ±5°C of their target temperatures during irradiation.[8] However, in FFTF Cycle 7 a severe overtemperature event caused many of the irradiation canisters in MOTA-ID to overheat (as much as 200°C at 600°C) for a period of ~1 hour. The presumed loss of experimental integrity lead to a programmatic decision to leave the MOTA in place but shift the priority of reactor operation to concerns not involving MOTA, these being primarily reactivity feedback tests. The MOTA was kept in the helium-purged mode while a large number of transient reactor tests were conducted during FFTF Cycle 8. Thus after the overtemperature event, all capsules subsequently operated over a range of temperatures, all of which were lower than the target temperatures. For those specimens that were reinserted into MOTA-IE in Cycle 9, however, the normal temperature control was maintained, and those specimens reached a cumulative exposure of 77 dpa.

The temperature control in the MOTA-2A experiment in FFTF Cycle 11 was essentially flawless, with all canisters controlled within ±5°C of their target temperatures. Three binary alloys (V-5Cr, V-2Si and V-1Zr, wt%) were irradiated in the annealed condition to 42-46 dpa at target temperatures of 427, 433, 519 and 600°C (Table 1). The specimens were in the form of microscopy disks and were irradiated in sealed helium-filled packets. An automated immersion density technique known to be accurate to ±0.16% swelling was used to determine the density changes of these alloys.

---

*Operated for the U.S. Department of Energy by Battelle Memorial Institute under Contract DE-AC06-76RLO 1830.

Location	Target Temperature °C	Neutron Fluence n/m^2 (E>0.1 MeV)	dpa*
3D-3	427	8.48×10^{26}	46.1
4D-4	430	7.72×10^{26}	42.0
3E-1	519	8.33×10^{26}	45.3
3F-1	600	8.35×10^{26}	45.4

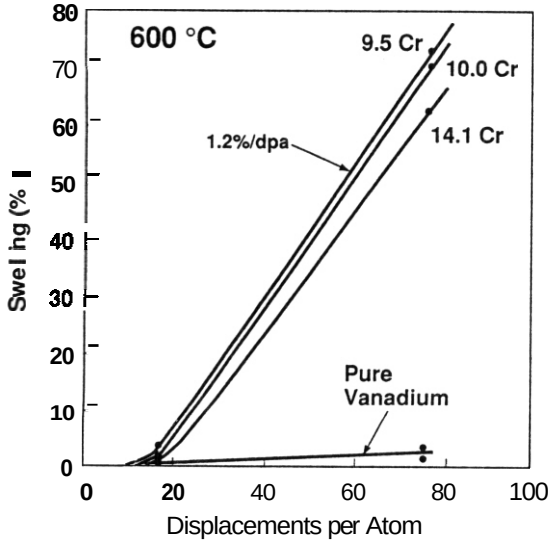

Fig. 1. Swelling observed in V-Cr alloys after irradiation to 17 and 77 dpa in FFTF cycles 7-9 at a target temperature of 600°C (ref. 5). The actual temperature in the first hail of the irradiation was rather complex, however.

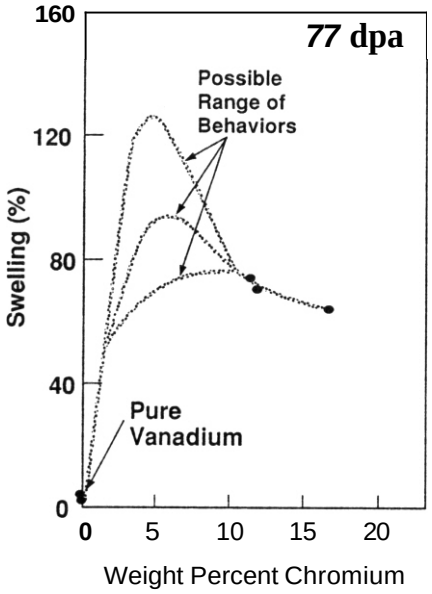

Fig. 2. Swelling data at 77 dpa from Fig. 1, plotted versus chromium content.

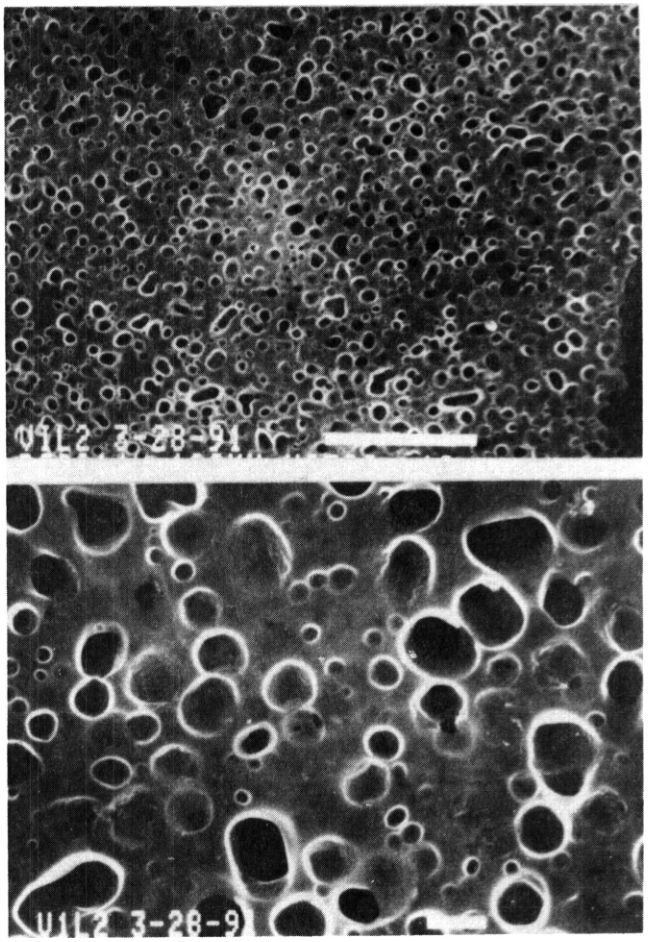

Results

Transmission electron microscopy of the Cycles 7-9 specimens with ~70% swelling was attempted but was found to be very difficult. Void sizes on the order of a micron or more were found, but penetration of the electropolishing solution into and through adjacent voids caused a loss of the void surface layers, rendering segregation studies of doubtful use. Figure 3 illustrates the extensive intersection of voids with the electropolished surface.

Figure 4 shows the swelling values obtained from the Cycle 7-8 irradiation sequence at a target temperature of 420°C and 520°C. Chromium appears to affect the swelling of vanadium at 400°C and possibly 520°C. In each case the swelling is less that at 600°C, although the swelling is not monotonic with temperature, however. In general, the levels reached in this highly complex irradiation were much larger than were observed in later isothermal irradiations that proceeded to higher displacement levels in Cycles 9 and 10 only.[9] This indicates that the complex temperature history strongly influenced the swelling.

The swelling values measured in the well-controlled MOTA-2A Cycle 11 experiment are shown in Figure 5. Where more than one nominally identical specimen was measured, swelling was somewhat variable. This is not surprising, Considering the high rate at which the specimens were found to be swelling. Assuming a very small incubation period, the V-2Si alloy reached a swelling rate of ~1%/dpa or greater.

The V-5Cr binary alloy exhibited a strongly temperature-dependent and monotonic swelling behavior during isothermal irradiation, in agreement with the general results of the non-isothermal experiment conducted at 420 and 600°C in Cycles 7-9. The V-2Si alloy also reached high swelling levels but did so with a temperature dependence opposite to that of V-5Cr alloy. The V-1Zr alloy swelled much less than either of the other two alloys, reaching only 2.7% at 600°C, and smaller amounts at lower temperatures. Density change measurements were not performed on pure vanadium from this experiment, since the irradiated specimens were found to be very brittle and might not have survived the automated measurement procedure. Several specimens disintegrated upon being picked up with tweezers.

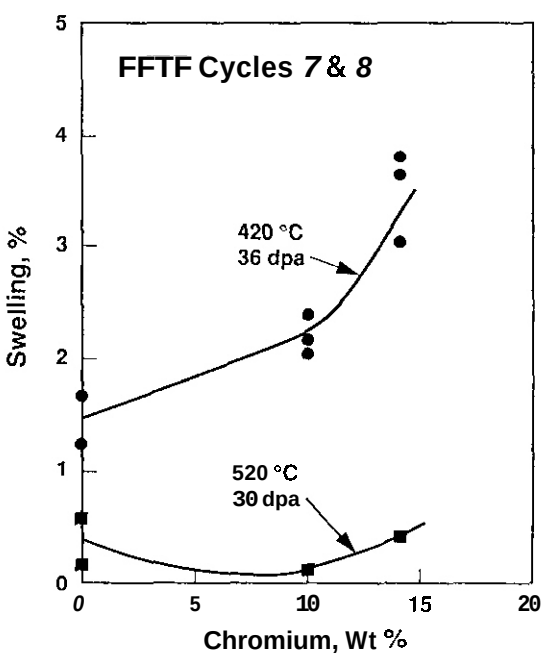

Fig. 4. Swelling observed in V-Cr alloys at 420 and 520°C after irradiation in FFTF Cycles 7-8.

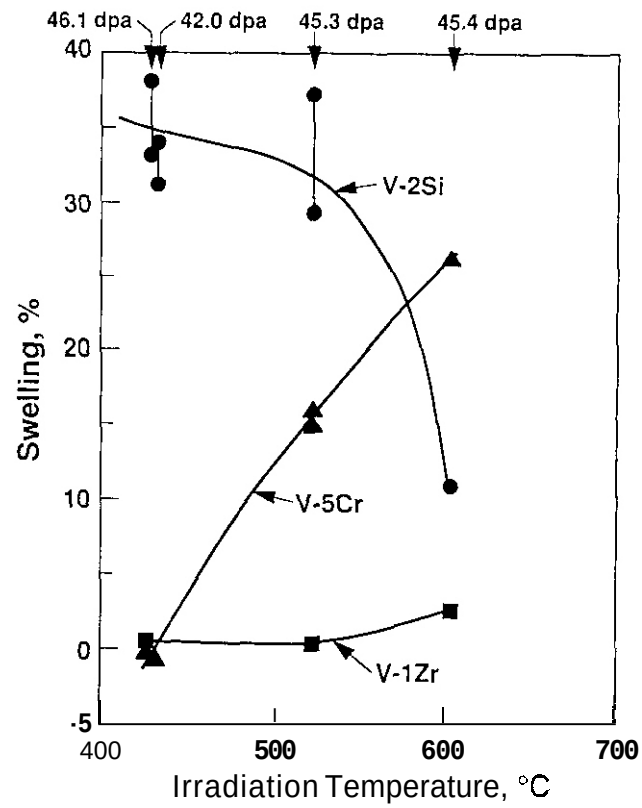

Fig. 5. Temperature-dependent swelling of three vanadium-binary alloys after irradiation in FFTF Cycle 11

Discussion and Conclusions

Nakajima and coworkers[10] have interpreted their swelling results in terms of the relative atomic size of each solute and found good agreement for data at 600°C for Fe, Cr and Si additions. The results of the current study at 600°C agree with their observations. As shown in Figure 5, however, a different relative swelling behavior was observed in this experiment at 420 and 520°C. Thus, atomic size arguments may not be generally applicable to these alloys.

Whatever mechanisms are later found to control the swelling of binary vanadium alloys, it appears that the role of buth crystal structure and irradiation temperature history will need to be closely examined in future studies on these and other specimens.

FUTURE WORK

Microscopy will proceed on these specimens

REFERENCES

1. H. Matsui, D.S. Gelles and Y. Kohno, Proc. 15th International Conference on Effects of Radiation on Materials (1991) in press.

2. H. Nakajima, S. Yoshida, Y. Kohno and H. Matsui, in ICFRM-5 conference.

3. H. Matsui and H. Nakajima, in ICFRM-5 conference.

4. F. A. Garner. J. Nucl. Mater., 122 & 123 (1984) 459.

5. B. A. Loomis, D. L. Smith and F. A. Garner, J. Nucl. Mater., 179-181 (1991) 771-774.

6. S. Ohnuki, D. S. Gelles, B. A. Loomis, F. A. Garner and H. Takahashi, J. Nucl. Mater., 179-181 (1991) 775-778.

7. S. Ohnuki, H. Takahashi, H. Kinoshita and R. Nagasaki, J. Nucl. Mater., 155-157 (1988) 935

8. R. J. Puigh and R. E. Schenter in Effects of Radiation on Materials, Twelfth International Symposium, ASTM STP 870 (1985) pp. 795-802.

9. B. A. Loomis, K. Abe, L. J. Nowicki, H. Chung and D. L. Smith, Fusion Reactor Materials Semiannual Prasress ReDort DOE/ER-0313/9, (1991) pp. 172-176.

10. H. Nakajima, S. Yoshida, Y Kohno and H. Matsui, in Annual Progress Report for Fusion Year 1990, Japan-USA Collaboration in FFTF MOTA (1991) pp. 71-77.

6.4 Copper Alloys

Irradiation Performance of Oxide Dispersion Strengthened Copper Alloys to 150 dpa at 415°C - D. J. Edwards and A. S. Kumar, (NORCUS Program) University of Missouri, K. R. Anderson and J. F. Stubbins, (NORCUS Program) University of Illinois, F. A Garner and M. L. Hamilton, Pacific Northwest Laboratory

OBJECTIVE

The objective of this effort is to provide design data for use of copper alloys in high heat flux structural applications.

SUMMARY

Results have been obtained on the post-irradiation properties of various oxide dispersion strengthened copper alloys irradiated from 34 to 150 dpa at 415°C in the Fast Flux Test Facility. The GlidCop™ alloys strengthened by Al_2O_3 continue to outperform other alloys with respect to swelling resistance, and retention of both electrical conductivity and yield strength. Several castable ODS alloys and a Cr_2O_3-strengthened alloy show increasingly poor resistance to radiation, especially in their swelling behavior. A HfO_2-strengthened alloy retains most of its strength and its electrical conductivity reaches a constant level after 50 dpa, but it exhibits a higher residual radioactivity.

PROGRESS AND STATUS

Introduction

Pure copper, which has a high thermal conductivity, is being considered for use as a high heat flux structural material in fusion reactors, in particular for divertor plate assemblies.[1-4] Pure copper is a poor candidate as a structural material, however, because of its low strength and low softening temperature. Furthermore, under irradiation pure copper has little resistance to void swelling. which rapidly degrades both mechanical properties and thermal conductivity. One approach to overcoming these limitations involves strengthening copper by oxide dispersion strengthening (ODS) and/or precipitation hardening (PH). To understand the possible effect of neutron irradiation on the properties of pure copper and various ODS and PH copper alloys, an exploratory experiment was conducted in the Materials Open Test Assembly MOTA) at the Fast Flux Test Facility (FFTF). The results revealed that the internally oxidized GlidCop™ (alloys exhibited the best overall radiation response.[5-7] Two follow-up experiments, designated Generation 1.5 and 2.0, incorporated a wider variety of ODS and PH alloys irradiated to exposures of 34, 50, 104, and 150 dpa. Some results for the specimens irradiated to 34 and 50 dpa have been reported.[8-10] In this report the results of tensile tests, density measurements, and electrical conductivity (used to estimate thermal conductivity) are presented for ODS specimens irradiated to 104 and 150 dpa at 415°C. The results on the PH alloys are presented elsewhere.[11]

Experimental Details

The GlidCop™ alloys employed were CuAl25 (50% cold worked (CW), 0.25 wt% Al as Al_2O_3), CuAl20 (20% CW), and CuAl15 (900°C/0.5 hr/air cooled (AC)) containing 200 ppm boron as a deoxidant. The GlidCop™ alloys were prepared by SCM Metal Products. Also used were Cu-Cr_2O_3 (3.5% Cr as Cr_2O_3, 20% CW, 450°C/0.5 hr/AC), and Cu-HfO_2 (1.1% Hf as HfO_2, 20% CW, 450°C/0.5 hr/AC). Both were obtained from Dr. N. Grant at the Massachusetts Institute of Technology. In addition there were four "castable" ODS alloys supplied by Technical Research Associates, INC., all in the 40% CW condition: ODS-1 and ODS-2, both with 0.25% Mg, 1% Al_2O_3; ODs-3 with 0.5% Mg and 1%ZrO_2; and ODS-4 with 0.5% Mg and 1%Al_2O_3. Both TEM disks and tensile specimens were punched from sheet stock of the various materials; TEM specimens only were punched from the ODs-2 stock. Additional tensile specimens of CuAl25 and ODS-1 were prepared from strips of *0.01"* thick sheet that had been cut and then joined together by laser welding. The specimens were punched from the welded sheet such that the weld was centered in the gage length. TEM disks were also punched from the welded regions.

Density measurements were obtained at room temperature from TEM disks using an immersion density technique known to have an accuracy of ±0.15% density change. Electrical conductivity measurements were made at room temperature on both miniature tensile specimens and TEM disks using a 4-point probe DC potential drop method described by Anderson and coworkers.[8] The miniature tensile specimens were flat specimens measuring 12.7 mm in length, 0.25 mm in thickness, 5.1 mm in gage length, ano 1.0 mm in gage width. Conductivity measurements on both types of specimens were in good agreement with each other. Tensile tests were performed after the conductivity measurements were completed using a miniature tensile testing apparatus developed specifically for this specimen geometry.[12] Tensile tests were performed at room temperature with a free-running crosshead speed of 0.0025 mm s^{-1}, which yields an initial strain rate of 4.8×10^{-4} s^{-1}.

Results

Figure 1a shows the swelling data for the four "castable" ODS alloys and $Cu-Cr_2O_3$. As a group, the swelling resistance of the four ODS alloys is very poor and parallels that of pure copper, with the ODs-4 alloy exhibiting the best overall swelling resistance. While the $Cu-Cr_2O_3$ exhibits roughly the same behavior, its overall swelling resistance is better than the four "castable" ODS alloys. In Figure 1b, the two GlidCop™ alloys, CuAl25 and CuAl20, and the $Cu-HfO_2$ alloy display the least swelling of all the ODS alloys. The CuAl25 and CuAl20 actually densify at the higher dpa levels, whereas the CuAl15 alloy begins to swell. Swelling data for the laser-welded CuAl25 are quite variable, ranging from 8% to 43% at 104 and 150 dpa.

Figure 2a demonstrates that the electrical conductivities of the various GlidCop™ alloys exhibit essentially the same behavior, decreasing with increasing radiation exposure. Laser welding decreases the conductivity both before and after irradiation. Figure 2b reveals that the conductivity of the $Cu-HfO_2$ levels off at ~80% IACS. The $Cu-Cr_2O_3$ alloy, on the other hand, steadily decreases in conductivity throughout the irradiatioc. In Figure 2c, the "castable" ODS alloys exhibit behavior similar to that of the GlidCop™ alloys in ihat the conductivity decrease for earh alloy lies within a common band, though the rate of decrease is more pronounced.

Figure 3 shows the ultimate tensile strengths and yield strengths for the GlidCop™ alloys, as well as $Cu-Cr_2O_3$ and $Cu-HfO_2$. The ultimate tensile strengths closely mirror the yield strength behavior. The decrease in yield strength of both CuAl25 anti CuAl20, as well as $Cu-HfO_2$, levels off after ~50 dpa, whereas the strength of the $Cu-Cr_2O_3$ continues to decrease. Data for CuAl15 are available only to 34.1 dpa, and suggest that the yield strength may be increasing with irradiation. The deleterious effect of laser welding is reflected in the poor strength of the welded CuAl25 alloy. Cverall, the CuAl25 alloy exhibits the best strength retention of the five alloys shown, with CuAl20 and $Cu-HfO_2$ exhibiting the next. best behaviors.

Figure 4 shows the strength data of the four "castable" ODS alloys. The yield strengths of the ODS-1 and *ODs-4* alloys decrease 50% or more after irradiation to 50 dpa, and then appear to level out. No ODS-3 specimens were placed in the 34 and 50 dpa experiments, but specimens were placed in the 104 and 150 dpa experiments. The limited data for the ODS-3 alloy matches the behavior of the ODS-1 alloy very closely. The ODS-1 welded specimens irradiated to 104 and 150 dpa failed before reaching the 0.2% offset yield strength. The welded ODS-1 specimen irradiated to 150 dpa failed in the weld.

Discussion

Of the various alloys studied, the GlidCop™ alloys continue to exhibit the best strength retention, swelling resistance, and electrical conductivity after irradiation to 150 dpa. The difference in cold work between the CuAl25 (50% CW) and the CuAl20 (20% CW) appears to have little effect on the conductivity and swelling resistance, but does appear to be responsible for the difference in strength shown in figure 3. After irradiation to 50 dpa, the CuAl20 was fully recrystallized. whereas the CuAl25 still retained some of its cold worked dislocation structure.[13,14] The higher Al_2O_3 content in CuAl25 is assumed to be responsible for the retention of cold work since the higher cold worked structure would normally recrystallize faster due to the yreater stored energy. The leveliny uff of the yield strength indicates that the Al_2O_3 particles are probably still present, though the morphology and distribution of the particles remains to be determined by microscopy. The unexpectedly high swelling values noted for CuAl15 at 104 dpa are probably due to a breakdown in the swelling resistance, perhaps due to an inhomogeneous distribution of either the Al_2O_3 or the boron.[13,14] The steady decrease in conductivity in these alloys results from increasing concentrations of transmutation products, primarily nickel and zinc.[15]

Laser welding has a pronounced effect on the mechanical properties, electrical conductivity, and swelling resistance of the CuAl25 alloy. It is iikely that the Al_2O_3 particles dissolved during the welding process, allowing the aluminum and oxygen to enter into solution. Butterworth[16] reports that aluminum in solution increases the resistivity by 2.88 μΩ-cm/wt% Al. Based on the assumption that the Al_2O_3 particles were completely dissolved, a preirradiation conductivity of 71% IACS was calculated for CuAl25 alloy compared to the measured value of 75.8%. Similar calculations indicated that placing the oxygen in solution would be expected to reduce the conductivity by an additional 3% IACS. The fact that the observed conductivity was not as low as the calculated value suggests that most but not all of the oxide in the weld zone was dissolved. Garner et al.[6] has shown that aluminum in solution enhances the swelling of copper, and Zinkle and Lee[17] have shown enhancement for small concentrations of oxygen in solution. The higher swelling of the welded CuAl25 alloy leads to the conclusion that at least part of the aluminum and oxygen was in solution. Further radiation-induced decreases in conductivity result from both enhanced swelling and transmutation.

The poor irradiation response of the "castable" ODS alloys has been attributed to the high residual oxygen levels introduced during casting.[13,14] Zinkle and Lee[17] suggest that oxygen stabilizes void formation by reducing the surface tension of the voids, making them more stable than dislocation loops and stacking fault tetrahedra. According to their results, the oxygen must be in solution for this to occur. The oxide dispersions may also be a source of oxygen if they are destroyed during irradiation by recoil resolution as suggested by Spitznagel and coworkers.[18] In contrast to the high swelling noted for tiie "castable" ODS

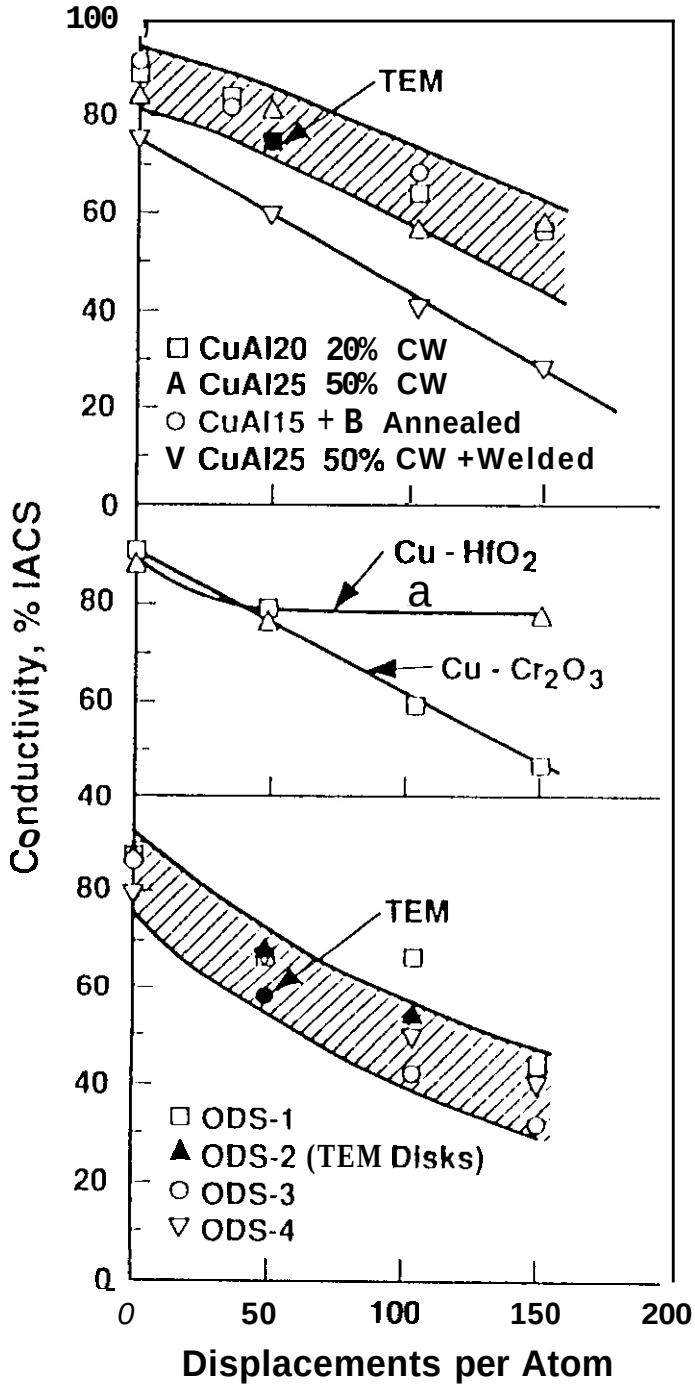

Figure 1. Swelling of (a) "castable" ODS alloys and $Cu\text{-}Cr_2O_3$ and (b) GlidCop™ alloys and $Cu\text{-}HfO_2$.

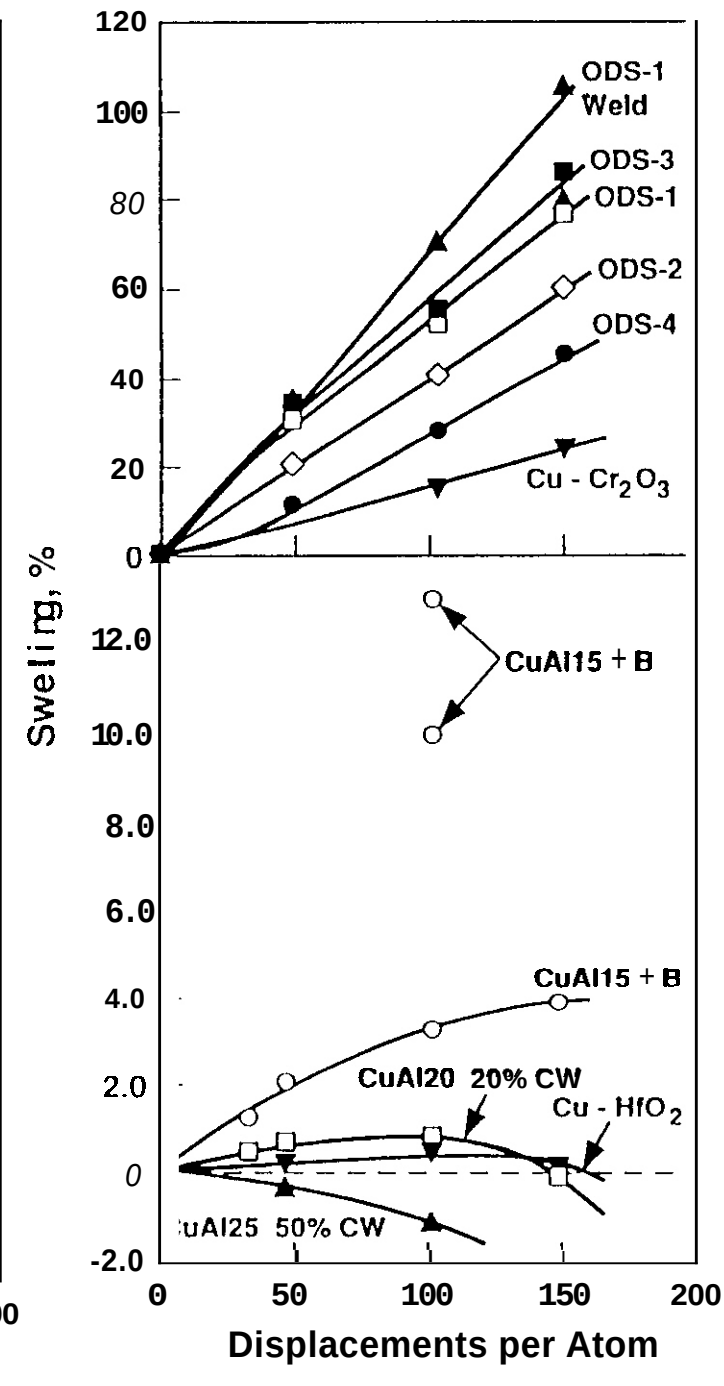

Figure 2. Effect of irradiation on electrical conductivity of (a) GlidCop™ alloys, (b) $Cu\text{-}HfO_2$ and $Cu\text{-}Cr_2O_3$, and (c) "castable" ODS alloys.

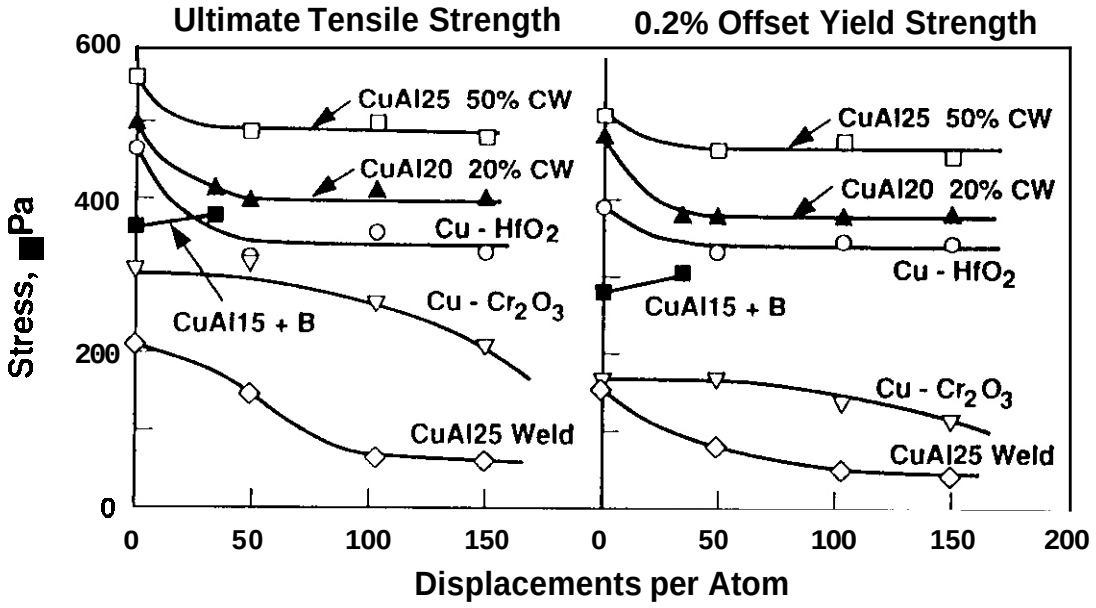

Fig. 3. Ultimate tensile strength and yield strength of GlidCop™, Cu-Cr_2O_3, and Cu-HfO_2.

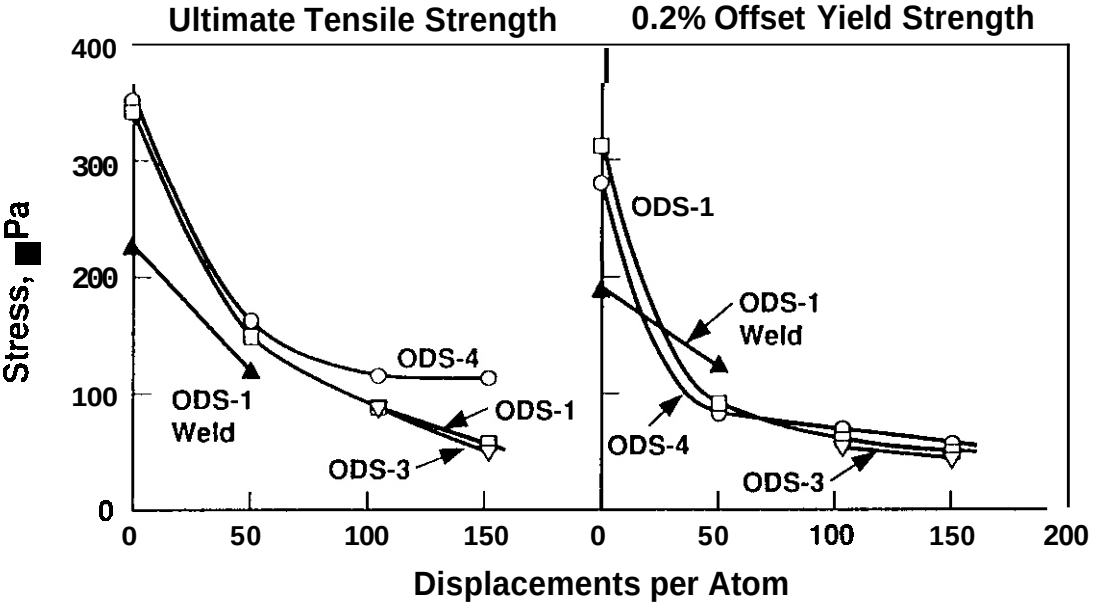

Fig. 4. Ultimate tensile strength and yield strength of "castable" ODS alloys.

alloys, the relatively low swelling of the CuAl25 and CuAl20 indicdtes thit if the Al_2O_3 undergoes recoil resolution, then the aluminum and oxygen do not stay in solution long enough to strongly influence swelling. Another possibility is that some other process such as reprecipitation is occurring to offset the resolution.

The Cu-HfO_2 alloy shows promise in view of the stability of both its conductivity and strength up to 150 dpa. Cu-HfO_2 is the only ODS alloy where the electrical conductivity remains constant when irradiated beyond 50 dpa. A possible explanation for this might reside in the low void swelling observed to 150 dpa, and possibly the redistribution of the hafnium observe? at 50 dpa.[13,14] The initial decrease in strength was found to be due to recovery and recrystallization,[13,14] but the constant level of strength after ~50 dpa probably iridicates that the redistributed hafnium and oxygen may continue to strengthen the material. One drawback to the Cu-HfO_2 alloy, however, is the long-lived radioactivity from Hf^{178}, making it somewhat less desirable for use as a structural material.

The poor mechanical properties of the Cu-Cr_2O_3 alloy are attributed to recovery and recrystallization and its high swelling. Redistribution of the Cr_2O_3 into smaller particles was observed at 50 dpa,[13,14] which is believed to increase the degree of Orowan strengthening. The subsequent decrease in both ultimate tensile strenath and vield strenuth at 104 and 150 dpa suggests that coarsening occurred in the oxide dispersion. The higher swelling-observed in the Cu-Cr_2O_3 alloy may also be a consequence of this, particularly if the some of the oxygen from the oxide was placed in solution.

The performance of the GlidCop™ alloys at ~400°C bodes well for applications at lower temperatures. The decrease in strength will most likely be less at the lower temperatures and fluences anticipated for ITER or other low fluence reactors, primarily because the kinetics for recovery and recrystallization decrease as the temperature decreases. Based on the data of Zinkle and Farrell[19] the role of swelling should not change significantly in the temperature range of 180°C to 400°C, and below 180°C swelling is expected not to occur. Although the swelling and strength data are probably valid fnr lower temperature/lower fluence reactor designs, Garner and coworkers[15] have pointed out that while the transmutation rate of zinc will decrease in a fusion spectra, the transmutation rate of nickel, which has a greater impact on conductivity than does zinc, will be higher. Therefore the conductivity data of this study must be adjusted before applying to fusion reactor designs. Garner and coworkers[5,15] also showed that the swelling was not very sensitive to the presence of nickel, implying that swelling should not be very sensitive to the difference between fission and fusion spectra.

CONCLUSIONS

After irradiation to 150 dpa at 415°C, the GlidCop™ alloys appear to be the most promising candidates for use as a high heat flux structural material in fusion reactors. In particular, the CuAl25 alloy exhibits excellent strength retention and swelling resistance.

The conductivity of the Cu-HfO_2 alloy at higher dpa levels is better than that of the GlidCop™ alloys. And although the Cu-HfO_2 alloy maintains moderate but lower strength than the GlidCop™ alloys, its higher residual radioactivity may be a drawback. The oxide dispersion in the Cu-Cr_2O_3 alloy loses its effectiveness after relatively low levels of irradiation, evident from the poor strength retention, low conductivity, and greater swelling compared to the other alloys studied. The "castable" ODS alloys do not warrant further consideration unless better casting techniques are found to lower the residual oxygen content.

FUTURE WORK

Fractography and electron microscopy will proceed on the various copper alloys.

ACKNOWLEOGEMENTS

The contribution of Edwards, Anderson, Stubbins, and Kurnar were made under the auspices of the Northwest Association for Colleges and Universities for Science (NORCUS), administering contract DE-FG06-89ER-75522 for the U.S. Department of Energy. Garner and Hamilton were supported by the U.S. DOE Office of Fusion Energy under contract DE-AC06-76RLO-1830.

REFERENCES

1. V. Renda and L. Papa, Fusion Technology, 20 (1991), 40.

2. W. B. Gauster, Nuclear Fusion, 30, no. 9 (1990), 1897.

3. E. E. Bloom, Nuclear Fusion, 30, no. 9 (1990) 1879.

4. J. L. Boutard, J. Nucl. Mater., 174 (1990) 240

5. F. A. Garner, H. R. Erager, and K. R. Anderson, J. Nucl. Mater., 179-181 (1991) 250

6. F. A Garner and K. R. Anderson, Fusion Reactor Materials Semiannual Progress Report DOE/ER-0313/7 (1989) p. 220.

7. H. R. Brager, J. Nucl. Mater. 141-143 (1986) 79,163

8. K. R. Anderson, F. A. Garner, M. L. Hamilton, and J. F. Stubbins, Fusion Reactor Materials Semiannual Progress Report DOE/ER 0313/6 (1989), p. 357.

9. F. A. Garner, K. R. Anderson, and T. Shikama, Fusion Reactor Semiannual Progress Report, DOE/ER-0313/9 (1990), p. 199.

10. T. Shikama, F. A Garner, M. L. Hamilton, and K. R. Anderson, Proceedings of the 15th ASTM International Symposium on Effects of Radiation on Mateiials, ASTM STP 1125 (in press).

11. F. A. Garner, M. L. Hamilton, T. Shikama, D. J. Edwards and J. W. Newkirk, in thi; semiannual report.

12. N. F. Panayotou, S.D. Atkin, R. J. Puigh, and B. A. Chin, ASTM STP 888 (1986), p. 201.

13. K. R. Anderson, Doctoral Thesis. University of Illinois at Urbana-Champaign (1990)

14. K. R. Anderson, F. A. Garner, M. L. Hamilton, and J. F. Stubbins, 15th ASTM International Symposium of Effects of Radiation on Materials, ASTM STP 1125, (in press).

15. F. A Garner, H. L. Heinisch, R. L. Simons, and F. M. Mann, Radiation Effects and Defects in Solids (1990) 229.

16. G. J. Butterworth, J. Nucl. Mater., 135 (1985) 160.

17. S. J. Zinkle and E. H. tee, Met. Trans.,21A, May (1990), 1037.

18. J. A. Spitznagel, N. J. Doyle, W. J Choyke, J. G. Greggi Jr., J. N. McGruer, and J. W. Davis. Nucl. Instr. and Meth. in Phys. Res. 616 (1986), p. 279.

19. S. J. Zinkle ana K. Farrell, J. Nucl. Mater., 168 (1989) 262

THE JOINING OF ALLOYS FOR FUSION REACTOR APPLICATIONS - BRAZING OF COPPER-ALUMINA ALLOYS AND THE WELDABILITY OF LOW-ACTIVATION FE-CR-MN-C STEELS - B.A. Chin, C.X. Lee (Auburn University), S.J. Zinkle (Oak Ridge National Laboratory), and R.C. Wilcox (Auburn University)

A. BRAZING OF COPPER-ALUMINA ALLAYS

OBJECTIVE

The objective of this research is the development of an induction brazing process for GLIDCOP Al-15 using a silver brazing alloy. The objective centers on minimizing the time required at elevated temperatures during the brazing process.

SUMMARY

Induction brazed butt joints were produced from which subsize fatigue samples were fabricated. Some fatigue- samples have-survived over 2 X 10^6 cycles in a tension-compression cantilever fatigue mode.

PROGRESS AND STATUS

Introduction

The copper-alumina alloy GLIDCOP A1-15 has been targeted for use in tokamak fusion reactors.[1,2] This choice was made because of the alloy's ability to retain the cold worked structure after high temperature brazing, coupled with its high heat carrying capacity, and high electrical conductivity.[3] However, the successful use of this alloy depends on the ability to join the alloy during fabrication without destroying these properties. Thus, a brazing process that does not alter the alloy's structure or properties is highly desirable.'

The objective of the research that is being conducted is the development of an induction brazing process for GLIDCOP A1-15 using a silver-base brazing alloy. This objective centers on minimizing the time required at elevated temperatures during the brazing process in order to eliminate excessive oxidation which occurs during furnace brazing.

ExDerimental procedure

Brazed joints of GLIDCOP-15 using the silver based brazing alloy BAg-5 (45 wt% Ag) were produced by using a 50 kW induction furnace with an oval shaped helical coil. For butt joints, the brazing time was 12 to 15 seconds. Shorter brazing times resulted in incomplete melting of the BAg-5 filler material. Longer brazing times resulted in overheating of the base metal.

Subsize cantilever type fatigue specimens were prepared by cutting rectangular pieces from the induction brazed butt joints. Each piece was then milled to size. The specimens were 0.762 mm thick and had two circular notches of 6.35 mm radius centered on the brazed joint. The gage length was 6.35 mm. Because fatigue properties at room temperature are sensitive to the surface finish[5], the subsize fatigue specimens were hand polished using emery papers and then electropolished using a 50% phosphoric acid, 50% water electrolyte at room temperature. The results yielded a polished surface completely free from machine marks.

Recent results

The preliminary results of fatigue testing of as-received GLIDCOP A1-15 and brazed butt joints are shown in Fig. 1. On a log-log plot, fatigue results can be represented by linear curves. The triangles and circles in Fig. 1 represent the as-received alloy and the induction brazed butt joint specimens, respectively. The fatigue results shown as solid circles in Fig. 1 were tests terminated after 30 days (a stress of 99 MPa and 2.5 x 10^7 cycles) and 55 days (a stress of 88 MPa and 4.5 x 10^7 cycles) without failing, while the solid triangle was a test terminated after 70 days (a stress of 286 MPa and 4.4 x 10^7 cycles) without failing.

Fatigue stresses as reported in Fig. 1 were calculated using the moment-deflection relationship for a cantilever beam and the value of 9.3 X 10^4 MPa (13.5 X 10^6 psi)' for the modulus of elasticity for the cold worked GLIDCOP A1-15 alloy. For the BAg-5 filler alloy, the average modulus of elasticity was determined from experimental tensile tests to be 2.76 X 10^4 MPa (4 X 10^6 psi). The results of fatigue testing can be represented by the Basquin[5] equation, $N\sigma_a^P = C$, where σ_a is the stress amplitude (MPa), and N is the number of cycles to failure. The value of P was found to be 17.7 and 7.5 for the butt joints and the as-received alloy, respectively. The constant C was determined to be 3.77 X 10^{42} and 1.04 X 10^{25} (MPa) for the butt joints and the as-received GLIDCOP Al-15 alloy, respectively.

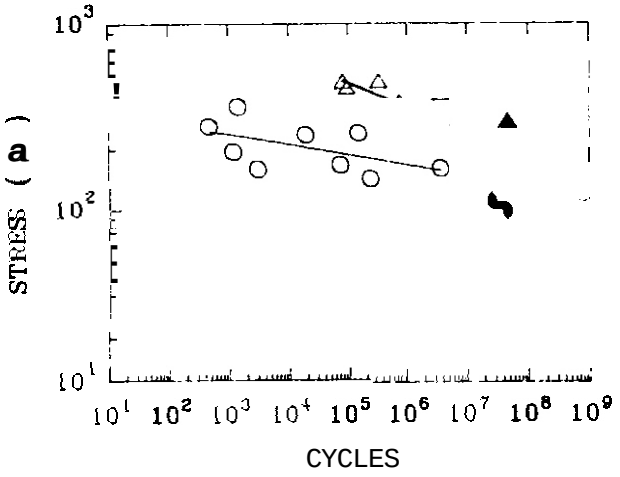

Fig. 1. Fatigue data for as-received GLIDCOP A1-15 (triangles) and induction brazed butt joints (circles).

Fig. 1 shows that the fatigue strength of induction brazed butt joints was less than the cold-worked GLIDCOP A1-15. These results were expected, because the tensile strength of the brazed BAg-5 (180 MPa) is much less than cold-worked GLIDCOP A1-15 alloy (486 MPa). Fatigue properties are frequently correlated with tensile properties[5].

The results of miniature fatigue specimens (3 mm diameter disks) were disappointing. These miniature specimens were to be used for electron microscopy studies. The problem stemmed from the difficulty in preparing such small specimens. These specimens were cut from larger brazed butt joints of GLIDCOP Al-15 that have about 40% voids. With the thickness of the specimens being only 0.25 mm, mechanical damage during electrical discharge machining caused specimens to fail. In order to reduce the mechanical damage and the cold-work effects during manufacturing, the miniature fatigue specimens were electron-polished. Because of the presence of about 40% voids in the brazed joint of such thin specimens, the braze filler material became anodic to the copper alloy and etched at a faster rate which again caused failure of the miniature specimens.

The presence of about 40% voids within the braze material of the butt joints was a major concern. Tensile specimens made from butt joints were tested in liquid N_2 to determine the origin of these voids. These tensile specimens failed in a brittle manner in the braze and still showed about 40% voids. These results indicated that these voids were created during the brazing process. Additional butt joints were designed in an effort to possibly eliminate the majority of these voids. However, through microscopic examination no evidence could be found that a decrease in amount of voids occurred.

Discussion

The results indicated that a satisfactory introduction brazing process for GLIDCOP A1-15 using a filler material that was 45 wt$ silver could be achieved. The properties obtained by induction brazing were as good as those produced in furnace brazing. One of the main objectives, perhaps the most important because it affects the achievement of other objectives, was to minimize the time to conduct the brazing sequence. All Glidcop A1-15 samples were brazed in less than 17 seconds. These results shows definite possibilities for induction brazing GLIDCOP A1-15 instead of furnace brazing. Optimizing joint dimensions will most likely produce stronger samples than furnace brazing. Even if stronger joints cannot be produced, induction brazing has a higher degree of manufactural ability for parts because there is no need for protective atmospheres or plating of the surfaces to prevent excessive oxidation.

B. THE PROPERTIES AND WELDABILITY OF FE-CR-MN-C STEELS

OBJECTIVE

The objective of this study was to characterize the welded microstructure andmechanical properties of two Fe-Cr-Mn-C steels.

SUMMARY

The effect of gas tungsten arc welding on the microhardness, tensile properties, and ductility of two low-activation Fe-Cr-Wn-C steels was investigated. Sound welds were produced in both steels.

PROGRESS AND STATUS

Introduction

Fe-Cr-Mn-C steels are being developed as candidates for the first wall and blanket structures of tokamak fusion reactors.[7] The objective of this study was to characterize the welded microstructure and mechanical properties of the two Fe-Cr-Mn-C steels. In order to explore the weldability of these steels, the structure and properties of autogenous bead-on-plate welds produced using the gas tungsten arc welding (GTAW) process was evaluated. Microhardness, weld bend and tensile tests were performed for the base metal, the heat affected zone and the fusion zone of the welded materials.

Both steels are fast induced-radioactivity decay (FIRD) austenitic steels and are to replace high-nickel stainless steels in fusion applications.[8] For a FIRD stainless steel, manganese is to be used as a replacement for nickel.[1]

Experimental Procedure

Two austenitic stainless steels, a Russian Steel (Fe-12Cr-19Mn-0.081C) and an U.S. Steel (Fe-12Cr-19Mn-.24C) were investigated in this study. Both steels contained about 1 wt.% W while the U.S. Steel also had 0.11 wt.% Ti and 0.007 wt% B. These steels, prepared by Combustion Engineering, Inc., were received from Oak Ridge National Laboratory (ORNL). The as-received steels were in sheet form 0.76 mm thick.

Autogenous bead-on-plate welds were produced using a GTAW process. The electrodes were 2 wt% thoriated tungsten with a diameter of 1.59 mm (1/16"). To reduce oxidation, the welding was carried out in a plexiglass chamber with an argon atmosphere. A full penetration weld with approximately a 2.5 mm fusion zone was obtained perpendicular to the prior sheet rolling direction.

To determine the hardness of the individual phases and to aid phase identification, microhardness measurements were conducted across the weld regions using a load of 50 or 100 grams for a duration of 10 seconds. Tensile specimens were cut perpendicular to the weld and had a reduced gage section of 12.7 mm long by 3.175 mm wide. A cross head speed of 0.508 mm/minute was used in all tensile tests. A three-point guide-bend test was used as an index to evaluate the weld soundness. Bend specimens were 43 mm x 8 mm x 0.76 mm.

Recent Results

Metallographic examination revealed an equiaxed grain structure in the as-received Russian Steel indicating that the steel was in the annealed condition. Elongated grains in the U.S. Steel indicated that this alloy was cold worked in the as-received state. Figs. 2 and 3 show the microstructure of these two steels after welding. Fig. 2 shows three distinct regions in the welded U.S. Steel: the fusion zone, the heat-affected zone (grain growth and grain refined regions), and the unaffected base metal. Fig. 3 shows only a fusion zone and the base metal for the Russian Steel. No visible heat affected zone was observed in the welded Russian Steel.

Microhardness measurements were made on all samples to obtain information relating to wear resistance. There was only a small change in microhardness from the fusion zone (332 VHN) to the base metal (309 VHN) of the Russian Steel in Fig. 4. Fig. 5 shows the microhardness in the fusion zone, the heat affected zone, and the base metal of the U.S. steel. The hardness in the heat-affected zone (259 VHN) was slightly lower than that of the

fusion zone (280 V'') and the base metal (267 VHN). The interface between the fusion zone and the heat affected zone had the lowest hardness (242 VHN). The hardness then increased slightly through the heat-affected zone to the interface adjacent to the base metal (268 V''). The loss in hardness in the heat affected zone was due to recrystallization and grain growth. This hardness profile is typical of cold-worked metal that has been welded and then quickly cooled.'

Tensile test strength data from the Russian Steel indicated that the welded specimens had an average 0.2% offset yield strength (YS) of 316 MPa and a tensile strength (TS) of 770 MPa with an uniform elongation of 40.1%. These roughly conformed to the average properties of the as-receive specimens (YS = 290 MPa, TS = 727 MPa, uniform elongation = 40.3%). The average property values for specimens failing within the fusion zone were 317 MPa YS and 768 MPa TS and 41.0% uniform elongation. These data were almost identical to the average property values of the welded specimens, which failed in the base metal. These average values were: YS = 315 MPa, TS = 770 MPa, and uniform elongation = 39.6%. Welded specimens of the Russian Steel failed randomly in the fusion zone or in the base metal. Excellent ductility (>40%) also was observed in this steel.

The tensile strength data for the U.S. Steel showed that the welded specimens had a lower yield strength (538 MPa), tensile strength (851 MPa) and elongation (14.3%) compared to the as-received steel (YS = 798 MPa, TS = 1063 MPa and elongation = 16.9%). The average YS (526 MPa), TS (861 MPa) and uniform elongation (14.8%) of specimens failing in the fusion zone was almost equal to the average values of the welded specimens which failed in the heat-affected

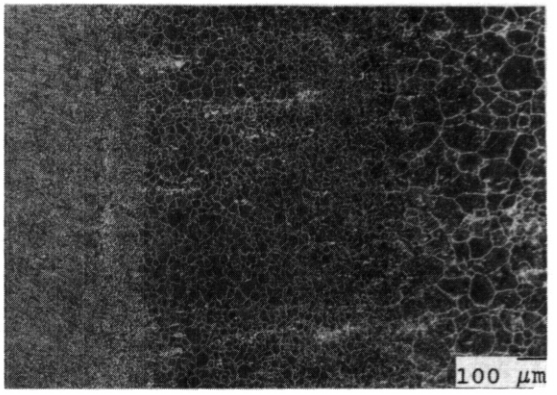

Fig. 2. Typical microstructure of the welded U.S. Steel.

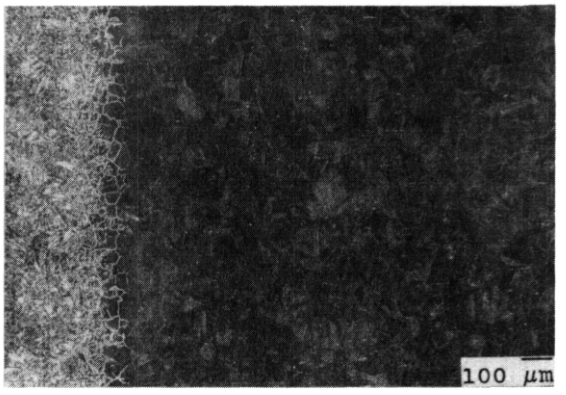

Fig. 3. Typical microstructure of the welded Russian Steel.

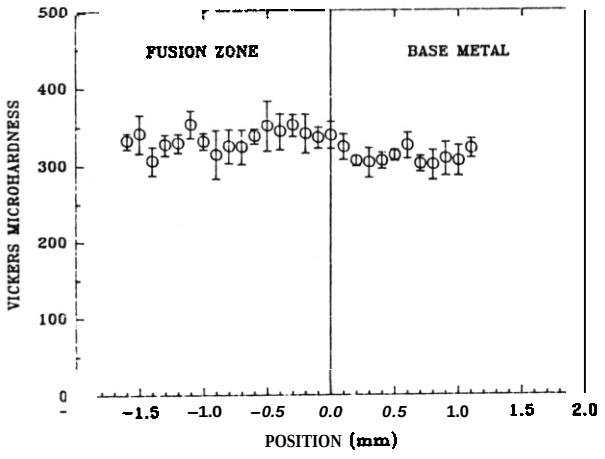

Fig. 4. Microhardness of the welded Russian Steel.

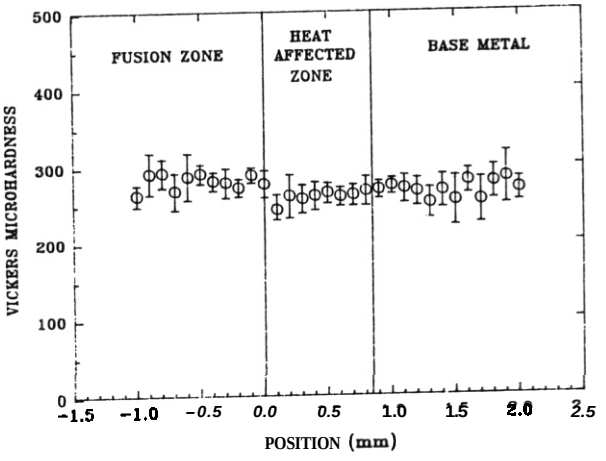

Fig. 5. Microhardness of the welded U.S. Steel.

zone (YS = 539 MPa, TS = 840 MPa and elongation = 13.7%). Generally, the strength of the fusion zone and the heat-affected zone are almost equal but were much less than the strength of the base metal. All welded specimens failed randomly, either in the fusion zone or in the heat-affected zone. The strength properties of the U.S. Steel were governed by the properties of the weld.

In three-point bend tests no cracks or failures were find in either steels. Gross welding flaws, such as incomplete fusion, inadequate joint penetration, or undercut were not observed. Bath heats of steels had excellent toughness and ductility.

Discussion

The study of Fe-Cr-Mn-C steels revealed that sound welds were achieved by gas tungsten arc welds in both the Russian Steel and the U.S. Steels. Mechanical properties were not altered after welding of the Russian Steel but in the U.S. Steel the cold-worked strength was reduced by the heat generated by the welding process.

REFERENCES

1. A. V. Nadkarni, E. Klar and W. M. Shafer, "A New Dispersion-Strengthened Copper" Metals Engineering Quarterly, 16, pp. 371-377 (1976).

2. R. W. Bild, "Neutron-Induced Particle Track Mapping of Elemental Distributions", Materials Research Society, Pittsburgh, Symposium Proceedings, 69, pp. 403-408 (1986).

3. E.N.C. Dalder, W. Ludeman and B. Schumacher, "Thermal Stability of Four High Strength, High Conductivity Copper Sheet Alloys", Lawrence Livermore National Laboratory, UCRL-89034, April, 1984.

4. J.B. Whitley, et.al. "Engineering Considerations for the TORE SUPRA Pump Limiter", Proceedings of the 14th Symposium on Fusion Technology, Avignon, France. September, 1986.

5. G.E. Dieter, Mechanical Metallurgy, McGraw-Hill, New York, 1986, pp. 379, 408, 415-416.

6. J.J. Stephens and D.T. Schmale, The Effect of High Temwerature Braze Thermal Cycles on Mechanical Properties of a Dispersion Strengthened Copper Alloy, Oak Ridge National Laboratory, SAND87-1296.

7. D.R. Harries, "Ferritic/Martensitic Steels for Use in Near-Term and Commercial Fusion Reactors", Proc. of Topical Conference on Ferritic Alloys for Use in Nuclear Energy Technology, TME/AIME, June 19-23, 1983, Snowbird, Utah, pp. 141-155.

8. R.L. Klueh and P.J. Maziasz, "The Development of Austenitic Stainless Steels for Fast Induced-Radioactivity Decay", Fusion Reactor Materials-Semiannual Progress Report, U.S. Department of Energy, March 31, 1990, pp. 217-221.

9. Donald R. Askeland, "The Science and Engineering of Materials", PWS Engineering, Boston, Massachusetts, 1984, pp. 225-227, 387.

6.5 Environmental Effects on Structural Materials

SLOW STRAIN RATE TENSILE TESTING OF FUSION SPECTRALLY-TAILORED TYPE 316 MATERIAL IRRADIATED BETWEEN 60 AND 400°C IN OXYGENATED. HIGH-PURITY WATER ENVIRONMENTS - G. E. C. Bell (Oak Ridge National Laboratory). T. Tsukada , K. Shiba, and H. Nakajima (Japan Atomic Energy Research Institute)

OBJECTIVE

To determine the susceptibility of a fusion-relevant alloy to irradiation-assisted stress corrosion cracking (IASCC) by performing slow strain rate tensile (SSRT) testing of fusion spectrally-tailored materials in aqueous environments.

SUMMARY

Specimens of a type 316 stainless steel (SS) that had been irradiated in the fusion spectrally-tailored MFE-6J/7J experiments in the Oak Ridge Research (ORR) to 7.4 dpa at temperatures of 400. 330, 200, and 60°C were SSRT tested in a recirculating autoclave system in oxygenated, high-purity water. Complete intergranular (IG) failure was observed only for the specimen irradiated at 400°C. Only 10% IG failure was observed for the 330°C irradiated specimen and no IG failure was observed for the specimens irradiated at 200 and 60°C.

INTRODUCTION AND BACKGROUND

IASCC is considered one of the major environmental degradation mechanisms of austentitic SS in water-cooled nuclear power systems.[1-3] IASCC has been observed in type 304 SS and other austentitic SS alloys, which have been exposed to a fast ($E > 1$ MeV) neutron fluence greater than about 5×10^{20} n/cm^2 in commercial boiling water reactors (BWRs) and in test reactor experiments at BWR conditions (288°C).[1] IASCC has been manifested in the form of intergranular stress corrosion cracking (IGSCC).[1] It has been suggested that changes in grain boundary composition caused by radiation-induced segregation (RIS) plays an important role in increasing the IASCC susceptibility of SS.[3-15] However. the precise mechanism of IASCC is not yet clear.

IASCC may also be a degradation mechanism for water-cooled austentitic steels in fusion reactors.[16-17] For fusion reactors, the RIS and IASCC characteristics of the materials will be different from those in light-water reactors (LWRs) because of the harder neutron spectrum and higher neutron flux (viz., higher damage rate and lower helium production).[18] Electrochemical testing performed at Oak Ridge National Laboratory (ORNL) on U.S. fusion alloys (USPCA). in cooperation with Japan Atomic Energy Research Institute (JAERI) and as part of the U.S.-Japan Collaborative Testing of First Wall and Blanket Structural Materials with Mixed Spectrum Fission Reactors, indicated that significant changes in the electrochemical properties could be detected in fusion spectrally-tailored specimens irradiated at temperatures as low as 200°C.[19] In some cases, changes in electrochemical properties can be related to susceptibility to IGSCC (IASCC).[20]

SSRT testing of similarly irradiated materials was the next step to determine if measured changes in electrochemical properties correlated with susceptibility to environmental cracking behavior (i.e., IASCC). An SSRT experiment is simply a tensile test performed in the environment of interest, in this case high-purity water. SSRT tests investigate the effect of the environment on the mechanical/cracking behavior of the material. Slow strain rates ($<10^{-6}$ s^{-1}) are required to allow sufficient time for environmental (corrosion) reactions to occur on the same time scale as the mechanical deformation. Susceotibility to IASCC in SSRT tests is determined by comparing the maximum stress, strain-to-failure, and fracture mode (percent IG failure) of irradiated specimens with similar SSRT measurements for unirradiated specimens and similar data from tensile tests in inert environments (e.g., vacuum).

EXPERIMENTAL

Specimens and Materials

Grodzinski specimens of two Japanese fusion alloys, designated JPCA and J316, were irradiated in the fusion spectrally-tailored MFE-6J/7J experiments in the Oak Ridge Research Reactor and were available for SSRT testing after irradiation. Details of the irradiation experiments and conditions have been reported elsewhere.[21-24] Grodrinski specimens are normally used to evaluate fatigue properties of materials. However, the geometry of a Grodrinski specimen is similar to that of a flat-sheet tensile specimen [Fig. 1 (ORNL-DWG-78-158)] and were adapted for use in SSRT testing. Grodrinski specimens of the material designated as 5316 in the solution annealed (SA = 1100°C x 30 min + water quench) irradiated at 60, 200, 330, and 400°C (specimens, GFC-30, GFC-45, GFC-01, and GFC-15, respectively) to a dose of 7.4 dpa under fusion spectrally-tailored conditions condition were selected for SSRT testing. The composition of 5316 is shown in Table 1. This material was chosen for SSRT testing because of the likelihood that a type-316 material will be selected as a structural material for the International Thermonuclear Experimental Reactor (ITER). In the fusion spectrally-tailored experiments (MFE-6J/7J), the dose rate (~ 2 x 10^{-7} dpa/s) and helium generation rate (15 appm-He/dpa) of the materials were maintained at values typical of components for fusion reactors, *e.g., the* first wall and blanket for the ITER.[25]

ORNL-OWG 80-*12052*

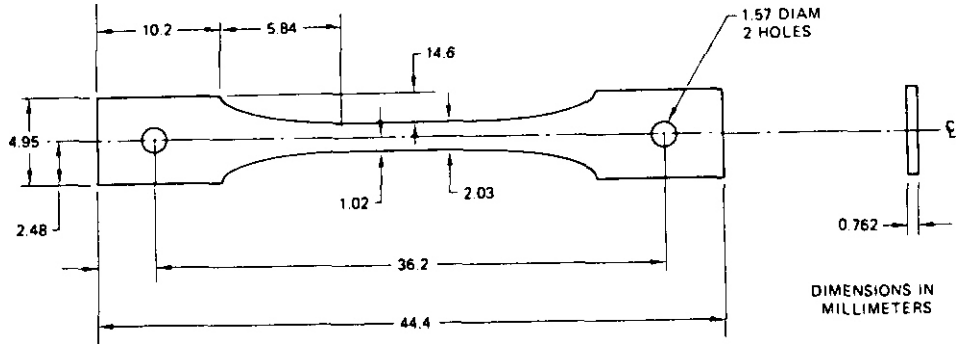

Figure 1. Grodzinski fatigue specimen.

TABLE 1. CHEMICAL COMPOSITION OF ALLOY J316

Alloy	C	Si	P	S	Ti	Cr	Mn	Fe	Ni	Mo
J316	0.058	0.61	0.028	0.003	0.005	16.7	1.80	bal	13.5	2.46

Heat Treatment: Solution Annealed = SA = 1100°C x 30 min + Water Quench

ORNL-DWG 91M-14388

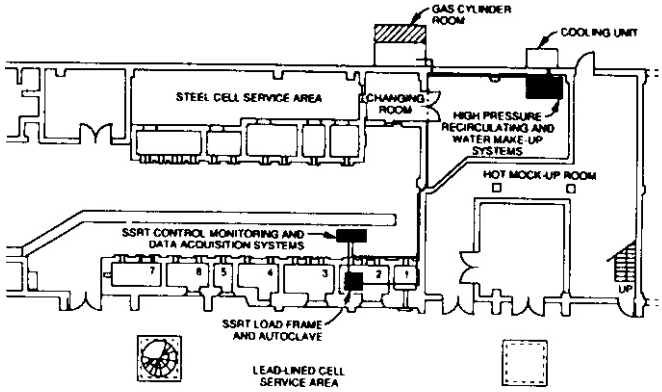

Figure 2. Floor Plan of Oarai Hot Laboratory.

TABLE 2. JAERI OARAI SSRT TEST FACILITY DESCIPTION

Load Frame

Maximum Load Capacity (kgf)	3000
Cross Head Speed (mm s^{-1})	-1.6×10^{-6} to 1.6×10^{-2}
Loading Methods	Constant toad
	Constant Extension Rate (a.k.a. SSR)
	Triangular Wave

Autoclave

Material	SUS316L
Volume (l)	1.7
Dimensions (mm)	90 ID x 270
Maximum Operating Temperature (°C)	300
Maximum Operating Pressure (MPa)	10.1
Electrochemical Electrodes	
	External Ag/AgCl Reference
	Platinum Counter
	Specimen (working) Electrodes

Flow Control System

Working Fluid	Pure Water
Dissolved Oxygen	10 ppb - 32 ppm
Flow Rate. Fixed (l/h)	5
Monitoring Capabilities	
	pH
	Conductivity
	Dissolved Oxygen
	Electrochemical Corrosion Potential (ECP)

Hot Cell timitation at Oarai Research Establishment

Equivalent ^{60}Co Activity	1 Curie

Equipment and Test Conditions

JAERI has installed an SSRT test facility for irradiated materials in a lead lined hot cell in the Hot Laboratory at the Oarai Research Establishment [Fig. 2 (ORNL-DWG 91M-14388)]. The manufacturer of the equipment was Toshin Kogyo, and a description of the facility is given in Table 2. A flow schematic of the SSRT system is showri in Fig. 3 (ORNL-OWG 91M-14387).

ORNL-DWG 91M-14387

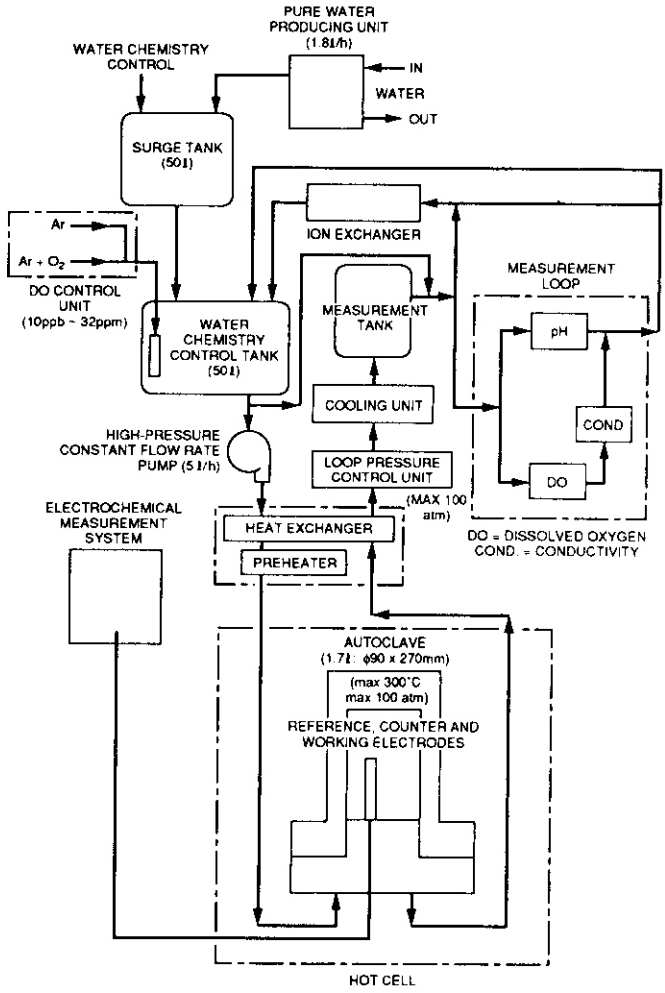

Figure 3. Schematic of SSRT Testing System.

The specimens irradiated at 400 and 330°C were tested with a water temperature of 300°C (different from their irradiation temperature) due to the system temperature limit. An unitradiated control specimen of 5316 (specimen GFC-026) was also tested in water at 300°C for comparison with the irradiated material. The 200 and 60°C specimens were SSRT tested in high-purity water at their respective irradiation temperatures. System pressure was maintained at 95 ± 1 kg-cm^{-2} for all five tests.

Oxygen-rich ervironments were chosen to maximize the sensitivity of the SSRT test to detecr IASCC. A condition of oxygen-saturated water in the surge tank (room temperature) was maintained by sparging with pure oxygen. Sparging produced dissolved oxygen (DO) contents to the inlet of the autoclave of ~ 32 ppm-DO for tests with the autoclave at 300°C. - 22 ppm-00 with the autoclave at 200°C and ~ 10 ppm-DO with the autoclave at 60°C. The autoclave outlet DO-value was typically 2 to 3 ppm less than the inlet DO-value. The conductivity of the water on inlet to the autoclave was less than 0.1 $\mu S \cdot cm^{-1}$ (typically 0.08$\mu S \cdot cm^{-1}$), and outlet from the autoclave was less than 1 $mS \cdot cm^{-1}$ (typically 0.6 $\mu S \cdot cm^{-1}$). The pH of the water in the system was - 6.4 measured at room temperature. The water flow rate was between 4.3 and 5.0 liters per hour. Specimens were pulled to failure at a constant cross head speed of 1.8 x 10^{-4} $mm \cdot s^{-1}$, except in the case of the 60°C specimen. For the 60°C specimen. it was necessary to accelerate the cross-head speed to 9 x 10^{-4} $mm \cdot s^{-1}$ after an extension of - 2.4 mm at 1.8 x 10^{-4} $mm \cdot s^{-1}$ (~ 13.2% total elongation) in order to complete the experiment prior to a previously scheduled Hot Laboratory shutdown. Test data (load. cross-head displacement, dissolved oxygen, pH, conductivity, system pressure, and temperature) were monitored and recorded by computer at intervals of ten minutes.

After testing. the specimen was inspected and measured optically. The fracture surface was then examined using a scanning electron microscope (SEM).

Results

Load versus Displacement in SSRT Tests:

The load versus displacement SSRT results of the four irradiated specimens. along witr that of the unirradiated control specimen (GFC-026), are shown in Fig. 4 (ORNL-DWG-91-15454).

For the specimen irradiated at 400°C (GFC-15), failure occurred at 0.80 mm. ~ 4.4% total eiongation (TE), of indicated extension and a maximum load of ~ 105 kg (s = 573 MPa). The failure was located approximately in the middle of the uniform gauge section. Sharp drops in load (~ 5 kg) were observed early in the test. Post-test measurement of the specimen showed good agreement betweer cross-head extensometer measurements and measured specimen elongation. The 330°C specimen also failed at 0.80 mm (~ 4.4% TE) of indicated extension. A maximum load of - 135 kg (s = 846 MPa) occurred early in the test. Failure occurred where the elliptical radius from the specimen shoulder meets the uniform gauge section of the specimen. One sharp drop in load was observed in the test before specimen failure occurred. Post-test measurement of the specimen also showed good agreement between in-situ extensometer measurements and measured specimen elongation. For the 200°C specimen, failure of the specimen occurred at 2.72 mm (~ 15.11% TE) of indicated extension and a maximum load of ~ 105 kg (s = 675 MPa). Upon removal of the specimen and specimen holder from the autoclave, it was found that the specimen had failed where the elliptical radius meets the uniform gauge section, but that slip in the gripping system had occurred during the extension. Post-test measurement of the specimen showed poor agreement between

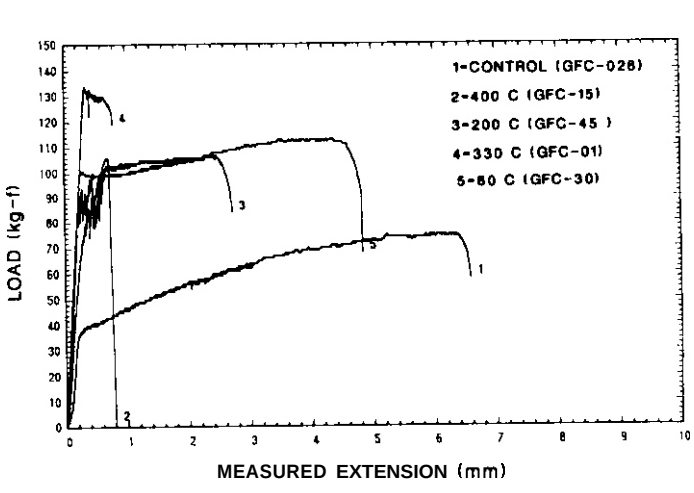

Figure 4. Load versus extension of MFE 65/75 irradiated J316.

in-situ extensometer measurements (2.72 mm) and measured specimen elongation (2.28 mm: ~ 12.7% TE) and confirmed slip of nearly 0.5 mm during the test. For the 60°C specimen. failure occurred at 4.83 mm of extension (~ 26.87 % TE) with a maximum load of ~ 113 kg (s = 713 kg/mm^2). Comparison between SSRT and tensile data for maximum stress and total elongation to failure is shown in Figs. 5 (ORNL-OWG 91-15445) and 6 CORNL-OWG 91-15443]. The tensile properties of the materials from these experiments have been reported previously in detail.[26]

ORNL-DWG 91-15445

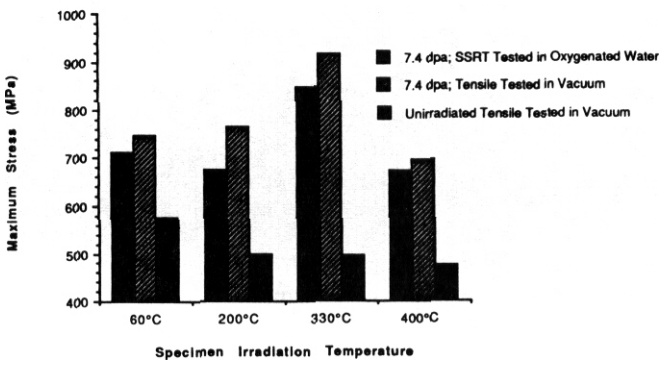

Figure 5. Maximum Stress attained during SSRT and vacuum tensile testing versus irradiation temperature for MFE-6J/7J irradiation J316.

ORNL-OWG 91-15443

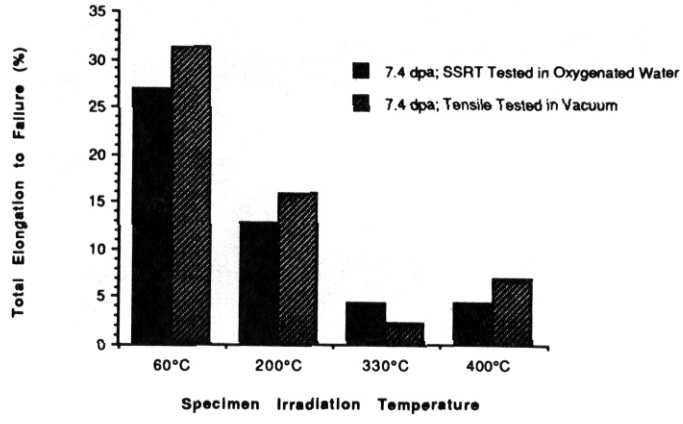

Figure 6. Total elonsation to failure as a function of irradiation temperature for SSRT and vacuum tensile test for MFE-6J/7J irradiated 5316.

Fracture Surface Morphology:

Figures 7 through 9 compare the fracture surfaces observed using an SEM for the 400, 330. and 200°C SSRT tested specimens with those of vacuum tensile tested specimens. Unfortunately, the fracture surface of the SSRT-tested 60°C specimen has not been examined. as yet. The 400°C [Fig. 7a] specimen showed nearly 100% IG failure when SSRT tested in high-purity, oxygenated water at 300°C. as compared to a completely ductile failure when test in vacuum at 400°C [Fig. 7bl. Secondary cracking was also observed on the SSRT-tested surface. Crack initiation. however. was not IG. The edge of the 400°C specimen fracture area was surrounded by a transgranular cleavage region. The fracture initiated by cleavage and propagated transgranularly for ~1 grain diameter, then branched IG upon meeting a grain boundary. The fracture surface of the 330°C specimen showed that only about 10% IG failure had occurred [Fig. 8al. Again, the vacuum tensile surface failed in a ductile mode by microvoid coalescence [Fig. 8b]. No secondary cracking was observed. Crack initiation in the region of IG failure was not IG. The periphery of the IG-failed specimen fracture area was surrounded by a region of transgranular cleavage. The fracture initiated and propagated transgranularly for ~ 1 grain diameter then branched IG upon meeting a grain boundary. The SSRT-tested 200°C specimen [Fig. 9a] showed no IG failure and was similar to the appearance of the vacuum tensile fracture surface [Fig. 9b].

DISCUSSION

The results from these SSRT tests are most interesting when viewed in light of the existing data on IASCC collected for light-water fission reactors (Fig. 10).[14] Only dose rate and temperature have been considered important to characterize the RIS and IASCC behavior of austenitic stainless steels by the fission reactor community. From this viewpoint, complete IG failure (i.e., IASCC) of the 400. 330, and most likely the 200°C

YP-13407

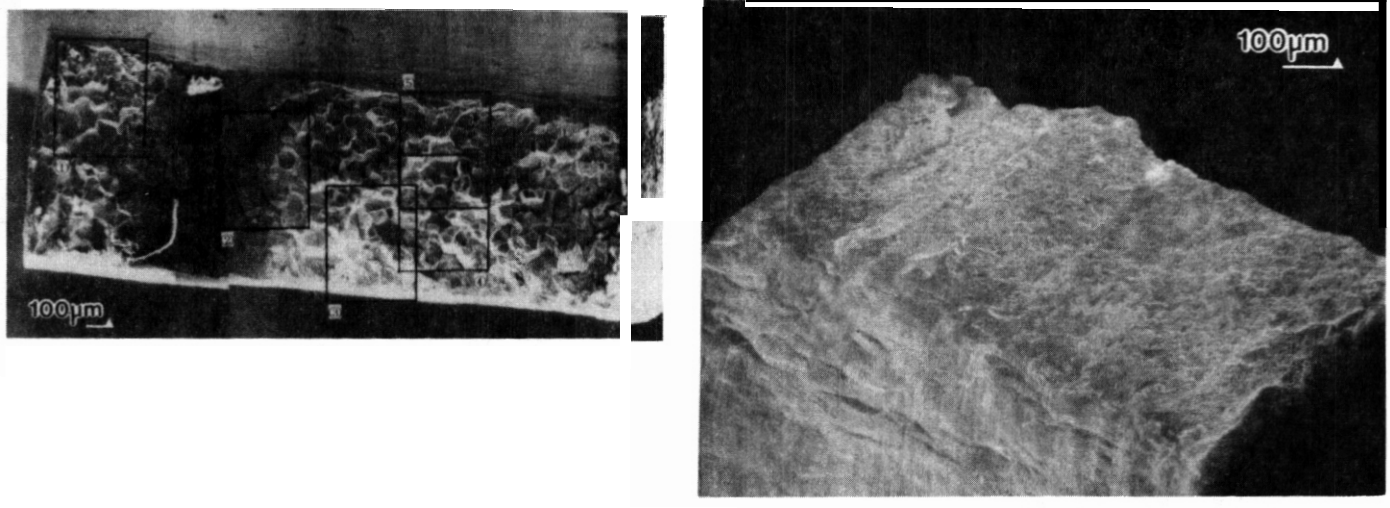

N000929

Fig. 7. Fracture surfaces of specimens of J316 irradiated at 400°C in MFE-6J/7J. (a) SSRT tested in oxygenated high-purity water at 300°C; (b) tensile tested in vacuum at 400°C.

YP-13406

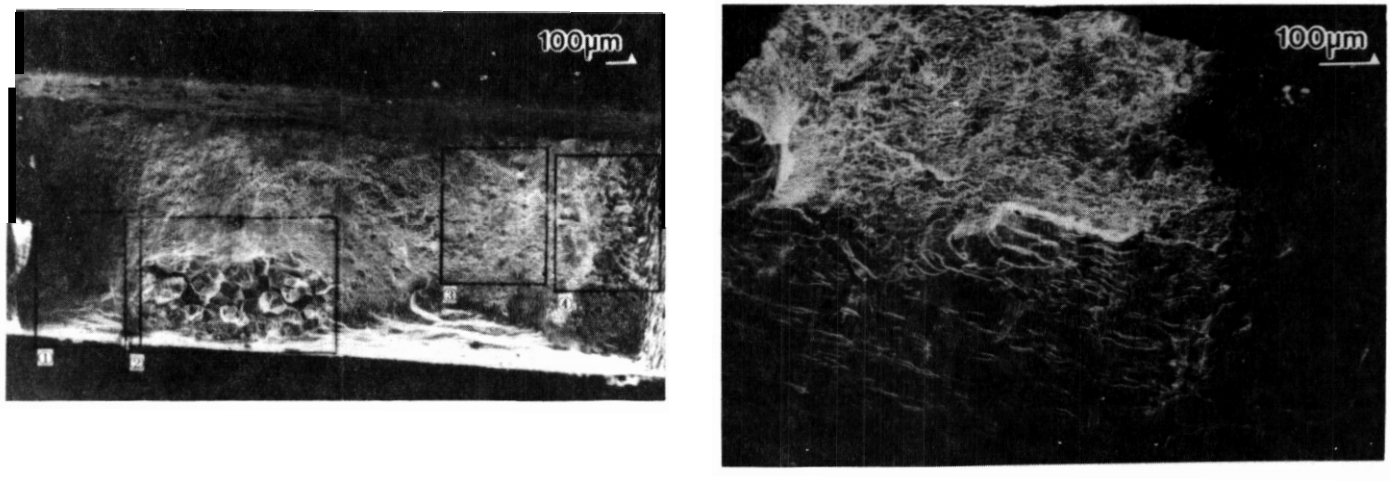

N000894

Fig. 8. Fracture surfaces of specimen of J316 irradiated at 330°C in MFE-6J/7J. (a) SSRT tested in oxygenated high-purity water at 300°C; (b) tensile tested in vacuum at 330°C.

specimens would have been predicted. The facts that the 330°C specimen showed only a small amount of IG failure and that the 200°C specimen showed no IG failure. are inconsistent with the fission reactor IASCC data base. While the SSRT data collected so far are inconsistent with the LWR fission data on IASCC. these SSRT data are consistent with the electrochemical data for similarly irradiated USPCA reported earlier.[19] When the surface of specimens of USPCA irradiated under fusion spectrally-tailored conditions in MFE-6J/7J at 60. 200, 330, and 400°C were examined after electrochemical potentiokinetic reactivation (EPR) testing, only the specimen irradiated at 400°C showed grain-boundary etching, indicating chromium depletion and sensitization.

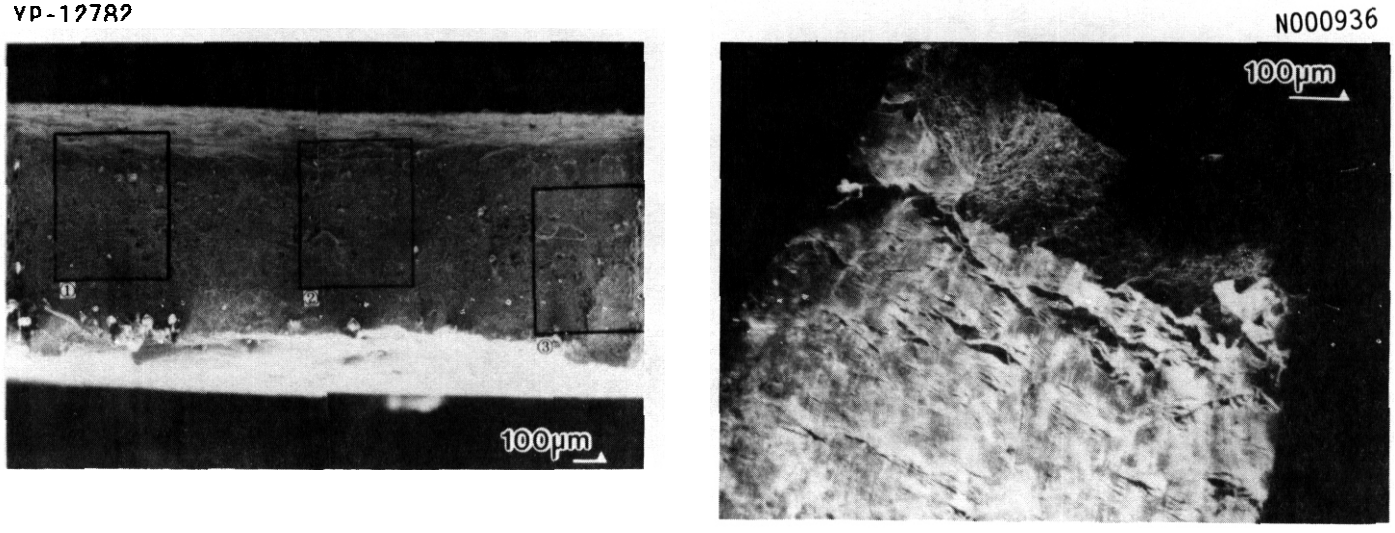

Fig. 9. Fracture surfaces of specimens of 5316 irradiated at 200°C in MFE-6J/7J. (a) SSRT tested in oxygenated, high-purity water at 200°C; (b) tensile tested in vacuum at 200°C.

There are several possible explanations for this apparent discrepancy between the LWR IASCC experience and these IASCC data from fusion spectrally-tailored experiments. First, the dose rate for MFE-6J/7J was about 10 to 20 times that of materials in operating LWRs. However, IASCC data from accelerated testing in test reactors (e.g., Advanced Test Reactor) with comparable dose rates (factor of 2 or 3 less) to MFE-6J/7J have been conducted and have shown behavior consistent with that in Fig. 10. Secondly, the non-uniform elongation that occurred in both the 200 and 330°C specimens may have caused the local strain rate to increase beyond that at which IASCC can be observed (i.e., local deformation of the material occurred on a faster time scale than the corrosion reactions). The fact that there was one sharp drop in load and, correspondingly, one small area of IG failure on the 330°C irradiated specimen supports this theory to some extent. This implies that perhaps the SSRT test method cannot correctly evaluate the SCC behavior of such materials. Constant load testing in oxygenated water may be more sensitive to detecting IASCC on materials that have little or no capacity to work harden. Lastly. helium generation rate in the MFE-6J/7J experiments was between a factor of 2 and a factor of 5 lower than that of a comparable material in an LWR (10 to 15 appm-He/dpa vs 20 to 50 appm-He/dpa). Helium exhibits a large influence on microstructure and microstructural development under irradiation by changing the number of radiation-produced defects which survive recombination. Since the migration of defects causes segregation, any process that changes the population of defects should affect the radiation-induced segregation and, thus, IASCC behavior. It is interesting to note that EPR testing of solution-annealed USPCA material irradiated in FFTF at 420°C to ~ 9 dpa with a lower helium generation rate (0.2 appm-He/dpa) showed deeper (as compared to MFE-6J/7J 400°C, 7.4 dpa), more continuous grain-boundary etching along with grain-face etching after electrochemical testing.[27] This observation suggests that RIS and IASCC decreases with increasing helium generation rate. Although the exact mechanism of how helium affects RIS/IASCC is not clear at this moment. it must be considered very carefully.

CONCLUSIONS

Only specimens irradiated at 400 (~ 100% IGSCC) and 330°C (~ 10% IGSCC) under fusion spectrally-tailored conditions showed any amount of IASCC when SSRT tested in oxygenated water at 300°C.

ORNL-DWG 91-15446

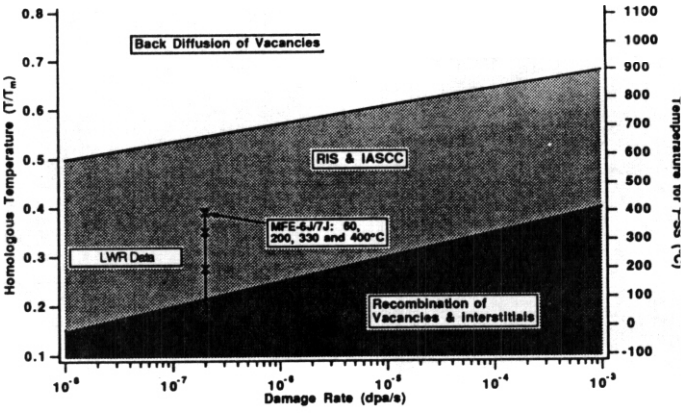

Fig. 10. Regions of **RIS and** IASCC **as functions of dose rate and irradiation temperature** for **austenitic stainless steels.**

Specimens irradiated at 200 and 60°C under fusion spectrally-tailored conditions showed no IASCC when SSRT tested in oxygenated water at their irradiation temperature.

Areas of IG fracture did not initiate intergranularly. Initiation was by cleavage fracture on the periphery of the specimen and branched to an IG mode after penetrating ~ 1 grain diameter and intersecting a grain-boundary.

It may be possible to correlate susceptibility to IASCC to post-EPR test grain boundary etching.

FUTURE WORK

Furture work in this area will include SSRT testing of spectrally-tailored JPCA to determine the effect of composition on IASCC. electrochemical testing of J316 and examination of post-EPR test surfaces to determine if post-EPR grain-boundary etching correlates to susceptibility to IASCC. and characterization of RIS in fusion spectrally-tailored materials via analytical electron microscopy.

ACKNOWLEDGMENTS

The authors thank the staff of the Hot Laboratory, Japan Atomic Energy Research Institute. at the Oarai Research Establishment for their assistance with this research and Ms. C. S. Lee for preparation of this manuscript.

REFERENCES

1. A. J. Jacobs. G. P. Wozadlo. "Availability Factor and Reliability Analysis." Proceedinas of International Conference on Nuclear Power Plant Aaing. American Society for Metals, Materials Park, Ohio, 1986. p. 173.

2. W. L. Clarke, A. J. Jacobs, "Materials in Nuclear Energy," Proceedings of International Conference, Metals Park. American Society Metals, Ohio 1982, p. 153.

3. R. N. Duncan, Stainless Steel Failure Investigation Program. Final Summary Report, GEAP-5530, General Electric Nuclear Energy, 1968.

4. K. Fukuya, S. Nakahigashi, S. Oraki, M. Terasawa, S. Shima. Proceedings of the Third International Symposium on Environmental Degradation of Materials in Nuclear Power Systems-Water Reactors, The Metallurgical Society of AIME. Warrendale, Pennsylvania, 1987, p.665.

5. A. J. Jacobs, G. P. Wuzadlo. N. Nakata, T. Yoshida. I. Masaoka. Proceedings of the Third International Symposium on Environmental Degradation of Materials in Nuclear Power Systems-Water Reactors, The Metallurgical Society of AIME, Warrendale, Pennsylvania, 1987, p.683.

6. E. P. Simonen. R. H. Jones. Proceedings of the Third International Symposium on Environmental Degradation of Materials in Nuclear Power Systems-Water Reactors, The Metallurgical Society of AIME, Warrendale, Pennsylvania, 1987. p.657.

7. H. Hanninen, Aho-Mantila, Proceedings of the Third International Symposium on Environmental Degradation of Materials in Nuclear Power Systems-Water Reactors, The Metallurgical Society of AIME. Warrendale. Pennsylvania, 1987. p.77,

8. F. Garzarolli, D. Alter. P. Dewes, J. L. Nelson, Proceedings of the Third International Symposium ON Environmental Degradation of Materials in Nuclear Power Systems-Water Reactors, The Metallurgical Society of AIME. Warrendale. Pennsylvania, 1987, p.657.

9. Aho-Mantila. H. Hanninen, "Materials for Nuclear Reactor Core Applications," Proceedings of International Conference. Vol. 1, British Nuclear Energy Society, London. England, 1987, p. 349.

10. E. A. Kenik, Proc. of Mat, Res. Soc. Symp. 62 (1986) 209.

11. D. I. R. Norris. C. Baker, J. M. Titchmarsh. Radiation-Induced Sensitization of Stainless Steels, CEGB 1987, Proceedings of the Symposium held at Berkeley Nuclear Laboratories, Berkeley, California, September 23, 1986, p.86.

12. J. M. Perks. A. D. Marwick, C. A. English, Radiation-Induced Sensitiration of Stainless Steels, CEGB 1987. Proceedings of the Symposium held at Berkeley Nuclear Laboratories, Berkeley, California, September 1986. p.15.

13. A. J. Jacobs, R. E. Clausing, L. Heatherly. R. M. Kruger, Irradiation-Assisted Stress Corrosion Cracking and Grain Boundary Searegation in Heat Treated Type 304SS, CONF-88063-3, Martin Marietta Energy Systems, Inc., Oak Ridge Natl. Lab.,1988.

14. P. L. Andresen, F. P. Ford, S. Murphy, J. Perks, Proceedings of the Fourth International Symposium on Environmental Degradation of Materials in Nuclear Power Systems-Water Reactors, National Association of Corrosion Engineers, Houston, Texas, 1990.

15. C. Taylor, Radiation-Induced Sensitization of Stainless Steels, CEGB 1987. Proceedings of the Symposium held at Berkeley Nuclear Laboratories, Berkeley, California, September 23, 1986, p.60.

16. C. C. Baker. Fusion Technology 15(1989) p.849.

17. R. H. Jones, Fusion Reactor Materials Semiannual Progress Report for the Period ending March 31. 1988. DOE/ER-0313/4, U.S. DOE, p.184.

18. S. Ohnuki, H. Takashi, R. Nagasaki, J. Nucl. Mater,. 155-157(1988) p.823.

19. T. Inarumi and G. E. C. Bell, "Radiation-induced Sensitization of PCA Under Spectrally-tailored Irradiation Conditions." Fusion Reactor Materials Semiannual Progress Report for the Period endino March 31. 1990, DOE/ER-031378, U.S. DOE, August 1990.

20. W. L. Clarke, V. M. Romero, J. C. Danko, Detection of Sensitization in Stainless Steels Using Electrochemical Techniques, GEAP-21382, General Electric Nuclear Energy 1976.

21. J. L. Scott et al.. First Annual Proaress Reoort on United States-Jaoan Collaborative Testing in the High Flux Isotooe Reactor and the Oak Ridge Research Reactor for the Period Endino September 30. 1984. ORNL/TM-9768, Martin Marietta Energy Systems, Inc., Oak Ridge Natl. Lab., October 1985.

22. J. L. Scott et al., Second Annual Progress Report on United States-Jaoan Collaborative Testing in the High Flux Isotope Reactor and the Oak Ridge Research Reactor for the Period Endina September 30. 1985, ORNL/TM-10102, Martin Marietta Energy Systems, Inc., Oak Ridge Natl. Lab., August 1986.

23. T. A. Gabriel. K. R. Thoms. and M. L. Grossbeck, "Design of Materials Irradiation Experiments in the ORR Utilizing Spectral Tailoring and Reencapsulation." ADIP Ouarterly Prooress Report March 31. 1979, DOE/ET-0058/5, U.S. DOE, p. 20.

24. T. A. Gabriel, K. R. Thorns. and J. W. Woods, "Design of Materials Irradiation Experiments Utilizing Spectral Tailoring," ADIP Ouarterlv Progress Reoort December 31. 1978. DOE/ET-0058/4, p. 10.

25. U. S. ITER Group, ITER and Blanket Work Package Report, ANL/FPP/88-1, Argonne Natl. Lab.. Argonne. Illinois, 1988.

26. M. L. Grossbeck et al., "Tensile Properties of Austenitic Stainless Steels Irradiated in the ORR Spectral Tailoring Experiment ORR-MFE-6J and 7J," Fusion Reactor Materials Semiannu. Prog. Rept., March 31. 1989, DOE/ER-0313/6, U.S. DOE, p. 259.

27. T. Inarumi. G. E. C. Bell, E. A. Kenik, K. Kiuchi. Corrosion, 46 (1990) 786.

7.0 SOLID BREEDING MATERIALS AND BERYLLIUM

DESORPTION CHARACTERISTICS OF THE Li_2O SYSTEM - A. K. Fischer and C. E. Johnson (Argonne National Laboratory)

OBJECTIVE

The objective is to describe the energetics and kinetics of desorption of $D_2O(g)$, $HDO(g)$, $H_2O(g)$, HO, and D_2, in the presence and absence of H_2, from the surface of ceramic tritium breeders (Li_2O in the present case) with data that facilitate predictions of the characteristics of tritium release.

SUMMARY

This reporting period is a time of transition during which temperature programmed desorption (TPD) measurements are being shifted from the $H_2O(g)$-H_2-$LiAlO_2$ system to the D_2-H_2-HD-HDO-H_2O-Li_2O system.

PROGRESS AND STATUS

Introduction

Earlier reports in this series discussed the background for the temperature programmed desorption (TPD) technique for measuring the activation energy and pre-exponential terms for the desorption rate equation. Most recently, measurements were reported for the H_2O-H_2-$LiAlO_2$ breeder system.[1] Characteristic desorption peaks were were identified according to their desorption activation energies. The reproducibility of a given activation energy under different conditions were ascribed to the desorption process occurring from specific types of surface sites. It was shown that the effectiveness of H_2 in enhancing the release of H_2O is not in modifying the activation energy of desorption and the pre-exponential terms for a given type of site, but rather in changing the populations of sites participating in the desorption processes so that sites with lower activation energies are increasingly involved.

Four types of sites were identified having activation energies of 18, *22,* 28 and **32 kcal/mol** for the desorption of $H_2O(g)$. These results were part of the input for a recent analysis of a MOZART tritium release test that provided excellent agreement between predicted and observed performance.[2]

With interest in the ITER program centering on Li_2O as the first choice of breeder, the focus of the TPD measurements has been shifted to develop understanding of desorption from Li_2O.

Discussion

Because numerous tritium release tests have indicated that the release is facilitated by H_2 in the sweep gas, there is much interest in determining the nature and quantitative aspects of this enhancement. In the forthcoming work with Li_2O, the sample will be loaded with deuterium and the desorption processes into a sweep gas containing H_2 will be measured. This will provide a close analog of the tritium release process in a reactor situation.

Preparation for the new work has required that the operation of the mass spectrometer be optimized for the new requirements. It was found, for example, that the voltage of the ionizing electrons that is conventionally used, 70 volts, leads only to a small $^{40}Ar^+$ peak and a large peak for $^{40}Ar^{+2}$ at mass 20 which would obscure the peak for D_2O. Conditions were found to restore acceptable mass spectrometer performance in this regard, but this requires that the instrument response for the other gaseous species be recalibrated.

FUTURE WORK

The future work is to perform and interpret the measurements for which preparations have been in progress. Blank runs without sample in the tube will be essential for separating sample desorption effects from tube wall effects. Beyond the measurements on Li_2O, analogous data will be needed for Li_2ZrO_3, the alternate ceramic breeder for ITER.

REFERENCES

1. A. K. Fischer and C. E. Johnson, "Desorption Characteristics of the $LiAlO_2$-H_2-$H_2O(g)$ System," Fusion Reactor Materials Semiannual Progress Report for the Period ending March 31, 1991, DOE/ER-0313/10, p. 284.

2. J. P. Kopasz, private communication.

Work supported by the U.S. Department of Energy, Office of Fusion Energy, under Contract W-31-109-Eng-38.

ANALYSIS OF IN-PILE TRITIUM RELEASE EXPERIMENTS - J. P. Kopasz, S. W. Tam, and C. E. Johnson

OBJECTIVE

Characterize tritium release behavior from lithium ceramics and develop insight into the underlying tritium release mechanisms.

SUMMARY

Analysis of tritium release data from recent laboratory experiments with lithium aluminate has identified physical processes which were previously unaccounted for in tritium release models. A new model that incorporates the recent data and provides for release from multiple sites rather than only one site was developed, Calculations of tritium release using this model are in excellent agreement with the tritium release behavior reported for the MOZART experiment.

PROGRESS AND STATUS

Introduction

Several different tritium release models have bee. used to interpret in-p'le tritium release tests.[1,2] However, in order to obtain good agreement with the test results, one or more parameters in the model were adjusted. This adjustment was required due to deficiencies in the data base needed for the models and deficiencies in the models themselves. The models gave goad agreement in the range of data for which the adjustable parameters were obtained, but often failed on other sets of data or outside the range of the adjustable parimeters.

Status

Tritium release from lithium ceramics has been modeled in the past as being controlled by diffusion or desorption from a single site. However, recent out-of-pile experiments suggest that this interpretation is an oversimplification of the tritium release mechanism. Laboratory isothermal anneal experiments performed on lithium aluminate at successively higher temperatures indicate that tritium release occurs from several different sites, with each site exhibiting different but discrete energies.[3,4] These results are in agreement with temperature programmed desorption (TPD) measurements on $LiAlO_2$ and Li_4SiO_4; the TPD curves show several overlapping peaks, indicating that tritium release occurs from different localized sites in these materials.[3,4,6] Thus, a shortcoming of our previous model[1] was that it was based on only one site for tritium release.

We have developed a model for tritium release that includes bulk diffusion and release from multiple sites. Since laboratory experiments indicate two sites dominate the release from $LiAlO_2$ when hydrogen is present in the purge gas,[4,5] our model considers release from two sites. The diffusion coefficient (D) used in the model is that determined by Bruning et al.[7] [$D = 3.09\times10^{-3} \exp(-19.3\ \text{kcal/mol/RT}) \text{cm}^2/\text{sec}$]. The first-order rate constants (K_1 and K_2) taken from recent laboratory experiments[5] are stated to be $K_1 = 4.04\times10^{-2} \exp(-28\ \text{kcal/mol/RT}) s^{-1}$ and $K_2 = 0.193 \exp(-32\ \text{kcal/mol/RT}) s^{-1}$. The distribution of tritium between the sites is calculated using the experimentally determined ratio of surface coverages for the two dominant sites obtained from TPD experiments and is expressed as $\theta_1/\theta_2 = 0.54$.[3,4]

Using this model, we have calculated the expected tritium release for some of the tests run in the MOZART experiment. No parameters were changed from the values observed in separate and independent laboratory experiments on material of similar size and structure. As examples of the applicability of the model, the calculated and observed tritium release was compared for a transient of a temperature increase and a temperature decrease. Figure 1 shows the results for a temperature increase from 600° to 650°C. The calculated release curve is of comparable magnitude to the observed curve, but indicates slightly slower kinetics. Figure 2 illustrates the results for a temperature decrease from 650° to 500°C. The magnitude of the decrease in release and the rate of the return to steady state of the calculated curve are in excellent agreement with the observed data. The agreement between observed and calculated results in these two plots has not been obtained previously without adjusting some of the input parameters.

FUTURE WORK

The model will be improved as additional experimental data become available describing how tritium is distributed between the sites and how this distribution changes with changing conditions, such as purge gas composition and temperature.

Work supported by the U.S. Department of Energy, Office of Fusion Energy, under Contract no. W-31-109-Eng-38.

REFERENCES

1. Modeling of Tritium Behavior in Ceramic Breeder Materials, J. P. Kopasz, S. W. Tam, and C. E. Johnson, J. Nucl. Mater. 155-157 (1988) 500.

2. Mistral: A Comprehensive Model for Tritium Transport in Lithium-Base Ceramics, G. Federici, A. R. Raffray, and M. A. Abdou, J. Nucl. Mater. 173 (1990) 214.

3. Mechanism of Tritium Release from Lithium Ceramics Irradiated with Neutrons, F. Botter, J. Mougin, B. Rasneur, S. Tistchenko, and J. Kopasz, 16th Symposium on Fusion Technology, London, England, 1990.

4. Investigation of Tritium Release and Retention in Lithium Aluminate, J. P. Kopasz, S. Tistchenko, and F. Botter, DOE/ER-0313/10, March 1991, p. 280.

5. Fusion Reactor Materials Semiannual Progress Report, A. Fischer and C. E. Johnson, DOE/ER-0313/10, March 1991, p. 284.

6. Tritium Release from Low-and High-density Lithium Meta- and Orthosilicate (Irradiation DELICE-2), W. Breitung, H. Elbel, H. Wedemeyer, and H. Werle, 16th Symposium on Fusion Technology, London, England, 1990.

7. The Diffusivity of Tritium in the System Li_2O-Al_2O_3, D. Bruning, D. Guggi, and H. R. Ihle, 12th International Symposium on Fusion Technology, Julich, FRG, 1982.

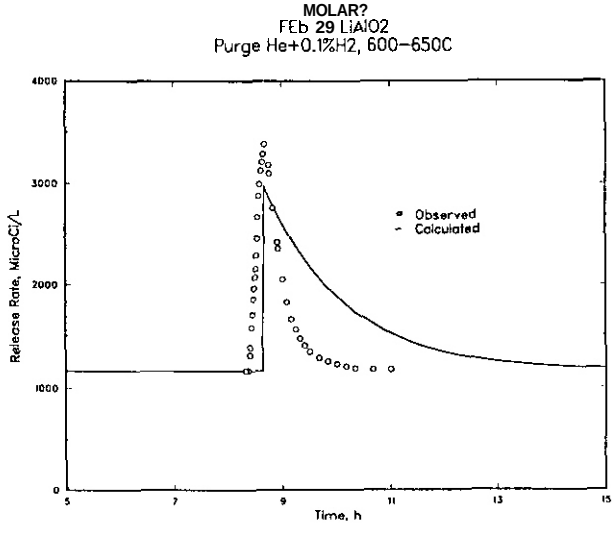

Fig. 1. Calculated and observed tritium release for a temperature increase from 600°-650°C for $LiAlO_2$ sample in the MOZART experiment.

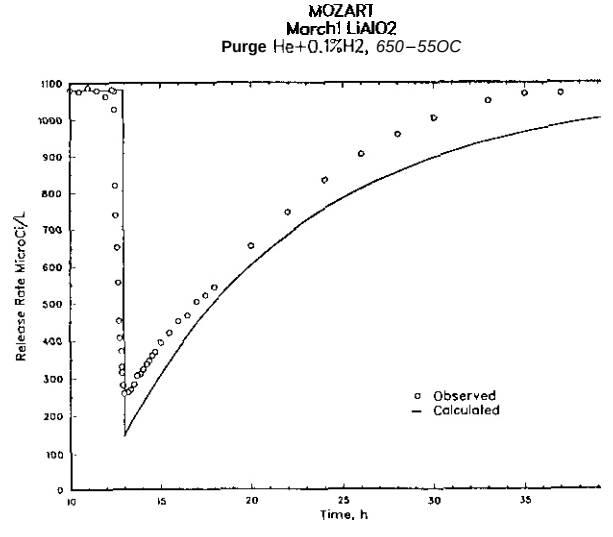

Fig. 2. Calculated and observed tritium release for a temperature decrease from 650°-550°C for $LiAlO_2$ sample in the MOZART experiment.

MICROSTRUCTURAL EXAMINATION OF BERYLLIUM IRRADIATED AT 500°C TO 1 DPA - D. S. Gelles, (Pacific Northwest Laboratory*)

OBJECTIVE

The objective of this study is to determine the suitability of beryllium as a neutron multiplier for blanket applications.

SUMMARY

The microstructure of commercial arc cast beryllium has been examined following irradidtion in FFTF at 500°C to 1 dpa. The major effect of irradiation is the development of helium bubbles on matrix and grain boundary dislocations.

PROGRESS AND STATUS

Introduction

Beryllium is being considered for use as a ileutron multiplier in iusion reactor blanket designs. In order to expedite the International Thermonuclear Experimental Reactor (ITER) design, specimens of pedigree beryllium that had previously been irradiated in the Fast Flux Test Facility Materials Open Test Assembly (FFTF/MOTA) are being examined. A previous report' described embrittlement of arc cast beryllium following irradiation in the FFTF MOTA at 400°C to 8 dpa, and attributed the embrittlement to irradiation hardening and helium bubble development. The present research extends that work to a higher temperature, 500°C.

Experimental Procedures

Sheet stock of commercial cast grade 99.7% pure beryllium was provided by J. B. Whitley, Sandia National Laboratory - Albuquerque (SNLA). Disk specimens 3 mm in diameter were punched from sheet stock of various thicknesses (0.05, 0.12, 0.20 and 1.14 mm), and fourteen of the specimens along with several copper alloy specimens were inserted into a helium filled stainless steel canister and were irradiated in the FFTF/MOTA cycle 1B in level 6 canister B. Level 6 is an above-core position. In that position, they received a dose of 3.4×10^{22} n/cm^2 or 1.25 dpa and about 10 appm He at 500°C.

Following irradiation, the beryllium specimens were removed from the helium filled stainless steel canister, and the 0.12 mm thick specimens were prepared for transmission electron microscopy following standard electropolishing procedures using a twin jet polishing unit. An electropolishing solution of 750 ml ethylene glycol, 75 ml nitric acid, 15 ml sulfuric acid, and 15 ml hydrochloric acid was used operating at 9 to 13 V and with the solution cooled. Typical polishing times approached three hours. Transmission electron microscopy (TEM) was performed on a scanning transmission machine operating at 120 KeV.

Results

The microstructure of the irradiated beryllium sheet specimens included a low density of dislocation tangles of a/3 <11•0> a-type Burgers vectors, possibly present before irradiation. No small loops were found. All matrix and grain boundary dislocations were decorated with helium bubbles. Examples are provided in Figure 1. Figure la shows a/3 <11•0> dislocations decorated with helium bubbles in a thin specimen. Figures lb and lc show subgrain boundaries and nearby dislocations decorated with helium bubbles. Helium bubble sizes vary but on a given dislocation, bubble sizes are fairly uniform. The bubble sizes appear to be proportional to the bubble spacing on a given dislocation, larger bubbles are farther apart. Bubbles are as large as 20 nm, but the average size for bubbles on dislocations is 10 ± 2 nm and the average size for bubbles on subgrain boundary dislocations is 6.6 ± 2 nm. On some of the largest bubbles, facets can be identified indicating that the largest bubbles have grown into voids. However, bubbles often appeared as bright circular features in weak beam dark field contrast even when dislocations were out of contrast, which is probably a further indication that they were pressurized and were therefore helium filled.

Discussion

The ITER team is expected to specify porous beryllium at levels between BO and 90% full density for neutron multiplication in the blanket. That material will be difficult to examine for microstructural stability because of the porosity and the resultant difficulties with specimen preparation. The present results on arc cast beryllium irradiated at 500°C to 1 dpa, combined with a previous effort on the same materials irradiated at 400°C to 8 dpa,[1] therefore provide a basis for understanding how such complex materiils

---

*Operated for the U.S. Department of Energy by Battelle Memorial institute under Contract DE-AC06-76RLO 1830.

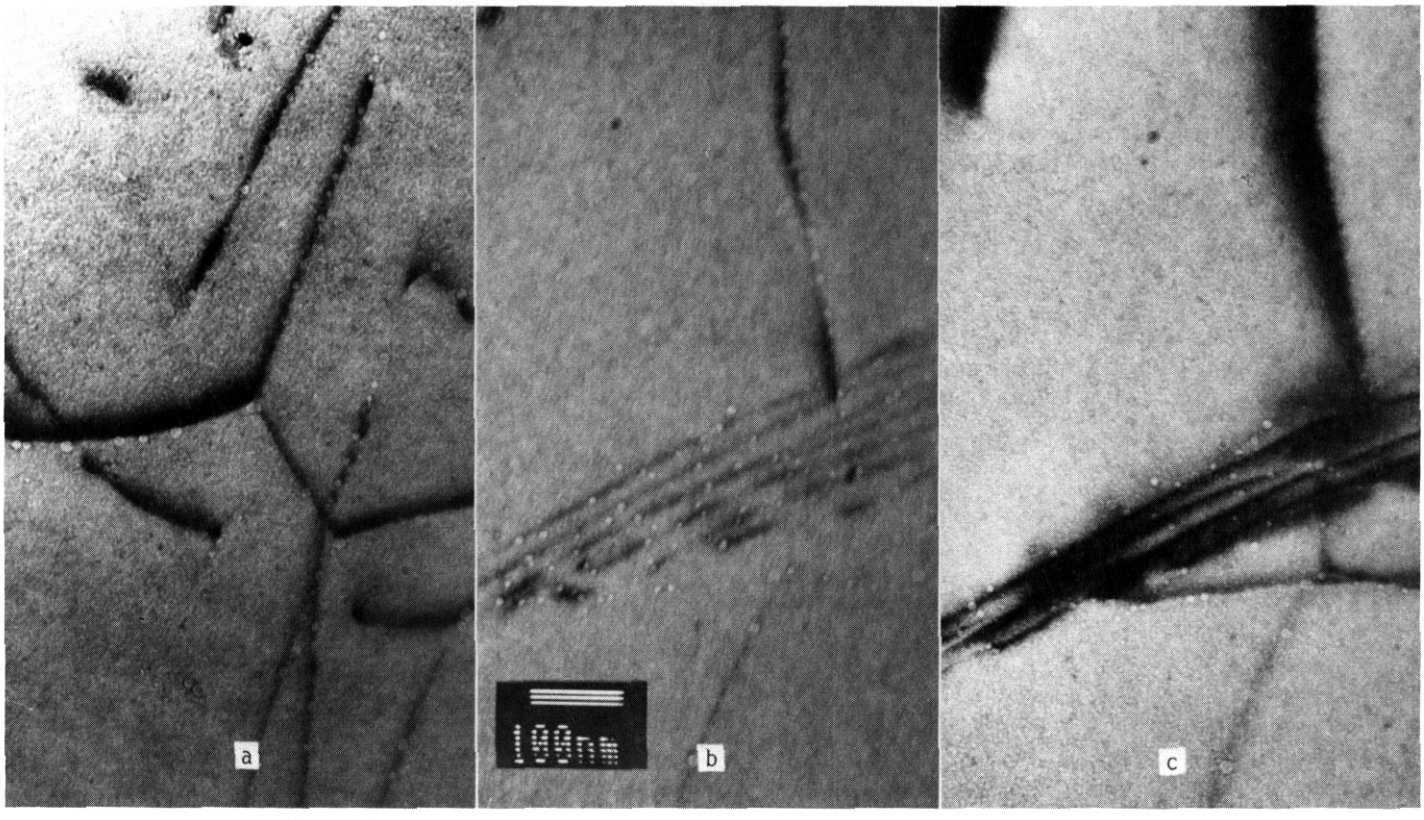

Fig. 1. Examples of helium bubbles in arc cast beryllium irradiated at 500°C to 1 dpa. **(a)** On matrix dislocations and **(b)** and (c) on subgrain boundaries and nearby matrix dislocations.

behave at fusion-relevant temperatures and irradiation conditions. Similar observations on the less dense, more fusion-prototypic beryllium will be more difficult to obtain.

The results of irradiation of beryllium in FFTF at 400°C to 8 dpa and at 500°C to 1 dpa indicate tnat the major effects of irradiation are dislocation evolution and helium bubble formation, probably leading to irradiation-induced swelling. Following irradiation at 400°C, a high density of small loops with c<00•1> c-type Burgers vectors and a high density of small bubbles 1.5 to 10 nm in diameter on dislocation: and grain boundaries are observed along with a severe loss in ductility. On the other hana, following irradiation at 500°C, small c-type loops are not found, and helium bubbles on matrix and grain boundary dislocations are much larger, on the order of 10 to 20 nm, despite a dose almost an order of magnitude lower. Therefore, embrittlement is expected to be much less severe following irradiation ai 500°C, but void swelling may become significant.

These results are in reasonable agreement with previous work. Barnes[2] and Walters et al[3] found a high density of dislocation loops following irradiation at 350°C to $2x10^{20}$ n/cm^2. Beeston and coworkers' found only void arrays at grain boundaries in a specimen irradiated at about 440°C to about 5 dpa, but otherwise the specimen contained no voids or bubbles. Hickman et al.[5] examined fracture surfaces of specimens irradiated to doses of 3.5 to $5.5x10^{20}$ nvt (or doses considerably below the present experiment) and found very few examples of bubbles on grain boundaries following irradiation at 450°C, but found many examples of bubbles on grain boundaries following irradiation at 550°C. However, all experiments except those of Beeston and coworkers involved doses considerably below the present levels.

Therefore, it can be anticipated that irradiation hardening will cause embrittlement of beryllium at temperatures on the order of 450°C and below, and helium embrittlement and perhaps swelling will be of concern for irradiation temperatures of 500°C and above.

CONCLUSIONS

Arc cast beryllium irradiated at 500°C to 1 dpa is found to contain a moderate density of a/3 <11•0> dislocations, and matrix and grain boundary dislocations decorated with helium bubbles 10 to 20 nm in diameter. The largest of the cavities appear to be facetted, indicating the onset of swelling.

FUTURE WORK

This work will be continued when cold pressed and sintered beryllium is available following irradiation at 420°C to 30 dpa.

REFERENCES

1. D. S. Gelles and H. L. Heinisch, Fusion Reactor Materials Semiannual Progress Report for the Period Ending September 30, 1989, DOE/ER-0313/7, 299.

2. R. S. Barnes, in The Metallurgy of Beryllium, Proceedings of an International Conference held in London, 16-18 October 1961, Institute of Metals Monograph and Report Series No. 28 (Chapman & Hall, London, 1963) 372.

3. G. P. Walters, C. M. Van Der Walt and M. J. Makin, J. Nucl. Mater., 11 (1964) 335.

4. J. M. Beeston, L. G. Miller, E. L. Wood, Jr. and R. W. Moir, J. Nucl. Mater., 122 & 123 (1984) 302.

5. B. S. Hickman, G. Bannister, J. H. Chate, J. G. McCracken, R. Smith and J. C. Be?.. "Irradiation of Beryllium at Elevated Temperatures, Part 1 Irradiation of Rig X-17 in HIFAR," TRG Report 540 (S/X), 1963.

8.0 CERAMICS

ANISOTROPIC DISLOCATION LOOP NUCLEATION IN ION-IRRADIATED $MgAl_2O_4$ - **S. J.** Zinkle (Oak Ridge National Laboratory)

OBJECTIVE

This work is intended to investigate the effects of transmutation products and varying ionizing-to-displaced damage ratio on microstructural evolution in ceramics.

SUMMARY

Polycrystalline disks of stoichiometric magnesium aluminate spinel ($MgAl_2O_4$) were irradiated with 2 MeV Al^+ ions at 650°C and subsequently analyzed in cross section using transmission electron microscopy (TEM). Interstitial dislocation loops were observed on {110} and {111} habit planes. The population of loops on both sets of habit planes was strongly dependent on their orientation with respect to the ion beam direction. The density of loops with habit plane normals nearly perpendicular to the ion beam direction was much higher than loops with habit plane normals nearly parallel to the ion beam direction. On the other hand, the loop size was nearly independent of habit plane orientation. This anisotropic loop nucleation does not occur in ion-irradiated metals such as copper and may be associated with the structure of displacement cascades in ceramics.

PROGRESS AND STATUS

1. Introduction

The successful operation of near-term fusion machines such as the International Thermonuclear Experimental Reactor (ITER) is dependent on the satisfactory performance of ceramics in various components, including diagnostic and resonant frequency heating systems. Irradiation studies of ceramics are more complex compared to metals due to the presence of multiple sublattices and ionic bonding effects. Hence, there is a relatively poor understanding of basic radiation-induced changes in ceramics. Ion accelerators are being utilized by several research groups to study the effects of radiation on the microstructure and electrical properties of insulating ceramics (e.g., refs. **1-4).**

A recent study has found that the microstructural evolution of ion-irradiated Al_2O_3, MgO, and $MgAl_2O_4$ is strongly dependent on the mass and energy of the irradiating ion.[5] Dislocation loop formation was suppressed in specimens irradiated with light ions such as protons. With increasing ion mass, the dislocation loop density increased and the mean loop size decreased for specimens irradiated at the same damage level and damage rate. This report concentrates on microstructural observations made on polycrystalline $MgAl_2O_4$ specimens irradiated with 2-MeV Al^+ ions.

2. Experimental Drocedure

Transmission electron microscopy **(TEM)** disks of stoichiometric polycrystalline magnesium aluminate spinel ($MgAl_2O_4$) were mechanically polished with 0.5 μm diamond paste and then bombarded in a 3 × 3 array at 650°C with 2-MeV Al^+ ions in the triple ion beam accelerator facility at the Oak Ridge National Laboratory (ORNL). The spinel grain size was 30 μm and the major chemical impurities were 1000 wt ppm Li and 200 wt ppm Fe (ref. **2).** The irradiation temperature was measured by a thermocouple spot-welded to the face of a stainless steel specimen that occupied one of the positions in the 9-specimen array, Specimens were irradiated to fluences of **4.6,** 15, and **37** × 10^{20} Al^+/m^2. This corresponds to calculated midrange (0.55 μm) damage levels of 3.2, **10,** and **24** displacements per atom (dpa). respectively, assuming an effective displacement energy of **40** eV (refs. 2,6). The calculated damage rate at this depth was ~7 × 10^{-4} dpa/s for all of the specimens, As detailed elsewhere,' cross-section TEM specimens were prepared by gluing an irradiated specimen face-to-face with a polished nonirradiated disk and sectioning perpendicular to the irradiation surface. The "sandwich" was mechanically dimpled and ion milled at room temperature until perforation occurred at the interface. TEM analysis was performed with a Philips **CM-12** microscope operating at **120** keV. Further experimental details are given elsewhere.[2,6,7]

3. Results and Analysis

Figure 1 shows the typical through-range microstructure observed in the irradiated specimens. There was no observable defect formation within ~**0.4** μm of the irradiated surface in any of the irradiated specimens. As discussed elsewhere,[5,6] this surface-denuded zone may be due to the high fraction of energy imparted to electronic excitation relative

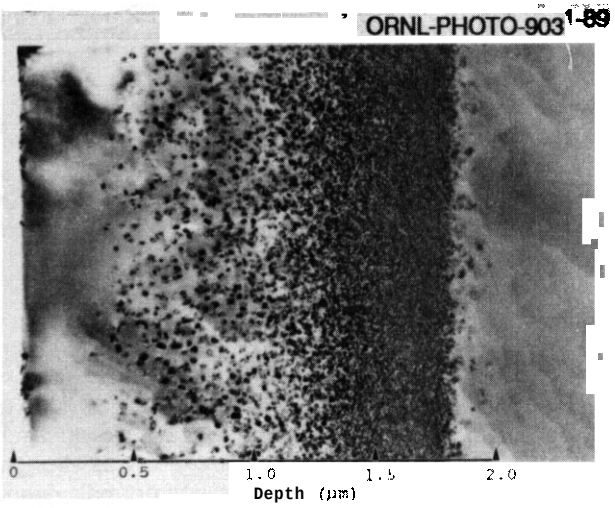

Fig. 1. Cross-section microstructure of spinel irradiated at 650°C to a fluence of 4.6×10^{20} Al^+/m^2.

to atomic displacements that occur in the near-surface regions of ceramic specimens irradiated with energetic light ions. A moderate density of interstitial-type dislocation loops lying on {110} and {111} habit planes was observed at intermediate depths of 0.4 to 1.0 μm from the irradiated surface. The loop density decreased and the size increased gradually with increasing fluence.[5] The loop density on {110} planes was significantly higher than on {111} planes. Metallic aluminum precipitates formed in a narrow band centered at a depth of ~1.5 μm (ref. 8), which coincided with the mean range of the 2-MeV Al+ ions. A dense array of dislocations was also visible in this ion-implanted region.

During the course of detailed loop analysts in the midrange regions of the irradiated specimens, it was discovered that loop nucleation was not occurring isotropically on the various habit planes. Figure 2 shows an example of the anisotropic distribution of loops on {110} habit planes. The two micrographs were taken from the same region in the irradiated foil, wkh the irradiated surface lying to the left side in each of the photographs. From the left-hand micrograph, it is apparent that there are only a few loops on the $(\bar{1}01)$ plane (visible as two half-arcs with a low-contrast axis that is perpendicular to the $[\bar{1}01]$ direction). On the other hand, the right-hand photograph shows more than 30 loops that lie on the $(01\bar{1})$ plane in this same region.

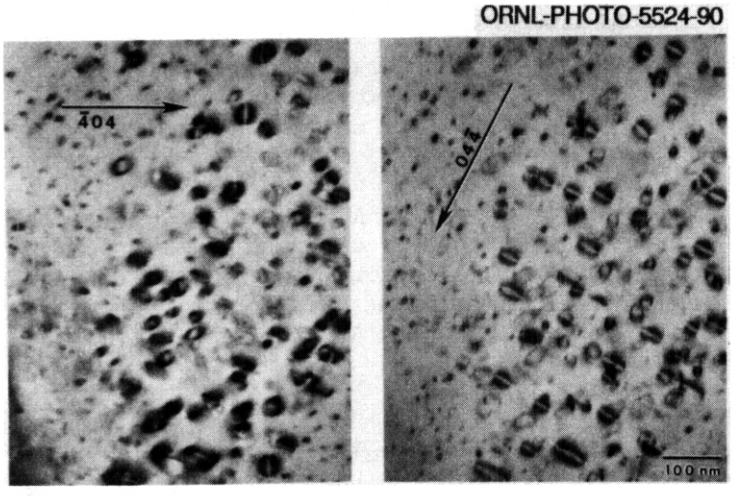

Fig. 2. Loop habit plane identification in spinel irradiated at 650°C to a fluence of 1.5×10^{21} Al^+/m^2 (same region imaged for both photographs). The foil normal is near [111], and the arrows indicate the magnitude and direction of the diffraction vector. The irradiated surface normal for this grain was near [312].

Figure 3 summarizes the results obtained from the habit plane analysis, performed using a specimen goniometer capable of high-angle x-y tilting. Typically, two different grains (with corresponding different surface normals) were examined for each of the three irradiation fluences. The dislocation loop population was very anisotropic for both the {110} and the {111} habit planes. Loop formation was clearly favored for habit planes with normals that are nearly perpendicular to the incident ion beam direction. This anisotropic behavior was maintained for all irradiation fluences that were investigated.

Figure 4 shows the corresponding variation in loop size with respect to habit plane orientation. The loops lying on {110} planes were generally larger than the {111} loops. In contrast to the loop density results, the loop size was independent of orientation. This clearly indicates that the physical mechanism responsible for the anisotropic distribution of loops on the various habit planes is related to loop nucleation, but not loop growth.

All of the analyzed loops on the {111} and {110} planes were determined to be interstitial in nature, with Burgers vectors of type $a/4\langle 110 \rangle$. This Burgers vector corresponds to a fully faulted defect (anion and cation sublattices) for the loops on {110} planes and a partially faulted defect (faulted cation and perfect anion sublattice) for the loops on {111} planes.

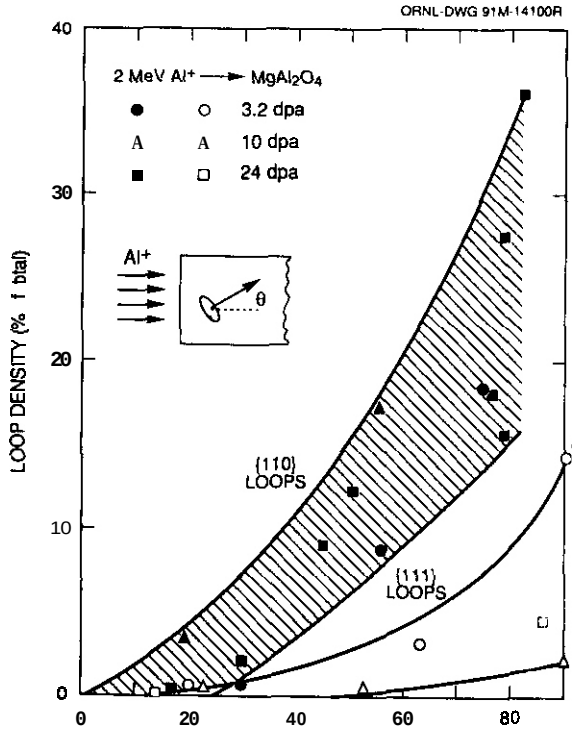

Fig. 3. Anisotropic loop formation in ion-irradiated spinel. The data points are normalized to the total measured loop density at each fluence.

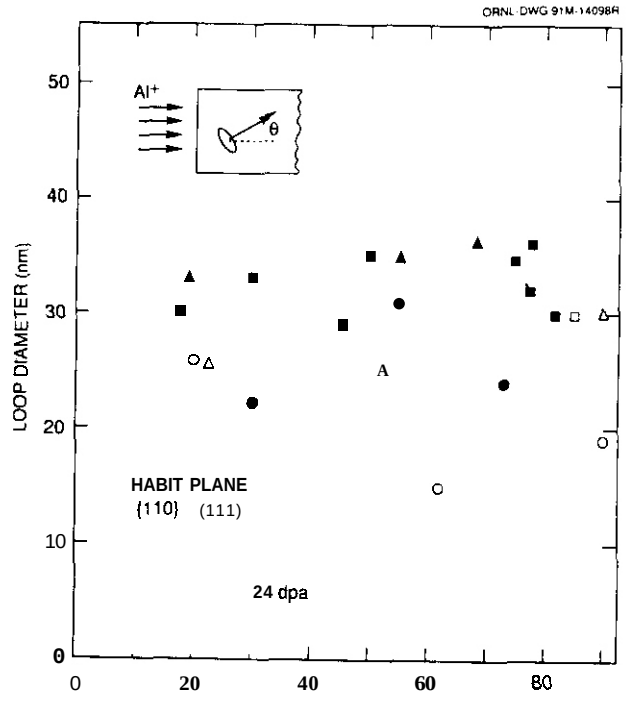

Fig. 4. Dislocation loop size in ion-irradiated spinel.

4. Discussion

Previous ion irradiation studies on metals such as copper have not detected any evidence of an orientation dependence for dislocation loop formation. For example, Stathopoulos et al.[9] found that the dislocation loops were equally distributed on the four {111} planes in copper irradiated with 30 keV Cu^+ ions. They noticed that the loops were slightly larger on habit planes with normals nearly perpendicular to the ion beam direction. which they took as evidence for slight elongation of the displacement cascades in the beam direction. We are not aware of any previous attempts to study the orientation dependence of dislocation loop formation in ion-irradiated ceramics.

The physical mechanism responsible for the observed habit plane orientation dependence on spinel is uncertain. Possible causes include: (1) stress effects associated with the implanted ions or the mechanical clamping of the specimen during irradiation; (2) surface image force effects; (3) electric field effects associated with the implantation of charged particles -- the resulting electric field potential and flow of electrical current between the surface and the implanted ion region could influence the diffusion of mobile interstitials; (4) anisotropic strain fields associated with the interstitial loops. This could lead to preferential capture by favorably oriented loops of the interstitials that are flowing toward the surface sink; (5) anisotropic displacement cascades that are elongated in the direction of the incoming ion -- the nucleation of an interstitial loop would then be statistically more probable on habit planes that are close to the ion beam direction (i.e., habit planes with normals that are nearly perpendicular to the ion beam direction).

Compressive stresses associated with ion implantation seem unlikely to be responsible since there was no evidence that the anisotropic loop nucleation was dependent on fluence. On the other hand, it is possible that the fluences in this study were too high to observe a transition from isotropic to stress-induced anisotropic loop nucleation. Compressive clamping stresses imposed on the specimen during irradiation may have aided anisotropic loop nucleation. Studies performed on metals have shown that external stress enhances interstitial loop nucleation on habit planes that experience the largest tensile stress, whereas subsequent growth is not appreciably affected.[10] Regarding the surface image mechanism. it is difficult to believe that image forces could be exerting such a strong influence at depths greater than 0.5 μm from the surface. The 3rd and 4th mechanisms appear to be unlikely, since anisotropic diffusion effects should also influence loop growth. As demonstrated in Figs. 3 and 4, the orientation dependence exists only for the loop density (nucleation) and not for the loop size (growth). The anisotropic displacement cascade mechanism is tentatively proposed

as the most likely cause of the observed dislocation loop orientation dependence, although the influence of compressive stresses associated with the ion implantation cannot be ruled out. Further work is planned to test these mechanisms, including an irradiation with the ion beam direction 30° from the surface normal of the samples.

In contrast to earlier neutron irradiation observations,[11,12] essentially all of the loops on {111} planes that form in stoichiometric spinel following Mg^+ or Al^+ ion irradiation at 25 and 650°C are of the type a/4 <110>{111} (refs 2,6). This type of loop does not contain an anion fault and is electrically more stable than faulted a/6 {111} Burgers vectors.[6] There was not any clear orientation relation between the Burgers vectors of the partially unfaulted loops and the ion beam direction. In addition, there is no apparent correlation between the unfaulted loop Burgers vectors and the foil normals of the cross-section specimens, which indicates that the loop unfaulting is not an artifact associated with the TEM specimen preparation. We have found some evidence that the partially unfaulted a/4 <110>{111} loops rotate toward {110} habit planes in a direction that would bring their habit plane normal to the <110> Burgers vector.

Nakai et al.[13] have recently reported similar results in spinel following neutron irradiation at 400 to 600°C. According to their observations, the {111} loops unfault on the anion sublattice at relatively low doses to form a/4 <110> {111} dislocation loops. These loops subsequently rotate along their glide cylinders to form a/4 <110> {110} loops. Previous neutron irradiation studies conducted on stoichiometric spinel at temperatures from 400 to 650°C have reported that the loops on {111} planes were always faulted on both sublattices, with a/6 <111> Burgers vectors.[11,12] It is uncertain why these earlier neutron irradiation studies[11,13] failed to observe the {111) loop unfaulting process.

Acknowledgments

The author thanks S.W. Cook for performing the ion irradiations and C.P. Haltom and A.M. Williams for preparing the TEM specimens.

References

1. C. Kinoshita, J. Nucl. Mater. 179-181 (1991) 53.
2. S. J. Zinkle, J. Am. Ceram. Soc. 72 (1989) 1343.
3. G. P. Pells et al., "Radiation Effects in Electrically Insulating Ceramics," Harwell Lab. AERE-R13222, Sept. 1988.
4. E. H. Farnum et al., these proceedings.
5. S. J. Zinkle, "Microstructural Changes in Oxide Ceramics Following Light Ion Irradiation," submitted to J. Mater. Res.; also Fusion Reactor Materials Semiann. Prog. Rept., DOE/ER-0313/10 (March 31, 1991).p. 302.
6. S. J. Zinkle, "Dislocation Loop Formation in Ion-Irradiated Polycrystalline Spinel and Alumina," in 15th Int. Symp. on Effects of Radiation on Materials, Nashville, TN, June 1990, ASTM STP 1125 (ASTM, Philadelphia), in press.
7. S. J. Zinkle, C. P. Haltom, L. C. Jenkins, and C.K.H. DuBose, J. Electron Microsc. Tech. 19 (1991) 452.
8. N. D. Evans, S. J. Zinkle, J. Bentley, and E. A. Kenik, Proc. 49th Ann. Mtg. of the Electron Microscopy Society of America (San Francisco Press, 1991). p. 728.
9. A. Y. Stathopoulos, C. A. English. B. L. Eyre. and P. B. Hirsch. Phil. Mag. A. 44 (1981) 285.
10. M. Suzuki and A. Sato, J. Nucl. Mater. 172 (1990) 97.
11. F. W. Clinard, Jr., G. F. Hurley, and L. W. Hobbs, J. Nucl. Mater. 108&109 (1982) 655.
12. F. W. Chard, Jr., G. F. Hurley, L. W. Hobbs. D. L. Rohr, and R. A. Youngman, J. Nucl. Mater. 122&123 (1984) 1386.
13. K. Nakai, K. Fukumoto, and C. Kinoshita. these proceedings.

THE EFFECT OF DISPLACIVE AND IONIZING RADIATION ON THE THERMAL CONDUCTIVITY OF Al_2O_3 --

Douglas P. White (Oak Ridge National Laboratory)

OBJECTIVE

This work is intended to provide information on the changes expected in the thermal conductivity of alumina under irradiation conditions.

SUMMARY

Recent measurements[1-3] have shown that the dielectric loss tangent of Al_2O_3 increases dramatically during irradiation by neutrons and protons. This large increase observed during in situ measurements has raised the question as to the effect of radiation on the thermal conductivity under irradiation conditions. The change in the lattice component of the thermal conductivity due to several phonon scattering mechanisms is calculated. The scattering due to intrinsic phonon-phonon interactions, vacancies, and to conduclion band electrons is considered. The vacancies produced by displacive radiation strongly scatter phonons in the high frequency portion of the phonon spectrum and the resulting fractional decrease in the thermal conductivity as a function of defect concentration is calculated. Ionizing radiation produces a large increase in the number of electrons in the conduction band and these electrons will scatter phonons in the low frequency portion of the phonon spectrum. The fractional decrease in the thermal conductivity as a function of the radiation induced electrical conductivity is calculated.

PROGRESS AND STATUS

Introduction

The transport of heat in ceramics is dominated by phonons and defects in the lattice which scatter phonons will bring about a reduction in the thermal conductivity. The lattice thermal conductivity *is* given by[4],

$$K=\frac{1}{3}\int S(\omega)\, v^2\, \tau(\omega)\, d\omega \quad , \tag{1}$$

where $S(\omega)$ is the specific heat per unit volume due to lanice modes of frequency $\omega d\omega$, v is the phonon velocity. and $\tau(\omega)$ is the phonon relaxation time. The reciprocal relaxation time is additively composed of the reciprocal relaxation time for each interaction separately so that,

$$\frac{1}{\tau(\omega)} = \sum_{\alpha} \frac{1}{\tau_{\alpha}(\omega)} \tag{2}$$

The interactions of interest in this case are intrinsic phonon-phonon scattering due to the anharmonicity ot the lanice, vacancy scattering, and phonon-electron scattering.

Vacancy Scattering

The reciprocal relaxation time due to intrinsic scattering is of the form[5,6],

$$\frac{1}{\tau_i}(\omega,T) = B\,\omega^2 \quad , \tag{3}$$

where T is the absolute temperature and B is a material dependent parameter which is proportional to T. The reciprocal relaxation time due to point defect scattering is of the form[4],

$$\frac{1}{\tau_p} = A\,\omega^4 \tag{4}$$

where A is proportional to the defect concentration and depends on the nature of the defect.

It has been shown[7,8] that at high temperatures ($T \geq \frac{\theta}{3}$, where θ is the Debye temperature) the fractional decrease in the thermal conductivity due to point defects is,

$$\frac{\delta K_p}{K_i} = 1 - \frac{\omega_0}{\omega_D} \tan^{-1}\left(\frac{\omega_D}{\omega_0}\right), \tag{5}$$

where ω_D is the Debye frequency and ω_0 is defined to be the frequency at which point defect scattering is equal to intrinsic scattering, that is $\tau_i(\omega_0) = \tau_p(\omega_0)$, so that,

$$\omega_0 = \sqrt{\frac{B}{A}}\,. \tag{6}$$

For a substitutional impurity of mass $M+\Delta M$[6],

$$A = C_d\,\Omega\left(\frac{\Delta M}{M}\right)^2 \frac{1}{4\pi v^3} \tag{7}$$

where C_d is the defect concentration, and Ω is the atomic volume. Equation 7 applies to the case of impurities which are chemically similar to the host lattice and which differ mainly in their mass, scattering by other defects may be described by an effective value of $\frac{\Delta M}{M}$ which also takes into account the local changes in the force constants. In the case of vacancies, which will be produced in the material by the radiation, a value of -3 can be ascribed to $\frac{\Delta M}{M}$[9].

For intrinsic scattering B has been estimated as[4],

$$B = 2\gamma^2 \frac{kT}{Mv^2} \frac{1}{\omega_D}\,, \tag{8}$$

where γ is the Gruneisen constant, M is the average atomic mass, and k is the Boltzmann constant. Thus in the case of vacancies,

$$\omega_0 = \left[\frac{8\pi kT\gamma^2 v}{C_v M \Omega \omega_D}\left(\frac{M}{\Delta M}\right)^2\right]^{1/2}\,, \tag{9}$$

where C_v denotes the vacancy concentration.

Phonon-Electron Scattering

The scattering of phonons by electrons may be neglected in insulators in non-radiation environments. However in a radiation environment the electrical conductivity is greatly increased[2,10,11,12] and this increase has a great effect on the dielectric loss tangent[2,3]. The effect of this increased conductivity on the thermal conductivity due to phonon-electron scattering must be calculated.

Energy and wave-vector conservation in the phonon-electron interaction dictates a maximum wave vector for those phonons allowed to interact with the electrons. If the maximum electron energy is chosen to be kT then the maximum frequency of interacting phonons is,

$$\omega_c = \frac{4nv}{h}(2mkT)^{1/2} \tag{10}$$

where h is Planck's constant, and m is the electron mass. Thus only phonons of frequency less than ω_c interact with the free electrons and the higher frequency part of the phonon spectrum is not scattered by electrons. Thus if ω_c is less than ω_D then the scattering due to vacancies and the scattering due to electrons are essentially independent of one another and the reduction in the thermal conductivity due to each scattering mechanism may be added.

Following the method of Klemens' the fractional reduction in the thermal conductivity due to phonon-electron scattering is found as follows. The intrinsic thermal conductivity is found by substituting equation 3 into equation 1 and using the high temperature limit for the specific heat,

$$S(\omega) = \frac{3k}{2\pi^2 v^3}\omega^2 \tag{11}$$

It is found that,

$$K_i = \frac{k}{2\pi^2 v}\int_0^{\theta/} \omega^2 \frac{1}{B\omega^2}\, d\omega = \frac{k\omega_D}{2\pi^2 vB} . \tag{12}$$

If the phonon relaxation time is assumed to be constant so that,

$$\frac{1}{\tau_{p-e}} = C , \tag{13}$$

then the thermal conductivity with the phonon-electron scattering included is, taking into account equation 2,

$$K_{p-e} = \frac{k}{2\pi^2 v}\left[\int_0^{\omega_c} \omega^2 \frac{1}{B\omega^2 + C}\, d\omega + \int_{\omega_c}^{\omega_D} \omega^2 \frac{1}{B\omega^2}\, d\omega\right] , \tag{14}$$

where equation 14 takes into account the fact that phonons of frequency greater than ω_c do not interact with the electrons. Evaluating equation 14,

$$K_{p-e} = \frac{k}{2\pi^2 v}\left[\frac{\omega_c}{B} - \frac{C}{B\sqrt{CB}}\tan^{-1}\left(\frac{B\omega_c}{\sqrt{CB}}\right)\right] + \frac{k}{2\pi^2 vB}(\omega_D - \omega_c)$$

$$= \frac{k\omega_D}{2\pi^2 vB}\left[1 - \frac{1}{\omega_D}\sqrt{\frac{C}{B}}\tan^{-1}\left(\omega_c\sqrt{\frac{B}{C}}\right)\right] . \tag{15}$$

Substituting equation 12 into this expression,

$$K_{p-e} = K_i\left[1 - \frac{1}{\omega_D}\sqrt{\frac{C}{B}}\tan^{-1}\left(\omega_c\sqrt{\frac{B}{C}}\right)\right]$$

so that,

$$\delta K_{p-e} = K_i - K = K_i\left[\frac{1}{\omega_D}\sqrt{\frac{C}{B}}\tan^{-1}\left(\omega_c\sqrt{\frac{B}{C}}\right)\right]$$

and **thus,**

$$\frac{\delta K_{p-e}}{K_i} = \frac{1}{\omega_D}\sqrt{\frac{C}{B}}\tan^{-1}\left(\omega_c\sqrt{\frac{B}{C}}\right) . \qquad (16)$$

In order to evaluate equation 16, B and C must be known. **As** before B has been estimated as,

$$B \approx 2\gamma^2 \frac{kT}{Mv^2}\frac{1}{\omega_D} , \qquad (8)$$

and it is *left* to determine C. It can be shown[13,14] that if one assumes that the phonons and electrons come to a mutual equilibrium through interactions with one another, then **the** time rate of change of the total momentum of the phonon gas must equal the time rate of change of the momentum of the electron gas, which may be expressed as;

$$\left|\frac{dP_e}{dt}\right| = \left|\frac{dP_p}{dt}\right| , \qquad (17)$$

and that this balance condition leads to the following expression for the phonon relaxation time,

$$\frac{1}{\tau_{p-e}} = C = \frac{n^2e^2v^2}{NkT\sigma}\frac{1}{\alpha}\left(\frac{\theta}{T}\right)^{3/2} , \qquad (18)$$

where,

$$\alpha = 4^3\left(\frac{\pi\Omega}{6}\right)^{1/2}\left(\frac{vm}{h}\right)^{3/2} ,$$

n is the conduction band electron concentration, *e* is the electronic charge, N is the number of atoms per unit volume. σ is the electrical conductivity, θ is the Debye temperature, and all other symbols have their previously defined meanings. To determine n the expression;

$$n = \frac{\sigma}{e\mu} \qquad (19)$$

is used, where μ is the electron mobility,

Fractional Chanae in Thermal Conductivity

It is now possible to calculate the fractional change in the thermal conductivity using equations **5** and 16. In order to do this, it is necessary to use the material constants specific to alumina. These are listed in Table 1.

γ	**1.35**[15]
θ_D	1000°K [16]
Ω	1.35 *x* 10^{-29} m^3 [17]
v	1 x 10^4 m/s
$\omega_D = vk_D = v\left(\frac{6\pi^2}{\Omega}\right)^{1/3}$	1.6 x 10^{14} s^{-1}
$M = .4(M_{Al}) + .6(M_O)$	**3.385**x 10^{-26} kg
μ	3 x 10^{-4} m^2/Vs [18]

$$\omega_D = 9.81 \times 10^{10}\sqrt{\frac{T}{C_v}} . \qquad (20)$$

Where C_v is !he vacancy concentration. Thus from equation 5,

$$\frac{\delta K_p}{K_i} = 1 - 6.13\times10^{-4}\sqrt{\frac{T}{C_v}}\tan^{-1}\left(\frac{1}{6.13\times10^{-4}}\sqrt{\frac{C_v}{T}}\right) \quad (21)$$

is the fractional decrease in the lattice thermal conductivity due to vacancy scattering. Substituting the values given in Table 1 into equation 16,

$$\frac{\delta K_{p-e}}{K_i} = 1.29\times10^{3}\,\frac{\sigma^{1/2}}{T^{7/4}}\tan^{-1}\left(4.61\times10^{-6}\,\frac{T^{9/4}}{\sigma^{1/2}}\right), \quad (22)$$

is the fractional decrease in the thermal conductivity due to phonon-electron scattering. Equations 21 and 22 are plotted in Fig. 1 and Fig. 2 respectively.

Predicted Change Durina Experiment

The fractional change in the thermal conductivity for specific experimental conditions may be calculated using equations 21 and 22. As an example, the fractional change in the lattice thermal conductivity expected under the irradiation conditions present in the experiments of Stoller et al.[1] will be calculated. In these experiments the alumina samples were irradiated at 306 °K for approximately 1.7×10^{-2} s and the displacement rate was 1.8×10^{-7} dpa/s. During displacive irradiation, the point defect concentrations initially increase at a linear rate". The time at which the defect concentrations deviate from this linearity is a function of temperature and the sink strength. For room temperature irradiation of ceramics, it is probably reasonable to assume this relationship holds over the time of the reactor pulse (this will give an upper bound to the fractional change in any case) then,

$$C_v = Gt \quad , \quad (23)$$

where G is the displacement rate in dpa/s and t is the time of the irradiation. The use of equation 23 also neglects any influence of the displacement cascades themselves. For times less than 10ps the effective vacancy concentration may be much higher within the cascade volume. Applying equation 23 in this case gives, $C_v = 3.06 \times 10^{-9}$, and substituting this value into equation 21 the fractional change in the thermal conductivity due *to* displacements is,

$$\frac{\delta K_p}{K_i} = 8.9 \times 10^{-6}. \quad (24)$$

This is an extremely small change in the thermal conductivity and would not be possible to measure. In order to calculate the fractional change in the thermal conductivity **due** to phonon-electron scattering it **is** necessary to estimate the value of the radiation induced conductivity produced by this radiation field. Extrapolating the data of **Pells** et al.[12] for the radiation induced conductivity in alumina vs. ionizing dose rate it is possible to estimate the radiation induced conductivity which was present in the experiments of Stoller et al.. The ionizing rate in these experiments was 5.83×10^{4} Gy/s and this corresponds to a radiation induced conductivity of $\sigma = 1.85 \times 10^{-6}$ $(\Omega\text{-m})^{-1}$. Using this value in equation 22 the fractional change in the thermal conductivity due to phonon-electron scattering under these irradiation conditions is,

$$\frac{\delta K_{p-e}}{K_i} = 1.2 \times 10^{-4} \quad (25)$$

This is also a negligibly small change in the lattice thermal conductivity.

DISCUSSION AND CONCLUSIONS

Large changes in the dielectric loss tangent have been observed in alumina under irradiation conditions and this has raised the question as to the effect these conditions have on the lattice thermai conductivity. It has been shown that the changes expected to occur in the thermal conductivity are negligible under these same conditions. In the dielectric measurements of Stoller et al. the dielectric **loss** was observed to increase from 5×10^{-5} to 8×10^{-3} while the calculated fractional change in the thermal conductivity was found to be 1.2×10^{-4} for the phonon-electron scattering and 8.9×10^{-6} for the vacancy scattering, which are negligibly small. The total fractional change in this case is given by the sum of these two and is essentially the reduction **due** to the phonon-electron interaction. Thus the small calculated reduction in the thermal conductivity is due to the increase in the number of free electrons under irradiation conditions which is probably also responsible for the large increase in the dielectric loss tangent. From these preliminary calculations it would appear that it is not necessary to perform in situ measurements of the thermai conductivity. This can be **seen** most clearly by referring to Figs. 1 and 2. From Fig. 1 it can be **seen** that in order to get even a one percent change in the thermal conductivity it is necessaly to have a vacancy concentration *of* about 2×10^{-6}. It should be noted that the vacancy concentration of interest here is not the total number of vacancies generated, but only those individual vacancies that would recombine quickly when the irradiation stops. It is not expected that the concentration of these transient vacancies will be as high as that necessaly to produce even a one percent change in the thermal conductivity. From Fig. 2 it can be seen that in order to produce a one percent change in the thermal conductivity a radiation induced conductivity of about 1×10^{-2} $(\text{ohm-m})^{-1}$ would be necessary and this is much higher than would be expected for fusion irradiation conditions.

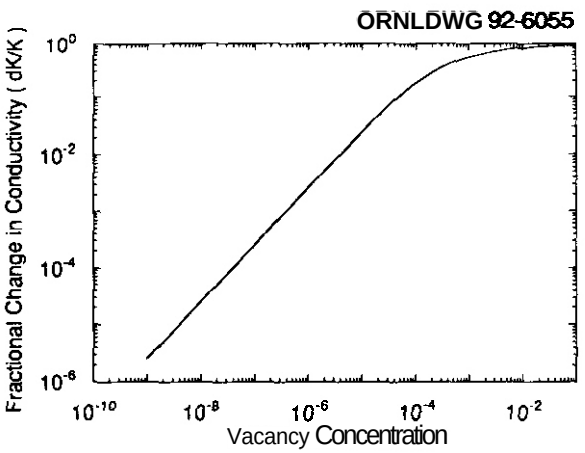

Figure 1: Fractional change in the lanice thermal conductivity versus the vacancy concentration, at 350 °K.

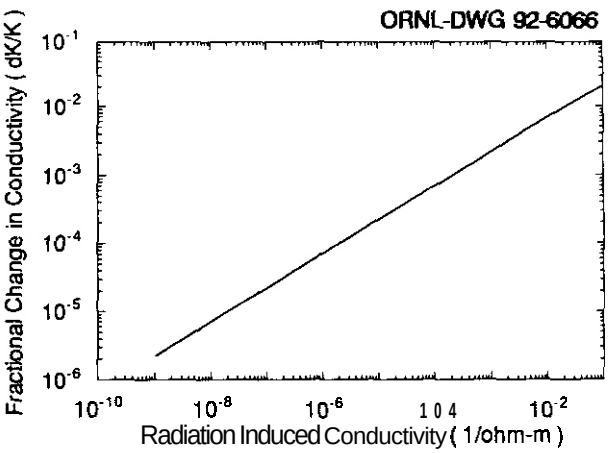

Figure 2: Fractional change in the lattice thermal conductivity versus the radiation induced conductivity, at 350 °K.

FUTURE WORK

The changes expected in the thermal conductivity due to other scattering mechanisms such as inclusions and grain boundaries will be calculated.

REFERENCES

1. R.E. Stoller, R.H. Goulding, and S.J. Zinkle, DOE/ER-0313/9, 317, (1990).
2. G.P. Pells, and G.J. Hill, J. Nucl. Mater., **141-143**, 375, (1986).
3. E.H. Farnum, J.M. Kennedy, and F.W. Clinard. DOE/ER-0313/10, 328. (1991).
4. P.G. Klemens, in *Thermal* Conductivity, ed., R.P. Tye, vol. 1, p. 1, Academic Press, London, (1969).
5. P.G. Klemens, Proc. Roy. Soc. (London). **A208**, 108, (1951).
6. P.G. Klemens, in Solid *State* Physics, eds. F. Seitz and D. Turnbull, Academic Press, New York, vol. **7,** (1958).
7. P.G. Klemens. Phys. Rev., 119, no. 2, 507, (1960).
8. **P.G.** Klemens. Nucl. Inst. Meth. Phy. Res., B1, 204, (1984).
9. C.A. Ratsifarifana, in Phonon Scattering in Condensed *Matter*, ed. H.J. Maris, Plenum Press, New York, 259, (1980).
10. R.W. Klaffky, B.H. Rose, A.N. Goland, and G.J. Dienes, Phys. Rev. B, vol. **21,** no. 8,3610, (1980).
11. G.P. Pells. Radiation Effects, vol. **97,** 199, (1986).
12. G.P. Pells, S.N. Buckley, P. Agnew, A.J.E. Foreman, M.J. Murphy, and S.A.B. Staunton-Lambert, AERE R-13222, (1988).
13. D.P. White, Doctoral dissertation. The University of Connecticut, Storrs, CT, (1991).
14. D.P. White, and P.G. Klemens. J. Appl. Phys.. (to be published).
15. Alois Schaur, Can. J. Phy., vol. 43, 523, (1965).
16. D. Billard, and F. Cabannes, High Temp.-High Press., vol. **3,** 201, (1971).
17. **W.E.** Lee , and K.P.D. Lagerlof, J. Elec. Micros. Tech., **2,** 247, (1985).
18. R.C. Hughes, Phys. Rev. B, **19**, 5318, (1979).
19. L.K. Mansur, Nucl. Tech., 40, 5-34, (1978).

HIGH-TEMPERATURE MECHANICAL AND MATERIAL DESIGN FOR SiC COMPOSITES" - N.M. Ghoniem, University of California, Los Angeles

OBJECTIVES

The objective of this effort is to review the data base on the manufacturing. radiation effects, mechanical properties, compatibility and design approach for SiC/SiC fiber reinforced composites.

SUMMARY

Silicon Carbide (SiC) fiber reinforced composites (FRC's) are strong potential candidate structural and high heat flux materials for fusion reactors. During this past decade, they have been vigorously developed for use in aerospace and transportation applications. Recent fusion reactor system studies, such as ARIES, have concluded that further development of SiC composites will result in significant safety, operational. and waste disposal advantages for fusion systems. A concise discussion of the main material and design issues related to the use of SiC FRC's as structural materials in future fusion systems is given in this paper. The status of material processing of SiC/SiC composites is first reviewed. The advantages and shortcomings of the leading processing technology, known as Chemical Vapor Infiltration are particularly highlighted. A brief outline of the design-relevant physical, mechanical, and radiation data base is then presented. SiC/SiC FRC's posses the advantage of increased apparent toughness under mechanical loading conditions. This increased toughness, however, is associated with the nucleation and propagation of small crack patterns in the structure. Design approaches and failure criteria under these conditions are discussed

PROGRESS AND STATUS

An important feature of fusion reactions is that the resulting radioactive products are short-lived. However, the interaction of neutrons with structural materials in fusion systems can lead to long-lived radioactive decay chains. Proper selection of structural materials can therefore lead to significant reductions in the level and duration of environmentally hazardous radioactive products. Several neutronic and conceptual fusion-reactor studies have concluded that the post-shutdown radioactive inventories of FW/B structures made of pure SiC are dramatically lower than any metallic alloy considered for fusion so far[1-4]. The same assessments have shown conclusively that decay heat generated in the reactor, in case of a loss of coolant accident, can be safely and passively removed without the danger of radioactivity release to the environment. It is also realized that long-term radioactive inventories will mainly be controlled by the level of impurities in the structure. Therefore, processing technologies which offer the potential for significant reductions in the level of impurities should be attractive for the development of SiC structures. Another important feature of SiC structural materials is their high temperature capabilities. Operational temperatures approaching 1000^0C are potentially attainable. which can lead to vastly improved thermal cycle efficiency. For these important reasons, the development of structural SiC components is perceived to be of paramount significance to the successful commercialization of fusion energy. In this article, we analyze and review the body of knowledge which is relevant to the application of SiC, as a structural material, in future fusion reactors. We do not intend, however, to make this an exhaustive literature search. Rather, brief discussions are given in the following areas: processing, data base and design approach.

Processing of SiC/SiC FRC's

Several methods have been developed for production of SiC fibers for use as re-inforcements in high-temperature composites. Continuous yams of 500 fibers are now in commercial production by Nippon Carbon Co.[I]. under the trade name Nicalon. The process starts by dechlorinating dichlorodimethylsilane with molten metallic sodium to produce the solid polymer. Further processing steps are polymerization, and densification of amorphous Si and C at high temperatures (1200^0C-1500^0C). The final microstructure is crystalline 0-Sic of density in the range 3.16 g/cmm^3,and of crystallite size of 20-50 μm. The final product is continuous multifilament tows comprised of 500 filaments.

SiC monofilaments can also be prepared by the chemical vapor deposition (CVD) process, as described in references[2,3]. SiC is deposited from vapor mixtures of alkyl silanes and H_2 onto a substrate formed by a resistance-heated W wire or C filament. The substrate has a diameter of 10-25 μm, and forms the fiber core. The final filament is commonly 100-150 μm in diameter. Although deposition at high temperatures (above 1300^0C) is fast, the resulting structure iscoarsecrystallineand is weaker than theamorphousstructureobtainedat lower temperatures. If any free silicon appears in the microstructure, further weakening will result

Whiskers of SiC can be prepared either from rice hulls[4], or by a vapor-liquid-solid (VLS) process[5]. Rice hull whiskers contain around 10% SiO_2 and between 0%-IO% Si_3N_4. Around 10%of SiC is in the 0 crystalline phase, and the remainder is composed of α-SiC particulates. Whiskers produced from rice hulls are short; with lengths around 50 μm. Longer and smoother whiskers are prepared at Los Alamos[5], by the VLS process. Such whiskers possess superb mechanical properties, with an average strength of 8.4 GPa and an average elastic modulus of 580 GPa.

Multifilament fibers can be assembled into 2- and 3-dimensional structures by interlacing, intertwining, or interlooping. Combining the high strength of fibers with proper matrix-fiber interface frictional properties, fiber architectures will expand the design options for tough and reliable fusion structural materials. Fiber architectures can be classified into four categories: discrete. continuous, 2-dimensional, and fully integrated (3-dimensional). Selection of one of these architectures for F/B or high heat flux applications will depend on a number of factors. These are: (I) the capability for in-plane multi-axial reinforcements, (2) through-thickness reinforcements, (3) the capability for final shape manufacturing, and (4) leak-tightness of the final components during high-temperature operation. Selection of a particular form of architecture for fusion may be premature at present, because matrix Processing techniques are still evolving. While 3-D architectures

provide an orthotropically tougher composite, the CVI technology employed at present is limited to low fiber volume fractions, and the procedure is quite lengthy. On the other hand, although 2-D laminates can be produced at much greater speed. and can achieve higher fiber volume fractions, final component mechanical properties will be anisotropic. this feature will certainly lead to reduced capabilities of components to carry shear loads. In summary, processing technologies for the manufacture of SiC/SiC FRM's are available at present. However, further development is needed for production of components on a commercial scale.

Data Base

SiC is known to have high intrinsic strength and stiffness (E= 450 GPa at RT), high-temperature stability (decomposition temperature =2830°C), and excellent oxidation resistance. Its relatively high conductivity (k-0.25 W cm^{-1} $^0C^{-1}$ at 200^{0}C) and low coefficient of thermal expansion (a-3.8~10'$^0C^{-1}$ at 200^{0}C) result in favorable thermal shock resistance when compared to other ceramic materials. The thermal conductivity of CVD SiC, k(W cm^{-1} $^0C^{-1}$), and the specific heat, C_p (J Kg^{-1} $^0C^{-1}$) are given by empirical equations of the form:

$$\text{property} = \sum_{i=1}^{4} M_i T^i$$

where **T** is temperature in "C. Values of the polynomial fit coefficients are shown in table(1). Graphical representation of these properties as functions of temperaure is shown in figure(1).

TABLE(1)
Coefficients of polynomial fits to selected properties of SiC

$$\textbf{Property} = \sum_{i=1}^{4} M_i T^i$$

Property / Coefficient	Thermal Conductivity W m^{-1} K^{-1}	Specific Heat J Kg^{-1} K^{-1}	Fracture Stress, σ_f MPa	Young's Modulus GPa	Swelling $\delta V/V$ < 1000°C	Swelling $\delta V/V$ > 1000°C
M_0	62.84	435.53	-993.9	605.632	1.43	-71.19
M_1	-0.04	3.08	1.42	-1.401	0.0059	0.15
M_2	6.25×10^{-6}	-0.0047	-0.013	0.003	-1.56×10^{-9}	1.09×10^{-4}
M_3	0	3.31×10^{-6}	9.54×10^{-6}	-2.081×10^{-6}	8.58×10^{-9}	2.56×10^{-8}
	0	-8.41 ×	-2.42×10^{-9}	0	0	0

Assessment of the data base and development of a proper fusion-specific SiC composite is an iterative process. For this reason, we discuss here the available mechanical and radiation effects data base, so that ways for further improvements can be found.

Mechanical Properties

The tensile strength of Nicalon fibers is statistical because of the existence of defects (e.g. voids and cracks) during the manufacturing process. It is also strongly influenced by heat treatment, test atmosphere and test temperature. Commercial Nicalon fibers in various atmospheres show degradation in strength at or above 1000C[6]. Strength deterioration is attributed to: (1) chemical reaction between SiO_2 and free C, leading to surface damage: (2) crystallization of the amorphous structure: (3) oxidation in gaseous atmospheres. The tensile strength of CVD-prepared SiC fibers on C cores is retained only up to 800^{0}C. The 100 h rupture strength of CVD fibers was shown to degrade greatly above 1100C[7]. While the average tensile strength of unirradiated monofilamenta is 2.8 GPa at temperatures below 900^{0}C, preform wires have an average flexural strength of only 1.3 GPa. The uniform elongation at fracture is 1.5-2.0%.

For CVD fibers, it was observed that fiber creep is anelastic (i.e. recoverable), and is a result of grain boundary sliding[8], controlled mainly by a small amount of free silicon in the grain boundary. Fiber creep activation energy of 480 kJ mole-' was concluded to be similar to sintered SiC material, and the resulting creep rafe is about an order of magnitude greater than the Nicalon fibers[8]. The lower creep resistance of the more commercial Nicalon fibers was attributed to the lower grain boundary (G.B.) viscosity of free Si, which results from the polymerization process. Diffusional creep by G.B sliding has an activation energy estimated at 611 kJ mole.', and a pre-exponential of 3.1x10-7 m^2 s^{-1} [9].

These observations indicate that high-temperature creep properties of the composite may be life-limiting in fusion. In particular, the crack bridging mechanism, which is the main feature for enhancement of the composite's toughness. will have to be critically examined since the bridging fibers may creep at a faster rate than the matrix itself.

The high-temperature deformation characteristics of hot-pressed SiC have been experimentally investigated, and may be taken as indicative of the matrix in a composite[8,9]. The activation energies for power law as well as lattice diffusion creep were found to be about 912 kJ $mole^{-1}$[9]. Transition from power law creep at high stresses to diffusional creep at low stresses was also observed[10]. However, the diffusional matrix creep rates were found to be very small. A power law index of 5 was found to be similar to that of pure Si. The mechanical

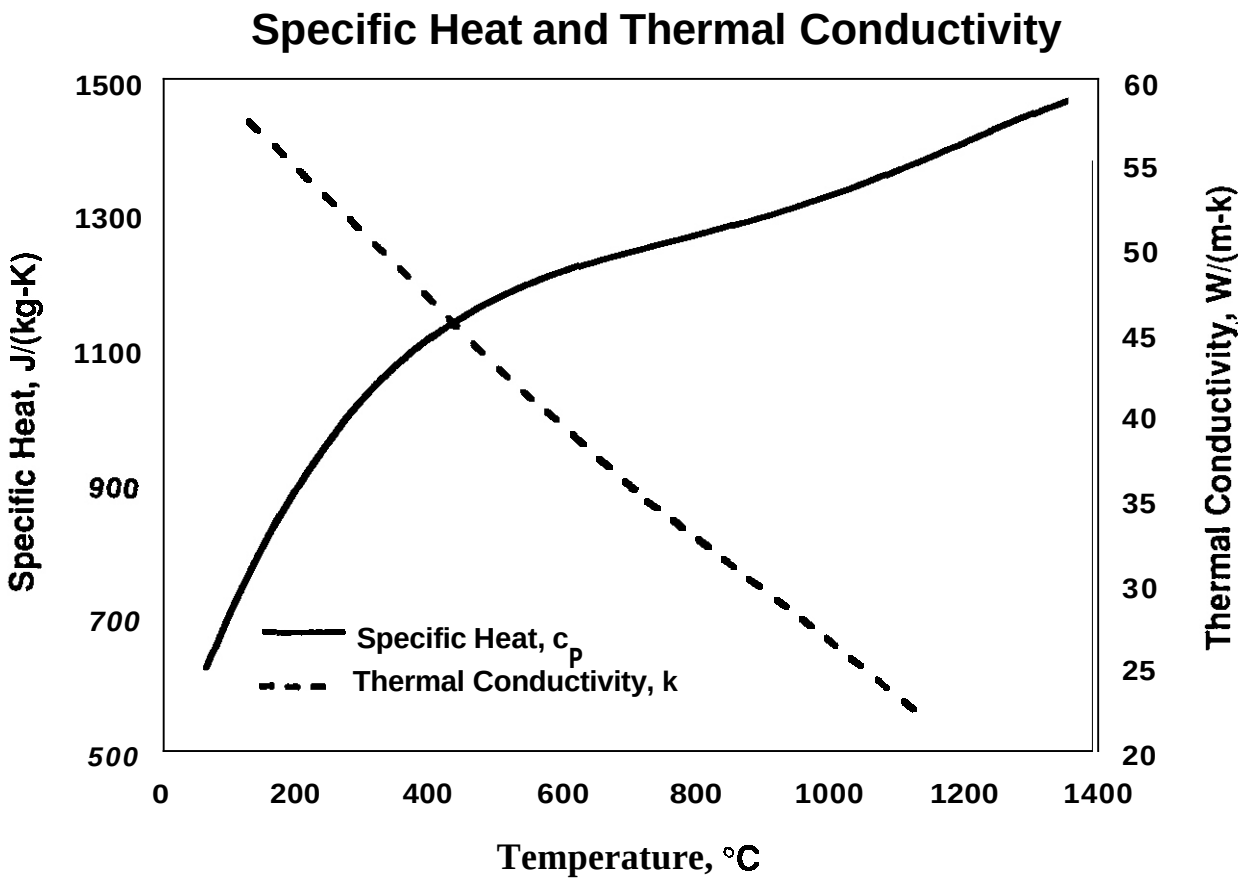

Fig. 1: Dependence of the specific heat and thermal conductivity of SiC on temperature.

properties of unirradiated reaction sintered SiC (i.e. Young's modulus, E (GPa), and bend strength. σ_f (MPa)) as functions of temperature. T (°C), are also given by polynomial fits, with coefficients defined in table(1). Graphical representation is shown in figure(2).

The critical stress intensity factor of the SiC matrix is expected to be low, as compared to metallic alloys. However, the bridging of cracks with the strong fibers will possibly allow for higher values of an apparent K_{IC}, especially when one is concerned with catastrophic through-thickness cracks. Room temperature values of K_{IC} for an unbridged hot pressed SiC range from 2.6 to 5.7 $MN.M^{-3/2}$, and is independent of temperature, up to 1000^0C. Sintered SiC shows temperature-independent K_{IC} of about 3 $MN.M^{-3/2}$, up to 1500^0C.

An allowable design stress for SiC FRC's will depend on a wide range of manufacturing and operational factors. For example, recent fracture test results at PNL at 800^0C on SiC FRM's from several vendors showed them to have strengths in the range 300-600 MPa in the unirradiated condition. Neutron irradiation at the same temperature, and up to approximately 10 dpa, showed that the fracture strength declined by about a factor of 2-2.5[11]. It is possible then, with modest technology extrapolation, that low pressure FW/B components would be designed to operate reliably in a fusion environment.

Coolant Compatibility

SiC has excellent resistance to oxidation up to 1000^0C, because of the formation of a protective stable SiO_2 layer. Rapid oxidation may occur, however, depending on the physical state of the oxide layer. between 1000^0C and 1300^0C. The porous oxide layer offers no resistance to the diffusion of oxygen to react with the SiC forming volatile Si and C oxides. The stability of the SiO_2 layer is dependent on the O_2 partial pressure, being unstable at pressures lower than 10^{-4} to 10^{-8} atmospheres[12]. In a primary helium loop, the partial pressure of O_2 is expected to exceed these values. However, the reaction of the interfacial layer between the fibers and the matrix with oxygen will ultimately determine the upper usable temperature of the composite, as far as compatibility is concerned. At present, this layer is either C, BC_4, or BN. while carbon oxidation will severely limit the upper temperature, the production of He and H from nuclear reactions in B compounds is expected to degrade the strength of SiC FRC's. An important factor which needs yet to be studied is the possible reduction of the passive SiO_2 layer by tritium or hydrogen.

Compatibility studies of SiC in molten Li indicated that intergranular penetration degrades its fracture strength[13]. Reaction with the glassy phase at the G.B is thought to be the cause of this rapid penetration. In a molten lithium environment, the uniform corrosion rate was reported to be extensive[13], however, the reported data was obtained at O_2 activities thought to be much higher than anticipated in a typical Li loop of a fusion reactor[11].

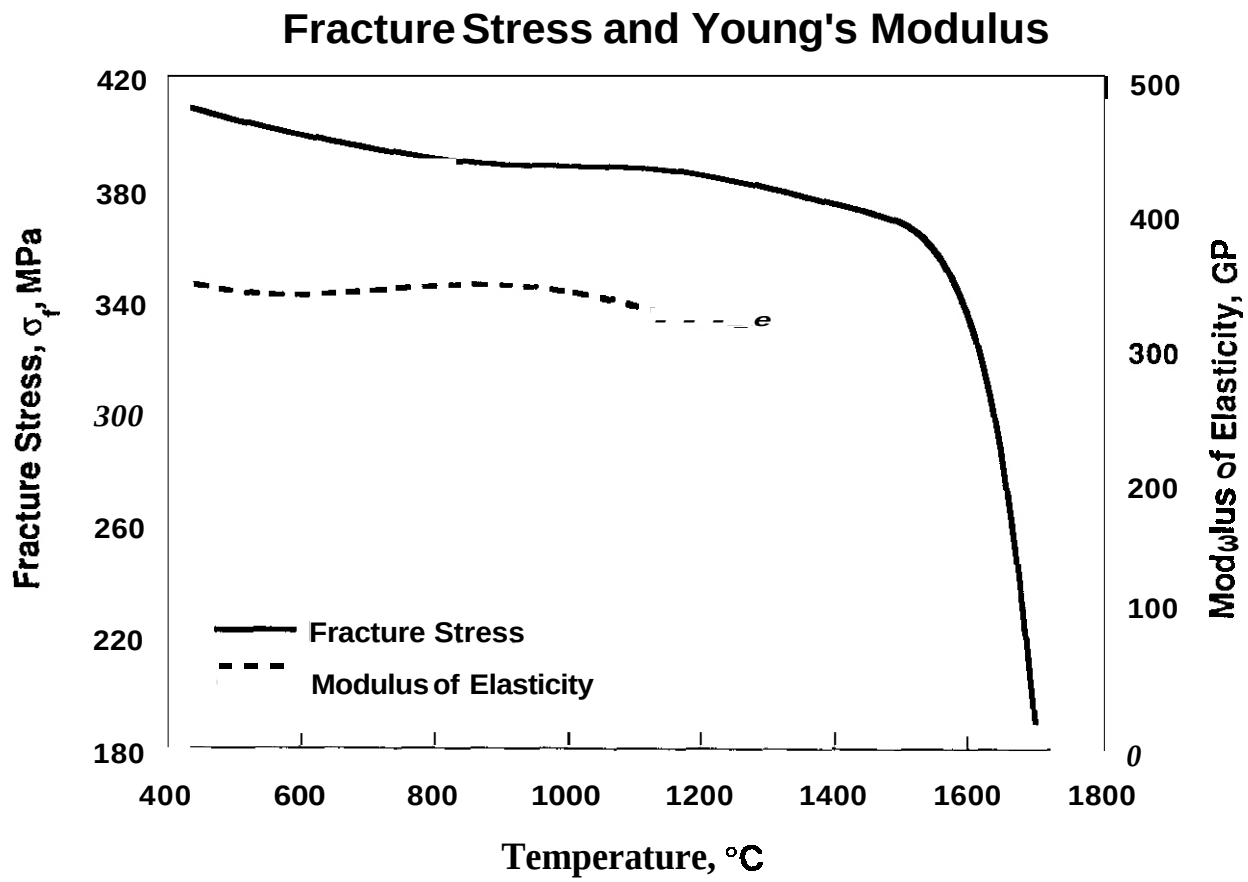

Fig. 2 Temperature dependence of the fracture stress and Young's modulus of Si.C.

Radiation effects

The strong directional bonding and the mass difference between Si and C atoms render the crystalline form of ß-SiC exceptional radiation resistance characteristics. Recent Molecular Dynamics (MD) studies[14] show that Replacement Collision Sequences (RCS's) are improbable, and that the displacement of C atoms is much easier than Si. MD computer simulations[14] show that while the average thresholddisplacement energy (E_d) is 10 eV for C, it is about 93 eV for Si. This result would leads directly to the conclusion that the stoichiometry of the displacement cascade will differ substantially from that of the matrix. It is also observed that energetic Si PKA's displace multiple C atoms which end up on <111> planes. Thus, C-rich interstitial dislocation loops wil tend to form on <111> planes. Experimental observations at temperatures below 1000°C tend to corraborate this conclusion[15]. Vacancies and He atoms exhibit considerable mobility above 1000°C. These fundamental considerations may explain some of the **observed** features of SiC dimensional changes, as function of temperature and fluence[15-18].

The ease by which C atoms can be displaced, as compared to Si, would indicate that C-rich interstitial loops may tend to be prevalent as a result of irradiation. Energetic Si atoms travelling the <111>-gap induce simultaneous displacements of multiple C atoms on {111} planes. Price[15] observed Frank-type loops on {111} planes which may be C-rich. Below 1000°C, point defects tend to form loops on {111} planes and swelling is therefore expected to saturate. Far example, Harrison and Correli[19] observed large loops (10-200 nm) in RB-SiC, after neutron irradiation to a fluence of 1.8×10^{23} cm^{-2}. At temperaures abve 1000°C, cavities form, and swelling does not saturate. The presence of helium results in further increases in the swelling rate by the known gas-driven swelling mechanism, as observed in the swelling of nuclear fuels. Swelling data with helium generation are scarse, and need future considerations. Swelling of ß-SiC in the temperature range 625-1500°C, and at a neutron fluence (E > 0.18 MeV) of 1.2×10^{22} [15] is represented by two separate polynomials, with two different sets of coefficients below and above 1000C, respectively. The coeffiecients, and the general swelling behavior as a function of temperature is shown in figure(3). Additional helium will drive swelling to higher values, particularly at temperatures above 1200°C[20].

A significant irradiation damage problem, which results in the deterioration of the mechanical properties of SiC is the crystalline-to-amorphous phase transition phenomenon. For example, the strength of Nicalon fibers is degraded by irradiation-induced re-crystallization. Crystallites growing out of the fibers into the matrix form nucleation sites for cracks leading *to* delamination of the interface. The limited accumulated evidence from radiation effects data indicate that the upper temperature limit for use of SiC in structural design is in the range of 900-1000°C.

Design with SiC/SiC comoosites

Design rules for SiC/SiC composites in the high-temperaure and radiation envirnment of fusion reactors are obviously not established, mainly because the test data base is not complete. This data base for mechanical properties must also be made on full-size components. It is interesting to note that the fracure behavior of the composite is totally different from monolithic behavior, and exhibits

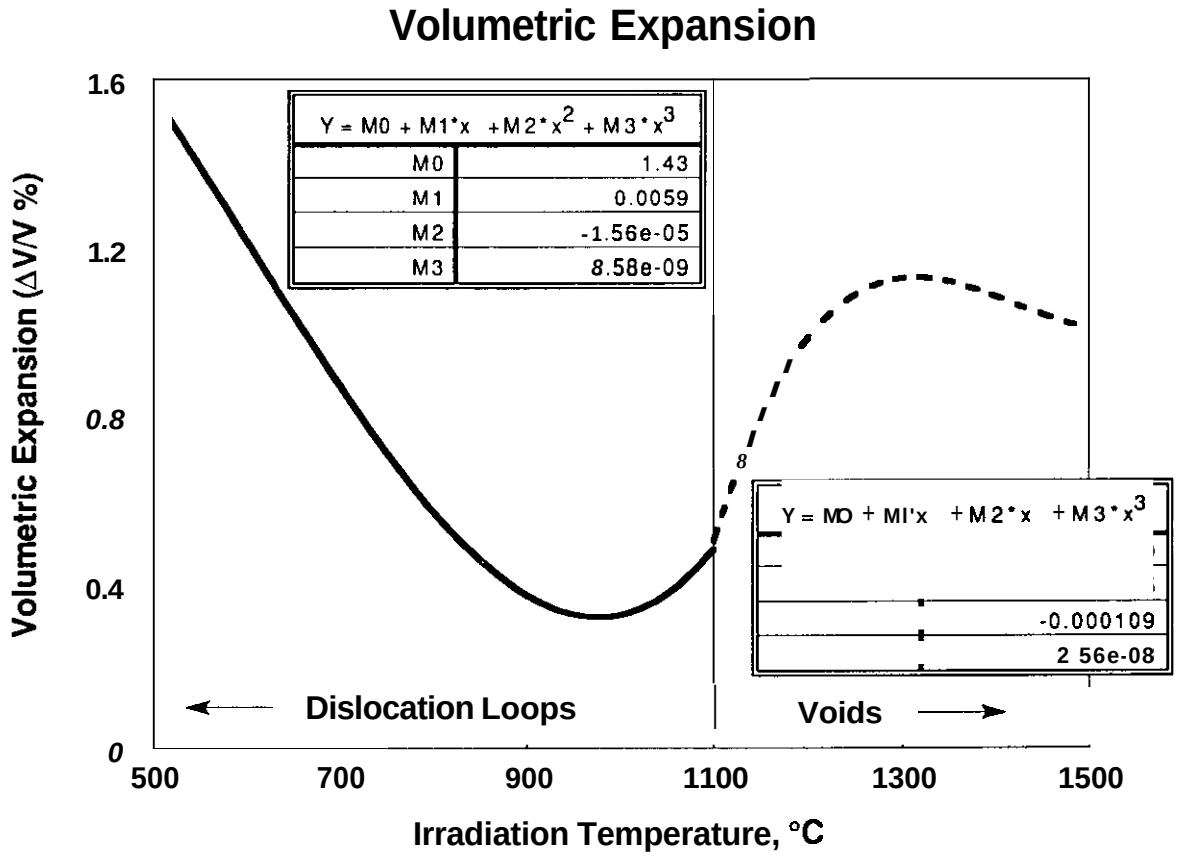

Fig. 3. Volumetric swelling of SiC as function of temperature at a neutron fluence of 1.2×10^{22} n cm^{-2} (E > 0.18 Mev).

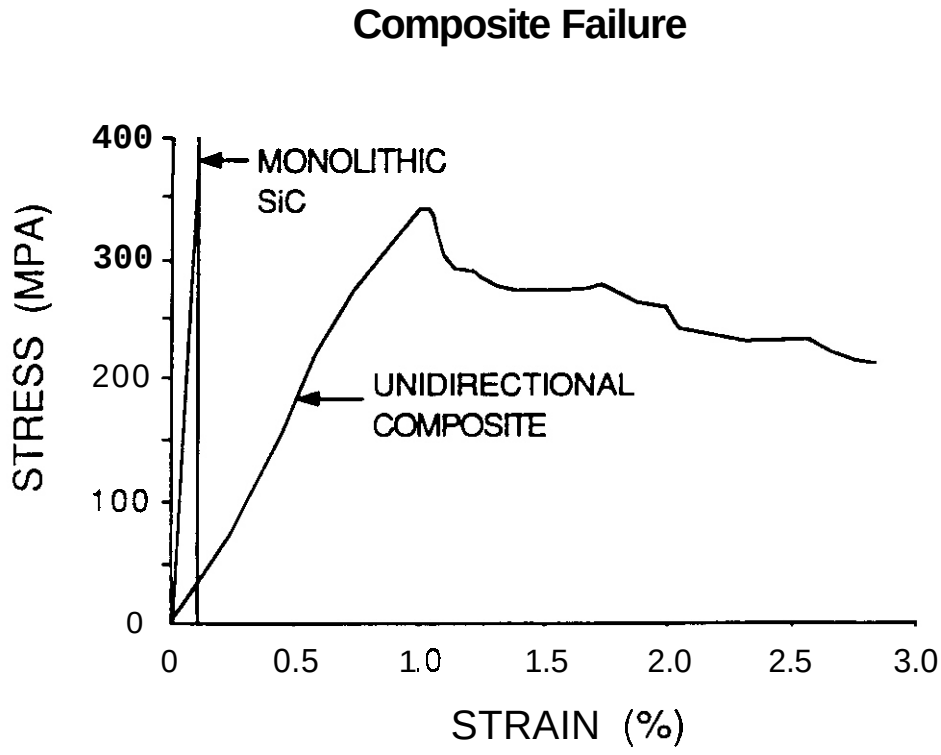

Fig. 4: Stress-strain behavior of monolithic and unidirectional composite SiC a room temperature

considerable apparant ductility, as shown in figure (4). However, this increased toughness is caused by the dissipation of the elastic energy in slow micro-cracking processes. Failure stresses will have to be determined for particular applications (e.g. load bearing but not leak-tight components, leak-tight components, components which resist thermal stresses, etc.). A promising failure approach would be to use an interactive theory, such as the Tsai-Wu criterion. In such an approach, the failure stress tensor is measured. This would give failure stress components in tension, compression. shear, for both in-plane and out-of-plane componenets. Structural analysis would be fairly complete, and would result in the definition of safety factors in each direction. This approach would take into account the probabilistic variability of properties, as determined by experimental measurements. There will be no need to use Weibull statistical analysis, because safety factors and the experimental failure tensor would guarantee safe operation, as desired from a particular component.

CONCLUSIONS AND FUTURE DIRECTIONS

SiC/SiC FRC's are excellent, low-activation and safe structural materials for the high-temperature and radiation envirnment in commercial fusion reactors. Their superior mechanical and physical properties would allow for operational temperatures approaching 900-1000°C, thus achieving high thermal cycle efficiencies. The strong covalent bond between Si and C results in promising resistance to the damaging effects of neutron irradiation. Increased toughness because of the reinforcement with strong fibers will make deterministic design approaches possible. However, considerable research and development will be needed before the material will be able to meet its promise.

REFERENCES

[1] S. Yajima, K. Okamura, J. Hayashi and M. Omori, J. Amer. Ceram. Soc., 59 (1976) 324.
[2] E. Fitzer, D. Kehr, and M. Shahibkar, in: Silicon Carbide-1973, Marshal. Faust and Ryan, Eds. (Univ. of South Carolina Press, USA, 1974) p33.
[3] H.E. DeBolt, V.J. Krukonis, and F.E. Wawne, in: ibid., p.168.
[4] I.B. Cutler, "Production of SiC from Rice Hulls," U.S. Patent # 3,754,076, 1976.
[5] G. Hurtley and J. Petrovic, in: Proc. Adv. Composites Conf., M.W. Liedtke and W.H.Todd, Eds., ASM, 1985, p.401.
[6] S. Yajima, H. Kayaro, K. Okamura, M. Omori, J. Hayashi, T. Matsuzwa, and K. Akutsu, Am. Chem. Soc. Bull., 55 (1976) 1065.
[7] I. Ahmad, D.N. Hill, and W. Hefferman, in: Proc. Inter. Conf. Comp. Mater., AIME, 1976, vol 1, p. 85.
[8] J. Decarlo, J. Mater. Sci., 21 (1986) 217.
[9] P.M. Sargent and M.F. Ashby, Scripta Met., 17 (1983) 951.
[10] A. Djemel, J. Cadoz and J. Philibert , in: Creep and Fracture of Engineering materials and Structures, B. Wilshire and D.R.J. Owen, Eds., Pineridge, Swansea, U.K., 1981, p. 381.
[11] R.H. Jones, in:Fusion Reactor Materials Semiannual Progress Report, March 1991. DOE/ER-0313/10, p. 215.
[12] E.A Gulbransen and S.A. Jansson, Oxid. Met., 4 (1972) 181.
[13] D.R. Curran and M.F. Amateau, Amer. Cer. Soc. Bull., 65 (1986) 1419.
[14] A. Elazab and N.M. Ghoniem. ICFRM-5 Proceedings, 1991.
[15] R.J. Price, J. Nucl. Mater., 46(1973)268.
[16] R. Blackstone and E.H. Voice, J. Nuci. Mater. 39(1971)319.
[17] A.M. Carey. F.J. Pineau, C.W. Lee, and J.C. Corelli, J. Nucl. Mater., 103&104(1981)789.
[18] K. Hojou and K. Izui, J. Nucl. Mater., 160(1988)334.
[19] S.D.Harrison and J.C. Corelli, J. Nucl. Mater., 122&123(1984) 833.
[20] T. Suzuki and T. Iseki, J. Nuci. Mater., 170(1990)113.

ACKNOWLEDGEMENTS

This work is supported by the US. Department of Energy/Office of Fusion Energy, Grant #DE-FG03-91 ER 5411S with UCLA.

COMPOSITE MATERIALS FOR FUSION APPLICATIONS - Russell H. Jones, Charles H. Henager, Jr. and Glenn W. Hollenberg, Pacific Northwest Laboratory, Richland, Washington 99352

OBJECTIVE

The purpose of this study is to review the data base on ceramic matrix composites relevant to the critical issues for their application as structural materials in fusion reactors.

SUMMARY

This report presents a review and analysis of the hermetic, thermal conductivity, corrosion, crack growth and radiation damage properties of CMCs. It was concluded that the leak rates of a gaseous coolant into the plasma chamber or tritium out of the blanket could exceed design criteria if matrix microcracking causes existing porosity to become interconnected. Thermal conductivities of unirradiated SiC/SiC and C/SiC materials are about 1/2 to 2/3 that of Type 316 SS whereas the thermal conductivity for C/C composites is seven times larger. The thermal stress figure-of-merit value for CMCs exceeds that of Type 316 SS for a single thermal cycle. SiC/SiC composites are very resistant to corrosion and are expected to be compatible with He or Li coolants if the O_2 concentrations are maintained at the appropriate levels. CMCs exhibit subcritical crack growth at elevated temperatures and the crack velocity is a function of the corrosion conditions. The radiation stability of CMCs will depend on the stability of the fiber, microcracking of the matrix, and the effects of gaseous transmutation products on properties.

PROGRESS AND STATUS

Introduction

Composite materials are being considered for a number of applications in fusion reactors including high heat flux surfaces, divertor structures, and first walls. In principle, composite materials are more "engineerable" than conventional metallic and cerdmic materials because they need not rely on equilibrium phases for reinforcement. Therefore, there is greater freedom to optimize their properties to meet the many challenging requirements presented by fusion reactor environments.

Metal matrix composites (MMCs) assembled from metallic matrices and particulate, whisker, or fiber shaped ceramic reinforcements are extensions of dispersion hardened materials made by mechanical alloying. Kohyama et al. (1,2) have evaluated the radiation response of Al/SiC and Al/C composite materials because of their potential for low activation and high temperature performance. They observed an increase in fracture strength for Al/SiC materials at a fast neutron fluence of 10^{25} n/m^2 at *123* K followed by a decrease at higher fluences. The strength response of these materials followed directly that of the fibers, as determined from extracted fibers and was related to radiation-enhanced crystallization of the amorphous Nicalon fibers. Cu/C composites are also being evaluated by Zinkle et al. (3) for divertor structural applications because of their thermal and mechanical properties. Radiation experiments are in progress.

Carbon/carbon composites are attractive for high-heat flux surfaces because of their high thermal conductivity (100 W/m-K) in a direction perpendicular to the fibers in 3-D and 4-D C/C composites (4). In directions parallel to the fibers, conductivity as high as 500 W/m-K has been obtained for 1-D C/C composite materials. This conductivity is important for minimizing thermal stresses, but heat remova? depends on through-thickness conductivity. For comparison, copper has a conductivity of around 400 W/m-k at 25°C. Radiation effects and thermal shock studies of C/C composites are in progress (5,6).

Other low activation CMCs that are being evaluated for high-heat flux and structural applications include C/SiC (graphite fibers in a SiC matrix), SiC/C and SiC/SiC (SiC fibers in graphite and SiC matrices). These materials offer a range of physical and mechanical properties because of variable fiber and matrix properties and fiber architectures. Although MMCs are being evaluated for selected fusion applications, the emphasis of this paper is to compare the properties of CMCs and issues regarding their potential applications in fusion reactors.

Property Comuarisons for Ceramic Composites

Continuous fiber composites reinforced with graphite or SiC fibers are produced with 1-D to n-D fiber architecture prepared from woven, knitted, or braided fibers. Most of the materials that are compared in this paper are simple 2-D composites with a 0/90° alignment. Although the properties become more isotropic with increasing dimensionality, the properties in the principal directions are usually diminished.

*Operated for the U.S. Department of Energy by Battelle Memorial Institute under Contract DE-AC06-76RLO 1830.

The properties of continuous fiber composites with about 40% graphite or SiC fibers are compared in Table 1. The graphite fibers are T-300 while the SiC fibers are Nicalon.[a] These are the highest strength versions of these respective fibers. The properties of C and SiC composites are also compared to Type 316 SS, although it is recognized that some of these comparisons are not strictly valid. The physical properties of the composite materials are relatively similar with the exception of C/C where the density and coefficient of expansion are the lowest and the thermal conductivity is the highest. The thermal conductivity reported in Table 1 for C/C is the highest reported value for .this material; earlier reported values were as low as 10 W/m-K for the same orientation. The C and SiC reinforced materials are much less dense and have lower codfficients of expansion than Type 316 SS, but the specific heat and thermal conductivity of the C/SiC and SiC/SiC composite materials are quite similar to that of Type 316 SS.

The mechanical property comparisons made in Table 1 are only useful for making qualitative comparisons since these parameters have different significance in CMCs and metallic materials. The SiC/SiC material has a similar modulus to that of Type 316 SS while the other materials all have lower modulii. The tensile strength in the CMCs refers to the ultimate stress following matrix microcracking and at the onset of significant crack extension, whereas the tensile strength in metallic materials refers to the ultimate stress following plastic flow and the onset of plastic instability. Although the physical processes which establish the tensile strength in CMCs and metallic materials are fundamentally different, the effect is somewhat similar. Therefore, the comparisons in Table 1 reveal that Type 316 SS ha; a tensile strength ranging between a factor of 2 to 3 greater than that of the C and SiC materials. Of the CMCs, the C/C material has the highest tensile strength while the SiC/SiC the lowest. This property is very amenable to "engineering" with the use of different fibers, fiber volume fraction, or fiber architecture so this trend could easily be reversed.

The interlaminar shear strength is a property that is significant for multi-ply materials such as the 2-D, 0/90° CMCs but is not a relevant parameter for metallic materials. For the CMC materials, those with SiC fibers have the highest interlaminar shear strengths but the differences are not great: Likewise, the fracture toughness values reported for the CMCs and Type 316 SS do not have equal significance for designing a component. The $K_{,}$ values listed in Table 1 illustrate that the CMCs have sufficient toughness so that in the unirradiated condition, the first wall and blanket (FWB) will be relatively flaw-insensitive as would a FWB built of Type 316 SS. Of course, the effects of multi-axial stresses, joining and radiation on these parameters must be considered for a riqorous assessment of these materials.

Property	C/C	C/SiC	SiC/C	SiC/SiC	316SS
Density g/cm^3	1.8	2.2	2.05	2.5	8.0
Specific Heat mJ/g-K	--	600	--	600	500
Coeff: [illegible] of Expansion, 10^{-6} K^{-1}	0.5	3	4	3	17
Thermal Conductivity, W/m-K	100	7	--	10	15
Modulus, GPa	100	90	70	230	210
Tensile Strength, MPa	320	340	205	200	600
MPa	20	35	43	40	--
Fracture Toughness MPa$\sqrt{m}$	--	35	--	30	150
He Generation Rate appm/MW-yr/m^2	2000	1800	1800	1600	150
H Generation Rate appm/MW-yr/m^2	--	240	160	400	880
Thermal Stress Factor W/cm	12,800	180	87*	50	17

Structural Applications of Ceramic Comoosites

The use of SiC as a low activation, first wall materidl was recommended several years ago by Hopkins et al. (7). More recently, the ARIES I design was based on the use of SiC/SiC composite material for the divertor and first wall (8). Operating temperatures were in the range of 800 to 1000°C with a tie coolant. A recent DOE workshop (9) was held to identify the potential feasibility issues in the structural applications of CMCs in fusion reartors. The following sections will review these issues and the status of our knowledge regarding these issues.

Feasibility Issues

The emphasis of the DOE workshop (9) was to identify key issues in the use of CMCs for fusion applications. This implies that there are other issues which were not addressed. These issues were not deemed unique to fusion but are generic to the CMC technology as a whole. The cost of material, fabrication scale-up, and other factors are issues which fall in this category. The issues identified by this workshop include: 1) hermeticity, 2) thermal conductivity, 3) chemical compatibility with coolant and blanket materials, 4) radiation stability, 5) joining, 5) thermal fatigue and thermal shock resistance, and 7) redefinition of design codes for brittle matrix-fiber strengthened materials.

Hermetic Properties of Ceramic Composites

Ceramic matrix composites made by the chemical vapor infiltration (CVI) technique generally contai? 10-15% porosity, as shown by the micrographs for a SiC/SiC composite in Figure 1. If CMCs are to function as a pressure boundary, the coolant leak rats into the plasma and the tritium leak rate out of the blanket will be a major design criteria. Ceramic composites made by the CVI process retain more porosity than those made by hot-pressing or the DuPont-Lanxide Composites DIMOX(b) process but continuous fiber composites that exhibit the highest fracture toughnesses are made primarily by the CVI process.

The porosity retained by the CVI process is not interconnected, as shown in Figure Ib, because tho porosity results from closure between adjacent fibers occurring during the matrix CVI process. Therefore, in the unirradiated condition, CMCs are expected to contain closed porosity. This will need to be verified, since some of the porosity may indeed interconnect. Also, the pores may become interconnected with the application of stresses above the matrix microcracking stress, or by creep, and irradiation induced microcracking. Therefore, the pores may in fact become interconnected with time and allow a pathway for gas leakage.

Jones (10) estimated the leak rate of He through a structure such as that shown in Figure 1 by using a gas flow equation for molecular flow through small orifices. Similar calculations have been performed previously (11) and compared to experimentally measured values for creep cracks in austenitic stainless steel. The agreement between measured and calculated values was quite good for flaws that were similar in size to those shown in Figure 1.

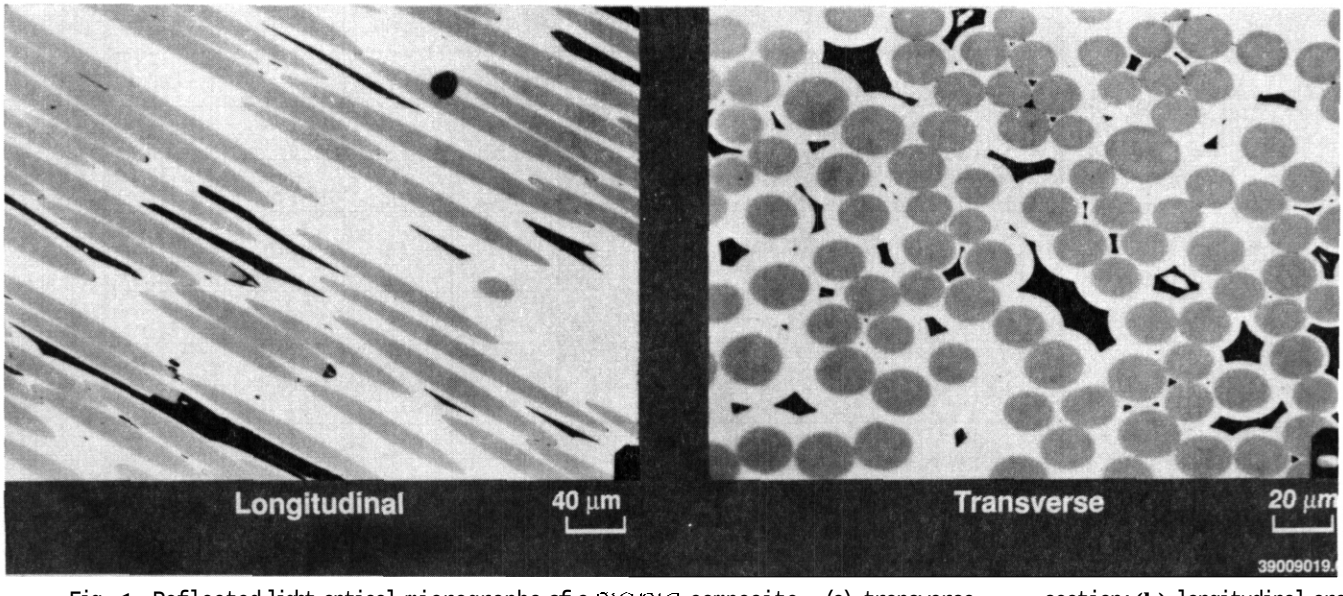

Fig. 1. Reflected light optical micrographs of a SiC/SiC composite. (a) transverse cross section; (b) longitudinal cross section.

The limiting leak rate established in a study by Jones, Conn and Schaffer (11) ranges between 10^{-1} moles/:; for a UWMAK II design to $4x\ 10^{-3}$ moles/s for a NUMAK reactor design. An upper bound value for the leak rate through a CMC was estimated by Jones (10) by assuming that the interconnection between all of the pores opened by creep to a value equal to the average pore size, 8 x 100 μm. Assuming the entire first wall is made of SiC/SiC and utilizing the pore density data obtained from micrographs, such as Figure **la,** an upper bound leak rate of 7×10^{5} moles/s was calculated. An alternative approach was to estimate the extent of opening between the pores that would produce the 10^{-1} moles/s limit. An opening of only 0.3 nm was required **if** all of the pores were connected. In reality, not all of the pores will become interconnected by microcracking or creep, but the calculated leak rates suggest that the pow hermetic properties of CMCs might require using a seal coat or metallic liner to reduce the coolant in-leakage or the tritium out-leakage to an acceptable level.

Thermal Conductivity of Ceramic Composites

Thermal conductivity is important for minimizing the stress in a material exposed to a thermal graoient and for removing heat from energy conversion systems. The thermal conductivity of CMCs are generally less than their monolithic counterparts because oi the high density of fiber/matrix inierfaces ana the higher porosity. Examples of the thermal conductivity for graphite and C/C composites is show in Figurt 2a (4) and examples of the thermal conductivity for SiC/SiC composites is shown in Figure 2b (12). The 1-D, 2-D, and 3-D [Z] values are for in-plane therma! conductivity, while the 4-D, 3-D [X] is through-thickness thermal conductivity. The through-thicknees value for a 3-D C/C composite is about a factor of ten less

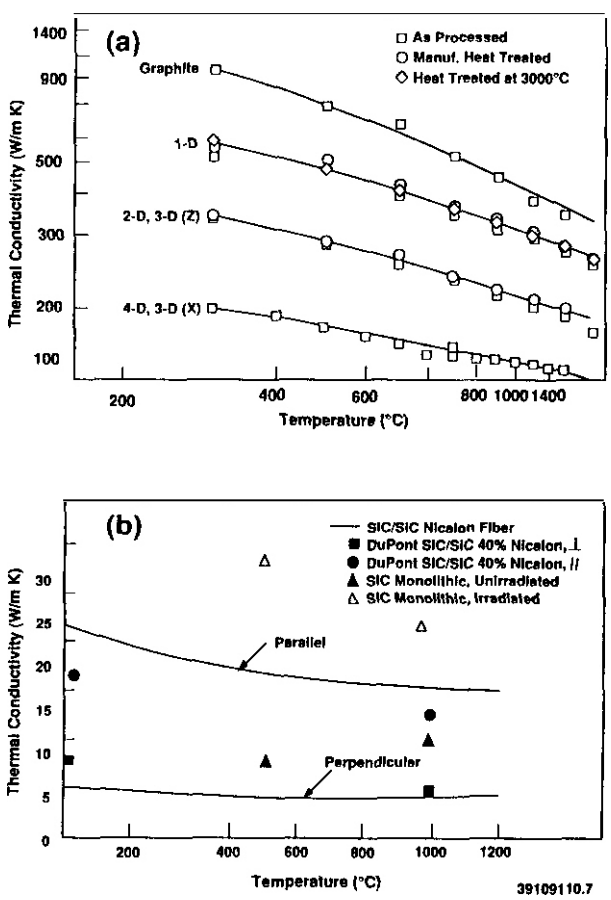

Fig. 2 Thermal conductivity of (a) C/C and (b) SiC/SiC composite materials.[4,12]

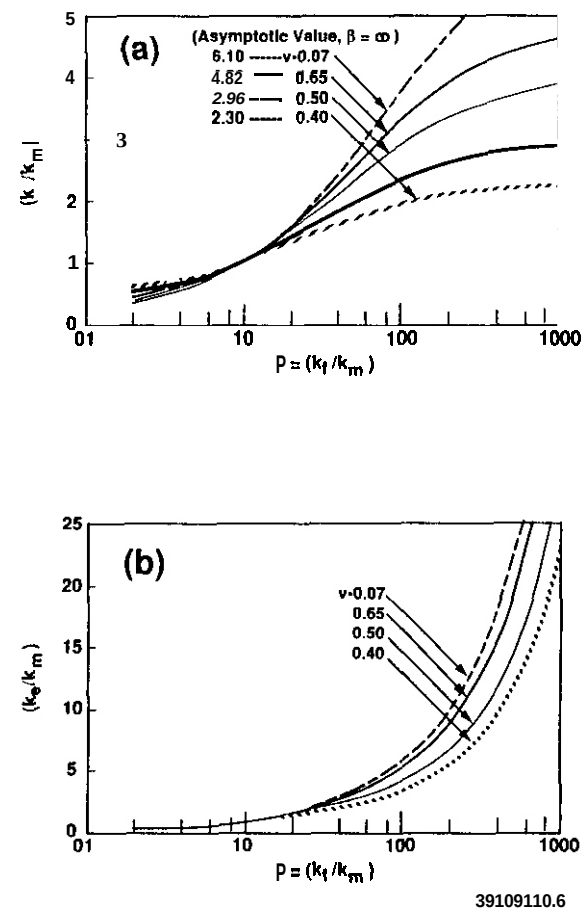

Fig. 3. **Calculated** effective thermal conductivities for 0/90 fiber composites for b/a = 2. (a) transverse/transverse orientation; (b) transverse-axial.[15]

than that for monolithic graphite. At 1000°C, the through-thickness thermal conductivity is about 35 W/m-K for C/C and about 6 W/m-K for SiC/SiC. Westwood and Notis (13) reported the thermal conductivity of single crystal SiC as 90 W/m-K at 25 to 150°C while BeO doped SiC had a thermal conductivity of 270 W/m-K at 25°C(7) and high-purity single crystal SiC a conductivity of 490 W/m-K (14). Thermal conductivity of polycrystalline SiC is a function of impurity content, processing method, etc. but has been reported as being between 12 to 35 W/m-K.

There is no data on thermal conductivitv of irradiated CMCs. although there is data for monolithic SiC irradiated to 10^{26} n/m^2 at the test temperatures shown in Figure 2b (7). The thermal conductivity decreased from 25 to 12 W/m-K, when irradiated at 1000°C and from 37 to 9 W/m-K, at 500°C. The ARIES I design temoerature for SiC/SiC was between 800 to 1000°C, so a decrease of a factor of 2 to 3 would be expected after a fluence of 10^{26} n/m^2. Whether the conductivity will continue to decrease with increasing fluence and the response of CMCs is unknown and will need to be determined before a fusion reactor can be designed and built with CMCs.

Improvements in the thermal conductivity are, in principle, possible with CMCs because of the "engineerable" aspect of these materials. Han and Cosner (15) have modeled the thermal conductivity of fiber reinforced composite materials with the results shown in Figure 3 for a 0/90° 2-D composite with a staggered fiber arrangement and a unit cell of b/a = 2. The through-thickness effective conductivity, K_e, normalized by the matrix value, K_m, is shown in Figure 3a relative to β, the ratio of the fiber conductivity, K_f, to K_m. Similar values are given for the in-plane conductivity in Figure 3b. These calculations indicate that the through-thickness conductivity can be doubled for a β value of 10 and a volume fraction (V_f) ,of 40% and increased by a factor of 4 for a β of 10 and a volume fraction of 70%. The in-plane conductivities would increase by more than a factor of 4 for similar p and V_f values. Much larger increases in the in-plane conductivity are possible with increasing values of β than for through-thickness conductivities that clearly reach limiting values at β between 10 to 100. A C/SiC composite would be expected to have a through-thickness conductivity of 12 and 24 W/m-K for a V_f of 40% and 70%, respectively. Increases in the conductivity of the C/C and SiC/SiC composites should be limited because the ratio of K_f/K_m is probably less than 1.

A thermal stress figure-of-merit derived for a range of materials has been reported by Whitley (16) as shown in Figure 4. The figure-of-merit value depends on thermal conductivity, yield strength, elastic modulii, and the coefficient of thermal expansion. Large values suggest a material that can tolerate higher heat loads; however, materials that undergo microcracking may have a high value for a single thermal cycle but could be degraded more rapidly with thermal cycling than materials that deform plastically. Clearly, C/C and graphite materials have the highest figure-of-merit values for a single thermal cycle; while SiC/SiC and C/SiC have much lower values, as indicated in Figure 4 and Table I. Type 316 SS has the lowest value of the metallic materials.

Chemical Compatibility Issues

Most ceramics are chemically stable and resistant to corrosion in many environments. Ceramic matrix composites are expected to also exhibit similar corrosion resistance; however, the stability of the fiber and interface may differ from monolithic ceramics and the method of manufacturing CMCs, i.e. CVI, can result in a relatively porous matrix that does not protect the fibers from the environment. Of particular concern, is the fiber/matrix interface through which CMCs gain their strength and toughness. Also, subcritical crack growth in CMCs is accompanied by the development of a bridging zone of fibers behind the crack. Exposure of these fibers and fiber/matrix interfaces to a corrosive environment could alter the subcritical crack growth behavior of CMCs, as demonstrated by the subcritical crack growth data presented in this paper.

Corrosion of Ceramic Composites

Ceramic composites used for structural applications in fusion reactors will require compatibility with coolants and blanket materials. Potential reactants include O_2, H_2, H_2O in a He coolant, Li in an Li cooled system or from Li ceramics used far breeding T and Be used as a neutron multiplier. Compatibility with the impurities in a He coolant might be a concern because of the large mass flow of impurities in flowing He.

Silicon carbide is thermodynamically unstable in O_2, H_2 and H_2O environments and will react with them in the following manner:

$$SiC(s) + O_2(g) = SiO(g) + CO(g) : Low\ Po_2 \quad (1a)$$

$$SiC(s) + 3/2O_2(g) = SiO_2(s) + CO(g) : High\ Po_2 \quad (1b)$$

$$SiC(s) + 2\,H_2(g) = Si + CH_4(g) \quad (2)$$

$$SiC(s) + 2\,H_2O(g) = SiO(g) + CO(g) + 2\,H_2(g) \quad (3)$$

The stability of SiC depends on the formation of a stable "passive" layer of SiO_2 with the active-passive oxidation behavior described by Figure 5 (17). Active oxidation of SiC occurs at around 10^{-8} atm of O_2 at 900°C, which is within the ARIES I temperature range. Obviously, it would be advantageous to maintain an adequate O_2 partial pressure in the He coolant to maintain SiC-based CMCs in the "passive" oxidation regime. Oxidation of C to CO or CO_2 is a concern for C/C and C/SiC as well as for SiC/SiC composite2 relying on a C interfacial layer for fracture toughness. An example of the oxidation resistance of uncoated SiC/C and C/C composites at 815°C is shown in Figure 6. Nicalon was the fiber used in the SiC/C composite and presumably a layer of SiO_2 may have formed to protect this composite even though the matrix was C. The instability of C/C type composites in an oxidizing atmosphere is clearly demonstrated by this data.

Hydrogen or tritium will be present in the He coolant if He is used as a sweep gas in the T breeding blanket, from out-leakage from the plasma or from out-gassing from materials in which it is generated by (n,p) reactions. Therefore, the stability of CMCs in $He/H_2/H_2O$ mixtures is also important. Jacobson, Eckel, Misra and Humphrey (18) have calculated the stability of SiC in an $Ar/H_2O/5\%\ H_2$ mixture with the results shown in Figure 7. Though these calculations are for a temperature about 300°C above that expected for a fusion reactor blanket constructed out of CMCs, it does illustrate some of the potential reactions. SiC could react with a $He/H_2/H_2O$ gas mixture to form CO, CH_4, and SiO gaseous products and all of these gaseous reaction products could be detrimental to the mechanical integrity of a SiC/SiC structural blanket. These data illustrate that these reactions are thermodynamically possible without details regarding the kinetics of these reactions. Detailed chemical compatibility studies for the CMCs that are applicable to fusion reactors will be necessary to determine corrosion and subcritical crack growth rates.

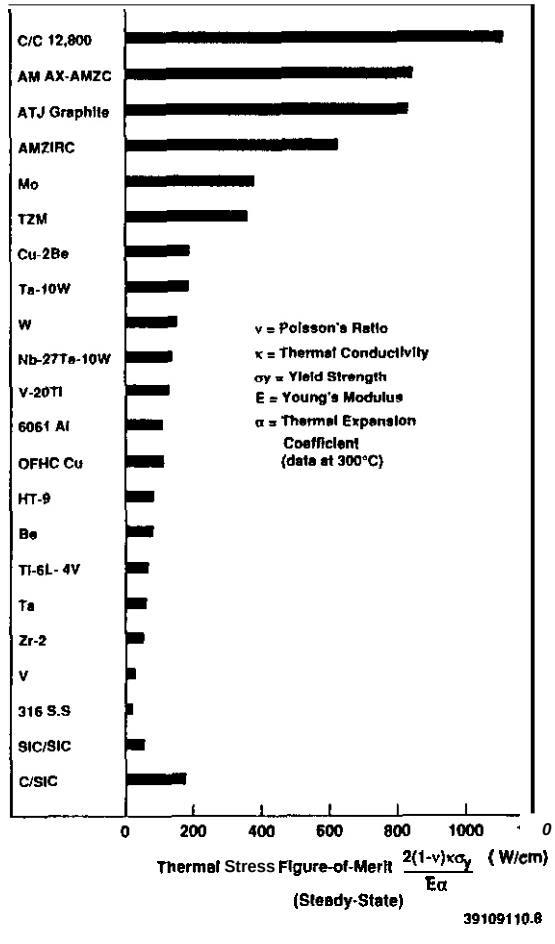

Fig. 4. A comparison of the surface thermal stress limits for a range of materials."

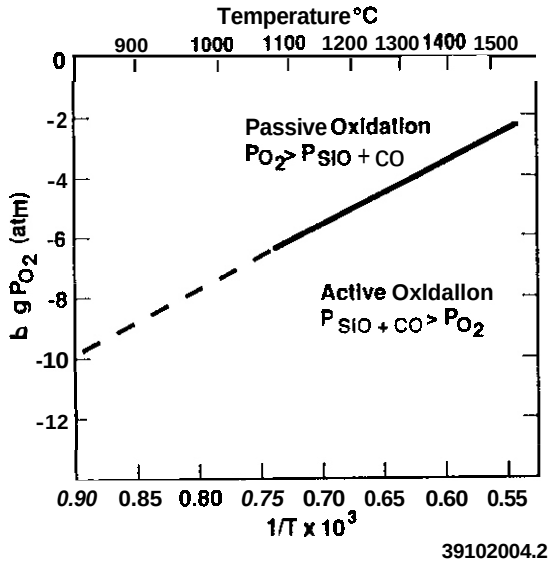

Fig. 5. Transition pressures for SiC active-passive oxidation vs. temperature, according to Gulbransen and Jansson."

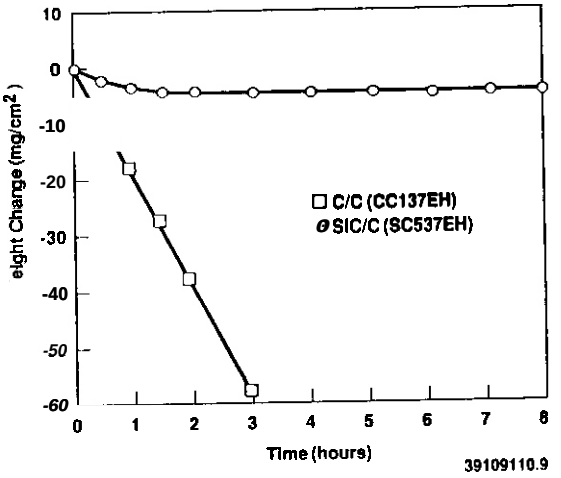

Fig. 6. Oxidation results for uncoated SiC/C and C/C composites at 815°C in air.

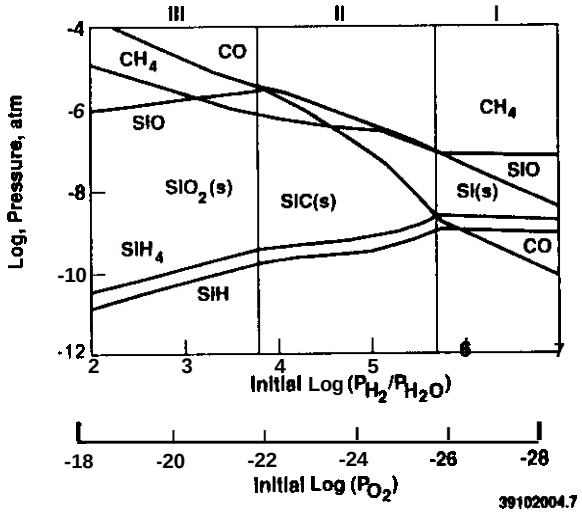

Fig. 7. Thermodynamic analysis of SiC + 5% H_2/Ar at 1300°C. All pressures are in atmospheres.'*

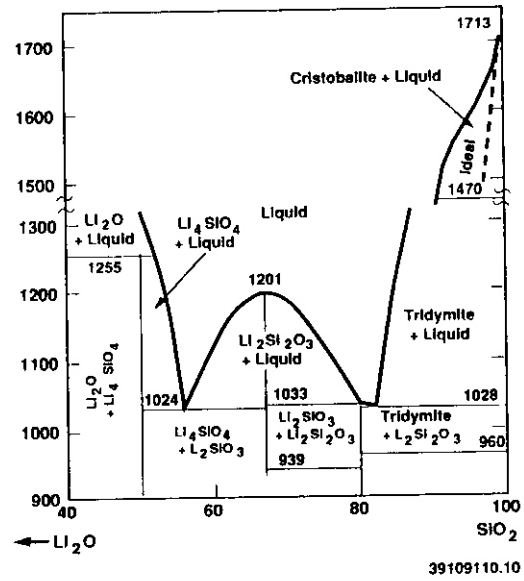

Fig, 8. Phase diagram for the SiO_2-Li_2O system.

CMCs can react with Li if Li is chosen as a coolant or from contact with Li ceramics used for T breeding. The major reaction between alkali metals and Si-based ceramics is the formation of a low melting temperature salt such as those shown by the Li_2O-SiO_2 phase diagram in Figure 8. Eutectics at 1024 and 1028°C are relatively close to the potential operating temperature of a fusion reactor constructed with CMCs. Reaction with SiO_2 is of concern because of its presence at grain boundaries and surfaces (i.e. reaction of SiC with O_2). Degradation of the protective "passive" SiO_2 layer and accelerated crack growth caused by the decreased viscosity of grain boundary glass phases in contact with alkali metals are two of the possible chemical compatibility concerns for SiC/SiC composites in contact with a Li coolant or Li ceramic. It is anticipated that the Li coolant would be maintained at very low O_2 activity, thus minimizing the possibility of forming the phases shown in Figure 8. However, this is not true with Li ceramics so it will be necessary to minimize contact between SiC and Li ceramics.

The corrosion and fracture behavior of SiC in molten Li has been evaluated by Curran and Amateau (19) and Cree and Amateau (20). Both studies were conducted on a-SiC exposed to a thin layer of molten Li in contact with the sample surface. A decrease in the room temperature fracture strength from about 350 MPa to about 150 MPa was found in both studies for exposures exceeding 500°C. The strength loss was related to Li penetration down SiC grain boundaries. Reaction with the glass phase in the SiC grain boundaries was considered to be the primary cause of the rapid intergranular penetration. Uniform corrosion rates were reported as being extensive but with no apparent effect on the fracture strength. Cree and Amateau (20) found a bi-modal distribution in the fracture strengths where the low strength group was related to intergranular Li penetration and the high strength group associated with the absenre of grain boundary penetration. In the absence of intergranular penetration, the fracture strength decreased slightly with increasing exposure temperature to a value of about 300 MPa after exposure at 800 nnd 1000°C.

Fracture toughness values were also reported by Curran and Amateau (19) using the direct-crack-measurement indentation method. The fracture toughness was determined from this method by measuring the crack length produced by indentation of the surface. This method is very sensitive to changes in the properties of the material near the surface and is subject to error associated with the compressive stresses created by the indentation process. The indentation fracture toughness measurements made by Curran and Amateauwere sensitive to the effects of surface corrosion reactions. They observed a decrease in the room temperature fracture toughness from about 4 $MPa\sqrt{m}$ to about 2 $MPa\sqrt{m}$ following exposure to molten Li for 30 min at 600°C. A 30-min exposure to Ar at 800°C caused a decrease to about 3 $MPa\sqrt{m}$, so the effects of Li are not due solely to a corrosion reaction but also to changes in the properties of the near-surface material.

The studies by Curran and Amateau (19) and Cree and Amateau (20) were conducted for relatively short exposure periods of 30 to 60 min. It was concluded in both studies that exposure time within these limits did not affect the properties; however, these exposure times are too short to suggest that further changes will not occur durina extended fusion reactor operation. Also. the reported studies were conducted with the SiC exposed to a limited supply of liquid Li. Exposure to a flowing Li coolant would likely produce a higher corrosion rate because the corrosion rate would be expected to decrease as Li becomes saturated with SiC and SiO_2.

Subcritical Crack Growth of Ceramic Composites

Subcritical crack growth in CMCs appears to be controlled by fundamentally different mechanisms compared to monolithic ceramics, with correspondingly different mechanical responses. Crack-wake bridging by long fibers in continuous fiber reinforced CMCs, which is responsible for the high fracture toughness of CMCs [19], dominates the mechanical response of these materials. Therefore, the time-dependent response of the bridging zone at elevated temperatures appears to be the dominant mechanism affecting subcritical crack growth in CMCs.

Experiments and micromechanical modeling conducted at PNL suggest that the bridging zone completely controls the mechanical response and subcritical crack growth rates in CMCs. Composites consisting of Nicalon[a] fiber cloth (0/90) and CVI SiC with and without carbon in the interfaces are currently being studied. Stepped load tests with load holding on single-edge notched bend bars (SENB) conducted at 1100°C in argon and argon plus 2000 ppm O_2 reveal a stage II regime in the V-K data that does not appear in V-K data for monolithic ceramics, Figure 9. For CMCs, the transition to power law crack growth, Stage IIJ, occurs at large values of stress intensity near the value of K_Q as determined from 4-point bending tests of SENB specimens. At present, there is little evidence to suggest the presence of a stage I regime at low K values.

The evidence for bridging zone domination of subcritical crack growth comes partly from experiments using argon plus oxygen in comparison with pure argon and partly from the micromechanical model being developed for this work. The addition of 2000 ppm oxygen to the 1100°C argon environment increases the crack velocity in the stage II regime and shifts the stdge 11-stage III transition to lower K values, as shown in Figure 9. The shift to lower K values for the transition to stage III crack growth is consistent with a reduction in the pinching forces imparted on the crack faces by the bridging fibers. SEM photomicrographs of the CMCs exposed to the 2000 ppm O_2 plus argon reveal the partial removal of the carbon interfaces caused by direct oxidation at 1100°C. The removal of this interface material can be expected to reduce the shear strength of the interface, the ability of the matrix to transfer load to the fibers, and the bridging

zone crack-tip shielding effectiveness. This is demonstrated in the micromechanical model calculations shown in Figure 10. A bridged crack of a fixed bridging zone length is simulated numerically and the fiber pinch force is allowed to vary as shown. A reduction in the interfacial shear strength, τ, would reduce the fiber pinching forces and shift the crack velocity to lower applied K values, which agrees with our recent experimental findings.

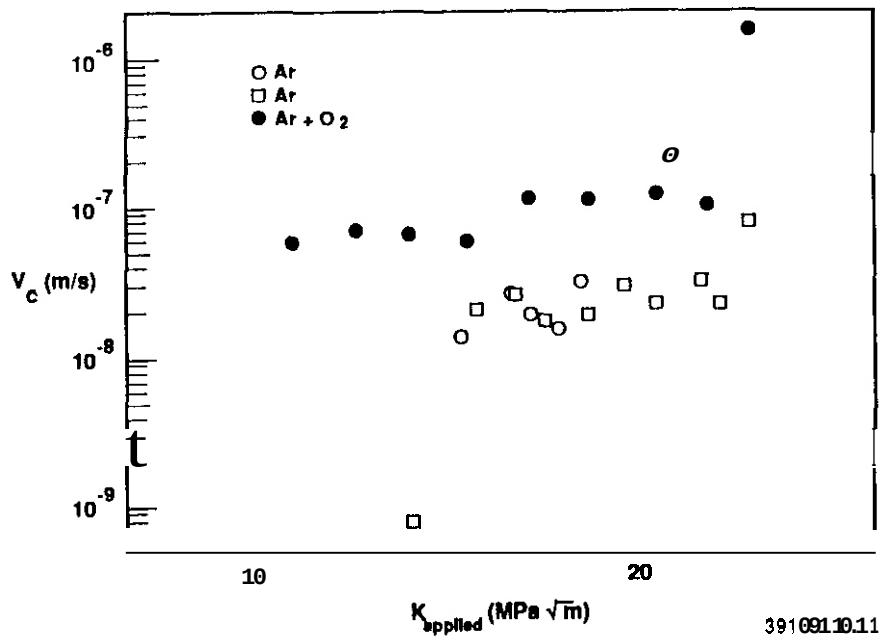

Fig. 9. Crack velocity as a function of applied K for SiC/SiC fiber composites tested at 1100°C with carbon fiber/matrix interfaces.

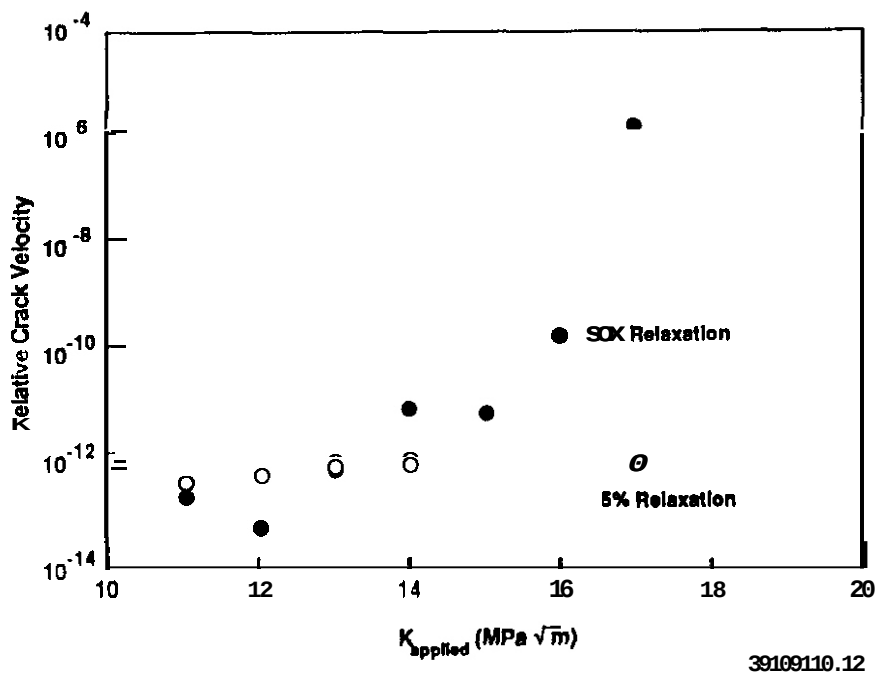

Fig. 10. Calculated crack velocities for a crack with a fixed bridging zone length. Fiber pinching forces relaxed 5% and 50% to simulate time dependent fiber or fiber matrix interface creep.

It is not surprising that these SiC/SiC(f) composites are sensitive to environmental effects since their mechanical response is dominated by the crack wake bridging zone that is completely exposed to the environment. Careful studies would be required to determine the effect of fusion environments on subcritical crack growth in CMCs. Mora severe environments that corrode the reinforcing fibers or the interfaces would be potentially very deleterious. In addition, radiation effects on CMCs would need to be factored into these studies. Uifferential matrix/fiber swelling, fiber/matrix interface dimensional and structural stability, fiber structural stability and fiber/matrix interface displacement mixing effects would all need to be determined for these materials.

Radiaticn Stability of Ceramic Composites

Radiation effects data on SiC/SiC is virtually nonexistent and the amount of data on monolithic SiC is also very sparse. Dimensional stability of β-SiC as a function of fast neutron fluence and irradiation temperature has been reported by Price (22), Figure 11. The linear expansion at fusion relevant temperatures of less than 1000°C shows a maximum expansion of less than 0.2% at 625°C at a fluence of 2 x 10^{25} n/m^2 and a linear expansion of about 0.1% at 900-1050°C at a fluence of 10^{26} n/m2. Mechanical property data for irradiated material is not available at fusion-relevant temperatures, but at 650°C there is a minimum in both the elastic modulus and the fracture strength with some recovery of these properties at higher fluences. The fracture strength decreases from about 320 MPa to about 220 MPa at a fluence of 10^{25} n/m^2, as shown in Figure 12.

When developing CMCs for radiation resistance, the damage to the fiber, fiber/matrix interface and the matrix must be Considered. High-temperature (400-1200°C) radiation effects studies of SiC/SiC composites are in progress a? PNL and will be reported at a future time. At present, it is only possible to list the potential effects of radiation on the physical and mechanical properties of these materials. For a Nicalon[a] fiber reinforced material, instability of the amorphous Nicalon[a] must be Considered. Kohyama et al. (2) have measured the fracture strength of Nicalon[a] fibers extracted from ar Al matrix following irradiation a? 450°C. There was an initial increase in the fracture strength at a fluence of 10^{24} to 10^{25} n/m^2 followed by a decrease to about 15% of the unirradiated value at a fluence of 10^{26} n/m^2. The loss in strength was related to crystallization of the amorphous fiber. It is expected that this crystallization will be accompanied by a volume contraction, whereas the β-SiC matrix would experience a small (<0.2%) but positive volume expansion at 10^{26} n/m^2. These dimensional instabilities could cause two very important effects: 1) the contraction of tne fiber away from the matrix and the consequent loss of load transfer capability and 2) microcracking of the matrix from residual stresses resulting from the differential dimensional changes of the fiber and the matrix. Microcracking of the matrix is likely to occur even without the stress imposed by fiber contraction. The reduction in the tensile nodulus and fracture strength of monolithic SiC, Figure 12, is likely the result of microcracking while the recovery of these properties is likely the result of mirrocrack healing.

The probable effect of irradiation on the fracture toughness of SiC/SiC is shown in Figure 13. The load-deflection response of continuous fiber composites exhibits a linear elastic region with deviation from linear elastic response, which results from matrix microcracking. Significant matrix and fiber bundle

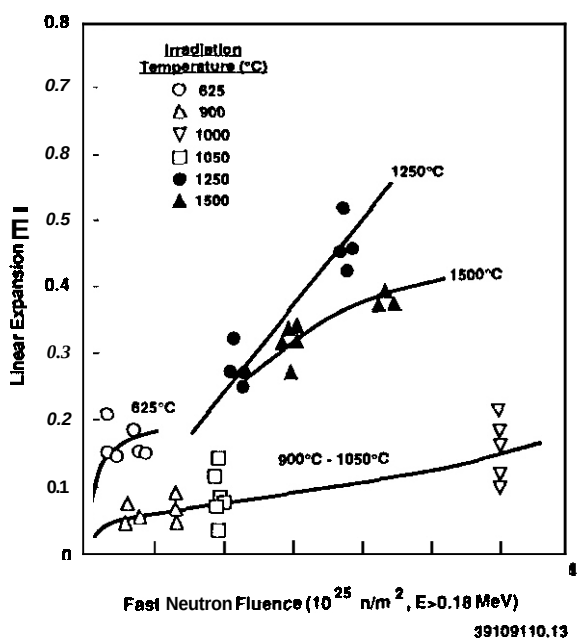

Fig. 11. Expansion of β-SiC as a function of fast neutron fluence at 625 to 1500°C (ref. 22).

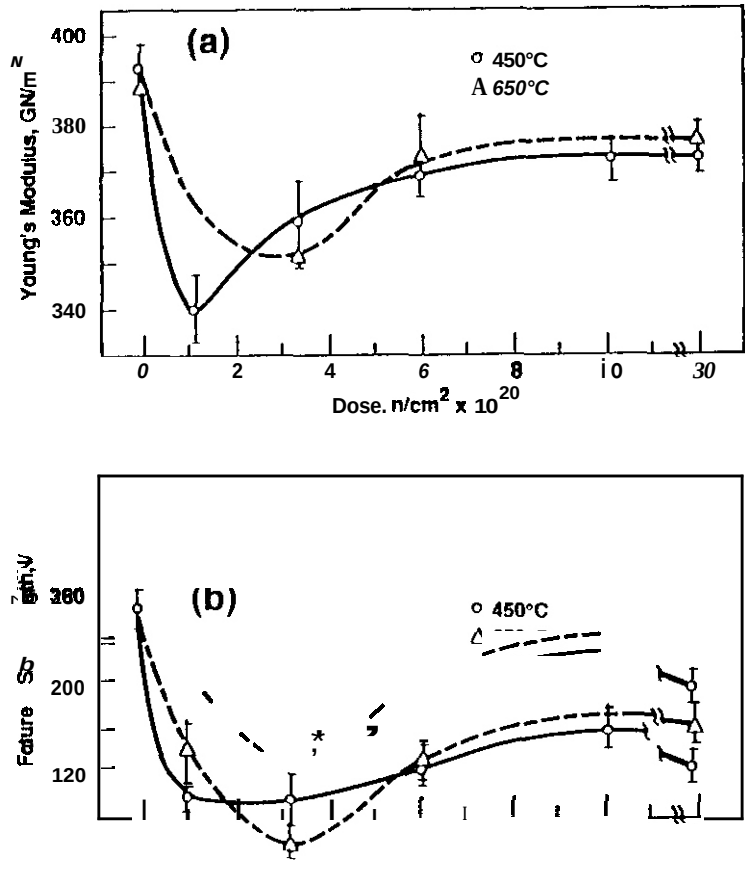

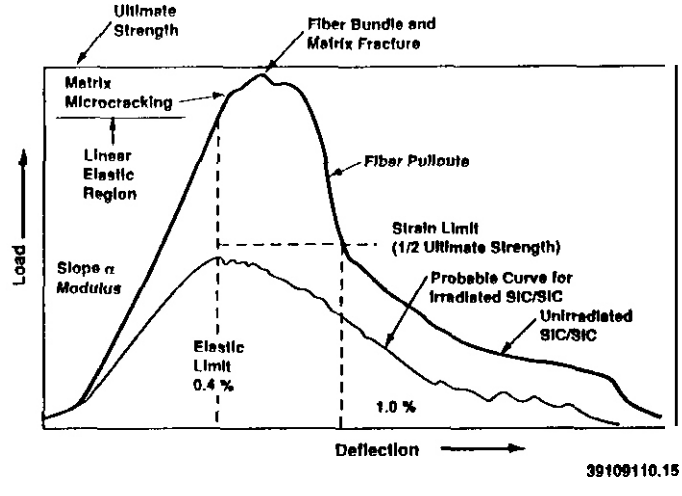

Fig. 13. Schematic of a load-deflection curve for ceramic matrix composites.

Gaseous transmutation products, such as He and H, could have an effect on tht mechanical properties of CMCs. The transmutation rates are summarized in Table I where it can be seen that the He generation rate is about 10 times that of Type 316 SS while the H generation rate for SiC bearing mdterials is between 1/4 to 1/2 that of Type 316 SS. The values for C/SiC and SiC/C were estimated from that for SiC/SiC assuming transmutation of only Si. The threshold for ^{12}C is 17 MeV which is above the neutron energy from a D+T reaction, therefore, the H transmutation rate was considered to be negligible for C.

Transmutation of C to He in the SiC fibers and matrix will shift the composition away from stoichiometry and could produce damage within the microstructure depending on the location of the He. If He is sufficiently mobile it could accumulate in the porous regions without causing serious damage; however, accumulation within the lattice could assist void formation as it does with metallic materials. Loss of C from the amorphous Si-C-O Nicalon™ fibers is probably not as detrimental as it will be in crystalline *p*-SiC. Radiation damage experiments must be conducted to fully characterize the response ar+ guide the development of rzdiation resistant CMCs.

Low neutron activation of SiC/SiC is Considered one of its greatest benefits for fusion structural applications. Seki et al. (23) calculated the γ-ray intensity decay for a high-purity C/SiC composite material containing only 700 ppm Ca, Figure 14. Following an irradiation to 10 MW-y/m^2 a C/SiC first wall reached a level of 2 mrem/hr after about 300 hours. The Ca concentration controlled the decay time although the production of ^{26}Al from ^{28}Si and ^{30}Si resulted in a low-levei decay lasting 10^6 y. The neutron activation of CMCs reinforced with Nicalon[a] which contains large quantities of O or other polymer-derived fibers such as the Tyranno or HPZ which contain N and O will be greater than that reported by Seki et.al. The N-containinq fibers have better high temperature stability than Nicalon"' and could also be more stable in an irradiation environment. Clearly, activation analysis must be conducted for material with the appropriate impurity concentration,

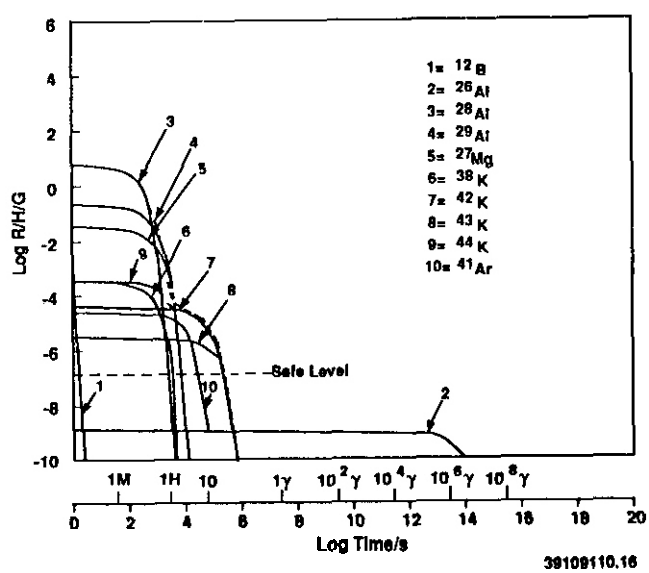

Fig. 14. Gamma ray intensity behavior of carbon fiber/SiC composite after irradiation to 10 MW-y/m^2. The dashed line shows a safe surface dose rate of 2.5 mrem/h for the first wall.[23]

Summary

Ceramic matrix composites offer tremendous potential as structural materials for fusion applications. High-temperature properties, low density, low thermal expansion and neutron activation are some of their positive attributes while hermeticity, radiation stability and joining are attributes that will need further research before CMCs can be considered suitable for fusion structural applications can be made.

SiC/SiC composites have densities that are about 1/4 and coefficients of expansion about 1/5 that of Type 316 SS while their thermal conductivitier and elastic modulii 8;e similar. Though tlie fracture strength and fracture toughness of SiC/SiC are less than Type 316 SS at 25°C, the strength of SiC/SiC is relatively independent of temperature up to 1200°C while the strength of Type 316 SS decreases rapidly above about 400°C.

teak ratec of a He coolant through SiC/SiC inio the plasma or T out-leakage may meet design limits in tlie unirradiated condition but matrix microcracking and creep crack growth are expected to result in leak rates that exceed the tolerable limits. Experimental determination of these values is needed to assess the leak rates and to evaluate possible solution!. if needed.

Thermal conductivities of SiC/C and C/SiC composites are comparable to those of lype 316 SS, though C/C composites have thermal conductivities that are 7 times greater. Thermal conductivity coupled with strength, elastic and thermal expansion properties determine the thermal stress factor where SiC/SiC has a value about 2.5 times greater than Type 316 SS and C/C a factor that is 10^3 times larger because of the large thermal conductivity and low thermal coefficient of expansion of C/C. Radiation-induced microcracking is expected to reduce the thermal conductivity of these materials.

Chemical compatibility of SiC/SiC composites should not be a factor for He or Li coolants if the O_2 concentration: are appropriately controllea. Intcraction with ti ceramics in the breeding blanket-could be a concern because of low meltiny temperature silicaies that could form. C/C composites may require protective coatings in He coolants because of the oxidation of C. He coolants will likely contain some H_2O/H_2 ratio as a result of H outgassing from the material or where He is used as a sweep gas to remove T from lithium ceramics. Large concentrations of H could destabilize the "passive" SiO_2 layer. Experiments to determine corrosion behavior in simulated reactor coolants will be necessary to assess long-term chemical stability of CMCs in contact with fusion reactor coolants although corrosion does not appear to be a major concern.

Radiation stability of both C/C and SiC/SiC materials is an area where further research is necessary. Large dimensional changes have been noted for C/C composite materials while SiC/SiC materials are expected to be much more stable. Radiation induced contraction and loss of strength of Nicalon fibers in SiC/SiC composites could lead to decreased modulii and fracture strengths as well as matrix microcracking. Formation of He and H by nuclear trazsmutation and the consequent change in stoichiometry is also a radiation stability issue which must be addressed but for which there is no existing data.

ACKNOWLEDGEMENTS

The assistance of S. M. Halazon in preparing the manuscript is graiefully acknowledged. This research was supported by the Office of Fusion Energv of the U.S. Department of Energy under contract DE-AC06-76RLO 1830 with Battelle Memorial Institute.

REFERENCES

1. A. Kohyama, H. Teruka, N. Igata, Y. Imai, H. Teranish and T. Ishikawa, J. of Nucl. Matls., vol. 141-143 (1986) 96.

2. A. Kohyama, S. Sato, H. Tezuka and M. Kondo, J. of Nucl. Matls, Vol. 179-181, (1991) 254

3. S. Zinkle, private communication

4. R. B. Dinwiddie, J. W. Sapp and O. A. Bowers, 20th Biennial Conference on Carbon, June 24-28, 1991, Santa Barbara, CA., DOE CONF 910645-1.

5. H. Takatsu, M. Seki, M. Araki, M. Yamamoto, K. Fukaya, M. Ogawa, M. Etoh, S. Yamasaki, S. Koga, and T. Kobayashi, J. of Nucl. Matls., Vol. 179-181 (1991) 344.

6. T. O. Burchell, in "Proceedings of the Office of Fusion Energy/DOE Workshop on Ceramic Matrix Composites for Structural Applications in Fusion Reactors," R. H. Jones and G. E. Lucas, eds., held in Santa Barbara, CA, May 21-22, 1990, PNL-SA-18743, CONF-9005225, p. 435.

7. G. R. Hopkins and J. Chin, J. of Nuclear materials, Vols 141-143 (1986) 148

8. C. P. C. Wong, E. T. Cheng, 8. McQuillan, E. E. Reis, Jr., K. R. Schultz, S. P. Grotz, M. F. Hasan, R. Martin, F. Najmabaci, S. Sharafat, T. Kunngi, J. S. Herring, D. K. Sze and the Aries Team, "Aries-I SiC Composite Low Activation Blanket Design", Fusion Technology, Vol. 19 (1991) 938.

9. "Prsceedinys of the Cffice of Fusion Energy/DOE Worksnop on Ceramic Matrix Composites for Structural Applications in Fusion Reactors," R. H. Jones and G. E. Lucas, eds., held in Santa Barbara, CA, May 21-22, 1990, PNL-SA-17843, CONF-9005225

10. R. H. Jones, "Gas Leak Rate Estimates for Ceramic Matrix Composites," Fusion Reactor Materials Semiannual Progress Report for Period Ending September 30, 1991, DOE/ER-0313/11.

11. R. H. Jones, R. W. Conn and R. F. Schaffer, "Effect of First Wall Flaws on Reactor Performance," Nuclear Engineering and Design/Fusion, 2 (1985), 175.

12. P. J. Lamicq, G. A. Bernhart, M. M. Danchier and J. G. Mace, "SiC/SiC Composite Ceramic:", Am Ceram Soc. Bull. 65 (1986) 336.

13. A. D. Westwood and M. R. Notis, JOM (June 195.1) 10.

14. CRC Handbook, *of* Chemistry and Physics, CRC Press West Palm Beach, FL, 59th Ed., p. E-5.

15. L. S. Han and A. A. Corner, J. of Heat Transfer, Vol. 103 (1981) 387.

16. J. Whitley, J. Nucl. Mater. Vol. 133 and 134(1985) 39.

17. E. A. Gulbransen and S. A. **Jansson,** Oxid. Met., 4 (1972) 181.

18. N. S. Jacobson, A. J. Eckel, A. K. Misra and D. L. Humphrey, J. Am. Ceram. Soc., 73 (1990) 2330.

19. D. R. Curran and M. F. Amateau, Am. Ceram. Bull., 65 (1986) 1419.

20. J. W. Cree and M. F. Amateau, J. Am. Ceram. Soc., 70 (1987) C-318.

21. A. G. Evans, J. Am. Ceram. Soc. 73(1990) 187.

22. R. J. Price, J. Nucl. Mate?. 33(1969) 17.

23. Y. Seki, I. Yamauchi, K. Yamada and H. Kawasaki, J. Fusion Energy 3(1984) 241.

GAS LEAK RATE ESTIMATES FOR CERAMIC MATRIX COMPOSITES

R. H. Jones (Pacific Northwest Laboratory*)

OBJECTIVE

To identify the coolant/plasma boundary-performance limits of ceramic matrix composites used for structural applications.

SUMMARY

Permeation rates for He through a SiC/SiC composite have been estimated using gas flow equations for viscous and molecular flow through small orifices. The total helium leak rate was determined for a composite material, SiC/SiC, utilized as a pressure boundary between a He coolant and the plasma. The calculated flow rates were determined for the residual porosity resulting from SiC/SiC manufacture and the total first wall surface area. This leak rate was compared to previous estimates of the tolerable leak rate limits established by plasma removal rates and recycling of He in a power reactor. The calculated estimates suggest that the He leak rates are within tolerable limits if the porosity is not interconnected or is interconnected by cracks with openings no larger than 0.3 nm. Increased crack openiny, induced by creep or more extensive microcracking induced by radiation or stress, could cause He leak rates to exceed the tolerable limit. These estimates suggest that the use of SiC/SiC composites for structural applications in fusion reactors will require the use of seal coatings if these materials must also perform as a pressure boundary. Similar conclusions should also apply for tritium containment.

PROGRESS AND STATUS

Introduction

Ceramic matrix composites (CMCs) have excellent high-temperature structural pruperties coupled with good low-temperature strength and toughness. Composites made of SiC fibers in a SiC matrix, SiC/SiC, also exhibit very low neutron activation. The properties of CMCs can be tailored through variations in the fiber type, volume fraction and architecture, matrix/fiber interface chemistry and structure and choice of matrix. However, these materials retain a significant volume fraction of porosity (5-15%) following processing. While the amount of porosity depends on the processing method, all processing routes result in some residual porosity. Therefore, the performance of these materials as pressure boundaries will depend on the rate at which the coolant or tritium permeates through the structure.

The elasticity and strength of these materials are a result of the combined properties of the fibers and matrix; however, the elastic response of CMCs deviate from linearity at applied stresses that induce matrix microcracking. If the design criteria allows for CMCs to be utilized at stresses exceeding the linear-elastic region to take full advantage of the fiber strength, then stress-induced matrix microcracks could also contribute to the leak rate of gases through these materials. Differences in radiation-induced dimensional changes between the fibers and matrix could also induce microcracking. It was recognized at a recent workshop on ceramic matrix composites for fusion reactor structural applications (1) that the hermeticity of CMCs is a key issue for their application in fusion reactors. The purpose of this report is to summarize estimated leak rates determined from CMC porosity data and gaseous flow rate equations.

Gaseous Leak Rates

Gas *Flow* Equations

Gas flow through an orifice can be expressed similarly to electrical current flow with F equal to the rate of flow per unit of pressure difference, Q analogous to the current and ΔP analogous to the electric potential. The gas conductance is then expressed as follows:

$$F = Q/(P_1 - P_2), \quad \ell/s. \qquad (1)$$

Porosity in SiC/SiC is elongated parallel to the fiber direction and the fiber direction is expected to be parallel to the first wall structure, as shown in Figure 1. Therefore, the pores can be considered as parallel channels separating the coolant and plasma such that the total conductance is the sum of the parallel conductances, in a manner analogous to electrical circuits.

---

*Operated for the U.S. Department of Energy by Battelle Memorial Institute under Contract DE-AC06-76RLO 1830.

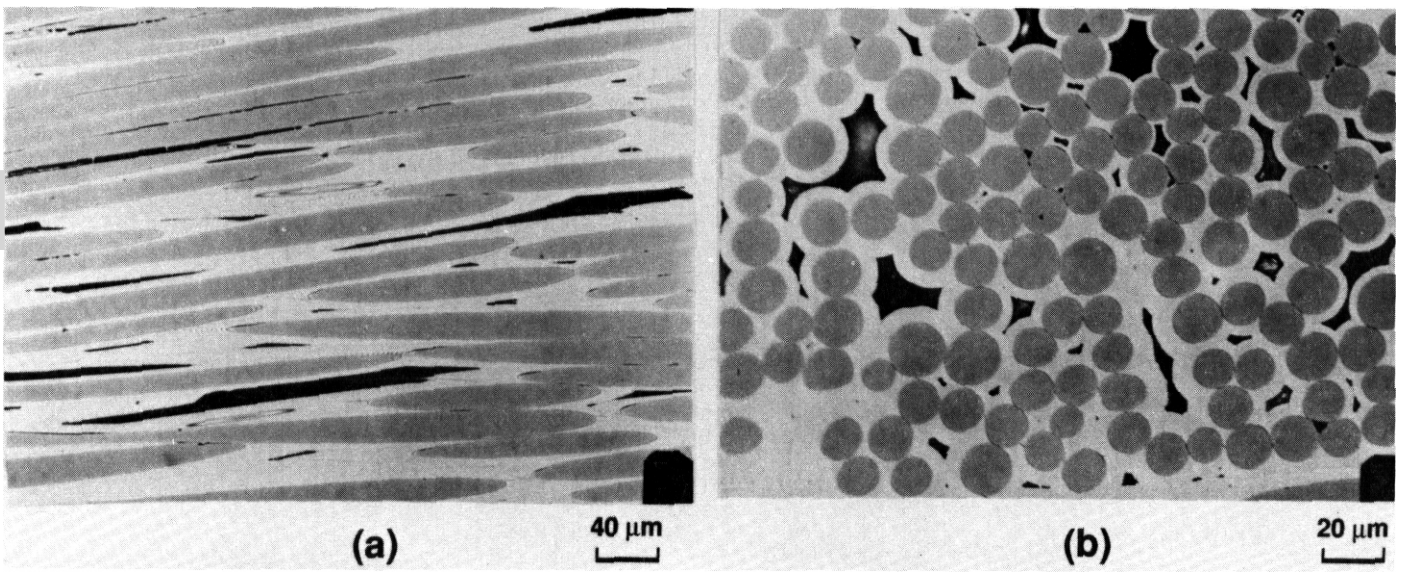

Figure 1. Reflected light optical micrographs of a SiC/SiC composite, a) longitudinal cross-section, b) transverse cross-section.

Gas flow through an orifice, or tube at high pressures, occurs with the mean free path of the gas molecules being substantially less than the dimensions of the channel. This type of gas flow is referred to as viscous flow and is described by the fallowing equation for a rectangular shaped channel:

$$Q = 0.26\, Y\, b^2c^2\, (P_1+P_2/2)(P_1-P_2)/t, \quad \mu\text{-}\ell/s \qquad (2)$$

where c is the pore length, b is the pore opening, t is the wall thickness, P_1 is the pressure on the plasma side and P, is the coolant pressure. All dimensions are in cm and pressures in μ of Hg. Y is a dimensionless parameter which is a function of c and b. A value for Y was estimated from data by Worden (2). The data given by Worden is for ducts with dimensions in cm while the small pores in CMCs have dimensions on the order of 8 μm for b and 100 μm for c. Worden's data is only given for b/c ratios extending to 0.1, while the b/c values for the pores were less than this. Therefore, calculations based on equation 2 for orifices the size of the pores in CMCs must be considered as very rough estimates of the actual flow rate.

Gas flaw through orifices at low pressures and under conditions where the collision of the molecules with the walls controls the flow rate is referred to as molecular flow and is described by the following equation for a rectangular shaped channel:

$$Q = 9.7\, b^2c^2\, (T/M)^{1/2}\, (P_1-P_2)/(b+c), \quad \mu\text{-}\ell/s \qquad (3)$$

where T is the temperature in K, M is the molecular weight of the gas and the other variables are the same as in equation 2. Again, all dimensions are in cm and pressures in μ of Hg The use of equation 3 has advantages over equation 2 because of the absence of the parameter Y, which required extrapolation beyond the available data set. Also, gas flow restricted by collision with the walls of the very small pores in CMCs is physically more realistic than viscous gas flow.

Yamawaki and Namba (3) have measured the permeability of H_2, CH_4 and Ar through porous graphite and concluded that molecular flow processes controlled the permeability over a pressure range of 0.5 to 100 MPa. The influence of pore size and distribution was described by the following equation:

$$J = 4P(2T/MR)^{1/2}\, k_p R_p'\, \beta/9x_o k^2 \qquad (4)$$

where J is the flux of gas molecules, P is the pressure differential across the membrane, T is temperature, M is molecular weight of the gas, R is the gas constant, k_p is the porosity, R' the average pore radius, k^2 describes the tortuosity, β is a function of pore distribution and x_o was undefined. This relationship is a refinement of the molecular flow equation 3 but requires considerable information about the pore structure before if can be used for predicting the leak rate through CMCs. Therefore, equation 3 was used for estimating the leak rate through SiC/SiC composites.

Estimates of the leak rate of He through small orifices and its effect on reactor performance have been made by Jones and Bruemmer (4), Jones, Conn and Schafer (5), and Hassanein (6). Jones and Bruemmer measured the leak rate of He gas through thin wall tubes in which cracks were developed by creep. They concluded that both the molecular and viscous flow equations, as expressed above, gave representative values of the experimental results for flaws with dimensions of about 15 by 100 μm. Jones, Conn and Schafer (5) determined that the limiting flow rate of He was 10^{-1} moles/s for a UWMAK II reactor design and 4 x 10^{-3} moles/s for a NUWMAK reactor design. These results were derived from He transport processes in the plasma and the resulting helium recycling and removal rates. Hassanein (6) estimated the critical leak rate by assuming that it must be less than the He generation rate within the plasma which can be expressed by:

$$Q_p = 5.9 \times 10^{-7} P_F, \quad \text{moles/s} \qquad (5)$$

where P_F is the fusion power in MW. For a 2000 MWth reactor the He ingress rate must be less than 1.2 x 10^{-3} moles/s. This approach gives a critical leak rate much smaller than the UWMAK and slightly smaller than for the NUWMAK reactor design. This differsnce probably results from He removal processes considered in the study by Jones, Conn and Schafer while equation 5 only considers the He generation rate without He removal. These previous leak rate studies suggest that the gas flow equations give reasonabla estimates of the He flow rate through small cracks and that the tolerable leak rate for a fusion reactor is between 10^{-3} and 10^{-1} moles/s.

Estimated Leak Rates for *SiC/SiC*

The material chosen for evaluation was a SiC/SiC composite with 40% Nicalon fibers in a SiC matrix produced by chemical vapor infiltration. The fiber architecture was 2-d with a 0/90° fiber orientation. Longitudinal and transverse cross-sections showing the fiber/pore geometry are given in Figure 2. The average pore size for this material is 8 μm by 100 μm with a pore density of 6 x 10^7 pore/m^2. These pores result from the cessation of the chemical vapor infiltration process as the space between the fibers fills in. Therefore, the pores are not interconnected in the transverse direction, Figure 2.

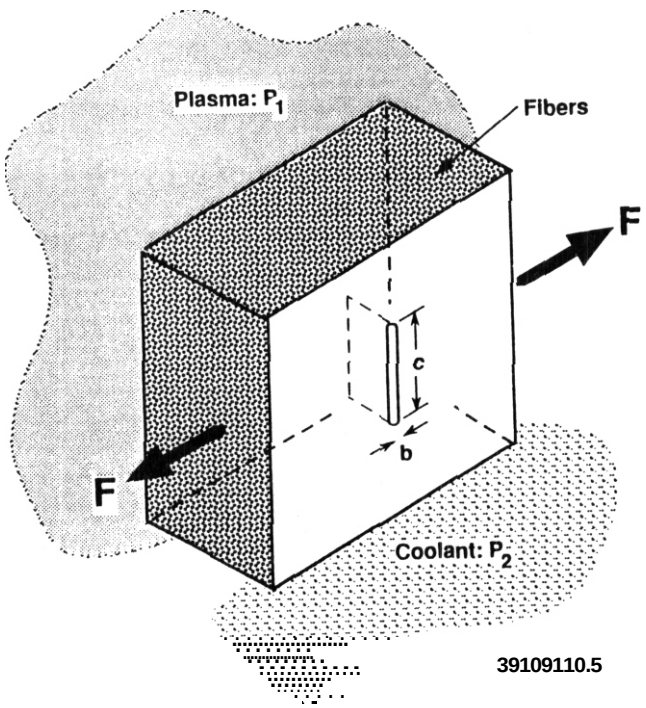

Figure 2. Schematic showing orientation of pores in a CMC relative to fiber orientation, plasma and helium coolant.

Two extreme pore size conditions were considered in estimating the leak rate. The lower limit was bounded by the condition that the pores become interconnected by microcracks with lengths equal to the pore lengths. Microcracks could develop from the applied stress or from differential radiation-induced dimensional change. The upper limit was bounded by the average pore size which assumes creep or other cracking processes open the channels between the pores to the same dimension as the pores. For both cases, it was assumed that all the pores become interconnected. These assumptions represent the worst case, since it is more likely that the size and number density of the openings between the pores will be time dependent.

Gas leak rate estimates were made for conditions similar to those used by Jones, Conn and Schafer in order to allow comparison with the previous analysis. Therefore, the gas temperature was taken as 500°C and the gas pressure as 10^7 MPa. Molecular gas flow, as described by equation 3, was assumed because of the small dimensions of the pores. A reactor first wall surface area of 4.3 x 10^3 m^2 was used to estimate the total He ingress rate. The upper bound leak rate is 7 x 10^{-5} moles/s for the assumption that all the pores are interconnected with channels equal to the average pore dimension. This is almost 7 orders of magnitude greater than the maximum tolerable leak rate of 0.1 moles/s. The lower bound condition was determined from the opening required to produce a leak rate of 0.1 moles/s if all the pores were connected with cracks equal in length to the pores. An opening of only 0.3 mm was necessary to produce a He leak rate of 0.1 moles/s. This small of an opening in the cracks interconnecting the pores would easily occur from the applied stress. Therefore, these results indicate the probable need for a seal coat for the surfaces of SiC/SiC materials used as a pressure boundary between a He coolant and the plasma.

Yamawaki and Namba (3) measured the leak rate of Ar through porous graphite and found a linear relationship between the flux of Ar and the pressure up to a pressure of 100 MPa at a temperature of 20 C. Extrapolation of their results to a pressure of 10^7 MPa gives a flux of 10^2 moles/m^2-s for a total leak rate into the reactor of 4.3 x 10^5 moles/s. Correction for temperature and molecular weight adjusts this value to 2.2 x 10^6 moles/s. The graphite had a similar volume fraction of porosity to the SiC/SiC but the pore size was considerably smaller. The average pore diameter was 0.1 μm for the graphite while the elongated porosity in the SiC/SiC was 8 μm x 100 μm. Correcting for the difference in pore size using equation 4 and the smallest dimension of the elongated porosity in SiC/SiC gives a leak rate 80 times higher or a value of about 1.6 x 10^8 moles/s. This value is considerably larger than that calculated with equation 3 but the effect of tortuosity, k_p and pore size distribution, β, was not considered. Nevertheless, the leak rate values obtained for porous graphite support the conclusion that the leak rate through CMCs is substantially higher than the reactor can tolerate.

The SiC/SiC material used for this analysis had an average porosity such that materials with less porosity could be produced. However, the CVI process has an upper limit of about 92% theoretical density because of the tendency for growth of the matrix to close off access of the chemical gas used to form the matrix. Nevertheless, small changes in the volume fraction and size of the porosity is not likely to eliminate the need for a seal coat since the estimated leak rates are well above the reactor limits. A process such as the DuPont Lanxide Composite Corporation's DIMOX process which has produced CMCs with near theoretical densities could be used; however, this process has not been used to produce SiC/SiC.

A SiC/SiC composite material was utilized in the ARIES-I design (7) which had different operating conditions than the UWMAK II and NUWMAK designs for which the leak rate analysis was made. Coolant temperature and reactor dimensions are the major differences between ARIES-I and the other designs. The coolant temperature in ARIES I was 900°C. With these differences and using equation 3 for the leak rate of He, it is possible to estimate that the leak rate for SiC/SiC in ARIES-I would be about 1/3 that of UWMAK II. This results in a leak rate that is still considerably greater than the 10^{-1} moles/s acceptable for UWMAK II. The ARIES I helium removal systems would have to be far superior to UWMAK II or NUWMAK for this high leak rate to be acceptable, but this is not expected.

FUTURE WORK

Experimental leak rate measurements are needed and will be conducted pending funding of a fusion CMC program. The capability to measure leak rates on unirradiated and irradiated materials is necessary. Comparison of measured leak rates to microstructural pore sizes will also be performed to build the basis for extrapolating the test results to other materials and conditions.

ACKNOWLEDGMENTS

Interest in the leak rate analysis of fusion reactor materials by A.M. Hassanein of ANL and Professor T. Min of North Carolina A & T Univ. is greatly appreciated. This work was supported by the U.S. Department of Energy under Contract DE-AC06-76RLO 1830 with Battelle Memorial Institute.

REFERENCES

1. Proceedings of the Office of Fusion Energy/DOE Workshop on Ceramic Matrix Composites for Structural Applications in Fusion Reactors, R. H. Jones and G. E. Lucas, eds., CONF-9005225, Nov. 1990, held at U.C. Santa Barbara, May 1990.

2. D. G. Worden, "Flow of Gases Through Tubes and Orifices" Scientific Foundations of Vacuum Technology, F. Dushman and J. M. Lafferty, Wiley and Sons, New York, 1962, p. 80.

3. M. Yamawaki and T. Namba, "Permeability of Hydrogen Isotopes and Surface Segregation of Impurities in First Wall Materials for Fusion Reactor", J. Nucl. Sci. and Tech., 28, 2, 1991, p. 178.

4. R. H. Jones and S. M. Bruemmer. Damage Analysis and Fundamental Studies Quarterly Report, DOE/ER-0046/4, 1980, p. 65.

5. R. H. Jones, R. W. Conn and R. F. Schaffer, "Effect of First Wall Flaws on Reactor Performance", Nuclear Engineering and Design/Fusion, 2, 1985, p. 175.

6. A. M. Hassanein, "Coolant Leakage Through Cracks in Fusion Reactors", presented at the 8th Topical Meeting on The Technology of Fusion Energy, Salt Lake City, Utah, Oct. 1988.

7. C. P. C. Wong, E. T. Cheno. B. McQuillan, E. E. Reis, Jr., K. R. Schultz. S. P. Grotz. M. F. Hasan, R Martin, F. Najmabaci, S. Sharafat, T. 'Kunngi, J. S. Herring, D. K. Sze and the Aries Team; "ARIES-I SiC Composite Low Activation Blanket Design", Fusion Technology, Vol. 19, 1991, p. 938.

Measurement of the Effect of Radiation Damage to Ceramic Composite Interfacial Strength. L.L. Snead, S. J. Zinkle (Oak Ridge National Laboratory), D. Steiner (Rensselaer Polytechnic Institute)

OBJECTIVE

To determine the effects of radiation on the physical and mechanical properties of silicon carbide composite materials.

SUMMARY

SiC/C/Nicalon Composite materials have been irradiated at 300°C in HFIR to a dose of 1 dpa. Three point bend tests demonstrate a marked decrease in ultimate tensile strength while showing added composite toughness. Both strength and toughness changes are shown to be caused by a large decrease in both interfacial shear strength and interfacial friction as measured using a thin section push-out test. The degradation in interfacial properties is attributed to a debonding at the fiber/interface interface due to fiber shrinkage during irradiation.

PROGRESS AND STATUS

1. Introduction

In recent years there has been a growing interest in ceramic composites for nuclear systems. A composite offers the possibility of reducing the possibility of catastrophic and unpredictable failure inherent in monolithic ceramics. A composite which offers some attractive features is the SiCICINicalon system. Through the incorporation of high strength Nicalon silicon carbide fibers into a chemically vapor deposited matrix, along with a fiber/matrix interfacial layer, the ceramic no longer fails in a catastrophic manner. The reason for this is that the interface serves the dual roles of being strong enough to transfer load between matrix and fiber to take advantage of the high fiber strength, and being compliant enough to inhibit crack propagation. Figure 1 shows the load/displacement behavior of such a composite made with varied thicknesses of a graphitic carbon interfacial layer. From the figure it is apparent that the composite with no interfacial coating failed at a relatively low load and in a brittle manner. This failure has occurred from a single flaw-induced crack which propagates through the entire material. As the interfacial layer becomes thicker, the failure becomes more gradual with the ultimate strength of the composite dramatically increasing. A thickness of 0.17 μm corresponds to the carbon interfacial layer which yields the greatest strength. It is important to note, however, that the increased strength of the composite for the SiC/C/SiC system corresponds to a large amount of matrix cracking and fiber pull out. Unlike the monolithic material, once a crack rains enough energy to propagate it does not cause failure. The interface serves to tie-up a crack and relieve some of the crack energy by debonding and sliding of the interface. The actual linear elastic region of the composite is significantly less than the ultimate strength; this must be considered when designing with these materials.

Due to the fundamental importance of the composite interface and the newness of direct interfacial measurement techniques, there has been growing interest in this area. There have been several recent papers in which experimenters have employed microindentation testing techniques to measure interfacial strength.[1-6] The technique of fiber push-out has been recently developed specifically for application to the SiCICINicalon system and utilizes a load controlled Nanoindenter. This techniaue has been described in detail elsewhere [5,6].

It is clear that for a fully bonded interface there will be at least two Competing resistances to fiber sliding. First, there will be a minimum force required to initiate a crack in the interfacial chemical bond which may or may not then have the required energy to propagate along the length of the fiber. This is referred to as the debond yield strength of Inter-Facial Shear (IFS). Second, there will be a frictional component to the resistance which is caused by the crack surfaces passing over each other as the fiber slides. This is generally referred to as the frictional resistance to sliding or Inter-Facial Friction (IFF). Both the IFS and IFF are calculated by noting the load at which the debonding or sliding begins and dividing by the fiber interfacial area:

$$\tau = \text{Load}/\pi D t.$$

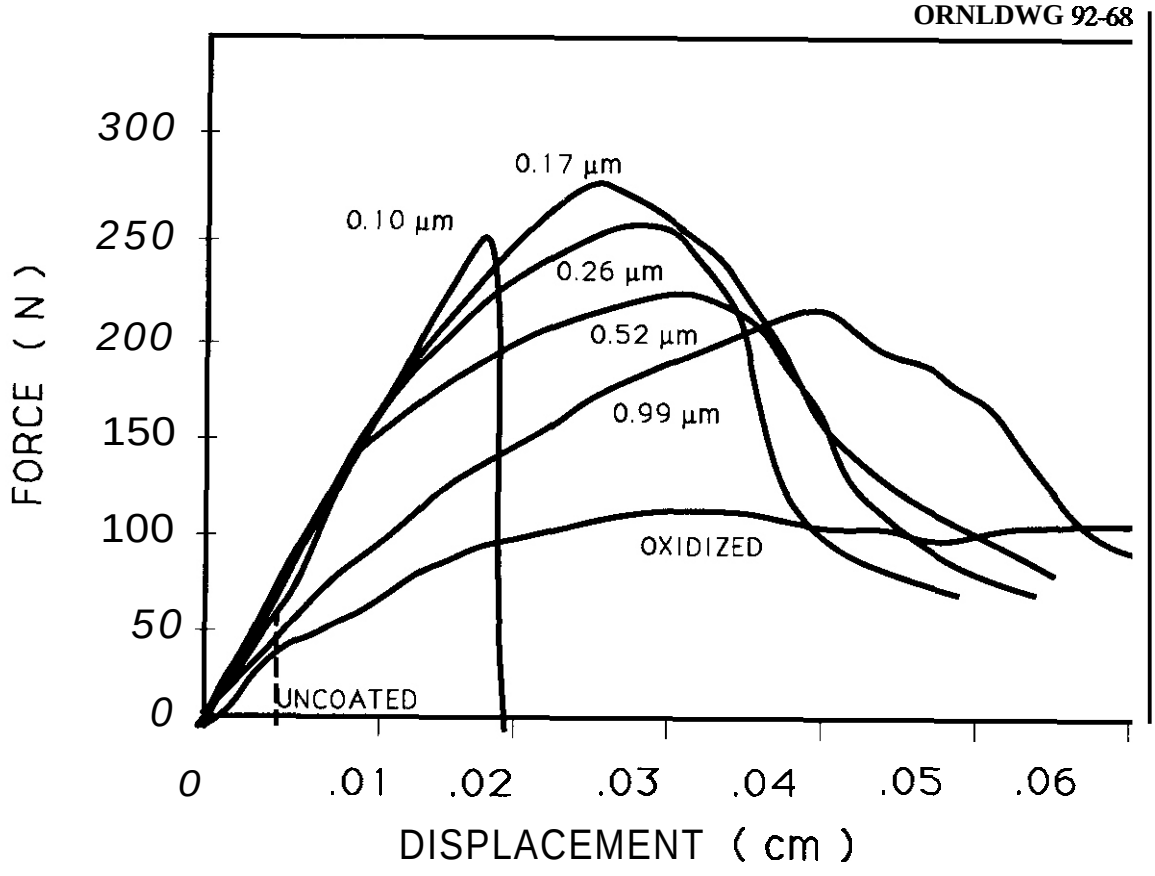

Figure 1: Load displacement curve demonstrating effect of interfacial thickness on SiC/C/Nicalon composite performance.

Here the diameter **D** is found using the Nanoindenter optics and the thickness t is constant of 35 µm for the composite sections.

Both the debond yield strength and the frictional resistance to sliding can be directly measured using the thin section push-out test. The basic technique is to thin a section of composite such that fibers which lay normal to the polished surface can have a load applied to their centers to the point of interfacial failure. This is the shear stress required to initiate a crack in the interface which travels along the length of the interface causing the fiber to be (partially) pushed out of the composite. The section is then repositioned such that those fibers which have been oushed out can be reloaded and pushed through the matrix in the opposite direction. By doing this, the resistance to fiber sliding of a debonded interface can be measured.

The purpose of this paper is to present results of interfacial measurements on unirradiated and irradiated SiC/C/Nicalon composites. Such results will be discussed in comparison with the conventional three point bend data taken on the same composite material.

2. ExDerimental

Composite bend bars were fabricated in a 30/60/90 fiber weave of Nicaion cloth infiltrated with SiC using the ORNL Forced Chemical Vapor Infiltration process.[7] The fiberlmatrix interface contains a 0.17 µm layer of graphitic carbon which was deposited onto the fibers from a polypropylene gas prior to SiC infiltration. Bend bars were then irradiated in the High Flux Isotope Reactor to 1 dpa (carbon) at 300°C.

Three point bend tests were performed on both irradiated and unirradiated specimens at a cross head displacement rate of 0.02 inlmin. The composites were then sliced into 250 µm sections with a low speed diamond saw and mechanically thinned and polished with 6.1 and 1/2 µm diamond paste to a final thickness of 22 pm. A final Syton polish was used. The sample was then mounted onto a polished aluminum holder such that the center of the sample

was positioned over a groove of 200 μm in width. The composite section was then held rigidly to the mount and fixed to the surface with crystal bond mounting wax. Care was taken during the thinning and mounting procedure to prevent bending the sample in order to avoid pre-cracking the interface.

A load controlled Nanoindenter microindentation hardness tester was used to apply a force to the fibers which lay normal to the composite surface. A good discussion of the Nanoindenter can be found elsewhere.[8] A constant loading rate of 300 μN/sec was used with a maximum loading capability of 0.12 N. Approximately 100 fibers were tested for both the irradiated and unirradiated material to ensure acceptable statistics.

3. Results and Discussion

Figure 2 shows the load displacement curve for the unirradiated and 1 dpa neutron modified composite. Three general observations can be made from the curves. The most obvious difference is that the composite ultimate strength for the irradiated composite is only 75% of the unirradiated bend bar. It should be noted that the composite selected for this test was for an interfacial layer of 0.17 μm, which by inspection of Fig. 1 is seen to correspond to the strongest composite. It can be inferred that, for unchanging fiber and matrix properties, the composite ultimate strength could only *be* decreased. The second observation from the load displacement curve is that after the composite is past its ultimate strength, the irradiated material does not have the load drop-off seen in the unirradiated sample. This would normally be described as having greater toughness or larger puli-out. The irradiated load-displacement curve has a shape similar to the 0.99 μm (weaker) interface material shown in Fig. 1. The third observation that can be made is that the initial slope of the irradiated material is less than that of the unirradiated. This result, that the modulus of the composite is reduced in the linear elastic region, is also consistent with fiber-matrix interfacial degradation. If the interface has been modified such that there is not adequate load transfer between matrix and fiber, the elastic modulus in the linear elastic region would be reduced.

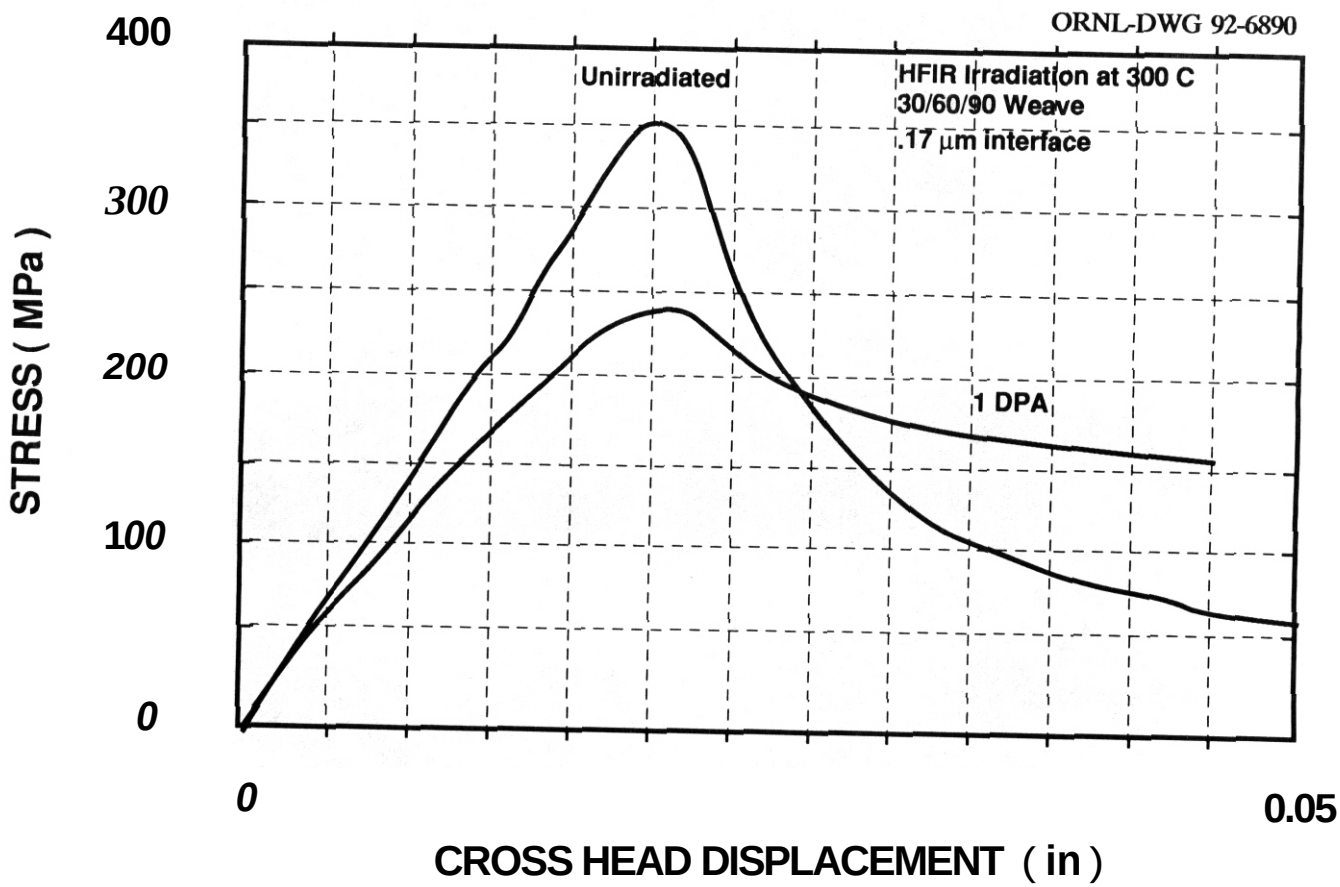

Figure 2: Load displacement curve from three point bending of unirradiated and 1 dpa neutron irradiated SiCICINicalon.

All three observations can be explained by a reduction in the fiber matrix interfacial strength. This is not conclusive, however, unless the radiation induced changes in the physical properties of the fiber and matrix are known and the interfacial strengths are measured. For example, by inspection of Fig. 2, the reduction in composite strength could as easily be explained by a reduction in fiber strength or a large change in either the fiber or the matrix elastic modulus.

Shown in Fig. 3 are scanning electron micrographs of fracture surfaces for the bend bars in Fig. 2. Figure **3** a and c show a nearly end on view of the entire bend bar. It is evident from these micrographs that there is a pronounced difference in the fracture surfaces between the unirradiated and 1 dpa specimens. By inspection of the same composite at higher magnification (b and d) it is seen that there is a much larger pull out of fibers for the irradiated composite.

Both the unirradiated and 1 dpa specimens were thinned to 35 μm and mounted for thin section push out tests. Approximately 100 fibers were tested and both interfacial shear strength and frictional resistance to sliding were measured. As the fibers were loaded two types of behavior are exhibited during interfacial failure. First, the load displacement curve follows the normal parabolic path until an interfacial crack is initiated. This is characterized by a departure from the parabolic curve characteristic of hardness measurements. A 2% departure from the parabolic curve has been adopted as the point of interfacial yield (IFS). After this crack is initiated, there is force required to propagate this crack front along the interface. Once this force has been reached and the crack has run the length of the fiber, push out occurs. This is characterized by a rapid failure and push out. When this fiber is reloaded in the opposite direction the fiber sliding occurs in a more graceful manner. Again, the point of sliding is taken to be a 2% departure from the parabolic. Shown in Fig. 4 is a scanning electron micrograph of a fiber which has undergone interfacial debonding and push out and which was then reloaded and pushed in the opposite direction to determine the interfacial friction (IFF).

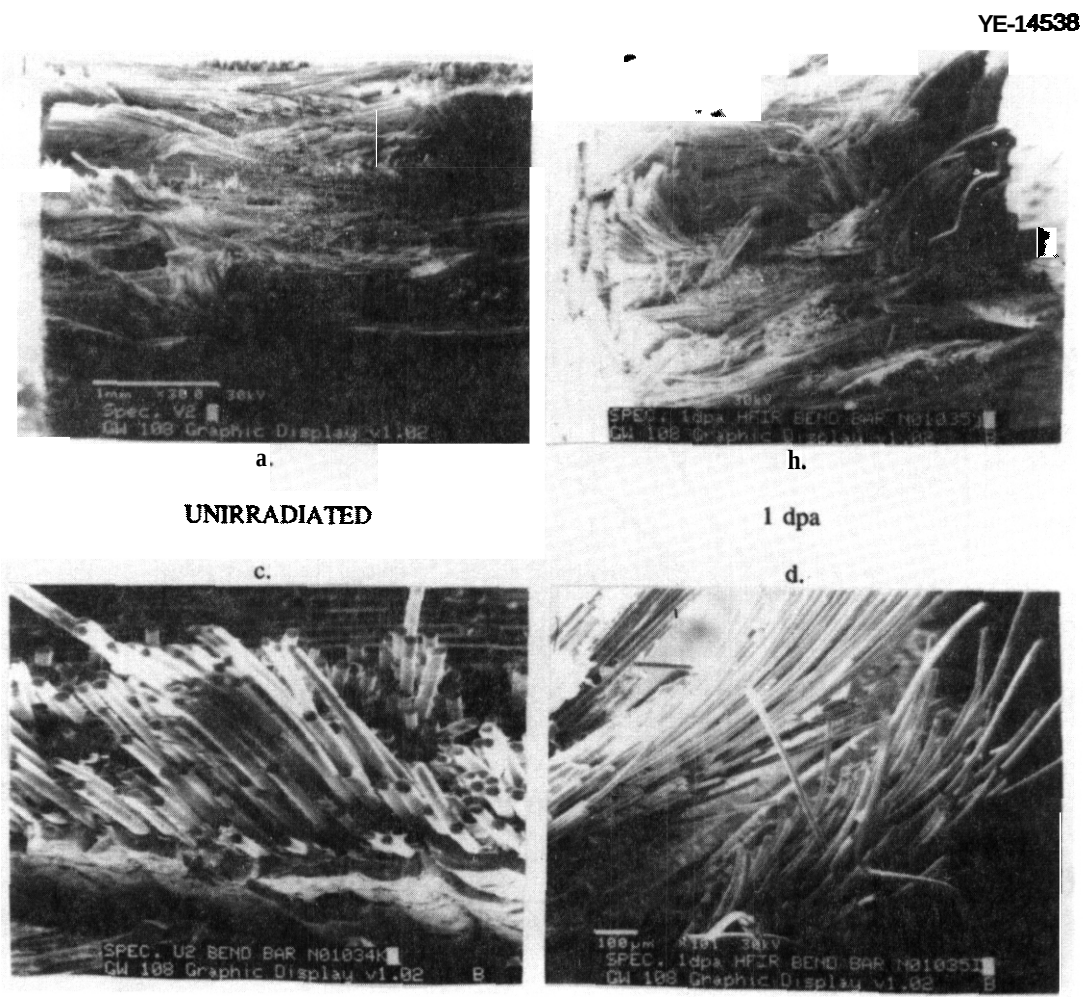

Figure **3:** Scanning electron micrographs of fracture surfaces of unirradiated and 1 dpa neutron irradiated SiC/C/Nicalon.
3 (a and c) : Unirradiated **3** (b and d) :1 dpa

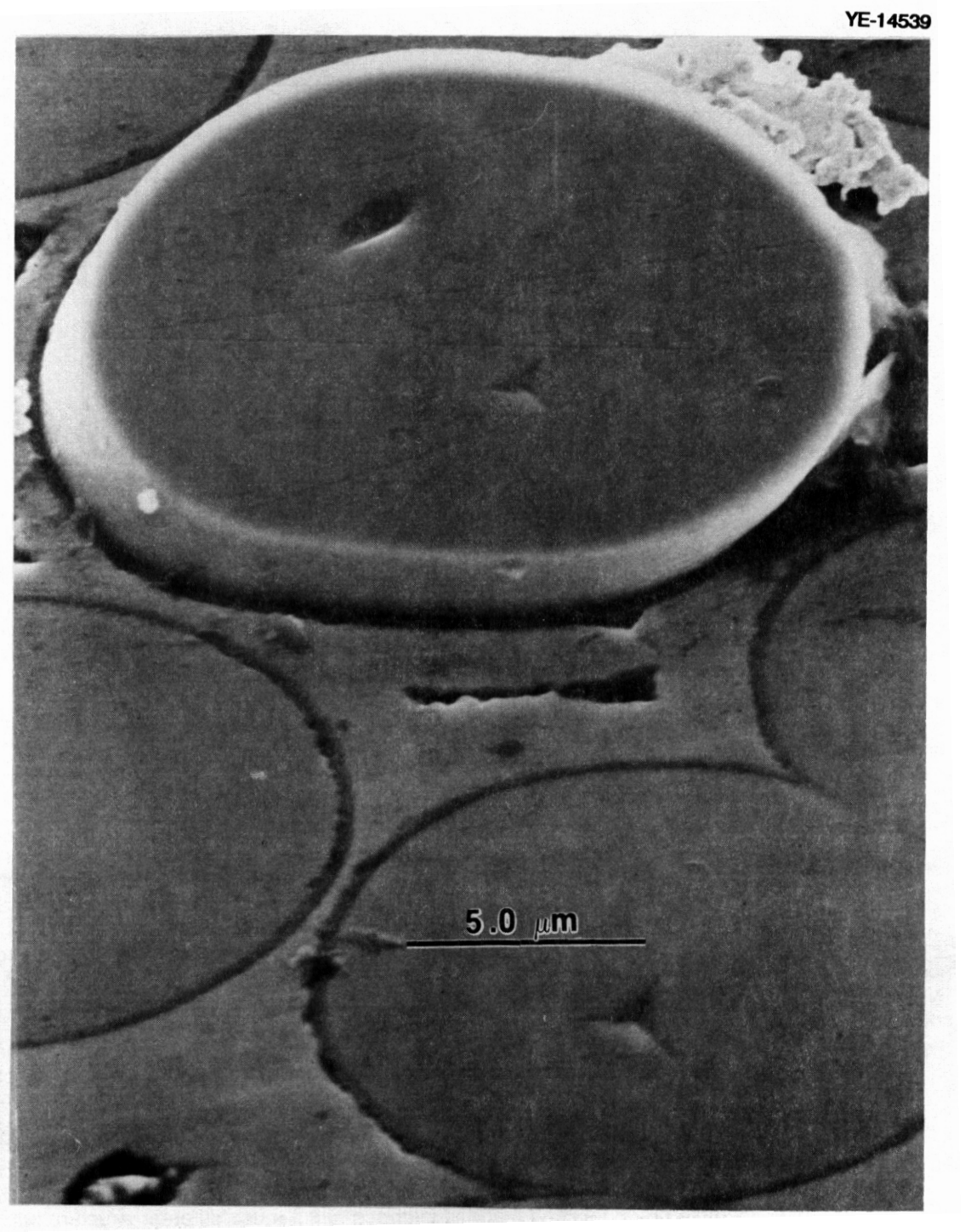

Figure 4 **Scanning electron micrographs** of **pushed** out **fiber.**

It has been previously reported [5,6] that the most accurate representation of interfacial strength data is found by applying a Weibull distribution. Figure *5* shows both the IFS and IFF for the unirradiated and irradiated composite material. The results from this figure quantitatively prove what was inferred from either the load displacement curves of Fig. **2** or the fracture surfaces of Fig. 3. Namely, the interfacial strength of the composite has been significantly reduced. By taking a Weibull average of the widely distributed data, the shear strength (IFS) has been reduced by almost an order of magnitude from 72.0 to *8.8* MPa. The interfacial friction (IFF) also shows a similar reduction for the irradiated material from 22.0 to **7.8** MPa in the irradiated condition.

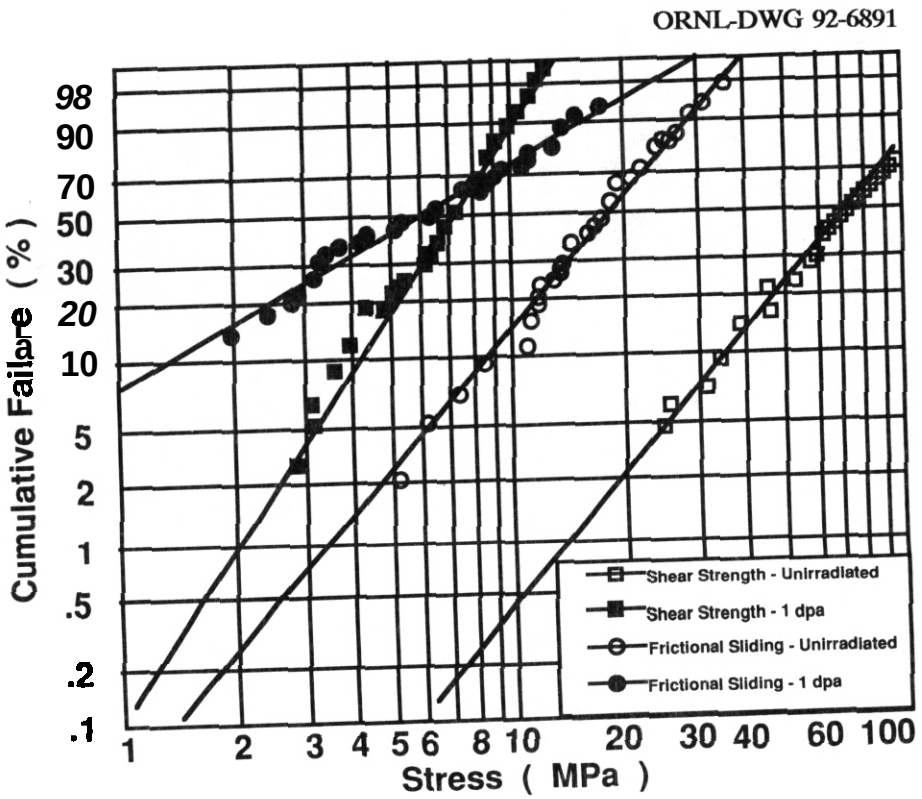

Figure *5:* Weibull plot of interfacial strengths for unirradiated and 1 dpa neutron irradiated SiC/C/Nicalon.

The choice of the chemically vapor deposited SiC/C/Nicalon composite has primarily been made because it is a state-of-the-art composite which is being produced both in the laboratory and on a commercial scale in many countries. It has become popular not only because of the good composite properties by also because the weavable Nicalon fiber is relatively inexpensive. This composite has also *been* used in fusion reactor design studies such as **ARIES.** It is not an ideal choice for nuclear systems, however. The Nicalon fiber is metastable and degrades at temperatures above 1000°C. The graphite interface also presents problems. It is well understood that carbon materials undergo extreme swelling at modest fluences. Graphite also goes through a densification prior to this swelling. For this reason a graphitic carbon interface will undergo changes which will significantly affect the composite strength.

The changes in hardness and modulus of both the CVD SiC and Nicalon fiber after irradiation have been discussed elsewhere[9]. It was found that the Nicalon fiber has a significant radiation induced increase in elastic modulus which is caused by densification. This densification in fact is the major factor in the reduction of interfacial strength. Transmission electron micrographs taken of fairly thick sections *of* composite show partial debonding at the fiber-interface interface, possibly the fiber has shrunk away from interface allowing interfacial yield at a lower stress.

In order to develop low activation ceramic composites it is critical to tailor the fiber, matrix and interface such that debonding is at least limited, if not avoided altogether. It is clear that ceramic composites require a fiber matrix interfacial structure to achieve desirable properties and that this interface has a much different structure than the matrix and fiber. For this reason there will be different responses to radiation in the fiber/matrix and interface. It would be beneficial then, to have very similar materials for the fiber and matrix so that there is no difference in radiation induced swelling (or other property changes) causing interfacial degradation. Once an acceptable fiber/matrix system is found the next step would be to find an interface which is radiation hardened or very compatible with the other composite constituents.

4. Concluding remarks

A method has been demonstrated to directly measure the effect of neutron modification to composite interfacial properties. Specifically, a neutron irradiated composite section has been thinned to 35 μm and a load controlled microindentation machine used to apply a force to individual fiber centers until fiber interfacial failure occurs; failed interfaces were then reloaded in the opposite direction allowing measurement of the fiber frictional sliding.

Chemically vapor deposited SiC/CINicalon composite samples irradiated to 1 dpa exhibited a marked decrease in both interfacial shear strength and frictional resistance to sliding. Such a result explains the load-displacement behavior observed during three point bend tests of the irradiated and unirradiated composite. Due to the significantly decreased interfacial shear strength, the composites ultimate strength has decreased by about 25% and the decreased frictional resistance to sliding has allowed much greater fiber pull-out yielding higher composite toughness.

The apparent reason for the reduction in interfacial strengths and reduced ultimate tensile strength of the composite is fiber shrinkage which causes a partial debonding of the fiber/matrix interface.

FUTURE WORK

In order to develop radiation hardened composites it will be necessary to first develop a fiber which has a radiation-induced volumetric change compatible with that of the matrix in order to avoid interfacial degradation. Higher density experimental silicon carbide fibers are currently being irradiated in HFIR and FFTF(MOTA).[10,11] Once such a fiber is found, the next step would be to develop a less radiation sensitive interface than graphite.

Acknowledgements

The authors would like to thank K. B. Alexander and L. T. Gibson for assistance with the SEM micrographs. We would also like to thank T. D. Burchell for providing space for composite irradiation in HFIR as well as the use of his specimen preparation and testing facilities. We would also like to thank Rick Lowden for providing composite material used in this experiment.

REFERENCES

1. A. G. Evans and D. D. Marshall, 'The Mechanical Behavior of Ceramic Matrix Composites," Acta Met. 37(10) (1989) 2567-83.

2. R. J. Kerans, R. S. Hay, N. J. Pagano, and T. A. Parthasarathy, 'The Role of the Fiber-Matrix Interface in Ceramic Composites," Ceram. Bull. 68(2) (1989) 429-42.

3. D. B. Marshall and W. C. Oliver, "Measurement of Interfacial Mechanical Properties in Fiber-Reinforced Ceramic Composites:' J. Am. Ceram. Soc. 70(8) (1987) 542-48.

4. J. D. Bright et al., "Interfacial Bondine and Friction in Silicon Carbide (filament)-Reinforced Ceramic and Glass-Matrix Composites,' J. Am. Ceram. Soc. 72(10) 71989) 1891-98.

5. L. L. Snead et al., "Measurement and Analysis of Nicalon/SiC Composite Interfacial Strengths Using a Thin Section Push Out Test," (submitted, 1991, to J. Mater. Res.).

6. L. L. Snead et al., "Development of Thin Section Push-Out Technique for Use in Measuring Radiation-Induced Modification of Composite Interfaces," Fusion Reactor Materials Semiann. Proe. Reat., DOE/ER-0313/9 (1989), pp. 306-16.

7. D. P. Stinton, A. J. Caputo, and R. A. Lowden, "Synthesis of Fiber-Reinforced SiC Composites by Chemical Vapor Infiltration," Ceram. Bull. 65(2) (1986) 347-SO.

8. W. C. Oliver et al., "Measurements of Hardness at Indentation Deaths as Low as 20 Nanometers," pp. 90-108 in ASTM Spec. Tech. Publ. No. 889, *Microindentation* Techniques *in Material Science and* Engineering (Ed. by P. J. Blau and B. R. Lawn, American Society for Testing and Materials, Philadelphia, PA, 1985.

9. L. L. Snead et al., "Radiation Induced Microstructure and Mechanical Property Evolution of SiC/C/SiC Composite Materials," presented at ICFRM-5, Clearwater, FL, Nov. 17-22, 1991.

10. S. J. Zinkle and L. L. Snead, "Irradiation of Conventionally and Isotopically Tailored Ceramics in HFIR," Fusion Reactor Materials Semiann. Proe. Rept., DOE/ER-0313/10 (1991), p. 314-16.

11. S. J. Zinkle and L. L. Snead, "Irradiation of Ceramics in FFTF," Fusion Reactor Materials Semiann. Proe. Reat., DOE/ER-0313/10 (1991), p. 317-19.

Radiation Induced Microstructure and Mechanical Property Evolution of SiC/C/SiC Composite Materials

L. L. Snead, S. J. Zinkle (Oak Ridge National Laboratory), D. Steiner (Rensselaer Polytechnic Institute)

OBJECTIVE

SiC/C/Nicalon composites have been neutron irradiated in both HFIR and FFTF from 1 to 15 dpa and have been ion beam damaged with 3 MeV carbon ions to 30 dpa in a temperature range from room temperature to 900°C. Room temperature ion irradiations have caused amorphization in both CVD SiC and Nicalon fiber though at different threshold levels of 15 dpa (carbon) and 1 dpa, respectively. A substantial change in both hardness and modulus is observed for both CVD SiC and Nicalon fiber. The objective of this paper is to present results obtained for radiation induced changes in hardness and modulus and to compare these results with observed microstructural changes.

SUMMARY

Room temperature carbon ion irradiations cause amorphization of both CVD SiC and Nicalon fiber. The elastic modulus and hardness have been measured using a microindentation method and the results compared with those of neutron irradiations in HFIR and FFTF at 300 and 435°C, respectively. It is observed that the randomization/amorphization of CVD SiC significantly reduces both hardness and modulus for both carbon beam and neutron irradiations. The Nicalon fiber shows the opposite behavior yielding higher modulus and hardness for both neutron and carbon irradiations. This change in Nicalon mechanical properties occurs whether the microstructure has been amorphized, as is the case for the room temperature carbon irradiations, or if the microstructure appears unchanged leading to the assertion that the cause of the mechanical property change is the densification of the fiber.

PROGRESS AND STATUS

1. Introduction

There has been increasing interest in the use of ceramic composites in fusion systems. The potential advantages of these materials include low activation and afterheat and the possibility of high temperature operation which would increase reactor thermal efficiency. Very little is known, however, about the performance of ceramics or ceramic composites in the demanding environment that fusion reactor materials are subjected.

One of the leading composites being considered for use in fusion reactors is the chemically vapor deposited (CVD) SiC/C/Nicalon system. Nicalon is a commercially available continuous fiber reinforcement which is nominally silicon carbide. The actual constituents of Nicalon are β SiC with 25% SiO_2 and 10% free carbon. Its density is only 81% that of the CVD SiC which is comprised mainly of heavily faulted β (cubic) SiC. Graphitic carbon is added to the system as an interfacial layer and is critical to the performance of the composite as it acts to tie-up cracks which are initiated and propagated through the CVD matrix. This interface is also important in that it acts to transfer load between the matrix and the fibers to take advantage of the high strength of the reinforcement.

2. ExDerimental

a) Irradiation Conditions and Material

Composite bend bars were fabricated from a 30/60/90 Nicalon fiber cloth infiltrated with SiC using the ORNL Forced Chemical Vapor Infiltration process.' The fiber/matrix interface contains a 0.17 μm layer of graphitic carbon which was deposited onto the fibers from a polypropylene gas prior to SiC infiltration.

The Triple Ion Beam Facility at Oak Ridge National Laboratory provided 3 MeV carbon ions with sample temperatures ranging from room temperature to 900°C at fluences of 1,10 and 30 dpa peak (normalized to steel). The carbon ions were implanted at a rate of 2.78 x 10^{-4} dpa/sec (peak) to an implantation depth of approximately 2.5 μm. Composite material was sliced with a low speed diamond saw and polished to a 1/2 μm diamond paste finish. Samples were then prepared in cross section for microstructural analysis and mechanical property measurement. Fission neutron irradiations were conducted to 1 and 3 dpa (carbon) in HFIR at a temperature of 300°C and to 15 dpa (steel) in FFTF at 365°C.

b) Microstructural Analysis

The carbon beam irradiated samples were prepared in cross section so that the carbon beam profile could be imaged. The composite surface which was subjected to the carbon beam was first glued to a virgin piece of composite with M-bond adhesive and this sandwich was sliced with a low speed diamond saw. The slices were then mechanically ground and polished to a 1/2 μm finish and ion milled to expose a thin area at the sandwich interface. A Phillips CM-30 transmission electron microscope (TEM) was used at 300 keV. The neutron irradiated composite material was simply ground and ion milled until perforation.

c) Mechanical Property Measurement

The modulus and hardness of a material can be obtained from the unloading portion of the load-displacement curve generated during indentation.2 A Nanoindenter load controlled microindentation machine was used to create a series of indents along the ion beam path. Figure 1 shows the Nanoindenter load displacement curve for CVD silicon carbide. The figure shows four separate loadings and unloadings for depths of 20, 40, 80 and 160 nm . While all four unloadings should give identical values for hardness and modulus for a uniform material, in the case of an ion irradiated material one would like to use the shallowest indent which still

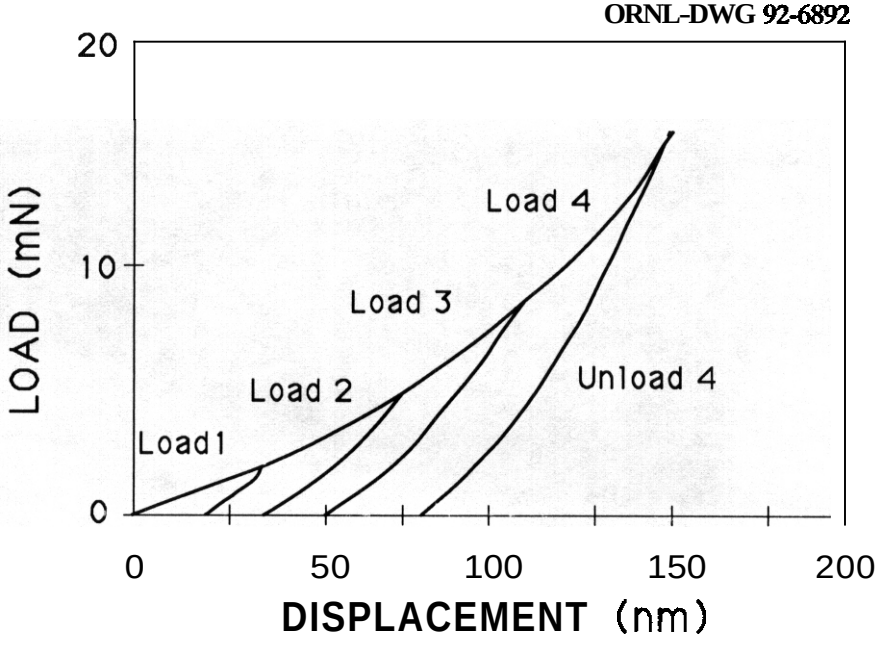

Figure 1: Nanoindenter Load-Displacement curves for CVD SiC.

provides reliable data. By doing this, the sensing volume associated with the indent is kept to a minimum and the most accurate modulus (or hardness)-vs- depth values are obtained.3

From the load displacement curves generated, it is straightforward2 to calculate the depth of plastic deformation by extrapolating a tangent line from the initial unloading curve to its intersection with the load axis. For metals, nearly all the unloading curve is linear. For materials such as ceramics, with high hardness to modulus ratio, there is substantial curvature in the unloading curve caused by the loss in indenter contact area. Even for materials such as silicon with a very high hardness to modulus ratio, however, the first 113 of the unloading curve is linear. thus an accurate determination of plastic depth can still be obtained.

The equation for the hardness is simply the load divided by the indenter area at that plastic depth and the equation for the elastic modulus can be shown[2] to be:

$$E_{sample} = \{Load/24.5\}^{1/2} (1/2h_p)\, dL/dD,$$

where h_p is the extrapolate plastic depth and dL/dD is the tangential slope of the unloading curve.

3. Results and Discussion

3a Microstructure

Shown in Fig. 2 is a cross sectional TEM micrograph of carbon implanted CVD silicon carbide irradiated to 30 dpa (peak in steel) at room temperature. It is clearly seen from the micrograph that near the end of range of the carbon ions the material has undergone a change. Higher magnification micrographs and diffraction patterns have determined that the CVD SiC has been amorphized due to the carbon beam irradiation. There is clearly a threshold tor amorphization for this material and by calculating a displacement profile using the EDEP code this threshold is found to be approximately 15 dpa. Previous studies4 have also seen such a threshold and through XRDA have concluded that there is a randomization of the silicon carbide at doses less than the threshold value.

YE-14541

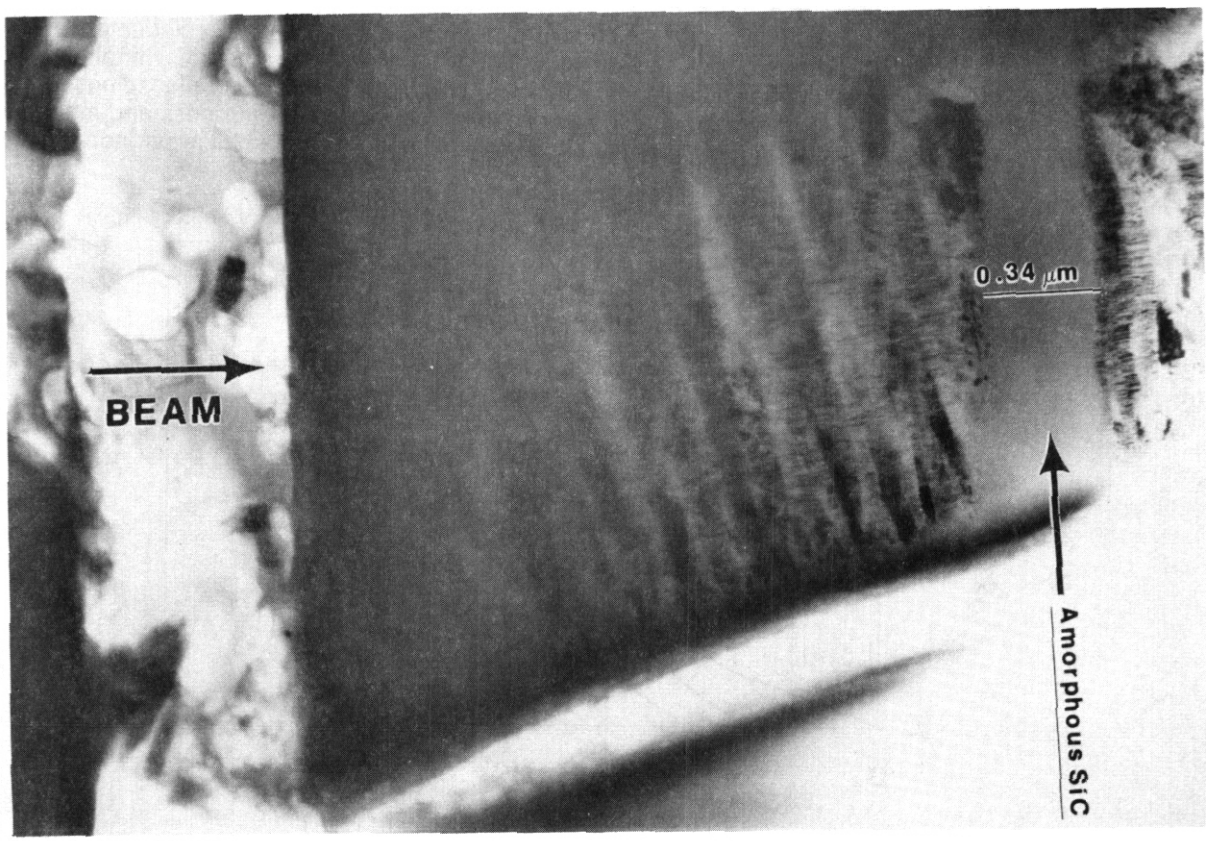

Figure 2: TEM Cross Sectional View of Carbon Modified CVD SiC.

Figure 3 shows the effect of room temperature carbon beam irradiation on Nicalon. The maximum dose for this case was 10 dpa. Nicalon is a very fine grained material and, as seen in the micrograph, the structure during room temperature irradiation becomes much finer. Diffraction patterns for both the unirradiated and irradiated material are identical (amorphous rings) with no apparent crystalline structure. This disagrees with previous works where it was claimed that neutron and nickel ion damage (peak irradiation temperature of 75°C) induces growth in the β SiC crystallites. From the figure it is seen that the beginningof-range structure is identical to the past range, or unirradiated. Nicalon structure. The threshold for microstructural change for the Nicalon is much less than that of CVD SiC and is approximately 1 dpa at room temperature.

The neutron irradiated material shows no apparent change in crystal structure for either the CVD SiC or Nicalon. Even at the highest displacement dose of 15 dpa (at 365°C in FFTF) there was no apparent change. This is most likely due Io the three hundred degree difference between the room temperature carbon and the neutron irradiations. Elevated temperature (900°C) carbon beam irradiation also showed no change in microstructure for the Nicalon. although amorphization of the CVD SiC was still observed.

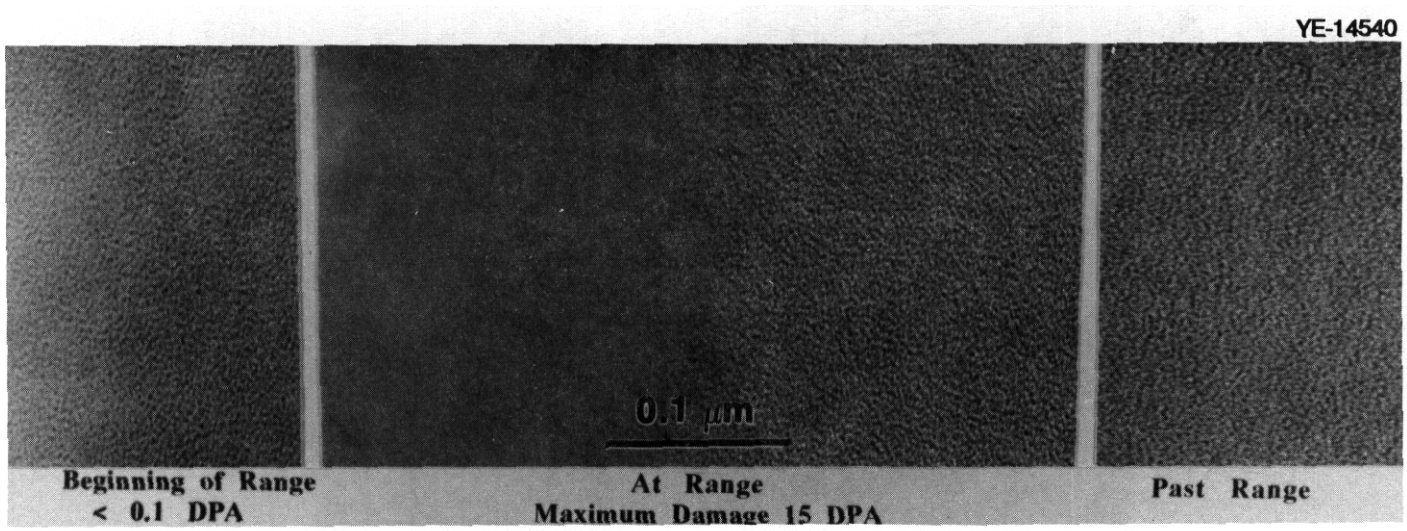

Fig. **3.** Composite TEM photo showing effect of carbon displacements on Nicalon.

3b. Hardness and Modulus Measurements

Hardness and modulus were measured for both carbon beam and neutron irradiated composites. For the carbon beam irradiated material, the sample was prepared in cross section and a series of indents were taken at a grazing angle to the interface. By doing this, a large number of indents could be taken within the irradiated band without spacing the indents so close together as to have interference between indents. Figure 4 shows a series of indents taken across a CVD SiC irradiated band of a room temperature carbon beam irradiated composite. By inspection of this figure, a light band is seen near the interface which corresponds to the carbon ion range. At the end of the carbon range (the light band) there is a distinct white band which indicates the amorphized region shown in Fig. 2. A similar series of indents was taken for Nicalon.

Figures 5 and 6 show the effect of room temperature carbon irradiation on the elastic modulus of CVD SIC and Nicalon. Figure 5 clearly shows that as the indents approach the maximum damage region (indicated by the EDEP profile) that the CVD SiC modulus sharply drops off. The modulus changes from approximately 400 GPa to a minimum in the amorphized region of 280 GPa. As the indents approach the interface. the carbon beam displacements decrease and the modulus begins to increase. At distances of less than 1.5 mm from the interface edge, the elastic modulus falls off due to edge curvature and overlapping of the indent sensing volume with the interface. This is discussed elsewhere[3].

Figure 6 indicates that Nicalon has the opposite behavior to that of CVD SiC. This figure shows the modulus from the four unloading curves. This data would normally be corrected using an area function which accounts for the departure from ideal indenter area. If this were done, the four curves would roughly fall on top of each other. By presenting the data in this manner one sees that the smoothest data is obtained from the deepest indent. In order to obtain the most precise value of hardness or modulus at a given dpa, one would desire the

YE-14543

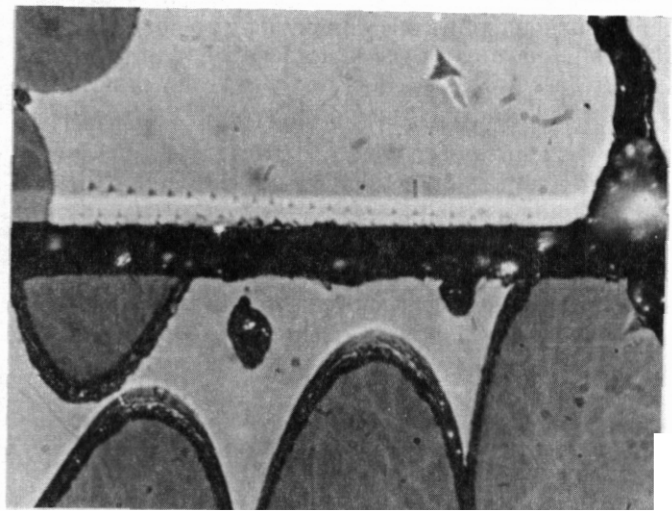

Fig. 4. Series of indents across irradiated band of CVD SiC.

ORNLDWG 92-6893

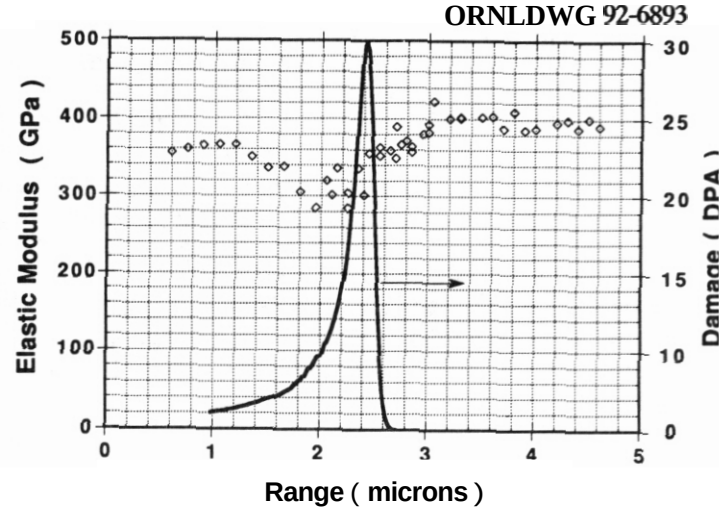

Fig. 5. Effect of room temperature carbon beam on CVD SiC.

ORNL-DWG 92-6894

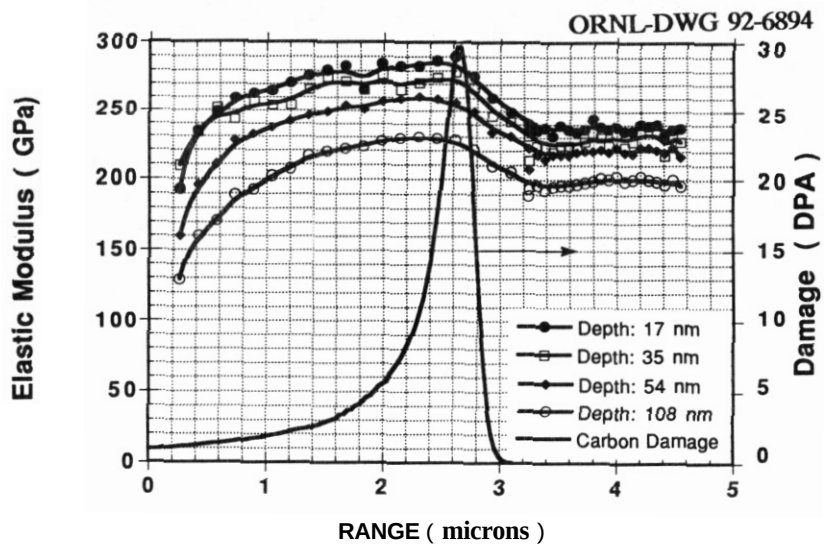

Figure 6: Effect of room temperature beam on Nicalon Fiber.

Shallowest indent possible in order to decrease the sensing volume associated with the indent. However, at shallower indents surface condition and other factors scatter the results. There is therefore a tradeoff that has to be made. The actual area function corrected modulus in this figure is very close to the value obtained from the unloading curve at the deepest indent depth (108 nm). The modulus is then seen to increase with increasing displacive dose from an unirradiated value of 200 GPa to an irradiated value of 230 GPa.

The trend in hardness and modulus for neutron irradiated material agrees with that seen in the carbon ion studies. The modulus for CVD SiC is seen to drop from over 400 GPa in the unirradiated case to 383 GPa in the 15 dpa FFTF irradiated material with the hardness dropping from about 41 GPa to 39.4. For the Case of the Nicalon fiber, the modulus has increased from 200 to 240 GPa for the 15 dpa FFTF irradiated material with a corresponding increase in hardness from 18 to 25 GPa.

4. Concluding Remarks

Both Nicalon SiC fiber and chemically vapor deposited silicon carbide have shown amorphization during room temperature carbon ion irradiations. The CVD SiC has a threshold amorphization value of approximately 15 dpa at room temperature as calculated using EDEP. Amorphization in the CVD SiC was still present at the 900°C carbon irradiation but from previous work6 recrystallization is expected to occur above 1000°C. Amorphization was not seen in 15 dpa neutron irradiated CVD. There was no observed change in microstructure for the neutron irradiated material studied. This may be due to the difference between the carbon and neutron irradiations or due to the difference in temperature for the irradiations. It is also possible that the implanted carbon ions have an effect on the microstructure although the straggling distance as calculated using TRIM-80 is approximately 0.14 μm. Due to the fact that the microstructural changes are occurring far from the implanted depth and that at room temperature there should be insignificant diffusion of the carbon ions, it is improbable that the carbon ions themselves are causing the observed microstructural changes.

Nicalon fiber structure becomes amorphous at room temperature at a lower threshold (~1 dpa) than that of the CVD SiC during room temperature irradiation. Amorphization is not evidenced at 900°C carbon irradiations or the 300 to 365°C neutron irradiations. This is in contrast with earlier work which attributed the increase in fiber modulus to crystallite growth in the fiber.[5]

Listed in Table 1 are the observed effects of the carbon beam and neutron irradiations on the hardness and modulus of CVD SiC and Nicalon fiber. While the CVD SiC modulus is reduced with increasing dose Nicalon fiber shows the opposite effect. The modulus and hardness of Nicalon increase with increasing displacing dose for both carbon ion and neutron irradiations. This change in mechanical properties occur independent of the amorphization of the fiber. This is evidenced by noting that there is no difference in bright field images or diffraction patterns for the Nicalon fiber subjected to 15 dpa in FFTF but the modulus has still increased. The most probable reason for the increase in elastic modulus is the densification of the Nicalon structure. Such fiber shrinkage has been observed optically and through TEM micrographs where the fiber has shrunk away from the matrix material. The magnitude of the densification has not been measured, however.

Table 1. Effect of displacing dose on CVD SiC and Nicalon fiber

Room-Temperature Carbon Ion Irradiation

	Threshold	Modulus (GPa)	Hardness (GPa)
CVD SiC	~15 dpa	400 to 275 (in 30 dpa)	41 to 32 (in 30 dpa)
Nicalon	~2 dpa	200 to 300 (in 30 dpa)	18 to 19 (in 15 dpa)

Neutron Irradiation

		Nicalon		CVD SiC	
dpa	T_{irr}	Modulus	Hardness	Modulus	Hardness
1	300	210	18.1	407	40.2
3	300	218	18.3	394	39.1
15	435	248	25.0	383	39.4

5. Acknowledgements

The authors would like to thank Rick Lowden for providing the material for this study.

FUTURE WORK

In order to develop radiation hardened composites, it will be necessary to first develop a fiber which has a radiation induced volumetric change which is compatible with that of the matrix in order to avoid interfacial degradation. Higher density experimental silicon carbide fibers are currently being irradiated in HFIR and FFTF(MOTA).[7,8] Once such a fiber is found, the next step would be to develop a less radiation sensitive interface than graphite.

References

1. T. M. Bessmann, R. A. Lowden. and D. P. Stinton, "A Method for Rapid Chemical Vapor Infiltration of Ceramic Composites," Proceedings of the Seventh European Conference on Chemical Vapor Deposition, Journal de Physique 50 (Conf-C-5). 229,239 (May 1989).

2. M. F. Doerner and W. D. Nix. " A Method for Interpreting the Data from Depth-Sensing Indentation Instruments." J. Mater Res, 1 (4), pp. 601-609. Jul/Aug, (1986).

3. L. L. Snead. S. J. Zinkle. D. Steiner. "Cross Sectional Measurement of Elastic Modulus for Carbon Beam Damaged Silicon Carbide" Fusion Reactor Materials Semiannual Report. DOE/ER-0313/10. Period Ending Apr. 30, 1991

4. J. M. Williams, et al. "Structural Alterations in SiC as a Result of Cr and N Implantation," Nucl. Intrum. and Methods, 209/210, pp. 317-323 (1983).

5. A. Kohyama. et al. "Radiation Induced Microstructural Evolution in SiC/Al Composite Materials." J. Nucl. Mat., 155-157, pp. 334-339, (1988).

6. H. G. Bonn, et al. "Recrystallization of ion-implanted a-Sic," J. Mater. Res. 2(1), pp. 107-117, Jan/Feb (1987.)

7 S. J. Zinkle and L. L. Snead. "Irradiation of Conventionally and Isotopically tailored ceramics in HFIR", Fusion Reactor Materials Semiannual Report, DOE/ER-0313/10. pg. 314 - 316.

8 S. J. Zinkle and L. L. Snead, "Irradiation of Ceramics in FFTF". Fusion Reactor Materials Semiannual Report, DOE/ER-0313/10. pg. 317-319.

IN-SITU MEASUREMENT OF RADIATION INDUCED CONDUCTIVITY IN CERAMICS---E. H. Farnum, J. M. Kennedy and F. W. Clinard (Los Alamos National Laboratory)

OBJECTIVE

The objective of this work is to develop a data base ana understanding of radiation-inauced changes in the electrical properties of ceramic insulators. and then use this intormation to identity or design new ceramic materials that will improve the performance of magnetic fusion reactors.

SUMMARY

Changes in the dielectric constant and loss tangent of alumina have been measured *in-situ* during proton irradiation. In these experiments, single crystal sapphire specimens were irradiated with 3 MeV protons which passed through the sample and were stopped in a copper-block heat sink. Dielectric properties were measured between 100 Hz and 10 MHz using a guard ring capacitor configuration. The proton irradiation caused an immediate increase in loss tangent from about 10^{-4} to more than 1.0. We have evaluated these changes at 300 K and 373 K, vsirradiation time, flux and frequency. While the *in-situ* radiation-induced conductivity (RIC) depends on these variables as well as on the history of previous irradiation, we believe that it is caused by a balance between the generation rate of electrons and holes, and their trapping and annihilation at displacement-type defects.

RESULTS AND DISCUSSION

1. Introduction

Radiation-induced electrical conductivity (RIC) in ceramics is a well-known phenomenon[1,2] that may dramatically affect crucial insulators in the next generation of deuterium-tritium burning fusion experiments such as BPX. NET and ITER. The fact that RIC is primarily a process that occurs during irradiation has also been recognized[3-5]. The effect is observed with gamma[4], electron[3], proton[4] and neutron5 irradiations, all of which have different ionization to atomic-displacement ratios. Protons, such as used in these experiments, create both electron-hole pairs and atomic displacements on both the aluminum and oxygen sublattices in alumina[6]. The RIC at the measured frequencies depends mainly on the concentration of free electrons, which is determined by the ionization (electron-hole pair generation) rate and the trapping and annihilation rate for these electrons and holes[7,8]. We have measured *in-situ* RIC during proton irradiation to try to understand the balance between these processes and to be able to predict the effect of irradiation on fusion insulators during the initial stages of experimental reactor operation.

2. Experimental procedure

Single crystal sapphire disks with face plane of $(11\bar{2}0)$, were purchased from Crystal Systems Inc.. These disks were HEMEX grade with manufacturer-specified total impurities less than 40 ppm. Major impurities and ppm concentration are: Fe, 8; Ce, 6 Sc, 4; N, 3; A, 3: K, 3; Cu. 2, and Mo. 1. All other impurities were specified as less than 1 ppm. The disks were coated with a gold/platinum thick-film composition, fired at 850 C for 5 min in air, and soldered or mounted with silver epoxy to a copper block. The mounted sample was then polished to 25-om-thickness. Titanium/gold electrodes, 0.25 μm thick, were applied to the top surface to form a guard-ring capacitor.

The copper block with sample was mounted on a heat sink in a vacuum chamber at the Los Alamos Ion Beam Materials Laboratory (IBML) where it was subjected to 3-MeV proton irradiation. In this configuration, the proton beam passes through the alumina sample, having a penetration depth in alumina of about 40 μm. An aperture 7.65 mm in diameter restricted the proton beam to a spot inside the center electrode. The capacitance and loss tangent were measured from 100 Hz to 10 MHz during the irradiation with a HP 4194A frequency-swept impedance analyzer. Irradiations were made at fluxes from 0.3 to 6 $\mu A/cm^2$, at ambient temperature (298 to 302 K) and at 373 K. During the experiments, the proton beam was turned on and off repeatedly to measure the transient response to irradiation, to measure beam current, and to establish the post-irradiation baseline.

The computer code TRIM90[9] was used to calculate ionization and instantaneous displacement rates in the sample. According to TRIM90, a proton current of 1 $\mu A/cm^2$ creates an ionization flux of 10^5 Gy/s and an average displacement flux for both the Al and O sublattices of 10^{-7} displacements per atom per second (dpa/s).

3. Results

The proton irradiation caused a large immediate increase in the loss tangent (tans) that then decreased with further irradiation. Figure 1 shows the measured loss tangent at 373 K as a function of frequency for several irradiation times. The initial loss tangent between 100 Hz and 10 MHz was about 10^{-4}. Immediately after onset of irradiation, we observe a loss peak near 470 Hz that moves to frequencies lower than 100 Hz in time. We currently believe that this peak is related to interfacial polarization and thus to the density of free charge carriers in the material during irradiation. Further analysis of this peak is underway. Figure 2 shows the product of tans and frequency *vs*. frequency for several irradiation times.

The low frequency drop at 100 s is caused by the loss peak. it has been shown[4] that

$$\tan\delta = a\,(\omega\,\varepsilon\,\varepsilon_o)^{-1} + X''/\varepsilon,$$

where ε_o is the permittivity of free space, ε the relative permittivity of the dielectric, $\omega = 2\pi$ times the frequency, X'' the imaginary part of the dielectric susceptibility, and s the ohmic conductivity. Our data show that at frequencies above the loss peak, tan6 is inversely proportional to frequency. This implies that the loss is dominated by the ohmic part of the conductivity[4]. Therefore, we have assumed that the second term in this equation is negligible in converting tans to conductivity in figures 3 and 5.

The increase in tans upon irradiation occurred in less than the 40 ms sampling time of our impedance analyzer. Similarly, tans dropped to nearly its pre-irradiation value in less than 40 ms when the beam was turned off. In fact, even fluctuations in the proton beam current show up as fluctuations (noise) in our data. Figure 3 shows the conductivity (calculated from tand) measured at 100 kHz during an experiment in which the proton beam was turned on at 0.6 $\mu a/cm^2$ and turned off several times. If the beam is turned off for a short time and then turned on. tanδ returns to its most recent beam-on value. However, preliminary observations show that this effect also decays in time and after 5 days of recovery at room temperature with no irradiation, the increase in tans when irradiation is resumed is nearly as high as it was for the unirradiated sample. Further studies of this recovery effect are planned.

The decay of the conductivity with irradiation time can be seen in Figure 3. The decay rate does not depend on frequency as shown in Figure 4 (again, the early time, low frequency data are influenced by the loss peak). Figure 4 also shows that after about 1500 s, the loss follows an exponential decay. In fact, the best fit to our data has been obtained with a double exponential with two time constants. We believe that this behavior reveals at least two mechanisms for trapping or annihilating the electrons and holes that cause RIC.

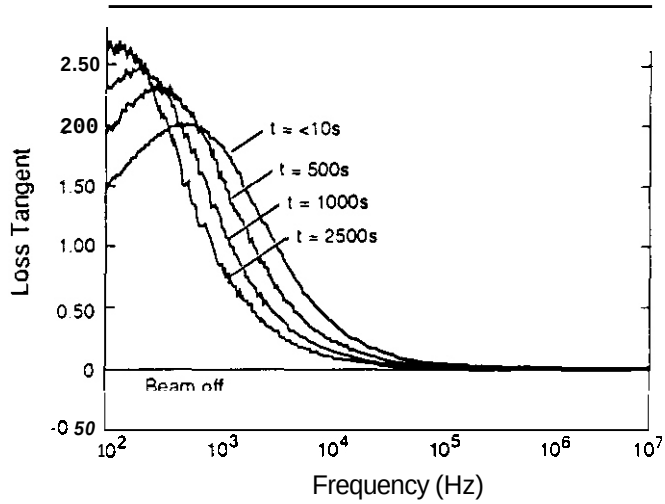

Figure 1 Loss tangent between 100 Hz and 10 MHz with the beam off and with the beam on after various irradiation times. Sapphire sample, 3 MeV protons, 1 $\mu A / cm^2$ beam current at a temperature of 373 K.

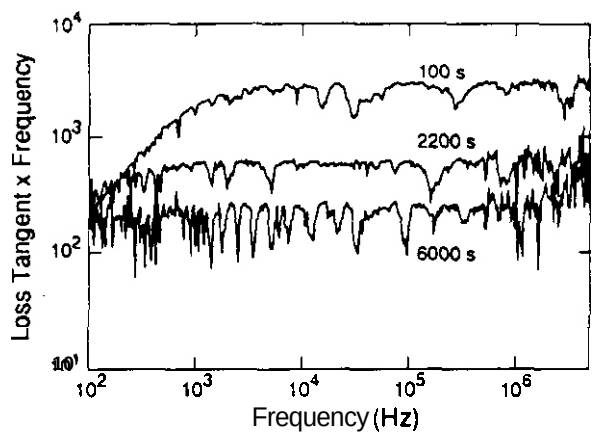

Figure 2 Loss tangent multiplied by the frequency vs. frequency with the beam on at various irradiation times. 3 Mev protons, 1 $\mu A / cm^2$ beam current at a temperature of 300 K.

When we increased the temperature from 300 K to 373 K, the relationship between these two exponential time constants and the relative importance of the two changed. Figure 5 shows the log of the ohmic conductivity *vs.* irradiation time for the two temperatures. The double exponential fit parameters are shown in Table 1.

We believe that these data show a dynamic equilibrium between ionization damage and displacement damage caused by the irradiation. During proton irradiation, both electron-hole and Frenkel pairs are generated. The electron-hole pairs, probably dominated by the relatively mobile electron. cause the RIC effect. The Frenkel pairs on both the aluminum and oxygen sublattices form a number of stable and metastable defects that act as traps and

annihilation centers for electrons and holes. Klaffkey[7] has discussed these traps in detail. During *the* irradiation, both *the* electron-hole and Frenkel pair generation rates are constant and depend on the temperature and flux (at least at low defect concentrations). The RIC depends on the steady-state concentration of electrons which establishes itself very quickly, probably in less than a millisecond. As the radiation progresses Frenkel pair defects, that trap and/or annihilate electrons and holes, increase. As a result, the steady-state concentration of conducting electrons decreases. Klaffkey's analysis describes a two-hole trap that disappears close to 373 K. It is possible that the change we see in one of the exponential time constants is related to the decay of the two-hole trap.

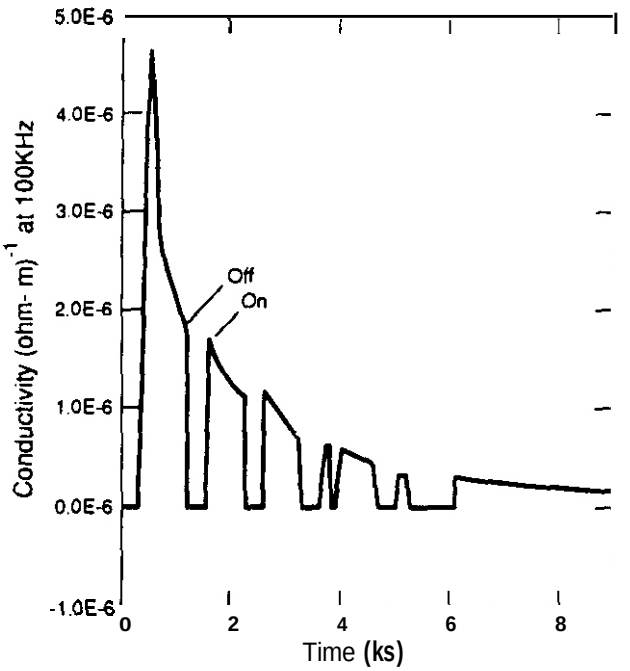

Figure 3 Ohmic electrical conductivity at 100 kHz *vs* chronographic time during an experimental run in which the proton beam was repeatedly turned on and off. Sapphire sample, 3 Mev Protons, 0.6 $\mu A / cm^2$ beam current at a temperature of 300 K.

In addition, Itoh et. al.[8] show the existence of transient defects, one of which is thought to be a self-trapped exciton (electron-hole pair). These defects may also affectthe steady-state concentration of free electrons However, when the proton beam is turned off and then on again after a short time, the RIC returns only to the value immediately prior to beam-off and not *to* the initial beam-on value as shown in Figure 3. Also, the fact that the RIC drops immediately when the proton beam is turned off implies that the traps are still active and quickly reduce the remaining free electrons. These facts suggest that the defects that cause the decrease in conductivity with time are not transient on a short (< hours) time scale. Itoh et. al. also suggest that high frequency dielectric loss will be dominated by transient defects other than electron-hole pairs or free

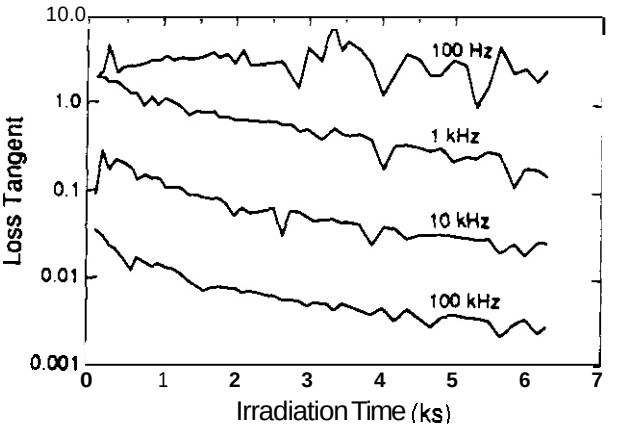

Figure 4 Loss tangent on a logarithmic scale *vs* irradiation time for various frequencies measured with the beam on. Beam *off* time has been subtracted from the chronographic time. Sapphire sample. 3 Mev Protons. 1.0 $\mu A / cm^2$ beam current at a temperature of 300 K.

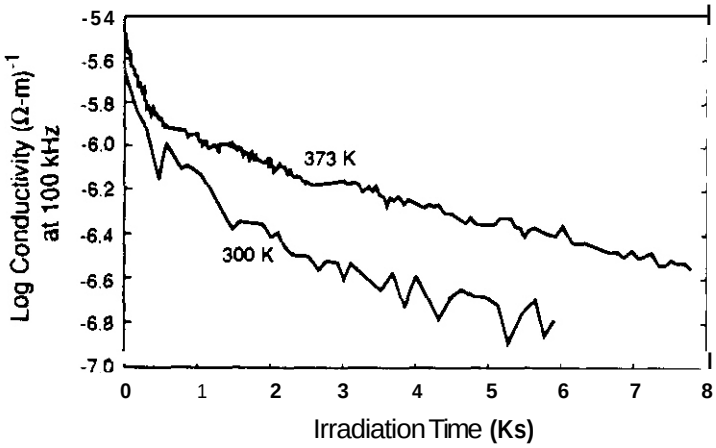

Figure 5 Logarithm of the ohmic electrical conductivity at 100 kHz vs irradiation time at 300 k and at 373 K. Table 1 shows the double exponential fit to this data. Sapphire sample, 3 Mev Protons, 1.0 $\mu A / cm^2$ beam current at temperatures of 300 K and 373 K.

Table 1

Figure 5 data fitted to:

$A \exp(-t/\tau_1) + B \exp(-t/\tau_2) + C$

Variable	300 K	373 K
τ_1 (s)	163	16?
τ_2 (s	1351	3205
A $(\Omega M)^{-1}$	1.0×10^{-6}	2.0×10^{-6}
B $(\Omega M)^{-1}$	1.1×10^{-6}	1.2×10^{-6}
C $(\Omega M)^{-1}$	1.6×10^{-7}	2.0×10^{-7}

electrons. Up to the limit of our measurements (10 MHz), at both temperatures, tan8 remains inversely proportional to frequency and no contribution to RIC from dipolar defects was observed. We have not yet analyzed the equations given by Itoh et. al. for our irradiation conditions, but we believe that the ratio of ionization to displacement damage, very different for electrons, protons and neutrons, will have a large effect on the ***in-situ*** RIC.

4. Conclusion

We have shown that upon irradiation there is an immediate increase in the dielectric loss in alumina. Loss tangents in excess of 1.0 were observed early in the irradiation. This loss depends on flux, time, temperature and radiation history, and is inversely proportional to frequency in the 100 Hz to 10 MHz range. We believe that it also depends on the ratio of ionization to displacement damage caused by the radiation. The data can be explained as a steady-state balance between the generation rate of electron-hole pair and Frenkel pair defects that trap and annihilate free electrons. Further work is needed to identify the defects that are responsible for trapping and annihilating charge carriers.

These observations are significant for diagnostic systems, blanket insulators and electrical feed-throughs in fusion experiments. The dependence of ***in-situ*** RIC on the ionization to displacement ratio emphasizes the importance of accurately predicting the fusion environment (both neutron and gamma radiation) and of trying to duplicate that in ***in-situ*** experiments. These data, in conjunction with the observations of Klaffkey et. al., suggest that it will be possible to design ceramic materials with built-in electron and hole traps that will mitigate the ***in situ*** RIC effect.

FUTURE PLANS

We intend to explore these prompt effects further by varying flux and also the beam-off time to determine flux dependence and recovery rates at room temperature. In addition, similar experiments will be conducted on sapphire doped with 150 ppm of titanium to explore the possible effect of additional trapping sites for the electron-hole pairs created by the ionizing part of the radiation.

REFERENCES

1. D. S. Billington and J. H. Crawford. Radiation Damage in Solids (Princeton University Press, Princeton, 1961) p. 249.

2. F. W. Clinard Jr. and L. W. Hobbs, in: Physics of Radiation Effects in Crystals, Ed. R. A. Johnson and A. N. Orlov (Elsevier Science Publishers, B. V., 1986) p 442.

3. E. R. Hodgson. in: DOE Task Force Meeting on Electrical Breakdown of Insulating Ceramics in a High Radiation Field (CONF-9105176, Vail. Colorado, USA.1991) 1.

4. G. P. Pells and G. J. Hill, J. Nucl. Mater. 141-143 (1986) 375.

5. R. E. Stoller. R. H, Goulding and S. J. Zinkle. in: Fusion Reactor Materials Semi-annual Progress Report for the Period Ending Sept. 30, 1990, DOE/ER-0313/9 (OSTI, Oak Ridge, TN, April 1991) 317.

6. D. M. Parkin and C. A. Coulter, J. Nucl. Mater. 101 (1981) 261

7. R. W. Klaffkey, B. H. Rose, A. N. Goland and G. J. Dienes, Phys. Rev. B 21 (1980) 3610

8. N. Itoh. T. Tanaka and F. W. Clinard, J. Nucl. Mater. 183 (1991) 25

9. J. F. Ziegler. J. P Biersack and U. L. Litmark, The Stopping and Range of Ions in Solids (Pergamon Press, GB. 1985).

DISTRIBUTION

1–16. Argonne National Laboratory, 9700 South Cass Avenue. Argonne, IL 60439

M. C. Billone	P. A. Finn	B. A. Loomis
P. E. Blackburn	A. K. Fisher	R. F. Mattas
O. K. Chopra	A. B. Hull	L. A. Neimark
R. G. Clemmer	C. E. Johnson	D. L. Smith
D. R. Diercks	F. Kassner	S. W. Tam
		H. Wiedersich

17. Argonne National Laboratory, EBR-II Division, Reactor Materials Section. P.O. Box 2528, Idaho Falls, ID 83403-2528
D. L. Porter

18. Auburn University, Department of Mechanical Engineering, 201 Ross Hall, Auburn, AL 36849
B. A. Chin

19–34. Battelle-Pacific Northwest Laboratory, P. O. Box 999, Richland, WA 99352

M. D. Freshley	M. L. Hamilton	J. M. McCarthy
F. A. Garner (5)	H. L. Heinisch	B. D. Shipp
D. S. Gelles	G. W. Hollenberg	O. D. Slagle
L. R. Greenwood	R. H. Jones	J. L. Straalsund

35. Carnegie Institute of Technology, Carnegie-Mellon University, Schenley Park, Pittsburgh, PA 15213
W. M. Garrison, Jr.

36. Oepartment of Energy, Richland Operations Office, Federal Bldg., MS A590, Richland, WA 99352
Paul Pak

37. EG&G Idaho, Inc., Fusion Safety Program, P.O. Box 1625, Idaho Falls, ID 83415-3523
D. F. Holland

38. GE Astrospace Division, San Jose Operations, 6835 via Deloro, P.O. Box 530954, San Jose, CA 95153-5354
Mike Kangilaski

39–42. General Atomics, P.O. Box 85608, San Diego, CA 92138

J. Raur	D. I. Roberts
T. A. Lechtenberg	K. R. Schultz

43. General Dynamics Corporation, 5001 Kearny Villa Road, San Diego, CA 92138
T. L. Cookson

44. Georgia Institute of Technology, School of Textile Engineering, Atlanta, GA 30332
D. S. Tucker

45. Grand Canyon University, Department of Natural Science, 3300 W. Camelback Rd., Phoenix, AZ 85017
W. A. Coghlan

46–48. Hokkaido University, Faculty of Engineering, Kita 13, Nishi 8, Kita-ku, Sapporo 060. Japan
Professor Heishichiro Takahashi Professor Akira Okada
Professor Somei Ohnuki

49–52. Japan Atomic Energy Research Institute, Tokai Research Establishment, Tokai-mura, Naka-gun, Ibaraki-ken 319-11, Japan
Dr. Tatsuo Kondo Dr. Akimichi Hishinuma (3)

53. Kyushu University, Department of Nuclear Engineering, Faculty of Engineering, Kyushu University 36, Hakozaki, Fukuoka 812, Japan
Professor C. Kinoshita

54. Kyushu University, Research Institute for Applied Mechanics, 6-1, Kasuga-Koen, Kasuga-Shi, Fukuoka-Ken 816, Japan
Professor Takeo Muroga

55–57. Lawrence Livermore National Laboratory, P.O. Box 808, Livermore, CA 94550

E.C.N. Dalder	J. Perkins
M. Guinan	

58–66. Los Alamos National Laboratory, P.O. Box 1663, Los Alamos, NM 87545
J. L. Anderson, L. D. Caudill, F. W. Clinard, E. H. Farnum, H. M. Frost, G. Hurley, C. D. Kise, R. Liepens, T. Iocco

67. Manlabs, Inc., 231 Erie Street, Cambridge, MA 02139
O. Tognarelli

68. Massachusetts Institute of Technology, Department of Metallurgy and Materials Science, Cambridge, MA 02139
L. W. Hohbs

6'370. Massachusetts Institute of Technology, Room 13-4069, Cambridge, MA 02139
N. J. Grant, K. C. Russell

71–72. Massachusetts Institute of Technology, Plasma Fusion Center Headquarters, Cambridge, MA 02139
H. D. Becker, D. B. Montgomery

73–74. Muroran Institute of Technology, Department of Metallurgical Engineering, 27-1 Mizumoto-cho, Muroran 050, Japan
Toshihei Misawa, Akihiko Kimura

75. McDonnell-Douglas Missile Systems Company, Mail Code 306 4204, P.O. Box 516, St. Louis, MO 63166
J. W. Davis

76-77. Nagoya University, Institute of Plasma Physics, Furo-Cho, Chikusa-ku, Nagoya 464-01, Japan
Professor Akira Miyahara, Dr. Chusei Namba

78. Nagoya University, Department of Nuclear Engineering, Furo-Cho, Chikusa-ku, Nagoya 464-01, Japan
Professor Michio Kiritani

79–81. National Institute for Fusion Science, Furo-cho, Chikusa-ku, Nagoya 464-01, Japan
Osamu Motojima, Nobuaki Noda, Chusei Namba

82–84. National Institute of Standards and Technology, Boulder, CO 80302
F. R. Fickett, R. P. Reed, H. [redacted]-McHenry

85. National Materials Advisory Board, 2101 Constitution Avenue, Washington, DC 20418
K. M. Zwilsky

86. National Research Institute for Metals, 1-2-1, Sengen, Tsukuba-shi, Ibaraki 305, Japan
Fujio Abe

87–88. National Research Institute for Metals, Tsukuba Branch, Sengen, Tsukuba-shi, Ibaraki-ken 305, Japan
Dr. Josei Naqakawa, Dr. Haruki Shiraishi

89. Naval Research Laboratory, Washington, DC 20375
J. A. Sprague

90–129. Oak Ridge National Laboratory, P.O. Box 2008, Oak Ridge, TN 37831
Central Research Library
Document Reference Section
Laboratory Records Department (2)
Laboratory Records—RC
Patent Section
D. J. Alexander
C. C. Baker
G.E.C. Bell
J. Bentley
E. E. Bloom
T. D. Burchell
R. H. Goulding
M. L. Grossbeck
E. A. Kenik
R. L. Klueh
Eal Lee
A. W. Longest
L. K. Mansur
P. J. Maziasz
T. C. Reuther
T. K. Roche
A. F. Rowcliffe (10)
R. L. Senn
J. Sheffield
L. Snead
R. E. Stoller
K. R. Thoms
P. F. Tortorelli
S. J. Zinkle
R. Yamada

130. Osaka University, Department of Nuclear Engineering, 2-1 Yamadaoka, Suita, Osaka 565, Japan
Tetuo Tanabe

131. PNC Oarai, 4002 Narita, Oarai, Ibaraki 311-13, Japan
Itaru Shibasaki

132–134. Princeton University, Princeton Plasma Physics Laboratory, P.O. Box 451, Princeton, NJ 08540
C. Bushnell
Long-Poe Ku
H. Furth

135-136. Rensselaer Polytechnic Institute, Troy, NY 12181
D. Steiner
David Duquette

137. Rockwell International Corporation, NA02, Rocketdyne Division, 6633 Canoga Avenue, Canoga Park, CA 91304
D. W. Kneff

138–139. Sandia National Laboratories, P.O. Box 5800, Albuquerque, NM 87185-5800
M. J. Davis
W. B. Gauster

140–141. Sandia National Laboratories, Livermore Division 8316, Livermore, CA 94550
W. Bauer
W. G. Wolfer

142. San Diego State University, Mechanical Engineering Dept., San Oiego, CA 92182-0191
L. D. Thompson

143. Science University of Tokyo, Department of Materials Science & Technology, 2641 Yamazaki Noda City, Chiba Prefecture 278 Japan
Naohira Igata

144. Tohoku University, Institute for Materials Research, Katahira 2-1-1, Sendai 980, Japan
Professor Hideki Matsui

145. Tohoku University, Institute for Materials Research, Oarai Branch, Oarai, Ibaraki 311-13, Japan
Tatsuo Shikama

146. Tohoku University, Institute for Materials Research, Orai Branch, Oarai, Higashi-Ibaraki-gun, Ibaraki-ken 311-13, Japan
Professor Hideo Kayano

147. Tohoku University, Oepartment of Nuclear Engineering, Tohoku University, Aoba, Aramaki, Sendai 980, Japan
Professor Katsunori Abe

148–149. University of California, Department of Chemical and Nuclear Engineering, Santa Barbara, CA 93106
G. E. Lucas
G. R. Odette

150–152. University of California. Department of Chemical, Nuclear and Thermal Engineering, Los Angeles, CA 90024
M. A. Abduo
N. M. Ghoniem
R. W. Conn

153. University of Michigan, Department of Nuclear Engineering, Ann Arbor, MI 48109
T. Kammash

154. University of Missouri, Department of Nuclear Engineering, Rolla, MO 65401
A. Kumar

155–156. University of Tokyo, Department of Nuclear Engineering, 3-1, Hongo 7-Chome, Runkyo-ku, Tokyo 113 Japan
Professor Shiori Ishino (2)

157–158. University of Tokyo, Department of Materials Science, 3-1, Hongo 7-Chome, Bunkyo-ku, Tokyo 113, Japan
Professor Akira Kohyama
Professor Yutaka Kohno

159. University of Tokyo, Nuclear Engineering Research Institute, 3-1, Hongo 7-Chome, Bunkyo-ku, Tokyo 113, Japan
Professor Naoto Sekimura

160–161. University of Wisconsin, Nuclear Engineering Dept., 1600 Johnson Drive, Madison, WI 53706
J. B. Rlanchard
G. L. Kulcinski

162–167. Westinghouse Hanford Company, P. O. Box 1970, Richland, WA 99352
ti. R. Brager
A. M. Ermi
G. D. Johnson
F. M. Mann
R. J. Puigh
R. L. Simons

168. Department of Energy, DOE Oak Ridge Field Office, P.O. Box 2008, Oak Ridge, TN 37831-6269
Assistant Manager for Energy Research and Development

169. Department of Energy, DOE Oak Ridge Field Office, P. O. Box 2008, Oak Ridge, TN 37831-6269
S. D. Frey

170. Department of Energy, Office of Basic Energy Sciences, Washington, DC 20585
J. R. Darby

171–176. Department of Energy, Office of Fusion Energy, Washington, DC 20585
S. E. Berk
M. M. Cohen
N. A. Davies
R. J. Dowling
R. E. Price
F. W. Wiffen

177–226. Department of Energy, Office of Scientific and Technical Information, Office of Information Services, P.O. Box 62, Oak Ridge, TN 37831
For distribution as shown in DOE/TIC-4500, Distribution Categories UC-423 (Magnetic Fusion Reactor Materials) and UC-424 (Magnetic Fusion Energy Systems)